

DECEMBER 2019

**AJNR**

VOLUME 40 • PP 1977-2171

# AJNR

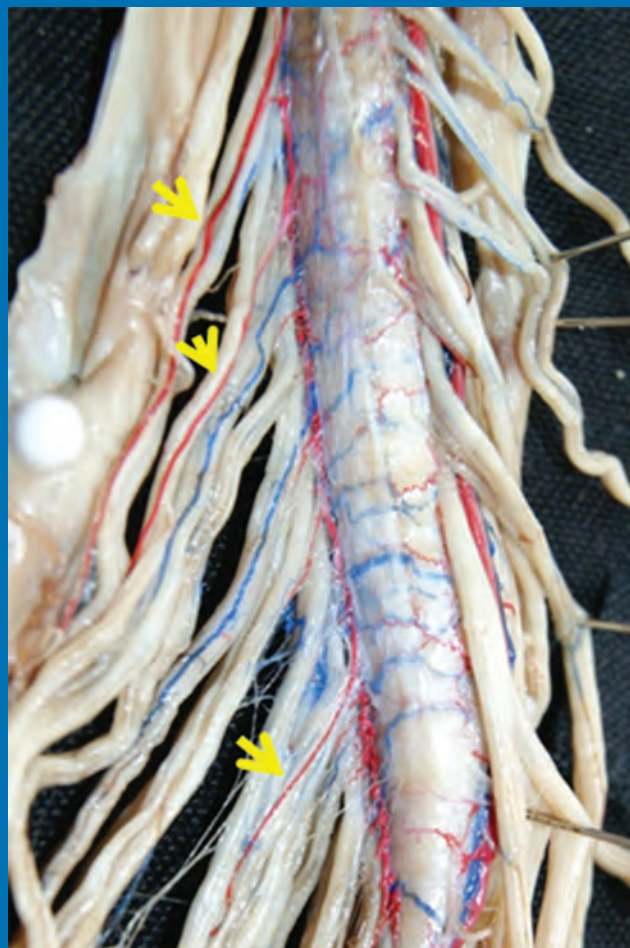
## AMERICAN JOURNAL OF NEURORADIOLOGY

DECEMBER 2019  
VOLUME 40  
NUMBER 12  
WWW.AJNR.ORG

THE JOURNAL OF DIAGNOSTIC AND  
INTERVENTIONAL NEURORADIOLOGY

Anatomy of posterior radiculomedullary arteries  
Intracranial atherosclerotic burden on 7T  
Monitoring response of gliomas to photodynamic therapy  
Middle cranial fossa floor pits and encephaloceles

Official Journal ASNR • ASFNR • ASHNR • ASPNR • ASSR





# ONE AND DONE

## INDICATIONS FOR USE:

The WEB Aneurysm Embolization System is indicated for use at the middle cerebral artery (MCA) bifurcation, internal carotid artery (ICA) terminus, anterior communicating artery (AComm) complex, or basilar artery apex for the endovascular treatment of adult patients with saccular, wide neck bifurcation intracranial aneurysms with dome diameter from 3 mm to 10 mm and either neck size 4 mm or greater or the dome-to-neck ratio is greater than 1 and less than 2.

The WEB Aneurysm Embolization System is contraindicated for patients with known bacterial infection that may interfere with or negatively affect the implantation procedure and patients with known hypersensitivity to nickel. For complete indications, contraindications, potential complications, warnings, precautions, and instructions, see instructions for use (IFU provided with the device).

The VIA® Catheter is intended for the introduction of non-liquid interventional devices (such as stents/\_ow diverters) and infusion of diagnostic (such as contrast media) or non-liquid therapeutic agents into the neuro, peripheral, and coronary vasculature. The VIA Catheter is contraindicated for use with liquid embolic materials, such as n-butyl 2-cyanoacrylate or ethylene vinyl alcohol & DMSO (dimethyl sulfoxide). The VIA Catheter is contraindicated for use in the pediatric population (<22 yrs of age).

Caution: Federal law restricts these devices to sale by or on the order of a physician.

# WEB<sup>®</sup>

## *Aneurysm Embolization System*

MicroVention<sup>®</sup> delivers the first intrasaccular solution for wide neck bifurcation aneurysms.

The **world leader**  
and **first**  
**PMA - approved**  
**device** in an  
important new  
category of  
intrasaccular  
flow disruptors.

The WEB<sup>®</sup> System is a safe  
and effective single-device  
solution for treating wide  
neck bifurcation aneurysms.



SL Device



SLS Device

Contact a MicroVention sales associate to learn more about integrating the WEB<sup>®</sup> device into your practice.



**MicroVention Worldwide  
Innovation Center**  
35 Enterprise  
Aliso Viejo, CA 92656 USA  
MicroVention UK Limited  
MicroVention Europe, S.A.R.L.  
MicroVention Deutschland GmbH  
[microvention.com](http://microvention.com)

PH +1.714.247.8000

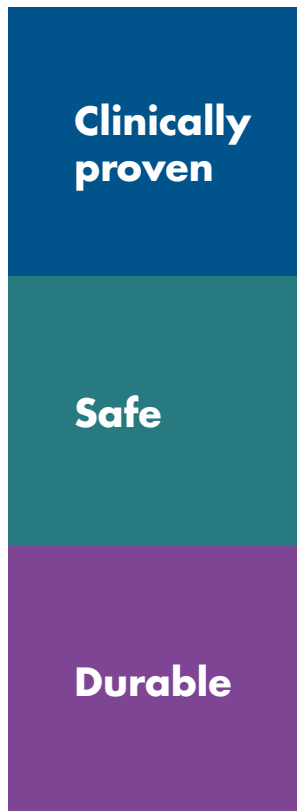
PH +44 (0) 191 258 6777

PH +33 (1) 39 21 77 46

PH +49 211 210 798-0

# The results say it all

Now **PMA** approved



**84.7%**

Primary efficacy endpoint

**4.4%**

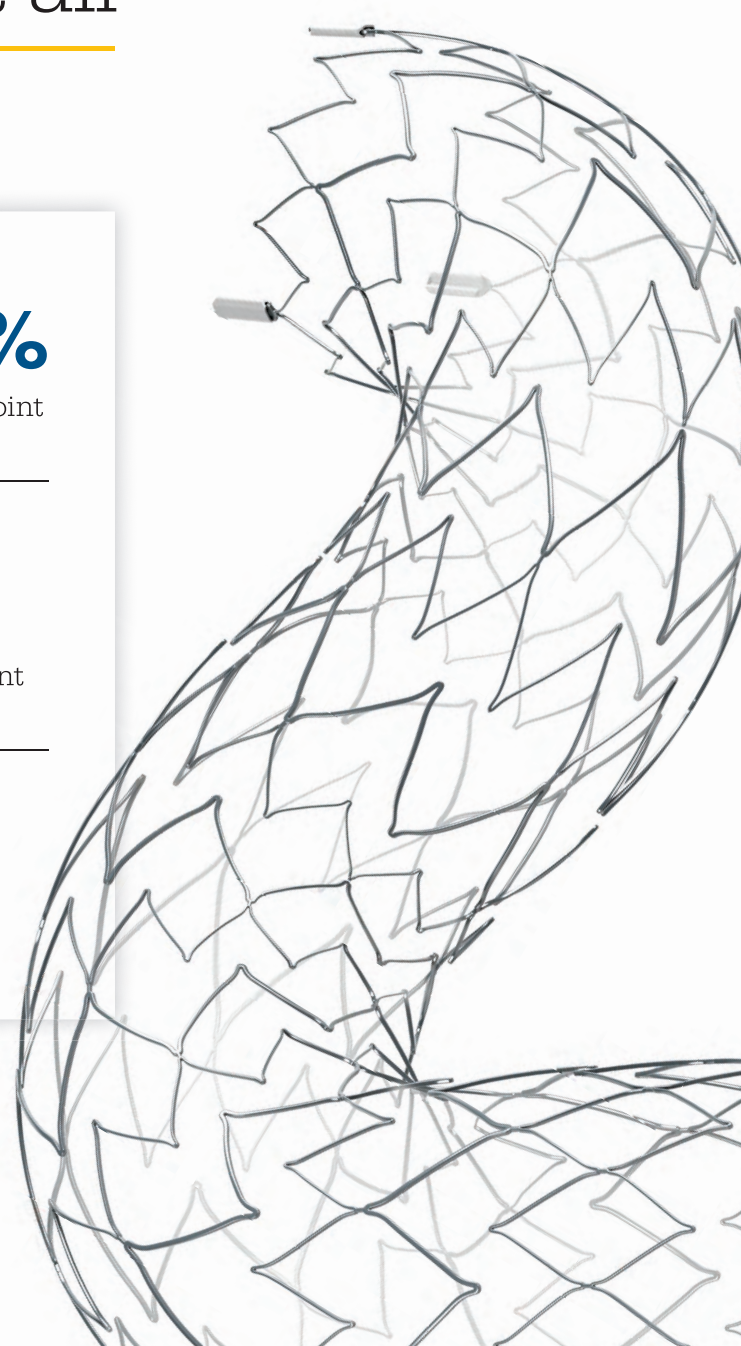
Primary safety endpoint

**3.8%**

Retreatment rate

The ATLAS IDE Study is the largest of its class with **182 patients treated.**

**Neuroform Atlas<sup>®</sup>**  
Stent System



# CALL FOR AJNR EDITORIAL FELLOWSHIP CANDIDATES

ASNR and AJNR are pleased once again to join efforts with other imaging-related journals that have training programs on editorial aspects of publishing for trainees or junior staff (<5 years on staff), including Radiology (Olmsted fellowship), AJR (Figley and Rogers fellowships), JACR (Bruce J. Hillman fellowship), and Radiologia.

## 2020 Candidate Information and Requirements

### GOALS

- Increase interest in editorial and publication-related activities in younger individuals.
- Increase understanding and participation in the AJNR review process.
- Incorporate into AJNR's Editorial Board younger individuals who have previous experience in the review and publication process.
- Fill a specific need in neuroradiology not offered by other similar fellowships.
- Increase the relationship between "new" generation of neuroradiologists and more established individuals.
- Increase visibility of AJNR among younger neuroradiologists.

### ACTIVITIES OF THE FELLOWSHIP

- Serve as Editorial Fellow for one year. This individual will be listed on the masthead as such.
- Review at least one manuscript per month for 12 months. Evaluate all review articles submitted to AJNR.
- Learn how electronic manuscript review systems work.
- Be involved in the final decision of selected manuscripts together with the Editor-in-Chief.
- Participate in all monthly Senior Editor telephone conference calls.
- Participate in all meetings of the Editors during the annual meetings of ASNR and RSNA and the Radiology Editors Forum as per candidate's availability. The Foundation of the ASNR will provide \$2000 funding for this activity.
- Evaluate progress and adjust program to specific needs in annual meeting or telephone conference with the Editor-in-Chief.
- Embark on an editorial scientific or bibliometric project that will lead to the submission of an article to AJNR or another appropriate journal as determined by the Editor-in-Chief. This project will be presented by the Editorial Fellow at the ASNR annual meeting.
- Serve as liaison between AJNR and ASNR's Young Professionals Network. Participate in meetings and telephone calls with this group. Design one electronic survey/year, polling the group regarding readership attitudes and wishes.
- Recruit trainees as reviewers as determined by the Editor-in-Chief.
- Organize and host a Fellows' Journal Club podcast.
- Serve as Guest Editor for an issue of AJNR's News Digest with a timely topic.

### QUALIFICATIONS

- Be a fellow in neuroradiology from North America, including Canada (this may be extended to include other countries).
- Be a junior faculty neuroradiology member (<5 years) in either an academic or private environment.
- Be an "in-training" or member of ASNR in any other category.

### APPLICATION

- Include a short letter of intent with statement of goals and desired research project. CV must be included.
- Include a letter of recommendation from the Division Chief or fellowship program director. A statement of protected time to perform the functions outlined is desirable.
- Applications will be evaluated by AJNR's Senior Editors prior to the ASNR meeting. The name of the selected individual will be announced at the meeting.
- Applications should be received by March 2, 2020 and sent to Ms. Karen Halm, AJNR Managing Editor, electronically at [khalm@asnr.org](mailto:khalm@asnr.org).

# AJNR *go green*

***AJNR* urges American Society of Neuroradiology members to reduce their environmental footprint by voluntarily suspending their print subscription.**

The savings in paper, printing, transportation, and postage directly fund new electronic enhancements and expanded content.

The digital edition of *AJNR* presents the print version in its entirety, along with extra features including:

- Publication Preview
- Case Collection
- Podcasts
- The *AJNR* News Digest
- The *AJNR* Blog

It also reaches subscribers much faster than print. An electronic table of contents will be sent directly to your mailbox to notify you as soon as it publishes.

Readers can search, reference, and bookmark current and archived content 24 hours a day on [www.ajnr.org](http://www.ajnr.org).

ASNR members who wish to opt out of print can do so by using the *AJNR* Go Green link on the *AJNR* Website (<http://www.ajnr.org/content/subscriber-help-and-services>). Just type your name in the email form to stop print and spare our ecosystem.



# Simplify the MOC Process



# Manage your CME Credits Online

## CMEgateway.org

### Available to Members of Participating Societies

American Board of Radiology (ABR)  
American College of Radiology (ACR)  
American Roentgen Ray Society (ARRS)  
American Society of Neuroradiology (ASNR)  
Commission on Accreditation of Medical  
Physics Educational Programs, Inc. (CAMPEP)  
Radiological Society of North America (RSNA)  
Society of Interventional Radiology (SIR)  
SNM  
The Society for Pediatric Radiology (SPR)

### It's Easy and Free!

Log on to CME Gateway to:

- View or print reports of your CME credits from multiple societies from a single access point.
- Print an aggregated report or certificate from each participating organization.
- Link to SAMs and other tools to help with maintenance of certification.

### American Board of Radiology (ABR) participation!

By activating ABR in your organizational profile, your MOC-fulfilling CME and SAM credits can be transferred to your own personalized database on the ABR Web site.

### Sign Up Today!

go to [CMEgateway.org](http://CMEgateway.org)

## Neuroform Atlas® Stent System

### RX ONLY

See package insert for complete indications, contraindications, warnings and instructions for use.

#### Indications for use

The Neuroform Atlas Stent System is indicated for use with neurovascular embolization coils in the anterior circulation of the neurovasculature for the endovascular treatment of patients  $\geq 18$  years of age with saccular wide-necked (neck width  $\geq 4$  mm or a dome-to-neck ratio of  $< 2$ ) intracranial aneurysms arising from a parent vessel with a diameter of  $\geq 0.5$  mm and  $\leq 4.5$  mm.

#### Contraindications

- Patients in whom the parent vessel size does not fall within the indicated range.
- Patients in whom antiplatelet and/or anticoagulation therapy (e.g., aspirin and clopidogrel) is contraindicated.
- Patients who have not received anti-platelet agents prior to stent implantation.
- Patients with an active bacterial infection.
- Patients in whom angiography demonstrates the anatomy is not appropriate for endovascular treatment due to conditions such as:
  - Severe intracranial vessel tortuosity or stenosis;
  - Intracranial vasospasm not responsive to medical therapy.
- Patients in whom a pre-existing stent is in place in the parent artery at the target intracranial aneurysm location.

#### Potential adverse events

The potential adverse events listed below, as well as others, may be associated with the use of the Neuroform Atlas Stent System or with the procedure:

- Aphasia
- Allergic reaction to Nitinol metal and medications
- Aneurysm perforation/rupture, leak or contrast extravasation
- Blindness
- Cardiac arrhythmia
- Coil herniation through stent into parent vessel
- Cranial neuropathy
- Death
- Embolus
- Headache
- Hemiplegia
- Hemorrhage (i.e., intracerebral, subarachnoid, retroperitoneal, or in other locations)
- Hydrocephalus
- In-stent stenosis
- Infection
- Ischemia

Stryker or its affiliated entities own, use, or have applied for the following trademarks or service marks: Neuroform Atlas, Stryker. All other trademarks are trademarks of their respective owners or holders.

The absence of a product, feature, or service name, or logo from this list does not constitute a waiver of Stryker's trademark or other intellectual property rights concerning that name or logo.

Copyright © 2019 Stryker  
AF002547 v2.0 | Page 2 of 2

## AXS Catalyst® Distal Access Catheter

### RX ONLY

See package insert for complete indications, complications, warnings, and instructions for use.

#### Indication for use as a conduit

The AXS Catalyst Distal Access Catheter is indicated for use in facilitating the insertion and guidance of appropriately sized interventional devices into a selected blood vessel in the peripheral and neurovascular systems. The AXS Catalyst Distal Access Catheter is also indicated for use as a conduit for retrieval devices.

#### Indication for use as a revascularization device

The AXS Catalyst Distal Access Catheter is indicated for use in the revascularization of patients with acute ischemic stroke secondary to intracranial large vessel occlusive disease (in the internal carotid, middle cerebral, M1 and M2 segments, basilar, and vertebral arteries) within 8 hours of symptom onset. Patients who are ineligible for intravenous tissue plasminogen activator (IV t-PA) or who failed IV t-PA are candidates for treatment.

#### Device description when use as a revascularization device

The AXS Universal Aspiration System is composed of the following components:

- AXS Catalyst Distal Access Catheter
- AXS Universal Aspiration Tubing
- Medela Dominant Flex Pump
- AXS Universal Liner Set

The AXS Universal Aspiration System is designed to remove thrombus from the neurovasculature using continuous aspiration.

The AXS Catalyst Distal Access Catheter delivers aspiration from the Medela Dominant Flex Pump directly to the site of the occlusion to remove the clot. The AXS Catalyst Distal Access Catheter is a sterile, single lumen, variable stiffness catheter. The catheter shaft has a hydrophilic coating to reduce friction during use, includes a radiopaque marker on the distal end for angiographic visualization, and includes a luer hub on the proximal end allowing attachments for flushing and aspiration. It is packaged with a Rotating Hemostasis Valve (RHV), Tuohy Borst Valve with Sideport, and Peel Away Introducer. The Rotating Hemostasis Valve and Tuohy Borst valve with sideport are used for flushing, insertion of catheters, and aspiration. The peel away introducer sheaths are designed to protect the distal tip of the catheter during insertion into the RHV or Tuohy Borst. The AXS Catalyst Distal Access Catheter is the only component of the AXS Universal Aspiration System that is used intravascularly.

#### AXS Universal Aspiration System

The AXS Universal Aspiration Tubing serves as a conduit to supply vacuum from the Medela Dominant Flex Pump to the distal tip of the AXS Catalyst Distal Access Catheter. The AXS Universal Aspiration Tubing provides a connection between the sterile and non-sterile environments. The proximal end of the AXS Universal Aspiration Tubing is connected to the AXS Universal Liner Set (outside of the sterile environment) while the distal end of the AXS

- Mass effect
- Myocardial infarction
- Neurological deficit/intracranial sequele
- Pseudoaneurysm
- Reaction to radiation exposure (i.e., alopecia, burns ranging in severity from skin reddening to ulcers, cataracts, or delayed neoplasia)
- Reactions to anti-platelet/anti-coagulant agents
- Renal failure
- Seizure
- Stent fracture, migration/embolization, or misplacement
- Stent thrombosis
- Stroke
- Transient ischemic attack
- Vasospasm
- Vessel occlusion or closure including parent vessel or non-target side-branches
- Vessel perforation/rupture, dissection, trauma or damage
- Vessel thrombosis
- Visual impairment
- Other procedural complications including but not limited to anesthetic and contrast media risks, hypotension, hypertension, access site complications (including pain, hematoma, local bleeding, local infection, and injury to the artery (i.e. dissection), vein, or adjacent nerves)
- Unplanned intervention

#### Warnings

Contents supplied STERILE using an ethylene oxide (EO) process. Do not use if sterile barrier is damaged. If damage is found, call your Stryker Neurovascular representative.

For single use only. Do not reuse, reprocess or resterilize. Reuse, reprocessing or resterilization may compromise the structural integrity of the device and/or lead to device failure which, in turn, may result in patient injury, illness or death. Reuse, reprocessing or resterilization may also create a risk of contamination of the device and/or cause patient infection or cross-infection, including, but not limited to, the transmission of infectious disease(s) from one patient to another. Contamination of the device may lead to injury, illness or death of the patient.

After use, dispose of product and packaging in accordance with hospital, administrative and/or local government policy.

- This device should only be used by physicians who have received appropriate training in interventional neuroradiology or interventional radiology and preclinical training on the use of this device as established by Stryker Neurovascular.
- Persons allergic to nickel titanium (Nitinol) may suffer an allergic response to this stent implant.
- Higher adverse event rates may be experienced for distal aneurysms located in the anterior and middle cerebral arteries.
- Do not use device to treat patients with ruptured intracranial aneurysms within a minimum of 30 days from the aneurysm rupture.

#### Cautions / precautions

- Take all necessary precautions to limit X-ray radiation doses to clinical operators by using sufficient shielding, reducing fluoroscopy times, and modifying X-ray technical factors whenever possible.
- The Neuroform Atlas stent may create local field inhomogeneity and susceptibility artifacts during magnetic resonance angiography (MRA), which may degrade the diagnostic quality to assess effective intracranial aneurysm occlusion.
- Safety and effectiveness of the Neuroform Atlas Stent System in patients below the age of 18 has not been established.
- The benefits may not outweigh the risks of device use in patients with small and medium asymptomatic extracranial intracranial aneurysms, including those located in the cavernous internal carotid artery.
- Carefully weigh the benefits vs. risks of device treatment for each individual patient based on their medical health status and risk factors for intracranial aneurysm rupture during their expected life time such as age, comorbidities, history of smoking, intracranial aneurysm size, location, and morphology, family history, history of prior asymptomatic subarachnoid hemorrhage (aSAH), documented growth of intracranial aneurysm on serial imaging, presence of multiple intracranial aneurysms, and presence of concurrent pathology. The benefits may not outweigh the risks associated with device use in certain patients; therefore, judicious patient selection is recommended based on clinical practice guidelines or tools to assess the life time risk of intracranial aneurysm rupture.

#### Safety Information Magnetic Resonance Conditional

Non-clinical testing and analysis have demonstrated that the Neuroform Atlas Stent is MR Conditional alone, or when overlapped with a second stent, and adjacent to a Stryker Neurovascular coil mass. A patient with the Neuroform Atlas Stent can be safely scanned immediately after placement of this implant, under the following conditions:

- Static magnetic field of 1.5 and 3.0 Tesla
- Maximum spatial gradient field up to 2500 Gauss/cm (25 Tesla/m)
- Maximum MR system reported whole body averaged specific absorption rate of 2 W/kg (Normal Operating Mode) and head averaged specific absorption rate of 3.2 W/kg.

Under the scan conditions defined above, the Neuroform Atlas Stent is expected to produce a maximum temperature rise of 4 °C after 15 minutes of continuous scanning. The Neuroform Atlas Stent should not migrate in this MRI environment.

In non-clinical testing, the image artifact caused by the device extends approximately 2 mm from the Neuroform Atlas Stent when imaged with a spin echo pulse sequence and 3 Tesla MRI System. The artifact may obscure the device lumen. It may be necessary to optimize MR imaging parameters for the presence of this implant. See additional precaution related to the image artifact from the implant in the "Precautions" section of this labeling.



**Stryker Neurovascular**  
47900 Bayside Parkway  
Fremont, CA 94538

[strykerneurovascular.com](http://strykerneurovascular.com)

Date of Release: MAY/2019

EX\_EN\_US

#### Warnings for both indications

Contents supplied STERILE using an ethylene oxide (EO) process. Do not use if sterile barrier is damaged. If damage is found, call your Stryker Neurovascular representative.

For single use only. Do not reuse, reprocess or resterilize. Reuse, reprocessing or resterilization may compromise the structural integrity of the device and/or lead to device failure which, in turn, may result in patient injury, illness or death. Reuse, reprocessing or resterilization may also create a risk of contamination of the device and/or cause patient infection or cross-infection, including, but not limited to, the transmission of infectious disease(s) from one patient to another. Contamination of the device may lead to injury, illness or death of the patient.

After use, dispose of product and packaging in accordance with hospital, administrative and/or local government policy.

- Limited testing has been performed with solutions such as contrast media, and saline. The use of these catheters for delivery of solutions other than the types that have been tested for compatibility is not recommended.
- Not intended for use with power injectors.
- If flow through catheter becomes restricted, do not attempt to clear catheter lumen by infusion. Doing so may cause catheter damage or patient injury. Remove and replace catheter.
- Never advance or withdraw an intravascular device against resistance until the cause of the resistance is determined by fluoroscopy. Movement of the device against resistance could dislodge a clot, perforate a vessel wall, or damage the device.

#### Additional warning for revascularization indication only

- Excessive aspiration may cause patient complications.

#### Precautions

- Carefully inspect all devices prior to use. Verify size, length, and condition are suitable for the specific procedure. Ensure the catheter's labeled outer diameter is smaller than the treatment vessel diameter. Do not use a device that has been damaged in any way. Damaged device may cause complications.
- To control the proper introduction, movement, positioning and removal of the catheter within the vascular system, users should employ standard clinical angiographic and fluoroscopic practices and techniques throughout the interventional procedure.
- Use the product prior to the "Use By" date printed on the label.
- To prevent thrombus formation and contrast media crystal formation, maintain a constant infusion of appropriate flush solution through catheter lumen.
- Torquing the catheter may cause damage which could result in kinking or separation of the catheter shaft.

Stryker or its affiliated entities own, use, or have applied for the following trademarks or service marks: AXS Catalyst, AXS Universal, ClotFinder, Stryker. All other trademarks are trademarks of their respective owners or holders.

The absence of a product, feature, or service name, or logo from this list does not constitute a waiver of Stryker's trademark or other intellectual property rights concerning that name or logo.

Copyright © 2019 Stryker  
AF002596 v1.0 | Page 2 of 2



**Stryker Neurovascular**  
47900 Bayside Parkway  
Fremont, CA 94538

[strykerneurovascular.com](http://strykerneurovascular.com)

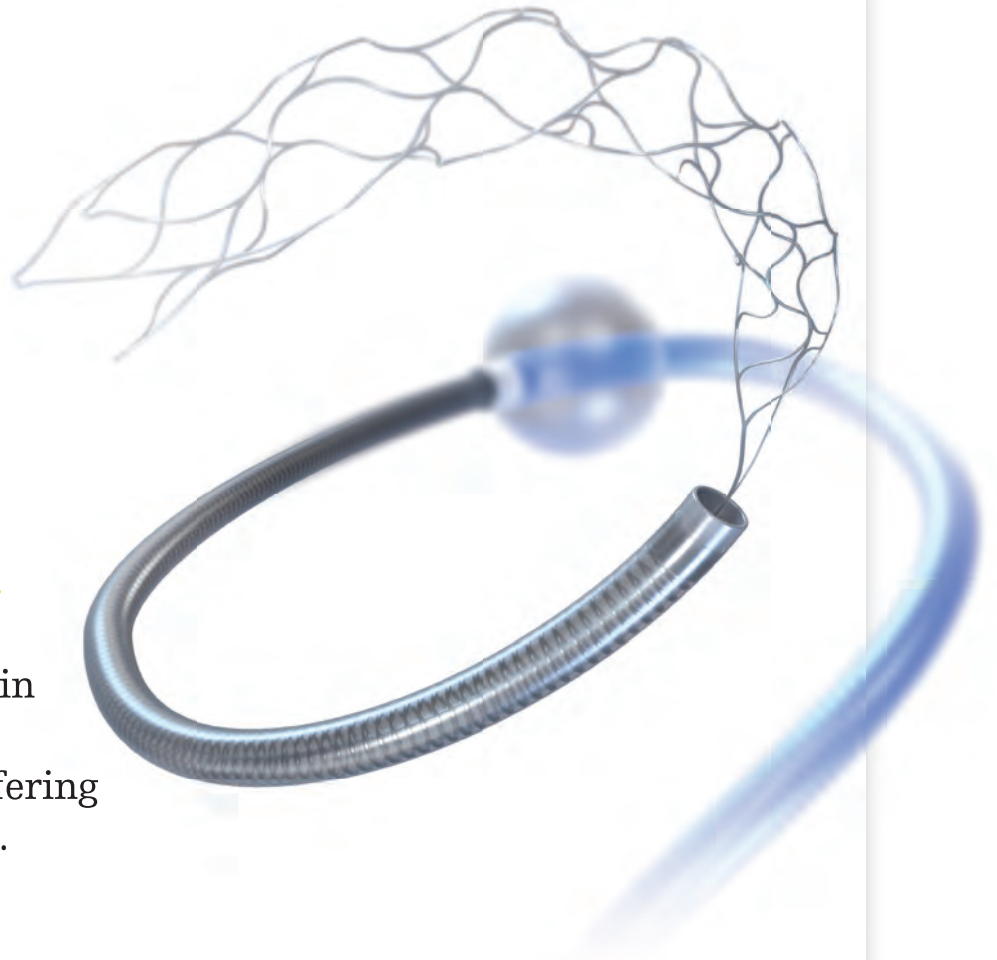
Date of Release: MAY/2019

EX\_EN\_US

# Trap more.

**Empowering first  
pass retrieval**

with the new 0.068in  
lumen CAT 7 Distal  
Access Catheter, offering  
ultimate versatility.



## **AXS Catalyst® 7** Distal Access Catheter

# AJNR

## AMERICAN JOURNAL OF NEURORADIOLOGY

DECEMBER 2019  
VOLUME 40  
NUMBER 12  
WWW.AJNR.ORG

Publication Preview at [www.ajnr.org](http://www.ajnr.org) features articles released in advance of print. Visit [www.ajnrblog.org](http://www.ajnrblog.org) to comment on AJNR content and chat with colleagues and AJNR's News Digest at <http://ajnrdigest.org> to read the stories behind the latest research in neuroimaging.

1977 **PERSPECTIVES** *Y. Bronstein*

### REVIEW ARTICLES

-  1978 **RESISTing the Need to Quantify: Putting Qualitative FDG-PET/CT Tumor Response Assessment Criteria into Daily Practice** *J.G. Peacock, et al.* **HEAD & NECK**
-  1987 **Imaging Findings Related to the Valsalva Maneuver in Head and Neck Radiology** *A.A. Madhavan, et al.* **HEAD & NECK**

### SOCIAL MEDIA VIGNETTE

- 1994 **Publicly Available Metrics Underestimate AJNR Twitter Impact and Follower Engagement** *C.M. Tomblinson, et al.*

### CLINICAL VIGNETTE

- 1998 **Lyme Disease: What the Neuroradiologist Needs to Know** *H.A. Valand, et al.*

### GENERAL CONTENTS

- 2001 **Safety and Diagnostic Efficacy of Gadobenate Dimeglumine in MRI of the Brain and Spine of Neonates and Infants** *D.S. Enterline, et al.* **PATIENT SAFETY  
PEDIATRICS**
-  2010 **Anatomy of the Great Posterior Radiculomedullary Artery** *V.H. Perez Perez, et al.* **SPINE**
-     2016 **Intracranial Atherosclerotic Burden on 7T MRI Is Associated with Markers of Extracranial Atherosclerosis: The SMART-MR Study** *M.H.T. Zwartbol, et al.* **ADULT BRAIN**
- 2023 **Commentary**  
**Intracranial and Extracranial Atherosclerosis: More Similar Than Different?** *L.L. Chan*
-   2025 **Qualitative Assessment and Reporting Quality of Intracranial Vessel Wall MR Imaging Studies: A Systematic Review** *J.W. Song, et al.* **ADULT BRAIN**
-  2033 **Automated ASPECTS in Acute Ischemic Stroke: A Comparative Analysis with CT Perfusion** *V.K. Sundaram, et al.* **ADULT BRAIN**
- 2039 **Are Linear Measurements of the Nucleus Basalis of Meynert Suitable as a Diagnostic Biomarker in Mild Cognitive Impairment and Alzheimer Disease?** *K.D. Jethwa, et al.* **ADULT BRAIN**
-  2045 **DWI for Monitoring the Acute Response of Malignant Gliomas to Photodynamic Therapy** *Y. Fujita, et al.* **ADULT BRAIN**

AJNR (Am J Neuroradiol ISSN 0195-6108) is a journal published monthly, owned and published by the American Society of Neuroradiology (ASNR), 800 Enterprise Drive, Suite 205, Oak Brook, IL 60523. Annual dues for the ASNR include approximately 21% for a journal subscription. The journal is printed by Cadmus Journal Services, 5457 Twin Knolls Road, Suite 200, Columbia, MD 21045; Periodicals postage paid at Oak Brook, IL and additional mailing offices. Printed in the U.S.A. POSTMASTER: Please send address changes to American Journal of Neuroradiology, P.O. Box 3000, Denville, NJ 07834, U.S.A. Subscription rates: nonmember \$410 (\$480 foreign) print and online, \$320 online only; institutions \$470 (\$540 foreign) print and basic online, \$935 (\$1000 foreign) print and extended online, \$380 online only (basic), extended online \$825; single copies are \$35 each (\$40 foreign). Indexed by PubMed/Medline, BIOSIS Previews, Current Contents (Clinical Medicine and Life Sciences), EMBASE, Google Scholar, HighWire Press, Q-Sensei, RefSeek, Science Citation Index, SCI Expanded, Meta/CZI, ReadCube, and Semantic Scholar. Copyright © American Society of Neuroradiology.

  	2052 Prognostic Predictions for Patients with Glioblastoma after Standard Treatment: Application of Contrast Leakage Information from DSC-MRI within Nonenhancing FLAIR High-Signal-Intensity Lesions <i>S.H. Kim, et al.</i>	ADULT BRAIN FUNCTIONAL
 	2059 Quantification of Iodine Leakage on Dual-Energy CT as a Marker of Blood-Brain Barrier Permeability in Traumatic Hemorrhagic Contusions: Prediction of Surgical Intervention for Intracranial Pressure Management <i>U.K. Bodanapally, et al.</i>	ADULT BRAIN FUNCTIONAL
	2066 Angiographic Analysis of Natural Anastomoses between the Posterior and Anterior Cerebral Arteries in Moyamoya Disease and Syndrome <i>S. Bonasia, et al.</i>	ADULT BRAIN
  	2073 Validation of Highly Accelerated Wave-CAIPI SWI Compared with Conventional SWI and T2*-Weighted Gradient Recalled-Echo for Routine Clinical Brain MRI at 3T <i>J. Conklin, et al.</i>	ADULT BRAIN
 	2081 Volumetry of Mesiotemporal Structures Reflects Serostatus in Patients with Limbic Encephalitis <i>L. Ernst, et al.</i>	ADULT BRAIN
	2090 Prevalence of Asymptomatic Middle Cranial Fossa Floor Pits and Encephaloceles on MR Imaging <i>J.C. Benson, et al.</i>	ADULT BRAIN
	2094 Outcome Study of the Pipeline Embolization Device with Shield Technology in Unruptured Aneurysms (PEDSU) <i>D. Atasoy, et al.</i>	INTERVENTIONAL
	2102 Comparing Morphology and Hemodynamics of Stable-versus-Growing and Grown Intracranial Aneurysms <i>E.L. Leemans, et al.</i>	INTERVENTIONAL
	2111 Identification of Vortex Cores in Cerebral Aneurysms on 4D Flow MRI <i>K. Futami, et al.</i>	INTERVENTIONAL
  	2117 How Flow Reduction Influences the Intracranial Aneurysm Occlusion: A Prospective 4D Phase-Contrast MRI Study <i>O. Brina, et al.</i>	INTERVENTIONAL
	2124 Optimizing the Quality of 4D-DSA Temporal Information <i>K.L. Ruedinger, et al.</i>	INTERVENTIONAL
	2130 The Influence of Angioarchitectural Features on the Success of Endovascular Embolization of Cranial Dural Arteriovenous Fistulas with Onyx <i>D.F. Vollherbst, et al.</i>	INTERVENTIONAL
   	2137 Ultra-High-Field Targeted Imaging of Focal Cortical Dysplasia: The Intracortical Black Line Sign in Type IIb <i>E. Bartolini, et al.</i>	PEDIATRICS
	2143 Cost and Utility of Routine Contrast-Enhanced Neck MRA in a Pediatric MRI Stroke Evaluation Protocol <i>A. Baltensperger, et al.</i>	PEDIATRICS
  	2146 Topological Alterations of the Structural Brain Connectivity Network in Children with Juvenile Neuronal Ceroid Lipofuscinosis <i>T. Roine, et al.</i>	PEDIATRICS FUNCTIONAL
 	2154 Cerebellar Heterotopias: Expanding the Phenotype of Cerebellar Dysgenesis in CHARGE Syndrome <i>J.N. Wright, et al.</i>	PEDIATRICS
	2161 White Matter Injury and Structural Anomalies in Infants with Prenatal Opioid Exposure <i>S.L. Merhar, et al.</i>	PEDIATRICS
	2166 Intraspinal Paragonimiasis in Children: MRI Findings and Suggestions for Pathogenesis <i>Y. Qin, et al.</i>	PEDIATRICS

## ONLINE FEATURES

### LETTERS

E65 **Methodologic Concerns on the Reported Values for Assessing Permeability of the Blood-Brain Barrier in the Hippocampus** *C.M. Lim, et al.*

E67 **Reply** *J. Ivanidze, et al.*

E69 **Multinodular and Vacuolating Neuronal Tumor of the Cerebrum: Does the Name Require Review?** *A. Agarwal, et al.*

### E71 ERRATUM

### BOOK REVIEWS

*R.M. Quencer, Section Editor*

Please visit [www.ajnrblog.org](http://www.ajnrblog.org) to read and comment on Book Reviews.



Multiple great radicular posterior radiculomedullary arteries shown in a specimen at the T11 level.



Indicates Editor's Choices selection



Indicates Fellows' Journal Club selection



Indicates open access to non-subscribers at [www.ajnr.org](http://www.ajnr.org)



Indicates article with supplemental on-line table



Indicates article with supplemental on-line photo



Indicates article with supplemental on-line video



Evidence-Based Medicine Level 1



Evidence-Based Medicine Level 2

### Official Journal:

American Society of Neuroradiology  
 American Society of Functional Neuroradiology  
 American Society of Head and Neck Radiology  
 American Society of Pediatric Neuroradiology  
 American Society of Spine Radiology

### EDITOR-IN-CHIEF

**Jeffrey S. Ross, MD**

Professor of Radiology, Department of Radiology,  
 Mayo Clinic College of Medicine, Phoenix, AZ

### SENIOR EDITORS

**Harry J. Cloft, MD, PhD**

Professor of Radiology and Neurosurgery,  
 Department of Radiology, Mayo Clinic College of  
 Medicine, Rochester, MN

**Thierry A.G.M. Huisman, MD**

Radiologist-in-Chief, Texas Children's Hospital,  
 Houston, TX

**Yvonne W. Lui, MD**

Associate Professor of Radiology,  
 Chief of Neuroradiology,  
 New York University School of Medicine,  
 New York, NY

**C.D. Phillips, MD, FACR**

Professor of Radiology, Weill Cornell Medical  
 College, Director of Head and Neck Imaging,  
 New York-Presbyterian Hospital, New York, NY

**Lubdha M. Shah, MD, MS**

Professor of Radiology and Director of Spine  
 Imaging, University of Utah Department of  
 Radiology and Imaging Sciences, Salt Lake City, UT

**Charles M. Strother, MD**

Professor of Radiology, Emeritus, University of  
 Wisconsin, Madison, WI

### STATISTICAL SENIOR EDITOR

**Bryan A. Comstock, MS**

Senior Biostatistician,  
 Department of Biostatistics,  
 University of Washington, Seattle, WA

### ARTIFICIAL INTELLIGENCE DEPUTY EDITOR

**Christopher G. Filippi, MD**

Professor and Vice Chair of Biomedical and  
 Translational Science,  
 Donald and Barbara Zucker School of Medicine at  
 Hofstra/Northwell,  
 Lenox Hill Hospital and Greenwich Village  
 Healthplex, New York, NY

### EDITORIAL BOARD

Ashley H. Aiken, *Atlanta, GA*  
 Lea M. Alhilali, *Phoenix, AZ*  
 Kubilay Aydin, *Istanbul, Turkey*  
 John D. Barr, *Dallas, TX*  
 Ari Blitz, *Baltimore, MD*  
 Barton F. Branstetter IV, *Pittsburgh, PA*  
 Jonathan L. Brisman, *Lake Success, NY*  
 Keith Cauley, *Danville, PA*  
 James Y. Chen, *San Diego, CA*  
 Asim F. Choudhri, *Memphis, TN*  
 Daniel Chow, *Irvine, CA*  
 J. Matthew Debnam, *Houston, TX*  
 Seena Dehkharghani, *New York, NY*  
 Yonghong Ding, *Rochester, MN*  
 Clifford J. Eskey, *Hanover, NH*  
 Saeed Fakhra, *Phoenix, AZ*  
 Massimo Filippi, *Milan, Italy*  
 Nils D. Forkert, *Calgary, Alberta, Canada*  
 Wende N. Gibbs, *Phoenix, AZ*  
 Christine M. Glastonbury, *San Francisco, CA*  
 John L. Go, *Los Angeles, CA*  
 Philipp Göltz, *Erlangen, Germany*  
 Allison Grayev, *Madison, WI*  
 Brent Griffith, *Detroit, MI*  
 Ajay Gupta, *New York, NY*  
 Rakesh Kumar Gupta, *Haryana, India*  
 Lotfi Hachein-Bey, *Sacramento, CA*  
 Christopher P. Hess, *San Francisco, CA*  
 Andrei Holodny, *New York, NY*  
 Benjamin Huang, *Chapel Hill, NC*  
 Mahesh V. Jayaraman, *Providence, RI*  
 Valerie Jewells, *Chapel Hill, NC*  
 Christof Karmonik, *Houston, TX*  
 Timothy J. Kaufmann, *Rochester, MN*  
 Hillary R. Kelly, *Boston, MA*  
 Toshibumi Kinoshita, *Akita, Japan*  
 Kenneth F. Layton, *Dallas, TX*  
 Alexander Lerner, *Los Angeles, CA*  
 Michael Lev, *Boston, MA*  
 Karl-Olof Lovblad, *Geneva, Switzerland*  
 Franklin A. Marden, *Chicago, IL*  
 Joseph C. McGowan, *Merion Station, PA*  
 Stephan Meckel, *Freiburg, Germany*  
 Christopher J. Moran, *St. Louis, MO*  
 Takahisa Mori, *Kamakura City, Japan*  
 Suresh Mukherji, *Ann Arbor, MI*  
 Alexander J. Nemeth, *Chicago, IL*  
 Renato Hoffmann Nunes, *Sao Paulo, Brazil*  
 Sasan Partovi, *Cleveland, OH*  
 Laurent Pierot, *Reims, France*  
 Jay J. Pillai, *Baltimore, MD*  
 Whitney B. Pope, *Los Angeles, CA*

Joana Ramalho, *Lisbon, Portugal*  
 Otto Rapalino, *Boston, MA*  
 Álex Rovira-Cañellas, *Barcelona, Spain*  
 Paul M. Ruggieri, *Cleveland, OH*  
 Amit M. Saindane, *Atlanta, GA*  
 Maksim Shapiro, *New York, NY*  
 Timothy Shepherd, *New York, NY*  
 Mark S. Shiroishi, *Los Angeles, CA*  
 Bruno P. Soares, *Baltimore, MD*  
 Maria Vittoria Spampinato, *Charleston, SC*  
 Khin Khin Tha, *Sapporo, Hokkaido, Japan*  
 Krishnamoorthy Thamburaj, *Hershey, PA*  
 Cheng Hong Toh, *Taipei, Taiwan*  
 Aquilla S. Turk, *Greenville, SC*  
 Anja G. van der Kolk, *Utrecht, the Netherlands*  
 Willem Jan van Rooij, *Tilburg, Netherlands*  
 Arastoo Vossough, *Philadelphia, PA*  
 Elysa Widjaja, *Toronto, Ontario, Canada*  
 Max Wintermark, *Stanford, CA*  
 Ronald L. Wolf, *Philadelphia, PA*  
 Kei Yamada, *Kyoto, Japan*  
 Carlos Zamora, *Chapel Hill, NC*  
 Vahe M. Zohrabian, *New Haven, CT*

### EDITORIAL FELLOW

Hediyeh Baradaran, *Salt Lake City, UT*

### SPECIAL CONSULTANTS TO THE EDITOR

#### AJNR Blog Editor

Neil Lall, *Denver, CO*

#### Case of the Month Editor

Nicholas Stence, *Aurora, CO*

#### Case of the Week Editors

Juan Pablo Cruz, *Santiago, Chile*

Sapna Rawal, *Toronto, Ontario, Canada*

#### Classic Case Editor

Sandy Cheng-Yu Chen, *Taipei, Taiwan*

#### Health Care and Socioeconomics Editor

Pina C. Sanelli, *New York, NY*

#### Physics Editor

Greg Zaharchuk, *Stanford, CA*

#### Podcast Editor

Wende N. Gibbs, *Phoenix, AZ*

#### Twitter Editor

Jennifer McCarty, *Houston, TX*

Founding Editor  
 Juan M. Taveras

Editors Emeriti  
 Mauricio Castillo, Robert I. Grossman,  
 Michael S. Huckman, Robert M. Quencer

Managing Editor  
 Karen Halm  
 Assistant Managing Editor  
 Laura Wilhelm  
 Editorial Assistant  
 Margaret B. Sabato  
 Executive Director, ASNR  
 Mary Beth Hepp



Title: Fog. This photograph was taken in Coburg, Oregon.

*Yulia Bronstein, MD, vRad (Virtual Radiologic) teleradiology service, Eugene, Oregon*

# RESISTING the Need to Quantify: Putting Qualitative FDG-PET/CT Tumor Response Assessment Criteria into Daily Practice

J.G. Peacock, C.T. Christensen, and K.P. Banks



## ABSTRACT

**SUMMARY:** Tumor response assessments are essential to evaluate cancer treatment efficacy and prognosticate survival in patients with cancer. Response criteria have evolved over multiple decades, including many imaging modalities and measurement schema. Advances in FDG-PET/CT have led to tumor response criteria that harness the power of metabolic imaging. Qualitative PET/CT assessment schema are easy to apply clinically, are reproducible, and yield good prognostic results. We present 3 such criteria, namely, the Lugano classification for lymphoma, the Hopkins criteria, and the Neck Imaging Reporting and Data Systems criteria for head and neck cancers. When comparing baseline PET/CTs with interim or end-of-treatment PET/CTs, radiologists can classify the tumor response as complete metabolic response, partial metabolic response, no metabolic response, or progressive disease, which has important implications in directing further cancer management and long-term patient prognosis. The purpose of this article is to review the progression of tumor response assessments from CT- and PET/CT-based quantitative and semi-quantitative systems to PET/CT-based qualitative systems; introduce the classification schema for these systems; and describe how to use these rapid, powerful, and qualitative PET/CT-based systems in daily practice through illustrative cases.

**ABBREVIATIONS:** CMR = complete metabolic response; D5PS = Deauville 5-point scale; NI-RADS = Neck Imaging Reporting and Data Systems; PD = relapsed/progressive disease; PERCIST = PET Response Criteria in Solid Tumors; RECIST = Response Evaluation Criteria in Solid Tumors; WHO = World Health Organization; HNSCCA = Head and Neck squamous cell carcinoma; ACR = American college of radiology; AUC = appropriate use criteria; SCCa = squamous cell carcinoma; PPD = product of the diameters; SPD = sum of the product of the diameters

## INTRODUCTION

Cancer is second only to cardiac disease with regard to leading causes of mortality in the United States.<sup>1</sup> Fortunately, the rate of cancer deaths is declining, with the prevalence of individuals surviving and living with cancer increasing.<sup>1</sup> New surgical and medical treatments, including immunotherapies and targeted molecular therapies, which are more and more frequently tailored to an individual's specific tumor, are to credit for much of these improvements in patient survival. Essential to any effective cancer treatment in this dawning era of personalized medicine is an

understanding of how each unique neoplasm responds to its customized therapy. As such, radiology plays an increasingly vital role in helping clinicians determine treatment success or failure; guiding decisions with regard to whose therapy may be de-escalated, which therapy reduces toxicity but preserves efficacy, and how to identify treatment failures in patients who would benefit from timely modification of their regimen to improve the likelihood of a positive outcome or determination of a course that leads to palliation and hospice care. In this article, we describe the development of tumor response assessments in radiology and review 3 easy-to-use, qualitative, FDG-PET/CT tumor response assessments used in head and neck tumors, including lymphoma.

### Evolution of Solid Tumor Response Evaluation

In 1976, the World Health Organization (WHO) introduced the concept of imaging-guided cancer therapy response assessment by using CT and quantitative tumor measurements.<sup>2</sup> This technique measures the longest axial dimension of a tumor and its perpendicular dimension, then calculates the product. The sum of the product of the diameters of multiple lesions were compared with previous results to quantify the overall response. The WHO system also included parameters for then classifying responses as complete remission/response,

Received February 9, 2019; accepted after revision September 11.

From the Department of Radiology (J.G.P., K.P.B.), Brooke Army Medical Center, San Antonio, Texas; Department of Radiology (C.T.C.), Wilford Hall Ambulatory Surgical Center, San Antonio, Texas; and Department of Radiology (K.P.B.), Uniformed Services University of the Health Sciences, Bethesda, Maryland

The views expressed herein are those of the authors and do not reflect the official policy or position of Brooke Army Medical Center, the U.S. Army Medical Department, the Department of the Air Force and Department of Defense or the U.S. Government.

Please address correspondence to Justin G. Peacock, MD, PhD, Brooke Army Medical Center, 3551 Roger Brooke Dr, San Antonio, TX 78234; e-mail: justin.g.peacock@gmail.com; @PeacockImaging

Indicates open access to non-subscribers at [www.ajnr.org](http://www.ajnr.org)

<http://dx.doi.org/10.3174/ajnr.A6294>

partial remission/response, no response, or relapsed/progressive disease (PD).<sup>2</sup> Although a step in the right direction, the WHO assessment had a degree of ambiguity because it did not specify the number or minimum size of lesions to be measured.<sup>2,3</sup> These limitations, among other factors, restricted its utility and curbed widespread use.

To better standardize the treatment response criteria, a new quantitative CT assessment tool called Response Evaluation Criteria in Solid Tumors (RECIST 1.0) was developed.<sup>2</sup> In RECIST 1.0, all lesions that were at least 1.0 cm in size were measured, with the maximum number capped at 10 lesions and no more than 5 lesions per organ. Also, lesion size was now quantified solely according to the longest dimension. RECIST underwent a slight modification, RECIST 1.1, to further simplify the technique by reducing the maximum number of lesions that needed to be characterized to 5 and no more than 2 per organ.<sup>3,4</sup> Although superior to previous assessment classifications in terms of ease of use and standardization, studies found a wide variation in sizes measured by different physicians.<sup>5,6</sup> Also, the criteria only looked at anatomic measurements, not at the metabolism of lesions. Therefore, it is unclear if a residual mass represents posttreatment inflammatory changes, tissue fibrosis, or viable tumor.<sup>6</sup>

FDG-PET/CT permits assessment not only of the anatomy but also the metabolism of lesions. This can provide valuable information with regard to the true efficacy of treatments, often much earlier than can be discerned by CT changes alone.<sup>7-10</sup> The first tumor response assessment to use PET/CT was the PET Response Criteria in Solid Tumors (PERCIST) tool.<sup>11</sup> PERCIST 1.0 incorporates FDG avidity in classifying tumor responses. PERCIST 1.0 involves calculating the standardized uptake value relative to the standardized uptake value of lean body mass for the liver and tumor target lesions. If the PET avidity is too low or not measurable, the classification defers to RECIST 1.1. The standardized uptake value relative to the lean body mass was chosen to reduce variability of metabolic measurements related to fluctuations in body weight and habitus. In PERCIST 1.0, disease response is classified as complete metabolic response (CMR), partial metabolic response, stable metabolic disease or no metabolic response, and progressive metabolic disease.

Clinical research demonstrated that PERCIST 1.0 is more sensitive and accurate than RECIST 1 for nonsmall cell lung cancer, malignant solid tumors, and colorectal cancer.<sup>6</sup> As with measurements, different patient factors, scanners, protocols, and PET software algorithms can all contribute to this variability.<sup>6</sup> Consequently, there was a need to develop an assessment classification that was easy to use, consistent, and prognostically valid.

### **Unique Lymphoma Response Evaluation**

In 1999, lymphoma treatment was classified according to the International Workshop Group.<sup>12,13</sup> The initial criteria were based on physical examination, CT, and gallium-SPECT findings. Quantification of size depended on the sum of the product of the diameters, with tumor response according to the WHO classes. An additional complete remission unconfirmed classification was applied when there was a significant decrease in lesion size but a residual mass. PET/CT improved the interpretation of these

complete remission unconfirmed lesions, so the International Workshop Group criteria were updated to include PET data, which led to the International Harmonization Project.<sup>14</sup> The complete remission unconfirmed classification was eliminated, with residual masses characterized as complete remission/response or partial remission/response based on the FDG avidity. Challenges in this International Harmonization Project classification again included interpreter variability in sum of the product of the diameters measurements, along with variability in PET standardized uptake value measurements and the need for a bone marrow biopsy.

### **Qualitative Tumor Response Evaluation**

The previously mentioned challenges in response assessment and the increased use of FDG-PET/CT have led to the current tools that are easy to use and useful for both prognostics and guiding therapy. The criteria rely on qualitative metrics that can be rapidly performed during the clinical interpretation of PET/CT examinations, often by analysis of the PET MIP views alone. Lymphoma, head and neck tumors, esophageal cancer, lung cancer, pancreatic cancer, rectal cancer, prostate cancer, and cervical cancer have all been assessed by using qualitative FDG-PET/CT tumor response evaluation techniques.<sup>15-22</sup> Three major response assessment criteria in neuroradiology that use this simplified approach are the Lugano criteria for lymphoma and the Hopkins and Neck Imaging Reporting and Data Systems (NI-RADS) criteria for solid tumors of the head and neck.<sup>15,16,23-26</sup> The Lugano and Hopkins criteria use relatively stable internal reference standards for metabolism found on every examination, blood pool, and liver intensities, which minimizes the variation in response assessments related to differences in patients, examination protocols, scanner characteristics, and readers.<sup>15,25</sup> The NI-RADS criteria use a combination of contrast-enhanced CT, together with the PET-CT findings, to provide anatomic evaluation in areas of increased metabolic activity.<sup>26</sup> In this article, we describe the development of these 3 criteria and their use in daily practice, and provide illustrative examples of the utility of these tools in the modern evaluation of tumor response.

## **THE LUGANO CLASSIFICATION FOR LYMPHOMA TREATMENT RESPONSE EVALUATION**

### **Development of the Lugano Classification**

In 2011, leaders in the field of malignant lymphoma met in Lugano, Switzerland, to create more effective treatment response classification guidelines based on previous trials, clinical experience, and research groups.<sup>23</sup> The results were published in 2014 as the Lugano classification for lymphoma staging and response assessment.<sup>15,23,27</sup> The novel classification included quantitative CT parameters for non-FDG-avid lymphomas and independent PET/CT parameters for FDG-avid lymphomas.<sup>15,23,27</sup> Although FDG-PET/CT was first included in the International Harmonization Project clinical response criteria, the Lugano system is the first to define the role of FDG-PET/CT for response assessment in all FDG-avid lymphomas.<sup>15,23,27</sup> In addition, the criteria eliminated the cumbersome need for a bone marrow biopsy in FDG-avid lymphomas, which allows

**Table 1: Lugano classification for CT-based lymphoma response<sup>a</sup>**

Technique	Complete Response	Partial Response	No Response	PD
CT	Complete disappearance of disease or decrease in the lymph node long axis to <1.5 cm	Multiple: $\geq$ 50% decrease in SPD of up to 6 lesions. Single: $\geq$ 50% decrease in PPD	No criteria for PD and <50% decrease in SPD of up to 6 lesions.	(1) New or increased lymphadenopathy (long axis >1.5 cm); new nodes, $\geq$ 50% increase in PPD, or >0.5 cm increase in diameter for $\leq$ 2 cm or >1.0 cm for >2 cm; (2) splenic volume increase: with splenomegaly, >50% increase in length, or without splenomegaly, $\geq$ 2 cm increase in length; (3) new or larger lesions; (4) recurrent previously resolved lesions; (5) new extranodal lesion >1 cm (or <1 cm if unequivocally lymphoma)
FDG-PET/CT	D5PS score of 1, 2, or 3 in disease sites, with or without residual mass	D5PS score of 4 or 5, with reduced uptake compared with baseline	D5PS score of 4 or 5, with no significant change in FDG uptake	D5PS score of 4 or 5, with increased uptake intensity compared with baseline and/or new FDG-avid foci

**Note:**—SPD indicates sum of the product of the diameters (PPD).

<sup>a</sup> For non-FDG avid lymphomas, the following CT-based measurement criteria are used to determine tumor response classification; adapted from Ref. 15.

**Table 2: D5PS<sup>a</sup>**

D5PS Score <sup>b</sup>	Lesion FDG Uptake
1	At or below background
2	Less than or equal to mediastinal blood pool
3	Greater than or equal to mediastinal, but less than hepatic blood pool
4	Greater than hepatic blood pool
5	Markedly greater than hepatic blood pool
X	Designator for nonlymphomatous lesion

<sup>a</sup> Adapted from Ref. 23.

<sup>b</sup> The D5PS score is used in the Lugano classification for grading lymphoma response.

response based solely on the single most metabolically active lesion.

**Using the Quantitative CT Lugano Parameters to Grade Lymphoma Response**

The Lugano criteria for CT lymphoma staging and response assessment are quantitative and reserved for non-FDG-avid lymphomas.<sup>23</sup> CT response assessment categories for interpretation of an interim

or end-of-treatment examination include complete remission/re-sponse, partial remission/response, no response, and PD.<sup>15,23</sup> CT criteria are based on measurement of lymph nodes, any extranodal lesions, and splenic sizes. Lymph nodes must have a long-axis measurement of >1.5 cm, whereas extranodal disease must be at least 1.0 cm. The bi-dimensional diameter product is calculated for single lesions and the sum of the product of the diameters for up to 6 nodal and/or extranodal target lesions. Complete remission/response occurs when all lymph node long-axis diameters are  $\leq$ 1.5 cm and there is no residual extranodal disease. PD occurs with new lymphadenopathy or extranodal lesions, splenic size increase, or increased size of pre-existing lesions. The complete response criteria are detailed in Table 1. The CT parameters, principally derived from the previous WHO schema, have similar challenges in interpreter measurement reliability.

**Deauville 5-Point Scale for Scoring FDG Avidity**

The Lugano classification incorporates the Deauville 5-point scale (D5PS) for grading FDG avidity.<sup>23,28</sup> A score is assigned based on the single most intense focus of FDG-avid lymphomatous disease, relative to mediastinal blood pool and hepatic activity (Table 2). A D5PS score of 1 indicates that the lesion does not demonstrate FDG uptake greater than background activity. A score of 2

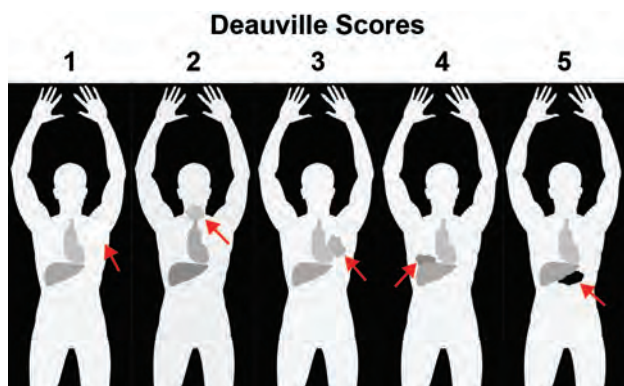


**FIG 1.** The D5PS scores of lesions qualitatively based on the FDG uptake relative to the mediastinal blood pool (MBP) and hepatic parenchymal FDG activity. The figure demonstrates hypothetical masses (arrows) and their FDG uptake relative to the MBP and liver activity. D5PS score of 1 for a left axillary mass with FDG uptake no greater than background activity. D5PS score of 2 for cervical mass with FDG uptake above background but less than MBP or liver. D5PS score of 3 for hilar mass with FDG uptake greater than MBP but less than or equal to the hepatic activity. A D5PS score of 4 for a mass in right lung base with FDG uptake greater than both MBP and liver. A D5PS score of 5 for a midabdominal mass with FDG uptake markedly greater than that of the liver.

for PET to serve as a surrogate for determining marrow involvement.<sup>23</sup> The FDG-PET/CT criteria also simplify interpretation by providing a qualitative assessment of the lymphoma treatment

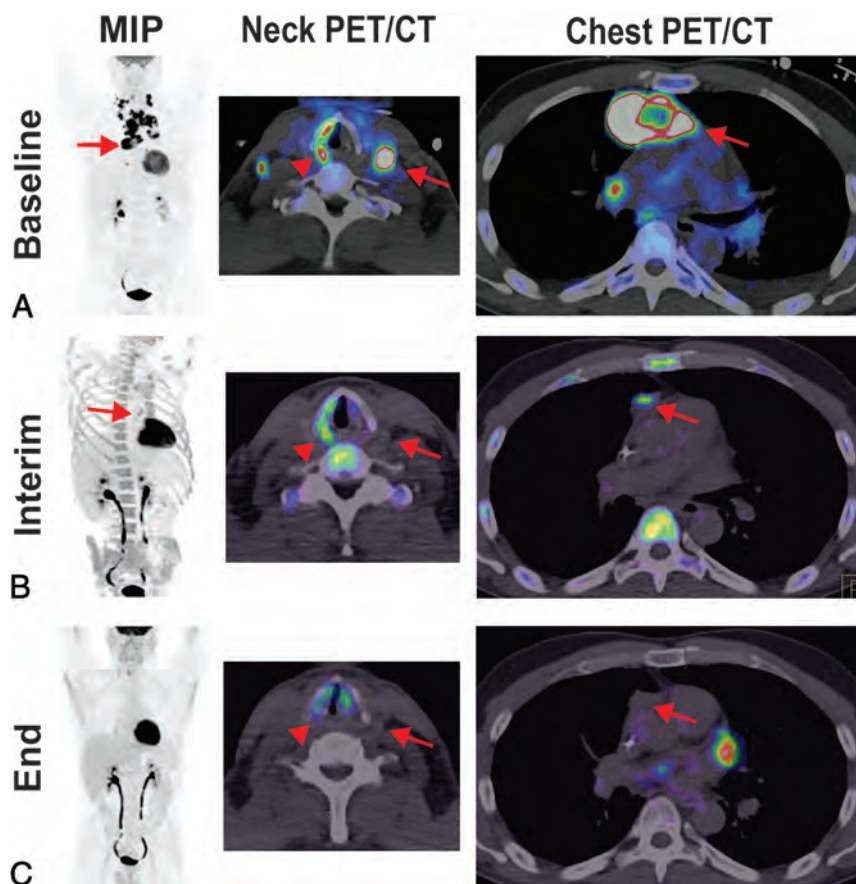


**FIG 2.** A partial metabolic response and CMR based on Lugano criteria. A 47-year-old man with diffuse large B-cell lymphoma demonstrates (A) baseline intense FDG avidity in mediastinal (MIP and PET/CT of the chest [arrows denote a large pericardial lymph node conglomerate]) and bilateral levels III and IV lymphadenopathy (PET/CT of the neck [arrow denotes a large level III node]), a D5PS score of 5. Incidentally, on the PET/CT of the neck, the arrowhead denotes a dysfunctional right vocal cord, likely due to disease impacting the ipsilateral recurrent laryngeal nerve. B, Interim imaging demonstrates reduced but persistent FDG uptake (2 times greater than the liver) in the retrosternal, pericardial mass (MIP and PET/CT of the chest [arrows]), consistent with a D5PS score of 5 but a Lugano designation of a partial metabolic response. There was interval resolution of the cervical lymphadenopathy. C, End-of-treatment imaging shows a residual pericardial mass on CT (arrow), without FDG uptake above background, consistent with a D5PS score of 1 and a Lugano designation of CMR.

indicates that the FDG uptake is less than or equal to mediastinal blood pool, whereas a score of 3 indicates that the lesion's FDG uptake is greater than the mediastinal blood pool and less than or equal to liver activity. D5PS scores of 4 and 5 indicate that the lesion's FDG uptake is moderately and markedly greater than the liver activity, respectively, with markedly greater considered to be at least 2–3 times more intense (Fig 1). A D5PS "X" designation may be used in conjunction with the 5-point scale to describe an FDG-avid nonlymphomatous lesion, such as sarcoid related hilar lymph nodes or focal thyroid uptake attributed to a primary thyroid neoplasm. By using these qualitative D5PS scores, rapid and reproducible assessment of posttreatment lymphoma response can be performed.

#### Using the Lugano Classification in Daily Practice

According to the 2019 International Workshop on Interim-PET scan in lymphoma, the D5PS score of the interim or end-of-

treatment examination should be compared with the score assigned to the most recent comparison,<sup>13,29</sup> which then lead to CMR, partial metabolic response, no metabolic response, or PD designations. Scores 1 and 2 on the interim or end-of-treatment examination denote a CMR (Fig 2). A D5PS score of 3 on follow-up imaging also likely signifies a CMR but may be interpreted as an inadequate response to avoid undertreating patients being considered for de-escalation of therapy.<sup>23</sup> In a separate article, by Mikhaeel et al,<sup>30</sup> these patients were found to have an intermediate overall survival and progression-free survival compared with patients with CMR and no metabolic response or PD. A D5PS score of 4 or 5 can indicate a partial metabolic response, no metabolic response, or PD designation, depending on whether the interim or end D5PS score is decreased, unchanged, or increased, respectively (Figs 2 and 3). In addition, any new FDG-avid lesions on an examination are classified as PD.<sup>15,23,27</sup>

The benefit of the D5PS and Lugano classification is that it provides well-defined guidelines for rapid qualitative tumor response assessment. The scores are based on internal standardized uptake value references, relatively similar from patient to patient and from examination to examination, which

means that individual variability in patients and PET/CT technology do not impact the assessment (Fig 1 and Table 1). Razek et al<sup>31</sup> reported excellent interobserver agreement (95.8% agreement,  $\kappa = 0.91$ ) in assigning D5PS scores and Lugano posttreatment responses. Burggraaff et al<sup>32</sup> reported treatment response assessments in diffuse large B-cell lymphoma by using dichotomization of D5PS 1–3 as negative and D5PS 4–5 as positive. The interim and end-of-treatment positive, negative, and overall agreements were 73.7%, 92.0%, and 87.7%, and 76.3%, 95.0%, and 91.7%, respectively.<sup>32</sup> By contrast, Kluge et al<sup>33</sup> (42% agreement,  $\kappa = 0.24$ ), Sawan et al<sup>34</sup> ( $\kappa = 0.082$ ), and Ceriani et al<sup>35</sup> ( $\kappa = 0.35$ – $0.72$ ) all reported poorer interobserver agreement for assigning individual D5PS to random scores. Kluge et al<sup>33</sup> reported that interobserver agreement improved when interpreters assigned a simple binary positive or negative result, such as reporting D5PS scores of 1, 2, or 3 as negative for recurrence and 4 or 5 as positive for disease or recurrence (86% agreement,

$\kappa = 0.56$ ). Sawan et al,<sup>34</sup> reported improved interobserver agreement as well as accuracy when second-opinion reports were obtained by oncologic radiologists who had training and experience in evaluating these studies ( $\kappa = 0.86$  and radiology-pathology concordance = 78%). Ceriani et al,<sup>35</sup> reported improved interobserver agreement after training ( $\kappa = 0.77$ – $0.87$ ). These studies demonstrate that simple binary scoring systems and training in the D5PS and Lugano criteria can improve the precision and accuracy in posttreatment response assessment.

Multiple studies demonstrate the significant prognostic value of the Lugano classification and D5PS score in interim and end-of-treatment PET/CTs for a variety of FDG-avid lymphomas, including Burkitt, Hodgkin, non-Hodgkin, mantle cell, follicular, natural killer, and T-cell lymphomas in pediatric and adult

patients.<sup>8,13,27,29,36-50</sup> These studies indicate that D5PS outperforms other indicators in overall survival and progression-free survival, including simple changes in standardized uptake values or CT-only measurements.<sup>23,29,46</sup> Specific test metrics depend on the lymphoma subtype and grade; Hodgkin lymphoma demonstrates high (90%–100%) positive predictive values and negative predictive values, and non-Hodgkin lymphoma demonstrates high negative predictive values (80%–100%), but lower positive predictive values (50%–100%).<sup>23,29</sup> Metabolically active disease in these non-Hodgkin lymphoma cases warrants further evaluation with imaging or biopsy because the activity may simply represent posttreatment inflammation.

### HOPKINS CRITERIA FOR HEAD AND NECK TUMOR RESPONSE EVALUATION

#### Development of the Hopkins Criteria for Head and Neck Tumors

Initially, the Hopkins criteria were developed to qualitatively assess head and neck tumor treatment response.<sup>16</sup> The criteria harnessed the well-documented power of FDG-PET/CT in head and neck tumors, which supersedes anatomic size changes in prognostic value.<sup>6,16</sup> Similar to the D5PS, lesions are classified into 5 scores relative to FDG avidity in the liver and the internal jugular vein blood pool, used in place of the mediastinum (Table 3). Lesions that demonstrate focal avidity less than the internal jugular vein have a score of 1, whereas those with focal avidity greater than internal jugular vein have a score of 2. In contrast to the D5PS, the Hopkins criteria address the presence of diffuse FDG avidity greater than internal jugular vein or liver, which is frequently seen after effective treatment and gives it a score of 3. Lesions with focal FDG avidity greater than the liver are given a score of 4, and focal and intense avidity greater than the liver are scored as 5.<sup>16</sup> These areas of FDG avidity are scored in the original tumor site, right neck, and left neck, and the overall score is the highest score. The scores correspond with the posttreatment response from CMR to posttreatment inflammation to residual tumor with overall scores of 1, 2, and 3 considered negative for residual disease, whereas scores of 4 or 5 are considered positive (Table 3).

Marcus et al<sup>16</sup> demonstrated a high interpreter reliability for scoring head and neck squamous cell carcinoma (HNSCCA) follow-up PET/CTs by using the Hopkins Criteria. They also demonstrated a robust specificity and negative predictive value of 92.2% and 91.1%, respectively, with an overall accuracy of 86.9%.

Importantly, the criteria demonstrated a significant clinical value by reversing management for approximately 64% of patients. Van den Wyngaert et al<sup>51</sup> in the European ECLYPS trial demonstrated similarly high specificity and negative predictive values, of 91.2% and 92.1%, respectively, by using the Hopkins criteria to grade head and neck squamous cell carcinoma tumor response. The sensitivity for residual

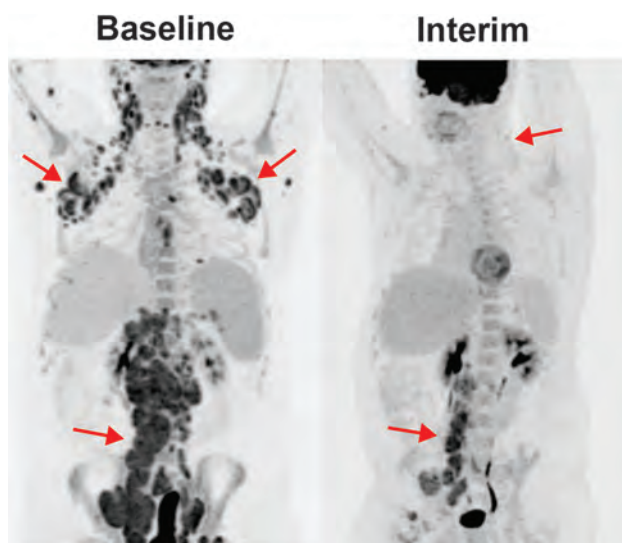


**FIG 3.** A posttreatment D5PS score of 5 but partial metabolic response based on Lugano criteria. Baseline imaging demonstrates diffuse lymphadenopathy, including cervical levels II–IV, axillary, mediastinal, abdominal periaortic/pericaval, and right greater than left iliac chains, with intense FDG avidity (arrows), consistent with a D5PS score of 5. Interim imaging during treatment demonstrates significantly reduced size and FDG avidity of the cervical, axillary, and mediastinal lymphadenopathy (arrows), now predominantly limited to the periaortic/pericaval regions and right greater than left iliac chains. The lymph nodes still have FDG avidity markedly greater than mediastinal blood pool and liver, consistent with a D5PS score of 5, but the reduction in size, number, and intensity results in a Lugano designation of a partial metabolic response.

**Table 3: Hopkins criteria scores for head and neck cancers<sup>a</sup>**

Hopkins Criteria Score <sup>b</sup>	Lesion FDG Uptake	Therapy Response
1	Focal uptake less than IJV	CMR
2	Focal uptake greater than IJV, but less than liver	Likely CMR
3	Diffuse uptake greater than IJV and liver	Likely posttreatment inflammation
4	Focal uptake greater than liver	Likely residual tumor
5	Focal uptake markedly greater than liver	Residual tumor

Note:—IJV indicates internal jugular vein.

<sup>a</sup> Adapted from Ref. 16.

<sup>b</sup> Five-point scale Hopkins criteria scores used to classify head and neck cancer response after treatment; new lesions are considered to be PD.

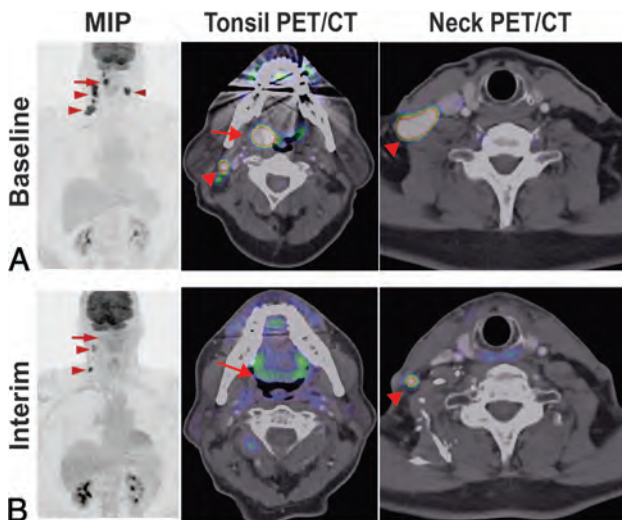


**FIG 4.** Hopkins criteria score of 5 in right tonsillar squamous cell carcinoma, consistent with residual tumor. A 71-year-old man with right tonsillar squamous cell carcinoma. MIP from baseline PET/CT demonstrates a Hopkins criteria score of 5 in the primary right tonsillar tumor (arrow) and right greater than left level II–IV cervical lymph nodes (arrowheads). Examination after radiation and chemotherapy shows resolution of the right tonsillar FDG uptake (arrow) and some of the cervical lymph nodes but persistent, focal, and intense FDG uptake in 2 ipsilateral level III and IV lymph nodes (arrowheads); a Hopkins criteria score of 5 is consistent with residual tumor.

disease was time dependent, and follow-up surveillance imaging was recommended at 1 year after therapy; however, guidelines with regard to posttreatment surveillance imaging are not well established, with some experienced Radiologists suggesting shorter intervals of as little as 12 weeks. Wray et al<sup>25</sup> demonstrated that the Hopkins criteria and FDG-PET/CT

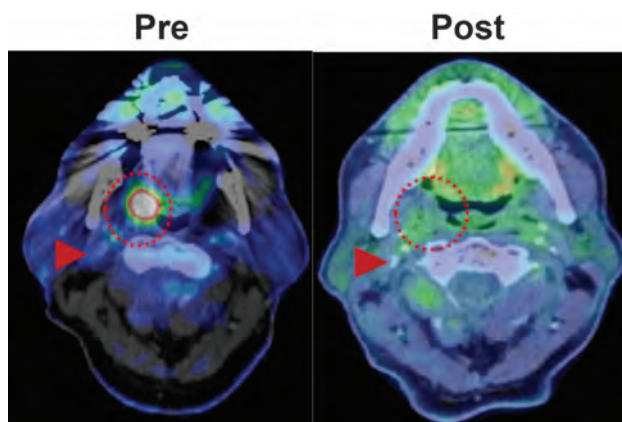


**FIG 5.** Hopkins criteria score of 2 and NI-RADS score of 1 in right tonsillar squamous cell carcinoma, consistent with a CMR. A 71-year-old man with an intensely FDG-avid right tonsillar squamous cell carcinoma (dotted circle) on pretreatment PET/CT. After treatment, the mass has resolved, with FDG uptake in the region just above the adjacent right internal jugular vein (arrowhead) but similar to the surrounding oropharyngeal soft tissues, consistent with a Hopkins criteria score of 2 and an NI-RADS score of 1 at the primary site. By using Hopkins or NI-RADS criteria, the findings are consistent with an overall CMR.

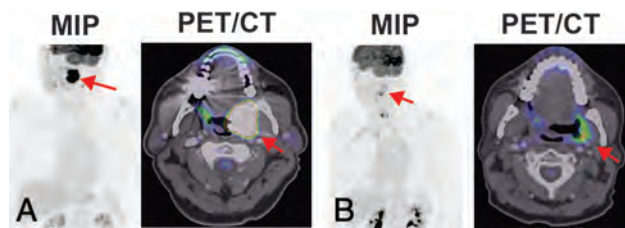


**FIG 6.** An NI-RADS score of 2a in left tonsillar squamous cell carcinoma (SCCa) after chemoradiation, consistent with a Hopkins criteria score of 3 and posttreatment inflammation. A 63-year-old man with a history of left tonsillar SCCa. A, Baseline oblique MIP shows markedly hypermetabolic primary left tonsillar SCCa (arrow). After completion of chemoradiation therapy, repeated FDG PET/CT was obtained. B, Oblique MIP and axial PET/CT show residual hypermetabolic mucosal activity of moderate intensity (arrow) throughout the tonsil bed. The findings are compatible with NI-RADS 2a. Linked management recommendations in the NI-RADS criteria suggest correlation with direct visualization given that such a finding typically represents non-neoplastic FDG uptake. As a comparison, the FDG uptake is greater than the liver and much greater than the internal jugular vein, this is consistent with a Hopkins criteria score of 3. The findings suggest benign posttreatment inflammation. Lesions with this score can be false-negatives and demonstrate intermediate overall survival and progression-free survival compared with scores of 1–2 and 4–5. Due to the false-negative probability, these lesions should be biopsied before altering the treatment plan.

assessment after head and neck squamous cell carcinoma chemoradiotherapy was significantly better than residual neck node size in predicting overall survival and progression-free survival. In an external validation study, Kendi et al<sup>24</sup> investigated the use of the Hopkins criteria in patients with head and neck squamous cell carcinoma after radiation therapy. They found similar degrees of interpreter reliability and overall test statistics, including a specificity of 87.3% and a negative predictive value of 96.5%. These studies demonstrate the widespread applicability of the Hopkins criteria in assessing posttreatment head and neck squamous cell carcinoma disease response.

#### Using the Hopkins Criteria for Evaluating Head and Neck Tumor Treatment Response

The Hopkins criteria in the studies described above were generally performed approximately 5 to 24 weeks after chemoradiotherapy or surgical treatment for head and neck squamous cell carcinoma. The timing and type of treatment seems to have a significant impact on the positive predictive value and sensitivity of the Hopkins criteria. Wray et al<sup>25</sup> indicate that posttreatment inflammatory changes or false-positives can mostly be avoided if the PET/CT is performed  $\geq 12$  weeks after the completion of radiation therapy. Taghipour et al<sup>52</sup> indicate that postsurgical patients may not have as much posttreatment inflammation as postradiation patients, so scans could potentially be performed earlier.

The beauty of qualitative therapy response assessment is again found in the ease and rapid assessment that can be performed, even on MIP images. The tumor response assessments, including CMR, partial metabolic response, no metabolic response, and

**Table 4: NI-RADS risk stratification guidelines<sup>a</sup>**

Description	Category	Imaging Findings	Management
Incomplete	0	New baseline study or unavailable previous imaging	Previous imaging
No evidence of recurrence	1	Posttreatment changes without mass or abnormal FDG uptake	Routine surveillance
Low suspicion (superficial)	2a	Enhancement without FDG uptake or mild/moderate FDG uptake without a mass	Direct visual inspection
Low suspicion (deep)	2b	Enhancement without FDG uptake or mild/moderate FDG uptake without a mass	Short imaging follow-up
High suspicion	3	New or enlarged mass or lymph node, enhancement, and intense FDG uptake	Biopsy
Definitive recurrence	4	Pathologically proved or definite progression	Clinical management

<sup>a</sup> The NI-RADS risk stratification guidelines grade head and neck tumor treatment response; adapted from Ref. 26.

PD, are based on FDG uptake before and after treatment (Figs 4 and 5). The challenge in the Hopkins criteria can often be scores of 3, which demonstrate diffuse areas of FDG avidity consistent with posttreatment inflammatory changes (Fig 6). Without the application of the Hopkins criteria, these areas can often lead to false-positive interpretation of persistent metabolically active tumor. However, even with appropriate use of the Hopkins criteria, false-negatives may occur, and thus Hopkins criteria scores of 3 demonstrate intermediate overall survival and progression-free survival compared with scores of 1–2 and 4–5. Consequently, Hopkins criteria scores of 3 may necessitate biopsy to confirm their posttreatment status.

## NI-RADS GUIDELINES FOR HEAD AND NECK TUMORS

### Development of the NI-RADS Criteria

In 2016, the American College of Radiology (ACR) convened the NI-RADS committee to formulate a reporting and management system with risk stratification for head and neck tumors.<sup>53,54</sup> The guidelines, modeled after BI-RADS, define 6 categories of posttreatment findings for head and neck tumors, which range from an incomplete study to definite disease recurrence, and recommend appropriate steps for follow-up.<sup>26</sup> The imaging findings are based on combined CT of the neck with contrast and FDG-PET/CT findings (Table 4).<sup>26</sup> The findings of the CT of the neck characterize disease recurrence by soft-tissue masses or enhancement, whereas the PET/CT findings characterize the recurrence by PET avidity of lesions relative to background (Table 4). The benefit of NI-RADS is that it combines the morphologic findings from the CT of the neck, including CT appearance, size, and enhancement, and the metabolic PET/CT findings (Figs 5 and 6).<sup>26</sup>

In 2017, Krieger et al<sup>54</sup> analyzed the accuracy of NI-RADS in follow-up scans for varying head and neck cancers. In analyzing 618 head and neck lesions, 85.4% were scored NI-RADS 1 and demonstrated a 3.8% recurrence, 9.4% were scored NI-RADS 2 and demonstrated a 17.2% recurrence, and 5.2% were scored NI-RADS 3 and demonstrated a 59.4% recurrence.<sup>54</sup> The overall AUC accuracy curve for the NI-RADS criteria gave a value of 0.787 (a perfect test would give a value of 1.0). They also demonstrated that the combination of a CT of the neck and PET/CT functioned better than either technique alone. In 2018, Wangaryattawanich

et al<sup>55</sup> demonstrated the ability of the NI-RADS criteria to rule out disease recurrence in head and neck cancers after treatment. When using 2-year disease-free survival as the reference standard, the negative predictive value for patients with NI-RADS 2 scores on the first posttreatment PET/CT was 85%, compared with 91% for patients with NI-RADS 1 scores.

### Comparison of the Hopkins and NI-RADS Criteria for Head and Neck Cancers

Similar to the Hopkins criteria, the NI-RADS guidelines use qualitative mechanisms for characterizing disease recurrence. Unlike the Hopkins criteria, the NI-RADS guidelines use both CT and PET/CT findings. Although the Hopkins criteria reference FDG uptake to internal jugular vein and liver uptake, the NI-RADS reference uptake is not standardized, and it is up to interpreters to determine what constitutes moderate versus intense FDG avidity relative to background, a significant factor in determining a score of NI-RADS 2 (low suspicion) versus 3 (high suspicion) (Figs 5 and 6).<sup>26</sup> The NI-RADS guidelines do incorporate recurrence risk rates and definitive management guidelines.<sup>26</sup> In addition, in using the morphologic or anatomic features on CT, NI-RADS can improve overall accuracy in interpreting non-neoplastic patterns of FDG uptake.<sup>56</sup>

## CONCLUSIONS

With the widespread institution of FDG-PET/CT, qualitative, tumor response classification systems have been developed that allow for simple, yet accurate, early evaluations of posttreatment response. The Lugano classification uses PET/CT to characterize the posttreatment lymphoma response. The Hopkins criteria were developed to similarly characterize the posttreatment response in head and neck tumors. The NI-RADS criteria use contrast CT and PET/CT to characterize posttreatment response. These 3 treatment response assessments use qualitative means of comparison that can be performed readily in the busy clinical setting with standard PET/CT equipment and software. The response assessments, particularly in well-trained interpreters, can accurately predict overall survival and progression-free survival. In addition, the response assessments can improve communication with clinicians to drive management decisions. We recommend that radiologists and nuclear medicine physicians

consider using these classifications when reporting posttreatment response on follow-up PET/CTs.

## REFERENCES

1. US Cancer Statistics Working Group. **US Cancer Statistics Data Visualizations Tool**. 2018 <https://www.cdc.gov/cancer/uscs/dataviz/index.htm>. Accessed October 16, 2019
2. Therasse P, Arbuick SG, Eisenhauer EA, et al. **New guidelines to evaluate the response to treatment in solid tumors**. European Organization for Research and Treatment of Cancer, National Cancer Institute of the United States, National Cancer Institute of Canada. *J Natl Cancer Inst* 2000;92:205–16 CrossRef Medline
3. Eisenhauer EA, Therasse P, Bogaerts J, et al. **New response evaluation criteria in solid tumours: Revised RECIST guideline (version 1.1)**. *Eur J Cancer* 2009;45:228–47 CrossRef Medline
4. Chalian H, Töre HG, Horowitz JM, et al. **Radiologic assessment of response to therapy: comparison of RECIST versions 1.1 and 1.0**. *Radiographics* 2011;31:2093–105 CrossRef Medline
5. Patel CN, Goldstone AR, Chowdhury FU, et al. **FDG PET/CT in oncology: “raising the bar”**. *Clin Radiol* 2010;65:522–35 CrossRef Medline
6. Sheikhabaei S, Mena E, Pattanayak P, et al. **Molecular imaging and precision medicine: PET/computed tomography and therapy response assessment in oncology**. *PET Clin* 2017;12:105–18 CrossRef Medline
7. Eugene T, Corradini N, Carlier T, et al. **<sup>18</sup>F-FDG-PET/CT in initial staging and assessment of early response to chemotherapy of pediatric rhabdomyosarcomas**. *Nucl Med Commun* 2012;33:1089–95 CrossRef Medline
8. MacManus MP, Seymour JF, Hicks RJ. **Overview of early response assessment in lymphoma with FDG-PET**. *Cancer Imaging* 2007;7:10–8 CrossRef Medline
9. Passero VA, Branstetter BF, Shuai Y, et al. **Response assessment by combined PET-CT scan versus CT scan alone using RECIST in patients with locally advanced head and neck cancer treated with chemoradiotherapy**. *Ann Oncol* 2010;21:2278–83 CrossRef Medline
10. Tiseo M, Ippolito M, Scarlattei M, et al. **Predictive and prognostic value of early response assessment using <sup>18</sup>FDG-PET in advanced non-small cell lung cancer patients treated with erlotinib**. *Cancer Chemother Pharmacol* 2014;73:299–307 CrossRef Medline
11. Wahl RL, Jacene H, Kasamon Y, et al. **From RECIST to PERCIST: Evolving considerations for PET response criteria in solid tumors**. *J Nucl Med* 2009;50(Suppl 1):122S–50S CrossRef Medline
12. Younes A, Hilden P, Coiffier B, et al. **International Working Group consensus response evaluation criteria in lymphoma (RECIL 2017)**. *Ann Oncol* 2017;28:1436–47 CrossRef
13. Meignan M, Gallamini A, Meignan M, et al. **Report on the First International Workshop on interim-PET scan in lymphoma**. *Leuk Lymphoma* 2009;50:1257–60 CrossRef Medline
14. Juweid ME, Stroobants S, Hoekstra OS, et al. **Use of positron emission tomography for response assessment of lymphoma: consensus of the Imaging Subcommittee of International Harmonization Project in Lymphoma**. *J Clin Oncol* 2007;25:571–78 CrossRef Medline
15. Johnson SA, Kumar A, Matasar MJ, et al. **Imaging for staging and response assessment in lymphoma**. *Radiology* 2015;276:323–38 CrossRef Medline
16. Marcus C, Ciarallo A, Tahari AK, et al. **Head and neck PET/CT: therapy response interpretation criteria (Hopkins criteria)—inter-reader reliability, accuracy, and survival outcomes**. *J Nucl Med* 2014;55:1411–16 CrossRef Medline
17. Valkema MJ, Noordman BJ, Wijnhoven BPL, et al. **Accuracy of <sup>18</sup>F-FDG PET/CT in predicting residual disease after neoadjuvant chemoradiotherapy for esophageal cancer**. *J Nucl Med* 2019;pii: jnmed.118.224196 [Epub ahead of print] CrossRef Medline
18. Sheikhabaei S, Mena E, Marcus C, et al. **<sup>18</sup>F-FDG PET/CT: therapy response assessment interpretation (Hopkins criteria) and survival outcomes in lung cancer patients**. *J Nucl Med* 2016;57:855–60 CrossRef Medline
19. Sheikhabaei S, Wray R, Young B, et al. **<sup>18</sup>F-FDG-PET/CT therapy assessment of locally advanced pancreatic adenocarcinoma: impact on management and utilization of quantitative parameters for patient survival prediction**. *Nucl Med Commun* 2016;37:231–38 CrossRef
20. Sole CV, Calvo FA, Alvarez E, et al. **Metabolic and molecular relative percentage coreduction in patients with locally advanced rectal cancer treated with neoadjuvant therapy**. *Eur J Nucl Med Mol Imaging* 2016;43:1444–52 CrossRef Medline
21. Rodado-Marina S, Coronado-Poggio M, García-Vicente AM, et al. **Clinical utility of <sup>18</sup>F-fluorocholine positron-emission tomography/computed tomography (PET/CT) in biochemical relapse of prostate cancer after radical treatment: results of a multicentre study**. *BJU Int* 2015;115:874–83 CrossRef Medline
22. Khiewvan B, Torigian DA, Emamzadehfard S, et al. **Update of the role of PET/CT and PET/MRI in the management of patients with cervical cancer**. *Hell J Nucl Med* 2016;19:254–68
23. Cheson BD, Fisher RI, Barrington SF, et al. **Recommendations for initial evaluation, staging, and response assessment of Hodgkin and non-Hodgkin lymphoma: the Lugano classification**. *J Clin Oncol* 2014;32:3059–68 CrossRef Medline
24. Kendi AT, Brandon D, Switchenko J, et al. **Head and neck PET/CT therapy response interpretation criteria (Hopkins criteria) - external validation study**. *Am J Nucl Med Mol Imaging* 2017;7:174–80 Medline
25. Wray R, Sheikhabaei S, Marcus C, et al. **Therapy response assessment and patient outcomes in head and neck squamous cell carcinoma: FDG PET Hopkins criteria versus residual neck node size and morphologic features**. *AJR Am J Roentgenol* 2016;207:641–47 CrossRef
26. Aiken AH, Rath TJ, Anzai Y, et al. **ACR Neck Imaging Reporting and Data Systems (NI-RADS): A White Paper of the ACR NI-RADS Committee**. *J Am Coll Radiol* 2018;15:1097–108 CrossRef Medline
27. Barrington SF, Mikhael NG, Kostakoglu L, et al. **Role of imaging in the staging and response assessment of lymphoma: consensus of the International Conference on Malignant Lymphomas Imaging Working Group**. *J Clin Oncol* 2014;32:3048–58 CrossRef Medline
28. Barrington SF, Qian W, Somer EJ, et al. **Concordance between four European centres of PET reporting criteria designed for use in multicentre trials in Hodgkin lymphoma**. *Eur J Nucl Med Mol Imaging* 2010;37:1824–33 CrossRef Medline
29. Barrington SF, Kluge R. **FDG PET for therapy monitoring in Hodgkin and non-Hodgkin lymphomas**. *Eur J Nucl Med Mol Imaging* 2017;44:97–110 CrossRef Medline
30. Mikhael NG, Hutchings M, Fields PA, et al. **FDG-PET after two to three cycles of chemotherapy predicts progression-free and overall survival in high-grade non-Hodgkin lymphoma**. *Ann Oncol* 2005;16:1514–23 CrossRef Medline
31. Razek A, Shamaa S, Lattif MA, et al. **Inter-observer agreement of whole-body computed tomography in staging and response assessment in lymphoma: The Lugano Classification**. *Pol J Radiol* 2017;82:441–47 CrossRef
32. Burggraaff CN, Cornelisse AC, Hoekstra OS, et al. **Interobserver agreement of interim and end-of-treatment <sup>18</sup>F-FDG PET/CT in diffuse large B-cell lymphoma: impact on clinical practice and trials**. *J Nucl Med* 2018;59:1831–36 CrossRef Medline
33. Kluge R, Chavdarova L, Hoffmann M, et al. **Inter-reader reliability of early FDG-PET/CT response assessment using the Deauville scale after 2 cycles of intensive chemotherapy (OEPA) in Hodgkin’s lymphoma**. *PLoS One* 2016;11:e0149072 CrossRef
34. Sawan P, Rebeiz K, Schoder H, et al. **Specialized second-opinion radiology review of PET/CT examinations for patients with diffuse**

- large B-cell lymphoma impacts patient care and management. *Medicine (Baltimore)* 2017;96:e9411 CrossRef
35. Ceriani L, Barrington S, Biggi A, et al. Training improves the inter-observer agreement of the expert positron emission tomography review panel in primary mediastinal B-cell lymphoma: interim analysis in the ongoing International Extranodal Lymphoma Study Group-37 study. *Hematol Oncol* 2017;35:548–53 CrossRef Medline
  36. Cheson DB. Staging and response assessment in lymphomas: the new Lugano classification. *Chin Clin Oncol* 2015;4:5
  37. Mylam KJ, El-Galaly TC, Hutchings M, et al. Prognostic impact of clinician-based interpretation of <sup>18</sup>F-fluorodeoxyglucose positron emission tomography/computed tomography reports obtained in patients with newly diagnosed diffuse large B-cell lymphoma. *Leuk Lymphoma* 2014;55:1563–69 CrossRef Medline
  38. Cottreau AS, El-Galaly TC, Becker S, et al. Predictive value of PET response combined with baseline metabolic tumor volume in peripheral T-cell lymphoma patients. *J Nucl Med* 2018;59:589–95 CrossRef Medline
  39. Albano D, Bosio G, Re A, et al. Metabolic behavior and prognostic value of early and end of treatment 18F-FDG PET/CT in adult Burkitt's lymphoma: the role of Deauville and IHP criteria. *Leuk Lymphoma* 2019;60:326–33 CrossRef Medline
  40. Qin C, Yang S, Sun X, et al. 18F-FDG PET/CT for prognostic stratification of patients with extranodal natural killer/t-cell lymphoma. *Clin Nucl Med* 2019;44:201–08 CrossRef Medline
  41. Gallamini A, Barrington SF, Biggi A, et al. The predictive role of interim positron emission tomography for Hodgkin lymphoma treatment outcome is confirmed using the interpretation criteria of the Deauville five-point scale. *Haematologica* 2014;99:1107–13 CrossRef Medline
  42. Jiang C, Su M, Kosik RO, et al. The Deauville 5-Point Scale improves the prognostic value of interim FDG PET/CT in extranodal natural killer/T-cell lymphoma. *Clin Nucl Med* 2015;40:767–73 CrossRef Medline
  43. Kong Y, Qu L, Li Y, et al. Predictive significance of a new prognostic score for patients with diffuse large B-cell lymphoma in the interim-positron emission tomography findings. *Medicine (Baltimore)* 2016;95:e2808. CrossRef
  44. Bakhshi S, Bhethanabhotla S, Kumar R, et al. Posttreatment PET/CT rather than interim PET/CT using Deauville criteria predicts outcome in pediatric Hodgkin lymphoma: A prospective study comparing PET/CT with conventional imaging. *J Nucl Med* 2017; 58:577–83 CrossRef Medline
  45. Lombion N, Robin P, Tempescul A, et al. Prognostic value of interim FDG PET-CT in patients older than 60 years with diffuse large B-cell lymphoma treated by PMitCEBO plus rituximab: comparison between Deauville 5-point scale and International Harmonization Project criteria. *Q J Nucl Med Mol Imaging* 2016 [Epub ahead of print] Medline
  46. Kim J, Song YS, Lee JS, et al. Risk stratification of diffuse large B-cell lymphoma with interim PET-CT based on different cutoff Deauville scores. *Leuk Lymphoma* 2018;59:340–47 CrossRef Medline
  47. Baratto L, Davidzon GA, Moghbel M, et al. Comparison between different PET and CT-based imaging interpretation criteria at interim imaging in patients with diffuse large B-cell lymphoma. *Clin Nucl Med* 2018;43:1–8 CrossRef Medline
  48. Yuan L, Kreissl MC, Su L, et al. Prognostic analysis of interim <sup>18</sup>F-FDG PET/CT in patients with diffuse large B cell lymphoma after one cycle versus two cycles of chemotherapy. *Eur J Nucl Med Mol Imaging* 2019;46:478–88 CrossRef Medline
  49. Isik EG, Kuyumcu S, Kebudi R, et al. Prediction of outcome in pediatric Hodgkin lymphoma based on interpretation of <sup>18</sup>F-FDG-PET/CT according to  $\Delta$ SUV<sub>max</sub>, Deauville 5-point scale and IHP criteria. *Ann Nucl Med* 2017;31:660–68 CrossRef Medline
  50. Kostakoglu L, Goy A, Martinelli G, et al. FDG-PET is prognostic and predictive for progression-free survival in relapsed follicular lymphoma: exploratory analysis of the GAUSS study. *Leuk Lymphoma* 2017;58:372–81 CrossRef Medline
  51. Van den Wyngaert T, Helsen N, Carp L, et al. Fluorodeoxyglucose-positron emission tomography/computed tomography after concurrent chemoradiotherapy in locally advanced head-and-neck squamous cell cancer: The ECLYPS Study. *J Clin Oncol* 2017; 35:3458–64 CrossRef Medline
  52. Taghipour M, Sheikhabahaei S, Wray R, et al. FDG PET/CT in patients with head and neck squamous cell carcinoma after primary surgical resection with or without chemoradiation therapy. *AJR Am J Roentgenol* 2016;206:1093–1100 CrossRef Medline
  53. Aiken AH, Farley A, Bagnon KL, et al. Implementation of a novel surveillance template for head and neck cancer: Neck Imaging Reporting and Data System (NI-RADS). *J Am Coll Radiol* 2016; 13:743–746.e1 CrossRef Medline
  54. Krieger DA, Hudgins PA, Nayak GK, et al. Initial performance of NI-RADS to predict residual or recurrent head and neck squamous cell carcinoma. *AJNR Am J Neuroradiol* 2017;38:1193–99 CrossRef Medline
  55. Wangaryattawanich P, Branstetter BF, Hughes M, et al. Negative predictive value of NI-RADS category 2 in the first posttreatment FDG-PET/CT in head and neck squamous cell carcinoma. *AJNR Am J Neuroradiol* 2018;39:1884–88 CrossRef Medline
  56. Rangaswamy B, Fardanesh MR, Genden EM, et al. Improvement in the detection of locoregional recurrence in head and neck malignancies: F-18 fluorodeoxyglucose-positron emission tomography/computed tomography compared to high-resolution contrast-enhanced computed tomography and endoscopic examination. *Laryngoscope* 2013;123:2664–69 CrossRef Medline

# Imaging Findings Related to the Valsalva Maneuver in Head and Neck Radiology

 A.A. Madhavan,  C.M. Carr,  M.L. Carlson, and  J.I. Lane



## ABSTRACT

**SUMMARY:** Forced exhalation against a closed glottis, known as the Valsalva maneuver, is an important clinical diagnostic and therapeutic tool due to its physiologic effects. Several unique conditions and anatomic changes can occur with repetitive or acute changes in pressure from the Valsalva maneuver. We will discuss and review various pertinent head and neck imaging cases with findings resulting from induced pressure gradients, including the Valsalva maneuver. Additionally, we will demonstrate the diagnostic utility of the Valsalva maneuver in head and neck radiology.

The Valsalva maneuver, defined as forceful exhalation against a closed glottis, has multiple physiologic effects. The maneuver can be divided into 4 major phases of physiologic response: First, the initial exhalation increases intrathoracic pressure and forces blood into the left atrium. Second, the high intrathoracic pressure causes decreased systemic venous return. Next, as intrathoracic pressure returns to normal, cardiac output oscillates due to mixed effects from aortic dilation and improving venous return. Finally, once thoracic pressure normalizes, cardiac output stabilizes and sometimes transiently increases above baseline.<sup>1</sup> Throughout this process, the maneuver also results in opening the Eustachian tube, partially due to contraction of the tensor veli palatini muscle. While the complex effects of the Valsalva maneuver have multiple clinical applications, the increase in intrathoracic pressure, decreased systemic venous return, and opening of the Eustachian tube are particularly relevant to the following discussion (Table 1). A wide spectrum of head and neck imaging findings has been attributed to the Valsalva maneuver or other similar induced-pressure gradients. Knowledge and recognition of these findings can be especially valuable to the neuroradiologist.

The goal of this review was to summarize common entities with imaging findings related to the Valsalva or similar physiologic maneuvers, accompanied by case examples (Table 2). Most cases had either a documented clinical history consistent with acute or chronic repetitive use of the Valsalva maneuver or were used to demonstrate how the Valsalva maneuver can be used during imaging to accentuate findings in a diagnostically beneficial way. A minority of cases had an uncertain-but-suspected clinical history of repetitive Valsalva maneuvers. These were included as classic examples of Valsalva-related pathology.

## VALSALVA-RELATED CASES BY ANATOMIC LOCATION

### Neck: Spontaneous Pneumomediastinum

Pneumomediastinum is a well-recognized condition commonly resulting from esophageal or airway trauma.<sup>2</sup> It is especially pertinent to neuroradiologists in the emergency setting because the findings may be initially seen on neck imaging as air dissects cranially from the superior mediastinum. Valsalva behaviors are among the most common causes of spontaneous pneumomediastinum. Overall, studies on pneumomediastinum have shown coughing, vomiting, drug inhalation, and physical activity to be among the most frequent inciting events.<sup>3</sup> For example, pneumomediastinum can occur due to barotrauma when users attempt inspiration through a high-resistance smoking apparatus, which causes an increase in alveolar air volume, a decrease in perialveolar pressure, and rupture due to the induced pressure gradient.<sup>4</sup> A similar phenomenon can occur with cocaine inhalation. In this case, pressure changes due to inhalation and chronic ischemic necrosis of the pharynx secondary to cocaine abuse lead to pharyngeal perforation and pneumomediastinum. Although less common, pneumomediastinum has also been

Received June 13, 2019; accepted after revision September 23.

From the Departments of Radiology (A.A.M., C.M.C., J.I.L.) and Otolaryngology-Head and Neck Surgery (M.L.C.), Mayo Clinic School of Medicine, Rochester, Minnesota.

Internal departmental funding was used without commercial sponsorship or support.

Paper previously presented at: Annual Meeting of the American Society of Head and Neck Radiology, September 26–20, 2018; Savannah, Georgia.

Please address correspondence to Ajay A. Madhavan, MD, Department of Radiology, Mayo Clinic, 200 1st St SW, Rochester, MN 55905; e-mail: madhavan.ajay@mayo.edu

 Indicates open access to non-subscribers at [www.ajnr.org](http://www.ajnr.org)

<http://dx.doi.org/10.3174/ajnr.A6309>

**Table 1: Net physiologic effects during the Valsalva maneuver**

Pressure Changes	Cardiovascular Effects
Increased intrathoracic pressure	Decreased thoracic venous return
Increased extrathoracic airway pressure	Distention of extrathoracic venous system
Increased middle ear pressure	Decreased stroke volume
Increased intracranial pressure	Decreased cardiac output
Opening of the Eustachian tube	Peripheral vascular constriction

**Table 2: Imaging findings associated with the Valsalva maneuver**

Neck	Skull Base/Face	Orbit/Head
Jugular phlebectasia	Nontraumatic orbital floor fracture	Orbital varix
Laryngocele Spontaneous pneumomediastinum	Pneumoparotid Hyperpneumatization of the skull base	Transient global amnesia Spontaneous pneumocephalus

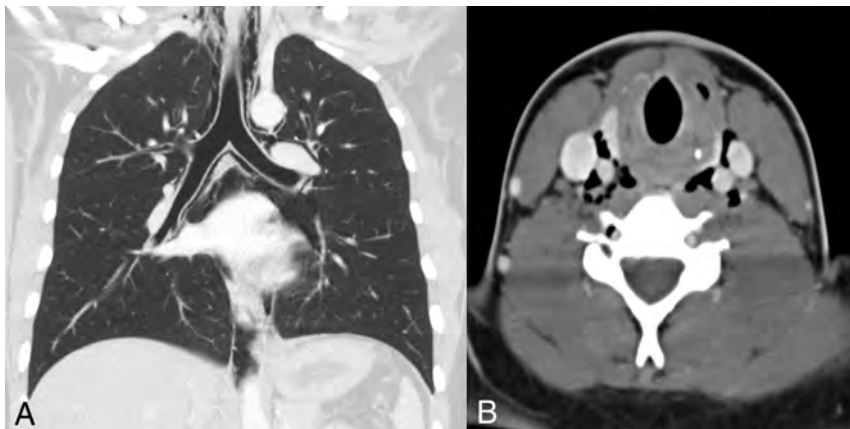


**FIG 1.** Spontaneous pneumomediastinum. A 19-year-old man with a history of cyclic vomiting syndrome presented to the emergency department after several bouts of severe vomiting with subsequent neck and chest pain. Chest (A) and neck (B) CT images show pneumomediastinum with air dissecting superiorly into both carotid spaces. An esophagram (not shown) demonstrated no evidence of esophageal perforation. The patient was observed for 3 days and discharged uneventfully.

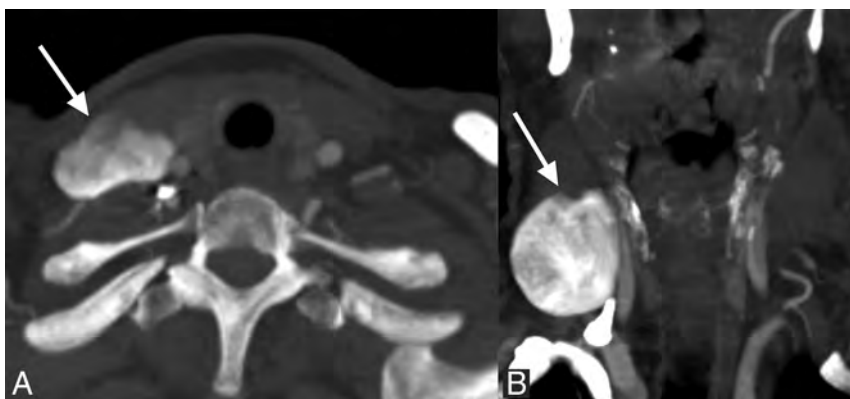


**FIG 2.** Jugular phlebectasia. A 72-year-old woman with headaches had a neck CTA performed to evaluate vascular disease. Axial (A) and coronal (B) CTA images show a large right jugular venous aneurysm (arrows). This was deemed to be benign without need for treatment.

previously reported with more benign Valsalva behaviors involving the airway, such as repetitively blowing into a bottle.<sup>5,6</sup>

Repetitive vomiting can also cause pneumomediastinum. For instance, cyclic vomiting syndrome (cannabinoid hyperemesis

syndrome), a rare condition of severe repeated bouts of vomiting in daily long-term users of marijuana, may cause pneumomediastinum by increasing intra-alveolar pressure (Fig 1).

Pneumomediastinum will slowly resolve as air is resorbed, provided that the underlying cause is reversed. The diagnosis is often made with a chest radiograph, though CT and an esophagram can help define the extent of the abnormality and suggest a cause.

### **Neck: Jugular Phlebectasia**

While it is very common to have asymmetry in the size of the internal jugular veins, there are uncommon reports of focal aneurysmal dilation of the jugular vein. Jugular phlebectasia is typically an incidental and benign finding but can present with neck pain or cosmetic concerns (Fig 2). This is often accentuated by straining or the Valsalva maneuver (Fig 3). While many of these cases present during childhood, this phenomenon has also been reported in adults. CT, sonography, and MR imaging can all be used to establish this diagnosis, but the use of the Valsalva maneuver is critical in inducing maximum dilation of the jugular vein. Treatment is not required if the patient is asymptomatic,<sup>7</sup> but surgery has been used in some cases due to symptoms or for cosmetic indications.<sup>8</sup>

### **Neck: Laryngocele**

Laryngoceles are air-filled dilations of the saccule of the laryngeal ventricle. Internal laryngoceles are confined to the ventricle, while external laryngoceles herniate beyond the thyrohyoid membrane. Laryngoceles are often asymptomatic and found incidentally at imaging (Fig 4A).<sup>9</sup> Laryngoceles usually contain air and communicate with the lumen of the larynx; however, if obstructed, they may fill with mucus (Fig 4B). External laryngoceles may be more visible and can present as a neck mass. Internal laryngoceles, when symptomatic, can contribute to airway dysfunction such as hoarseness, coughing, dysphonia, or, less commonly, airway compromise. Laryngoceles are associated with Valsalva-related maneuvers. For example, chronic cough and occupations such as glassblowing can cause

laryngoceles. Additionally, laryngoceles have been observed to enlarge in real-time with the Valsalva maneuver, which could be used to increase diagnostic certainty in unclear cases.<sup>9</sup> In some cases, an etiology for laryngoceles may not be found.<sup>10</sup> Because these are usually incidental, the role of imaging is often to exclude a malignant cause, such as laryngeal cancer causing a

secondary laryngocele. Simple excision can be performed for symptomatic cases.<sup>11</sup>

### Skull Base/Face: Periorbital Emphysema and Nontraumatic Orbital Floor Fracture

Periorbital emphysema, often in the setting of blowout fractures of the orbit, is commonly seen in trauma. However, several cases of periorbital emphysema and even nontraumatic orbital fractures have been reported. These have been reported to occur with activities that cause increased intranasal pressure often related to forceful Valsalva maneuvers and include weight-lifting, pressure changes from airplane travel or free diving, and even forceful nose-blowing (Fig 5). In addition, some of these have occurred in the setting of chronic paranasal sinus disease, which has been hypothesized to weaken the orbital floor, making these individuals more susceptible to nontraumatic pathologic fractures.<sup>12</sup> Treatment is similar to that of traumatic cases and depends on the presence of surgical abnormalities, such as entrapment, compartment syndrome, or persistent diplopia. If no surgical treatment is required, patients are educated to avoid any activities that raise intranasal pressure.

### Skull Base/Face: Pneumoparotid

The term “pneumoparotid” indicates the presence of air within the parotid gland parenchyma, which may extend from forced air through the parotid duct. This may occur with an intraoral pressure increase (eg, blowing up a balloon, playing the trumpet, or with mask anesthesia), which causes air to reflux through the Stenson duct. Pneumoparotid is more likely to occur in patients with compromised natural protective mechanisms. For example, dilation of the Stenson duct, masseter hypertrophy, or buccinator muscle weakness can predispose to pneumoparotid by altering the anatomy of the mucosa normally sealing the duct entrance.<sup>13</sup>

Acute cases can occur in the setting of dental procedures using air-powered cleaning devices that rapidly increase intraoral pressure up to 20-fold above normal.<sup>14</sup> Chronic or recurrent

cases often occur in occupational settings such as glassblowing or wind instrument playing. Nonoccupational causes include cystic fibrosis, obstructive pulmonary disease, or other diseases that lead to a chronic cough.<sup>15</sup> Additionally, pneumoparotid can be seen in patients with repetitive psychosocial-related Valsalva behaviors (Fig 6). Patients may be misdiagnosed with parotitis because they will appear to have swelling and pain localized to the parotid region. In some cases, pneumoparotid can be clinically distinguished from parotitis by the presence of crepitus with external palpation of the gland. Most pneumoparotid cases will have concomitant infection/inflammation due to the abundant oral flora refluxing into

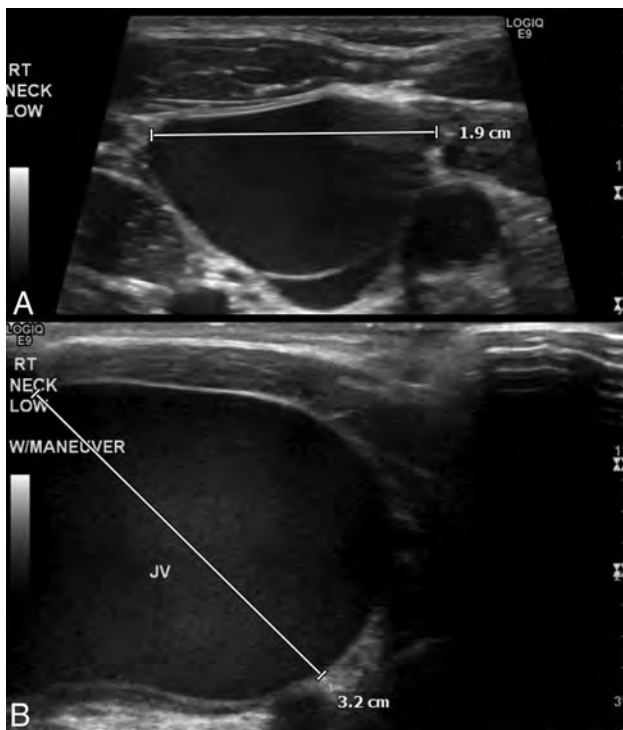


**FIG 3.** Inducible jugular phlebectasia. A 3-year-old boy presented with intermittent right-neck swelling. Sonographic images of the right neck with (A) and without (B) the use of the Valsalva maneuver show significant enlargement of the right internal jugular vein with Valsalva. After additional work-up to exclude any associated cardiovascular or genetic abnormality, the family was reassured that this was consistent with benign jugular phlebectasia.

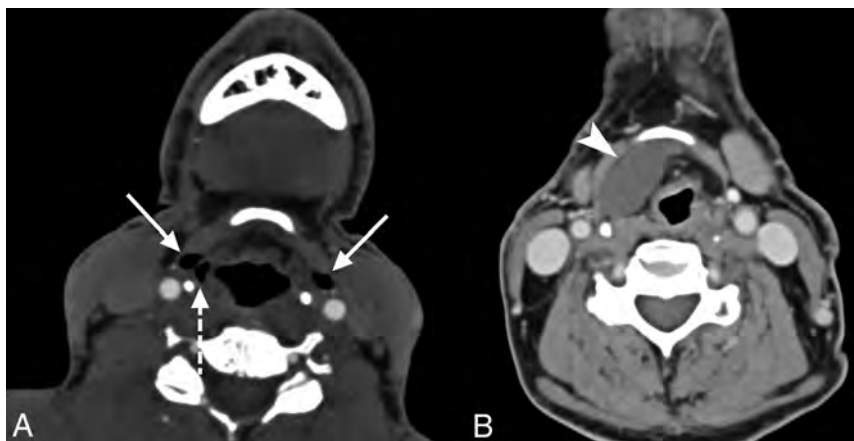


**FIG 4.** Laryngocele. A 54-year-old with recent viral upper respiratory infection underwent a contrast-enhanced neck CT. Axial contrast images from this patient show mixed internal and external laryngoceles (A, solid and dashed arrows, respectively). Axial contrast-enhanced CT in an asymptomatic 69-year-old (B) shows a fluid-filled internal laryngocele (arrowhead), which was subsequently resected to confirm the diagnosis.

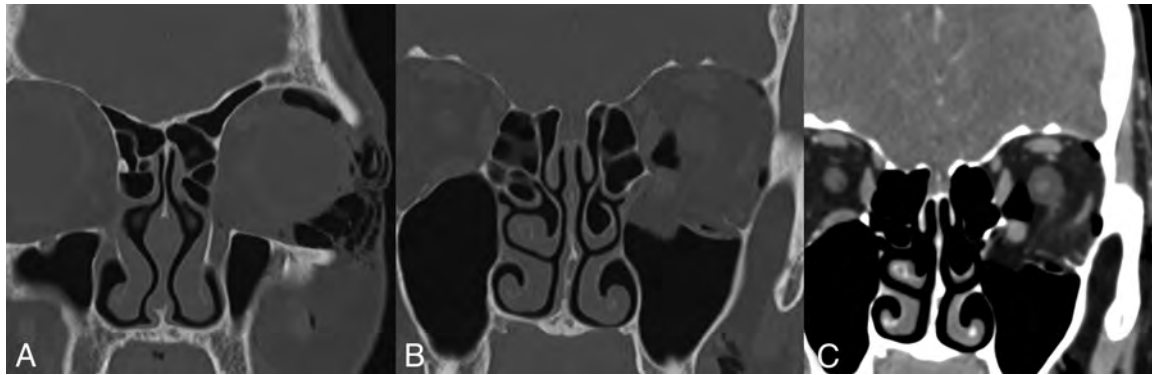


**FIG 5.** Spontaneous orbital floor fracture. A 58-year-old woman with chronic sinusitis who presented with sudden left periorbital swelling that started after forcefully blowing her nose. Coronal noncontrast CT images with bone (A and B) and soft-tissue (C) windows demonstrate an open-door-type left orbital floor fracture and orbital/periorbital emphysema. After ophthalmology consultation, which excluded any evidence of orbital muscle entrapment or compartment syndrome, she was discharged with a short course of antibiotics without incident.

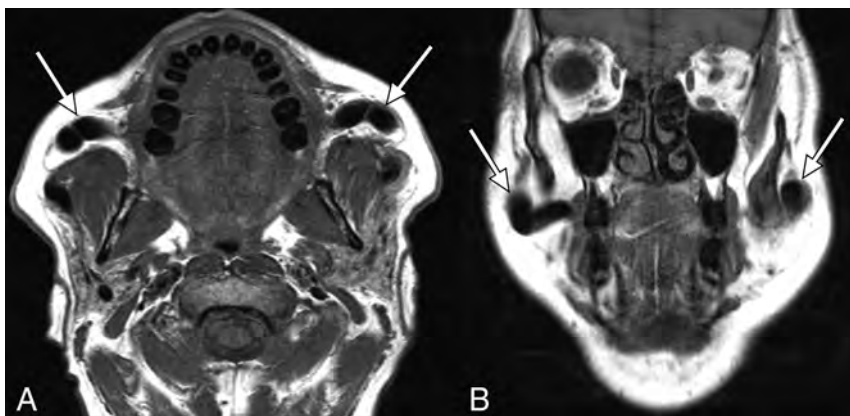


**FIG 6.** Pneumoparotid. A 57-year-old man was referred to the Ear, Nose and Throat department for chronic bilateral parotid swelling and pain, having been previously treated with antibiotics for parotitis with no symptom improvement. The patient reported periodically massaging his parotid glands, which expressed bubbly saliva into his mouth and temporarily alleviated his symptoms. Axial T1-weighted noncontrast axial (A) and coronal (B) MR images demonstrate marked dilation of the parotid ducts bilaterally (arrows). On further questioning, the patient recalled that he had been chronically pursing his lips and putting pressure inside his mouth. He was advised to avoid this in the future and to return should his symptoms worsen.

the duct. The main role of cross-sectional imaging is to identify air in the parotid gland/duct and evaluate the extent of disease. Moreover, imaging may identify dissection of air into the parapharyngeal or retropharyngeal spaces, which can occur in cases of a particularly high-pressure pneumoparotid.<sup>16</sup> Treatment is usually conservative, with patient education being key.

#### **Skull Base/Face: Hyperpneumatization of the Skull Base**

Pneumatization of the skull base and paranasal sinuses occurs in 3 stages: infant (younger than 2 years), transitional (2–4 years), and adult. Pneumatization can be developmentally exuberant, which is considered a normal variant.<sup>17</sup> However, hyperpneumatization and pneumatization of unusual locations like the craniocervical junction have also been associated with repetitive Valsalva maneuvers. It is thought that during the Valsalva maneuver, a ball valve mechanism occurs wherein air is forced into the Eustachian tube and subsequently trapped (Fig 7).<sup>18</sup> Coughing and high-altitude travel can lead to

hyperpneumatization as well, putatively through the same mechanism. Skull base hyperpneumatization through these mechanisms is not entirely benign. The high pressure associated with this process can induce bone ischemia and lead to microfractures.<sup>19</sup> Additionally, hyperpneumatization has been reported to extend to the craniocervical junction and epidural space.<sup>20</sup> This likely occurs due to venous transmission of air and the presence of microfractures, respectively. Fortunately, hyperpneumatization and epidural air have been shown to be reversible, sometimes by simply instructing patients to avoid repetitive Valsalva maneuvers. However, more aggressive treatment such as tympanic pressure equalization via ventilation tubes can be necessary.

Patients with skull base hyperpneumatization should be advised to avoid contact sports due to the increased risk of traumatic fracture.<sup>19</sup>

It is important to document the presence of skull base hyperpneumatization. Skull base surgical approaches may be altered if important neurovascular structures may have unexpected anatomy due to extended areas of dehiscence. Extreme skull base pneumatization also carries an elevated risk of CSF leak during a skull base or intracranial operation. Last, hyperpneumatization must be clearly differentiated from pathologic osseous lucency.<sup>17</sup>

#### **Orbit: Orbital Varix**

Orbital varices can be classified as primary (congenital/idiopathic) or secondary, often due to upstream high-flow vascular lesions such as intracranial arteriovenous malformations, carotid cavernous fistulas, or dural arteriovenous fistulas. Overall, they are quite rare and make up a minority of orbital lesions (approximately 1%–2%). They typically present in the second or third decade affecting males and females equally. Most exhibit

characteristic distension with maneuvers that increase venous pressure (eg, coughing, breath-holding) because they have a large communication with the venous system. This is termed “stress proptosis,” which is dramatic protrusion of the eye with any Valsalva-type maneuver. This ability to enlarge with a Valsalva maneuver is key to imaging and confirming the diagnosis (Fig 8). Occasionally, the venous communication is minimal, and these

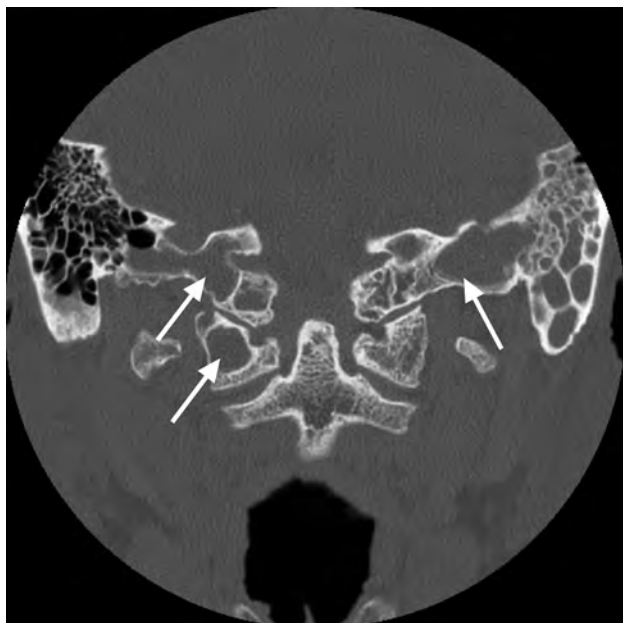


**FIG 7.** Hyperpneumatization of the skull base. A 47-year-old woman was referred to the Ear, Nose and Throat department for chronic allergies that caused her to habitually clear her throat. Coronal noncontrast CT of the skull base shows hyperpneumatization of the temporal bones, CI ring, and dens, which are secondarily opacified (arrows).



**FIG 8.** Orbital varix. A 70-year-old woman who presented due to an orbital mass incidentally discovered on an outside brain MR imaging. Axial (A and C) and coronal (B and D) CT images of the orbits without (A and B) and with (C and D) a Valsalva maneuver demonstrate inducible enlargement of a lobular structure in the right orbit (arrows), consistent with a varix. The patient subsequently reported right-eye fullness when bending over. No additional treatment was pursued.

cases can present with acute onset of painful proptosis relating to thrombosis and hemorrhage.<sup>21</sup> Intervention, either surgical or endovascular, is usually reserved for symptomatic cases resulting from mass effect or thrombosis.<sup>22</sup>

#### **Cranial: Transient Global Amnesia**

Transient global amnesia is defined as an episode of anterograde or retrograde amnesia lasting <24 hours. It has been reported to be associated with diffusion restriction in the CA1 subfield of the hippocampus. There have been several previously reported cases in association with the Valsalva maneuver and a variety of physical activities.<sup>23,24</sup> It is possible that transient global amnesia occurs due to retrograde flow in the internal jugular vein induced by the Valsalva maneuver, leading to temporary cerebral venous congestion. Others have theorized that paradoxical emboli precipitated by the Valsalva maneuver might lead to transient global amnesia, though patients with transient global amnesia have not been shown to have a higher incidence of right-to-left shunts.<sup>24</sup> Ultimately, the exact pathogenesis of transient global amnesia is uncertain, but its correlation with the Valsalva maneuver is quite diagnostically useful. We have seen hippocampal infarcts associated with transient global amnesia after weight-lifting (Fig 9A, -B) and associated with sexual intercourse (Fig 9C, -D).

#### **Cranial: Spontaneous Nontraumatic Pneumocephalus**

Pneumocephalus refers to the abnormal presence of intracranial air, which is usually due to trauma or an operation. However, rare cases of spontaneous pneumocephalus have been reported in the literature, typically related to the Valsalva maneuver, cranial defects, infection, or neoplasm.<sup>25</sup> Sometimes, predisposing factors such as sinus osteomas can be seen in association with spontaneous nontraumatic pneumocephalus (Fig 10). Osteomas may lead to osseous erosion, providing a conduit for air to enter the skull from paranasal sinuses or air cells. The air then may become trapped through a ball valve mechanism as the cranial defect is sealed by the arachnoid membrane.<sup>26</sup> Regardless of the cause, pneumocephalus is important to recognize because it can cause headache or sensations of increased pressure. In cases of unexpected clinical decompensation, particularly in postoperative patients, mass effect on the brain from pneumocephalus (tension pneumocephalus) is an important consideration that requires prompt surgical attention.

#### **CONCLUSIONS**

The unique physiologic changes that occur from the Valsalva maneuver can result in a variety of head and neck abnormalities with characteristic imaging findings. Additionally,

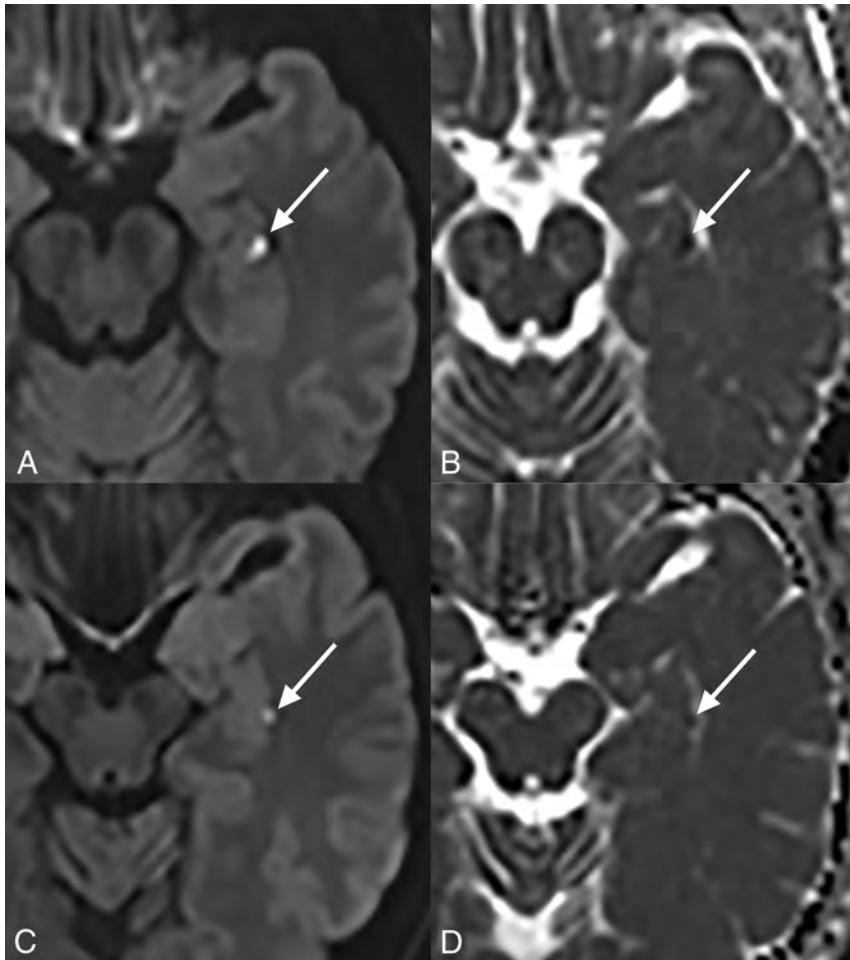


**FIG 9.** Transient global amnesia. A 58-year-old man who presented with retrograde amnesia. He had gone to the gym and completed his usual workout routine including bench-pressing earlier that day. When he returned home, he had no memory of being at the gym despite having recorded his exercises in his daily workout log. An axial diffusion-weighted MR image (A) and a corresponding ADC map (B) show a focus of diffusion restriction in the left hippocampus (arrows). The same findings (arrows) are demonstrated on axial diffusion-weighted (C) and ADC (D) images from a 57-year-old man with mixed retrograde/anterograde amnesia following sexual intercourse.

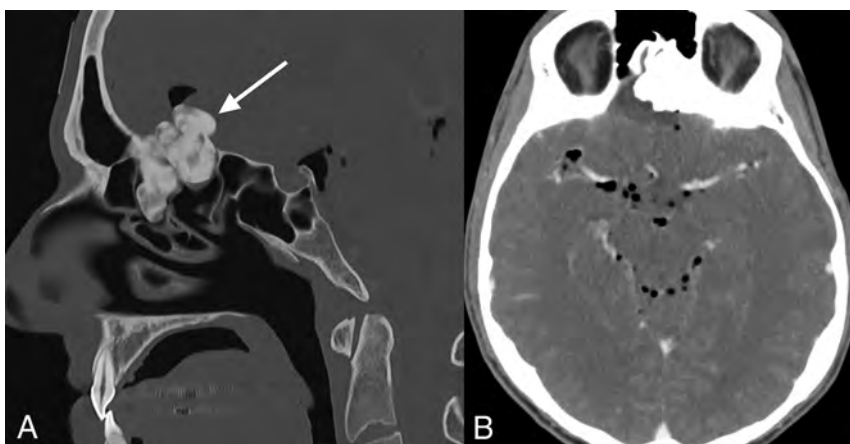


**FIG 10.** Spontaneous pneumocephalus. A 27-year-old ex-Marine with a recent history of clear rhinorrhea for 1 week presented with acute, severe head pressure that started during weight-lifting. Sagittal CT (A) shows a giant osteoma extending superiorly from the ethmoid air cells (arrow). There is extensive subarachnoid pneumocephalus (A and B).

the Valsalva maneuver can be intentionally used during imaging to aid in diagnosing various conditions. Identification of Valsalva-related imaging abnormalities can help prompt clinicians to elicit relevant history from patients. Thus, it is important to recognize these findings, carefully correlate them with relevant clinical history, and communicate with referring clinicians if additional history must be obtained. It is also helpful to have knowledge of lesions commonly encountered on routine imaging that predispose patients to the Valsalva or other pressure gradient-related effects.

Some of the entities presented are incidental findings and do not necessarily have immediate clinical significance. However, it is important to recognize these findings as well to avoid incorrect diagnoses or unnecessary additional work-up, especially true in cases in which use of the Valsalva maneuver during imaging supports the benignity of a lesion. Recognition of these cases will help clinicians make clinically relevant diagnoses and prevent undue treatment of benign, incidental findings.

Disclosures: Ajay A. Madhavan—RELATED: Support for Travel to Meetings for the Study or Other Purposes: Mayo Clinic, Comments: travel/conference reimbursement to present work at the American Society of Head and Neck Radiology 2018 Annual Meeting in Savannah, Georgia.

## ACKNOWLEDGMENTS

The authors acknowledge the assistance of Sonia Watson, PhD, in editing the manuscript.

## REFERENCES

1. Luster EA, Baumgartner N, Adams WC, et al. **Effects of hypovolemia and posture on responses to the Valsalva maneuver.** *Aviat Space Environ Med* 1996;67:308–13 Medline
2. Vianello A, et al. **Spontaneous pneumomediastinum complicating severe acute asthma exacerbation in adult patients.** *J Asthma* 2017:1–77 CrossRef Medline
3. Sahni S, Verma S, Grullon J, et al. **Spontaneous pneumomediastinum: time for consensus.** *N Am J Med Sci* 2013;5:460–64 CrossRef Medline
4. Weiss ZF, Gore S, Foderaro A. **Pneumomediastinum in marijuana users:**

- a retrospective review of 14 cases. *BMJ Open Respir Res* 2019;6:e000391 CrossRef Medline
5. Swe T, Naing AT, Lixon A, et al. **Spontaneous pneumomediastinum, pneumoretroperitoneum, and cervicofacial subcutaneous emphysema after repeatedly and forcefully blowing into a bottle.** *J Community Hosp Intern Med Perspect* 2016;6:33361 CrossRef Medline
  6. Pittman JA, Pounsford JC. **Spontaneous pneumomediastinum and Ecstasy abuse.** *J Accid Emerg Med* 1997;14:335–36 CrossRef Medline
  7. Bora MK. **Internal jugular phlebectasia: diagnosis by ultrasonography, Doppler and contrast CT.** *J Clin Diagn Res* 2013;7:1194–96 CrossRef Medline
  8. Hu X, Li J, Hu T, et al. **Congenital jugular vein phlebectasia.** *Am J Otolaryngol* 2005;26:172–74 CrossRef Medline
  9. Upile T, Jerjes W, Sipaul F, et al. **Laryngocele: a rare complication of surgical tracheostomy.** *BMC Surg* 2006;6:14 CrossRef Medline
  10. Spinosi MC, Mezzedimi C, Monciatti G, et al. **Internal laryngocele: unusual onset in a 91-year-old female patient.** *Sultan Qaboos Univ Med J* 2018;18:e104–06 CrossRef Medline
  11. Glazer HS, Mauro MA, Aronberg DJ, et al. **Computed tomography of laryngoceles.** *AJR Am J Roentgenol* 1983;140:549–52 CrossRef Medline
  12. Sandhu RS, Shah AD. **Nontraumatic orbital floor fracture after nose-blowing.** *Radiology Case Rep* 2016;11:1–3 CrossRef Medline
  13. Markowitz-Spence L, Brodsky L, Seidell G, et al. **Self-induced pneumoparotitis in an adolescent: report of a case and review of the literature.** *Int J Pediatr Otorhinolaryngol* 1987;14:113–21 CrossRef Medline
  14. Martin-Granizo R, et al. **Pneumoparotid in childhood: report of two cases.** *J Oral Maxillofac Surg* 1999;57:1468–71 CrossRef Medline
  15. Brodie HA, Chole RA. **Recurrent pneumosialadenitis: a case presentation and new surgical intervention.** *Otolaryngol Head Neck Surg* 1988;98:350–53 CrossRef Medline
  16. Luaces R, Ferreras J, Patiño B, et al. **Pneumoparotid: a case report and review of the literature.** *J Oral Maxillofac Surg* 2008;66:362–65 CrossRef Medline
  17. Wemhoff M, Jain R, Rock J. **Hyperpneumatization of the skull base: case report.** *Neurosurgery* 2012;70:E789–93 discussion E793–94. CrossRef Medline
  18. Quigley AJ, Shannon H. **Craniocervical pneumatization.** *J Radiol Case Rep* 2013;7:27–33 CrossRef Medline
  19. Francies O, Morley S, Beale T. **Skull base and craniocervical bone pneumatisation: two case reports of differing presentations and a review of the literature.** *J Radiol Case Rep* 2017;11:1–10 CrossRef Medline
  20. Littrell LA, Leutmer PH, Lane JJ, et al. **Progressive calvarial and upper cervical pneumatization associated with habitual Valsalva maneuver in a 70-year-old man.** *AJNR Am J Neuroradiol* 2004;25:491–93 Medline
  21. Smoker WR, Gentry LR, Yee NK, et al. **Vascular lesions of the orbit: more than meets the eye.** *Radiographics* 2008;28:185–204; quiz 325 CrossRef Medline
  22. Weill A, Cognard C, Castaings L, et al. **Embolization of an orbital varix after surgical exposure.** *AJNR Am J Neuroradiol* 1998;19:921–23 Medline
  23. Mariaca AF, Valdeza JM, Gaebel C, et al. **Simultaneous transient global amnesia and right MCA stroke after Valsalva manoeuvre.** *BMJ Case Rep* 2017 CrossRef Medline
  24. Owen D, Paranandi B, Sivakumar R, et al. **Classical diseases revisited: transient global amnesia.** *Postgrad Med J* 2007;83:236–39 CrossRef Medline
  25. Pishbin E, Azarfardian N, Salarirad M, et al. **Spontaneous nontraumatic pneumocephalus: a case report.** *Iran Red Crescent Med J* 2015;17:e23920 CrossRef Medline
  26. Umredkar AB, Disawal A, Anand A, et al. **Frontal sinus osteoma with pneumocephalus: a rare cause of progressive hemiparesis.** *Indian J Radiol Imaging* 2017;27:46–48 CrossRef Medline

# Publicly Available Metrics Underestimate *AJNR* Twitter Impact and Follower Engagement

 C.M. Tomblinson,  V. Wadhwa,  E. Latimer,  C.H. Gauss, and  J.L. McCarty

## ABSTRACT

**SUMMARY:** Social media use by professional organizations has increased as a platform to disseminate information, affording an alternative avenue to engage membership and the public. The *American Journal of Neuroradiology* (*AJNR*) posts cases and articles, hosts Tweet chats, advertises podcasts, and more on its Twitter account (@TheAJNR). The objective of this study was to determine whether user engagement is underestimated on the basis of publicly available metrics and to assess the engagement rate. This study demonstrated that engagement extends beyond visible metrics, suggesting an *AJNR* “silent” following beyond what is readily apparent. Median engagement rates from the @TheAJNR account from 2017 to 2019 appear stable since last reported in 2016 and are comparable with those reported in other professional medical journals.

**ABBREVIATION:** ER = engagement rate

Twitter continues to be an active social media platform for radiologists, trainees, and academic organizations. Although Twitter was originally a personal communication platform, its dynamic and rapidly changing information stream encourages propagation of topics of interest in the medical community. Currently, this platform is routinely used to disseminate information for large medical societies, including the American Society of Neuroradiology.

Twitter has become a catalyst for real-life meet-ups by conference attendees and allows virtual participation for those unable to attend. In the field of neuroradiology, Radmanesh et al<sup>1</sup> first described social media incorporation and use patterns by analyzing data from the 2014 Annual Meeting of the American Society of Neuroradiology (ASNR). When tweets from the *Journal of the American College of Radiology* targeted topics of member interest, Web site traffic increased 31%, and unique Web site visitors increased 20%.<sup>2</sup> Studies by Koontz et al<sup>3</sup> and Patel et al<sup>4</sup> found that social media use among radiologists and radiology trainees ranged from 59% to 91%, with usage rates varying by generation. Furthermore, Patel et al noted

that 60% of radiologists in their study used Twitter for professional purposes. These high rates of use demonstrate a new digital era in which information is being consumed on-line.

While many of the interactions are visible to the public (retweets, likes, and replies), some of the more important metrics for content engagement are not visible (impressions, engagements, engagement rate, URL clicks) to the public but can be accessed by the account owner (Fig 1). The *American Journal of Neuroradiology* (*AJNR*) Twitter account (@TheAJNR) has been in existence since 2013, now garnering more than 6400 followers and 7300 tweets at the time of publication. Each @TheAJNR posted case and published article is paired with a unique URL link to route users to the corresponding *AJNR* Web page.

All social media activity is designed to increase engagement with users. However, the type of engagement important for an academic journal such as *AJNR* includes URL clicks, in addition to likes and retweets. One objective of this study was to assess whether case views and article readership resulting from Twitter posts (indicated by the number of URL clicks) exceed the number of visible engagements (particularly, retweets and likes), implying a “silent” Twitter following and educational outreach beyond what is readily apparent. Another objective of the study was to assess the engagement rate of the @TheAJNR account since the most recent reporting of *AJNR* engagement rate data from 2015 to 2016.<sup>5</sup>

## MATERIALS AND METHODS

### Data Source

Twitter Analytics data were obtained from the *AJNR* Twitter account for tweets published from January 2017 to June 2019.

Received July 31, 2019; accepted after revision September 16.

From the Department of Radiology and Radiological Sciences (C.M.T.), Vanderbilt University Medical Center, Nashville, Tennessee; Departments of Radiology (V.W., E.L.) and Biostatistics (C.H.G.), University of Arkansas for Medical Sciences, Little Rock, Arkansas; and Department of Diagnostic and Interventional Imaging (J.L.M.), University of Texas Health Science Center, Houston, Texas.

Paper previously presented at: Annual Meeting of the American Society of Neuroradiology, June 2–7, 2018; Vancouver, British Columbia, Canada.

Please address correspondence to Jennifer L. McCarty, MD, 6431 Fannin St, MSB 2.130, Houston, TX 77030; e-mail: jennifermccartymd@gmail.com; @cmtomblinson; @JMcCartyMD

<http://dx.doi.org/10.3174/ajnr.A6299>

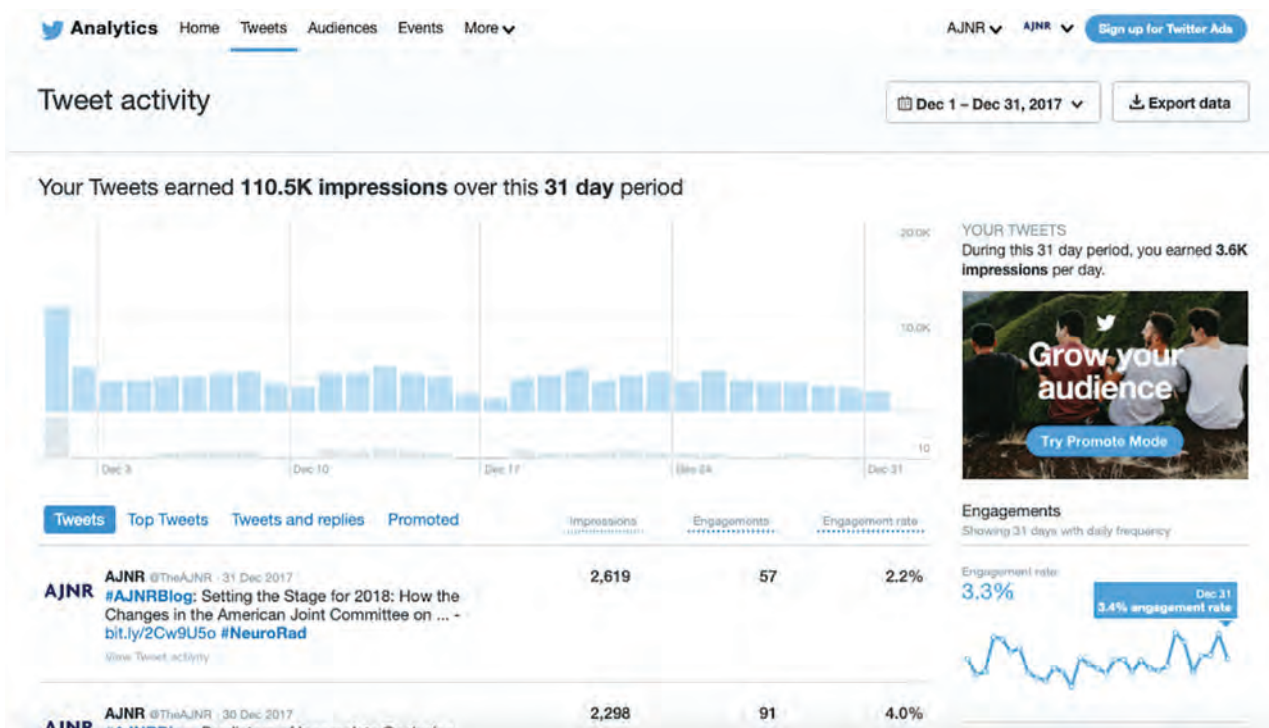


**FIG 1.** Twitter Analytics. The free Twitter Analytics page provides data for the account and for each individual tweet from the account over designated time periods that can be viewed on-line or exported to Excel (Microsoft, Redmond, Washington). Only the account user has access to this page. The exported data include impressions, engagements, URL clicks, retweets, likes, and all other metrics collected for this project.

Available Twitter Analytics data include impressions, engagements, and engagement rate for each tweet.

“Impressions” refer to the number of times a tweet passes through user timelines or is included in a search.

“Engagements” are defined by the total number of times a user interacted with a tweet through a click for any purpose (retweet, reply, follow, like, URL link, hashtag, photo, or tweet expansion). The engagements of interest for our study were retweets, likes, and URL clicks.

“Engagement rate” (ER) is defined by total number of engagements divided by total number of impressions.

Likes and retweets can be seen by any Twitter user and were considered publicly visible engagements. The number of URL clicks data is only accessible by the owner of the Twitter account, thus considered a form of private engagement only visible to the account owner.

Tweet types were classified into 3 categories: cases, articles, and other. The “other” category included Tweet chats, blog posts, news announcements, advertisements for podcasts, upcoming meeting information, and deadline reminders.

### Statistical Analysis

Summary statistics were obtained for URL clicks, retweets, likes, and replies for each of the 3 tweet types from January to December 2017. Both the difference between the number of URL clicks and the number of retweets and the difference between the number of URL clicks and the number of likes were computed for each tweet of each type (AJNR case, article, and other). Both difference response variables were analyzed

separately using a 1-way analysis of variance with unequal variances to test for a difference among the 3 tweet-type population mean differences. Subsequently, for both the URL-click-retweet differences and the URL-click-like differences, case and article tweets were compared using a statistical contrast that used a *t* test. Also, subsequent to the 1-way analysis of variance, for each tweet type, a *t* test was performed to determine whether there was sufficient statistical evidence to suggest that the population mean number of URL clicks was greater than that of retweets, and a similar *t* test was performed for URL clicks and likes. To assess the level of engagement based on URL clicks, we obtained an estimate of the percentage of combined case and article tweets that had at least 25 URL clicks, and similar percentages were obtained for that same set of combined tweets that had at least 50, at least 75, and at least 100 URL clicks. These statistical analyses were conducted using SAS 9.4 (SAS Institute, Cary, North Carolina).

Using Twitter Analytics data available from January 2017 through June 2019, we calculated descriptive statistics for engagement rate, which included medians along with 25th and 75th percentiles by year and overall. These statistics were obtained using SPSS, Version 23 (IBM, Armonk, New York).

### RESULTS

Nine hundred one tweets were analyzed, including 173 cases, 366 articles, and 362 others for the first objective of the study. There was evidence to suggest that at least 2 of the population mean differences among the 3 tweet types were significantly different for

the URL click-retweet differences ( $P < .001$ ) and the URL click-like differences ( $P < .001$ ).

Of particular interest was the comparison between tweets for *AJNR* articles and *AJNR* cases. For the difference between URL clicks and retweets, the mean difference was statistically significantly greater for cases than articles (50.1 versus 13.0,  $P < .001$ ). The same was true for the difference between URL clicks and likes (49.8 versus 11.8,  $P < .001$ ).

**Table 1: Tweet metrics by type<sup>a</sup>**

Tweet Type No.	Variable	Mean	SD	Min	Max
AJNR case 173	URL clicks	54.6	38.6	7	205
	Retweets	4.6	3.7	0	19
	Likes	4.9	4.6	0	20
	Replies	1.6	4.3	0	33
AJNR article 366	URL clicks	18.1	18.0	0	140
	Retweets	5.0	4.9	0	39
	Likes	6.3	6.7	0	59
	Replies	1.5	4.3	0	32
Other 362	URL clicks	7.3	9.4	0	56
	Retweets	1.5	2.0	0	12
	Likes	3.0	3.6	0	22
	Replies	0.7	1.7	0	14

**Note:**—Min indicates minimum; Max, maximum

<sup>a</sup> Across tweet-type categories, there was a significant difference among the mean URL-click-retweet differences ( $P < .001$ ) and among the mean URL-click-like differences ( $P < .001$ ), which was greater for cases compared with articles for both differences ( $P < .001$ ). Within each tweet-type category, the mean number of URL clicks was significantly greater than that of retweets ( $P < .001$ ) and likes ( $P < .001$ ).

**Table 2: Frequency of engagement (URL clicks) with cases and articles**

Frequency of Cases and Articles		
No. of URL Clicks	No. of Tweets	%
≥25	215	39.9
≥50	95	17.6
≥75	48	8.9
≥100	23	4.3

For all 3 tweet types, the mean number of URL clicks was significantly greater than the mean number of retweets (cases, 54.6 versus 4.6,  $P < .001$ ; articles, 18.1 versus 5.0,  $P < .001$ ; other, 7.3 versus 1.5,  $P < .001$ ) and the mean number of likes (case, 54.6 versus 4.9,  $P < .001$ ; articles, 18.1 versus 6.3,  $P < .001$ ; other, 7.3 versus 3.0,  $P < .001$ ) (Table 1).

The second objective of the study entailing an assessment of the engagement rate of the @TheAJNR account used 2187 tweets (893 from 2017, 911 from 2018, and 383 from January to June 2019). The median ER for 2017 was 4.1% (25th percentile = 2.3%, 75th percentile = 7.3%); for 2018 was 3.0% (1.7%, 5.2%), and was 3.5% (2.0%, 6.0%) for the first 6 months of 2019. The overall median ER was 3.5% (1.9%, 6.2%).

## DISCUSSION

Free to users and available only to the owner of an account, the Twitter Analytics page offers data to the user that extend far beyond publicly visible metrics. In addition to likes, retweets, and replies that are available to the public, the account owner can evaluate trends in the engagement of his or her tweets based on other private metrics such as impressions, detail expands, URL clicks, and engagement rate.

Our URL click-retweet and URL click-like differences highlight this engagement of URL clicks visible only to the account owner that far outnumber the popular publicly visible metrics of retweets and likes. This feature is of particular importance because URL clicks are the best indicator of *AJNR* readership. A user who clicks the URL link is interested in reading more than the small snippet of information previewed in the Twitter post (limited to 280 characters and 4 pictures). Such a user is actively engaged in the *AJNR* content, but that interaction will leave no publicly visible footprint unless that same user likes, retweets, or comments.

When evaluating the frequency of URL clicks, we found that almost 40% of case and article tweets combined from the *AJNR* account get at least 25 URL clicks. A little over 4% reach at least 100 URL clicks, with the most popular case during our study receiving 205 URL clicks (Tables 1 and 2).

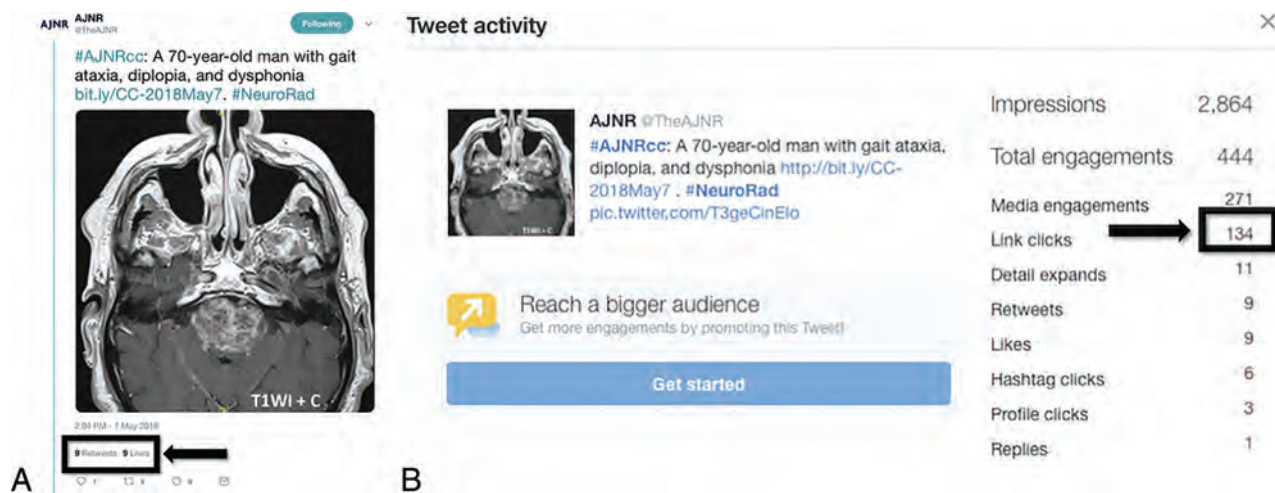


**FIG 2.** Link clicks far exceed publicly visible metrics. For this *AJNR* Classic Case top tweet, there were only 9 retweets and 9 likes (A, black arrow and box), 2 publicly visible metrics. B, Twitter Analytics revealed that the link was clicked 134 times (black arrow and box), a metric only visible to the @TheAJNR Twitter account user and indicating a large silent-but-active following.

Each week, the *AJNR* posts a “Classic Case” submitted by readers (Fig 2). On May 7, 2018, a case of CLIPPERS received only 9 retweets and likes each but had 134 URL clicks, which channel the Twitter user directly to the *AJNR* site for full viewing.<sup>6</sup> Thirty percent of the engagement for this particular tweet was through a link click. For each aforementioned case, *AJNR* posts a quiz where users can vote on a diagnosis. The corresponding case quiz for that week received 1033 votes, at least 42 of which came from Twitter but possibly more through direct funneling to the Web site, equaling about 4% of total quiz votes.

One social media primer for radiologists states that “engagements track the deepest level of interaction with social media” and are “the most powerful metric, one not available with print media.”<sup>7</sup> When evaluating article engagement, we found that a recent review article posted on May 16, 2017, had 25 likes and 15 retweets; however, the article link was clicked 85 times, taking viewers directly to the article abstract.<sup>8</sup> Web site analytics show that this article has been accessed 1433 times and downloaded 773 times. Here, a full 62% of the tweet engagement was in the form of a link click. Similar to a previous study by Hoang et al,<sup>9</sup> this study supports that posting *AJNR* content on social media may expose viewers to the society’s content and funnel traffic to the Web site, increasing member and nonmember engagement with existing materials diligently curated by *AJNR*. Certainly, most of these accessions and downloads are independent of Twitter, however the fact remains that accessions through URL clicks are higher than what meets the eye visually.

Our review of the literature revealed a paucity of studies that serve as benchmarks for end-user engagement on social media in the scientific community, but the most commonly used metric has been ER. Leary et al<sup>10</sup> examined the use of a social media campaign at the Resuscitation Science Symposium at the American Heart Association’s Scientific Sessions using Twitter Analytics data of 8 professional bloggers who live-tweeted during the sessions and used dedicated hashtags. The median ER for these bloggers was 2.4%. In another study analyzing the engagement data for the *Journal of Vascular and Interventional Radiology (JVIR)*, Wadhwa et al<sup>11</sup> showed that the median ER for @JVIRmedia steadily increased with time from 1.96% in 2014 to 4.47% in 2017. Another similar study by Wadhwa et al<sup>5</sup> analyzing Twitter Analytics data for *AJNR* from August 2015 to July 2016 showed a median ER of 3.4%. When we expanded on this prior study on *AJNR* Twitter, further analysis showed that the median ER for @TheAJNR in the years 2017 and 2018 and the first 6 months of 2019 (January to June) was 4.1%, 3.0%, and 3.5%, respectively. The median ERs from our study are similar to the median ERs from other studies related to medical journals and use of social media described above. Further studies by other professional societies will be needed to more accurately define end-user engagement benchmarks for our industry, which include ER.

It is known from the prior work of Wadhwa et al<sup>5</sup> that tweets containing an image or a hashtag or published in the morning hours have a higher ER. Their study also found that *AJNR* cases were the most popular style of tweet, concordant with the current study.<sup>5</sup>

There are several important limitations of this study. For instance, the presence of a URL click does not imply that a viewer

is reading the article in full or looking through an entire case, and this has been reported previously by Hoang et al.<sup>9</sup> Next, it cannot be ascertained what proportion of *AJNR* Web site activity is driven by Twitter at the current time, but this represents an area for future growth if the hope is to direct traffic to the *AJNR* Web site through social media. Last, the study was performed during a relatively short time frame since one of the authors (J.L.M.) assumed Twitter editorship in January 2017.

## CONCLUSIONS

The *AJNR* Twitter account has an ever-present silent following with a far broader audience reach than previously recognized. This study suggests that the extent of viewership and on-line engagement should not be measured by likes and retweets of *AJNR* cases and articles alone. Rather, the number of URL clicks is more representative of the viewership of *AJNR* on-line content and outnumbers both retweets and likes. Also, median engagement rates from the @TheAJNR account from 2017 to 2019 appear stable since last reported in 2016 and are comparable with those reported in other professional medical journals, helping to inform the end-user engagement benchmarks for this industry.

## REFERENCES

1. Radmanesh A, Kotsenas AL. **Social media and scientific meetings: an analysis of Twitter use at the annual meeting of the American Society of Neuroradiology.** *AJNR Am J Neuroradiol* 2016;37:25–27 CrossRef Medline
2. Hawkins CM, Hillman BJ, Carlos RC, et al. **The impact of social media on readership of a peer-reviewed medical journal.** *J Am Coll Radiol* 2014;11:1038–43 CrossRef Medline
3. Koontz NA, Kamer AP, Dodson SC, et al. **Social media utilization at an academic radiology practice.** *Acad Radiol* 2018;25:111–17 CrossRef Medline
4. Patel SS, Hawkins CM, Rawson JV, et al. **Professional social networking in radiology: who is there and what are they doing?** *Acad Radiol* 2017;24:574–79 CrossRef Medline
5. Wadhwa V, Latimer E, Chatterjee K, et al. **Maximizing the tweet engagement rate in academia: analysis of the AJNR Twitter feed.** *AJNR Am J Neuroradiol* 2017;38:1866–68 CrossRef Medline
6. **Classic Case. A 70-year-old man with gait ataxia, diplopia, and dysphonia.** <http://bit.ly/CC-2018May7>. #NeuroRad. Twitter. Accessed May 31, 2018
7. Kohli MD, Daye D, Towbin AJ, et al. **Social media tools for department and practice communication and branding in the digital age.** *Radiographics* 2018;38:1773–85 CrossRef Medline
8. @TheAJNR. **#ReviewArticle: Vertebroplasty and kyphoplasty for osteoporotic vertebral fractures: what are the latest data?** <http://bit.ly/2IIYSiN> @JoshuaAHirsch #NeuroRad #Spine #NeuroIR. Twitter. Accessed May 31, 2017
9. Hoang JK, McCall J, Dixon AF, et al. **Using social media to share your radiology research: how effective is a blog post?** *J Am Coll Radiol* 2015;12:760–65 CrossRef Medline
10. Leary M, McGovern S, Dainty KN, et al. **Examining the use of a social media campaign to increase engagement for the American Heart Association 2017 Resuscitation Science Symposium.** *J Am Heart Assoc* 2018;7 CrossRef Medline
11. Wadhwa V, Devgan A, Patel MV, et al. **Factors increasing tweet engagement rate for the Journal of Vascular and Interventional Radiology Twitter feed.** *J Vasc Interv Radiol* 2018;29:1057–59 CrossRef Medline

# Lyme Disease: What the Neuroradiologist Needs to Know

H.A. Valand, A. Goyal, D.A. Melendez, S.S. Matharu, H.S. Mangat, and R.K. Tu

## ABSTRACT

**SUMMARY:** Lyme disease is the most common tick-borne disease in Canada and the United States, caused by *Borrelia burgdorferi*, which affects multiple organ systems. Epidemiology, clinical presentation, and neuroimaging findings are reviewed.

### What Is Lyme Disease?

Lyme disease, known as Lyme borreliosis, was first described in 1976 by William E. Mast and William M. Burrows in Old Lyme, Connecticut.<sup>1</sup> It is the most commonly reported vector-borne disease in North America. In the United States, it is caused by *Borrelia burgdorferi*, a spirochete, closely related clinically to *Treponema pallidum* (syphilis) and transmitted via the bite of an infected *Ixodes* tick.<sup>2,3</sup> Lyme disease is predominantly seen in the mid-Atlantic (primarily New England) and upper Midwest regions (Wisconsin, Minnesota, and Great Lakes region) but is also prevalent in parts of the Pacific coast (Oregon and Washington).<sup>4</sup> Transmission of this tick-borne zoonosis requires both infected reservoirs in the small mammalian hosts and vector blacklegged ticks. Large mammals like humans are seldom hosts and are mainly affected by nymphal ticks.<sup>5</sup> The incidence of Lyme disease is approximately 30,000 or 0.5 per 1000 individuals in endemic areas per the Centers for Disease Control and Prevention.<sup>2,6</sup> However, under-reporting and misclassification are the common drawbacks of any surveillance system. The Centers for Disease Control and Prevention report that highly Lyme endemic states may have considerably higher prevalence than that recorded.<sup>7</sup>

### What Are the Clinical Manifestations of Lyme Disease?

Lyme disease can be classified in 3 stages: early localized (stage 1), early disseminated (stage 2), and late disseminated (stage 3). In

the early localized stage, erythema migrans is the first and most common sign, seen in up to 70%–80% of the individuals with a tick bite. It appears within 3 to 32 days at the tick bite site and may be asymptomatic, pruritic, or, rarely, painful. In untreated individuals, this lesion can expand up to 61 cm in diameter.<sup>8–13</sup> Early dissemination begins within weeks to months after the appearance of erythema migrans. It mainly presents as nonspecific flulike symptoms such as fatigue, malaise, fever, arthralgias, myalgias, and lymphadenopathies.<sup>14</sup> In addition, ~15% and ~8% of patients may develop neurologic and cardiac abnormalities, respectively. The most common neurologic manifestations are lymphocytic meningitis, meningoencephalitis, cranial nerve neuritis, and sensorimotor radiculopathies.<sup>15</sup> Patients with cardiac involvement mainly have a spectrum of atrioventricular nodal block.<sup>16,17</sup> In late dissemination, arthritis mainly affecting the large joints (most commonly the knees) is the most common presentation. Because most patients are treated with antibiotics, <10% develop arthritis.<sup>13,18–20</sup> Neurologic deficits such as loss of short-term memory, word amnesia, and progressive loss of multi-tasking ability with new-onset attention deficit–type symptoms are being increasingly recognized.<sup>21</sup>

### How to Diagnose and Treat Lyme Disease

Lyme disease is diagnosed by combining the clinical examination with serologic testing. The early localized stage of Lyme disease is typically diagnosed with clinical signs and symptoms.<sup>22</sup>

Many physicians use the Centers for Disease Control and Prevention criteria of a Lyme reflex test, measuring the antibody titers to Lyme, and, if positive, performing a western blot to Lyme.<sup>23</sup> The Centers for Disease Control and Prevention recommend a 2-step quantitative assay to detect antibodies against *B burgdorferi*. The first step involves the use of an enzyme immunoassay or an indirect immunofluorescence assay. If the result is negative, no further testing is required, but if the test is positive or equivocal, step 2 is performed. Step 2 uses an immunoblotting technique such as a western blot. The test is deemed positive

Received August 23, 2019; accepted after revision August 27.

From the American University of Integrative Sciences (H.A.V.), Brampton, Ontario, Canada; George Washington University (A.G., D.A.M.), Washington, DC; The Fischell Department of Bioengineering (S.S.M.), University of Maryland College Park, College Park, Maryland; Germantown Medical Center (H.S.M.), Germantown, Maryland; and Progressive Radiology (R.K.T.), George Washington University, United Medical Center, Washington, DC.

Please address correspondence to Raymond K. Tu, MD, MS, FACR, Progressive Radiology, George Washington University, United Medical Center, 2121 K St NW, Suite 100, Washington, DC 20037; e-mail: Raymond.Tu@progressiveradiology.net; @RayTu10

<http://dx.doi.org/10.3174/ajnr.A6301>

## Neuroradiologic findings in Lyme disease

Location	Neurologic Presentation	Comments
PNS	Subacute meningitis <sup>24</sup> Plexus neuritis or mononeuritis multiplex <sup>25</sup> Bannwarth syndrome <sup>15</sup>	Most common presentation in North America <sup>24</sup> 5%–10% cases <sup>25</sup> Uncommon in North America <sup>15</sup>
Cranial nerve	Facial nerve neuritis <sup>26,27</sup> CN III and CNV <sup>28,29</sup>	Most commonly involved cranial nerve <sup>26</sup> Few case reports <sup>28,29</sup>
CNS	Nonspecific bifrontal white matter T2 hyperintensity <sup>15</sup> Encephalitis-rhombencephalitis pattern likely <sup>25</sup> Vasculitis <sup>15</sup>	50% of cases with CNS involvement <sup>15</sup> Rare <sup>15</sup> Rare <sup>15</sup>
Spinal cord	Nonspecific areas of T2 prolongation <sup>15</sup>	Most common pattern in spinal cord involvement <sup>15</sup>
Ocular	Conjunctivitis and episcleritis, early stages <sup>33,34</sup> Uveitis, orbital myositis, chronic intraocular inflammation <sup>33,34</sup>	Rare <sup>33,34</sup> Rare <sup>33,34</sup>
Pediatric	Cranial neuritis and meningitis <sup>35,36</sup> Peripheral neuritis, myelitis, Bannwarth syndrome <sup>37,38</sup> Prominent Virchow-Robin spaces <sup>37,38</sup>	Most common pediatric neurologic presentation <sup>35,36</sup> Rare <sup>37,38</sup> Less common <sup>37,38</sup>

**Note:**—CN indicates cranial nerve; PNS, peripheral nervous system.

when both steps are positive. Doxycycline, amoxicillin, or cefuroxime axetil is the first-line treatment, and results in complete resolution of a patient's symptoms. Cases resistant to these antibiotics are treated with macrolides.<sup>18</sup>

### What Are the Neuroradiologic Findings in Patients with Lyme Disease?

There are several neurologic manifestations of Lyme disease. Imaging can be helpful in the assessment of peripheral Lyme disease. A clinical presentation of radiculitis in an endemic region should raise suspicion for the disease. The summary of these neurologic finding is in the Table.

**Peripheral Nervous System.** In the North American population, the peripheral manifestations are likely an extension of subacute meningitis, such as plexus neuritis or mononeuritis multiplex seen in 5%–10% of cases.<sup>24,25</sup> Bannwarth syndrome, another complication of Lyme disease less frequently seen in North America, would be indicative of meningoradiculitis. On MR imaging, meningoradiculitis presents as an increased T2 signal of the affected nerve roots, which enhances with gadolinium contrast medium.<sup>15</sup>

**Cranial Nerves.** Facial nerve involvement is seen in approximately 80% of the cases, presenting as cranial neuritis. Of these, approximately 25% of cases show bilaterality. On MR imaging, enhancement of the affected nerve can be seen.<sup>26,27</sup> Cranial nerve III and V involvement has also been reported.<sup>28,29</sup> There still remains a lack of specificity to diagnose Lyme disease on imaging alone. In the clinical setting, attention should be paid to asymmetry or marked intensity of enhancement in the course of facial nerve geniculate ganglion and beyond. Enhancement of the typically nonenhancing facial nerve segments proximal to geniculate ganglion should also raise the suspicion.<sup>25</sup>

**Central Nervous System.** Half of the affected patients with CNS involvement show nonspecific abnormal signal in the frontal lobe white matter. This signal may persist even after clinical resolution post-antibiotic treatment.<sup>15</sup> On a molecular level, the immune

response to Lyme disease and MS has been found to be relatively similar, yet T-cell lines demonstrate only weak cross-reactivity between myelin basic protein and *B burgdorferi*.<sup>30</sup> On magnetization transfer and DTI sequences, the presence of occult brain and cervical cord pathology in otherwise normal white matter would be more indicative of MS.<sup>31</sup> Progression of CNS involvement can lead to encephalitis. Although there is no specific pattern of involvement, there have been a few cases showing a rhombencephalitis pattern of involvement affecting the brain stem and cerebellum, though this pattern of involvement can also be seen in tubercular or *Listeria* infection.<sup>25</sup> There have been a few case reports of Lyme-related vasculitis and subsequent stroke-like symptoms. Lyme disease rarely affects the spinal cord.<sup>15</sup> In affected patients, it is characterized by diffuse or multifocal areas of T2 prolongation. In contrast to MS, there are no occult lesions on magnetization-transfer images. Postcontrast images are helpful to demonstrate any associated nerve root enhancement.<sup>31,32</sup>

**Ocular.** The most common orbital/ocular manifestations of Lyme disease in the early stages are conjunctivitis, episcleritis, and subtle keratitis. Later stages may present as uveitis, orbital myositis, or chronic intraocular inflammation presenting with floaters and photophobia. Later stages of chronic intraocular inflammation can mimic orbital pseudotumor (due to raised intracranial pressure) or lymphoma.<sup>33,34</sup> The clinical and imaging manifestations of orbital myositis in Lyme disease closely mimics those orbital pseudotumor; lymphoma and thyroid dysorbitopathy are possible differential diagnoses.<sup>15,33</sup>

**Pediatric Patients.** Facial neuritis and meningitis are the most common neurologic presentations in the pediatric population.<sup>35,36</sup> Peripheral neuritis, myelitis, and Bannwarth syndrome are rare in children. The overall clinical course is milder and shorter compared with adults. Affected pediatric patients may show prominent Virchow-Robin spaces and T2 hyperintense lesions.<sup>37,38</sup>

## CONCLUSIONS

This Clinical Vignette reviews the most common tickborne disease in Canada and the United States and important neuroradiologic

findings. Heightened interpretive sensitivity to the myriad nonspecific imaging findings may provide critical clinical information to diagnose and monitor *Borrelia burgdorferi* infection.

## REFERENCES

1. Mast WE, Burrows WM. Erythema Chronicum Migrans in the United States. *JAMA* 1976;236:859–60 CrossRef Medline
2. Shapiro ED. *Borrelia burgdorferi* (Lyme disease). *Pediatr Rev* 2014;35:500–09 CrossRef Medline
3. Centers for Disease Control and Prevention. Lyme Disease. <https://www.cdc.gov/lyme/index.html>. Last reviewed June 3, 2019. Accessed June 25, 2019
4. Schwartz AM, Hinckley AF, Mead PS, et al. Surveillance for Lyme disease: United States, 2008–2015. *Surveillance Summaries* 2017;66:1–12 CrossRef
5. National Collaborating Centre for Infectious Diseases. ARCHIVED: Lyme Disease in Canada. An Update on the Epidemiology. <https://nccid.ca/publications/lyme-disease-in-canada-an-update-on-the-epidemiology/>. Published April 2014. Accessed June 25, 2019
6. Centers for Disease Control and Prevention. Data and Surveillance. <https://www.cdc.gov/lyme/datasurveillance/index.html>. Accessed June 25, 2019
7. Centers for Disease Control and Prevention. Lyme disease surveillance and available data. <https://www.cdc.gov/lyme/stats/survfaq.html>. Accessed August 19, 2019
8. Bush LM, Perez MT. Lyme Disease: Infectious Diseases. Merck Manuals Professional Edition. <https://www.merckmanuals.com/professional/infectious-diseases/spirochetes/lyme-disease>. Accessed June 25, 2019.
9. Shapiro ED. Lyme disease. *N Engl J Med* 2014;371:683–84 CrossRef Medline
10. Tibbles CD, Edlow JA. Does this patient have erythema migrans? *JAMA* 2007;297:2617–27 CrossRef Medline
11. Steere AC, Sikand VK. The presenting manifestations of Lyme disease and the outcomes of treatment. *N Engl J Med* 2003;348:2472–74 CrossRef Medline
12. Nadelman RB, Nowakowski J, Forseter G, et al. The clinical spectrum of early Lyme borreliosis in patients with culture confirmed erythema migrans. *Am J Med* 1996;100:502–08 CrossRef Medline
13. Smith RP, Schoen RT, Rahn DW, et al. Clinical characteristics and treatment outcome of early Lyme disease in patients with microbiologically confirmed erythema migrans. *Ann Intern Med* 2002;136:421 CrossRef Medline
14. Wormser GP. Early Lyme disease. *N Engl J Med* 2006;354:2794–2801 CrossRef Medline
15. Hildenbrand P, Craven D, Jones R, et al. Lyme neuroborreliosis: manifestations of a rapidly emerging zoonosis. *AJNR Am J Neuroradiol* 2009;30:1079–87 CrossRef Medline
16. Steere AC. Lyme disease. *N Engl J Med* 1989;321:586–96 CrossRef Medline
17. Forrester JD, Meiman J, Mullins J, et al. Notes from the field: update on Lyme carditis, groups at high risk, and frequency of associated sudden cardiac death—United States. *MMWR Morb Mortal Wkly Rep* 2014;63:982–83 Medline
18. Wormser GP, Dattwyler RJ, Shapiro ED, et al. The clinical assessment, treatment, and prevention of Lyme disease, human Granulocytic Anaplasmosis, and Babesiosis: Clinical Practice Guidelines by the Infectious Diseases Society of America. *Clin Infect Dis* 2006;43:1089–1134 CrossRef Medline
19. Stanek G, Wormser GP, Gray J, et al. Lyme borreliosis. *Lancet* 2012;379:461–73 CrossRef Medline
20. Wormser GP, McKenna D, Carlin J, et al. Brief communication: hematogenous dissemination in early Lyme disease. *Ann Intern Med* 2005;142:751 CrossRef Medline
21. Bransfield RC. Neuropsychiatric Lyme borreliosis: an overview with a focus on a specialty psychiatrist's clinical practice. *Healthcare (Basel)* 2018;6:104 CrossRef Medline
22. Steere A. Lyme disease. *N Engl J Med* 2001;345:115–25 CrossRef Medline
23. Centers for Disease Control and Prevention. Lyme Disease. Laboratory testing. <https://www.cdc.gov/lyme/diagnosistesting/index.html>. Accessed October 11, 2019
24. Schwenkenbecher P, Pul R, Wurster U, et al. Common and uncommon neurological manifestations of neuroborreliosis leading to hospitalization. *BMC Infect Dis* 2017;17:90 CrossRef Medline
25. Lindland ES, Solheim AM, Andreassen S, et al. Imaging in Lyme neuroborreliosis. *Insights Imaging* 2018;9:833–44 CrossRef Medline
26. Halperin JJ. Nervous system Lyme disease. *Infect Dis Clin North Am* 2015;29:241–53 CrossRef Medline
27. Strle F, Stanek G. Clinical manifestations and diagnosis of Lyme borreliosis: current problems in dermatology Lyme Borreliosis. *Curr Probl Dermatol* 2009;37:51–110 CrossRef Medline
28. Savas R, Sommer A, Gueckel F, et al. Isolated oculomotor nerve paralysis in Lyme disease: MRI. *Neuroradiology* 1997;39:139–41 CrossRef Medline
29. Nelson JA, Wolf MD, Yuh WT, et al. Cranial nerve involvement with Lyme borreliosis demonstrated by magnetic resonance imaging. *Neurology* 1992;42:671–71 CrossRef Medline
30. Pohl-Koppe A, Logigian EL, Steere AC, et al. Reactivity of *Borrelia burgdorferi* and myelin basic protein-specific T-cells is not observed in borreliac encephalomyelitis. *Cell Immunol* 1999;194:118–23 CrossRef Medline
31. Agosta F, Rocca MA, Benedetti B, et al. MR imaging assessment of brain and cervical cord damage in patients with neuroborreliosis. *AJNR Am J Neuroradiol* 2006;27:892–94 Medline
32. Hattingen E, Weidauer S, Kieslich M, et al. MR imaging in neuroborreliosis of the cervical spinal cord. *Eur Radiology* 2004;14:2072–75 CrossRef Medline
33. Lesser RL. Ocular manifestations of Lyme disease. *Am J Med* 1995;98:60S CrossRef
34. Zagorski Z, Biziorek B, et al. Ophthalmic manifestations in Lyme borreliosis [in Polish]. *Przegl Epidemiol* 2002;56(Suppl 1):85–90 Medline
35. Shapiro E, Seltzer E. Lyme disease in children. *Semin Neurol* 1997;17:39–44 CrossRef Medline
36. Belman AL, Iyer M, Coyle PK, et al. Neurologic manifestations in children with North American Lyme disease. *Neurology* 1993;43:2609–14 CrossRef Medline
37. Belman AL, Coyle PK, Roque C, et al. MRI findings in children infected by *Borrelia burgdorferi*. *Pediatr Neurol* 1992;8:428–31 CrossRef Medline
38. Vanzielegheem B, Lemmerling M, Carton D, et al. Lyme disease in a child presenting with bilateral facial nerve palsy: MRI findings and review of the literature. *Neuroradiology* 1998;40:739–42 CrossRef Medline

# Safety and Diagnostic Efficacy of Gadobenate Dimeglumine in MRI of the Brain and Spine of Neonates and Infants

 D.S. Enterline,  K.W. Martin,  H.A. Parmar,  F.M. Triulzi, and  C. Colosimo

## ABSTRACT

**BACKGROUND AND PURPOSE:** Contrast-enhanced MR imaging provides essential information for pediatric imaging applications. We evaluated gadobenate dimeglumine for contrast-enhanced MR imaging of infants younger than 2 years of age.

**MATERIALS AND METHODS:** Ninety children younger than 2 years of age (including 55 children younger than 1 year) who underwent enhanced MR imaging of the CNS with gadobenate dimeglumine at 0.1 mmol/kg body weight  $\pm$  25% by volume were retrospectively enrolled at 2 imaging centers. Safety data were assessed for adverse events and, when available, vital signs and electrocardiogram and clinical laboratory values obtained from 48 hours before until 48 hours after the MR imaging examination. The efficacy of gadobenate dimeglumine-enhanced MR imaging was evaluated prospectively by 3 blinded, unaffiliated readers in terms of the accuracy of combined pre- and postcontrast images relative to precontrast images alone for differentiation of tumor from non-neoplastic disease and the correct diagnosis of specific disease. Differences were tested using the McNemar test. A possible effect of dose on diagnostic accuracy was assessed using the Fisher exact test.

**RESULTS:** Nine nonserious adverse events were reported for 8 (8.8%) patients. Five adverse events occurred in patients 12 months of age or older. All events occurred at least 24 hours after gadobenate dimeglumine administration, and in each case, the investigating radiologist considered that there was no reasonable possibility of a relationship to gadobenate dimeglumine. No clinically meaningful changes in vital signs, electrocardiogram results, or laboratory parameters were reported. Accurate differentiation of tumor from non-neoplastic disease and exact matching of each specific MR imaging-determined diagnosis with the on-site final diagnosis were achieved in significantly more patients by each reader following evaluation of combined pre- and postcontrast images relative to precontrast images alone (91.0%–94.4% versus 75.3%–87.6%,  $P < .04$ , and 66.3%–73.0% versus 52.8%–58.4%,  $P < .02$ , respectively). No significant differences ( $P > .133$ ) in diagnostic accuracy were noted between patients receiving  $\leq 0.08$  mmol/kg of gadobenate dimeglumine and patients receiving  $> 0.08$  mmol/kg of gadobenate dimeglumine.

**CONCLUSIONS:** Gadobenate dimeglumine is safe and effective for pediatric MR imaging.

**ABBREVIATIONS:** ECG = electrocardiogram; GBCA = gadolinium-based contrast agent; Gd = gadolinium

The choice of MR imaging contrast agents for use in pediatric subjects, particularly in neonates and infants younger than

2 years of age, is increasingly driven by concerns over potential differences in safety among available gadolinium-based contrast agents (GBCAs). Early concern over the potential increased risk of nephrogenic systemic fibrosis in young children with immature renal function<sup>1–3</sup> has been overshadowed in recent years by a perceived risk associated with gadolinium (Gd) retention following multiple exposures to certain types of GBCAs.<sup>4–7</sup> Such concerns have led to a change in practice at some centers, with many departments opting to use macrocyclic GBCAs, which are considered more stable and, consequently, safer for potentially more vulnerable pediatric subjects.<sup>8</sup> Recent evidence demonstrating T1 signal increases suggestive of Gd retention in the pediatric brain after the exclusive administration of macrocyclic GBCAs<sup>9</sup> should encourage practitioners to look more closely at the available evidence and to select the most appropriate GBCA on the basis of

Received July 26, 2019; accepted after revision September 18.

From the Department of Radiology (D.S.E.), Duke University, Durham, North Carolina; Department of Diagnostic Imaging (K.W.M.), University of California, San Francisco, Benioff Children's Hospital, Oakland, California; Department of Radiology (H.A.P.), University of Michigan, C.S. Mott Children's Hospital, Ann Arbor, Michigan; Department of Neuroradiology (F.M.T.), Fondazione Istituto di Ricovero e Cura a Carattere Scientifico Cà Granda Ospedale Maggiore Policlinic, Milan, Italy; and Radiodiagnostica e Neuroradiologia (C.C.), Institute of Radiology, Fondazione Policlinico Universitario 'A. Gemelli', Università Cattolica del Sacro Cuore, Rome, Italy.

Grants from Bracco Diagnostics, specifically to enroll patients, were awarded to the University of California, San Francisco, CSF Benioff Children's Hospital in Oakland, California (Kenneth W. Martin) and the University of Michigan, C.S. Mott Children's Hospital in Ann Arbor, Michigan (Hemant A. Parmar).

Please address correspondence to David S. Enterline, MD, Duke University Medical Center, 3808 Erwin Rd, Durham, NC 27710; e-mail: david.enterline@duke.edu  
<http://dx.doi.org/10.3174/ajnr.A6319>

not only the potential for Gd deposition but also diagnostic efficacy and other safety parameters such as the risk for immediate adverse events.<sup>10</sup>

Gadobenate dimeglumine (MultiHance; Bracco Diagnostics, Princeton, New Jersey) is a GBCA that has been proved safe among adult and pediatric (older than 2 years of age) subjects for a variety of indications.<sup>11-14</sup> Compared with other GBCAs, gadobenate dimeglumine has 2 unique features that make it advantageous for contrast-enhanced MR imaging of children; on the one hand, it has increased relaxivity,<sup>15</sup> which enables better depiction of very small or poorly enhancing lesions compared with other agents at equivalent doses,<sup>16</sup> and on the other hand, it is partially eliminated (up to 5% of the injected dose) by the hepatobiliary route, rendering it suitable for both dynamic and delayed hepatobiliary phase imaging of the liver at a reduced dose.<sup>17</sup> In terms of the risk of nephrogenic systemic fibrosis, numerous studies point to its safety in patients with severely compromised renal function,<sup>18,19</sup> and it is classified, together with the 3 macrocyclic agents, as a group II (lowest risk of nephrogenic systemic fibrosis) GBCA by the American College of Radiology.<sup>2</sup> Studies of T1 signal changes in the pediatric brain following cumulative gadobenate dimeglumine exposure have revealed no differences relative to GBCA-naïve subjects in non-neurologic subjects (including in infants younger than 2 years of age at first exposure) who received between 5 and 15 doses of gadobenate dimeglumine at a dose of 0.05 mmol/kg.<sup>20</sup> Conversely, elevations of T1 signal were seen in 2 of 60 untreated (no radiochemotherapy) children with neurologic disease, but only after 16 and 20 injections of gadobenate dimeglumine at a higher dose of 0.1 mmol/kg.<sup>21</sup>

A recent study in 200 pediatric hospital in-patients from 4 days to 15 years of age revealed an excellent safety profile for gadobenate dimeglumine with no adverse events or abnormal clinical laboratory values reported during the 24-hour monitoring period, even among patients who received several gadobenate dimeglumine exposures.<sup>14</sup> Among these patients were 57 who were 2 years of age or younger, of whom 47 were 1 year of age or younger at first exposure (including 18 that were 1 month or younger). Gadobenate dimeglumine is currently approved in Europe for liver imaging and in the United States and elsewhere for a range of indications, including enhanced MR imaging of the CNS in children younger than 2 years of age.<sup>22</sup> The present study was performed to further evaluate the safety and efficacy of gadobenate dimeglumine in neonates and infants 2 years of age or younger referred for routine diagnostic MR imaging of the CNS.

## MATERIALS AND METHODS

This was a retrospective evaluation of safety data for patients 2 years of age or younger with suspected or known disease of the CNS who had undergone contrast-enhanced MR imaging with gadobenate dimeglumine as part of the clinical work-up. An additional prospectively designed blinded read of images from these patients was performed to confirm the efficacy of gadobenate dimeglumine. Patients underwent imaging at 2 centers (Benioff Children's Hospital, Oakland, California; C.S. Mott Children's Hospital, Ann Arbor, Michigan) in the United States between June 12, 2008, and December 5, 2014. The

study was conducted in accordance with the International Congress on Harmonization, Good Clinical Practice, US FDA regulations, and ethical principles outlined in the Declaration of Helsinki and all applicable local regulations. The study protocol was reviewed and approved by the institutional review board at each center, was compliant with the Health Insurance Portability and Accountability Act, and was registered at [www.clinicaltrials.gov](http://www.clinicaltrials.gov).

## Patients

Male and female patients were eligible for inclusion if they were 2 years of age or younger, received gadobenate dimeglumine at a documented nominal dose of 0.1 mmol/kg body weight ( $\pm$  25% in volume administered) for known or highly suspected enhancing disease of the brain or spine, and had complete demographic and safety data available. Eligible patients were included consecutively from a prospectively defined start date (December 5, 2014) and continued chronologically backward in strict order until the prospectively designed enrollment was attained. A prospective, blinded assessment of efficacy was then performed for all patients who were eligible for the safety evaluation for whom pre- and postdose T1-weighted spin-echo/FSE and/or gradient recalled-echo images as well as T2-weighted spin-echo/FSE and FLAIR (if acquired) images were available.

## MR Imaging

MR imaging was performed at 1.5T (Ingenia and Gyroscan Intera; Philips Healthcare, Best, the Netherlands) for all patients apart from 7 subjects whose images were acquired at 3T (Ingenia and Achieva; Philips Healthcare). A standard protocol comprising T1-weighted spin-echo, T1-weighted gradient recalled-echo, T2-weighted FSE, and T2-weighted FLAIR acquisitions before contrast injection, and T1-weighted spin-echo and T1-weighted gradient recalled-echo acquisitions after injection ensured protocol uniformity across the 2 sites and in individual patients. Gadobenate dimeglumine was administered manually as a nominal bolus dose of 0.1 mmol/kg body weight (0.2 mL/kg). However, due to the retrospective nature of the study, a dose of 0.1 mmol/kg  $\pm$  25% by volume was prospectively defined for patient inclusion.

## Safety Assessments

Safety data recorded by the investigating radiologist at the time of the examination were evaluated in terms of clinical adverse events and, when available, vital signs and electrocardiogram (ECG) and clinical laboratory determinations. An adverse event was defined as any untoward medical occurrence during the timeframe associated with the administration of gadobenate dimeglumine that did not necessarily need to be causally related to the administration of gadobenate dimeglumine. If an adverse event was considered related to sedation or anesthesia, this was recorded as part of the event description.

All safety data obtained from 48 hours before until 48 hours after the examination were recorded on an individual, patient-specific case report form. Adverse events with unknown onset times were counted beginning during the timeframe associated with gadobenate dimeglumine administration. If laboratory data

**Table 1: Patient demographic characteristics and details regarding type of MR examination, exposure to gadobenate dimeglumine, and sedation during examination**

Demographic	Overall	0 to <1 Month	1 to <6 Months	6 to <12 Months	12–24 Months
No. of subjects	90	13	23	19	35
Male/female	48:42	4:9	11:12	16:3	17:18
Age (mo)					
Mean	9.7 ± 7.5	0.3 ± 0.3	3.0 ± 1.3	9.1 ± 1.8	17.9 ± 3.1
Range	0.1–23.3	0.1–0.8	1.1–5.6	6.0–11.5	12.2–23.3
Weight (Kg)					
Mean	7.9 ± 3.3	3.5 ± 0.7	5.4 ± 1.5	8.6 ± 1.8	10.8 ± 2.0
Range	2.3–16.3	2.3–4.8	2.6–9.6	5.2–12.1	7.4–16.3
Height (cm)					
Mean	68.4 ± 13.5	46.4 ± 6.7	59.4 ± 6.4	68.7 ± 5.2	81.0 ± 5.8
Range	32–91	32–51	47–71	61–76	70–91
Type of examination					
Brain	83	12	23	17	31
Spine	7	1	0	2	4
Dose (mmol/kg)					
Mean	0.084 ± 0.015	0.092 ± 0.025	0.089 ± 0.018	0.085 ± 0.01	0.078 ± 0.006
Range	0.07–0.13	0.07–0.13	0.07–0.13	0.07–0.10	0.07–0.10
Sedation/anesthesia <sup>a</sup>					
Yes	72	7	16	15	34
No	7	3	3	1	0
NA	11	3	4	3	1

**Note:**—NA indicates not available.

<sup>a</sup>Patients may have received >1 drug for sedation.

were available, the normal ranges for the parameters measured were included. The last laboratory measurement before the administration of gadobenate dimeglumine was taken as the baseline value.

### Efficacy Assessments

MR images were evaluated by 3 independent neuroradiologists (C.C., D.S.E., and F.M.T.; each with >20 years' experience) who were unaffiliated with the enrollment centers and blinded to all patient clinical profiles. Evaluation was performed using the thin client of the AquariusNet server (Version 4.4.5.36; TeraRecon, San Mateo, California). Blinded reads consisted of independent assessments of precontrast images and combined pre- and postcontrast images in a randomized order.

Patient diagnoses were determined at the disease (tumor versus non-neoplastic) level and at specific diagnosis levels from a list of 54 coded diagnoses covering brain and spinal diseases of different natures (including neoplastic, inflammatory, degenerative, vascular, and postoperative conditions). Diagnoses by the blinded readers were subsequently matched with the final on-site patient diagnosis which, in each case, was determined by the investigating radiologist on the basis of all available clinical, pathologic, radiologic, and surgical information.

Finally, each reader was asked whether the postcontrast images provided additional information over precontrast images based on applicable categories described elsewhere.<sup>23</sup>

### Statistical Analysis

Statistical analyses were performed using SAS software (Version 9.3; SAS Institute, Cary, North Carolina). Continuous measurements were reported as mean ± SD, while categorical assessments were described as number (%). The final diagnosis made at each investigator site was considered the reference standard. Diagnostic accuracy on precontrast and combined

pre- and postcontrast images was estimated for each reader for both the differentiation of tumor from non-neoplastic disease and the correct diagnosis at specific disease level. The McNemar test was used to test the difference in diagnostic accuracy between precontrast and combined pre- and postcontrast image sets by reader. The Fisher exact test was used to test the difference in diagnostic accuracy for combined pre- and postcontrast image sets for contrast doses of ≤0.08 mmol/kg body weight and >0.08 mmol/kg body weight.

Assuming an expected difference in accuracy between precontrast and combined pre- and postcontrast image sets of 10% with 12% discordant pairs, we calculated a sample size of 90 patients to provide >85% power for a McNemar test of equality in accuracy.

### RESULTS

Ninety patients meeting the inclusion criteria were included in the safety evaluation. Of these 90 patients, 89 (98%) had pre- and postdose efficacy data available and were included in the prospective blinded evaluation of gadobenate dimeglumine efficacy. One patient 13 months of age was excluded from the efficacy evaluation due to image acquisitions occurring on different days, with different equipment, and in different planes.

Demographic details for the 90 patients evaluated for safety are shown in Table 1. Patient ages ranged from 0.1 month (2 days postnatal) to 23.3 months (23 months, 7 days). The age distribution included 35 (39%) between 12 and younger than 24 months; 19 (21%) between 6 and younger than 12 months, 23 (26%) between 1 and younger than 6 months; and 13 (14%) younger than 1 month. An MR imaging examination of the brain was performed in 83 (92.2%) cases, while MR imaging of the spine was performed in 7 (7.8%) cases.

A summary of relevant medical history is given in Table 2. At least 1 finding was reported for 71 (78.9%) patients. The most

commonly reported medical history findings were oncologic, occurring in 23 of the 71 patients with available information.

Serum creatinine values measured before and in close temporal proximity to the administration of gadobenate dimeglumine were available for 61 patients (Table 3). Estimated glomerular filtration rate values calculated using the Schwartz formula for patients younger than 2 years of age<sup>24</sup> were reported for 40 patients with available height data. Mean and median values across the age groups were consistent with those reported for children with normal age-related renal function; immaturity of clearance was observed in infants younger than 1 month and a gradual decline of serum creatinine levels was observed during the first year, reflecting normal kidney maturation and muscle mass accretion.<sup>25</sup>

Administration of sedation and/or anesthesia before the examination was reported for 72 (80%) patients. Seven patients did not receive sedation or anesthesia before the examination. No information could be retrieved from clinical records for 11 subjects. Propofol, alone or in combination with other drugs, including sevoflurane, isoflurane, fentanyl, midazolam, nitrous oxide, succinylcholine, vecuronium bromide, and cisatracurium besilate, was administered to 56/72 (77.8%) patients without complications.

The distribution of gadobenate dimeglumine doses is presented in Table 4. Overall, 52/89 (58.4%) patients received a dose of  $\leq 0.08$  mmol/kg body weight (0.065–0.08 mmol/kg), while 37/89 (41.6%) patients received a dose of  $> 0.08$  mmol/kg body weight (0.082–0.132 mmol/kg). Gadobenate dimeglumine was administered in accordance with the standard practice at each investigating center.

**Table 2: Relevant medical history of evaluated patients<sup>a</sup>**

History	
No. of patients included	<i>n</i> = 90
No. of patients with at least 1 finding	71 (78.9)
No. of patients by finding	
Oncology	23 (25.6)
Metabolic	1 (1.1)
Congenital	6 (6.7)
Other	48 (53.3)
Cerebrovascular	23 (25.6)
Hemorrhagic	3 (3.3)
Infarct	3 (3.3)
Ischemic	13 (14.4)
Vascular	4 (4.4)
Hydrocephalus	3 (3.3)
Inflammatory/Infectious	15 (16.7)
Injury	7 (7.8)
Seizure	4 (4.4)
Other findings	6 (6.7)

<sup>a</sup> Numbers add up to  $> 100\%$  because a patient may have findings in  $> 1$  category. Data in parentheses are percentages of total [*n* = 90] patients.

**Table 3: Serum creatinine values**

Demographic	Overall	0 to <1 Month	1 to <6 Months	6 to <12 Months	12–24 Months
No. of subjects	61	12	16	11	22
SCr (mg/mL)					
Mean	0.3 ± 0.19	0.5 ± 0.23	0.3 ± 0.25	0.2 ± 0.07	0.3 ± 0.07
Range	0.1–1.2	0.2–0.9	0.1–1.2	0.1–0.4	0.2–0.4
eGFR (mL/min/1.73m <sup>2</sup> )					
Mean	131.7 ± 60.3	59.3 ± 31.7	92.4 ± 43.2	150.4 ± 18.3	176.3 ± 47.2
Range	17.6–255.6	24.0–114.8	17.6–153.9	114.0–168.8	99.0–255.6

**Note:**—SCr indicates serum creatinine; eGFR, estimated glomerular filtration rate.

## Safety Findings

**Adverse Events.** Nine nonserious adverse events were reported for 8 (8.8%) patients. Six adverse events were reported in 5 patients 12 months of age or older. Three adverse events (2 cases of fever, 1 of poor urine output) were considered mild, and 6 (malignant hyperthermia, 3 cases of seizures/seizurelike activity, hypokinesia, decreased responsiveness) were moderate in intensity. All events occurred at or  $> 24$  hours after gadobenate dimeglumine administration, and in all cases, the investigating radiologist considered that there was no reasonable possibility of a relationship to the administration of gadobenate dimeglumine. All patients recovered, though 1 patient recovered with sequelae following an operation.

**Vital Signs.** Vital signs were monitored at standard intervals for all sedated patients (52/90 [57.8%]) but were not routinely monitored for nonsedated patients. No clinically meaningful changes were recorded by the investigators.

**ECGs.** ECG data from at least 1 postdose time point were available for 48/90 (53.3%) patients. No clinically meaningful changes from baseline were observed in any patient with data available.

**Clinical Laboratory Values.** Data for hematology and clinical chemistry at pre- and postdose were available for 47/90 (52.2%) patients. On the basis of available data, no clinically meaningful changes from baseline in any hematology or clinical chemistry parameter were reported for any patient.

## Efficacy Results

Accurate differentiation of neoplastic from non-neoplastic disease was achieved by all 3 blinded readers in significantly ( $P < .05$ ) more patients following evaluation of combined pre- and postcontrast images relative to precontrast images alone (91.0%–94.4% versus 75.3%–87.6%, Table 5). Three-reader agreement for the differential diagnosis was achieved for 63/89 (70.8%) patients based on precontrast images alone, but for 77/89 (86.5%) patients based on the evaluation of combined pre- and postcontrast images.

Similar results were obtained when each reader was asked to ascribe a specific lesion diagnosis from a list of 54 coded diagnoses. Each reader assigned a correct diagnosis relative to the on-site final clinical diagnosis in significantly ( $P \leq .02$ ) more patients based on assessment of combined pre- and postcontrast images relative to precontrast images alone (66.3%–73.0% versus 52.8%–58.4%, Table 5). No reader provided an accurate diagnosis for 22/89 (24.7%) patients based on the evaluation of precontrast images alone. The number of patients for whom an accurate diagnosis

was not made was lower (17/89; 19.1%) when assessment was made of combined pre- and postcontrast images. Agreement on an accurate specific diagnosis by all 3 readers was achieved for 29/89 (32.6%) patients based on precontrast images alone but for 50/89 (56.2%) patients when evaluation was made of combined pre- and postcontrast images.

No differences in either the differential diagnosis (neoplastic-versus-non-neoplastic disease,  $P < .133$ ) or a specific disease diagnosis ( $P > .344$ ) were noted by any reader for patients who received a gadobenate dimeglumine dose of  $\leq 0.08$  mmol/kg body weight compared with patients who received a dose of  $> 0.08$  mmol/kg body weight (Table 6).

The presence and pattern of contrast enhancement were considered radiologically helpful in 78/89 (87.6%), 85/89 (95.5%), and 57/89 (64%) patients by readers 1, 2, and 3, respectively. The primary benefit was considered the improvement in lesion conspicuity as defined by an improved visualization of the size, extent, and/or margins of a lesion or better prediction of the grade, histologic type, vascularity, and/or aggressiveness of a lesion (Figs 1–3). Lack of enhancement was also recognized as a potentially useful factor in image interpretation but in a smaller percentage of patients (6.0%, 16.8%, and 4.5%; readers 1, 2, and 3, respectively).

**Table 4: Gadobenate dimeglumine dose distribution**

Volume/Dose Classes		No. of Patients
Volume Administered (mL/kg)	Dose Administered (mmol/kg)	
$\leq 0.14$	$\leq 0.07$	2
0.142–0.15	0.071–0.075	25
0.152–0.16	0.076–0.08	25
0.162–0.18	0.081–0.09	20
0.182–0.2	0.091–0.1	7
0.202–0.264	0.101–0.132	11
Total		90

**Table 5: Evaluation of diagnostic performance on combined pre- and postcontrast MR images relative to precontrast images alone**

End Point	Reader	Precontrast (n = 89)	Pre- + Postcontrast (n = 89)	P Value <sup>a</sup>
Tumor vs nontumor	1	75 (84.3%)	84 (94.4%)	.003
	2	67 (75.3%)	81 (91.0%)	<.001
	3	78 (87.6%)	82 (92.1%)	.046
Specific diagnosis	1	52 (58.4%)	65 (73.0%)	.003
	2	47 (52.8%)	63 (70.8%)	<.001
	3	50 (56.2%)	59 (66.3%)	.02

<sup>a</sup> McNemar test.

**Table 6: Comparison of diagnostic performance on combined pre- and postcontrast images in patients administered gadobenate dimeglumine at doses of  $\leq 0.08$  mmol/kg body weight compared with doses  $> 0.08$  mmol/kg body weight**

End Point	Reader	$\leq 0.08$ mmol/kg (n = 52)	$> 0.08$ mmol/kg (n = 37)	P Value <sup>a</sup>
Tumor vs nontumor	1	50 (96.2%)	34 (91.9%)	.645
	2	45 (86.5%)	36 (97.3%)	.133
	3	47 (90.4%)	35 (94.6%)	.695
Specific diagnosis	1	40 (76.9%)	25 (67.6%)	.344
	2	38 (73.1%)	25 (67.6%)	.64
	3	35 (67.3%)	24 (64.9%)	.824

<sup>a</sup> Fisher exact test.

## DISCUSSION

Whereas the accumulated experience in MR imaging of the CNS of adult patients is helpful for imaging the pediatric population, pediatric imaging presents unique challenges in terms of approaches to image acquisition and, in particular, concerns about patient safety.<sup>26,27</sup> Nevertheless, despite numerous recent studies that have focused on potential safety issues associated with GBCA use in the pediatric population,<sup>1, 3–9</sup> little, if any, evidence of increased risk due to GBCA administration has been demonstrated in the roughly 30 years since the approval of the first GBCA. As with all contrast-enhanced studies, the fear of adverse consequences, no matter how rare the event or unfounded the fear, should be off-set against the clinically relevant diagnostic information available from the examination. In the case of pediatric neuroimaging, GBCA-enhanced MR imaging provides essential information on a variety of conditions, including congenital malformations, tumors, infections, metabolic disorders, epilepsy, and inflammatory and cerebrovascular diseases. Postcontrast imaging provides detailed information on the location, type, and number of lesions that are essential for diagnosis and treatment planning.

The safety and efficacy profiles of GBCAs in children 2 years of age or older are relatively well-established, in part because most GBCAs have regulatory approval for children 2 years of age or older. Much more limited information is available for children younger than 2 years of age. One of the principal concerns relating to young children, and particularly neonates, is that the hepatic and renal clearance mechanisms are relatively underdeveloped compared with those in adults.<sup>28,29</sup> In full-term infants, glomerular filtration efficiency roughly equivalent to adult levels does not occur until about 6 months.<sup>30</sup> Nevertheless, pharmacokinetic studies of renally excreted drugs, including GBCAs, in healthy neonates have revealed kinetic behavior comparable with that in older children and adults.<sup>30,31</sup>

Our study revealed no evidence of any adverse events attributable to gadobenate dimeglumine administration in children younger than 2 years of age, even among the youngest children

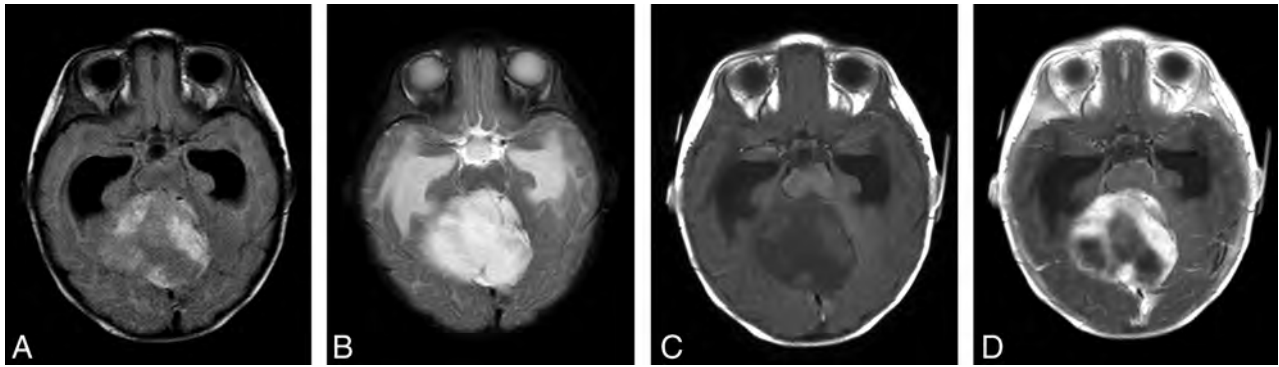


**FIG 1.** MR imaging in a 4.3-month-old infant with cerebellar pilocytic astrocytoma shows a large intra-axial mass, which is hyperintense on FLAIR (A) and T2-weighted (B) images with surrounding edema. The lesion is hypointense on the T1-weighted precontrast image (C) and shows heterogeneous-but-avid postcontrast enhancement (D) after contrast administration (0.08 mmol/kg of gadobenate dimeglumine [1 mL] administered as a manual bolus). Also note marked obstructive hydrocephalus with enlarged bilateral temporal horns.

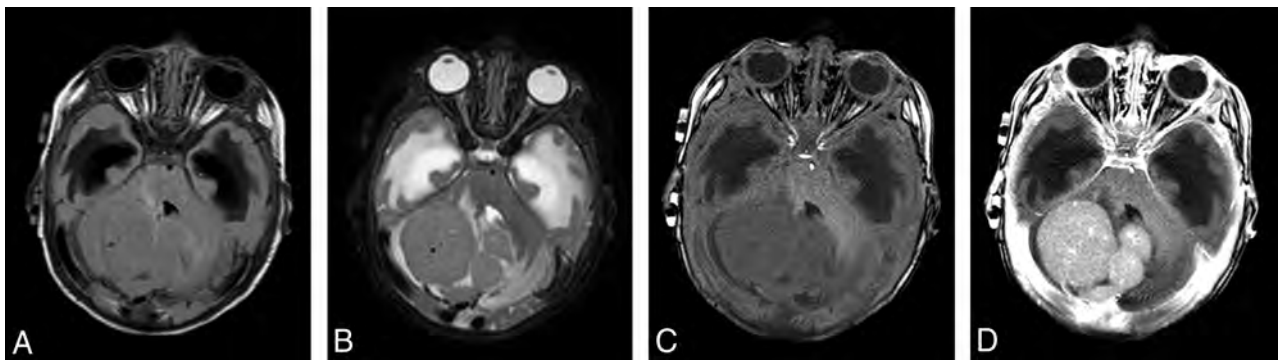


**FIG 2.** MR imaging in a 2.3-month-old infant with desmoplastic medulloblastoma shows a large multinodular intra-axial mass, which is isointense on FLAIR (A) and T2-weighted (B) images with mild surrounding edema. The lesion is slightly hypointense on the T1-weighted precontrast image (C) and shows moderate homogeneous enhancement (D) after contrast administration (0.07 mmol/kg of gadobenate dimeglumine, 0.8 mL administered as a manual bolus). Also noted is obstructive hydrocephalus with extensive periventricular interstitial edema.

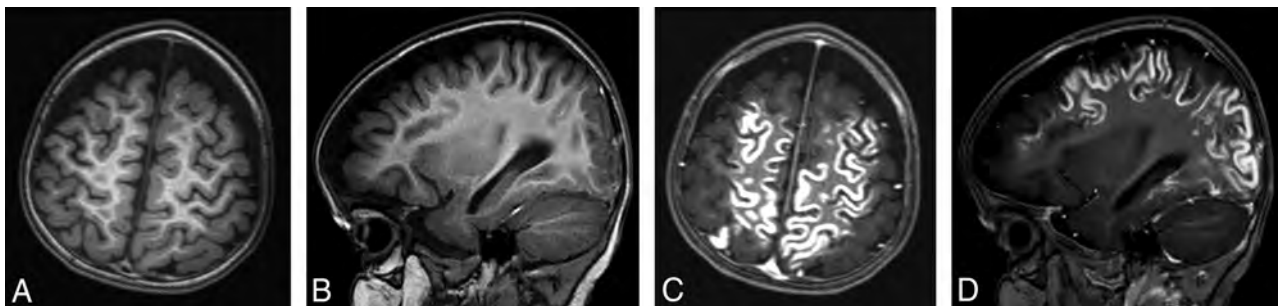


**FIG 3.** MR imaging in a 15-month-old girl with known subacute infarctions. Axial and sagittal T1-weighted images acquired before (A and B) and after (C and D) contrast administration (0.08 mmol/kg gadobenate dimeglumine [1.5 mL] administered as a manual bolus). Extensive gyral enhancement in the cerebral hemispheres is clearly demonstrated on postcontrast images.

evaluated. Overall, just 9 adverse events were reported, each of which occurred at least 24 hours after gadobenate dimeglumine administration and none of which were considered attributable to the administration of gadobenate dimeglumine. In terms of the safety profile, our findings are in agreement with those of Schneider et al,<sup>14</sup> who evaluated gadobenate dimeglumine safety in 200 pediatric patients from 4 days to 15 years of age (including 47 patients 1 year of age or younger). In their study, no adverse

events were reported after the administration of up to 10 injections of gadobenate dimeglumine, and no changes in creatinine or bilirubin levels were noted, even among the very youngest children.

In common with the study by Schneider et al,<sup>14</sup> approximately 80% of our patients were imaged under heavy sedation or general anesthesia. The need for sedation reflects the need for the child to lie still in the magnet for a relatively long time. One benefit of

sedation in very young children is that changes in vital signs, ECG traces, and even laboratory measurements from acquired blood samples can more readily be assessed objectively. In our study, as in the study by Schneider et al,<sup>14</sup> no clinically meaningful changes from baseline were noted for any patient for ECG intervals, vital signs, or laboratory values. Our results also compare very favorably with safety findings reported for the macrocyclic GBCAs gadoterate meglumine<sup>32,33</sup> and gadobutrol.<sup>31,34</sup> Those studies similarly reported no,<sup>33,34</sup> or at most 1,<sup>31,32</sup> adverse event in children younger than 2 years of age that was considered related to the administration of GBCA.

In terms of diagnostic efficacy, gadobenate dimeglumine has proved efficacious in pediatric subjects not only for body applications<sup>14</sup> but also specifically for brain tumor imaging.<sup>16</sup> Our findings confirm those of previous studies in demonstrating excellent accuracy (>91% for all 3 readers) for the differentiation of neoplastic from non-neoplastic disease. Most important, the distribution of neoplastic-versus-non-neoplastic disease in the patients' diagnoses was balanced in our study (57.3% versus 42.3%, respectively), with roughly equivalent representation of both intra- and extra-axial tumors in patients with neoplasms. Regarding the more challenging assessment of accuracy for a specific diagnosis, values from 66.3% to 73.0% were obtained for the 3 blinded readers. These values should be considered very good, given the fully blinded and independent reading conditions under which the images were evaluated. It is well-established that knowledge of clinical data significantly improves lesion diagnosis for other contrast-enhanced MR imaging applications<sup>35</sup> and thus it is to be expected that more correct specific diagnoses would have been made in this study had the readers been aware of the medical history and clinical characteristics of the patients.

Compared with other GBCAs, gadobenate dimeglumine has considerably higher r1 relaxivity,<sup>15</sup> which translates into significantly better diagnostic performance for brain tumor imaging when administered at a dose equivalent to that of a comparator GBCA.<sup>36,37</sup> Recent studies have highlighted the value of this higher r1 relaxivity in permitting lower gadobenate dimeglumine doses without the loss of diagnostic information relative to that attained with a comparator GBCA at higher dose.<sup>37-41</sup> Our evaluation revealed no significant differences between doses lower and higher than 0.08 mmol/kg body weight for either differential or specific disease diagnoses. These findings lend support to previous studies that have looked at reduced doses of gadobenate dimeglumine for neuroimaging applications<sup>37-41</sup> and suggest that a gadobenate dimeglumine dose lower than the standard GBCA dose (0.1 mmol/kg body weight) may be appropriate for neuroimaging in many cases. Notably, the gadobenate dimeglumine dose approved by the US FDA for enhanced MR imaging of the CNS in children younger than 2 years of age is 0.1–0.2 mL/kg body weight, corresponding to 0.05–0.1 mmol/kg body weight.<sup>22</sup>

Such dose-lowering opportunities might be considered highly clinically relevant, given the current concern over T1 hyperintensity and gadolinium retention following GBCA administration. In this regard, a study in pediatric non-neurologic subjects who received between 5 and 15 doses of 0.05

mmol/kg of gadobenate dimeglumine revealed no evidence of T1 hyperintensity in the dentate nucleus or globus pallidus compared with age- and weight-matched control subjects who had never been administered any GBCA.<sup>20</sup> Conversely, a study in neurologic patients revealed T1 hyperintensity in 2 of 60 pediatric subjects who received 16 and 20 doses of 0.1 mmol/kg of gadobenate dimeglumine.<sup>21</sup> Whether the T1 signal changes noted in these 2 subjects reflected the higher dose used (0.1 versus 0.05 mmol/kg) or whether they were a consequence of the different underlying clinical condition of the patients (neurologic versus non-neurologic) is unclear and should be the subject of further study. However, the 16 and 20 doses given to these 2 patients were the highest cumulative doses across the entire patient cohort.<sup>21</sup> It should be noted that T1 signal changes in the pediatric brain have also been seen after the exclusive administration of macrocyclic GBCAs,<sup>9</sup> and that confirmed gadolinium presence has been reported in the brains of postmortem subjects even after the administration of single doses of macrocyclic GBCA.<sup>42</sup>

Most important, no clinical manifestations or adverse clinical outcomes related to T1 signal changes or brain Gd retention have been observed at this time following the repeat administration of any GBCA, and there is no evidence of any effect on cognitive or neurobehavioral development, as also recognized by the US FDA. Although studies to assess the impact of cumulative GBCA administration on human development and neurologic function are difficult to perform, studies in animals, which are invariably taken as indicative of the human situation, have revealed no impact of gadobenate dimeglumine on growth, maturation, behavior, or cognitive function of neonatal and juvenile rats, even after very high cumulative doses (15 mmol/kg; corresponding to about 25 injections of a standard 0.1-mmol/kg dose in humans).<sup>43</sup>

A limitation of our study was its retrospective design. However, whereas patients were enrolled retrospectively at each of the 2 sites, patient inclusion began from a prospectively defined start date and continued chronologically backward in strict order until the planned enrollment was attained. This enrollment procedure ensured an unbiased approach to patient inclusion. Furthermore, image assessment was performed in a prospective manner by 3 independent readers who were unaffiliated with the enrollment centers and fully blinded to all patient information.

## CONCLUSIONS

Our findings confirm that contrast-enhanced MR imaging of the CNS with gadobenate dimeglumine at a dose between 0.065 and 0.132 mmol/kg body weight is safe, well-tolerated, and effective in patients younger than 2 years of age. The potential to lower the administered dose because of the higher r1 relaxivity of gadobenate dimeglumine may be considered beneficial in pediatric patients, particularly considering the cumulative nature of gadolinium retention in the brain.

Disclosures: David S. Enterline—UNRELATED: Board Membership: Bracco Diagnostics, Comments: Scientific Advisory Board; Consultancy: Bracco Diagnostics. Kenneth W. Martin—RELATED: Grant: Children's Hospital and Research Center Oakland.\* Hemant

A. Parmar—RELATED: Other: Bracco Diagnostics, Comments: research grant to enroll study patients.\* Cesare Colosimo—UNRELATED: Consultancy: Bracco Diagnostics, Comments: €5000 as a blinded reader for evaluating MR images of the enrolled patients. \*Money paid to the institution.

## REFERENCES

1. Nardone B, Saddleton E, Laumann AE, et al. **Pediatric nephrogenic systemic fibrosis is rarely reported: a RADAR report.** *Pediatr Radiol* 2014;44:173–80 CrossRef Medline
2. American College of Radiology. *ACR Manual on Contrast Media, Version 10.3.* Reston: American College of Radiology; 2017
3. Bedoya MA, White AM, Edgar JC, et al. **Effect of intravenous administration of contrast media on serum creatinine levels in neonates.** *Radiology* 2017;284:530–40 CrossRef Medline
4. Roberts DR, Chatterjee AR, Yazdani M, et al. **Pediatric patients demonstrate progressive T1-weighted hyperintensity in the dentate nucleus following multiple doses of gadolinium-based contrast agent.** *AJNR Am J Neuroradiol* 2016;37:2340–47 CrossRef Medline
5. Hu HH, Pokorney A, Towbin RB, et al. **Increased signal intensities in the dentate nucleus and globus pallidus on unenhanced T1-weighted images: evidence in children undergoing multiple gadolinium MRI exams.** *Pediatr Radiol* 2016;46:1590–98 CrossRef Medline
6. Flood TF, Stence NV, Maloney JA, et al. **Pediatric brain: repeated exposure to linear gadolinium-based contrast material is associated with increased signal intensity at unenhanced T1-weighted MR imaging.** *Radiology* 2017;282:222–28 CrossRef Medline
7. Radbruch A, Haase R, Kickingereder P, et al. **Pediatric brain: no increased signal intensity in the dentate nucleus on unenhanced T1-weighted MR images after consecutive exposure to a macrocyclic gadolinium-based contrast agent.** *Radiology* 2017;283:828–36 CrossRef Medline
8. Blumfield E, Moore MM, Drake MK, et al. **Survey of gadolinium-based contrast agent utilization among the members of the Society for Pediatric Radiology: a Quality and Safety Committee report.** *Pediatr Radiol* 2017;47:665–73 CrossRef Medline
9. Rossi Espagnet MC, Bernardi B, Pasquini L, et al. **Signal intensity at unenhanced T1-weighted magnetic resonance in the globus pallidus and dentate nucleus after serial administrations of a macrocyclic gadolinium-based contrast agent in children.** *Pediatr Radiol* 2017;47:1345–52 CrossRef Medline
10. Gulani V, Calamante F, Shellock FG, et al; International Society for Magnetic Resonance in Medicine. **Gadolinium deposition in the brain: summary of evidence and recommendations.** *Lancet Neurol* 2017;16:564–70 CrossRef Medline
11. Kirchin MA, Pirovano G, Venetianer C, et al. **Safety assessment of gadobenate dimeglumine (MultiHance®): extended clinical experience from Phase I studies to post-marketing surveillance.** *J Magn Reson Imaging* 2001;14:281–94 CrossRef Medline
12. Shellock FG, Parker JR, Venetianer C, et al. **Safety of gadobenate dimeglumine: summary of findings from clinical studies and post-marketing surveillance.** *Invest Radiol* 2006;41:500–09 CrossRef Medline
13. Bleicher AG, Kanal E. **Assessment of adverse reaction rates to a newly approved MRI contrast agent: review of 23,553 administrations of gadobenate dimeglumine.** *AJR Am J Roentgenol* 2008;191:W307–11 CrossRef Medline
14. Schneider G, Schürholz H, Kirchin MA, et al. **Safety and adverse effects during 24 hours after contrast-enhanced MRI with gadobenate dimeglumine (MultiHance) in children.** *Pediatr Radiol* 2013;43:202–11 CrossRef Medline
15. Shen Y, Goerner FL, Snyder C, et al. **T1 relaxivities of gadolinium-based magnetic resonance contrast agents in human whole blood at 1.5, 3, and 7 T.** *Invest Radiol* 2015;50:330–08 CrossRef Medline
16. Colosimo C, Demaerel P, Tortori-Donati P, et al. **Comparison of gadobenate dimeglumine (Gd-BOPTA) with gadopentetate dimeglumine (Gd-DTPA) for enhanced MR imaging of brain and spine tumors in pediatric subjects.** *Pediatr Radiol* 2005;35:501–10 CrossRef Medline
17. Schneider G, Maas R, Schultze Kool L, et al. **Low-dose gadobenate dimeglumine versus standard dose gadopentetate dimeglumine for contrast-enhanced magnetic resonance imaging of the liver: an intra-individual crossover comparison.** *Invest Radiol* 2003;38:85–94 CrossRef Medline
18. Nandwana SB, Moreno CC, Osipow MT, et al. **Gadobenate dimeglumine administration and nephrogenic systemic fibrosis: is there a real risk in patients with impaired renal function?** *Radiology* 2015;276:741–47 CrossRef Medline
19. Bruce R, Wentland AL, Haemel AK, et al. **Incidence of nephrogenic systemic fibrosis using gadobenate dimeglumine in 1423 patients with renal insufficiency compared with gadodiamide.** *Invest Radiol* 2016;51:701–05 CrossRef Medline
20. Schneider GK, Stroeder J, Roditi G, et al. **T1 signal measurements in pediatric brain: findings after multiple exposures to gadobenate dimeglumine for imaging of nonneurologic disease.** *AJNR Am J Neuroradiol* 2017;38:1799–806 CrossRef Medline
21. Kinner S, Schubert TB, Bruce RJ, et al. **Deep brain nuclei T1 shortening after gadobenate dimeglumine in children: influence of radiation and chemotherapy.** *AJNR Am J Neuroradiol* 2018;39:24–30 CrossRef Medline
22. MultiHance prescribing information in the USA. [https://www.accessdata.fda.gov/drugsatfda\\_docs/label/2018/021357s016s017,021358s015s016bl.pdf](https://www.accessdata.fda.gov/drugsatfda_docs/label/2018/021357s016s017,021358s015s016bl.pdf). Accessed September 5, 2019
23. Elster AD, Moody DM, Ball MR, et al. **Is Gd-DTPA required for routine cranial MR imaging?** *Radiology* 1989;173:231–38 CrossRef Medline
24. Schwartz GJ, Brion LP, Spitzer A. **The use of plasma creatinine concentration for estimating glomerular filtration rate in infants, children, and adolescents.** *Pediatr Clin North Am* 1987;34:571–90 CrossRef Medline
25. Hellerstein S. **Fluids and electrolytes: physiology.** *Pediatr Rev* 1993;14:70–79 CrossRef Medline
26. Bhargava R, Hahn G, Hirsch W, et al. **Contrast-enhanced magnetic resonance imaging in pediatric patients: review and recommendations for current practice.** *Magn Reson Insights* 2013;6:95–111 CrossRef Medline
27. Raschle N, Zuk J, Ortiz-Mantilla S, et al. **Pediatric neuroimaging in early childhood and infancy: challenges and practical guidelines.** *Ann N Y Acad Sci* 2012;1252:43–50 CrossRef Medline
28. Alcorn J, McNamara PJ. **Ontogeny of hepatic and renal systemic clearance pathways in infants, Part I.** *Clin Pharmacokinet* 2002;41:959–98 CrossRef Medline
29. Fernandez E, Perez R, Hernandez A, et al. **Factors and mechanisms for pharmacokinetic differences between pediatric population and adults.** *Pharmaceutics* 2011;3:53–72 CrossRef Medline
30. Ginsberg G, Hattis D, Sonawane B, et al. **Evaluation of child/adult pharmacokinetic differences from a database derived from the therapeutic drug literature.** *Toxicol Sci* 2002;66:185–200 CrossRef Medline
31. Kunze C, Mentzel HJ, Krishnamurthy R, et al. **Pharmacokinetics and safety of macrocyclic gadobutrol in children aged younger than 2 years including term newborns in comparison to older populations.** *Invest Radiol* 2016;51:50–57 CrossRef Medline
32. Scala M, Koob M, de Buttet S, et al. **A pharmacokinetics, efficacy, and safety study of gadoterate meglumine in pediatric subjects aged younger than 2 years.** *Invest Radiol* 2018;53:70–79 CrossRef Medline
33. Emond S, Brunelle F. **Gd-DOTA administration at MRI in children younger than 18 months of age: immediate adverse reactions.** *Pediatr Radiol* 2011;41:1401–06 CrossRef Medline
34. Bhargava R, Noga M. **Safety and efficacy of gadobutrol-enhanced MRI in patients aged under 2 years: a single-center, observational study.** *Magn Reson Insights* 2013;6:1–12 CrossRef Medline

35. Hamm B, Thoeni RF, Gould RG, et al. **Focal liver lesions: characterization with nonenhanced and dynamic contrast material-enhanced MR imaging.** *Radiology* 1994;190:417–23 CrossRef Medline
36. Kanal E, Maravilla K, Rowley HA. **Gadolinium contrast agents for CNS imaging: current concepts and clinical evidence.** *AJNR Am J Neuroradiol* 2014;35:2215–26 CrossRef Medline
37. Vaneckova M, Herman M, Smith MP, et al. **The benefits of high relaxivity for brain tumor imaging: results of a multicenter intraindividual crossover comparison of gadobenate dimeglumine with gadoterate meglumine (The BENEFIT Study).** *AJNR Am J Neuroradiol* 2015;36:1589–98 CrossRef Medline
38. Khouri Chalouhi K, Papini GD, Bandirali M, et al. **Less is better? Intraindividual and interindividual comparison between 0.075 mmol/kg of gadobenate dimeglumine and 0.1 mmol/kg of gadoterate meglumine for cranial MRI.** *Eur J Radiol* 2014;83:1245–49 CrossRef Medline
39. Huang B, Liang CH, Liu HJ, et al. **Low dose contrast-enhanced magnetic resonance imaging of brain metastases at 3.0T using high-relaxivity contrast agents.** *Acta Radiol* 2010;51:78–84 CrossRef Medline
40. Crisi G, Filice S, Erb G, et al. **Effectiveness of a high relaxivity contrast agent administered at half dose in dynamic susceptibility contrast MRI of brain gliomas.** *J Magn Reson Imaging* 2017;45:500–06 CrossRef Medline
41. Filice S, Crisi G, Erb G. **T2\*-correction in dynamic contrast-enhanced magnetic resonance imaging of glioblastoma from a half dose of high-relaxivity contrast agent.** *J Comput Assist Tomogr* 2017;41:816–21 CrossRef Medline
42. Murata N, Gonzalez-Cuyar LF, Murata K, et al. **Macrocyclic and other non-group 1 gadolinium contrast agents deposit low levels of gadolinium in brain and bone tissue: preliminary results from 9 patients with normal renal function.** *Invest Radiol* 2016;51:447–53 CrossRef Medline
43. Bussi S, Penard L, Bonafè R, et al. **Non-clinical assessment of safety and gadolinium deposition after cumulative administration of gadobenate dimeglumine (MultiHance®) to neonatal and juvenile rats.** *Regul Toxicol Pharmacol* 2018;92:268–27 CrossRef Medline

# Anatomy of the Great Posterior Radiculomedullary Artery

V.H. Perez Perez, J. Hernesniemi, and J.E. Small



## ABSTRACT

**BACKGROUND AND PURPOSE:** Although considerable variability exists as to the overall caliber of radiculomedullary arteries, dominant radiculomedullary arteries such as the artery of Adamkiewicz exist. The existence of a great posterior radiculomedullary artery has attracted little attention and has been a matter of debate. The aim of this anatomic study was to determine the presence or absence of the great posterior radiculomedullary artery.

**MATERIALS AND METHODS:** We performed microsurgical dissection on formaldehyde-fixed cadaveric human spinal cords. The artery of Adamkiewicz in the spinal cord specimens ( $n=50$ ) was injected with colored latex until the small-caliber arterial vessels were filled and the great posterior radiculomedullary artery was identified. The course, diameter, and location of great posterior radiculomedullary artery were documented.

**RESULTS:** A great posterior radiculomedullary artery was identified in 36 (72%) spinal cord specimens. In 11 (22%) specimens, bilateral great posterior radiculomedullary arteries were present. In 13 cases (26%), a unilateral left-sided great posterior radiculomedullary artery was identified. In 11 cases (22%), a unilateral right-sided great posterior radiculomedullary artery was identified. In 1 specimen (2%), 3 right-sided great posterior radiculomedullary arteries were noted. The average size of the great posterior radiculomedullary arteries was 0.44 mm (range, 0.120–0.678 mm on the left and 0.260–0.635 mm on the right).

**CONCLUSIONS:** A great posterior radiculomedullary artery is present in most (72%) individuals. The authors describe the microsurgical anatomy of the great posterior radiculomedullary artery with emphasis on its morphometric parameters as well as its implications for spinal cord blood supply. Variations of the arterial supply to the dorsal cord are of great importance due to their implications for ischemic events, endovascular procedures, and surgical approaches.

**ABBREVIATIONS:** AKA = artery of Adamkiewicz; ASA = anterior spinal artery; GPRA = great posterior radiculomedullary artery; PSA = posterior spinal artery

Understanding the basic vascular anatomy of the spinal cord is of utmost importance for imaging interpretation and endovascular and surgical management of spinal cord vascular malformations. Advances in diagnostic and therapeutic interventions have led to a need for more detailed and specific understanding of the microvasculature of the spinal cord. In particular,

attention to the anatomic variations of the smaller caliber circulatory supply to the spinal cord allows tailored management of a specific patient.

At its most basic, the spinal cord derives circulatory supply from 1 ventral (anterior spinal artery) and 2 dorsal (posterior spinal arteries) arterial trunks. The anterior spinal artery (ASA) courses along the anterior sulcus of the spinal cord and supplies the anterior two-thirds of the spinal cord (including the anterior horns and spinothalamic and corticospinal tracts). The ASA exhibits a variable caliber along its course, ranging in size from 0.2 to 0.8 mm.<sup>1,2</sup> The pair of posterior spinal arteries (PSAs) courses along the posterolateral surface of the spinal cord. The PSAs generally have a caliber of 0.1–0.4 mm<sup>2,3</sup> and supply the posterior third of the spinal cord (including the posterior columns, dorsal gray matter, and superficial dorsal aspect of the lateral columns).

A variable number of radicular arteries originating from segmental arteries or homologous vessels make arterial contributions

Received August 28, 2019; accepted after revision September 19.

From the Department of Neurosurgery (V.H.P.P.), Instituto de Ciencias Forenses, TSJ Ciudad de México, Centro Medico Siglo XXI, Mexico City, Mexico; Department of Neurosurgery (J.H.), International Center for Neurosurgery, Henan Provincial People's Hospital, Zhengzhou, China; and Department of Radiology (J.E.S.), Neuroradiology Section, Lahey Hospital and Medical Center, Burlington, Massachusetts.

Paper previously presented as an oral presentation at: Annual Meeting of the American Society of Neuroradiology, May 18–23, 2019; Boston, Massachusetts.

Please address correspondence to Juan E. Small, MD, MSc, Department of Radiology, Lahey Hospital & Medical Center, 41 Mall Road, Burlington, MA 01805; e-mail: Juan.E.Small@Lahey.org

<http://dx.doi.org/10.3174/ajnr.A6304>

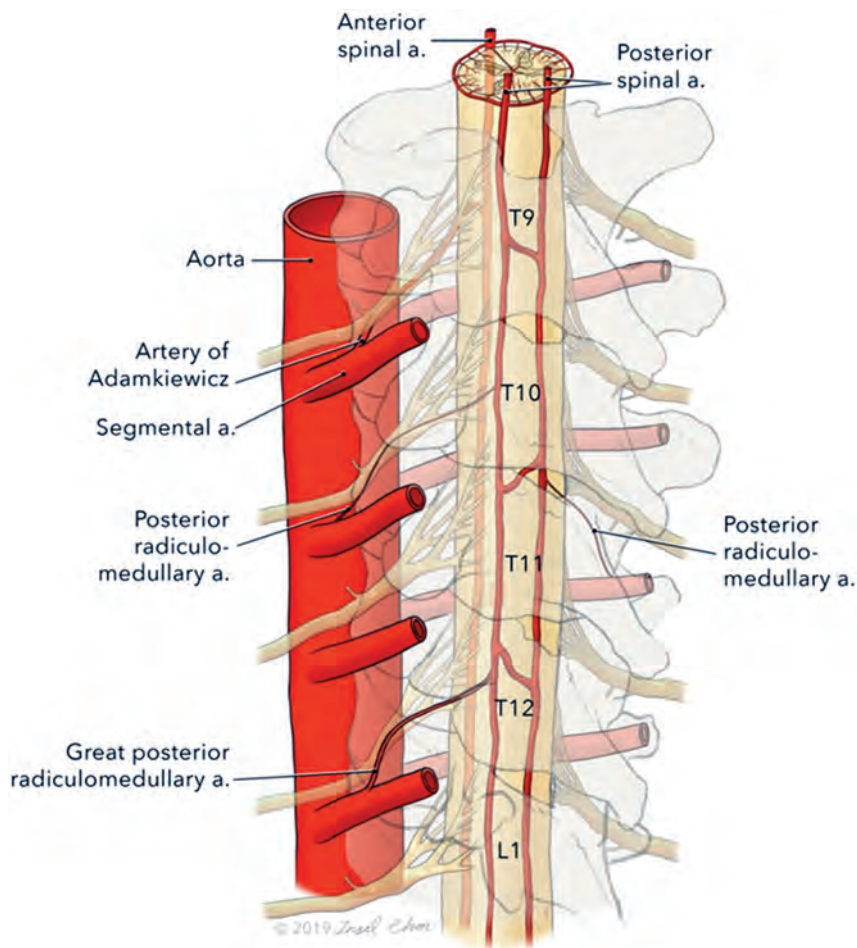


**FIG 1.** Illustration of the arterial radiculomedullary supply to the spinal cord. A posterior view of the distal spinal cord demonstrates the radiculomedullary supply of the distal cord. Ventrally, the artery of Adamkiewicz can be seen as the dominant anterior radiculomedullary supply. A dominant posterior radiculomedullary arterial feeder is referred to as the great posterior radiculomedullary artery. Image © 2019 Insil Choi. Reproduced with permission.

as lateral feeders along the course of the spine. These radicular arteries are of small-but-differing calibers. Most of these radicular arteries supply nerve roots, the dura, or the pial plexus. Only a few of these radicular arteries specifically provide arterial supply to the collateral network of vessels supplying the spinal cord.<sup>4,5</sup> These vessels are specifically termed radiculomedullary arteries. Radicular branches contributing to the ASA are referred to as anterior radiculomedullary arteries. The paired posterior spinal arteries are supplied by the posterior radiculomedullary arteries. The variability in number, caliber, and entrance level of anterior and posterior radiculomedullary arteries has been studied.<sup>6-8</sup> The number of anterior radiculomedullary arteries ranges from 2 to 14.<sup>1</sup> Approximately 11–16 radiculomedullary arteries supply the PSAs along their course.<sup>1</sup> The collateral network established by the anterior and posterior radiculomedullary arteries aids in spinal cord perfusion by allowing the redundancy of an anastomotic network of vessels. In this sense, the anterior and posterolateral spinal arteries are not typical arteries. They are, instead, systems of longitudinal anastomoses

connecting with ascending and descending radiculomedullary artery branches.<sup>3</sup>

An inverse correlation between the caliber and number of anterior radiculomedullary vessels supplying the entire spinal cord has been described.<sup>6,8</sup> When few in number (2–5), they are referred to as a pauci-segmental type with larger caliber vessels. When they number at least 6, they are referred to as a pluri-segmental type with smaller caliber vessels.<sup>3</sup>

Although variability exists as to the overall caliber of radiculomedullary arteries, dominant radiculomedullary arteries are present. The most important radiculomedullary artery is the arteria radicularis magna, otherwise known as the artery of Adamkiewicz (AKA). The AKA arises in the thoracolumbar region between T8 and L2 in 75% of patients and has a diameter of 0.5–1.2 mm.<sup>1,2</sup>

The arterial supply to the posterior spinal arteries has attracted considerably less attention compared with the anterior spinal arterial supply. Because the posterior vessels are considerably smaller in diameter, they are difficult to identify on angiography and very few studies have analyzed their lumbosacral anatomy in cadavers. The arterial radiculomedullary supply to

the posterior spinal system in the region of the AKA often includes 2 dorsal feeders of similar caliber, generally 400–500  $\mu\text{m}$ .<sup>3</sup> The existence of a great posterior radiculomedullary artery (GPRA) has been a matter of debate (Fig 1). The presence of such an artery corresponding with the AKA, with a distinctly greater caliber than other posterior radiculomedullary arteries, has been acknowledged by a few authors<sup>3,5,7,8</sup> but denied by others.<sup>8-10</sup>

The aim of this anatomic study was to analyze the lumbosacral arterial supply to the dorsal spinal cord and determine the presence or absence of the GPRA. In addition, we set out to analyze its morphometric characteristics.

## MATERIALS AND METHODS

We conducted an institutional review board–approved study of 50 (49 men and 1 woman) unembalmed cadaveric specimens at the Institute of Forensic Sciences of Mexico City (Instituto de Ciencias Forenses de la Ciudad de Mexico). Specimens with any spinal pathology were excluded from the analysis. The cadavers ranged in age from 20 to 70 years (median age, 40 years). The

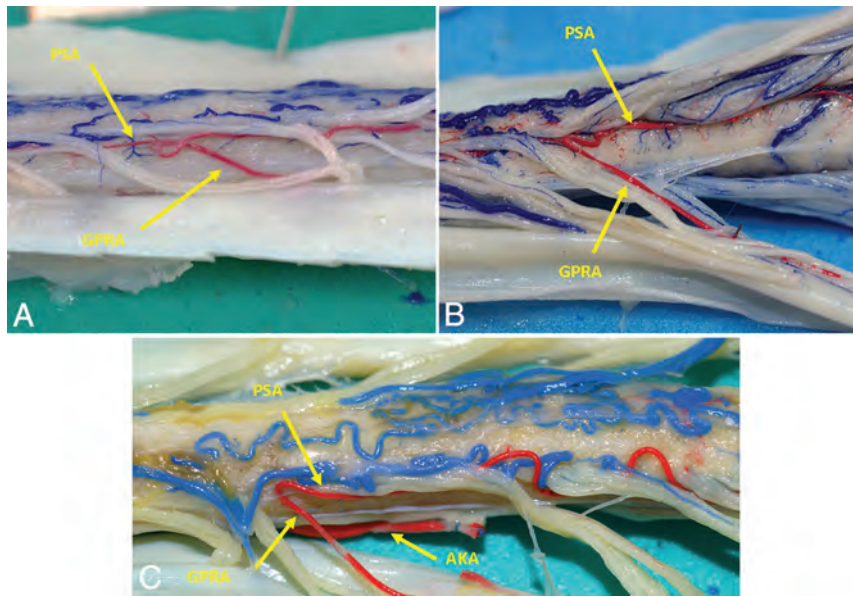


**FIG 2.** The great posterior radiculomedullary artery. Dorsolateral views from 3 different spinal cord specimens (A–C) reveal clear evidence of a dominant GPRA.

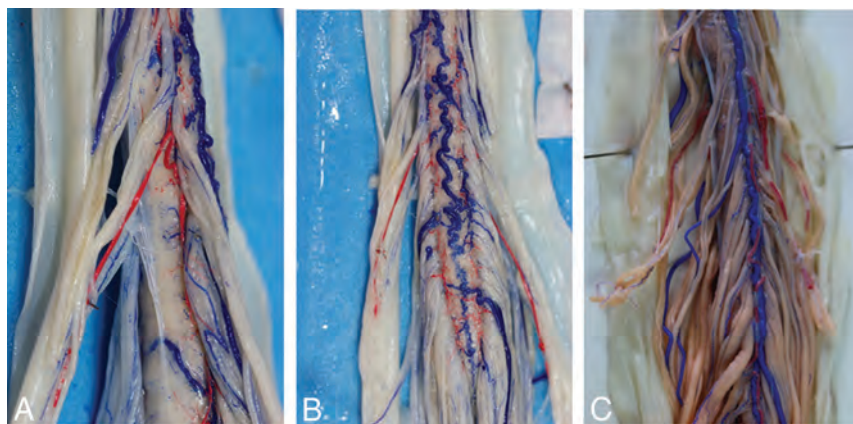


**FIG 3.** GPRA position. Photographs of the posterior aspect of the spinal cord in 3 different specimens show a left-sided GPRA (A), bilateral GPRAs (B), and a right-sided GPRA (C). A unilateral left-sided GPRA was seen in 13 (26%) specimens; a unilateral right-sided GPRA, in 11 cases (22%); and bilateral GPRAs, in 11 specimens (22%).

spinal cords were extracted via a longitudinal midline posterior incision from the occiput to the sacrum. Anatomic dissection was performed until reaching the vertebral lamina. Laminectomies were performed from C1 to L5. The spinal nerves were cut with care so as not to lesion the dura. With the use of surgical loupes, ventral and dorsal longitudinal midline durotomies were performed. The spinal cord was irrigated with saline. The vascular system was irrigated with saline to purge residual blood and blood clots. The AKA was identified and cannulated with an angi catheter of commensurate size. Red natural latex was injected into the AKA under moderate pressure and close visual inspection to avoid contrast extravasation. The injection was continued until latex filled distal small caliber arterial vessels, including the posterior spinal arteries. Veins were injected with blue natural latex. No evidence of spinal cord pathology, including vascular malformations or fistulas, was identified in any of the

samples included in this analysis. The specimens were then fixed in a 5% formaldehyde solution. Two weeks after fixation, the spinal cord specimens were studied with surgical loupes (5×). We identified the artery of Adamkiewicz as well as the major posterior arterial radicular arteries. We conducted measurements with digital Vernier calipers in conjunction with digital measurements of computerized photographic images with a scale included in the photographic image. In particular, we searched for the presence or absence of the GPRA.

## RESULTS

A GPRA was identified in 72% of spinal cord specimens (36/50) (Fig 2). This total included specimens in which unilateral and bilateral GPRAs were found, as well as a single case in which 3 GPRAs were evident. In 26% of the specimens, a unilateral left-sided GPRA was present (13/50). A unilateral right-sided GPRA was present in 22% of the specimens (11/50). In 22% of the specimens, bilateral GPRAs were present (11/50) (Fig 3). One specimen demonstrated 3 right-sided GPRAs (Fig 4). The laterality and spinal level of GPRAs are summarized in Table 1. Including unilateral and bilateral specimens, a total of 24 GPRAs were present on the left extending from T9 through L2. Including unilateral, bilateral, and triplicated specimens, a total of 25 right-sided GPRAs were present with their distribution ranging from T9 through L3. A GPRA was most frequently identified at the level of T12, with 9 left- and 9 right-sided specimens identified at this level. Of the 11 specimens with bilateral GPRAs, 8 demonstrated GPRAs at the same level (most often T12).

Average GPRA size was 0.44 mm with a range of 0.120–0.678 mm on the left and 0.260–0.635 mm on the right. Although the caliber of the GPRAs did not approximate that of the AKA, the vessels were truly dominant and easily distinguished from the tiny caliber of the radicular arteries, which accompany posterior spinal nerves. In the specimen that demonstrated 3 right-sided GPRAs, they were seen at T11 (0.371 mm), T12 (0.319 mm), and L1 (0.240 mm). Of note, no absolute cutoff measurement was used to establish the presence of a GPRA because establishing the presence of a dominant arterial feeder is a relative process specific to each patient. For instance, the pauci-segmental and pluri-

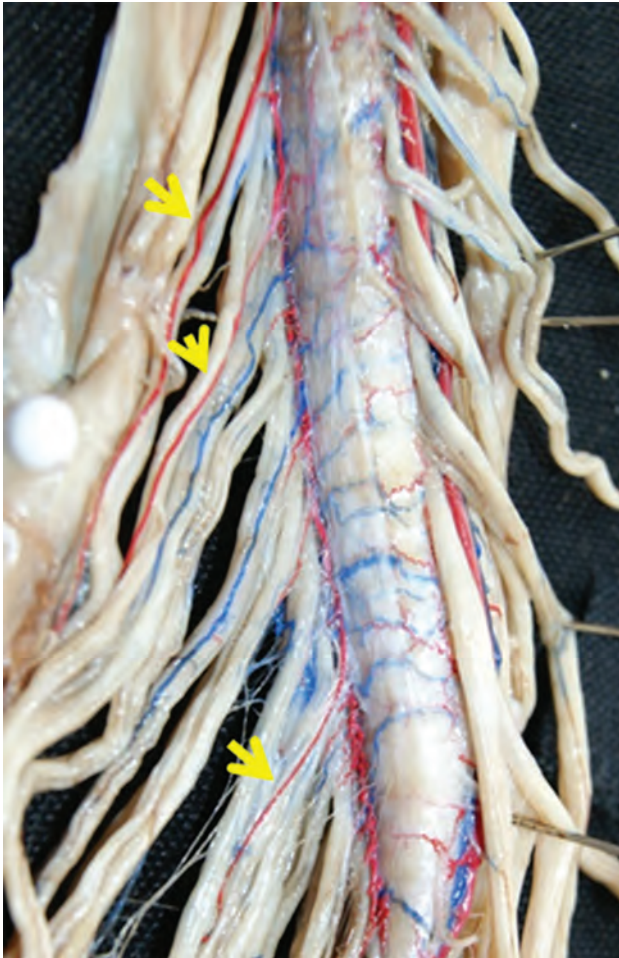


**FIG 4.** Multiple GPRAs. In 1 specimen, a total of 3 dominant right-sided GPRAs are evident (arrows), present at the level of T11 (0.371 mm), T12 (0.319 mm), and L1 (0.240 mm).

**Table 1: Distribution of GPRAs based on side and spinal level**

Spinal Level	Left-Sided GPRAs (24/36)	Right-Sided GPRAs (25/36)
T9	2	3
T10	4	2
T11	2	3
T12	9	9
L1	5	6
L2	2	1
L3	0	1

segmental ASA circulations are associated with markedly differing calibers of the AKA. In the same manner, pauci-segmental and pluri-segmental PSA circulations are associated with differing calibers of the GPRAs.

A GPRAs was not identified in 28% of specimens (14/50). In all the spinal cord specimens in which a GPRAs was not present, the ventral distal ASA trifurcated distally into a tiny midline artery that coursed toward the filum terminale and 2 small-caliber lateral branches along the anterolateral surface of the conus, which formed termino-terminal anastomoses with the corresponding PSAs (Fig 5). Each of the 2 lateral arteries originating from the distal ASA trifurcation measured, on average, 0.35 mm

on the right and 0.31 mm on the left. If the ASA did not exhibit this trifurcation branching pattern, the distal dorsal spinal cord was instead supplied by a GPRAs. In the specimens in which the distal ASA did not exhibit a trifurcation pattern, the distal ASA gradually-but-drastically became diminished in caliber as it reached the conus. Careful analysis of the posterior spinal nerves in these cases established the presence of a GPRAs in every case without exception.

With respect to the artery of Adamkiewicz, a left-sided vessel was present in 45 specimens and a right-sided AKA was present in 5 specimens. Of these, 6 specimens demonstrated duplicated AKAs with 3 having 2 separate AKAs, both on the left side, and 3 having bilateral AKAs (1 left and 1 right). Of the left-side duplications, 2 cases demonstrated duplicated left-sided AKAs at T8 and T12 and 1 case demonstrated duplicated T11 and T12 with left-sided origins. The bilateral duplications were present at T8 on the left and T12 on the right, T9 on the left and T10 on the right, and T11 on the left and T8 on the right. The AKA most frequently originated on the left at the level of T9 in 13 specimens and at the level of T8 in 10 specimens. The side and spinal levels of AKAs are summarized in Table 2.

The most proximal AKA was evident at the T3 level on the left, and the most distal, at the L2 level of on the left. On average, the diameter of the AKA was 0.82 mm, with the smallest caliber AKA measuring 0.49 mm and the largest measuring 1.21 mm. When 2 AKAs were present, the smallest caliber vessel measured 0.4 mm and the largest measured 0.79 mm.

## DISCUSSION

Spinal cord ischemia remains an infrequent-yet-devastating consequence of spinal and thoraco-abdominal surgical and endovascular procedures. Radiculomedullary arteries, which provide arterial supply to the spinal cord, are variable in location and few in number. In particular, the dominant radiculomedullary artery supplying the ASA, termed the AKA, has received extensive attention in the literature. However, the caliber of the anterior circulation with a usual ASA diameter of 0.2–0.8 mm and an AKA diameter of 0.5–1.0 mm<sup>3</sup> allows these vessels to be reliably visualized via in vivo imaging studies.<sup>2,11,12</sup> Although the anatomy of the ASA and its supplying branches has been well-studied and is currently well-understood, the more complex configuration of the paired PSAs has received much less attention, often yielding complicated, confusing, and, at times, discordant results. In particular, the smaller radiculomedullary arteries supplying the posterior spinal arteries have received scant attention. In part, the decreased attention stems from the smaller size of the posterior circulation branches, making them more difficult to detect and rendering them less consequential to ischemic deficits when occluded. The posterior spinal arteries are usually 0.1–0.4 mm in diameter, and the posterior radiculomedullary arteries are typically smaller. Thus, the posterior radiculomedullary arteries are rarely well-depicted in vivo during spinal angiography.

In vivo studies of the remainder of the spinal cord vasculature are extremely difficult owing to the smaller caliber of these vessels often beyond the resolution of imaging. In addition, the substantial anatomic variability of these vessels and their complex course makes their identification virtually unattainable. Nonetheless, to

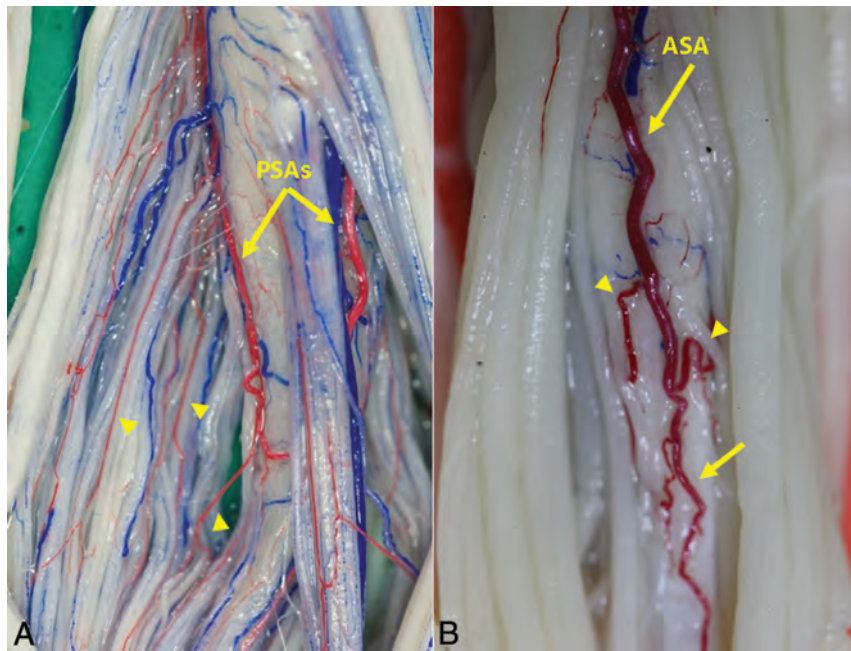


**FIG 5.** Absence of a GPRA. In specimen A, bilateral PSAs are evident along the dorsal aspect of the cord (A, arrows), with numerous small-caliber posterior radiculomedullary arteries supplying the left PSA (A, arrowheads). A posterior radiculomedullary artery with a dominant caliber could not be identified. No GPRA is evident in this case. In cases in which a GPRA is absent, a typical trifurcation pattern of the ASA is evident along the ventral aspect of the cord (B). The distal ASA typically trifurcates distally into a small midline artery (B, arrow), which courses toward the filum terminale and 2 small-caliber lateral branches (B, arrowheads) along the anterolateral surface of the conus, which form termino-terminal anastomoses with the corresponding PSAs (often referred to as the basket of the conus medullaris).

**Table 2: Artery of Adamkiewicz side and level of origin<sup>a</sup>**

Spinal Level	Left-Sided AKA	Right-Sided AKA
T3	1	0
T4	0	0
T5	1	0
T6	1	0
T7	2	1
T8	10	1
T9	13	1
T10	6	3
T11	5	1
T12	5	1
L1	2	0
L2	2	0

<sup>a</sup> Six of the specimens demonstrated duplicated AKAs.

interpret imaging findings with abnormally dilated branches and plan surgical or endovascular procedures, we must have a more extensive knowledge of the spinal cord vascular anatomy. Therefore, we must necessarily turn to postmortem studies to obtain information related to the small-caliber spinal cord circulation. Because postmortem studies of the spinal cord circulation are so infrequent and technically demanding, our knowledge regarding the posterior radiculomedullary arteries to this date is scant. Of those studies available in the literature, conflicting evidence and inaccuracies are not uncommon. In addition, the nomenclature for the same vessel often varies, leading to further confusion.

The results of this study demonstrate that in most individuals, there is a posterior radiculomedullary artery in the region of the lumbar spine, which distinguishes itself as the dominant arterial supply from other posterior medullary arteries due to its size. This prominent posterior artery supplying the spinal cord may be considered the GPRA, and our findings conclusively describe its presence. The definitive identification of a GPRA in 72% of our cases corroborates the disputed findings of Gillian (1958),<sup>13</sup> Lazorthes et al (1958),<sup>14</sup> Jellinger (1966),<sup>7</sup> and Thron (2016)<sup>3</sup> and refute the findings of Corbin (1961),<sup>9</sup> Clemens (1966),<sup>10</sup> and Pisco (1972).<sup>8</sup> Our study adds new information highlighting the importance of a dominant posterior radiculomedullary artery to the arterial supply of the posterior distal spinal cord.

Our results also have implications for the anatomic understanding of the arterial cruciate anastomosis (arterial basket) of the conus medullaris and its associated variations and watershed zones.<sup>15-17</sup>

As previously noted, the caudal ASA diminishes in caliber and branches into 2 small lateral branches, which curve dorsally and anastomose with the paired PSAs. In the study conducted by Rodriguez-Baeza et al (1991),<sup>18</sup> they noted that the AKA was accompanied by a posterior radiculomedullary artery in 63% of cases. Unfortunately, they only documented the size of anterior radiculomedullary arteries and therefore failed to identify the dominant posterior radiculomedullary supply. This finding contrasts with that of Lazorthes et al (1957),<sup>19</sup> who described a posterior radiculomedullary artery always associated with the AKA and Houdart et al (1965)<sup>20</sup> and Tveten (1976),<sup>21</sup> who noted that this association was found in only one-third of cases. As noted in these previous articles,<sup>16,17</sup> different configurations of the arterial basket have been identified. As our results indicate, the presence or absence of a GPRA correlates with different anastomotic configurations.

The substantial number of specimens examined in this study gives us confidence regarding the reliability of our vessel distribution, laterality, and diameter determinations. However, almost all anatomic specimens were from male cadavers. Therefore, the unlikely possibility that sex differences exist cannot be definitively excluded. In addition, the possibility of racial variations cannot be excluded on the basis of this study.

## CONCLUSIONS

A GPRA is conclusively present in most (72%) individuals. Understanding this intricate anatomy and its variations is critical

for addressing vascular malformations of the spinal cord. A better understanding of the spinal cord circulation will lead to reduced risk of surgical and endovascular spinal and aortic procedures.

## REFERENCES

1. Santillan A, Nacarino V, Greenberg E, et al. **Vascular anatomy of the spinal cord.** *J Neurointerv Surg* 2012;4:67–74 CrossRef Medline
2. Vargas MI, Gariani J, Sztajzel R, et al. **Spinal cord ischemia: practical imaging tips, pearls, and pitfalls.** *AJNR Am J Neuroradiol* 2015;36:825–30 CrossRef Medline
3. Thron AK. *Vascular Anatomy of the Spinal Cord.* Palgrave: Macmillan; 2016
4. Etz CD, Kari FA, Mueller CS. **The collateral network concept: a reassessment of the anatomy of spinal cord perfusion.** *J Thorac Cardiovasc Surg* 2011;141:1020–28 CrossRef Medline
5. Griep RB, Griep EB. **Spinal cord perfusion and protection during descending thoracic and thoracoabdominal aortic surgery: the collateral network concept.** *Ann Thorac Surg* 2007;83:S865–69 CrossRef Medline
6. Kadyi H. *Über die Blutgefäße des menschlichen Rückenmarks.* Lemberg: Gubrynoxicz u Schmidt; 1889
7. Jellinger K. *Zur Orthologie und Pathologie der Rückenmarksdurchblutung.* Vienna: Springer Vienna; 1966
8. Pisco K. *Die Blutversorgung des Rückenmarks und ihre klinische Relevanz.* New York: Springer-Verlag; 1972
9. Corbin JL. **Arteries of the spinal cord and medullary ischemic pathology.** *Presse Med* 1961;69:1341–44 Medline
10. Clemens HJ. **Beitrag des morpholegen zum problem der spinalen mangeldurchblutung.** *Verh Dtsch Kongr.inn. Med* 1966;1059–80
11. Backes WH, Nijenhuis RJ. **Advances in spinal cord MR angiography.** *AJNR Am J Neuroradiol* 2008;29:619–31 CrossRef Medline
12. Nijenhuis RJ, Backes WH. **Optimal preoperative imaging of spinal cord blood supply.** *AJNR Am J Neuroradiol* 2009;30:E38–39 CrossRef Medline
13. Gillian LA. **The arterial blood supply of the human spinal cord.** *J Comp Neurol* 1958;110:75–103 CrossRef Medline
14. Lazorthes G, Poulhes J, Bastide G, et al. **Arterial vascularization of the spine; anatomic research and applications in pathology of the spinal cord and aorta** (in French). *Neurochirurgie* 1958;4:3–19
15. Gailloud P, Gregg L, Galan P, et al. **Periconal arterial anastomotic circle and posterior lumbosacral watershed zone of the spinal cord.** *J Neurointerv Surg* 2015;7:848–53 CrossRef Medline
16. Martirosyan NL, Kalani MY, Lemole GM Jr, et al. **Microsurgical anatomy of the arterial basket of the conus medullaris.** *J Neurosurg Spine* 2015;22:672–76 CrossRef Medline
17. Rojas S, Ortega M, Rodríguez-Baeza A. **Vascular configurations of anastomotic basket of conus medullaris in human spinal cord.** *Clin Anat* 2018;31:441–48 CrossRef Medline
18. Rodríguez-Baeza A, Muset-Lara A, Rodríguez-Pazos M, et al. **The arterial supply of the human spinal cord: a new approach to the arteria radicularis magna of Adamkiewicz.** *Acta Neurochir (Wein)* 1991;109:57–62 CrossRef Medline
19. Lazorthes G, Poulhes J, Bastide G, et al. **Research on the arterial vascularization of the medulla; applications to medullary pathology.** *Bull Acad Natl Med* 1957;141:464–77 Medline
20. Houdart R, Djindjian R, Julian H, et al. **New data on the vascularization of the dorso-lumbar spinal cord. (Radiological application and surgical interest)** (in French). *Rev Neurol (Paris)* 1965;112:472–76 Medline
21. Tveten L. **Spinal cord vascularity, I: extraspinal sources of spinal cord arteries in man.** *Acta Radiology Diagn (Stockh)* 1976;17:1–16 CrossRef Medline

# Intracranial Atherosclerotic Burden on 7T MRI Is Associated with Markers of Extracranial Atherosclerosis: The SMART-MR Study

M.H.T. Zwartbol, M.I. Geerlings, R. Ghaznawi, J. Hendrikse, and A.G. van der Kolk, on behalf of the UCC-SMART Study Group



## ABSTRACT

**BACKGROUND AND PURPOSE:** Intracranial atherosclerosis, a major risk factor for ischemic stroke, is thought to have different atherogenic mechanisms than extracranial atherosclerosis. Studies investigating their relationship in vivo are sparse and report inconsistent results. We studied the relationship between intracranial atherosclerosis and extracranial atherosclerosis in a cohort of patients with a history of vascular disease.

**MATERIALS AND METHODS:** Within the Second Manifestations of ARterial disease–Magnetic Resonance (SMART) study, cross-sectional analyses were performed in 130 patients (mean age, 68 ± 9 years) with a history of vascular disease and with assessable 7T intracranial vessel wall MR imaging data. Intracranial atherosclerosis burden was defined as the number of intracranial vessel wall lesions in the circle of Willis and its major branches. Age- and sex-adjusted unstandardized regression coefficients (*b*-value) were calculated with intracranial atherosclerosis burden as the dependent variable and extracranial atherosclerosis markers as independent variables.

**RESULTS:** Ninety-six percent of patients had ≥1 vessel wall lesion, with a mean intracranial atherosclerosis burden of 8.5 ± 5.7 lesions. Significant associations were observed between higher intracranial atherosclerosis burden and carotid intima-media thickness (*b* = 0.53 lesions per +0.1 mm; 95% CI, 0.1–1.0 lesions), 50%–100% carotid stenosis versus no stenosis (*b* = 6.6 lesions; 95% CI, 2.3–10.9 lesions), ankle-brachial index ≤ 0.9 versus >0.9 (*b* = 4.9 lesions; 95% CI, 1.7–8.0 lesions), and estimated glomerular filtration rate (*b* = –0.77 lesions per +10 mL/min; 95% CI, –1.50 to –0.03 lesions). No significant differences in intracranial atherosclerosis burden were found among different categories of vascular disease.

**CONCLUSIONS:** Intracranial atherosclerosis was associated with various extracranial markers of atherosclerosis, not supporting a different etiology.

**ABBREVIATIONS:** ABI = ankle-brachial index; cIMT = carotid intima-media thickness; ECAS = extracranial atherosclerosis; eGFR = estimated glomerular filtration rate; ICAS = intracranial atherosclerosis

Intracranial atherosclerosis (ICAS) is a major cause of adverse cerebrovascular events such as ischemic stroke.<sup>1</sup> Furthermore,

it is associated with an increased risk of cognitive decline and dementia.<sup>2</sup> A wide range of prevalence estimates for ICAS has been reported, ranging from 4%–51% in asymptomatic populations to 43%–70% in patients with ischemic stroke.<sup>3,4</sup>

ICAS is currently seen as the intracranial phenotype of atherosclerosis, a generalized disease that can affect all large arteries. Nonetheless, correlations between intracranial and extracranial atherosclerotic disease in postmortem studies are modest.<sup>5</sup> Furthermore, ICAS has a later time of onset, slower rate of progression, and different plaque morphology compared with other arterial territories.<sup>6–8</sup> As a result, it has been suggested that ICAS might have a different etiology than extracranial disease. Studies investigating the relationship between intracranial and extracranial disease in vivo are sparse and often limited to one extracranial vessel bed. Furthermore, all of these studies have used lumenographic imaging methods, which can assess only luminal stenosis.<sup>9,10</sup> Therefore, intracranial plaques without stenosis (ie,

Received July 27, 2019; accepted after revision September 24.

From the Department of Radiology (M.H.T.Z., R.G., J.H., A.G.v.d.K.) and Julius Center for Health Sciences and Primary Care (M.I.G., R.G.), University Medical Center Utrecht and Utrecht University, Utrecht, the Netherlands.

Jeroen Hendrikse has received funding from the European Research Council under the European Union's Horizon 2020 Program (H2020)/European Research Council grant agreement No. 637024 (HEARTOFSTROKE) and H2020 grant agreement No. 666881, SVDs@target, and is supported by the Netherlands Organization for Scientific Research under grant No. 91712322.

Please address correspondence to Mirjam I. Geerlings, PhD, University Medical Center Utrecht, Julius Center for Health Sciences and Primary Care, PO Box 85500, Stratenum 6.131, 3508 GA Utrecht, the Netherlands; e-mail: m.geerlings@umcutrecht.nl

Indicates open access to non-subscribers at www.ajnr.org

Indicates article with supplemental on-line tables.

Indicates article with supplemental on-line photo.

<http://dx.doi.org/10.3174/ajnr.A6308>

due to arterial remodeling) will not be detected, leading to an underestimation of the actual ICAS burden.<sup>11</sup>

Vessel wall lesions are a novel neuroimaging marker of ICAS, which can be assessed using intracranial vessel wall MR imaging.<sup>12</sup> Vessel wall MR imaging enables visualization of the intracranial arterial walls, allowing a more direct evaluation of ICAS.<sup>13</sup> Currently, 7T is the highest field strength at which vessel wall MR imaging has been performed in humans *in vivo* and has been shown to be superior to lower field strengths in the detection of vessel wall anomalies.<sup>14</sup>

In the current study, we investigated, in patients with atherosclerotic disease, to what extent markers of extracranial atherosclerosis (ECAS) were associated with the burden of ICAS measured by 7T vessel wall MR imaging, thereby providing insight into the etiology of ICAS and its relationship with ECAS.

## MATERIALS AND METHODS

### Study Sample

Data were used from the Second Manifestations of ARterial disease–Magnetic Resonance (SMART-MR) study, a prospective cohort study at our institution with the aim of investigating risk factors and clinical outcomes of MR neuroimaging markers in patients with arterial disease.<sup>15</sup> In brief, from 2001 through 2005, thirteen hundred nine patients newly referred to our institution with cerebrovascular disease, peripheral arterial disease, coronary artery disease, or abdominal aortic aneurysm without MR imaging contraindications were enrolled in the SMART-MR study. On a 1-day visit to our institution's hospital, the participants underwent 1.5T MR imaging of the brain, a physical examination, ankle-brachial index (ABI) assessment, ultrasonography of the carotid arteries, blood and urine sampling, and questionnaires to assess risk factors, medical history, and daily functioning. Follow-up examinations of the SMART-MR cohort were performed in 2006–2009 and 2013–2017.

From June 2016 to October 2017, we included 147 patients participating in the second follow-up examination of the SMART-MR study who had intracranial vessel wall MR imaging performed as part of a 7T MR imaging of the brain.<sup>12</sup> A flowchart of the study sample is provided in the On-line Figure. Seventeen patients were excluded from the current study because of artifacts hampering vessel wall MR imaging assessment of  $\geq 1$  major segment of the circle of Willis (major segments included the distal internal carotid artery and primary branches [M1, A1, P1] of the anterior, middle, and posterior cerebral arteries), leaving 130 patients for the final analysis. For the current study, measurements of extracranial atherosclerosis and risk factor assessment, including questionnaire data and blood and urine sampling, were obtained (median, 2.3 years; range, 0.6–8.6 years) before the 7T MR imaging.

Comparison of ECAS markers between the excluded patients and the patients for final analysis showed a higher prevalence of 50%–100% carotid stenosis in the excluded patients (7.0% versus 23.5%;  $P = .04$ ,  $\chi^2$  test). Also, the excluded patients were older, though this feature was not statistically significant ( $70 \pm 7$  versus  $68 \pm 9$  years;  $P = .11$ , Student  $t$  test). Sex distribution did not differ between included and excluded patients (88% versus 88% men;  $P = .95$ ,  $\chi^2$  test).

### Vascular Risk Factors

Information on general vascular risk factors was obtained by questionnaires, physical examination, and blood sampling. Height and weight were used to calculate the body mass index (kilogram/square meter). Systolic blood pressure (millimeter of mercury) and diastolic blood pressure (millimeter of mercury) were measured by averaging 3 separate measurements with a sphygmomanometer. Hypertension was defined as a systolic blood pressure of  $>140$  mm Hg, a mean diastolic blood pressure of  $>90$  mm Hg, or self-reported use of antihypertensive drugs. Diabetes mellitus was defined as fasting serum glucose levels of  $\geq 7.0$  mmol/L and/or use of glucose-lowering medication and/or a known history of diabetes. Patients who did not meet these criteria, but with a fasting plasma glucose level  $\geq 7.0$  mmol/L at baseline, were considered to have diabetes at baseline if they received treatment with glucose-lowering medication within 1 year after baseline. Hyperlipidemia was defined as a total cholesterol of  $>5.0$  mmol/L, a low-density lipoprotein cholesterol of  $>3.2$  mmol/L, or use of lipid-lowering medication. Metabolic syndrome was determined by the National Cholesterol Education Program Expert Panel III criteria.<sup>16</sup>

### Markers of Extracranial Atherosclerosis

An experienced technician performed carotid ultrasonography with a 10-MHz linear-array transducer. Mean carotid intima-media thickness (cIMT) was calculated from 6 measurements (anterolateral, posterolateral, and mediolateral in both common carotid arteries). Extracranial carotid stenosis was ultrasonographically assessed and defined according to standard criteria based on the peak systolic velocity.<sup>17</sup> ABI measurements were conducted by experienced technicians and were calculated from the highest systolic blood pressure measured at the posterior tibial and dorsal pedal arteries by Doppler sonography and at both brachial arteries by a semiautomatic oscillometric device with the patient in the supine position. Renal function was assessed using the estimated glomerular filtration rate (eGFR) calculated by the Cockcroft-Gault equation adjusted for body weight and body mass index.<sup>18</sup>

Coronary artery disease was defined as a history of myocardial infarction or a history of coronary artery bypass graft surgery or percutaneous transluminal coronary angioplasty at inclusion or in the past. Cerebrovascular disease was defined as transient ischemic attack or stroke at inclusion or in the past. Peripheral artery disease was defined as intermittent claudication or rest pain at inclusion or a history of surgery or angioplasty of the arteries supplying the lower extremities. Abdominal aortic aneurysm was defined as the presence of an abdominal aortic aneurysm (distal aortic anteroposterior diameter of  $\geq 3$  cm) or a previous abdominal aortic aneurysm operation. Multivascular disease was defined as the presence of  $\geq 2$  of the above-defined vascular diseases.

### 7T MR Imaging Protocol

A 7T whole-body system (Philips Healthcare, Best, the Netherlands) was used with a volume/transmit coil for transmission and a 32-channel receive head coil (Nova Medical, Wilmington, Massachusetts). Vessel wall MR imaging was performed using a T1-weighted magnetization-prepared inversion recovery TSE sequence, with the following parameters: FOV =

250 × 250 × 190 mm<sup>3</sup>, acquired resolution = 0.8 × 0.8 × 0.8 mm<sup>3</sup> (reconstructed to 0.49 × 0.49 × 0.4 mm<sup>3</sup>), TR/TI/TE = 3952/1375/37 ms, acquisition time = 10 minutes 40 seconds.<sup>19</sup> In addition, an SWI sequence was performed, with the following parameters: FOV = 200 × 200 × 120 mm<sup>3</sup>, acquired resolution = 0.5 × 0.5 × 0.7 mm<sup>3</sup> (reconstructed to 0.4 × 0.4 × 0.35 mm<sup>3</sup>), TR/TE 1/TE 2 = 20/6.9/15.8 ms, flip angle = 12°, acquisition time = 9 minutes 17 seconds.

### Assessment of Intracranial Atherosclerosis

For the assessment of vessel wall lesions, axial multiplanar reconstructions were calculated from the T1-weighted magnetization-prepared inversion recovery TSE sequence (section thickness = 0.8 mm; no section gap), angulated to the nasion-foramen magnum line. One observer (M.H.T.Z. with over 5 years of experience in neuroradiology) assessed all images, blinded to patient characteristics. M.H.T.Z. was trained by a senior observer with 8 years of experience in interpreting vessel wall MR images (A.G.v.d.K.), using a practice set of 15 patients from the intracranial vessel wall imaging (IVI) study<sup>20</sup> and a consensus set of 20 patients from the current study. An interobserver agreement of 0.75 (Dice similarity coefficient) was obtained, which was regarded as good.

Vessel wall lesions were rated according to the methodology previously published by Lindenholtz et al.<sup>21</sup> A lesion was defined as either a focal or more diffuse thickening of the arterial wall of >50%, assessed visually, using the normal contralateral or neighboring arterial wall as a reference. Uncertain lesions were verified in multiple planes. After a lesion was identified, it was subsequently classified as eccentric (≤50% wall circumference) or concentric (>50% wall circumference) and by arterial segment location: internal carotid arteries (C6, C7), middle cerebral arteries (M1, M2), anterior cerebral arteries (A1, A2), posterior communicating arteries, posterior cerebral arteries (P1, P2, and P1–P2 bifurcation), basilar artery, and vertebral arteries (V4). One single segment could contain multiple lesions, making the total lesion count theoretically unlimited. Lesions that extended into multiple segments were counted as separate lesions for each involved segment. Furthermore, lesions with eccentric and concentric components were regarded as separate lesions.

A maximum intensity projection of the SWI was used to assess the course of smaller arteries (M2, A1, P2, posterior communicating artery). We did not assess luminal stenosis because the SWI quality in our study did not permit accurate measurement, especially of small lesions. Of note, we did not perform a refined MRA because it was logistically not feasible, and at the time of study design, the diagnostic accuracy of MRA in the detection and grading of intracranial stenosis was still relatively low.<sup>22</sup>

### Statistical Analysis

First, characteristics of the study sample were described. Next, the association of ECAS markers with ICAS burden was estimated using linear regression analyses, with the ECAS measure as the independent variable and ICAS burden as the dependent variable. ICAS burden was defined as the total number of intracranial vessel wall lesions. All analyses were adjusted for age and sex. ECAS measures were entered into the model as continuous and/or dichotomous variables. ABI was dichotomized by the

**Table 1: Markers of extracranial atherosclerosis (N = 130)<sup>a</sup>**

Markers	
Age (yr)	68 ± 9
Male	88%
Carotid IMT (mm)	0.84 ± 0.22
Carotid stenosis <sup>b</sup>	
No stenosis	23%
1%–49% stenosis	70%
50%–100% stenosis <sup>c</sup>	7%
Ankle-brachial index	
ABI	1.09 ± 0.18
ABI ≤ 0.9	11%
Renal function	
eGFR (mL/min)	72.8 ± 17.3
eGFR <60 mL/min	21%
History of vascular disease <sup>d</sup>	
Cerebrovascular disease	9%
Coronary artery disease	65%
Peripheral artery disease	9%
Multivascular disease	17%

**Note:**—IMT indicates intima-media thickness.

<sup>a</sup> Values are presented as mean ± SD for continuous variables and percentages for categorical variables.

<sup>b</sup> Categories are mutually exclusive. Patients were categorized according to most severe stenosis grade.

<sup>c</sup> Includes 4 patients with ≥1 carotid artery occlusion.

<sup>d</sup> Categories are mutually exclusive. The multivascular category consisted of 22 patients with a history of ≥2 vascular diseases: Ninety-five percent had coronary artery disease; 60%, cerebrovascular disease; 60%, peripheral artery disease; and 14% abdominal aortic aneurysm.

clinical cutoff for peripheral artery disease (≤0.9).<sup>23</sup> For eGFR, the clinical threshold for chronic kidney disease (<60 mL/min) was used. cIMT was categorized into quartiles. Categorization of carotid stenosis was based on the most severe lesion in the bilateral extracranial common or internal carotid arteries. In the analyses of vascular disease, patients with ≥2 vascular diseases were categorized as having multivascular disease, making categories mutually exclusive. Patients with only coronary artery disease were used as the reference category. A sensitivity analysis was performed to control for the time interval (in days) between the date of ECAS measurements and date of the 7T MR imaging.

Statistical analyses were performed using SPSS, Version 25.0 for Windows (IBM, Armonk, New York).

## RESULTS

Table 1 shows the characteristics of the 130 patients. Eighty-eight percent were men, and the mean age was 68 ± 9 years. Twenty-five percent had multivascular disease. Although 19% of the population had cerebrovascular disease, in just 9% was it the only disease. A majority of 65% had a sole history of coronary artery disease. An overview of vascular risk factors can be found in Online Table 1. Of the 130 patients, 96% had ≥1 intracranial vessel wall lesion and a mean ICAS burden of 8.5 ± 5.7 lesions (median, 7 lesions; range, 0–32 lesions). Furthermore, in the anterior circulation, a mean ICAS burden of 5.3 ± 3.2 lesions (median, 4 lesions; range, 0–14 lesions) was found, which was 3.8 ± 3.0 lesions (median, 3 lesions; range, 0–18 lesions) for the posterior circulation. More details regarding arterial or segmental distribution can be found in our prior publication.<sup>12</sup> Examples of vessel wall lesions in a 76-year-old male patient are shown in the Figure.



**FIGURE.** Examples of intracranial vessel wall lesions on vessel wall MR imaging in a 76-year-old male patient with a history of coronary artery disease. A detailed description of the rating criteria can be found in the Materials and Methods section. A, Lesion in lateral wall of the right P2 segment (arrow) versus the nondiscernable normal neighboring medial wall (arrowhead). B, Lesion in the right vertebral (arrow) and left vertebral (arrowhead) arteries. C, Lesion in the proximal basilar artery (arrow), with coronal orientation shown in enclosed panel (arrowhead). D, Lesion in the C7 segment of the right ICA (arrow), compared with the normal-appearing contralateral C7 segment (arrowhead) and proximal right M1 segment. Furthermore, note the long lesion in the distal half of the right P2 segment (gray arrow) and focal lesion in the left P2 segment (dual arrow).

**Table 2: Association between carotid atherosclerosis and ICAS burden**

	ICAS Burden ( <i>b</i> -value) <sup>a</sup> (95% CI)
cIMT, per +0.1 mm	0.53 (0.06–0.98)
cIMT quartiles	
Quartile 1	0 (Reference)
Quartile 2	0.62 (–2.31–3.55)
Quartile 3	0.40 (–2.61–3.41)
Quartile 4	2.89 (–0.01–5.80)
Carotid stenosis	
No stenosis	0 (Reference)
1%–49% stenosis	2.48 (0.08–4.89)
50%–100% stenosis	6.62 (2.34–10.93)

<sup>a</sup> *B*-values are unstandardized linear regression coefficients adjusted for age and sex.

Age- and sex-adjusted linear regression analyses showed that cIMT was significantly associated with a higher ICAS burden ( $b = 0.53$  lesions per +0.1 mm; 95% CI, 0.06–0.98 lesions). Analysis of cIMT in quartiles indicated a threshold effect, with only quartile 4 suggesting an association with ICAS burden.

However, because the 95% confidence interval contained 0.00, it was not statistically significant (Table 2).

Carotid stenosis of 1%–49% was found to be associated with a higher ICAS burden compared with no carotid stenosis ( $b = 2.5$  lesions for presence of 1%–49% carotid stenosis; 95% CI, 0.08–4.89 lesions). Carotid stenosis of 50%–100% was also associated with a higher ICAS burden ( $b = 6.6$  lesions for the presence of 50%–100% carotid stenosis; 95% CI, 2.34–10.93 lesions) (Table 2).

ABI did not show a significant association with ICAS burden when analyzed as a continuous variable. However, when dichotomized by 0.9, the clinical threshold for peripheral artery disease, a significant association with a higher ICAS burden was found, compared with ABI > 0.9 ( $b = 4.9$  lesions for the presence of ABI ≤ 0.9; 95% CI, 1.74–7.99 lesions) (Table 3).

eGFR was significantly associated with ICAS burden when analyzed as a continuous variable ( $b = -0.77$  lesions per +10 mL/min; 95% CI, -1.50 to -0.03 lesions). Furthermore, renal dysfunction (eGFR of <60 mL/min) was also associated with a higher ICAS burden, compared with eGFR of ≥60 mL/min ( $b = 3.2$  lesions; 95% CI, 0.45–5.91 lesions) (Table 4).

No significant differences in ICAS burden were observed among cerebrovascular, peripheral artery, or multivascular disease groups compared with only coronary heart disease (Table 5).

As a sensitivity analysis, all models were additionally adjusted for the time interval between the date of ECAS measurement and date of 7T MR imaging. On-line Tables 2–5 show the results of these analyses. Although the estimates slightly differed compared with the estimates without time interval adjustment, this did not lead to a change in statistical significance.

## DISCUSSION

This study examined the association between the ICAS measured with intracranial vessel wall MR imaging at 7T and several markers of ECAS, in a cohort of patients with a history of vascular disease. Our results show that increasing cIMT, the presence of extracranial carotid stenosis, ABI ≤ 0.9, and decreasing eGFR were all associated with a higher ICAS burden, defined as the number of intracranial vessel wall lesions. No differences in ICAS burden were observed between the presence of peripheral, cerebrovascular, or multivascular disease compared with coronary heart disease, the main disease in our population.

**Table 3: Association between ABI and ICAS burden**

	ICAS Burden (b-value) <sup>a</sup> (95% CI)
ABI, per +0.1 in ratio	-0.36 (-0.91-0.19)
ABI > 0.9	0 (Reference)
ABI ≤ 0.9	4.86 (1.74-7.99)

<sup>a</sup> B-values are unstandardized linear regression coefficients adjusted for age and sex.

**Table 4: Association between renal function and ICAS burden**

	ICAS Burden (b-value) <sup>a</sup> (95% CI)
eGFR, per +10 mL/min	-0.77 (-1.50 to -0.03)
eGFR ≥60 mL/min	0 (Reference)
eGFR <60 mL/min	3.18 (0.45-5.91)

<sup>a</sup> B-values are unstandardized linear regression coefficients adjusted for age and sex.

**Table 5: Association between history of vascular disease and ICAS burden**

	ICAS Burden (b-value) <sup>a</sup> (95% CI)
Coronary artery disease	0 (Reference)
Peripheral artery disease	-0.22 (-3.99-3.55)
Cerebrovascular disease	0.01 (-3.46-3.48)
Multivascular disease	2.08 (-0.60-4.76)

<sup>a</sup> B-values are unstandardized linear regression coefficients adjusted for age and sex. Categories are mutually exclusive.

Cerebral arteries are thought to have a different response to vascular risk factors than extracranial arteries, and the relationship between ECAS and ICAS may therefore be relatively weak or absent.<sup>8,24,25</sup> However, studies investigating this hypothesis in vivo have been based on the detection of arterial calcification or hemodynamically significant stenosis, both related to a more advanced stage of atherosclerotic disease. Furthermore, the heterogeneous etiology of arterial calcification and localization restricted to the proximal cerebral arteries might obscure detection of an association. Vessel wall MR imaging directly visualizes the pathologic vessel wall, enabling more accurate measurement of the ICAS burden.<sup>11,12,26</sup>

A very high frequency of ICAS was found in the current population,<sup>12</sup> especially compared with other neuroimaging studies. This is in line with early postmortem studies that reported frequencies approaching 100% in older age.<sup>27,28</sup> Furthermore, the distribution of vessel wall lesions, which we recently reported,<sup>12</sup> was also in line with the distribution of plaques in those postmortem studies, particularly the increased involvement of the larger cerebral arteries compared with the smaller ones. These findings suggest that vessel wall MR imaging at 7T allows a more accurate approximation of the ICAS burden, compared with other neuroimaging methods. However, more studies in different populations regarding age, sex, and disease status are needed to confirm this finding.

cIMT is an established marker of generalized atherosclerosis,<sup>29</sup> though studies on its association with ICAS are limited. Our results are in line with a postmortem study, which reported an association of cIMT with the intima-media ratio of the cerebral vasculature.<sup>30</sup> Furthermore, a longitudinal study in patients with intracranial stenosis found that patients with progressive stenosis on MRA had a larger cIMT compared with those

without progression, though this difference was not statistically significant.<sup>31</sup>

Extracranial carotid disease and ICAS are often assessed separately, likely because their prevalence varies among different ethnic populations.<sup>32</sup> Notably, ICAS is thought to be most prevalent in populations of African and Asian descent, where it is a major cause of ischemic stroke, whereas in whites, it was thought to be less prevalent and a minor cause of ischemic stroke. However, recent studies have shown that the prevalence and importance of ICAS in whites may have been underestimated.<sup>12,33,34</sup> Our results show a strong association between extracranial carotid stenosis and ICAS, a finding that is in concordance with a recent Asian study.<sup>35</sup> Hence, our findings question the current segregation and suggest that they should not be assessed separately.

Low ABI has been associated with hemodynamically significant intracranial stenosis in community-based and ischemic stroke cohorts.<sup>36-38</sup> Our results are in line with these findings and also show that a low ABI is associated with the more continuous spectrum of disease measured by ICAS burden, not just hemodynamic stenosis.

Renal dysfunction is an independent risk factor for cardiovascular disease<sup>39</sup> and has been linked to ischemic stroke, cerebral small vessel disease, and medial arterial calcification.<sup>40,41</sup> A recent scientific abstract reported an association between renal dysfunction and intracranial arterial wall thickening, which is in concordance with our results.<sup>42</sup>

No significant differences in ICAS burden were observed in patients with a history of cerebrovascular, peripheral artery, or multivascular disease compared with coronary heart disease. An association with cerebrovascular disease might have been expected because ICAS is a major cause of ischemic stroke.<sup>1</sup> In our prior study, we did find an association between ICAS burden and the presence of ischemic infarcts.<sup>12</sup> However, in the current analyses, the outcome was clinical stroke and/or TIA, which is an overlapping-but-different entity. Furthermore, small sample sizes of all categories, except for coronary heart disease, may also have prevented observation of significant relationships. Notably, earlier studies from our group in patients with acute ischemic stroke and controls also did not find an association between the number of vessel wall lesions and ischemic stroke.<sup>43</sup>

A main strength of this study is the use of vessel wall MR imaging at 7T, one of the most accurate methods to assess intracranial atherosclerosis in vivo, which enabled visualization of atherosclerosis beyond stenosis. Furthermore, it provided a large coverage area, which allowed assessment of the circle of Willis' branches over a great length. Moreover, the increased contrast-to-noise ratio facilitated a more reliable identification of lesions than is possible at lower field strengths. A last strength is the various measures of ECAS, which allowed an integrated assessment of multiple arterial beds in the same patient.

Several limitations also need to be addressed. First, there is a paucity of radiopathologic studies on vessel wall lesions, making it possible that not all lesions are atherosclerotic. Second, our sample size, though large compared with previous 7T studies, is still relatively small compared with other epidemiologic studies. Third, our cohort consisted of patients with a history of vascular disease with most being men, which may limit generalization of

our results to other populations. Fourth, we used a basic uniparametric score to quantify ICAS burden, which does not account for other quantitative features, such as wall thickness. However, accurate quantitative assessment of lesions, especially the very small lesions visible at 7T, is limited at current spatial resolutions.<sup>44</sup> As a result, grading lesions is a qualitative process and inherently less objective than quantitative grading. Nonetheless, increased objectivity can be obtained by training, experience, and attaining good reproducibility compared with senior observers, as in the current study. Furthermore, we did not assess luminal stenosis because we did not include a refined MRA in the protocol. As advancements to current vessel wall sequences are starting to enable more accurate measurements, development of multiparametric scoring systems (eg, the Gensini score for coronary artery disease), taking into account lesion location, stenosis grade, different geometric characteristics (eg, remodeling index), signal intensity on various weightings, and contrast-enhanced MR imaging, may enable a more versatile way to study the relation among ICAS, ECAS, and clinical outcomes. Last, due to logistic reasons, the ECAS assessment and the 7T MR imaging were not performed on the same day, and in a number of participants, the time interval was quite large. Because ECAS markers could have changed during this interval, this feature may have influenced the observed associations. However, most estimates differed only slightly and did not lead to different conclusions.

## CONCLUSIONS

In patients with a history of various manifestations of vascular disease, ICAS burden, defined as the number of intracranial vessel wall lesions, was associated with atherosclerotic disease in all extracranial arterial beds, not supporting a different etiology. Our results may be used to further elucidate the etiology of ICAS and may be of interest to clinical studies looking for effective ways to select patients at risk of ICAS.

## ACKNOWLEDGMENTS

Members of the Utrecht Cardiovascular Cohort-Second Manifestations of ARterial disease Study Group (UCC-SMART Study Group): F.W. Asselbergs and H.M. Nathoe, Department of Cardiology; G.J. de Borst, Department of Vascular Surgery; M.L. Bots and M.I. Geerlings, Julius Center for Health Sciences and Primary Care; M.H. Emmelot, Department of Geriatrics; P.A. de Jong and T. Leiner, Department of Radiology; A.T. Lely, Department of Obstetrics and Gynecology; N.P. van der Kaaij, Department of Cardiothoracic Surgery; L.J. Kappelle and Y.M. Ruigrok, Department of Neurology; M.C. Verhaar, Department of Nephrology; F.L.J. Visseren (Chair) and J. Westerink, Department of Vascular Medicine, University Medical Center Utrecht and Utrecht University.

## REFERENCES

1. Qureshi AI, Caplan LR. **Intracranial atherosclerosis.** *Lancet* 2014;383:984–98 CrossRef Medline
2. Dearborn JL, Zhang Y, Qiao Y, et al. **Intracranial atherosclerosis and dementia.** *Neurology* 2017;88:1556–63 CrossRef Medline
3. Gorelick P, Wong KS, Liu L. **Epidemiology.** *Front Neurol Neurosci* 2016;40:34–46 CrossRef Medline
4. Qiao Y, Suri FK, Zhang Y, et al. **Racial differences in prevalence and risk for intracranial atherosclerosis in a US community-based population.** *JAMA Cardiol* 2017;2:1341–48 CrossRef Medline
5. Sternby NH. **Atherosclerosis in a defined population: an autopsy survey in Malmö, Sweden.** *Acta Pathol Microbiol Scand* 1968;Suppl 194:5+ Medline
6. D'Armiento FP, Bianchi A, de Nigris F, et al. **Age-related effects on atherogenesis and scavenger enzymes of intracranial and extracranial arteries in men without classic risk factors for atherosclerosis.** *Stroke* 2001;32:2472–79 CrossRef Medline
7. Kiechl S, Willeit J. **The natural course of atherosclerosis, Part I: incidence and progression.** *Arter Thromb Vasc Biol* 1999;19:1484–90 CrossRef Medline
8. Ritz K, Denswil NP, Stam O, et al. **Cause and mechanisms of intracranial atherosclerosis.** *Circulation* 2014;130:1407–14 CrossRef Medline
9. Suri MF, Qiao Y, Ma X, et al. **Prevalence of intracranial atherosclerotic stenosis using high-resolution magnetic resonance angiography in the general population: the Atherosclerosis Risk in Communities study.** *Stroke* 2016;47:1187–93 CrossRef Medline
10. López-Cancio E, Dorado L, Millán M, et al. **The Barcelona-Asymptomatic Intracranial Atherosclerosis (AsIA) study: prevalence and risk factors.** *Atherosclerosis* 2012;221:221–25 CrossRef Medline
11. Qiao Y, Anwar Z, Intrapromkul J, et al. **Patterns and implications of intracranial arterial remodeling in stroke patients.** *Stroke* 2016;47:434–40 CrossRef Medline
12. Zwartbol MHT, van der Kolk AG, Ghaznawi R, et al. **Intracranial vessel wall lesions on 7T MRI.** *Stroke* 2019;50:88–94 CrossRef Medline
13. Bhogal P, Navaei E, Makalanda HL, et al. **Intracranial vessel wall MRI.** *Clin Radiol* 2016;71:293–303 CrossRef Medline
14. Hartevelde AA, van der Kolk AG, van der Worp HB, et al. **High-resolution intracranial vessel wall MRI in an elderly asymptomatic population: comparison of 3T and 7T.** *Eur Radiol* 2017;27:1585–95 CrossRef Medline
15. Geerlings MI, Appelman AP, Vincken KL, et al. **Brain volumes and cerebrovascular lesions on MRI in patients with atherosclerotic disease: the SMART-MR study.** *Atherosclerosis* 2010;210:130–36 CrossRef Medline
16. National Cholesterol Education Program (NCEP) Expert Panel on Detection, Evaluation, and Treatment of High Blood Cholesterol in Adults (Adult Treatment Panel III). **Third Report of the National Cholesterol Education Program (NCEP) Expert Panel on Detection, Evaluation, and Treatment of High Blood Cholesterol in Adults (Adult Treatment Panel III) final report.** *Circulation* 2002;106:3143–421 Medline
17. Simons PC, Algra A, Van De Laak MF, et al. **Second manifestations of ARterial disease (SMART) study: rationale and design.** *Eur J Epidemiol* 1999;15:773–81 CrossRef Medline
18. Winter MA, Guhr KN, Berg GM. **Impact of various body weights and serum creatinine concentrations on the bias and accuracy of the Cockcroft-Gault Equation.** *Pharmacother J Hum Pharmacol Drug Ther* 2012;32:604–12 CrossRef Medline
19. van der Kolk AG, Hendrikse J, Brundel M, et al. **Multi-sequence whole-brain intracranial vessel wall imaging at 7.0 Tesla.** *Eur Radiol* 2013;23:2996–3004 CrossRef Medline
20. van der Kolk AG, Zwanenburg JJ, Brundel M, et al. **Distribution and natural course of intracranial vessel wall lesions in patients with ischemic stroke or TIA at 7.0 Tesla MRI.** *Eur Radiol* 2015;25:1692–700 CrossRef Medline
21. Lindenholz A, van der Kolk AG, Zwanenburg JJ, et al. **The use and pitfalls of intracranial vessel wall imaging: how we do it.** *Radiology* 2018;286:12–28 CrossRef Medline

22. Holmstedt CA, Turan TN, Chimowitz MI. **Atherosclerotic intracranial arterial stenosis: risk factors, diagnosis, and treatment.** *Lancet Neurol* 2013;12:1106–14 CrossRef Medline
23. Aboyans V, Criqui MH, Abraham P, et al. **Measurement and interpretation of the Ankle-Brachial Index: a scientific statement from the American Heart Association.** *Circulation* 2012;126:2890–909 CrossRef Medline
24. López-Cancio E, Galán A, Dorado L, et al. **Biological signatures of asymptomatic extra- and intracranial atherosclerosis: the Barcelona-AsIA (Asymptomatic Intracranial Atherosclerosis) study.** *Stroke* 2012;43:2712–19 CrossRef Medline
25. Odink AE, van der Lugt A, Hofman A, et al. **Association between calcification in the coronary arteries, aortic arch and carotid arteries: the Rotterdam study.** *Atherosclerosis* 2007;193:408–13 CrossRef Medline
26. Mandell DM, Mossa-Basha M, Qiao Y, et al. **Intracranial Vessel Wall MRI: Principles and Expert Consensus Recommendations of the American Society of Neuroradiology.** *AJNR Am J Neuroradiol* 2017;38:218–29 CrossRef Medline
27. Resch JA, Baker AB. **Etiologic mechanisms in cerebral atherosclerosis: preliminary study of 3,839 cases.** *Arch Neurol* 1964;10:617–28 CrossRef Medline
28. Mathur KS, Kashyap SK, Kumar V. **Correlation of the extent and severity of atherosclerosis in the coronary and cerebral arteries.** *Circulation* 1963;27:929–34 CrossRef Medline
29. Bots ML, Sutton-Tyrrell K. **Lessons from the past and promises for the future for carotid intima-media thickness.** *J Am Coll Cardiol* 2012;60:1599–604 CrossRef Medline
30. Iwakiri T, Yano Y, Sato Y, et al. **Usefulness of carotid intima-media thickness measurement as an indicator of generalized atherosclerosis: findings from autopsy analysis.** *Atherosclerosis* 2012;225:359–62 CrossRef Medline
31. Mizukami H, Shimizu T, Maki F, et al. **Progression of intracranial major artery stenosis is associated with baseline carotid and intracranial atherosclerosis.** *J Atheroscler Thromb* 2015;22:183–90 CrossRef Medline
32. Caplan LR, Gorelick PB, Hier DB. **Race, sex and occlusive cerebrovascular disease: a review.** *Stroke* 1986;17:648–55 CrossRef Medline
33. Bos D, van der Rijk MJ, Geeraedts TE, et al. **Intracranial carotid artery atherosclerosis: prevalence and risk factors in the general population.** *Stroke* 2012;43:1878–84 CrossRef Medline
34. Bos D, Portegies ML, van der Lugt A, et al. **Intracranial carotid artery atherosclerosis and the risk of stroke in whites.** *JAMA Neurol* 2014;71:405 CrossRef Medline
35. Man BL, Fu YP. **Concurrent stenoses: a common etiology of stroke in Asians.** *World J Clin Cases* 2014;2:201–05 CrossRef Medline
36. Manzano JJ, De Silva DA, Pascual JL, et al. **Associations of ankle-brachial index (ABI) with cerebral arterial disease and vascular events following ischemic stroke.** *Atherosclerosis* 2012;223:219–22 CrossRef Medline
37. Nakano T, Ohkuma H, Suzuki S. **Measurement of ankle brachial index for assessment of atherosclerosis in patients with stroke.** *Cerebrovasc Dis* 2004;17:212–17 CrossRef Medline
38. Jiménez M, Dorado L, Hernández-Pérez M, et al. **Ankle-brachial index in screening for asymptomatic carotid and intracranial atherosclerosis.** *Atherosclerosis* 2014;233:72–75 CrossRef Medline
39. Manjunath G, Tighiouart H, Ibrahim H, et al. **Level of kidney function as a risk factor for atherosclerotic cardiovascular outcomes in the community.** *J Am Coll Cardiol* 2003;41:47–55 CrossRef Medline
40. Makin SD, Cook FA, Dennis MS, et al. **Cerebral small vessel disease and renal function: systematic review and meta-analysis.** *Cerebrovasc Dis* 2015;39:39–52 CrossRef Medline
41. Power A, Chan K, Haydar A, et al. **Intracranial arterial calcification is highly prevalent in hemodialysis patients but does not associate with acute ischemic stroke.** *Hemodial Int* 2011;15:256–63 CrossRef Medline
42. Qing HA, Gottesman R, Qiao Y, et al. **Abstract TMP52: Association of chronic kidney disease and intracranial atherosclerotic disease by high resolution vessel wall MRI: the ARIC study.** *Stroke* 2018;49 (Suppl 1) CrossRef
43. Hartevelde AA, van der Kolk AG, van der Worp HB, et al. **Detecting intracranial vessel wall lesions with 7T-magnetic resonance imaging: patients with posterior circulation ischemia versus healthy controls.** *Stroke* 2017;48:2601–04 CrossRef Medline
44. van Hespelen KM, Zwanenburg JJ, Hartevelde AA, et al. **Intracranial vessel wall magnetic resonance imaging does not allow for accurate and precise wall thickness measurements.** *Stroke* 2019;50:e283–84 CrossRef

## Intracranial and Extracranial Atherosclerosis: More Similar Than Different?

**A**therosclerosis involves gradual arterial hardening secondary to the building up of lipid-laden plaques in the vessel wall, which may cause vascular stenosis, thromboembolism, or overgrowth across perforator arterial ostia.<sup>1,2</sup> Despite common vascular risk factors and overlapping atherogenic molecular pathways, differential prevalence, onset, and progression of atherosclerosis exist across arterial beds and ethnic groups (eg, inordinate prevalence of intracranial atherosclerosis in Asians and Africans in epidemiologic data), suggesting multifactorial variation underlying the expression of this systemic disease.<sup>2-8</sup> Intracranial large-artery atherosclerosis is a known strong risk factor for ischemic stroke, associated with a high risk of recurrent ischemic stroke.<sup>1</sup> However, it is generally perceived to be etiologically different from extracranial disease.<sup>3-5,8</sup>

Recent technologic advances improving the clinical applicability of 3D high-resolution intracranial vessel wall imaging challenge these traditional assumptions.<sup>5-7,9</sup> Because vascular remodeling in the form of compensatory dilation may occur secondary to plaque formation, traditional lumen-based approaches such as CT or MR angiography on which some historical epidemiologic or symptomatic stroke studies were based could underestimate the true prevalence of underlying intracranial atherosclerosis.<sup>4,6-10</sup> In contrast, vessel wall imaging allows simultaneous study of both stenotic and nonstenotic atherosclerotic vessel wall lesions, better reflecting the true prevalence of intracranial atherosclerotic burden.<sup>7,9</sup> Hence, vessel wall imaging offers the opportunity to elucidate the pathophysiologic underpinnings of intracranial large-artery atherosclerosis, which may serve as potential targets for stroke prevention and treatment.<sup>5,7</sup> Recent interest has been directed to the reliability of vessel wall imaging in epidemiologic characterization of intracranial atherosclerotic burden in population-based studies.<sup>7,9</sup>

The article by Zwartbol et al<sup>11</sup> in this issue of the *American Journal of Neuroradiology* offers incipient evidence of an association of extracranial atherosclerosis and intracranial atherosclerotic burden based on a simple uniparametric score of vessel wall lesion count. Using 7T vessel wall MR imaging, the authors reported on the intracranial atherosclerotic burden on a cross-

sectional analysis of 130 patients with second manifestations of arterial disease in various vessel beds, recruited under the SMART-MR study. Besides a clear majority (96%) of patients having at least 1 intracranial arterial vessel wall lesion, there is a significant association of intracranial atherosclerotic burden with atherosclerotic disease in all examined extracranial arteries (ie, carotid intima-media thickening, 50%–100% carotid stenosis, an ankle-brachial index of  $\leq 0.9$ , and renal dysfunction), leading the authors to conclude that contrary to popular belief, intracranial and extracranial atherosclerosis were more similar than different in atherogenic mechanisms and etiology.

Literature on the relationship between systemic and intracranial atherosclerotic disease is scant and wanting. A recent French study of 403 patients with stroke by Hoshino et al<sup>12</sup> found significant ( $\geq 50\%$ ) intracranial atherosclerotic stenosis in only a 36.2% minority by lumenographic imaging, with concomitant aortic arch and coronary artery atherosclerosis more often coexisting. While the male-dominant cohort studied by Zwartbol et al<sup>11</sup> is small in epidemiologic terms, it is valuable and useful as one of the largest studied with 7T vessel wall MR imaging to date.<sup>7,9</sup> The analysis of extracranial atherosclerosis was comprehensive, and the team should be commended for their clear and succinct charting of the markers of extracranial atherosclerosis and assessment of vascular risk factors. The authors are well-established and competent in vessel wall imaging assessment.<sup>13</sup> Improved accuracy with ultra-high-field in vivo vessel wall MR imaging<sup>14</sup> and a detailed description of vessel wall lesion rating criteria lend credibility to their findings of high intracranial plaque burden, which were consistent with postmortem reporting of plaque frequency and distribution.<sup>15</sup>

We eagerly await validation of these findings in larger prospective population studies incorporating intracranial vessel wall MR imaging with systemic atherosclerosis assessment, and especially in vulnerable cohorts such as Asians and Africans.<sup>1,3</sup> Future evaluation of luminal stenosis and vessel wall MR imaging in tandem, in addition to brain ischemic events, would allow even more comprehensive appraisal and characterization of intracranial atherosclerotic burden with respect to severity, vascular remodeling, and hemodynamic impact. Technologic and protocol refinements further

reducing scan time, while maintaining spatial and contrast resolution,<sup>13</sup> could also make vessel wall MR imaging more clinically accessible to the patient in this age of precision medicine and could deepen our insights into stroke pathophysiology.

## REFERENCES

1. Qureshi AI, Caplan LR. **Intracranial atherosclerosis.** *Lancet* 2014;383:984–98 CrossRef Medline
2. Hopkins PN. **Molecular biology of atherosclerosis.** *Physiol Rev* 2013;93:1317–542 CrossRef Medline
3. Bravata DM, Wells CK, Gulanski B, et al. **Racial disparities in stroke risk factors: the impact of socioeconomic status.** *Stroke* 2005;36:1507–11 CrossRef Medline
4. Kiechl S, Willeit J. Group for the BS. **The natural course of atherosclerosis, Part I: incidence and progression.** *Arter Thromb Vasc Biol* 1999;19:1484–90 CrossRef Medline
5. Ritz K, Denswil NP, Stam O, et al. **Cause and mechanisms of intracranial atherosclerosis.** *Circulation* 2014;130:1407–14 CrossRef Medline
6. Holmstedt CA, Turan TN, Chimowitz MI. **Atherosclerotic intracranial arterial stenosis: risk factors, diagnosis, and treatment.** *Lancet Neurol* 2013;12:1106–14 CrossRef Medline
7. Qiao Y, Suri FK, Zhang Y, et al. **Racial differences in prevalence and risk for intracranial atherosclerosis in a US community-based population.** *JAMA Cardiol* 2017;2:1341–48 CrossRef Medline
8. López-Cancio E, Galán A, Dorado L, et al. **Biological signatures of asymptomatic extra- and intracranial atherosclerosis: the Barcelona-AsIA (Asymptomatic Intracranial Atherosclerosis) study.** *Stroke* 2012;43:2712–19 CrossRef Medline
9. Qiao Y, Guallar E, Suri FK, et al. **MR imaging measures of intracranial atherosclerosis in a population-based study.** *Radiology* 2016;280:860–68 CrossRef Medline
10. Qiao Y, Anwar Z, Intrapromkul J, et al. **Patterns and implications of intracranial arterial remodeling in stroke patients.** *Stroke* 2016;47:434–40 CrossRef Medline
11. Zwartbol MH, Geerlings MI, Ghaznawi R, et al. **Intracranial atherosclerotic burden on 7T MRI is associated with markers of extracranial atherosclerosis: the SMART-MR study.** *AJNR Am J Neuroradiol* 2019;40
12. Hoshino T, Sissani L, Labreuche J, et al; AMISTAD Investigators. **Prevalence of systemic atherosclerosis burdens and overlapping stroke etiologies and their associations with long-term vascular prognosis in stroke with intracranial atherosclerotic disease.** *JAMA Neurol* 2018;75:203–11 CrossRef Medline
13. Lindenholz A, van der Kolk AG, Zwanenburg JJM, et al. **The use and pitfalls of intracranial vessel wall imaging: how we do it.** *Radiology* 2018;286:12–28 CrossRef Medline
14. Hartevelde AA, van der Kolk AG, van der Worp HB, et al. **High-resolution intracranial vessel wall MRI in an elderly asymptomatic population: comparison of 3T and 7T.** *Eur Radiol* 2017;27:1585–95 CrossRef Medline
15. Resch JA, Baker AB. **Etiologic mechanisms in cerebral atherosclerosis: preliminary study of 3,839 cases.** *Arch Neurol* 1964;10:617–28 CrossRef Medline

 L.L. Chan

Department of Diagnostic Radiology  
Singapore General Hospital

Associate Professor

Radiological Sciences, Neuroscience & Behavioural Disorders  
Duke-NUS Medical School

Singapore

<http://dx.doi.org/10.3174/ajnr.A6349>

# Qualitative Assessment and Reporting Quality of Intracranial Vessel Wall MR Imaging Studies: A Systematic Review

J.W. Song, S.C. Guiry, H. Shou, S. Wang, W.R. Witschey, S.R. Messé, S.E. Kasner, and L.A. Loevner



## ABSTRACT

**BACKGROUND:** Over the last quarter-century, the number of publications using vessel wall MR imaging has increased. Although many narrative reviews offer insight into technique and diagnostic applications, a systematic review of publication trends and reporting quality has not been conducted to identify unmet needs and future directions.

**PURPOSE:** We aimed to identify which intracranial vasculopathies need more data and to highlight areas of strengths and weaknesses in reporting.

**DATA SOURCES:** PubMed, EMBASE, and MEDLINE databases were searched up to September 2018 in accordance with the Preferred Reporting Items for Systematic Reviews and Meta-Analyses guidelines.

**DATA ANALYSIS:** Two independent reviewers screened and extracted data from 128 articles. The Strengthening the Reporting of Observational Studies in Epidemiology guidelines were used to assess the reporting quality of analytic observational studies.

**DATA SYNTHESIS:** There has been an exponentially increasing trend in the number of vessel wall MR imaging publications during the past 24 years ( $P < .0001$ ). Intracranial atherosclerosis is the most commonly studied intracranial vasculopathy (49%), followed by dissections (13%), aneurysms (8%), and vasculitis (5%). Analytic observational study designs composed 48% of the studies. Transcontinental collaborations showed nonsignificantly higher reporting quality compared with work originating from single continents ( $P = .20$ ).

**LIMITATIONS:** A limitation is the heterogeneity in study designs.

**CONCLUSIONS:** Investigations on the diagnostic utility of vessel wall MR imaging in less commonly studied intracranial vasculopathies such as dissections, aneurysms, and vasculitis are warranted. More consistent adherence to the Strengthening the Reporting of Observational Studies in Epidemiology guidelines should improve transparency and maximize effective synthesis for clinical translation. Diverse collaborative teams are encouraged to advance the understanding of intracranial vasculopathies using vessel wall MR imaging.

**ABBREVIATIONS:** CRS = complete reporting score; ICAD = intracranial atherosclerotic disease; STROBE = Strengthening the Reporting of Observational Studies in Epidemiology; VWI = vessel wall MR imaging

Vessel wall MR imaging (VWI) is being increasingly used worldwide to evaluate intracranial vasculopathies.<sup>1</sup> This increased utilization has paralleled a rise in the number of publications using VWI. Many narrative reviews report the application and utility of VWI for different types of vasculopathies.<sup>2,3</sup> However, no study has systematically assessed the frequency or

trends of VWI publications for all intracranial vasculopathies or the reporting quality.

Interpretation of data and secondary analyses from observational studies is often limited by the methodology and completeness of reporting. Reporting quality is important to critically

Received July 15, 2019; accepted after revision September 24.

From the Departments of Radiology (J.W.S., S.C.G., S.W., W.R.W., L.A.L.), Neurology (S.R.M., S.E.K.), Otolaryngology (L.A.L.), and Neurosurgery (L.A.L.), Hospital of the University of Pennsylvania, Philadelphia, Pennsylvania; and Department of Biostatistics, Epidemiology and Informatics (H.S.), University of Pennsylvania, Philadelphia, Pennsylvania.

This work was supported by the Radiological Society of North America Research and Education Foundation, through grant No. RSCH1929; the Institute for Translational Medicine and Therapeutics/Thomas B. McCabe and Jeannette E. Laws McCabe Fund for Junior Faculty (J.W.S.); and National Institutes of Health National Heart, Lung, and Blood Institute, R01 HL137984 (W.R.W.).

The content is solely the responsibility of the authors and does not necessarily represent the official views of the Radiological Society of North America Research and Education Foundation.

Please address correspondence to Jae W. Song, MD, MS, Department of Radiology, Division of Neuroradiology, Hospital of the University of Pennsylvania, 3400 Spruce St, Philadelphia, PA 19104; e-mail: jae.song@pennmedicine.upenn.edu; @jsongmd

Indicates open access to non-subscribers at www.ajnr.org

Indicates article with supplemental on-line tables.

<http://dx.doi.org/10.3174/ajnr.A6317>

assess the strengths of studies, weaknesses, and generalizability as well as for investigators who want to assess the reproducibility of a study. The clinical and scientific utility of research data may be lost in poorly reported studies. The Strengthening the Reporting of Observational Studies in Epidemiology (STROBE) guidelines were developed to improve the quality of reporting of observational studies in medical research.<sup>4,5</sup> We set out to systematically survey VWI publications by examining the types of vasculopathies studied as well as assessing the quality of reporting of analytic observational studies using the STROBE checklist. The aims of this study were to identify which intracranial vasculopathies may need more data and to highlight areas of reporting that could be improved.

## MATERIALS AND METHODS

### Search Strategy

The systematic review was conducted in accordance with the Preferred Reporting Items for Systematic Reviews and Meta-Analyses guidelines. PubMed, EMBASE, and MEDLINE were searched on September 12, 2018. To identify eligible studies, we searched keywords using the Boolean operators “OR” and “AND.” Keywords covered imaging, vessel wall imaging, intracranial circulation, vasculopathy, and vascular disease terms (On-line Table 1). A manual review of the citations of each included article was also performed. All foreign language articles were translated.

### Study Selection

Two researchers independently reviewed all publications for inclusion. Inclusion criteria were the following: 1) case series or observational studies, 2) imaging humans, 3) intracranial arteries, 4) intracranial vasculopathies, 5) imaging of the arterial wall, and 6) MR imaging. Single case reports, conference abstracts, animal studies, and studies of the pediatric population were excluded.

### Data Extraction

Two reviewers independently screened and extracted data from each study that fulfilled the inclusion and exclusion criteria. Disagreements were resolved by consensus. We collected the following data: publication characteristics (year of publication, countries of publication, funding sources), type of vasculopathy studied, study design (case series or analytic observational study), and subject enrollment design (prospective or retrospective). Analytic observational studies were identified using a published study design classification algorithm<sup>6</sup> and included studies with comparator groups or that were designed as prevalence/cross-sectional or diagnostic accuracy studies.<sup>7-9</sup> Studies that reported obtaining informed consent or explicitly reported prospective enrollment by the authors were categorized as prospective. Transcontinental collaborative publications were identified by author affiliations. Reporting quality was assessed using the STROBE checklist.<sup>4</sup> Each STROBE item was assessed as 1 = reported, 0.5 = partly reported, or 0 = not reported. A complete reporting score (CRS) per publication was calculated by summing the total number of items divided by 22 (the total number of STROBE criteria). Scores by article section (introduction, methods, results, and conclusions) were also calculated.

### Statistical and Sensitivity Analysis

Categorical variables are expressed in counts and percentages. Distributions of continuous variables are summarized with means and SDs or medians and interquartile ranges. Agreement was calculated with an unweighted Cohen  $\kappa$ . Based on the goodness of fit, exponential and linear regression analyses were fit to test trends across time in the total number of VWI studies and analytic observational studies by year, respectively. The Shapiro-Wilks test was used to test normal distributions of CRS measures. CRS measures were calculated by a summary statistic (mean or median) based on the test for a normal distribution. The Kruskal-Wallis test assessed differences among CRS scores by continent. Two sensitivity analyses assessed the robustness of the results. The first sensitivity analysis considered fulfillment of STROBE items reported in footnotes, bylines, and different sections of the article. A second analysis was conducted by considering fulfillment of STROBE items that were “partly reported” in any part of the article, including footnotes and bylines. Publication bias was assessed using the likelihood ratio  $\chi^2$  test to compare the distributions of the intracranial vasculopathies of the included studies versus the excluded conference abstracts. SPSS Version 19 (IBM, Armonk, New York) was used for statistical analysis.

## RESULTS

### Search

The search strategy identified 2431 publications, among which 1635 were screened by title/abstract ( $\kappa = 0.77$ ; 95% CI, 0.71–0.83;  $P < .01$ ). Of those, 234 articles were selected for full-text review ( $\kappa = 0.89$ ; 95% CI 0.82–0.96;  $P < .01$ ). Manual review of the citations of the included articles yielded 807 citations, which were further screened by title/abstract ( $\kappa = 0.73$ ; 95% CI, 0.52–0.93;  $P < .01$ ). Full data extraction for qualitative synthesis was performed on 128 articles identified from the initial and manual citation review (Fig 1; references in the On-line Appendix).

### Publication Trends

The first article evaluating intracranial vessel wall characteristics from this systematic review was reported in 1994 evaluating intramural hematomas in dissections.<sup>10</sup> The second publication was in 1995 and evaluated vessel walls for cerebral atherosclerosis.<sup>11</sup> An exponentially increasing trend in the number of VWI publications during the past 24 years was seen (Fig 2) ( $\beta = 0.14$ ; 95% CI, 0.11–0.17;  $P < .0001$ ). Asia published the highest number of publications (61%) during the 24 years, followed by North America ( $n = 19$ ) and Europe ( $n = 18$ ). In 2014, transcontinental collaborative publications emerged, composing 10% of the included publications. Asia was part of 92% of the transcontinental collaborations (Fig 3A), and 46% of the transcontinental collaborations were between Asia and North America.

Most investigations were solely federally funded (39%). Publications with mixed types of funding sources accounted for 21%, with the most common combination being federal and medical society sources (54%). No funding source was reported for 30% of all publications (Fig 3B).

Survey of studies focused on 1 vasculopathy revealed intracranial atherosclerotic disease (ICAD) to be the most commonly studied vasculopathy (49%,  $n = 62$ , references in the On-line

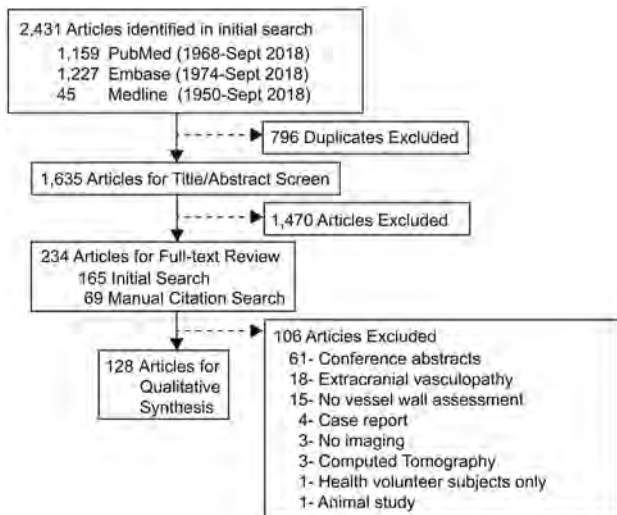


**FIG 1.** Systematic review of the data bases. From the initial data base search, 165 articles were identified for full-text review. Manual review of the citations of those 165 articles identified 807 citations that were further screened by title and abstract. This resulted in 69 articles for full-text review from the manual citation search. A total of 234 articles underwent full-text review, from which 128 articles met the predetermined inclusion and exclusion criteria.

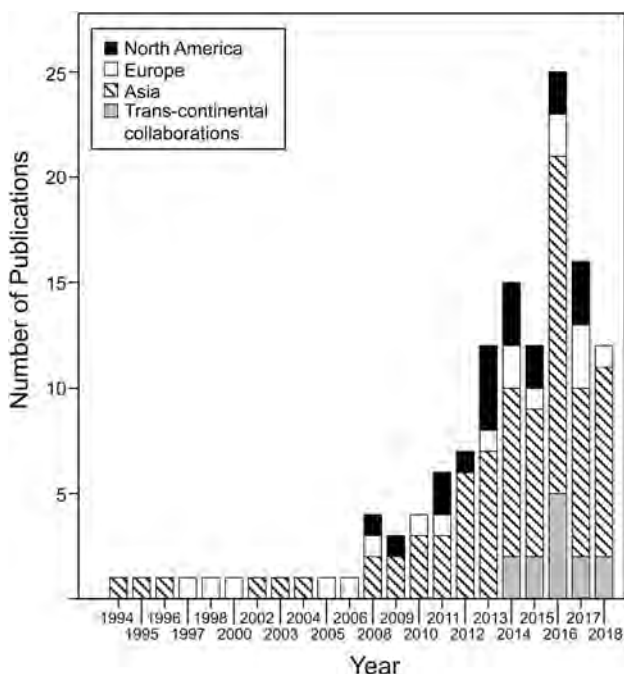


**FIG 2.** Annual number of publications using vessel wall MR imaging.

Appendix), followed by arterial dissection (13%,  $n = 16$ ),<sup>10,12-26</sup> aneurysm (8%,  $n = 10$ ),<sup>27-36</sup> vasculitis (5%,  $n = 6$ ),<sup>37-42</sup> Moyamoya disease (3%,  $n = 4$ ),<sup>43-46</sup> postendovascular changes (2%,  $n = 3$ ),<sup>47-49</sup> and reversible cerebral vasoconstriction syndrome (1%,  $n = 1$ )<sup>50</sup> (Fig 3C). Among the 16 publications investigating arterial dissections, 11 used VWI<sup>12,14-18,22-26</sup> and the other 5 publications<sup>10,13,19-21</sup> assessed intramural hematoma signal characteristics on conventional MR imaging. Note that 21% of the studies examined  $\geq 2$  types of vasculopathies; a breakdown of the types of vasculopathies

studied among these publications is further illustrated in the pie-in-pie chart.

Publication bias was assessed by comparing the number of intracranial vasculopathy types that were included in this study with excluded conference abstracts; the comparison showed no significant difference (On-line Table 2,  $P = .95$ ).

### Study Designs

Case series composed 52% of the publications, and 48% were analytic observational study designs. There was a significant yearly increase in analytic observational studies since 2000 ( $\beta = 0.39$ ; 95% CI, 0.26–0.51;  $P < .0001$ ). Most studies were conducted with prospective subject enrollment (50%) compared with retrospective subject identification (44%). Examples of prospective case series include studies that obtained written informed consent to study circle of Willis cadaveric specimens and characterize intracranial atherosclerotic plaque components,<sup>51</sup> recruited 3 subjects to describe atherosclerosis enhancement characteristics by VWI,<sup>52</sup> and methodologic articles reporting interrater/intrater reliability<sup>53</sup> and scan-rescan reproducibility.<sup>54</sup>

### STROBE Reporting Assessment

The 62 analytic observational studies were evaluated for reporting quality using the STROBE checklist (Table) ( $\kappa = 0.76$ ; 95% CI, 0.72–0.79;  $P < .001$ ). The mean CRS for all studies was  $0.64 \pm 0.10$ . The introduction section had the highest and the methods had the lowest scores. Transcontinental collaborative publications showed higher scores ( $CRS_{all} = 0.67 \pm 0.05$ ) compared with single-continent studies (Table) and multisite/single-continent collaborations ( $CRS_{all} = 0.63 \pm 0.12$ ), though these results did not reach statistical significance ( $P = .20$ ).

Two sensitivity analyses were performed that showed the same direction of the results but notably did not reach statistical significance. First, a sensitivity analysis evaluating each study for items reported in any part of the article, including footnotes and bylines, showed higher scores from transcontinental collaborations compared with single-continent studies ( $P = .30$ ). A second sensitivity analysis considered all partially reported criteria as fulfilling reporting and also showed higher CRS measures by transcontinental collaborations than North American and European studies. The studies from Asia had only marginally higher CRS measures ( $P = .27$ ) (On-line Table 3).

On-line Table 4 reports the mean score per STROBE item for the 62 articles and checklist descriptions. Items 1 and 22 were scored separately because they reflect title/abstract and funding reporting, respectively. Most studies provided an informative abstract but did not indicate the study design in the title (item 1) to fully meet the STROBE criterion, resulting in a score of  $0.52 \pm 0.13$ . Also, 70% of the studies did not disclose whether there was a funding source (item 22), resulting in a score of  $0.71 \pm 0.46$ . The 2 introduction section criteria, evaluating the reporting of the scientific background and rationale (item 2) and specific objectives or hypothesis (item 3), scored the highest among all sections.

The methods section included 9 criteria. No publication reported a sample size determination (item 10). Explicitly presenting key elements of the study (item 4) also scored low

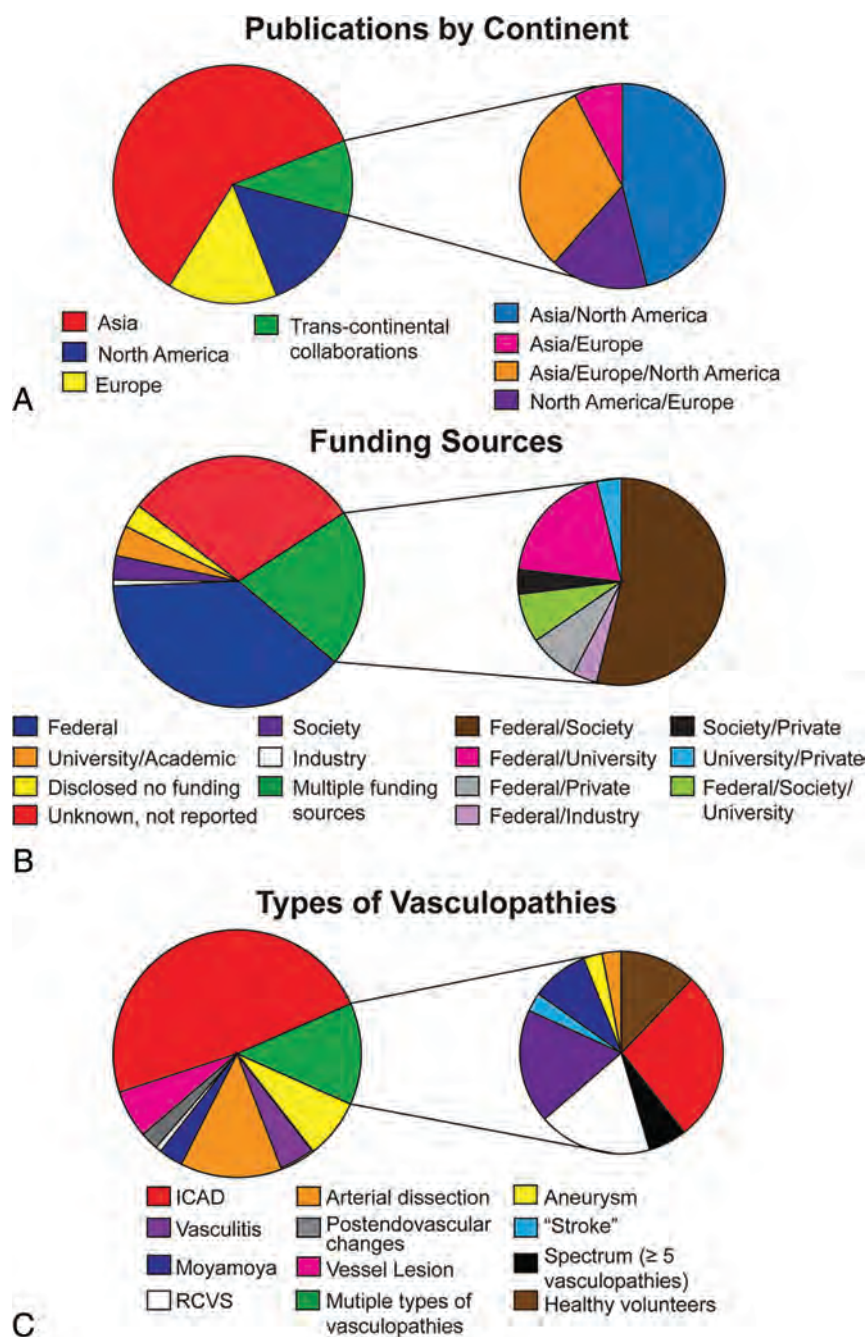


**FIG 3.** Distribution of publications by funding source, continent and intracranial vasculopathy. *A*, Distribution of publications by continent is shown. Distribution of transcontinental collaborations is further elaborated to show 4 different groups of collaborating partners. *B*, Distribution of different funding sources and the combination of funding sources are shown. *C*, Distribution of studied intracranial vasculopathies are shown. RCVS indicates reversible cerebral vasoconstriction syndrome.

( $0.08 \pm 0.24$ ). Although 73% of the studies reported a prospective or retrospective subject enrollment method, few studies named the study design type.<sup>5</sup> Clearly defining outcomes, exposures, predictors, confounders, and diagnostic criteria (item 7) also had a low score ( $0.34 \pm 0.32$ ); for example, only 14% of the 43 publications studying ICAD reported diagnostic criteria for cardiovascular risk factors such as hypertension. The importance of reporting diagnostic criteria for hypertension is emphasized in light of the new 2017 American Heart Association classifications of hypertension and evolving definitions.<sup>55</sup>

Five criteria were included in the results section. Reporting of the study participants and information on exposures and potential confounders (item 14) was suboptimal ( $0.45 + 0.19$ ). Publications lacking information on confounders such as race/ethnicity were scored as partial reporting. Only 8 studies<sup>18,56-62</sup> reported race/ethnicity, among which 5 studies<sup>18,56-59</sup> reported the information in the discussion section as a limitation of generalizability. Twenty-four publications originated from Asia, were single-center studies, and did not report a description of ethnicity; in these studies, one could assume that all enrolled subjects were Asian but clarity in reporting could be strengthened.

In the discussion section, generalizability (item 21) scored the lowest ( $0.26 \pm 0.44$ ). Most studies were single-center studies (74.2%), but this was not commonly addressed as a limitation for external validity. A discussion on limitations and reporting direction/magnitude of potential bias (item 19) also scored

**STROBE complete reporting scores<sup>a</sup>**

	CRS <sub>All</sub>	CRS <sub>Introduction</sub>	CRS <sub>Methods</sub>	CRS <sub>Results</sub>	CRS <sub>Discussion</sub>
All ( <i>n</i> = 62)	0.64 (0.10)	1.00 (0)	0.56 (0.22)	0.60 (0.20)	0.63 (0.25)
North America ( <i>n</i> = 11)	0.62 (0.10)	1.00 (0)	0.52 (0.11)	0.56 (0.22)	0.69 (0.28)
Asia ( <i>n</i> = 40)	0.65 (0.11)	1.00 (0)	0.61 (0.17)	0.65 (0.20)	0.63 (0.25)
Europe ( <i>n</i> = 6)	0.58 (0.14)	1.00 (0)	0.42 (0.15)	0.60 (0.15)	0.63 (0.19)
Trans-continental collaborations ( <i>n</i> = 5)	0.67 (0.05)	1.00 (0)	0.60 (0.07)	0.64 (0.11)	0.73 (0.10)

<sup>a</sup> CRS measures reported in means (SDs) or medians (interquartile range). Summary statistics were chosen on the basis of the test for normality.

poorly ( $0.55 \pm 0.24$ ), with most studies partially fulfilling this item due to an absence of a discussion on the direction and magnitude of the bias.

## DISCUSSION

The increasing trend in the number of VWI publications and more transcontinental collaborations during the past 24 years suggest the widespread interest in the diagnostic utility of VWI. Evaluation of the reporting quality of analytic observational studies using the STROBE checklist highlighted strengths and weaknesses in the current literature. Subgroup analyses showed that transcontinental collaborations yielded higher CRS measures compared with single-center/single-continent and multicenter/single-continent publications, suggesting an advantage for multicultural, diverse collaborative teams. Notably, the results did not reach significance, potentially due to the relatively small number of transcontinental publications.

A survey of the literature to date shows Asia as the leading contributor of VWI publications and ICAD to be the most commonly studied vasculopathy. Fewer VWI studies were identified evaluating arterial dissections, aneurysms, vasculitis, and Moyamoya disease. More effort is warranted to further understand the diagnostic utility of VWI in these less commonly studied intracranial vasculopathies.

Given that stroke is one of the leading causes of morbidity and mortality worldwide and a widespread public health problem, it is not surprising to see federal funding supporting many of the VWI investigations across all continents. Medical societies such as the Dutch Heart Foundation, American Society of Neuroradiology, Radiological Society of North America, and American Heart Association also emerged as common funding sources, showing societal missions to improve stroke outcomes. Nearly one-third of the studies did not disclose a funding source, reflecting either no funding source or funding that was not disclosed.

The availability of the STROBE guidelines has encouraged many research domains and medical specialties to improve reporting quality<sup>63,64</sup> and ultimately improve research reproducibility. Assessment of reporting quality of VWI publications has not yet been evaluated. Our results show a CRS of 0.64 for the 62 analytic observational VWI studies. The results of this study highlight areas where reporting of analytic observational studies are good, along with other areas where improvements are needed. In particular, there is a need for studies to improve the clear reporting of definitions of exposures, predictors, and potential confounders (item 7). The lack of clearly defined diagnostic criteria becomes important when, for example, guidelines are updated; in 2017, the American Heart Association changed the blood pressure guidelines, with some secondary analyses suggesting that the new classification correlates with different prevalence rates and outcomes.<sup>65,66</sup>

Study size calculations (item 10) were not reported in any study. Sample size estimates are informative because they indicate the magnitude of the aimed effect and address whether there were challenges with recruitment due to drop-out or attrition bias.<sup>5</sup>

Additional areas of weakness in reporting included the description of study design (item 4) and settings and locations (item 5). Reporting a prospective or retrospective enrollment design only is insufficient. For example, a cross-sectional study could assess imaging findings on a subject at 1 time point using a prospective enrollment design or the subject could be identified retrospectively from a registry.

In the discussion, reporting the generalizability or external validity (item 21) of the results was also noted to be a weakness. Generalizability is evaluating the extent to which the results of the publication can be applied to other settings and populations and is important for the reader to see whether the results are applicable to his or her own practice setting.

Analysis of reporting quality by continent showed that transcontinental collaborations had higher CRS measures (Table). Collaborations are encouraged for the cross-pollination of ideas, to increase recruitment, or to enhance generalizability by coordinating a multisite study, among other advantages.<sup>67</sup> Our findings suggest an additional advantage of higher reporting quality. Multilingual authors and increased diversity within teams from different continents may be possible explanations for this finding.

This systematic review has some limitations. First, neuro-radiology research often reports innovative techniques and drives cutting-edge methods that are not tested as part of larger epidemiologic studies. These technologic-advancement publications are typically of smaller scale and are “proof of concept” studies that are designed differently but may have larger impact. The STROBE guidelines do not always fit this radiology research framework. However, as an assessment for completeness of reporting with consistency in evaluation by 2 independent raters, the results provide at least a basis of reporting quality among VWI publications. Second, classifying studies as case series or analytic observational studies was often challenging due to the heterogeneity in study designs. Many of the included studies did not fit traditional epidemiologic study designs. This challenge has been addressed in other systematic review methodologies, and an algorithm has been tested to appropriately classify study designs for systematic reviews. We based our classification as descriptive (case series) or analytic observational studies following a simplified version of this algorithm.<sup>6</sup> Third, methodologic quality was not assessed because the aim was to identify trends in VWI publications rather than conduct a quantitative meta-analysis. Instead, an assessment of reporting quality was conducted to highlight areas for improvement.

Fourth, use of the STROBE checklist is inconsistently recommended in author guidelines among journals, which could be a confounder in our analysis. Notably, some journals have their own checklists requiring a statement on data-sharing and open-source availability, which also improve transparency of the conducted research. As a future direction, an assessment of the journals can be conducted to assess CRS measures by journal Impact Factor as well as explicit author instructions to follow the STROBE checklist. Finally, the CRS was calculated using the STROBE guidelines, and items were scored by section as determined by the STROBE checklist. Studies that did not report items

in the correct section per the STROBE guidelines were not considered as fulfilling the criteria. This method may underestimate CRS measures. To account for this issue, we performed a sensitivity analysis with items scored as reported if present in any part of the article, including footnotes and author bylines. This sensitivity analysis yielded similar conclusions. A second sensitivity analysis considering partially reported items as completely reported showed a similar direction of the results.

## CONCLUSIONS

We systematically assess VWI publications to identify trends and assess reporting quality. Our results show that ICAD is the most common intracranial vasculopathy studied. The utility of VWI for ICAD, and for other types of intracranial vasculopathies will likely benefit from additional rigorous studies. We also highlight deficiencies in the reporting of analytic observational VWI studies. Transcontinental collaborative effort yielded a higher reporting quality, though this result did not reach statistical significance. Nonetheless, there may be advantages to diverse and multilingual cross-cultural teams. More consistent adherence to STROBE guidelines should improve transparency and maximize effective synthesis and clinical translation of findings for future studies.

Disclosures: Jae W. Song—RELATED: Grant: Radiological Society of North America, Comments: Radiological Society of North America Scholar Grant.\* Walter R. Witschey—RELATED: Grant: National Institutes of Health.\* Scott E. Kasner—UNRELATED: Consultancy: Bristol Myers Squibb, Bayer, Boehringer Ingelheim, Medtronic; Expert testimony: Janssen; Grants/Grants Pending: BMS, Bayer, Medtronic, WL Gore\*; Royalties: UpToDate. Laurie A. Loevner—UNRELATED: Board Membership: American Society of Neuroradiology, Foundation of the American Society of Neuroradiology, Comments: Co-Chair of the Foundation of the American Society of Neuroradiology, Board of Trustees, Board of Directors. \*Money paid to the institution.

## REFERENCES

- Arenillas JF, Dieleman N, Bos D. **Intracranial arterial wall imaging: techniques, clinical applicability, and future perspectives.** *Int J Stroke* 2019;14:564–73 CrossRef Medline
- Lindenholz A, van der Kolk AG, Zwanenburg JJM, et al. **The use and pitfalls of intracranial vessel wall imaging: how we do it.** *Radiology* 2018;286:12–28 CrossRef Medline
- Mandell DM, Mossa-Basha M, Qiao Y, et al. **Intracranial vessel wall MRI: principles and expert consensus recommendations of the American Society of Neuroradiology.** *AJNR Am J Neuroradiol* 2017;38:218–29 CrossRef Medline
- von Elm E, Altman DG, Egger M, et al. **The strengthening of reporting of observational studies in epidemiology (STROBE) statement: guidelines for reporting observational studies.** *Lancet* 2007;370:1453–57 CrossRef Medline
- Vandenbroucke JP, von Elm E, Altman DG, et al. **Strengthening the reporting of observational studies in epidemiology (STROBE): explanation and elaboration.** *Epidemiology* 2007;18:805–35 CrossRef Medline
- Seo HJ, Kim SY, Lee YJ, et al. **A newly developed tool for classifying study designs in systematic reviews of interventions and exposures showed substantial reliability and validity.** *J Clin Epidemiol* 2016;70:200–25 CrossRef Medline
- Song JW, Chung KC. **Observational studies: cohort and case-control studies.** *Plast Reconstr Surg* 2010;126:2234–42 CrossRef Medline
- Grimes DA, Schulz KF. **An overview of clinical research: the lay of the land.** *Lancet* 2002;359:57–61 CrossRef Medline
- Rutjes AW, Reitsma JB, Vandenbroucke JP, et al. **Case-control and two-gate designs in diagnostic accuracy studies.** *Clin Chem* 2005;51:1335–41 CrossRef Medline
- Kitanaka C, Tanaka J, Kuwahara M, et al. **Magnetic resonance imaging study of intracranial vertebrobasilar artery dissections.** *Stroke* 1994;25:571–75 CrossRef Medline
- Aoki S, Shirouzu I, Sasaki Y, et al. **Enhancement of the intracranial arterial wall at MR imaging: relationship to cerebral atherosclerosis.** *Radiology* 1995;194:477–81 CrossRef Medline
- Natori T, Sasaki M, Miyoshi M, et al. **Detection of vessel wall lesions in spontaneous symptomatic vertebrobasilar artery dissection using T1-weighted 3-dimensional imaging.** *J Stroke Cerebrovasc Dis* 2014;23:2419–24 CrossRef Medline
- Urbach H, Meyer-Lindenberg A, Bendszus M, et al. **Dissections of the basilar artery [in German].** *Rofu* 1998;169:170–74 CrossRef Medline
- Ishitsuka K, Sakaki Y, Sakai S, et al. **Diagnosis and follow-up of posterior inferior cerebellar artery dissection complicated with ischemic stroke assisted by T1-VISTA: a report of two cases.** *BMC Neurol* 2016;16:121 CrossRef Medline
- Sakurai K, Miura T, Sagisaka T, et al. **Evaluation of luminal and vessel wall abnormalities in subacute and other stages of intracranial vertebrobasilar artery dissections using the volume isotropic turbo-spin-echo acquisition (VISTA) sequence: a preliminary study.** *J Neuroradiol* 2013;40:19–28 CrossRef Medline
- Choi JW, Han M, Hong JM, et al. **Feasibility of improved motion-sensitized driven-equilibrium (iMSDE) prepared 3D T1-weighted imaging in the diagnosis of vertebrobasilar artery dissection.** *J Neuroradiol* 2018;45:186–91 CrossRef Medline
- Wang Y, Lou X, Li Y, et al. **Imaging investigation of intracranial arterial dissecting aneurysms by using 3 T high-resolution MRI and DSA: from the interventional neuroradiologists' view.** *Acta Neurochir (Wien)* 2014;156:515–25 CrossRef Medline
- Kwon JY, Kim N, Suh DC, et al. **Intracranial and extracranial arterial dissection presenting with ischemic stroke: lesion location and stroke mechanism.** *J Neurol Sci* 2015;358:371–76 CrossRef Medline
- Hirai T, Korogi Y, Murata Y, et al. **Intracranial artery dissections: serial evaluation with MR imaging, MR angiography, and source images of MR angiography.** *Radiat Med* 2003;21:86–93 Medline
- Kim T, Choi HS, Koo J, et al. **Intramural hematoma detection by susceptibility-weighted imaging in intracranial vertebral artery dissection.** *Cerebrovasc Dis* 2013;36:292–98 CrossRef Medline
- Mascalchi M, Bianchi MC, Mangiafico S, et al. **MRI and MR angiography of vertebral artery dissection.** *Neuroradiology* 1997;39:329–40 CrossRef Medline
- Takano K, Yamashita S, Takemoto K, et al. **MRI of intracranial vertebral artery dissection: evaluation of intramural haematoma using a black blood, variable-flip-angle 3D turbo spin-echo sequence.** *Neuroradiology* 2013;55:845–51 CrossRef Medline
- Park KJ, Jung SC, Kim HS, et al. **Multi-contrast high-resolution magnetic resonance findings of spontaneous and unruptured intracranial vertebral artery dissection: qualitative and quantitative analysis according to stages.** *Cerebrovasc Dis* 2016;42:23–31 CrossRef Medline
- Jung SC, Kim HS, Choi C, et al. **Spontaneous and unruptured chronic intracranial artery dissection: high-resolution magnetic resonance imaging findings.** *Clin Neuroradiol* 2018;28:171–81 CrossRef Medline
- Yun SY, Heo YJ, Jeong HW, et al. **Spontaneous intracranial vertebral artery dissection with acute ischemic stroke: high-resolution magnetic resonance imaging findings.** *Neuroradiol J* 2018;31:262–69 CrossRef Medline
- Madokoro Y, Sakurai K, Kato D, et al. **Utility of T1- and T2-weighted high-resolution vessel wall imaging for the diagnosis and follow up of isolated posterior inferior cerebellar artery dissection with ischemic stroke: report of 4 cases and review of the**

- literature. *J Stroke Cerebrovasc Dis* 2017;26:2645–51 CrossRef Medline
27. Mizutani T. A fatal, chronically growing basilar artery: a new type of dissecting aneurysm. *J Neurosurg* 1996;84:962–71 CrossRef Medline
  28. Edjlali M, Gentric J, Régent-Rodriguez C, et al. Does aneurysmal wall enhancement on vessel wall MRI help to distinguish stable from unstable intracranial aneurysms? *Stroke* 2014;45:3704–06 CrossRef Medline
  29. Park JK, Lee CS, Sim KB, et al. Imaging of the walls of saccular cerebral aneurysms with double inversion recovery black-blood sequence. *J Magn Reson Imaging* 2009;30:1179–83 CrossRef Medline
  30. Boussel L, Wintermark M, Martin A, et al. Monitoring serial change in the lumen and outer wall of vertebrobasilar aneurysms. *AJNR Am J Neuroradiol* 2008;29:259–64 CrossRef Medline
  31. Martin AJ, Hetts SW, Dillon WP, et al. MR imaging of partially thrombosed cerebral aneurysms: characteristics and evolution. *AJNR Am J Neuroradiol* 2011;32:346–51 CrossRef Medline
  32. Omodaka S, Endo H, Niizuma K, et al. Quantitative assessment of circumferential enhancement along the wall of cerebral aneurysms using MR imaging. *AJNR Am J Neuroradiol* 2016;37:1262–66 CrossRef Medline
  33. Blankena R, Kleinloog R, Verweij BH, et al. Thinner regions of intracranial aneurysm wall correlate with regions of higher wall shear stress: a 7T MRI study. *AJNR Am J Neuroradiol* 2016;37:1310–17 CrossRef Medline
  34. Matouk CC, Mandell DM, Günel M, et al. Vessel wall magnetic resonance imaging identifies the site of rupture in patients with multiple intracranial aneurysms: proof of principle. *Neurosurgery* 2013;72:492–96 CrossRef Medline
  35. Kleinloog R, Korkmaz E, Zwaneburg JJM, et al. Visualization of the aneurysm wall: a 7.0-Tesla magnetic resonance imaging study. *Neurosurgery* 2014;75:614–22 CrossRef Medline
  36. Nagahata S, Nagahata M, Obara M, et al. Wall enhancement of the intracranial aneurysms revealed by magnetic resonance vessel wall imaging using three-dimensional turbo spin-echo sequence with motion-sensitized driven-equilibrium: a sign of ruptured aneurysm? *Clin Neuroradiol* 2016;26:277–83 CrossRef Medline
  37. Cheng-Ching E, Jones S, Hui FK, et al. High-resolution MRI vessel wall imaging in varicella zoster virus vasculopathy. *J Neurol Sci* 2015;351:168–73 CrossRef Medline
  38. Ide S, Kakeda S, Miyata M, et al. Intracranial vessel wall lesions in patients with systemic lupus erythematosus: vessel wall lesions in SLE patients. *J Magn Reson Imaging* 2018;48:1237–46 CrossRef Medline
  39. Berkefeld J, Enzensberger W, Lanfermann H. MRI in human immunodeficiency virus-associated cerebral vasculitis. *Neuroradiology* 2000;42:526–28 CrossRef Medline
  40. Thaler C, Kaufmann-Bühler A, Gansukh T, et al. Neuroradiologic characteristics of primary angiitis of the central nervous system according to the affected vessel size. *Clin Neuroradiol* 2019;29:37–44 CrossRef Medline
  41. Schuster S, Bachmann H, Thom V, et al. Subtypes of primary angiitis of the CNS identified by MRI patterns reflect the size of affected vessels. *J Neurol Neurosurg Psychiatry* 2017;88:749–55 CrossRef Medline
  42. Küker W, Gaertner S, Nagele T, et al. Vessel wall contrast enhancement: a diagnostic sign of cerebral vasculitis. *Cerebrovasc Dis* 2008;26:23–29 CrossRef Medline
  43. Han C, Li M, Xu Y, et al. Adult Moyamoya-atherosclerosis syndrome: clinical and vessel wall imaging features. *J Neurol Sci* 2016;369:181–84 CrossRef Medline
  44. Muraoka S, Araki Y, Taoka T, et al. Prediction of intracranial arterial stenosis progression in patients with Moyamoya vasculopathy: contrast-enhanced high-resolution magnetic resonance vessel wall imaging. *World Neurosurg* 2018;116:e1114–21 CrossRef Medline
  45. Yu L, He H, Zhao J, et al. More precise imaging analysis and diagnosis of Moyamoya disease and Moyamoya syndrome using high-resolution magnetic resonance imaging. *World Neurosurg* 2016;96:252–60 CrossRef Medline
  46. Wang M, Yang Y, Zhou F, et al. The contrast enhancement of intracranial arterial wall on high-resolution MRI and its clinical relevance in patients with Moyamoya vasculopathy. *Sci Rep* 2017;7:44264 CrossRef Medline
  47. Seo W, Oh K, Suh S, et al. Clinical significance of wall changes after recanalization therapy in acute stroke: high-resolution vessel wall imaging. *Stroke* 2017;48:1077–80 CrossRef Medline
  48. Power S, Matouk C, Casaubon LK, et al. Vessel wall magnetic resonance imaging in acute ischemic stroke: effects of embolism and mechanical thrombectomy on the arterial wall. *Stroke* 2014;45:2330–34 CrossRef Medline
  49. Abraham P, Scott Pannell J, Santiago-Dieppa D, et al. Vessel wall signal enhancement on 3-T MRI in acute stroke patients after stent retriever thrombectomy. *Neurosurg Focus* 2017;42:E20 CrossRef Medline
  50. Chen C, Chen S, Fuh J, et al. Vascular wall imaging in reversible cerebral vasoconstriction syndrome: a 3-T contrast-enhanced MRI study. *J Headache Pain* 2018;19:74 CrossRef Medline
  51. Jiang Y, Zhu C, Peng W, et al. Ex-vivo imaging and plaque type classification of intracranial atherosclerotic plaque using high resolution MRI. *Atherosclerosis* 2016;249:10–16 CrossRef Medline
  52. Jiang W, Yu W, Ma N, et al. High resolution MRI guided endovascular intervention of basilar artery disease. *J Neurointerv Surg* 2011;3:375–78 CrossRef Medline
  53. Ma N, Jiang WJ, Lou X, et al. Arterial remodeling of advanced basilar atherosclerosis: a 3-Tesla MRI study. *Neurology* 2010;75:253–58 CrossRef Medline
  54. Zhang X, Zhu C, Peng W, et al. Scan-rescan reproducibility of high-resolution magnetic resonance imaging of atherosclerotic plaque in the middle cerebral artery. *PLoS One* 2015;10:e0134913 CrossRef Medline
  55. Whelton PK, Carey RM, Aronow WS, et al. 2017 ACC/AHA/AAPA/ABC/ACPM/AGS/APhA/ASH/ASPC/NMA/PCNA guideline for the prevention, detection, evaluation, and management of high blood pressure in adults: executive summary—a Report of the American College of Cardiology/American Heart Association Task Force on Clinical Practice Guidelines. *Hypertension* 2018;71:1269–324 CrossRef Medline
  56. Xu W, Li M, Niu J, et al. Intracranial artery atherosclerosis and lumen dilation in cerebral small-vessel diseases: a high-resolution MRI study. *CNS Neurosci Ther* 2014;20:364–67 CrossRef Medline
  57. Kim J, Jung K, Sohn C, et al. Intracranial plaque enhancement from high resolution vessel wall magnetic resonance imaging predicts stroke recurrence. *Int J Stroke* 2016;11:171–79 CrossRef Medline
  58. Kim YS, Lim S, Oh K, et al. The advantage of high-resolution MRI in evaluating basilar plaques: a comparison study with MRA. *Atherosclerosis* 2012;224:411–16 CrossRef Medline
  59. Ahn S, Lee J, Kim Y, et al. Isolated MCA disease in patients without significant atherosclerotic risk factors: a high-resolution magnetic resonance imaging study. *Stroke* 2015;46:697–703 CrossRef Medline
  60. Niu P, Yu Y, Zhou H, et al. Vessel wall differences between middle cerebral artery and basilar artery plaques on magnetic resonance imaging. *Sci Rep* 2016;6:38534 CrossRef Medline
  61. Dieleman N, Yang W, Abrigo JM, et al. Magnetic resonance imaging of plaque morphology, burden, and distribution in patients with symptomatic middle cerebral artery stenosis. *Stroke* 2016;47:1797–802 CrossRef Medline
  62. Qiao Y, Anwar Z, Intrapromkul J, et al. Patterns and implications of intracranial arterial remodeling in stroke patients. *Stroke* 2016;47:434–40 CrossRef Medline

63. Langan S, Schmitt J, Coenraads PJ, et al. **The reporting of observational research studies in dermatology journals: a literature-based study.** *Arch Dermatol* 2010;146:534–41 CrossRef Medline
64. Fung AE, Palanki R, Bakri SJ, et al. **Applying the CONSORT and STROBE statements to evaluate the reporting quality of neovascular age-related macular degeneration studies.** *Ophthalmology* 2009;116:286–96 CrossRef Medline
65. Papaioannou TG, Soulis D, Tousoulis D. **Reversibility of hypertension-induced subclinical vascular changes: do the new ACC/AHA 2017 blood pressure guidelines and heart rate changes make a difference?** *J Clin Hypertens (Greenwich)* 2019; 21:1242 CrossRef
66. Muntner P, Carey RM, Gidding S, et al. **Potential US population impact of the 2017 ACC/AHA high blood pressure guideline.** *Circulation* 2018;137:109–18 CrossRef Medline
67. Hall KL, Vogel AL, Huang GC, et al. **The science of team science: a review of the empirical evidence and research gaps on collaboration in science.** *Am Psychol* 2018;73:532–48 CrossRef Medline

# Automated ASPECTS in Acute Ischemic Stroke: A Comparative Analysis with CT Perfusion

V.K. Sundaram, J. Goldstein, D. Wheelwright, A. Aggarwal, P.S. Pawha, A. Doshi, J.T. Fifi, R. De Leacy, J. Mocco, J. Puig, and K. Nael



## ABSTRACT

**BACKGROUND AND PURPOSE:** Automated ASPECTS has the potential of reducing interobserver variability in the determination of early ischemic changes. We aimed to assess the performance of an automated ASPECTS software against the assessment of a neuroradiologist in a comparative analysis with concurrent CTP-based CBV ASPECTS.

**MATERIALS AND METHODS:** Patients with anterior circulation stroke who had baseline NCCT and CTP and underwent successful mechanical thrombectomy were included. NCCT-ASPECTS was assessed by 2 neuroradiologists, and discrepancies were resolved by consensus. CTP-CBV ASPECTS was assessed by a different neuroradiologist. Automated ASPECTS was provided by Brainomix software. ASPECTS was dichotomized (ASPECTS  $\geq 6$  or  $< 6$ ) and was also based on the time from onset ( $> 6$  or  $\leq 6$  hours).

**RESULTS:** A total of 58 patients were included. The interobserver agreement for NCCT ASPECTS was moderate ( $\kappa = 0.48$ ) and marginally improved ( $\kappa = 0.64$ ) for dichotomized data. Automated ASPECTS showed excellent agreement with consensus reads ( $\kappa = 0.84$ ) and CTP-CBV ASPECTS ( $\kappa = 0.84$ ). Intraclass correlation coefficients for ASPECTS across all 3 groups were 0.84 (95% CI, 0.76–0.90, raw scores) and 0.94 (95% CI, 0.91–0.96, dichotomized scores). Automated scores were comparable with consensus reads and CTP-CBV ASPECTS in patients when grouped on the basis of time from symptom onset ( $> 6$  or  $\leq 6$  hours). There was significant ( $P < .001$ ) negative correlation with final infarction volume and the 3 ASPECTS groups ( $r = -0.52$ , consensus reads;  $-0.58$ , CTP-CBV; and  $-0.66$ , automated).

**CONCLUSIONS:** ASPECTS derived from an automated software performs equally as well as consensus reads of expert neuroradiologists and concurrent CTP-CBV ASPECTS and can be used to standardize ASPECTS reporting and minimize interpretation variability.

**ABBREVIATIONS:** AIS = acute ischemic stroke; IQR = interquartile range

The ASPECTS was initially developed in an effort to standardize assessment of the extent of early ischemic change on NCCT of the head in patients with acute ischemic stroke (AIS).<sup>1</sup> The ASPECTS assessment has been increasingly incorporated in treatment decision-making and has been used in several randomized clinical trials for endovascular treatment decision-making.<sup>2,3</sup> ASPECTS  $\geq 6$  is now included in the latest version of the

American Heart Association guidelines as an imaging eligibility criterion for endovascular treatment for patients presenting in the early treatment window ( $< 6$  hours).<sup>4</sup>

The major drawback of the ASPECTS evaluation is its modest interobserver agreement and reproducibility. Early ischemic changes are often difficult to detect on NCCT, with low interobserver agreement for presence and extent.<sup>5-7</sup>

One solution to decrease variability in the detection of early ischemic changes is to use artificial intelligence and deep learning techniques to minimize the variability factor related to human interaction.<sup>8,9</sup> Today automated software programs are commercially available to automatically calculate the ASPECTS using NCCT, with promising results in comparison with human interpretation.<sup>10-12</sup>

By providing hemodynamic and physiologic information, CTP delivers an improved delineation of early ischemia in comparison with NCCT. Applying ASPECTS to CTP-CBV maps has

Received July 4, 2019; accepted after revision September 18.

From the Department of Radiology (V.K.S., J.G., A.A., P.S.P., A.D., K.N.), Neuroimaging Advanced and Exploratory Lab, Department of Neurology (D.W., J.T.F., R.D.L.), and Department of Neurosurgery (J.T.F., R.D.L., J.M.), Icahn School of Medicine at Mount Sinai, New York, New York; and Department of Radiology (J.P.), University of Manitoba, Winnipeg, Manitoba, Canada.

Please address correspondence to Kambiz Nael, MD, Icahn School of Medicine at Mount Sinai, Department of Radiology, One Gustave L. Levy Place, New York, New York 10128; e-mail: kambiznael@gmail.com; @kambiznael

Indicates open access to non-subscribers at www.ajnr.org

<http://dx.doi.org/10.3174/ajnr.A6303>

shown promising results in terms of the accuracy of detecting early ischemic changes, reduced variability, and prediction of functional outcome over NCCT ASPECTS.<sup>5,13-15</sup>

In this study, we aimed to evaluate the performance of automated ASPECTS obtained from a software-based analysis (Brainomix, Oxford, UK; [www.brainomix.com](http://www.brainomix.com)) against the assessment of neuroradiologists in a comparative analysis with concurrent CT perfusion in a cohort of patients with acute ischemic stroke. This study was exploratory without a prespecified hypothesis.

## MATERIALS AND METHODS

### Patient Selection

This study was approved by the local institutional review board (Mount Sinai Health System, New York). We retrospectively reviewed consecutive patients with AIS who presented to our institution between January 2016 and July 2018 and met the following inclusion criteria: 1) time from symptom onset <24 hours, 2) anterior circulation ischemic stroke with large-vessel occlusion (intracranial carotid artery or MCA), 3) baseline NCCT, 4) technically adequate pretreatment CTP, and 5) successful recanalization defined by TIC1 (thrombolysis in cerebral infarction)  $\geq 2b$  via mechanical thrombectomy.<sup>16</sup>

We recorded clinical data, including patients' age, sex, baseline NIHSS scores, time from stroke onset/last well known, location of large-vessel occlusion, time from CT to recanalization, data on receiving intravenous tissue plasminogen activator before mechanical thrombectomy, grade of recanalization using the TIC1 scale, and 90-day mRS when available. mRS scores of 0–2 were classified as indicating a good functional outcome.

### Image Acquisition

CT image acquisition was performed using 2 CT scanners, including a LightSpeed VCT (GE Healthcare, Milwaukee, Wisconsin) and a Somatom Definition (Siemens, Erlangen, Germany). Helical NCCT (120 kV, 100–350 auto-mA) was performed using a 5-mm section thickness from the foramen magnum through the vertex. CTP was performed with the following scan parameters: 100-mm coverage in the z-axis, 80 kV, 150 mA, effective dose = 3.3 mSv, section thickness = 5 mm, collimation =  $64 \times 0.625$  mm. Total acquisition time was 60 seconds (30 consecutive spiral acquisitions, each 2 seconds). A total of 50 mL of iopamidol (Isovue-370; Bracco, Princeton, New Jersey) was injected intravenously followed by a 20-mL saline flush at 5 mL/s.

### Image Analysis

Two board-certified neuroradiologists independently reviewed all baseline NCCTs and assigned an ASPECTS using a 10-point scale.<sup>1</sup> The site of arterial occlusion (right or left) was presented at the time of image interpretation. Discrepancies between 2 readers were resolved using a consensus read in a separate reading session.

In addition, an automated software-based analysis (Brainomix) was used to calculate automated ASPECTS (e-ASPECTS; <https://brainomix.com/e-aspects>). Axial isotropic sequences from NCCT for each patient were uploaded to the software, and automated ASPECTS was calculated without human interaction. The

neuroradiologists and automated ASPECTS were then exported to an Excel spreadsheet (Microsoft; Redmond, Washington) for analysis.

Subsequently, CTP data were processed using FDA-approved postprocessing software (Olea Sphere, Version 6.0; Olea Medical, La Ciotat, France). First, the arterial input function was detected automatically using a cluster-analysis algorithm.<sup>17</sup> This arterial input function was subsequently used by the Bayesian probabilistic method<sup>18</sup> to generate several perfusion parametric maps including CBV and CBF. To avoid recall bias, a board-certified neuroradiologist (different from the one who determined ASPECTS on NCCT) reviewed CTP-CBV maps and assigned an ASPECTS for each patient.

The volume of final infarction was calculated by applying a volume of interest to the DWI hyperintense region using a voxel-based signal intensity method subsampling the entire region of DWI hyperintensity. When follow-up MR imaging was not available ( $n = 13$ ), follow-up CT within 24–48 hours from thrombectomy was used for determination of final infarction volume. In these patients, infarct (defined as established hypodense regions) was manually delineated by a neuroradiologist with 10 years of experience.

### Statistical Analysis

Clinical and demographic data were presented as mean (SD) or median (interquartile range) as appropriate. ASPECTS values were presented as median (interquartile range). Comparison of ASPECTS was performed using both the raw/original scores and dichotomized ASPECTS using  $\geq 6$  and  $< 6$  as a cutoff. Interobserver agreement between 2 neuroradiologists was performed using a weighted  $\kappa$  test with calculation of the 95% CI. Agreement and correlation among neuroradiologist consensus reads, CTP-CBV, and automated ASPECTS were performed using the intraclass correlation coefficient with 95% CI. Comparative analysis between ASPECTS based on the time of symptom onset ( $< 6$  or  $> 6$  hours) was also performed. Finally, clinical and imaging variables were compared between groups with good-versus-poor functional outcome (using 90-day mRS  $> 2$  as a cutoff), using a combination of  $t$  tests and  $\chi^2$  tests as appropriate.

## RESULTS

### Demographic and Clinical Data

A total of 58 patients met our inclusion criteria (27 men, 31 women; mean age,  $69.9 \pm 12.5$  years). The mean of time from symptom onset was  $8.4 \pm 5.3$  hours. The median and interquartile range (IQR) of the NIHSS were 15 and 10–21. A total of 42 patients had proximal middle cerebral artery occlusion, and 16 patients had intracranial internal carotid occlusion. Thirteen of 56 patients received IV-tPA before mechanical thrombectomy (this information was not available in 2 patients). The final mean infarct volume was  $41 \pm 56$  mL. The median and IQR of 90-day mRS available in 50 patients were 3 and 1–5. The final recanalization (TIC1) scores were 2b ( $n = 16$ ), 2c ( $n = 10$ ), and 3 ( $n = 32$ ).

### Human Interpretation

The median for ASPECTS was 9 (IQR, 7–10) for reader 1 and 8 (IQR, 6–9) for reader 2. The interobserver agreement was moderate

with  $\kappa = 0.48$  (95% CI, 0.33–0.62). For the dichotomized ASPECTS (ASPECTS  $\geq 6$  or  $< 6$ ), the interobserver agreement was improved with  $\kappa = 0.64$  (95% CI, 0.32–0.95). For the final consensus read, the median for ASPECTS was 7 (IQR, 7–9). In the dichotomized consensus read, a total of 54 patients had ASPECTS  $\geq 6$  and 4 patients had ASPECTS  $< 6$ .

For CTP-CBV ASPECTS, the median was 8 (IQR, 7–9). A total of 50 patients had ASPECTS  $< 6$ , while 8 had ASPECTS  $\geq 6$ . When ASPECTS values were evaluated between CTP and NCCT (human consensus reads), there was excellent agreement ( $\kappa = 0.84$ ; 95% CI, 0.62–1.0) for the dichotomized scores and moderate agreement ( $\kappa = 0.57$ ; 95% CI, 0.38–0.76) for the raw scores.

### Automated ASPECTS of NCCT

The median was 9 (IQR, 8–10) for automated ASPECTS. The breakdown of dichotomized ASPECTS (ASPECTS  $\geq 6$ /ASPECTS  $< 6$ ) was 52/6 for automated ASPECTS. There was excellent agreement ( $\kappa = 0.84$ ; 95% CI, 0.62–1.0) between automated and consensus dichotomized ASPECTS. In only 2 patients, the software overestimated the extent of early ischemic changes by providing an automated ASPECTS  $< 6$ , while the score was  $> 6$  by consensus read.

There was also excellent agreement ( $\kappa = 0.84$ ; 95% CI, 0.62–1.0) between automated and CTP-CBV dichotomized ASPECTS. In only 2 patients did the software underestimate the extent of early ischemic changes by providing an automated ASPECTS  $> 6$ , while the CTP-CBV ASPECTS was  $< 6$ .

Intraclass correlation coefficients were 0.84 (95% CI, 0.76–0.90) for the original ASPECTS and 0.94 (95% CI, 0.91–0.96) for the dichotomized ASPECTS across all 3 groups (consensus, CTP-CBV, and automated ASPECTS). Comparative scatterplots of ASPECTS across all 3 groups are shown in Fig 1.

Figure 2 demonstrates an example of ASPECTS and comparative analysis among humans, software, and CTP.

Comparative analysis between ASPECTS values based on the time of symptom onset ( $< 6$  or  $> 6$  hours) did not show any significant difference for neuroradiologists, CTP-CBV, or automated ASPECTS (Table 1).

In 50 patients who had a 90-day mRS, 22 patients (44%) had good functional outcome using 90-day mRS  $\leq 2$ , while 28 patients (56%) had poor (mRS  $> 2$ ) functional outcome. Patients with poor functional

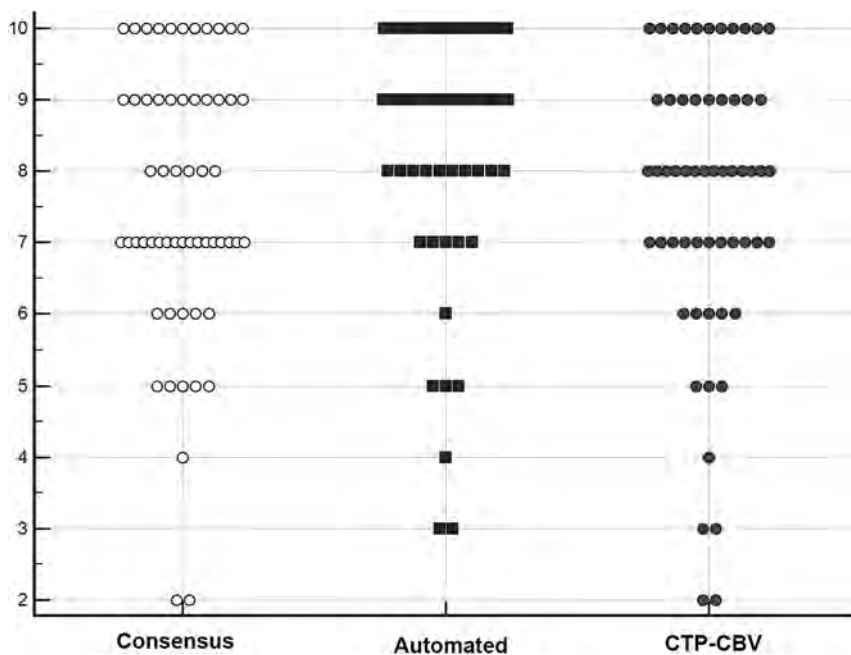


**FIG 1.** Comparative illustration of the distribution of ASPECTS from consensus reads of 2 neuro-radiologists, software-based automated ASPECTS, and CTP-CBV for all patients in our study population (each marker represents a patient's score). Automated ASPECTS showed excellent agreement ( $\kappa = 0.84$ ; 95% CI, 0.62–1.0) with both consensus and CTP-CBV ASPECTS. The intraclass correlation coefficient was 0.84 (95% CI, 0.76–0.90) across all 3 groups.

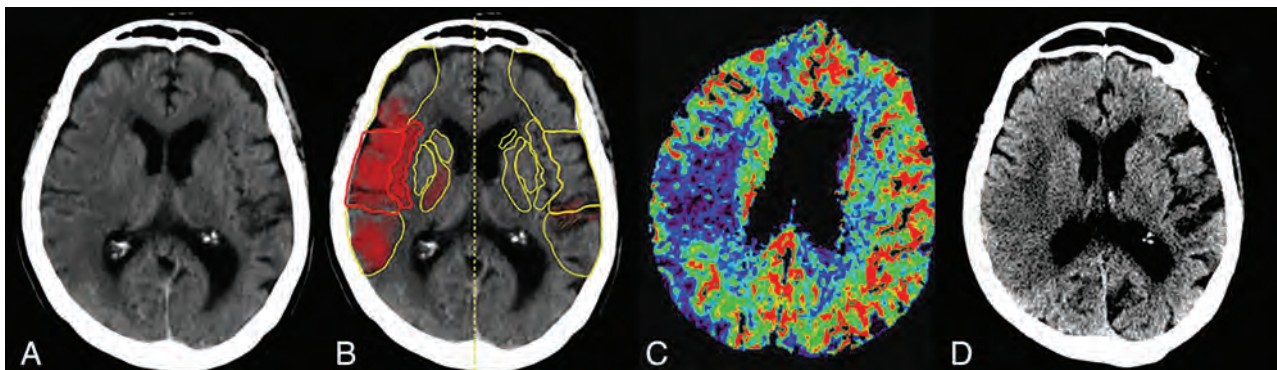


**FIG 2.** An 82-year-old woman who presented with right MCA MI occlusion and an NIHSS score of 18. She underwent successful mechanical thrombectomy (TICI 3) with a CT-to-recanalization time of 50 minutes. Axial NCCT (A), automated ASPECTS (B), axial CTP-CBV (C), and axial NCCT 48 hours after endovascular treatment (D) are shown. For the 2 human readers, one scored 6 and the other, 7 (consensus ASPECTS, 6). B, Automated software assigned an ASPECTS of 6. CTP-CBV ASPECTS was 7. There is good topographic correlation with the final infarction volume.

outcome had significantly higher NIHSS ( $P = .001$ ), older age ( $P = .02$ ), and higher infarction volume ( $P = .03$ ). Of note, none of the ASPECTS values (consensus read, CTP-CBV, or e-ASPECTS) were discriminatory between patients with good-versus-poor functional outcome. Clinical and imaging variables compared in groups with good-versus-poor functional outcome are summarized in Table 2.

All 3 ASPECTS groups had significant ( $P < .001$ ) negative correlation with final infarction volume, with a correlation coefficient ( $r$ ) of  $-0.52$  for the consensus reads,  $-0.58$  for CTP-CBV, and  $-0.66$  for automated ASPECTS. Figure 3 shows correlation scatterplots of ASPECTS and final infarction volumes.

## DISCUSSION

ASPECTS has become increasingly integrated into the decision-making process for intervention in patients with AIS. According to current guidelines, absence of a large infarction core via NCCT defined by ASPECTS  $\geq 6$  is sufficient for treatment decision-making in patients with anterior circulation large-vessel occlusion within the first 6 hours from the symptom onset.<sup>4</sup> For the same population of patients if presenting between 6 and 24 hours from symptom onset, there is a lack of data supporting the use of

NCCT ASPECTS alone for treatment selection,<sup>19</sup> and additional imaging including CTP or MR imaging is recommended.<sup>4</sup>

Our results reaffirmed the concern of interobserver variability for ASPECTS assessment by showing only fair interobserver agreement ( $\kappa = 0.48$ ), even for experienced neuroradiologists. This has been attributed to factors such as physician training and experience, time pressure, and personal bias of expected findings (for example, from the ordering or treatment teams), among other factors that have been noted as potential reasons for the variability of ASPECTS.<sup>11,20,21</sup> Similar to other investigators, using dichotomized ASPECTS ( $\geq 6$  or  $< 6$ ), we showed marginal improvement in interobserver agreement ( $\kappa = 0.64$ ).<sup>13,22</sup> However, there remains substantial variability in ASPECTS assessment, which can introduce uncertainty for all physicians involved in the care of patients with stroke and affect the clinical management and implementation of a guideline-based approach for stroke treatment.<sup>4</sup>

With the introduction of software packages trained on deep learning algorithms, attempts have been made to use automated ASPECTS as a way to address variability associated with human interpretation with some success.<sup>10-12,23-25</sup> In this study, we showed that automated ASPECTS has a similar diagnostic performance to consensus reading of experienced neuroradiologists with excellent agreement ( $\kappa = 0.84$ ). In a recent study by Maegerlein et al<sup>11</sup> using a different software package, similar results were shown with substantial agreement ( $\kappa = 0.9$ ) between automated and consensus reads. Most important, we showed that automated ASPECTS performed equally well compared with consensus reads

with excellent agreement ( $\kappa = 0.84$ ). In a recent study by Maegerlein et al<sup>11</sup> using a different software package, similar results were shown with substantial agreement ( $\kappa = 0.9$ ) between automated and consensus reads. Most important, we showed that automated ASPECTS performed equally well compared with consensus reads

**Table 1: Comparative analysis among ASPECTS scores categorized on the basis of time of symptom onset<sup>a</sup>**

	Onset Symptoms $\leq 6$ hrs (24)	Onset Symptoms $> 6$ hrs (34)	P Value
Consensus ASPECTS (2 neuroradiologists)	8 (6–9)	7 (7–9)	.46
Automated ASPECTS	9 (7–10)	9 (8–9)	.64
CTP-CBV ASPECTS	8 (6–9)	8 (7–9)	.73

<sup>a</sup>Data are presented in median (IQR).

**Table 2: Clinical and imaging data in patients with good-versus-poor functional outcome using mRS  $> 2$  as a cutoff**

Variable	Overall (n = 50)	Good Outcome (n = 22)	Poor Outcome (n = 28)	P Value
Age (mean) (SD) (yr)	70.0 (13.0)	65.1 (12.8)	73.8 (12.1)	.02
Sex (M/F)	23:27	13:9	10:18	.10
Baseline NIHSS (median) (IQR)	15 (11–21)	11 (8–14)	20 (14–22)	.001
Time from symptom onset (mean) (SD) (hr)	8.4 (5.6)	8.8 (6.7)	8.1 (4.6)	.62
Consensus ASPECTS $\geq 6$ (No.) (%)	43	21 (95%)	22 (78%)	.10
Automated ASPECTS $\geq 6$ (No.) (%)	45	21 (95%)	24 (85%)	.26
CTP-CBV ASPECTS $\geq 6$ (No.) (%)	43	21 (95%)	22 (78%)	.10
Final infarction volume (mean) (SD) (mL)	49	24.4 (29.0)	57.5 (64.7)	.03

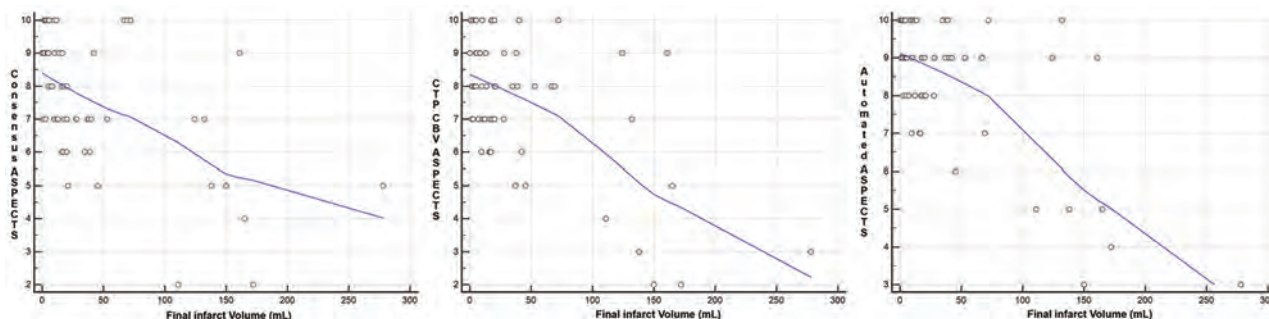


**FIG 3.** Scatterplots for correlation between ASPECTS and final infarction volume for all 3 ASPECTS groups showing significant ( $P < .001$ ) negative correlation ( $r = -0.52$  for the consensus reads,  $-0.58$  for CTP-CBV, and  $-0.66$  for automated ASPECTS).

regardless of the time from onset ( $\geq 6$  or  $< 6$  hours). Assuming that consensus ASPECTS of 2 neuroradiologists can be used as an “operation criterion standard” in an acute setting, it is plausible to use automated ASPECTS to standardize NCCT interpretation in the acute setting and avoid variability associated with individual human interpretation, ensuring that all patients receive equivalent care and are triaged with appropriate treatment options.

Our second finding is that the described automated ASPECTS provides similar diagnostic performance to concurrently performed CTP-CBV ASPECTS. CTP provides more sensitive assessment of early ischemic changes in AIS because it contains physiologic and hemodynamic information about the ischemia. CTP ASPECTS has been used successfully in the triage of patients with AIS with the potential added value of improving reliability and reducing variability in the assessment of early ischemic changes compared with NCCT ASPECTS, in particular in earlier treatment windows.<sup>15,26-29</sup> In a study of 227 patients, Naylor et al<sup>15</sup> showed improvement in the reliability of early ischemic changes using CTP ASPECTS over NCCT ASPECTS.

In our study, having similar diagnostic performance and excellent agreement ( $\kappa = 0.84$ ) between automated software and CTP is reassuring and strengthens the validity of the automated ASPECTS and the argument that it can be used in clinical practice with confidence. In our study using a cutoff for time from symptom onset at 6 hours that has been used in the current guidelines, we did not find any significant discrepancy among our ASPECTS groups.

Finally, we showed that none of our ASPECTS groups (human, automated, or CTP) were predictive of functional outcome as it was measured by 90-day mRS. Although there are several reports supporting a favorable association between higher ASPECTS and good functional outcome,<sup>1,30,31</sup> others have debated the ability of ASPECTS to predict outcome.<sup>20,32</sup> There are also some reports that showed the predictive ability of CTP ASPECTS for determination of functional outcome.<sup>27,33</sup> In a recent study by Pfaff et al,<sup>24</sup> automated ASPECTS was shown to be predictive of functional outcome. One reason for the lack of association between ASPECTS and functional outcome in our study could be an insufficient number of patients with ASPECTS  $< 6$  (only 6 patients using automated ASPECTS). In fact, 21/22 patients who had good functional outcome had a baseline automated ASPECTS score of  $\geq 6$ .

Although ASPECTS values were not predictive of functional outcome in our study, they were predictive of final infarction volume concordant with prior reports.<sup>34</sup> Using automated ASPECTS, a recent study by Demeestere et al<sup>34</sup> showed findings similar to ours by demonstrating a lack of association with functional outcome but significant correlation in the determination of final infarction volume. We found 3 variables, including age, NIHSS, and final infarction volume, as significant contributors to predicting functional outcome. Most interesting, 2 of these (age and NIHSS) have been used in a prior established predictive score (Houston Intra-Arterial Therapy 2 score, which combines age, glucose level, NIHSS, and ASPECTS) for improved prediction of functional outcome in patients with AIS.<sup>35</sup>

There are several limitations to our study. Retrospective design can introduce unknown bias. There was selection bias because only patients with AIS were included. The sample size was relatively small, and further validation studies with larger sample sizes are required to validate the practical application of our automated software as a stand-alone tool in the triage of patients with AIS. Similarly, we had only a small group of patients with low ASPECTS, and this limits assessment of the association with functional outcome. Infarct extension and increased volume are possible between CT and the follow-up imaging after endovascular thrombectomy, which was used for final infarction determination. We tried to minimize this confounding factor by including patients with successful recanalization. Another limitation is that the final imaging study used for determination of final infarction volume was CT in a subset of patients (22%), which is less than ideal in comparison with MR imaging and can possibly introduce inconsistencies into our analysis. Finally, the CTP-CBV ASPECTS values were assessed by only 1 observer.

## CONCLUSIONS

We showed that automated ASPECTS provided by the described software performs equally well compared with a consensus read of expert neuroradiologists and concurrent CTP-CBV ASPECTS in patients presenting with acute ischemic stroke. If its potential is realized, automated ASPECTS can be used as a stand-alone tool for triage and treatment decision-making in patients with acute ischemic stroke.

Disclosures: J. Mocco—RELATED: Board Membership: Neurotechnology Investors; Consultancy: Imperative Care, Cerebrotech inc., Vison, EndoStream Medical, Rebound Therapeutics, Vastrax; UNRELATED: Stock/Stock Options: Neurotechnology Investors, comet inc., Neurvana inc, Cardinal Consulting, Vison, Echovate, Serenity, RIST, Spinaker, inc., Blockade Medical, Kambiz Nael—RELATED: Board Membership: Olea Medical, Comments: Medical Advisory Board.

## REFERENCES

1. Barber PA, Demchuk AM, Zhang J, et al. **Validity and reliability of a quantitative computed tomography score in predicting outcome of hyperacute stroke before thrombolytic therapy: ASPECTS Study Group—Alberta Stroke Programme Early CT Score.** *Lancet* 2000;355:1670–74 CrossRef Medline
2. Goyal M, Demchuk AM, Menon BK, et al. **Randomized assessment of rapid endovascular treatment of ischemic stroke.** *N Engl J Med* 2015;372:1019–30 CrossRef Medline
3. Saver JL, Goyal M, Bonafe A, et al. **Stent-retriever thrombectomy after intravenous t-PA vs. t-PA alone in stroke.** *N Engl J Med* 2015;372:2285–95 CrossRef Medline
4. Powers WJ, Rabinstein AA, Ackerson T, et al. **2018 Guidelines for the Early Management of Patients With Acute Ischemic Stroke: A Guideline for Healthcare Professionals From the American Heart Association/American Stroke Association.** *Stroke* 2018;49:e46–e110 CrossRef Medline
5. Finlayson O, John V, Yeung R, et al. **Interobserver agreement of ASPECT score distribution for noncontrast CT, CT angiography, and CT perfusion in acute stroke.** *Stroke* 2013;44:234–36 CrossRef Medline
6. Mak HK, Yau KK, Khong PL, et al. **Hypodensity of  $> 1/3$  middle cerebral artery territory versus Alberta Stroke Programme Early CT Score (ASPECTS): comparison of two methods of quantitative evaluation of early CT changes in hyperacute ischemic stroke in the community setting.** *Stroke* 2003;34:1194–96 CrossRef Medline

7. Wardlaw JM, Dorman PJ, Lewis SC, et al. **Can stroke physicians and neuroradiologists identify signs of early cerebral infarction on CT?** *J Neurol Neurosurg Psychiatry* 1999;67:651–53 CrossRef Medline
8. Bentley P, Ganesalingam J, Carlton Jones AL, et al. **Prediction of stroke thrombolysis outcome using CT brain machine learning.** *Neuroimage Clin* 2014;4:635–40 CrossRef Medline
9. Tang FH, Ng DK, Chow DH. **An image feature approach for computer-aided detection of ischemic stroke.** *Comput Biol Med* 2011; 41:529–36 CrossRef Medline
10. Herweh C, Ringleb PA, Rauch G, et al. **Performance of e-ASPECTS software in comparison to that of stroke physicians on assessing CT scans of acute ischemic stroke patients.** *Int J Stroke* 2016;11: 438–45 CrossRef Medline
11. Maegerlein C, Fischer J, Monch S, et al. **Automated calculation of the Alberta Stroke Program Early CT Score: feasibility and reliability.** *Radiology* 2019;291:141–48 CrossRef Medline
12. Nagel S, Sinha D, Day D, et al. **e-ASPECTS software is non-inferior to neuroradiologists in applying the ASPECT score to computed tomography scans of acute ischemic stroke patients.** *Int J Stroke* 2017;12:615–22 CrossRef Medline
13. Aviv RI, Mandelcorn J, Chakraborty S, et al. **Alberta Stroke Program Early CT Scoring of CT perfusion in early stroke visualization and assessment.** *AJNR Am J Neuroradiol* 2007;28:1975–80 CrossRef Medline
14. Parsons MW, Pepper EM, Chan V, et al. **Perfusion computed tomography: prediction of final infarct extent and stroke outcome.** *Ann Neurol* 2005;58:672–79 CrossRef Medline
15. Naylor J, Churilov L, Chen Z, et al. **Reliability, reproducibility and prognostic accuracy of the Alberta Stroke Program Early CT Score on CT perfusion and non-contrast CT in hyperacute stroke.** *Cerebrovasc Dis* 2017;44:195–202 CrossRef Medline
16. Tomsick T, Broderick J, Carrozella J, et al. **Revascularization results in the Interventional Management of Stroke II trial.** *AJNR Am J Neuroradiol* 2008;29:582–87 CrossRef Medline
17. Mouridsen K, Christensen S, Gyldensted L, et al. **Automatic selection of arterial input function using cluster analysis.** *Magn Reson Med* 2006;55:524–31 CrossRef Medline
18. Boutelier T, Kudo K, Pautot F, et al. **Bayesian hemodynamic parameter estimation by bolus tracking perfusion weighted imaging.** *IEEE Trans Med Imaging* 2012;31:1381–95 CrossRef Medline
19. Saver JL, Goyal M, van der Lugt A, et al. **Time to treatment with endovascular thrombectomy and outcomes from ischemic stroke: a meta-analysis.** *JAMA* 2016;316:1279–88 CrossRef Medline
20. McTaggart RA, Jovin TG, Lansberg MG, et al. **Alberta stroke program early computed tomographic scoring performance in a series of patients undergoing computed tomography and MRI: reader agreement, modality agreement, and outcome prediction.** *Stroke* 2015;46:407–12 CrossRef Medline
21. Kobkitsuksakul C, Tritanon O, Suraratdecha V. **Interobserver agreement between senior radiology resident, neuroradiology fellow, and experienced neuroradiologist in the rating of Alberta Stroke Program Early Computed Tomography Score (ASPECTS).** *Diagn Interv Radiol* 2018;24:104–07 CrossRef Medline
22. Gupta AC, Schaefer PW, Chaudhry ZA, et al. **Interobserver reliability of baseline noncontrast CT Alberta Stroke Program Early CT Score for intra-arterial stroke treatment selection.** *AJNR Am J Neuroradiol* 2012;33:1046–49 CrossRef Medline
23. Kuang H, Najm M, Chakraborty D, et al. **Automated ASPECTS on noncontrast CT scans in patients with acute ischemic stroke using machine learning.** *AJNR Am J Neuroradiol* 2019;40:33–38 CrossRef Medline
24. Pfaff J, Herweh C, Schieber S, et al. **e-ASPECTS correlates with and is predictive of outcome after mechanical thrombectomy.** *AJNR Am J Neuroradiol* 2017;38:1594–99 CrossRef Medline
25. Guberina N, Dietrich U, Radbruch A, et al. **Detection of early infarction signs with machine learning-based diagnosis by means of the Alberta Stroke Program Early CT Score (ASPECTS) in the clinical routine.** *Neuroradiology* 2018;60:889–901 CrossRef Medline
26. Padroni M, Boned S, Ribo M, et al. **CBV\_ASPECTS improvement over CT\_ASPECTS on determining irreversible ischemic lesion decreases over time.** *Intervent Neurol* 2016;5:140–147 CrossRef Medline
27. Padroni M, Bernardoni A, Tamborino C, et al. **Cerebral blood volume ASPECTS is the best predictor of clinical outcome in acute ischemic stroke: a retrospective, combined semi-quantitative and quantitative assessment.** *PLoS One* 2016;11:e0147910 CrossRef Medline
28. Liu ZW, Jiang Y, Wang R, et al. **Combined application of multi-parameter semiquantitative Alberta Stroke Program Early CT Score to assess infarction severity in acute ischemic stroke [In Chinese; Abstract available in Chinese from the publisher].** *Zhonghua Yi Xue Za Zhi* 2018;98:1697–1702 CrossRef Medline
29. Psychogios MN, Knauth M, Bshara R, et al. **Computed tomography perfusion-based selection of endovascularly treated acute ischaemic stroke patients: are there lessons to be learned from the pre-evidence era?** *Neuroradiol J* 2017;30:138–43 CrossRef Medline
30. Olive-Gadea M, Martins N, Boned S, et al. **Baseline ASPECTS and e-ASPECTS correlation with infarct volume and functional outcome in patients undergoing mechanical thrombectomy.** *J Neuroimaging* 2019;29:198–202 CrossRef
31. Dzialowski I, Hill MD, Coutts SB, et al. **Extent of early ischemic changes on computed tomography (CT) before thrombolysis: prognostic value of the Alberta Stroke Program Early CT Score in ECASS II.** *Stroke* 2006;37:973–78 CrossRef Medline
32. Weir NU, Pexman JH, Hill MD, et al. **How well does ASPECTS predict the outcome of acute stroke treated with IV tPA?** *Neurology* 2006;67:516–18 CrossRef Medline
33. Lee JY, Kim SH, Lee MS, et al. **Prediction of clinical outcome with baseline and 24-hour perfusion CT in acute middle cerebral artery territory ischemic stroke treated with intravenous recanalization therapy.** *Neuroradiology* 2008;50:391–96 CrossRef Medline
34. Demeestere J, Scheldeman L, Cornelissen SA, et al. **Alberta Stroke Program Early CT Score versus computed tomographic perfusion to predict functional outcome after successful reperfusion in acute ischemic stroke.** *Stroke* 2018;49:2361–67 CrossRef Medline
35. Sarraj A, Albright K, Barreto AD, et al. **Optimizing prediction scores for poor outcome after intra-arterial therapy in anterior circulation acute ischemic stroke.** *Stroke* 2013;44:3324–30 CrossRef Medline

# Are Linear Measurements of the Nucleus Basalis of Meynert Suitable as a Diagnostic Biomarker in Mild Cognitive Impairment and Alzheimer Disease?

K.D. Jethwa, P. Dhillon, D. Meng, and D.P. Auer,  
for the Alzheimer's Disease Neuroimaging Initiative

## ABSTRACT

**BACKGROUND AND PURPOSE:** Cell loss within the nucleus basalis of Meynert is an early event in Alzheimer disease. The thickness of the nucleus basalis of Meynert (NBM) can be measured on structural MR imaging. We investigated NBM thickness in relation to cognitive state and biochemical markers.

**MATERIALS AND METHODS:** Mean bilateral nucleus basalis of Meynert thickness was measured on coronal T1-weighted MR imaging scans from the Alzheimer's Disease Neuroimaging Initiative dataset. Three hundred and fifteen scans (80 controls, 79 cases of early mild cognitive impairment, 77 cases of late mild cognitive impairment and 79 cases of Alzheimer disease) were assessed. Alzheimer's Disease Assessment Scale-Cognitive scores, CSF tau, and amyloid quantification were extracted. Group differences in NBM thickness, their correlates and measurement reliability were assessed.

**RESULTS:** Mean NBM thickness  $\pm$  SD progressively declined from  $2.9 \pm 0.3$ ,  $2.5 \pm 0.3$ , and  $2.3 \pm 0.3$  to  $1.8 \pm 0.4$  mm in healthy controls, patients with early mild cognitive impairment, late mild cognitive impairment and Alzheimer disease respectively ( $P < .001$ ). NBM thickness was negatively correlated with Alzheimer's Disease Assessment Scale-Cognitive scores ( $r = -0.53$ ,  $P < .001$ ) and weakly positively correlated with CSF amyloid ( $r = 0.250$ ,  $P < .001$ ) respectively. No association with CSF tau was found. NBM thickness showed excellent diagnostic accuracy to differentiate Alzheimer disease (area under the curve, 0.986) and late mild cognitive impairment from controls (area under the curve, 0.936) with excellent sensitivity, but lower specificity 66.7%. Intra- and inter-rater reliability for measurements was 0.66 and 0.47 ( $P < .001$ ).

**CONCLUSIONS:** There is progressive NBM thinning across the aging-dementia spectrum, which correlates with cognitive decline and CSF markers of amyloid- $\beta$  pathology. We show high diagnostic accuracy but limited reliability, representing an area for future improvement. NBM thickness is a promising, readily available MR imaging biomarker of Alzheimer disease warranting diagnostic-accuracy testing in clinical practice.

**ABBREVIATIONS:**  $A\beta$  = amyloid  $\beta$ ; AD = Alzheimer disease; ADAS-cog = Alzheimer's Disease Assessment Scale-Cognitive; ADNI = Alzheimer's Disease Neuroimaging Initiative; EMCI = early mild cognitive impairment; LMCI = late mild cognitive impairment; MCI = mild cognitive impairment; NBM = nucleus basalis of Meynert; P-tau = phospho-tau

Alzheimer disease (AD) is a common neuropsychiatric disorder characterized by progressive cognitive impairment, behavioral disturbance, and functional decline. There are currently

around 850,000 individuals living with the disorder in the United Kingdom, and this number is set to rise with an aging population.<sup>1</sup> Impaired quality of life and increased caregiver burden are associated with health service use and associated costs.

There has been much research interest into the pathologic mechanisms that underlie the disorder.<sup>2</sup> The presence of extracellular aggregates (or "plaques") of misfolded amyloid- $\beta$  protein

Received May 30, 2019; accepted after revision September 3.

From the Department of Radiological Sciences, Division of Clinical Neuroscience, School of Medicine; Sir Peter Mansfield Imaging Centre, School of Medicine; and National Institute for Health Research Nottingham Biomedical Research Centre (K.D.J., P.D., D.M., D.P.A.), Queen's Medical Centre, University of Nottingham, Nottingham, UK.

Data used in preparation of this article were obtained from the Alzheimer's Disease Neuroimaging Initiative data base (adni.loni.usc.edu). Thus, the investigators within the Alzheimer's Disease Neuroimaging Initiative contributed to the design and implementation of Alzheimer's Disease Neuroimaging Initiative and/or provided data but did not participate in analysis or writing of this report. A complete listing of Alzheimer's Disease Neuroimaging Initiative investigators can be found at: [http://adni.loni.usc.edu/wp-content/uploads/how\\_to\\_apply/ADNI\\_Acknowledgement\\_List.pdf](http://adni.loni.usc.edu/wp-content/uploads/how_to_apply/ADNI_Acknowledgement_List.pdf).

K.D.J. and P.D. are supported by a National Institute of Health Research Academic Clinical Fellowship in Radiology.

Part of this work was previously presented as a poster at: European Congress of Neuropsychopharmacology, March 8–10, 2018; Nice, France.

Please address correspondence to K.D. Jethwa, FRCR, Radiological Sciences, University of Nottingham, Queens Medical Centre, Derby Rd, Nottingham, NG7 2UH UK; e-mail: [ketan.jethwa@nottingham.ac.uk](mailto:ketan.jethwa@nottingham.ac.uk)  
<http://dx.doi.org/10.3174/ajnr.A6313>

and intracellular “tangles” of hyperphosphorylated tau protein are the pathologic hallmarks of the disease.<sup>3</sup> The presence of these plaques and tangles results in neuroinflammation, neurodegeneration, and subsequent cognitive impairment.<sup>2</sup> Abnormal amyloid- $\beta$  accumulates principally within neocortical areas, while tau is found mainly within the basal forebrain and limbic regions before involving the neocortex, spreading via corticocortical axonal projections. The burden of tau pathology is mostly correlated with the degree of neurodegeneration and cognitive impairment observed clinically.<sup>4</sup>

The nucleus basalis of Meynert (NBM) consists of a population of hyperchromic, magnocellular neurons within the basal forebrain, which represent the main source of cortical cholinergic innervation.<sup>5</sup> The internal structure of the nucleus basalis of Meynert is complex, lacking strict anatomic boundaries, with differentially located neurons projecting to distinct areas of the allocortex and neocortex.<sup>6</sup>

Neurons within the NBM are particularly susceptible to tau pathology, being affected more severely and at an earlier stage of the disease.<sup>5,6</sup> There is a long latent period during which there is increasing tau deposition and cell damage, which precedes cell death and the emergence of clinical symptoms. This latent period may coincide with the presymptomatic and mild cognitive impairment (MCI) phases of AD. Atrophy of temporal lobe structures, including the hippocampal formation and entorhinal cortex, is observed later in the course of AD.<sup>7,8</sup>

Stepwise reductions in NBM volumes have been documented as subjects progress from cognitively normal to MCI and AD.<sup>9</sup> NBM atrophy may also predict MCI-to-AD conversion.<sup>10,11</sup> NBM atrophy may identify patients with late-life depression who are at an increased risk of developing dementia, probably due to a basal forebrain cholinergic deficit.<sup>12</sup> NBM atrophy also appears to be associated with treatment response to cholinesterase inhibitors.<sup>13,14</sup> However, this effect may diminish as NBM atrophy progresses in later stages of the disease.<sup>15</sup> MR imaging functional connectivity analyses have also demonstrated reduced NBM-cortical connectivity in dementia, which may also be of value in predicting treatment response.<sup>16</sup>

The NBM can be readily identified on structural neuroimaging, and its thickness can be measured. NBM thickness measurement is a potentially practical tool, which could be easily used by clinicians to assess subtle pathologic changes in patients with cognitive impairment. There is currently a knowledge gap in terms of whether simple measurements of the basal cholinergic nuclei are altered across the aging-dementia spectrum and whether they are correlated with clinical and biochemical markers of disease.

In this study, we investigated the potential of NBM thickness measurements as a diagnostic marker of Alzheimer disease. We analyzed a well-characterized cohort of 315 subjects from the Alzheimer's Disease Neuroimaging Initiative data base (ADNI; [adni.loni.usc.edu](http://adni.loni.usc.edu)) across the aging-dementia spectrum to test the following hypotheses: that NBM thickness 1) progressively decreases in cognitively healthy elderly subjects during early and late MCI to AD, 2) correlates positively with cognitive performance and negatively with CSF disease markers (phospho-tau [P-tau] and amyloid load), and 3) has potential as clinical

diagnostic marker based on diagnostic accuracy and reliability assessment.

## MATERIALS AND METHODS

### Study Participants

Data used in the preparation of this article were obtained from the ADNI data base. ADNI was launched in 2003 as a public-private partnership. The primary goal of ADNI is to test whether serial MR imaging, PET, other biologic markers, and clinical and neuropsychological assessments can be combined to measure the progression of MCI and early AD. Written informed consent was obtained from all individuals.

A retrospective cohort study was performed using 315 coronally acquired T1-weighted MPRAGE scans from this dataset. Cases were selected consecutively from the dataset. Imaging was acquired on 3T systems across multiple sites and providers with the same ADNI 3T imaging protocol. The sample included 80 healthy controls, 79 individuals with early MCI, 77 with late MCI, and 79 with AD (diagnostic criteria: <https://adni.loni.usc.edu/wp-content/uploads/2008/07/adni2-procedures-manual.pdf>). All patients were 55–90 years of age (inclusive). Sex and years of education were also extracted. Clinical cognitive assessments included the Mini-Mental State Examination and Alzheimer Disease Assessment Scale-Cognitive subscale (ADAS-Cog). Stable dose cholinesterase inhibitors were permitted for patients with MCI and AD (ie, no dose change during the preceding 12 weeks).

### CSF Amyloid and Tau Pathology

We manually extracted the presence of CSF amyloid- $\beta$  ( $A\beta$ ) 42 and P-tau from <http://www.ADN.org>. The details of how we extracted the information have been documented previously.<sup>16</sup> The cutoffs for abnormal CSF amyloid  $\beta$ -42 used in this study have been reported previously and were as follows: normal CSF amyloid- $\beta$ -42 (participants with negative CSF  $A\beta$ -42 status), >201.6 ng/L and abnormal amyloid- $\beta$  42 (participants with positive CSF  $A\beta$ -42 status), <182.4 ng/L.<sup>17</sup> We also used the cutoffs for abnormal P-tau as follows: P-tau-positive ( $\geq 23$  pg/mL) and P-tau-negative (<23 pg/mL). There is some overlap between normality and disease states (MCI/AD) for these cutoffs. Detailed protocols for the ADNI2 cohort can be found on-line at: <http://adni.loni.usc.edu/adni-go-adni-2-clinical-data-available/>.

### Measurement of NBM Thickness

Images were analyzed using ITK-SNAP software ([www.itknap.org](http://www.itknap.org)).<sup>18</sup> A vertical line was drawn from the ventral pallidum to the base of the brain at the section where the anterior commissure crosses the midline. NBM thickness (in millimeters) was measured bilaterally, and a mean NBM thickness was calculated for each case. Figs 1 and 2 demonstrate the anatomic localization of the NBM on MR imaging.

A second rater (P.D., with 3 years of experience) measured the NBM thickness on both hemispheres independently in 40 participants (10 from each clinical group) following the same method as the first rater (K.D.J., with 3 years of experience) to test the interrater reliability. The intrarater measurements were undertaken by the same assessor with a 4-week interval.

## Statistical Analysis

All statistical analyses were conducted in SPSS (Version 24; IBM, Armonk, New York). One-way ANOVA and  $\chi^2$  tests were used to compare demographics, CSF amyloid pathology, CSF tau pathology, and *apolipoprotein E 4* (*APOE 4*) status among healthy controls and those with early mild cognitive impairment (EMCI), late mild cognitive impairment (LMCI), and AD.

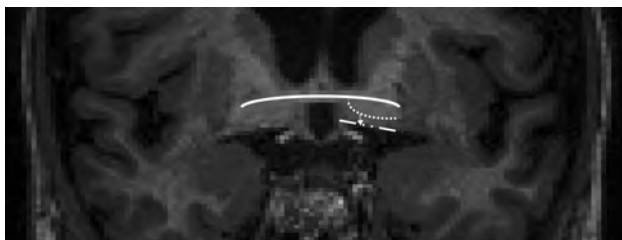


**FIG 1.** Representative coronal MPRAGE brain image showing the localization of the NBM and thickness measurement (arrow). The NBM was measured at its midpoint at the level of the decussation of the anterior commissure (solid line). The NBM sits between the chiasmatic cistern inferiorly (line-dot) and the ventral pallidum superiorly (dotted line). Contrast was maximized on individual cases to improve visualization.

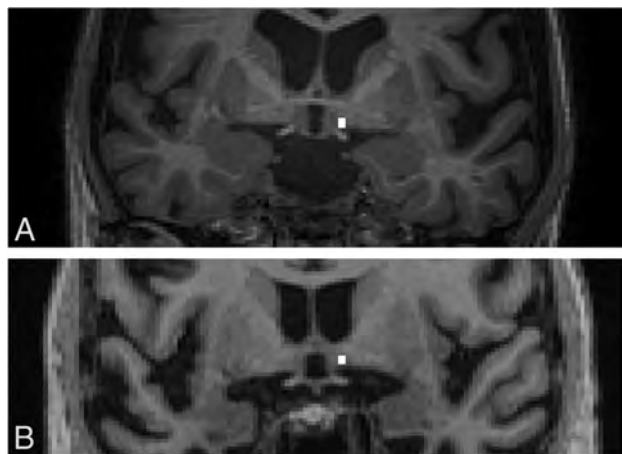


**FIG 2.** Representative coronal MPRAGE brain images showing the localization of the NBM and thickness measurement (white line). A, A patient with AD shows reduced NBM thickness. B, Control. Measurements were made using the ITK-SNAP software.

Due to the between-group differences in age, we then assessed whether NBM thickness was affected by age or sex in our study sample and also explored laterality effects to assess the appropriateness of averaging.

To test our first hypothesis that the averaged NBM thickness was significantly different across healthy controls, EMCI, LMCI, and AD, we used 1-way ANOVA. Data are given as mean  $\pm$  SD unless stated otherwise. Significance was set at  $P < .05$ .

To test our second hypothesis that NBM thickness was declining with increasing cognitive decline and increasing biochemical disease load, we used univariate linear regression analysis to investigate the correlation between averaged NBM thickness and the ADAS-cog score, CSF amyloid- $\beta$  pathology, and CSF tau load. The significance level was set at  $P < .05$ .

To test our third hypothesis that NBM thickness has diagnostic biomarker potential, we used receiver operating characteristic analysis. The choice of the most suitable NBM thickness cutoff to diagnose AD and those at risk based on the Youden index ( $J$ ) which the maximum value of the index may be used as a criterion for selecting the optimum cutoff point.<sup>19</sup>  $J$  can be formally defined as  $J = \text{Sensitivity} + \text{Specificity} - 1$ . We analyzed 2 classification tasks: AD versus controls and LMCI versus controls. We split the sample into 50 controls and 50 cases of AD/LMCI, respectively, to determine the best cutoff and used the remaining 30 controls versus 29 cases of AD and 27 of LMCI, respectively, for validation. We report sensitivity and specificity.

Lastly, using the average value of NBM thickness of the left and right hemispheres, intraclass correlation coefficients were calculated as a measure of interrater (2-way random effects, absolute consistency) and intrarater reliability (mixed-effects model) between 2 radiology trainees to explore the feasibility of clinical implementation. Intraclass correlation coefficient  $> 0.75$  represents excellent reliability; 0.60–0.74, good reliability; 0.41–0.59, fair reliability; and  $< 0.40$ , poor reliability.<sup>20</sup>

## RESULTS

A total of 315 participants (mean age,  $73.2 \pm 7.4$  years; 145 women [46%] and 170 men [54%]) were included. Age ( $P < .001$ ), years of education ( $P = .022$ ), and ADAS-cog scores ( $P < .001$ ) were significantly different among healthy controls and those with EMCI, LMCI, and AD (Table).

### Demographics and clinical information

Whole Sample	Healthy Controls (n = 80)	EMCI (n = 79)	LMCI (n = 77)	AD (n = 79)	P
Age (mean) (yr)	75.2 $\pm$ 6.4	70.2 $\pm$ 7.7	72.3 $\pm$ 7.2	75.0 $\pm$ 7.5	<.001 <sup>a</sup>
Female (No.) (%)	41 (51.3)	36 (45.6)	32 (41.6)	36 (45.6)	.680
Education (mean) (yr)	16.4 $\pm$ 2.3	15.9 $\pm$ 2.7	16.5 $\pm$ 2.7	15.3 $\pm$ 3.1	.022 <sup>a</sup>
ADAS-cog score (mean)	9.7 $\pm$ 4.3	11.9 $\pm$ 5.4	18.3 $\pm$ 6.2	30.4 $\pm$ 6.9	<.001 <sup>a</sup>
CSF amyloid subsample	(n = 53)	(n = 68)	(n = 54)	(n = 47)	
CSF A $\beta$ -42 (ng/L) (mean)	192.5 $\pm$ 56.3	193.5 $\pm$ 50	166.6 $\pm$ 52.3	137.4 $\pm$ 32	<.001 <sup>a</sup>
Positive CSF A $\beta$ -42 status (No.) (%)	26 (49.1)	25 (36.8)	36 (66.7)	45 (95.7)	<.001 <sup>a</sup>
CSF tau subsample	(n = 31)	(n = 68)	(n = 48)	(n = 20)	
CSF P-tau (pg/mL) (mean)	38.9 $\pm$ 28.8	35.1 $\pm$ 21.7	44.1 $\pm$ 21.0	58.1 $\pm$ 26.2	.002 <sup>a</sup>
Positive CSF P-tau status (No.) (%)	22 (71.0)	42 (61.8)	41 (85.4)	19 (95.0)	.004 <sup>a</sup>
APOE subsample	(n = 78)	(n = 75)	(n = 74)	(n = 77)	
APOE-4 carriers (No.) (%)	25 (32.1)	31 (41.3)	37 (50.0)	50 (64.9)	<.001 <sup>a</sup>

<sup>a</sup>Significant.

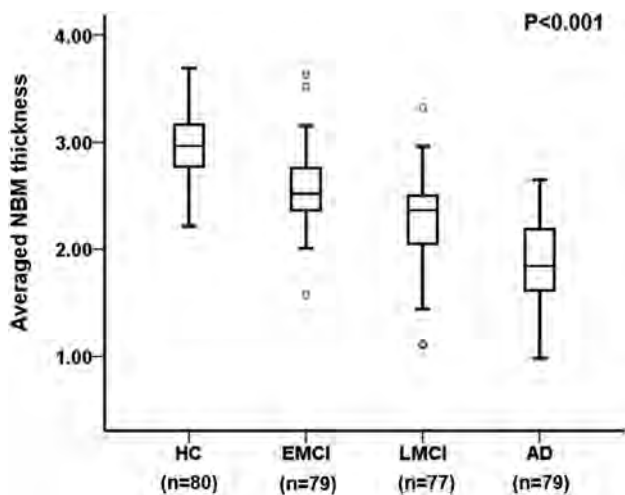


**FIG 3.** Boxplot showing averaged NBM thickness across healthy controls ( $n=80$ ) and individuals with mild cognitive impairment, considered to be early ( $n=79$ ); those with late mild cognitive impairment ( $n=77$ ); and those with AD ( $n=79$ ). NBM thickness differed significantly across cognitive subgroups ( $P < .001$ ).

These significant differences of age ( $P = .006$ ), years of education ( $P = .042$ ), and ADAS-cog scores ( $P < .001$ ) among healthy controls and those with EMCI, LMCI, and AD were also observed in the subsample of participants who had CSF  $A\beta$ -42 measurements ( $n = 222$ ). However, in the subsample of participants who had the measurement of CSF P-tau ( $n = 167$ ), only the ADAS-cog score ( $P < .001$ ) was significantly different among healthy controls and those with EMCI, LMCI, and AD.

NBM thickness was not significantly affected by age or sex or laterality. Hence, we averaged right and left metrics and did not control for demographic variables. There were statistically significant differences among cognitive subgroup means: healthy controls,  $2.9 \pm 0.3$  mm; early MCI,  $2.5 \pm 0.3$  mm; late MCI,  $2.3 \pm 0.3$  mm; clinical AD,  $1.8 \pm 0.4$  mm as determined by 1-way ANOVA ( $F[3,311] = 128.5, P < .001$ ) (Fig 3).

NBM thickness was significantly correlated with cognitive performance with higher ADAS-cog scores found in subjects with thinner NBMs, explaining 33% of the mutual variance ( $r^2 = 0.334, P < .001$ , Fig 4). There was also a mild association between a thinner NBM and lower CSF- $A\beta$ -42 ( $r^2 = 0.06, P < .001$ , Fig 5). Conversely, CSF P-tau did not correlate with NBM thickness.

The receiver operating characteristic showed excellent diagnostic accuracy to differentiate healthy controls from those with AD (area under the curve, 0.986;  $P < .001$ ; 95% CI, 0.969–1.000; Fig 6A) in the discovery dataset (sensitivity, 92%; specificity, 100%), using a cutoff score of 2.7025 mm. Applying this cutoff to the validation data of 30 controls and 29 patients with AD, we achieved 100% sensitivity but only 66.7% specificity. Considerable overlap of error bars in boxplots among different groups (Fig 3) may account for this specificity value.

Diagnostic accuracy was also excellent to differentiate those with LMCI and controls using the receiver operating characteristic in the discovery subgroup that identified a cutoff of 2.687 mm (area under the curve, 0.936;  $P < .001$ ; 95% CI, 0.884–0.988; Fig 6B) with a sensitivity of 92% and specificity of 90%. Validation in

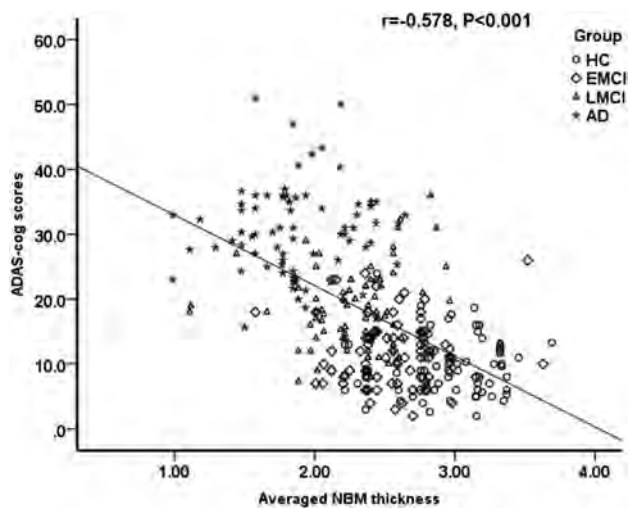


**FIG 4.** Scatterplot shows a negative correlation between cognitive performance (ADAS-cog score) and averaged NBM thickness (in millimeters).

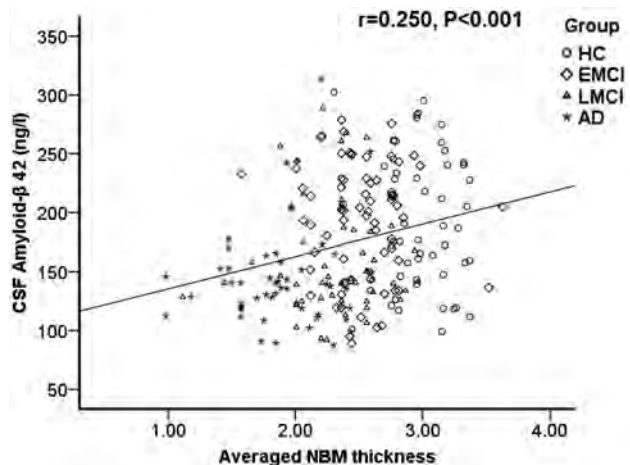


**FIG 5.** Scatterplot shows a positive correlation between CSF  $A\beta$ -42 and averaged NBM thickness.

the remainder of healthy controls and the LMCI cohort (30 healthy controls versus 27 with LMCI) achieved excellent sensitivity (92.5%), at a lower specificity of 66.7%.

A sample of 40 scans was reviewed twice by the same assessor following a 4-week interval to assess intrarater reliability. The interrater reliability was considered fair (intraclass correlation coefficient [2,2] = 0.468 [95% CI,  $-0.227$ – $0.774$ ],  $P < .001$ ), and the intrarater reliability was good (intraclass correlation coefficient [2,2] = 0.658 [95% CI, 0.266–0.831],  $P < .001$ ).

## DISCUSSION

In this large retrospective study of a well-phenotyped cohort from the ADNI data base, we undertook a series of qualification studies to assess the potential of a simplified NBM thickness measurement as a novel diagnostic biomarker of AD. We demonstrate progressive thinning of the NBM in subjects with early and late MCI and AD compared with cognitively healthy

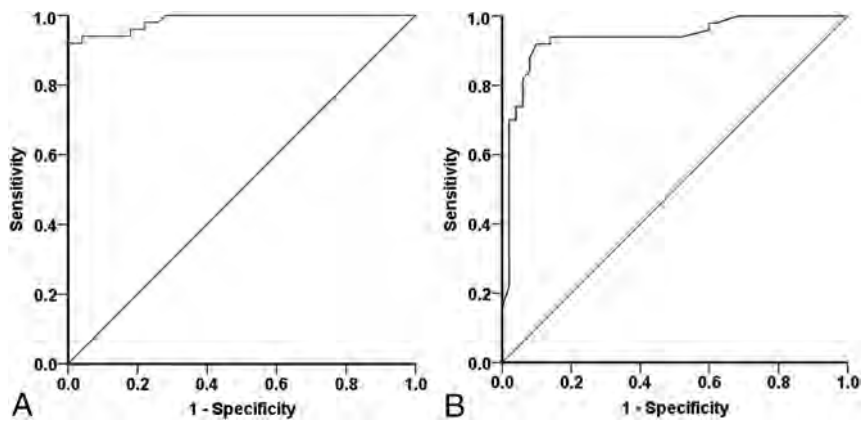


**FIG 6.** Receiver operating characteristic curves to differentiate those with AD from controls (A) and those with LMCI from controls (B).

subjects. Second, we show that linear NBM thickness measures are correlated with measures of cognitive impairment and CSF- $A\beta$ . Lastly, NBM thickness proved promising to differentiate those with AD and late MCI from cognitively healthy controls.

NBM thinning in AD has face validity as a diagnostic marker of AD based on the established cell loss within the NBM in AD, which is well-documented in the pathologic<sup>6</sup> and clinical imaging literature.<sup>9,10</sup> Our findings, using a simple linear assessment of the width of the NBM, closely mirror the reported progressive NBM volumetric reductions in clinical groups with increasing clinical cognitive impairment.<sup>9</sup> Accurate volumetric assessment of the NBM, however, does not form part of routine assessment, and the software required is not available on reporting workstations. Given that the NBM can be readily identified on coronal MR imaging, thickness measurement at the level of the decussation of the anterior commissure may represent a novel and simple-to-use imaging biomarker for routine assessment in memory clinics with no additional scan or software license costs. Small observational studies have previously highlighted differences in NBM thickness between controls and patients with AD and reported mean NBM thicknesses of up to 3.0 mm in controls and 2.1 mm in those with AD.<sup>21</sup> These reports are quantitatively consistent with our findings of 2.9 and 1.8 mm in controls and patients with AD, respectively.

To further qualify MR imaging-defined NBM thickness assessment as a potential biomarker of AD, we sought to address the requirement of a direct association with clinical symptoms and biochemical disease markers. As an important proof of concept, we demonstrated that NBM thinning was significantly correlated with cognitive decline. We found a moderate negative correlation between NBM thickness and ADAS-cog scores, explaining a third of the mutual variance, which corroborates the expected direct role of cholinergic projections from the NBM and cognitive functioning. Preclinical studies have shown memory impairment and learning deficits after lesioning of the NBM.<sup>22</sup> A previous MR imaging study found a significant-albeit-weaker ( $r^2 = 0.12$ ) correlation between the volume of the substantia innominata and memory scores in a cohort of healthy elderly and those with amnesic MCI and AD.<sup>23</sup>

CSF  $A\beta$ -42 is an accepted biomarker of cerebral amyloid accumulation, with high diagnostic accuracy for AD.<sup>24</sup> In a subset of the ADNI cohort with available CSF  $A\beta$ -42 data, we show that reduced  $A\beta$ -42 was associated with reduced NBM thickness, which is consistent with a link between cerebral amyloid pathology and NBM degeneration in AD. There is evidence that NBM atrophy may correlate more closely with cortical amyloid burden than hippocampal atrophy and may predict disease trajectory.<sup>11,25</sup>

The burden of tau pathology is mostly correlated with the degree of clinical cognitive impairment.<sup>4</sup> Hyperphosphorylated tau is preferentially deposited within the basal forebrain early in the course of AD. However, no significant association between CSF P-tau and NBM thickness was identified. A possible explanation is that given that tau is an intracellular protein, there may be limited correlation between CSF levels and the actual cortical burden. A CSF-pathologic correlative study has found no correlation between CSF P-tau levels and the Braak staging criteria, which are used to pathologically assess the burden of cellular tau deposition.<sup>26</sup>

NBM thickness measurement sensitivity and specificity compare favorably with those of currently used structural brain rating scales, including the medial temporal lobe atrophy scale (85% and 82% sensitivity and specificity, respectively).<sup>27</sup> A 2.7-mm cutoff provides superior sensitivity and specificity for distinguishing controls and those with AD as well as controls and those with LMCI in our discovery data, with high sensitivity in the validation data pointing to the potential clinical diagnostic value of NBM thickness as screening biomarker for AD.

The cross-sectional nature of this project and lack of out-of-sample validation are a limitation of this study. Longitudinal analysis is warranted to assess the trajectory of NBM thickness and the power to differentiate stable MCI from MCI-to-AD converters. Second, NBM atrophy measurements are indirect markers of cellular damage and may also reflect changes in other neuronal or glial components within the basal forebrain. Without a postmortem sample, the relationship between NBM thickness and cell count remains unclear. Suboptimal measurement reliability is another limitation of this study. There is fair intrarater and good interobserver reliability for repeat NBM thickness measurements. It is possible that this may be improved with additional rater training and optimizing sequences with better contrast resolution between the NBM and surrounding structures.<sup>28</sup>

## CONCLUSIONS

There is progressive nucleus basalis of Meynert thinning across the aging-dementia spectrum, which correlates with cognitive decline and CSF markers of amyloid- $\beta$  pathology. We show high diagnostic accuracy but limited reliability measurement, which

could be improved by optimising contrast resolution at the base of the brain. Nucleus basalis of Meynert thickness is a promising, readily available MR imaging biomarker of Alzheimer disease which warrants diagnostic-accuracy testing in clinical practice.

Disclosures: Ketan D. Jethwa—UNRELATED: Employment: National Institute of Health Research, Comments: K.D.J. and P.D. are National Institute of Health Research academic clinical fellows whose salary is partly funded by the National Institute of Health Research. This fellowship also includes a bursary for research/educational purposes. Dorothee P. Auer—UNRELATED: Grants/Grants Pending: National Institute of Health Research, Parkinson's UK, Versus Arthritis, Michael J Fox Foundation, Comments: grant funding for unrelated work\*; Other: Biogen, Comments: research support for neuromelanin imaging in Parkinson disease. \*Money paid to the institution.

## REFERENCES

1. What is dementia? Factsheet 400LP January 2017. [https://www.alzheimers.org.uk/Download/Downloads/Id/3416/What\\_Is\\_Dementia.pdf](https://www.alzheimers.org.uk/Download/Downloads/Id/3416/What_Is_Dementia.pdf). Accessed May 3, 2017
2. Esiri MM, Morris JH. *The Neuropathology of Dementia*. Cambridge: Cambridge University Press; 2009
3. Selkoe DJ. Alzheimer's disease: genes, proteins, and therapy. *Physiol Rev* 2001;81:741–66 CrossRef Medline
4. Braak H, Alafuzoff I, Arzberger T, et al. Staging of Alzheimer disease-associated neurofibrillary pathology using paraffin sections and immunocytochemistry. *Acta Neuropathol* 2006;112:389–404 CrossRef Medline
5. Mesulam MM. Cholinergic circuitry of the human nucleus basalis and its fate in Alzheimer's disease. *J Comp Neurol* 2013;521:4124–44 CrossRef Medline
6. Liu AK, Chang RC, Pearce RK, et al. Nucleus basalis of Meynert revisited: anatomy, history and differential involvement in Alzheimer's and Parkinson's disease. *Acta Neuropathol* 2015;129:527–40 CrossRef Medline
7. Sassin I, Schultz C, Thal DR, et al. Evolution of Alzheimer's disease-related cytoskeletal changes in the basal nucleus of Meynert. *Acta Neuropathol* 2000;100:259–69 CrossRef Medline
8. Insausti R, Juottonen K, Soininen H, et al. MR volumetric analysis of the human entorhinal, perirhinal, and temporopolar cortices. *AJNR Am J Neuroradiol* 1998;19:659–71 Medline
9. Teipel SJ, Flatz WH, Heinsen H, et al. Measurement of basal forebrain atrophy in Alzheimer's disease using MRI. *Brain* 2005;128:2626–44 CrossRef Medline
10. Grothe M, Heinsen H, Teipel SJ. Atrophy of the cholinergic basal forebrain over the adult age range and in early stages of Alzheimer's disease. *Biol Psychiatry* 2012;71:805–13 CrossRef Medline
11. Grothe MJ, Ewers M, Krause B, et al. Basal forebrain atrophy and cortical amyloid deposition in nondemented elderly subjects. *Alzheimers Dement* 2014;10:S344–53 CrossRef Medline
12. Förstl H, Levy R, Burns A, et al. Disproportionate loss of noradrenergic and cholinergic neurons as cause of depression in Alzheimer's disease: a hypothesis. *Pharmacopsychiatry* 1994;27:11–15 CrossRef Medline
13. Bottini G, Berlinger M, Basilio S, et al. Good or bad responder? Behavioural and neuroanatomical markers of clinical response to donepezil in dementia. *Behav Neurol* 2012;25:61–72 Medline
14. Hanyu H, Tanaka Y, Sakurai H, et al. Atrophy of the substantia innominata on magnetic resonance imaging and response to donepezil treatment in Alzheimer's disease. *Neurosci Lett* 2002;319:33–36 CrossRef Medline
15. Kanetaka H, Hanyu H, Hirao K, et al. Prediction of response to donepezil in Alzheimer's disease: combined MRI analysis of the substantia innominata and SPECT measurement of cerebral perfusion. *Nucl Med Commun* 2008;29:568–73 CrossRef Medline
16. Meng D, Li X, Bauer M, et al. Alzheimer's disease neuroimaging, I: altered nucleus basalis connectivity predicts treatment response in mild cognitive impairment. *Radiology* 2018;289:775–85 CrossRef Medline
17. Palmqvist S, Mattsson N, Hansson O. Cerebrospinal fluid analysis detects cerebral amyloid- $\beta$  accumulation earlier than positron emission tomography. *Brain* 2016;139:1226–36 CrossRef Medline
18. Yushkevich P, Piven J, Hazlett H, et al. User-guided 3D active contour segmentation of anatomical structures: significantly improved efficiency and reliability. *Neuroimage* 2006;31:1116–28 CrossRef Medline
19. Youden WJ. Index for rating diagnostic tests. *Cancer* 1950;3:32–35 CrossRef
20. Cicchetti D, Sparrow A. Developing criteria for establishing interrater reliability of specific items: applications to assessment of adaptive behavior. *Am J Ment Defic* 1981;86:127–37 Medline
21. Hanyu H, Asano T, Sakurai F, et al. MR analysis of the substantia innominata in normal aging. *AJNR Am J Neuroradiol* 2002;23:27–32 Medline
22. Berger-Sweeney J, Heckers S, Mesulam MM, et al. Differential effects on spatial navigation of immunotoxin-induced cholinergic lesions of the medial septal area and nucleus basalis magnocellularis. *J Neurosci* 1994;14:4507–19 CrossRef Medline
23. George S, Mufson EJ, Leurgans S, et al. MRI-based volumetric measurement of the substantia innominata in amnesic MCI and mild AD. *Neurobiol Aging* 2011;32:1756–64 CrossRef Medline
24. Dubois B, Feldman HH, Jacova C, et al. Advancing research diagnostic criteria for Alzheimer's disease: the IWG-2 criteria. *Lancet Neurol* 2014;13:614–29 CrossRef Medline
25. Grothe MJ, Heinsen H, Amaro E, et al. Cognitive correlates of basal forebrain atrophy and associated cortical hypometabolism in mild cognitive impairment. *Cereb Cortex* 2016;26:2411–26 CrossRef Medline
26. Buerger K, Alafuzoff I, Ewers M, et al. No correlation between CSF tau protein phosphorylated at threonine 181 with neocortical neurofibrillary pathology in Alzheimer's disease. *Brain* 2007;130:E82 CrossRef Medline
27. Duara R, Loewenstein DA, Potter E, et al. Medial temporal lobe atrophy on MRI scans and the diagnosis of Alzheimer disease. *Neurology* 2008;71:1986–92 CrossRef Medline
28. Jethwa K, Aphiwatthanasumet K, Mougou O, et al. Phase enhanced PSIR T1-weighted imaging improves contrast resolution of the nucleus basalis of Meynert at 7 T: a preliminary study. *Magn Reson Imaging* 2019;61:296–99 CrossRef Medline

# DWI for Monitoring the Acute Response of Malignant Gliomas to Photodynamic Therapy

Y. Fujita, T. Sasayama, K. Tanaka, K. Kyotani, H. Nagashima, M. Kohta, H. Kimura, A. Fujita, and E. Kohmura



## ABSTRACT

**BACKGROUND AND PURPOSE:** Photodynamic therapy is a novel treatment that provides effective local control, but little is known about photodynamic therapy–induced changes on MR imaging. The aim of this study was to assess the utility of DWI and ADC in monitoring the response of malignant gliomas to photodynamic therapy.

**MATERIALS AND METHODS:** Time-dependent changes in DWI and ADC values after photodynamic therapy were analyzed in a group that received photodynamic therapy in comparison with a group that did not.

**RESULTS:** Twenty-four patients were enrolled (photodynamic therapy,  $n=14$ ; non-photodynamic therapy,  $n=10$ ). In all patients who received photodynamic therapy, linear high signals on DWI in the irradiated area were detected adjacent to the resection cavity and were 5–7 mm in depth from 1 day posttreatment and disappeared in about 30 days without any neurologic deterioration. The non-photodynamic therapy group did not show this change. The photodynamic therapy group had significantly lower ADC values from 1 day posttreatment ( $P < .001$ ), which increased steadily and disappeared by 30 days. There was no decline or time-dependent change in ADC values in the non-photodynamic therapy group.

**CONCLUSIONS:** The acute response of malignant gliomas to photodynamic therapy was detected as linear high signals on DWI and as a decrease in ADC values. These findings were asymptomatic and transient. Although the photodynamic therapy–induced acute response on MR imaging disappeared after approximately 30 days, it may be helpful for confirming the photodynamic therapy–irradiated area.

**ABBREVIATIONS:** CE = contrast-enhanced; PDT = photodynamic therapy

Standard therapy for malignant glioma, the most aggressive primary malignant brain tumor, includes maximal possible surgical resection followed by radiation therapy and concomitant temozolomide-based chemotherapy, which results in a median survival of 14.6 months.<sup>1</sup> The major problem with malignant glioma is its invasiveness. It is extremely difficult to remove all the tumor cells that have invaded the peripheral normal brain tissue.

Consequently, local recurrence develops in many cases.<sup>2,3</sup> Development of novel treatments that have both potency and high selectivity for tumor cells in the peripheral zone where normal brain cells and tumor cells coexist is desirable. Photodynamic therapy (PDT) is a novel treatment that could overcome these issues.

PDT is a light-activated treatment technique that harnesses tumor-selective accumulation of photosensitizer and a photochemical reaction on semiconductor laser irradiation. The oxygen in the tumor tissue is converted from the ground state to the excited state, singlet oxygen, which is cytotoxic and exerts an antitumor effect.<sup>4</sup> The concept of PDT was first reported in 1900,<sup>5</sup> developed as a treatment technique in the 1960s,<sup>6,7</sup> and entered into clinical trials for several types of cancer during the 1980s and 1990s.<sup>8–13</sup> The potential use of PDT for brain tumors was first reported in 1980,<sup>14</sup> and its effectiveness with porfimer sodium, a first-generation photosensitizer, for malignant brain tumors was reported in the 2000s.<sup>15–17</sup> In 2013, the safety and effectiveness of PDT with talaporfin sodium, a second-generation photosensitizer, for primary malignant brain tumors was established in a Phase II clinical trial in Japan. PDT for malignant

Received August 5, 2019; accepted after revision September 13.

From the Department of Neurosurgery (Y.F., T.S., K.T., M.K., H.K., A.F., E.K.), Kobe University Graduate School of Medicine, Kobe, Hyogo, Japan; Center for Radiology and Radiation Oncology (K.K.), Kobe University Graduate School of Medicine and Kobe University Hospital, Kobe, Hyogo, Japan; and Department of Neurosurgery (H.N.), Massachusetts General Hospital Research Institute, Boston, Massachusetts.

This work was supported, in part, by a Grant-in-Aid for Scientific Research to Kazuhiro Tanaka (17K10864) and Takashi Sasayama (17K10863) from the Japanese Ministry of Education, Culture, Sports, Science and Technology.

Please address correspondence to Takashi Sasayama, MD, Department of Neurosurgery, Kobe University Graduate School of Medicine, 7-5-1 Kusunoki-cho, Chuo-ku, Kobe, Hyogo 650-0017, Japan; e-mail: takasasa@med.kobe-u.ac.jp

Indicates open access to non-subscribers at www.ajnr.org

<http://dx.doi.org/10.3174/ajnr.A6300>

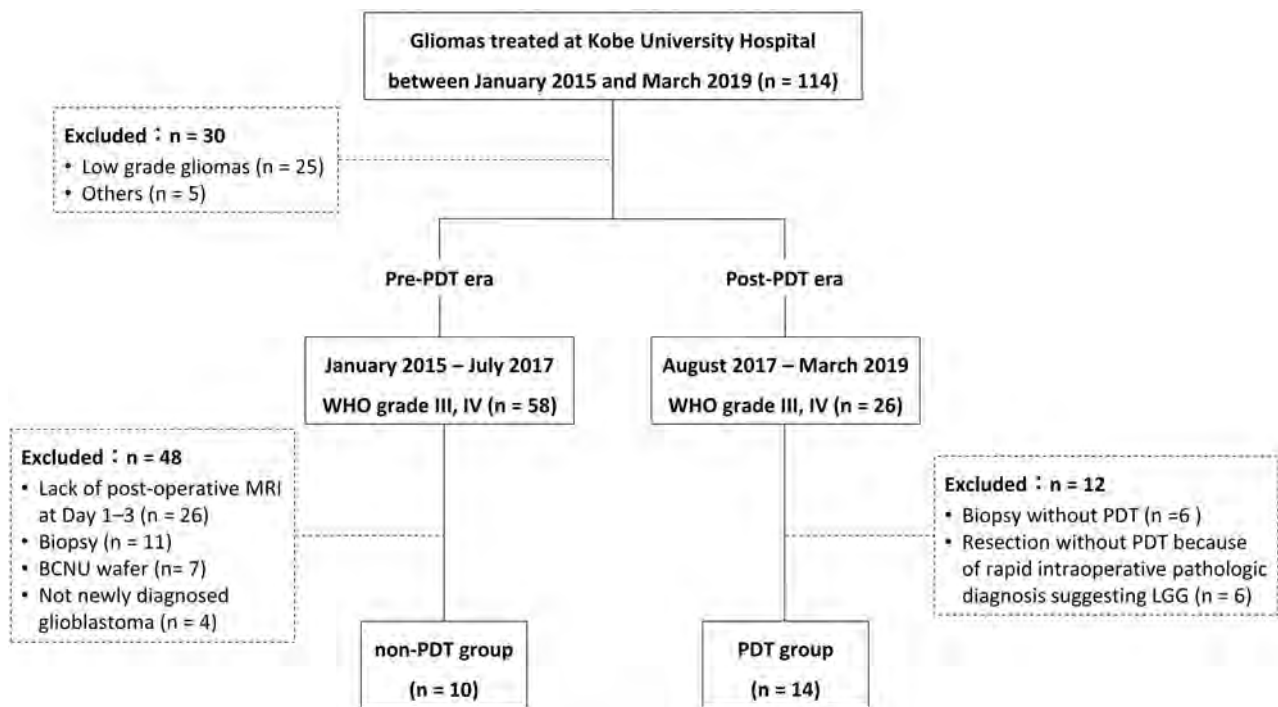


**FIG 1.** Flow chart showing the patient selection process. LGG indicates low-grade glioma; BCNU, biodegradable carmustine.

brain tumors was subsequently approved for coverage under Japanese national health insurance.<sup>18</sup>

Postoperative follow-up is generally performed using MR imaging. Although a contrast effect in the resected cavity wall and fluid retention have been reported to be transient MR imaging abnormalities after PDT,<sup>19</sup> these changes can also occur after conventional brain tumor surgery.<sup>20</sup> It is unclear how purely PDT-induced changes in the tumor microenvironment are reflected on postoperative imaging. Therefore, it would be useful to clarify the characteristic changes on MR imaging after PDT to monitor the therapeutic response. Given the evidence for DWI and ADC in ischemic stroke,<sup>21–23</sup> we hypothesized that post-PDT changes in brain tumors could be captured by DWI and ADC. The aim of this study was to elucidate the changes on MR imaging that are purely attributable to PDT for malignant glioma to test this hypothesis.

## MATERIALS AND METHODS

### Study Design and Study Patients

The study was approved by the institutional review board (Kobe University Hospital) (protocol number B190100) and conducted according to institutional and national ethical guidelines and in accordance with the Helsinki Declaration.

Since August 2017, our institution has used PDT in combination with conventional surgery without a biodegradable carmustine wafer in patients with World Health Organization grade III or IV glioma confirmed by rapid intraoperative pathologic diagnosis who underwent >90% (gross-total or subtotal) resection or intentional partial resection because of involvement of eloquent areas. Between January 2015 and March 2019, eighty-four of 114 patients with glioma treated at our institution were confirmed histopathologically to have World Health Organization grade III or IV

glioma. Twenty-six of these 84 patients were treated during our post-PDT era, from August 2017 to March 2019. Fourteen of these patients underwent PDT and were enrolled in this study as the PDT group; the remaining 12 patients were excluded because they had undergone biopsy without PDT ( $n = 6$ ) or resection without PDT because of an intraoperative pathologic diagnosis suggesting low-grade glioma ( $n = 6$ ). We analyzed the post-PDT time-dependent changes on DWI, in ADC values, and on contrast-enhanced T1WI (CE-T1WI) and T2-weighted FLAIR images obtained on days 1, 7, 14, 30, and 60 after the operation. Furthermore, to confirm whether the findings were specific for PDT, we compared the PDT group with a non-PDT group selected using the following criteria: newly diagnosed glioblastoma treated without PDT and without a biodegradable carmustine wafer at our institution during the pre-PDT era from January 2015 to July 2017, >90% resection or intentional partial resection because of involvement of eloquent areas, and adequate MR imaging scans obtained at least once during each of the following periods: 1–3 days, 14–30 days, and 60 days after the operation. Of the 58 patients with World Health Organization grade III or IV glioma treated during the pre-PDT era, 10 met the inclusion criteria and were selected as the non-PDT group and 48 were excluded because of lack of postoperative MR imaging at 1–3 days ( $n = 26$ ), biopsy ( $n = 11$ ), surgery with a biodegradable carmustine wafer ( $n = 7$ ), or not having a newly diagnosed glioblastoma ( $n = 4$ ). The flow chart outlining the patient-selection process is shown in Fig 1. The histopathologic diagnosis was performed according to the 2016 World Health Organization guidelines.<sup>24</sup>

### Surgical Treatment with PDT

Patients who were scheduled for PDT received a single intravenous injection of talaporfin sodium (Laserphyrin; Meiji Seika

**Patient characteristics**

Characteristic	PDT (n = 14)	Non-PDT (n = 10)	P Value
Age (yr)			.98
Median (range)	61.5 (35–70)	61.0 (36–72)	
Sex (No.) (%)			.92
Male	8 (57)	6 (60)	
Female	6 (43)	4 (40)	
Preoperative Karnofsky Performance Status Scale score			.17
Median (range)	80 (30–100)	70 (30–100)	
Tumor locations (No.) (%)			.67
Frontal	9 (64)	5 (50)	
Temporal	3 (21)	4 (40)	
Parietal	1 (7)	1 (10)	
Basal ganglia	1 (7)	0 (0)	
Preoperative tumor volume (cm <sup>3</sup> )			.07
Median (range)	31.7 (2.2–140.0)	70.3 (16.4–153.5)	
Extent of resection (No.) (%)			.91
Gross-total	10 (71)	7 (70)	
Subtotal	2 (14)	1 (10)	
Partial	2 (14)	2 (20)	
Histopathology (No.) (%)			.14
Glioblastoma	11 (79)	10 (10)	
Anaplastic astrocytoma	1 (7)	0 (0)	
Anaplastic oligodendroglioma	2 (14)	0 (0)	
Isocitrate dehydrogenase mutation status (No.) (%)			.50
Wild-type	11 (79)	9 (90)	
Mutant	3 (21)	1 (10)	
MIB-1 index			.65
Median (range)	20 (10–80)	20 (8–40)	

Pharma, Tokyo, Japan) at a dose of 40 mg/m<sup>2</sup> 22–26 hours before the operation. After maximum resection of the enhanced lesion, the entire resection cavity was irradiated with a 664-nm semiconductor laser (PD laser; Meiji Seika Pharma, Tokyo, Japan) (diameter, 1.5 cm; radiation power density, 150 mW/cm<sup>2</sup>; radiation energy density, 27 J/cm<sup>2</sup>). Each irradiation was performed for 3 minutes per spot without overlap of the previously irradiated area and without limitation of the number of irradiation spots. The canopy walls were irradiated by reflecting the beam using a mirror. The large blood vessels were protected by aluminum foil so as not to be directly irradiated. Post-therapeutic light protection (<500 lux) was performed for 10–14 days to prevent photosensitive dermatosis.

**Imaging Analysis**

DWI was performed with a 3T MR imaging scanner (Achieva; Philips Healthcare, Best, the Netherlands) using echo-planar imaging and the

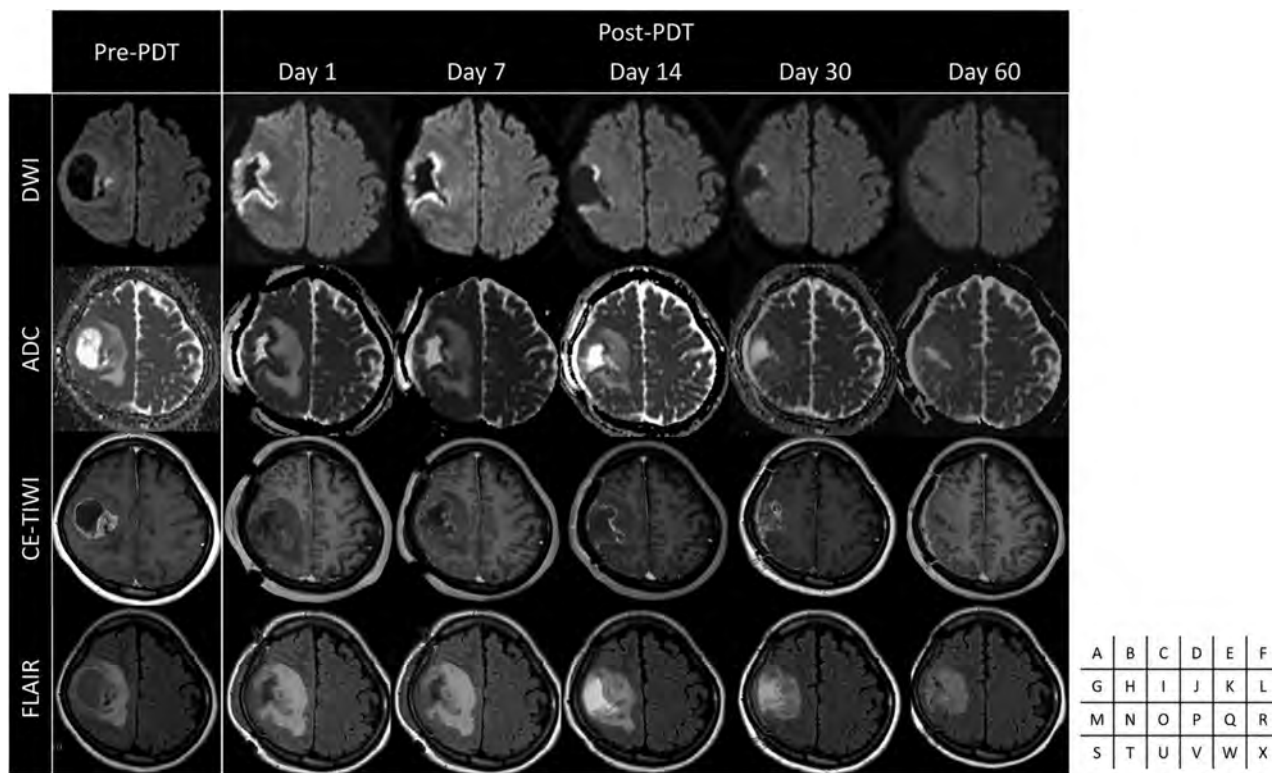


**FIG 2.** A representative case in the PDT group. Preoperative DWI (A), ADC map (G), CE-T1WI (M), and FLAIR (S) demonstrate the lesion with a cyst in the right frontal lobe. Postoperative DWI (B–F), ADC map (H–L), CE-T1WI (N–R), and FLAIR (T–X) show time-dependent changes after PDT.

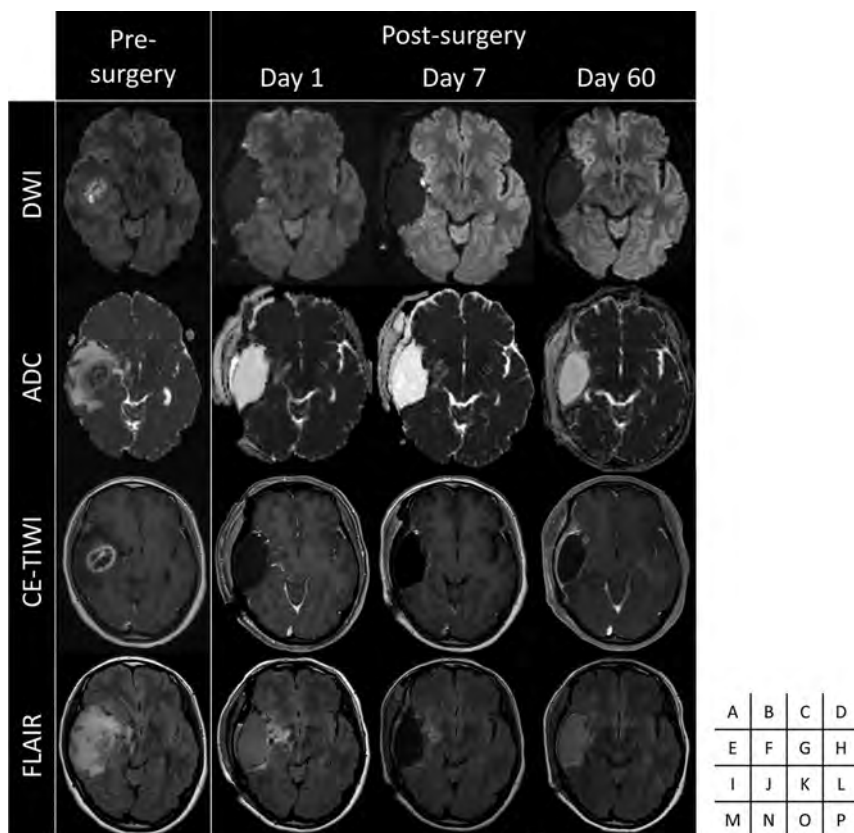


**FIG 3.** A representative case in the non-PDT group. Preoperative DWI (A), ADC map (E), CE-T1WI (I), and FLAIR (M) demonstrate the lesion in the right temporal lobe. Postoperative DWI (B–D), ADC map (F–H), CE-T1WI (J–L), and FLAIR (N–P) show time-dependent changes after the operation.

following parameters: b-values, 0 and 1000 s/mm<sup>2</sup>; TR/TE, 4500/75 ms; FOV, 240 mm; section thickness, 4 mm; section gap, 1 mm; matrix, 109 × 128; and flip angle, 90°. The ADC values from DWI of 2 types (b-values, 0 and 1000 s/mm<sup>2</sup>) were calculated per voxel to create the ADC map. An ROI measuring 10–20 mm<sup>2</sup> was drawn manually on a representative DWI section of the largest resection cavity and was set on the PDT-irradiated area in the PDT group and on the surgical resection margin in the non-PDT group. The ROI was then reflected to the ADC map. To assess time-dependent changes, we set ROIs numbered 1–5, respectively, with a wide and balanced distribution and followed them at the same anatomic locations. The mean of the ADC values within the ROIs was used for statistical analysis. The ROIs were drawn by a single neurosurgeon (Y.F.) and confirmed by another neurosurgeon (T.S.).

The conventional MR imaging sequences included FLAIR (TR/TE/TI, 4500/148/1600 ms; FOV, 240 mm; matrix, 240 × 240; section thickness, 1.0 mm) and 3D T1WI (TR/TE/TI, 6.4/2.8/1200 ms; FOV, 260 mm; matrix, 320 × 320; section thickness, 0.8 mm) before and after injection of the intravenous gadolinium contrast agent (0.2 mL/kg, Magnescope; Meglumine gadoterate, Guerbet, Paris, France).

### Statistical Analysis

The characteristics of each group were compared using the Fisher exact test and the Mann–Whitney *U* test. The Friedman test was

used to assess the postoperative time-dependent change in ADC values. The Bonferroni test was used for post hoc comparisons. The Mann–Whitney *U* test was used to compare ADC values between the groups. All statistical analyses were performed with EZR (Saitama Medical Center, Jichi Medical University, Saitama, Japan), which is a graphic user interface for R statistical and computing software (<http://www.r-project.org/>).<sup>25</sup> A 2-sided *P* value of <.05 was considered statistically significant.

## RESULTS

### Patient Characteristics

In total, 24 patients were included in the study. There were 14 patients (8 men, 6 women; median age, 61.5 years [range, 35–70 years]) in the PDT group and 10 patients (6 men, 4 women; median age, 61.0 years [range, 36–72 years]) in the non-PDT group (Fig 1). The characteristics of the patients in both groups are summarized in the Table. There were no statistically significant between-group differences in age, sex, preoperative Karnofsky Performance Status Scale score, tumor location, preoperative tumor volume, or extent of resection

at baseline. Intraoperative MR imaging was performed in 12 patients (86%) in the PDT group and 8 (80%) in the non-PDT group. In the PDT group, all 12 patients who underwent intraoperative MR imaging had no evidence of surgery-related ischemia or hemorrhage before PDT. Awake surgery was performed in 1 (7%) of the patients in the PDT group and 3 (30%) of those in the non-PDT group because the tumors were close to the Broca area. There was no statistically significant difference in histology, *isocitrate dehydrogenase* status, or the MIB-1 index between the 2 groups. The median number of irradiation spots was 13 (range, 5–31) in the PDT group. No patient in either group showed neurologic deterioration postoperatively or a deterioration in Karnofsky Performance Status Scale score at 60 days.

### Post-PDT MR Imaging

In all patients in the PDT group, linear high signals on DWI in the irradiated area were detected adjacent to the resection cavity and were 5–7 mm in depth from 1 day posttreatment and disappeared in about 30 days without any neurologic deterioration (Fig 2). The area on the ADC map corresponding to the high signals on DWI was hypointense. None of the patients in the non-PDT group showed this change (Fig 3).

These changes in DWI were also tracked by the ADC value. The PDT group had lower ADC values from 1 day after PDT. The ADC values (expressed as 10<sup>–6</sup> mm<sup>2</sup>/s) increased in a time-dependent manner, continued to increase significantly up to

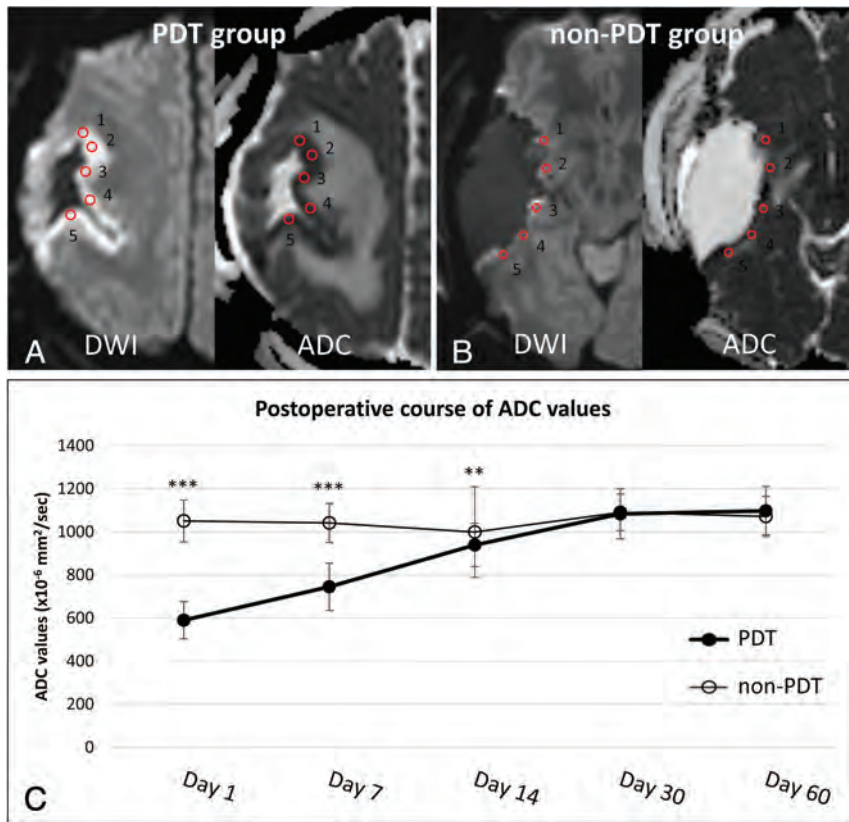


**FIG 4.** Postoperative DWI (left) and ADC map (right) demonstrate representative settings for the ROIs in the PDT group (A) and non-PDT group (B). The small circles labeled 1–5 indicate the ROIs used for analysis of the ADC values. A line graph demonstrates the postoperative time-dependent change in ADC values in the PDT group (thick line) and non-PDT group (thin line) (C). Double asterisks indicate  $P < .01$ ; triple asterisks,  $P < .001$ , Mann-Whitney U test.

30 days after PDT ( $589.8 \pm 86.7$  on day 1;  $745.1 \pm 109.9$  on day 7,  $939.1 \pm 100.3$  on day 14, and  $1083.2 \pm 116.2$  on day 30;  $P < .001$ ), and reached a plateau ( $1097.6 \pm 112.2$  on day 60;  $P = 1.0$ , Fig 4). In contrast, there was no decline and time-dependent change in ADC values after the operation in the non-PDT group ( $1050.8 \pm 96.9$  on day 1,  $1041.2 \pm 91.0$  on day 7,  $998.8 \pm 210.3$  on day 14,  $1090.4 \pm 84.7$  on day 30, and  $1071.5 \pm 92.8$  on day 60;  $P = .44$ , Fig 4). The ADC values in the PDT group were significantly lower than those in the non-PDT group until 14 days after the operation; thereafter, the difference was no longer statistically significant (day 1,  $P < .001$ ; day 7,  $P < .001$ ; day 14,  $P = .002$ ; day 30,  $P = .33$ ; and day 60,  $P = .36$ ; Fig 4).

One patient in the PDT group had both PDT-irradiated and nonirradiated areas because the middle cerebral artery ran through the center of the resected cavity. In this case, the nonirradiated area showed neither high signal on DWI nor a decline in the ADC value. ADC values in the nonirradiated area remained in the range of  $1000\text{--}1200 \times 10^{-6} \text{ mm}^2/\text{s}$  from day 1 to day 60 after the operation with PDT (Fig 5).

On CE-T1WI, all patients in both groups showed thin linear contrast effects along the resected cavity wall at 1–2 weeks after the operation. Fluid retention was observed on FLAIR in 9 patients (64%) in the PDT group and 7 (70%) of those in the non-PDT group. The difference between the 2 groups was not statistically significant ( $P = .56$ ).

## DISCUSSION

Surgery combined with PDT is a novel localized treatment for malignant glioma that can selectively kill tumor cells invading from the surgical resection margin to the peripheral normal brain. Previous studies have demonstrated its safety and effectiveness.<sup>18,19,26</sup> PDT with talaporfin sodium, a second-generation photosensitizer, has been safely used in patients with malignant glioma at our institution since August 2017. In this study, we identified specific changes on MR imaging scans that can be used to monitor the early response to PDT. The PDT-irradiated site showed linear high signals of 5–7 mm on DWI from the acute phase after PDT that were transient and asymptomatic. Furthermore, the high signals on DWI had concurrently lower ADC values, which improved in a time-dependent manner parallel to the signal intensity on DWI.

DWI is an MR imaging sequence that images the Brownian motion of water molecules in tissue. The ADC is less susceptible to T2 shimming, which is a problem with DWI, and accurately reflects the diffusivity of water molecules. Cellular swelling and narrowing of the extracellular space due to effects of cytotoxicity such as ischemia, known as cytotoxic edema, restrict the movement of water.<sup>21,23</sup> In general, regions with cell damage show high signals on DWI and low ADC values.

Three main mechanisms are known to underpin the effect of PDT: 1) direct tumor cell killing including apoptosis and necrosis,<sup>26,27</sup> 2) tumor-associated vascular damage,<sup>28,29</sup> and 3) activation of the immune response against tumor cells.<sup>30–32</sup> These mechanisms also influence each other.<sup>33,34</sup> The antitumor effects cannot be attributed to the photosensitizer alone or the laser alone.<sup>35,36</sup> The photosensitizer used in PDT is transformed from its ground state into an electronically excited state by laser light of a specific wavelength and transfers the energy directly to triplet oxygen to form singlet oxygen (a type II reaction), which exerts an antitumor effect.<sup>4</sup> We could capture the PDT-induced early response as high signals on DWI and low ADC values because the cell damage and microcirculatory impairment caused by PDT led to restricted diffusivity of water molecules. These changes in DWI and ADC values were observed only in the PDT-irradiated area and not in the nonirradiated area, even in the same patient.

Furthermore, the tissue transmittance of the laser depends on the wavelength and irradiation power. The semiconductor laser used in this study ( $664 \text{ nm}$ ,  $150 \text{ mW}/\text{cm}^2$ ) has been reported to penetrate to an approximate tissue depth of 5 mm.<sup>19</sup> The match of the width of the DWI high signal and the depth of penetration

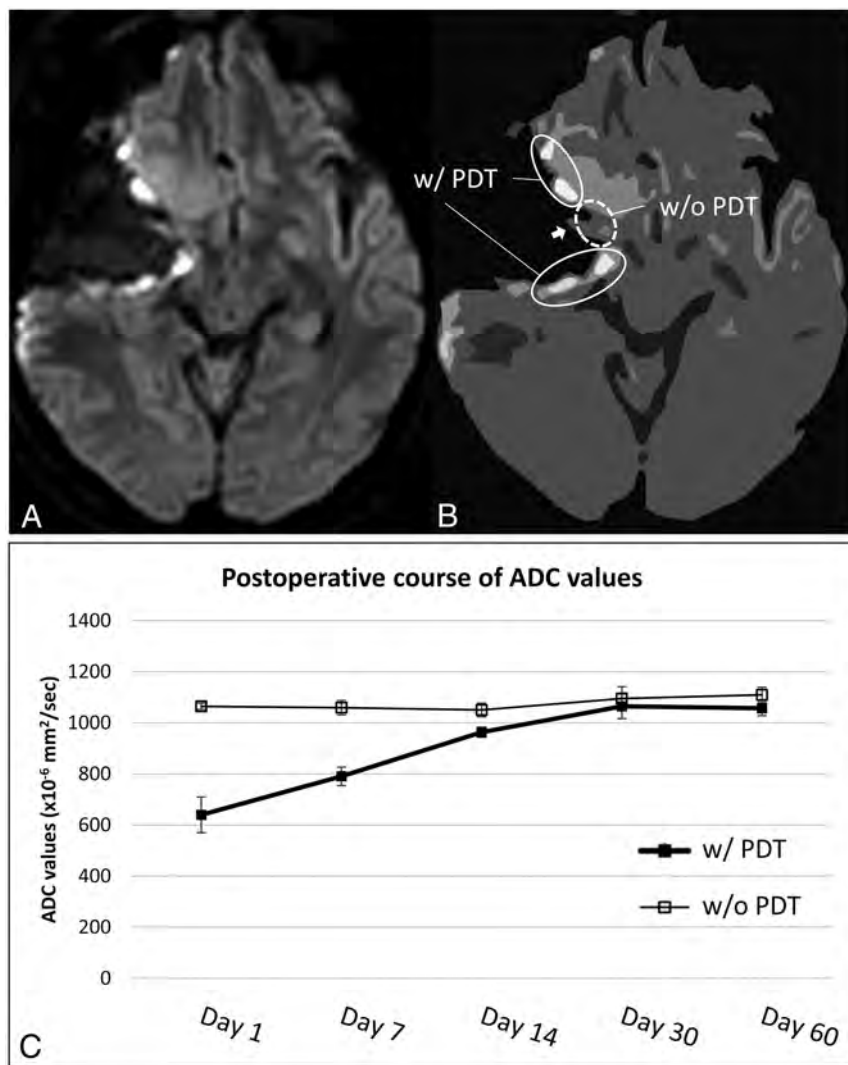


**FIG 5.** DWI (A) and a schematic illustration of A (B) show the post-PDT changes in irradiated and nonirradiated areas on day 1 for 1 patient in the PDT group. The circle with the solid line indicates the area with PDT irradiation (w/PDT). The circle with the dotted line indicates the area without PDT irradiation (w/o PDT). The white arrow indicates the middle cerebral artery. The line graph shows the postoperative time-dependent changes in ADC values in areas with PDT (thick line) and without PDT (thin line) (C).

of the laser strongly suggests that the abnormal findings on DWI and ADC were caused by the effect of PDT. Although the level and postoperative course of the ADC values in the PDT group were similar to those in ischemic stroke, the initial recovery of the ADC values was found to be more rapid after PDT than after stroke.<sup>23</sup> Moreover, all the changes in DWI and ADC values in the PDT group were asymptomatic in this study. PDT is able to attack only tumor cells with accumulated photosensitizer while preserving the surrounding normal brain cells without a bystander effect because singlet oxygen has a short migration distance of 0.02–1  $\mu\text{m}$  and a short lifetime in the range of 0.04–4  $\mu\text{s}$ .<sup>37,38</sup> Therefore, the asymptomatic nature of our findings on DWI and ADC further supports our hypothesis.

The other abnormalities seen on CE-T1WI and FLAIR were similar to those reported previously<sup>19,20</sup> and could not be used

to distinguish between the PDT and non-PDT groups. These findings were transiently observed in the subacute phase after the operation but not in the acute phase, which might reflect inflammation and immunoreactivity after surgery and PDT.

In summary, our findings suggest that a linear high signal on DWI accompanied by a decline in ADC values after PDT are purely PDT-induced MR imaging changes. Although PDT-induced MR imaging changes on DWI and in ADC values are transient and disappear by around 30 days, they seem to be useful for confirming the PDT-irradiated area. To our knowledge, this is the first study to show the usefulness of DWI and ADC values for monitoring the PDT-induced acute response of malignant glioma. However, our study also had several limitations. First, the number of patients treated with PDT was small. Second, the study was conducted at a single institution. Third, the ROIs for the ADC values reflected some but not all of the regions in which PDT was suspected to have had an effect. Fourth, surgery-related changes before PDT were not confirmed intraoperatively in 2 of the 14 patients in the PDT group. Finally, this study could not fully examine the utility of DWI and ADC values when monitoring recurrence and progression after PDT because the follow-up time was relatively short. Six of 14 patients in the PDT group experienced tumor recurrence, and only 3 patients exhibited local recurrence during follow-up. In

contrast, all patients in the non-PDT group had recurrence, which was local in 6 patients. Most interesting, all the local recurrences in the PDT group arose from the nonirradiated area, which did not show a high signal on DWI. Further studies are needed to clarify the association of our findings with pathologic mechanisms and their long-term impact. Nevertheless, findings that the visually apparent changes on DWI and the change in ADC values were consistent across all PDT patients in this study are clinically worthwhile.

## CONCLUSIONS

This study provided new evidence that the acute response of malignant glioma to PDT could be detected as linear high signals on DWI and a decline in ADC values that were asymptomatic and transient. These linear high signals on DWI may be useful for confirming the PDT-irradiated area.

## ACKNOWLEDGMENTS

We thank Miss Takiko Uno for molecular analysis of the *isocitrate dehydrogenase* mutation status of patients in this study.

Disclosures: Yuichi Fujita—RELATED: Grant: Grant-in-Aid for Scientific Research (KAKENHI) from the Japanese Ministry of Education, Culture, Sports, Science and Technology, Comments: 17K10864, 17K10863.\* Eiji Kohmura—UNRELATED: Grants/Grants Pending: Takeda Pharmaceutical Company, Sanofi, Chugai Pharmaceutical Company, Pfizer, Comments: academic contributions\*; Payment for Lectures Including Service on Speakers Bureaus: Olympus, Comments: honorarium.\*Money paid to the institution.

## REFERENCES

1. Stupp R, Mason WP, van den Bent MJ, et al. **Radiotherapy plus concomitant and adjuvant temozolomide for glioblastoma.** *N Engl J Med* 2005;352:987–96 CrossRef Medline
2. Konishi Y, Muragaki Y, Iseki H, et al. **Patterns of intracranial glioblastoma recurrence after aggressive surgical resection and adjuvant management: retrospective analysis of 43 cases.** *Neurol Med Chir (Tokyo)* 2012;52:577–86 CrossRef
3. Gaspar LE, Fisher BJ, Macdonald DR, et al. **Supratentorial malignant glioma: Patterns of recurrence and implications for external beam local treatment.** *Int J Radiat Oncol* 1992;24:55–57 CrossRef Medline
4. Henderson BW, Dougherty TJ. **How does photodynamic therapy work?** *Photochem Photobiol* 1992;55:145–57 CrossRef Medline
5. Raab O. **Über die Wirkung Fluorescirender Stoffe auf Infusorien.** *Z Biol* 1900;39:524–46
6. Lipson RL, Baldesi EJ. **The photodynamic properties of a particular hematoporphyrin derivative.** *Arch Dermatol* 1960;82:508–16 CrossRef Medline
7. Lipson RL, Baldesi EJ, Olsen AM. **The use of a derivative of hematoporphyrin in tumor detection.** *J Natl Cancer Inst* 1961;26:1–11 Medline
8. Hayata Y, Kato H, Konaka C, et al. **Hematoporphyrin derivative and laser photoradiation in the treatment of lung cancer.** *Chest* 1982;81:269–77 CrossRef Medline
9. McCaughan JS, Hicks W, Laufman L, et al. **Palliation of esophageal malignancy with photoradiation therapy.** *Cancer* 1984;54:2905–10 CrossRef Medline
10. Hayata Y, Kato H, Okitsu H, et al. **Photodynamic therapy with hematoporphyrin derivative in cancer of the upper gastrointestinal tract.** *Semin Surg Oncol* 1985;1:1–11 CrossRef Medline
11. Mang TS, Allison R, Hewson G, et al. **A phase II/III clinical study of tin ethyl etiopurpurin (Purlytin)-induced photodynamic therapy for the treatment of recurrent cutaneous metastatic breast cancer.** *Cancer J Sci Am* 1998;4:378–84 Medline
12. Ward BG, Forbes IJ, Cowled PA, et al. **The treatment of vaginal recurrences of gynecologic malignancy with phototherapy following hematoporphyrin derivative pretreatment.** *Am J Obstet Gynecol* 1982;142:356–57 CrossRef Medline
13. Schweitzer VG. **Photodynamic therapy for treatment of head and neck cancer.** *Otolaryngol Head Neck Surg* 1990;102:225–32 CrossRef Medline
14. Perria C, Capuzzo T, Cavagnaro G, et al. **Fast attempts at the photodynamic treatment of human gliomas.** *J Neurosurg Sci* 1980;24:119–29 Medline
15. Stylli SS, Kaye AH, MacGregor L, et al. **Photodynamic therapy of high-grade glioma: long-term survival.** *J Clin Neurosci* 2005;12:389–98 CrossRef Medline
16. Muller PJ, Wilson BC. **Photodynamic therapy of brain tumors: a work in progress.** *Lasers Surg Med* 2006;38:384–89 CrossRef Medline
17. Eljamel S. **Photodynamic applications in brain tumors: a comprehensive review of the literature.** *Photodiagnosis Photodyn Ther* 2010;7:76–85 CrossRef Medline
18. Muragaki Y, Akimoto J, Maruyama T, et al. **Phase II clinical study on intraoperative photodynamic therapy with talaporfin sodium and semiconductor laser in patients with malignant brain tumors.** *J Neurosurg* 2013;119:845–52 CrossRef Medline
19. Nitta M, Muragaki Y, Maruyama T, et al. **Role of photodynamic therapy using talaporfin sodium and a semiconductor laser in patients with newly diagnosed glioblastoma.** *J Neurosurg* 2018;1–8 CrossRef Medline
20. Sato N, Bronen RA, Sze G, et al. **Postoperative changes in the brain: MR imaging findings in patients without neoplasms.** *Radiology* 1997;204:839–46 CrossRef Medline
21. Latchaw RE, Alberts MJ, Lev MH, et al. **Recommendations for imaging of acute ischemic stroke: a scientific statement from the American Heart Association.** *Stroke* 2009;40:3646–78 CrossRef Medline
22. Moseley ME, Cohen Y, Mintorovitch J, et al. **Early detection of regional cerebral ischemia in cats: comparison of diffusion- and T2-weighted MRI and spectroscopy.** *Magn Reson Med* 1990;14:330–46 CrossRef Medline
23. Huang I-J, Chen C-Y, Chung H-W, et al. **Time course of cerebral infarction in the middle cerebral arterial territory: deep watershed versus territorial subtypes on diffusion-weighted MR images.** *Radiology* 2001;221:35–42 CrossRef Medline
24. Louis DN, Perry A, Reifenberger G, et al. **The 2016 World Health Organization classification of tumors of the central nervous system: a summary.** *Acta Neuropathol* 2016;131:803–20 CrossRef Medline
25. Kanda Y. **Investigation of the freely available easy-to-use software “EZR” for medical statistics.** *Bone Marrow Transplant* 2013;48:452–58 CrossRef Medline
26. Akimoto J. **Photodynamic therapy for malignant brain tumors.** *Neurol Med Chir (Tokyo)* 2016;56:151–57 CrossRef Medline
27. Henderson BW, Waldow SM, Mang TS, et al. **Tumor destruction and kinetics of tumor cell death in two experimental mouse tumors following photodynamic therapy.** *Cancer Res* 1985;45:572–76 Medline
28. Fingar VH, Wieman TJ, Haydon PS. **The effects of thrombocytopenia on vessel stasis and macromolecular leakage after photodynamic therapy using photofrin.** *Photochem Photobiol* 1997;66:513–17 CrossRef Medline
29. Ferrario A, von Tiehl KF, Rucker N, et al. **Antiangiogenic treatment enhances photodynamic therapy responsiveness in a mouse mammary carcinoma.** *Cancer Res* 2000;60:4066–69 Medline
30. Shumaker BP, Hetzel FW. **Clinical laser photodynamic therapy in the treatment of bladder carcinoma.** *Photochem Photobiol* 1987;46:899–901 CrossRef Medline
31. de Vree WJ, Essers MC, de Bruijn HS, et al. **Evidence for an important role of neutrophils in the efficacy of photodynamic therapy in vivo.** *Cancer Res* 1996;56:2908–11 Medline
32. Gollnick SO, Liu X, Owczarczak B, et al. **Altered expression of interleukin 6 and interleukin 10 as a result of photodynamic therapy in vivo.** *Cancer Res* 1997;57:3904–09 Medline
33. Dolmans D, Fukumura D, Jain RK. **Photodynamic therapy for cancer.** *Nat Rev Cancer* 2003;3:380–87 CrossRef Medline
34. Castano AP, Mroz P, Hamblin MR. **Photodynamic therapy and anti-tumour immunity.** *Nat Rev Cancer* 2006;6:535–45 CrossRef Medline
35. Fujiwara Y, Miki Y, Akimoto J, et al. **Effect of talaporfin sodium-mediated photodynamic therapy on cell death modalities in human glioblastoma T98G cells.** *J Toxicol Sci* 2014;39:821–27 CrossRef Medline
36. Ohashi S, Kikuchi O, Tsurumaki M, et al. **Preclinical validation of talaporfin sodium-mediated photodynamic therapy for esophageal squamous cell carcinoma.** *PLoS One* 2014;9:e103126 CrossRef Medline
37. Moan J, Berg K. **The photodegradation of porphyrins in cells can be used to estimate the lifetime of singlet oxygen.** *Photochem Photobiol* 1991;53:549–53 CrossRef Medline
38. Stylli SS, Kaye AH. **Photodynamic therapy of cerebral glioma: a review, Part I: a biological basis.** *J Clin Neurosci* 2006;13:615–25 CrossRef Medline

# Prognostic Predictions for Patients with Glioblastoma after Standard Treatment: Application of Contrast Leakage Information from DSC-MRI within Nonenhancing FLAIR High-Signal-Intensity Lesions

S.H. Kim, K.H. Cho, S.H. Choi, T.M. Kim, C.K. Park, S.H. Park, J.K. Won, I.H. Kim, and S.T. Lee



## ABSTRACT

**BACKGROUND AND PURPOSE:** Attempts have been made to quantify the microvascular leakiness of glioblastomas and use it as an imaging biomarker to predict the prognosis of the tumor. The purpose of our study was to evaluate whether the extraction fraction value from DSC-MR imaging within nonenhancing FLAIR hyperintense lesions was a better prognostic imaging biomarker than dynamic contrast-enhanced MR imaging parameters for patients with glioblastoma.

**MATERIALS AND METHODS:** A total of 102 patients with glioblastoma who received a preoperative dynamic contrast-enhanced MR imaging and DSC-MR imaging were included in this retrospective study. Patients were classified into the progression ( $n=87$ ) or non-progression ( $n=15$ ) groups at 24 months after surgery. We extracted the means and 95th percentile values for the contrast leakage information parameters from both modalities within the nonenhancing FLAIR high-signal-intensity lesions.

**RESULTS:** The extraction fraction 95th percentile value was higher in the progression-free survival group of  $>24$  months than at  $\leq 24$  months. The median progression-free survival of the group with an extraction fraction 95th percentile value of  $>13.32$  was 17 months, whereas that of the group of  $\leq 13.32$  was 12 months. In addition, it was an independent predictor variable for progression-free survival in the patients regardless of their ages and genetic information.

**CONCLUSIONS:** The extraction fraction 95th percentile value was the only independent parameter for prognostic prediction in patients with glioblastoma among the contrast leakage information, which has no statistically significant correlations with the DCE-MR imaging parameters.

**ABBREVIATIONS:** DCE = dynamic contrast-enhanced; EF = extraction fraction;  $K^{trans}$  = volume transfer constant; MGMT = *O*6-methylguanine methyltransferase; PFS = progression-free survival;  $V_e$  = volume of extravascular extracellular space;  $V_p$  = volume of vascular plasma space; IDH = isocitrate dehydrogenase

**G**lioblastoma multiforme is a hypervascular tumor, and its aggressive portion is known to disrupt the BBB, resulting in enhancement on contrast-enhanced MR imaging. In addition,

glioblastoma tumor cells have an infiltrative nature that shows only high signal intensity on FLAIR images without definite enhancement. This characteristic of the tumor is highly related to microvasculature disruption, which may be demonstrated as BBB leakiness.<sup>1-3</sup> The standard treatment for glioblastoma is surgical resection, followed by concomitant chemoradiotherapy with adjuvant temozolomide.<sup>4,5</sup> The surgical resection is performed mainly at the contrast-enhancing portion of the tumor based on imaging guidance. Nonenhancing infiltrative tumor cells remain after the operation, which explains most of the local recurrences at the

Received June 18, 2019; accepted after revision September 16.

From the Departments of Radiology (S.H.K., K.H.C., S.H.C.), Pathology (S.H.P., J.K.W.), and Neurology (S.T.L.), Seoul National University College of Medicine, Seoul, Korea; Center for Nanoparticle Research (S.H.C.), Institute for Basic Science, Seoul, Korea; School of Chemical and Biological Engineering (S.H.C.), Seoul National University, Seoul, Korea; Departments of Internal Medicine (T.M.K.) and Radiation Oncology (I.H.K.), Cancer Research Institute, Seoul National University College of Medicine, Seoul, Korea; and Department of Neurosurgery (C.K.P.), Biomedical Research Institute, Seoul National University College of Medicine, Seoul, Korea.

S.H. Kim and K.H. Cho contributed equally to this work.

This study was supported by a grant from the Korea Healthcare Technology R&D Projects, Ministry of Health, Welfare & Family Affairs (HI16C111), by the Bio & Medical Technology Development Program of the National Research Foundation of Korea funded by the Korean government, Ministry of Science, Information & Community Technology and Future Planning (NRF-2015M3A9A7029740), by the Brain Research Program through the National Research Foundation of Korea funded by the Ministry of Science, Information & Community Technology and Future Planning (2016M3C7A1914002), by the Creative-Pioneering Researchers Program through Seoul National University, and by Project Code (IBS-R006-D1).

Please address correspondence to Seung Hong Choi, MD, PhD, Department of Radiology, Seoul National University College of Medicine, 28, Yongon-dong, Chongno-gu, 110-744, Seoul, Korea; e-mail: verocay@snuh.org

Indicates open access to non-subscribers at www.ajnr.org

Indicates article with supplemental on-line appendix and tables.

Indicates article with supplemental on-line photos.

<http://dx.doi.org/10.3174/ajnr.A6297>

resection margin.<sup>6</sup> Those infiltrative tumor cells intermingle with reactive edema on T2WI or T2 FLAIR images, thereby increasing the difficulty of their identification. Therefore, non-enhancing FLAIR high-signal-intensity lesions have clinical significance.<sup>7</sup>

Attempts have been made to quantify the microvascular leakiness of a tumor and use it as a biomarker to predict the level of aggressiveness and the prognosis of a tumor. One approach is the use of dynamic contrast-enhanced (DCE) MR imaging, which is an imaging technology that provides BBB permeability information, to analyze nonenhancing FLAIR high-signal-intensity lesions of glioblastoma.<sup>8</sup> Gliomas with high-permeability parameters from DCE-MR imaging have been reported to show a poor prognosis due to a large proportion of leaky vasculature.<sup>9-11</sup> To date, many studies have revealed the utility of DCE-MR imaging for predicting the tumor grade and/or tumor progression in patients with glioblastoma.<sup>12</sup>

Recently, a new method that can reveal contrast leakage information (ie, the extraction fraction [EF]) using DSC-MR imaging has been reported; this method has well-known advantages over DCE-MR imaging, such as providing perfusion information, a shorter scan time, and higher contrast.<sup>13</sup> However, no studies have investigated the application of EF for prognostication in patients with glioblastoma receiving standard treatment. Thus, the aim of our study was to evaluate whether the EF parameter from DSC-MR imaging has correlation with contrast leakage information from DCE-MR imaging and whether the EF value from nonenhancing FLAIR high-signal-intensity lesions was a better prognostic imaging biomarker than DCE-MR imaging parameters in patients with glioblastoma receiving standard treatment.

## MATERIALS AND METHODS

### Patients

This retrospective study was approved by the Institutional Review Board of Seoul National University Hospital. The requirement for informed consent was waived. A total of 134 patients diagnosed with glioblastoma from April 2010 to September 2018 at Seoul National University Hospital were enrolled in this study. The following were the inclusion criteria: adult patients (older than 18 years of age) who were initially diagnosed with glioblastoma based on the 2016 World Health Organization classification of central nervous system tumors, underwent both preoperative DCE- and DSC-MR imaging, and received the standard treatment, including surgical resection of the contrast-enhancing lesion, followed by concomitant chemoradiotherapy with temozolomide and adjuvant temozolomide. Patients with lost raw data ( $n = 14$ ) or inadequate image quality for analysis ( $n = 17$ ) or who were lost to follow-up ( $n = 1$ ) were excluded from the study. Under these inclusion and exclusion criteria, 102 patients were enrolled in our study.

All patients underwent a follow-up MR imaging while visiting the outpatient clinic. On the basis of the clinical features and radiologic results, we categorized our study population into disease progression and nonprogression groups according to the Response Assessment in Neuro-Oncology criteria at 24 months after the operation. Patients satisfying any of the following

Response Assessment in Neuro-Oncology criteria were considered to have disease progression<sup>14</sup>: 1) a >25% increase in the sum of the products of the perpendicular diameters of the enhancing lesions with the smallest tumor measurement, 2) any new lesion, 3) clear clinical deterioration not attributable to causes other than the tumor, and 4) clear progression of nonmeasurable disease. Accordingly, 15 patients (14.7%) were grouped into the nonprogression group, and 87 patients (85.3%) were classified into the disease-progression group.

The flow diagram in On-line Fig 1 shows the inclusion and exclusion of patients in this study. Image acquisition is summarized in the On-line Appendix.

### Image Processing and Analysis

MR images were acquired from the PACS workstation and transferred to a personal computer using a software package (NordicICE, Version 4.1.2; Nordic-NeuroLab, Bergen, Norway) for analysis. On-line Figure 2 shows the schematic diagram of the imaging analysis.

The DCE and DSC perfusion MR imaging analysis methods based on the 2-compartment pharmacokinetic model were performed with the DCE- and DSC-MR imaging data to calculate contrast leakage information parameters, which were presented as parametric maps. The parameters of interest were volume transfer constant ( $K^{trans}$ ), volume of extravascular extracellular space ( $V_e$ ), volume of vascular plasma space ( $V_p$ ), and EF.<sup>15</sup> For preprocessing, the noise threshold and noise level were set to dispose of noise during parameter extraction from the MR imaging. In addition, a motion-correction function was used for spatial and temporal smoothing of the MR imaging. After preprocessing, vascular deconvolution with the arterial input function was executed by determining it in the intracranial tumor-supplying arteries near the tumor for DCE-MR imaging. This step was assisted by the software's automatic detection function for arterial input function, which still required manual setting of the arterial input function search region within the tumor. Subsequently, the arterial input function curves and concentration-time curve were generated, which indicated the tumor-supplying artery within the ROI. To find the ideal relationship between the arterial input function curve and the concentration-time curve, we manually defined the ROI, and an appropriate arterial input function curve was selected by 2 well-trained medical students (S.H.K. and K.H.C.) supervised by 1 neuroradiologist (S.H.C., with 16 years of experience in brain MR imaging). The baseline T1 was fixed at 1000 ms in this study.<sup>16</sup>

A recently introduced contrast leakage information parameter (EF) from DSC-MR imaging is defined as the ratio of permeability ( $K^{trans}$ ) to perfusion (fractional tissue perfusion). EF describes the fraction of contrast agent that is extracted during the first passage through tissue following an instantaneous tracer bolus. Assisted by automated arterial input function detection, EF is obtained by a novel contrast agent extravasation-correction method that is based on fitting the tissue residue function, including both apparent tissue extravasation and a perfusion component, to the 2-compartment uptake kinetic model.<sup>17-20</sup> Both the arterial input function and the tissue residue function were estimated from the T1- and T2\*-dominant leakage effect. Then, the

value of F derived from the tissue residue function was applied to the equation to calculate the EF.<sup>17,21</sup>

A multiplanar reconstruction tool was used to convert contrast-enhanced, T1-weighted, multiplanar images into axial images. These axial contrast-enhanced T1WI and FLAIR images were deployed for structural imaging. The coregistration algorithm of the software allows users to resample the number of target image sets to that of a reference image set based on the geometric information stored in each dataset. In our case, the target image set was structural images, whereas the reference image set was parametric maps from the DCE- and DSC-MR imaging.<sup>22,23</sup>

Afterwards, the parametric maps were coregistered with the structural images from the FLAIR and contrast-enhanced T1WI. Then, the ROIs of the nonenhancing FLAIR high-signal-intensity lesion on each axial image were determined manually by reviewers blinded to any information regarding the patient's prognosis. Additionally, the necrotic and cystic regions as well as large vessels were excluded from the ROI. All manual tasks were performed by consensus to minimize reviewer bias.

We used the ROI analysis function provided by the software to calculate the contrast leakage information, including the  $K^{\text{trans}}$ , Vp, Ve, and EF, from every pixel within the range of the ROI on every axial image and thereby acquired the sum of values from all pixels in the ROI. The total parametric values from the entire nonenhancing FLAIR high-signal-intensity lesion were obtained for each tumor. Finally, the mean values and 95th percentile values for  $K^{\text{trans}}$ , Vp, Ve, and EF were derived from the cumulative histograms (the  $x$ th percentile point is the point at which  $x\%$  of the pixel values that form the histogram are found to the left of the histogram).

### Statistical Analysis

All statistical analyses were performed by using MedCalc for Windows, Version 18.11 (MedCalc Software, Mariakerke, Belgium). For all analyses, only  $P < .05$  was considered statistically significant. Clinical characteristics, including age, sex, date of the operation, radiation dose, date of progression, and genetic information, were recorded for each patient. The Fisher exact test was performed for categorical data. The data for each parameter were assessed for normality with the Kolmogorov-Smirnov test. An unpaired Student  $t$  test was performed to compare data between the disease progression and nonprogression groups, in which patients with a follow-up period of  $>24$  months or progression-free survival (PFS) of  $\leq 24$  months were enrolled.

The Pearson correlation analysis for parametric data was performed to assess the correlations between the EF from DSC-MR imaging and contrast leakage information (eg,  $K^{\text{trans}}$ , Ve, and Vp) from DCE-MR imaging, which were obtained from contrast-enhancing areas as well as nonenhancing FLAIR high-signal-intensity lesions. To further assess the correlation analysis, we calculated intraclass correlation coefficients. Intraclass correlation coefficient values of  $<0$ ,  $0-0.20$ ,  $0.21-0.40$ ,  $0.41-0.60$ ,  $0.61-0.80$ , or  $>0.81$  were interpreted as negative, positive but poor, fair, moderate, good, or excellent agreement, respectively.

Receiver operating characteristic curve analysis was performed to set the optimum cutoff value for each contrast leakage parameter with an aim of distinguishing between the disease progression and nonprogression groups and to calculate the diagnostic performances of the contrast leakage information.

PFS was assessed using the Kaplan-Meier method according to the contrast leakage information and was compared using the log-rank test. We only recorded the first progression. PFS was calculated from the date of the operation to that of glioblastoma progression, the patient's death, the last confirmation of no evidence of disease, or the most recent follow-up examination. Patients without an event were censored at the date of the most recent follow-up regardless of whether they were scheduled for future follow-ups or had been lost to follow-up. Receiver operating characteristic curve analysis was performed to determine the thresholds for each contrast leakage information parameter for PFS. Multivariate analysis was performed using the Cox proportional hazards model adjusted for prognostic factors, including age, the *isocitrate dehydrogenase (IDH) 1/2* mutation, and the *O6-methylguanine methyltransferase (MGMT)* promoter methylation status.

Finally, the prediction performance of the 95th percentile EF was evaluated via the leave-one-out method. This method was performed by selecting 1 patient as a testing sample, with the remaining patients used as the training samples. The cutoff values determined by receiver operating characteristic curve analysis on the training samples were used to distinguish whether the testing sample belonged to the early disease progression or the nonprogression group. As a result of these validation rounds, we acquired the sensitivity, specificity, and accuracy of the total study population's 95th percentile EF as the cutoff value.

## RESULTS

### Patient Clinical Characteristics

The mean age of the patients with glioblastoma in the disease progression group ( $n=87$ ) was slightly higher than that of the patients in the nonprogression group ( $n=15$ ) ( $59.24 \pm 13.50$  versus  $51.33 \pm 13.96$  years, respectively,  $P=.04$ ). The other clinical characteristics, including the radiation dose, sex, *MGMT* promoter methylation status and *IDH 1/2* mutation status, were not statistically significantly different between the 2 groups (all,  $P > .05$ ; Table 1).

Correlation analyses between EF from DSC-MR imaging and contrast leakage information from DCE-MR imaging are given in the On-line Appendix and On-line Fig 3.

### Comparison of Contrast Leakage Information and Imaging Findings between the Early Disease Progression and Nonprogression Groups

These analyses enrolled patients with a follow-up period of  $>24$  months without progression ( $n=15$ ) or PFS of  $\leq 24$  months ( $n=71$ ), as mentioned above. On the basis of the unpaired Student  $t$  test, the EF 95th percentile value was higher for the patients in the nonprogression group than for those in the disease-progression group ( $15.7895\% \pm 8.6931\%$  versus

11.0527%  $\pm$  7.6511%, respectively,  $P = .0363$ ). However, no statistically significant differences in the other parameters were found between the 2 groups (all,  $P > .05$ ; Table 2).

Here, sensitivity and specificity are defined for identification of early disease progression and nonprogression, respectively, using receiver operating characteristic curve analysis. The EF 95th percentile value also showed statistical significance in receiver operating characteristic curve analysis, with an area under curve of 0.71 (95% CI, 0.599–0.800, and  $P = .008$ ). The best cutoff criterion for the EF 95th percentile value was 13.32, with a sensitivity of 60.0% and a specificity of 78.9%. Two representative cases with disease progression and nonprogression with parametric maps of EF,  $K^{trans}$ ,  $V_e$ , and  $V_p$  are shown in Figs 1 and 2, respectively.

**Table 1: Clinical characteristics of the study population<sup>a</sup>**

Characteristics	Total (n = 102)	Progression (n = 87)	Nonprogression (n = 15)	P Value
Mean age (yr)	56.9	59.2 $\pm$ 13.5	51.3 $\pm$ 14.0	.04 <sup>b</sup>
Mean radiation dose (Gy)	51.9	52.5 $\pm$ 18.4	48.6 $\pm$ 0.6	.43 <sup>b</sup>
Sex				.40 <sup>c</sup>
Male	59	52	7	
Female	43	35	8	
Methylated <i>MGMT</i> promoter				.09 <sup>c</sup>
Positive	59	47	12	
Negative	42	39	3	
<i>IDH1/2</i> mutation				.28 <sup>c</sup>
Positive	7	5	2	
Negative	94	81	13	

<sup>a</sup> Unless otherwise specified, data are given as the number of patients.

<sup>b</sup> Calculated with an unpaired Student *t* test.

<sup>c</sup> Calculated with the Fisher exact test.

**Table 2: Comparison of the parametric values of the progression and nonprogression groups<sup>a</sup>**

Parameters	Progression (n = 71)	Nonprogression (n = 15)	P Value <sup>b</sup>
Mean tumor volume (mL)	119.84 $\pm$ 85.65	161.81 $\pm$ 102.59	.10
EF 95th PV (%)	11.053 $\pm$ 7.651	15.790 $\pm$ 8.693	.04
EF mean (%)	2.473 $\pm$ 1.552	3.140 $\pm$ 1.463	.13
$K^{trans}$ 95th PV ( $\text{min}^{-1}$ )	0.140 $\pm$ 0.118	0.177 $\pm$ 0.132	.28
$K^{trans}$ mean ( $\text{min}^{-1}$ )	0.022 $\pm$ 0.024	0.0260 $\pm$ 0.021	.59
$V_e$ 95th PV	51.604 $\pm$ 71.965	44.480 $\pm$ 29.773	.71
$V_e$ mean	7.750 $\pm$ 16.050	6.209 $\pm$ 4.917	.71
$V_p$ 95th PV	5.334 $\pm$ 5.488	6.594 $\pm$ 4.807	.41
$V_p$ mean	1.264 $\pm$ 1.352	1.384 $\pm$ 0.100	.75

**Note:**—PV indicates percentile value.

<sup>a</sup> Patients with a follow-up period of  $>24$  months without progression ( $n = 15$ ) or PFS of  $\leq 24$  months ( $n = 71$ ) were analyzed.

<sup>b</sup> Calculated with an unpaired Student *t* test.

Correlation analysis between the EF from DSC-MR imaging and contrast leakage information from DCE-MR imaging is given in the On-line Appendix and On-line Table 1.

### Leave-One-Out Cross-Validation

In the leave-one-out cross-validation of the EF 95th percentile value, the cross-validated values for the prediction of glioblastoma disease progression were found, with corresponding sensitivity (46.67%), specificity (77.46%), and accuracy (72.09%).

**Contrast Leakage Information Correlated with PFS.** In all patients, PFS was correlated with the EF 95th percentile value with an optimum cutoff value of 13.32% obtained from receiver operating characteristic curve analysis, which showed statistical significance ( $P = 0.02$ ) (On-line Fig 4).

Then, we performed Cox proportional hazards model analysis, including the EF 95th percentile value, which was significantly associated with PFS, and previously reported prognostic genetic factors, including the *IDH1/2* mutation and *MGMT* promoter methylation status. The analysis revealed that only the EF 95th percentile value was significant among these factors ( $P = .01$ , On-line Table 2). In all patients, a significant difference in PFS was found between patients with high and low EF 95th percentile values (median, 17.0 months [95% CI, 12.0–36.0 months] versus 12.0 months [95% CI, 9.0–15.0 months];  $P = .02$ , log-rank test), which was independent of age, the *IDH1/2* mutation, and the *MGMT* promoter methylation status.

### DISCUSSION

In our study, contrast leakage information from both DCE- and DSC-MR imaging, including the EF,  $K^{trans}$ ,  $V_e$ , and  $V_p$ , was analyzed for prognostication in patients with glioblastoma treated with standard methods. Most interesting, the EF value from DSC-MR imaging had no significant

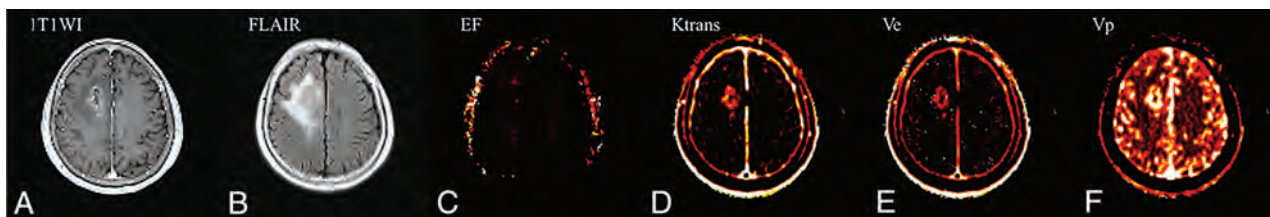


**FIG 1.** A 64-year-old patient with glioblastoma who had early disease progression (PFS = 14 months) after standard treatment. The preoperative axial contrast-enhanced T1WI (A) and FLAIR (B) images represent an enhancing area and nonenhancing FLAIR high-signal-intensity lesions, respectively. The preoperative parametric maps of contrast leakage information (EF,  $K^{trans}$ ,  $V_e$ , and  $V_p$ ) are shown (C, D, E, and F, respectively). A low EF value on the nonenhancing FLAIR high-signal-intensity lesion was observed, with an EF 95th percentile value of 5.67.

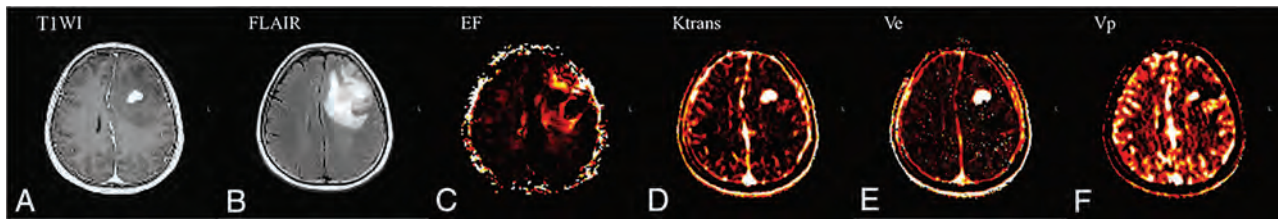


**FIG 2.** A 60-year-old patient with glioblastoma who had nonprogression (PFS = 31 months) after standard treatment. The preoperative axial contrast-enhanced T1WI (A) and FLAIR (B) images represent an enhancing area and a nonenhancing FLAIR high-signal-intensity lesion, respectively. The preoperative parametric maps of contrast leakage information (EF,  $K^{trans}$ , Ve, and Vp) are shown (C, D, E, and F, respectively). A high EF value on a nonenhancing FLAIR high-signal-intensity lesion was noted, with an EF 95th percentile value of 16.69.

correlation with any DCE-MR imaging parameters. We found that the EF 95th percentile value was higher in patients with nonprogression than in patients with disease progression within 2 years. We also found that patients with a higher EF 95th percentile value had longer PFS than those with a lower value. PFS also had a significant correlation with the EF 95th percentile value, which was the most important prognostic marker, regardless of age, *IDH1/2* mutation, and the *MGMT* promoter methylation status.

Microscopic infiltrative glioblastoma cells commonly are unenhanced on contrast-enhanced T1WI and are indistinguishable from peritumoral edema components, features increasing the difficulty of response prediction for patients with glioblastoma. DCE- and DSC-MR imaging have been used to evaluate microscopic infiltrative glioblastoma cells in nonenhancing FLAIR high-signal-intensity lesions.<sup>8,24</sup> DCE-MR imaging parameters, including the  $K^{trans}$ , Ve, and Vp, can reflect vascular permeability, which usually is increased in the glioblastoma vasculature.<sup>10-12,25</sup> Extensive studies have been performed to determine the survival-associated parameters of DCE-MR imaging in patients with glioblastoma. Despite some controversies, patients with glioblastoma with high contrast leakage information parameters on DCE-MR imaging are known to have a poor prognosis.<sup>26-30</sup> However, no controlled studies have been established to evaluate the EF on the basis of DSC-MR imaging as a survival-associated parameter.

In our study, although a weak correlation was found between the mean EF and Vp values in the Pearson correlation analysis, no statistical correlation was found with the other parameters, and the intraclass correlation coefficients did not show any significant correlations between the EF and the DCE-MR imaging parameters. These results are supported by previous studies in patients with glioblastoma that indicated a nonlinear relationship between the  $K^{trans}$  obtained from DCE-MR imaging and that obtained by DSC-MR imaging, probably due to the mixed contributions from the T1- and T2\*-dominant leakage effects in DSC-MR imaging.<sup>13,21</sup> Even for the EF, because the estimation of perfusion theoretically is independent of leakage, varying contributions of the 2 relaxation effects by postextravasation would directly influence the magnitude of the resulting EF value. Therefore, even though both DCE- and DSC-MR imaging use a contrast agent extravasation-correction method, the EF parameter from DSC-MR imaging cannot replace the parameters from DCE-MR imaging; however, the EF may be a noteworthy parameter that is affected by the T2\* effect from contrast agents

and may be more sensitive to contrast leakage than the parameters that are mainly determined by the T1 effect from DCE-MR imaging.

We believe that the EF value needs clinical validation before use as a potential imaging biomarker for prognostication in patients with glioblastoma treated with a standard method. Contrast leakage information can be translated into drug-delivery predictions, especially within nonenhancing FLAIR high-signal-intensity lesions after near-complete resection of the enhancing portions. In nonenhancing FLAIR high-signal-intensity lesions in patients with glioblastoma after the operation, the BBB is still an effective barrier that prevents entry of the drug into the brain tissue; hence, BBB disruption accounts for a better prognosis of patients with glioblastoma due to more efficient drug delivery.<sup>31-34</sup> The improved tumor response to chemotherapy after radiation-induced vascular damage also supports the association between permeability and drug delivery.<sup>35</sup> We found that a high EF within nonenhancing FLAIR high-signal-intensity lesions was an independent prognostic biomarker for longer PFS in patients with glioblastoma in our study, which suggested that the EF value could effectively reflect BBB disruption related to the chemotherapy response.

The *MGMT* gene encodes the MGMT protein, which has DNA repair activity.<sup>36,37</sup> Some studies have shown a significant correlation between the *MGMT* promoter methylation status and the outcome of alkylating chemotherapeutic substances, such as temozolomide.<sup>38</sup> Additionally, mutations of the *IDH1/2* gene encoding the cytosolic nicotinamide adenine dinucleotide phosphate+-dependent isocitrate dehydrogenase have been shown to be correlated with the outcome in patients with malignant gliomas.<sup>39,40</sup> To examine whether these genetic statuses influence PFS as confounding factors of the EF 95th percentile value, we performed Cox proportional hazards regression analysis in our study. The analysis revealed that the EF 95th percentile value was a predictive parameter of PFS independent of *MGMT* promoter methylation and the *IDH1/2* mutation status in patients with glioblastoma. Some studies have shown that decreased vascular permeability can cause treatment resistance in patients with gliomas.<sup>41</sup> Similarly, in our study, improved drug delivery by increased vascular permeability in patients with glioblastoma could have resulted in a better prognosis regardless of genetic variances.

Our study has some limitations, including the nature of its retrospective design. First, the patients with glioblastoma in our study were not perfectly balanced because the mean age of the

disease-progression group was slightly older than that of the non-progression group, whereas no significant differences were found in any of the other clinical characteristics. However, according to Cox proportional hazards regression, the age of the patients with glioblastoma did not affect the significance of the EF 95th percentile value. Second, we manually marked the nonenhancing FLAIR high-signal-intensity lesions as ROIs using image-analysis software, which might have resulted in observer bias. However, we carefully drew the ROIs under supervision of an expert neuroradiologist. Third, our study enrolled patients who received a double dose of contrast medium for both DSC- and DCE-MR imaging. This could increase the risk of nephrogenic systemic fibrosis and gadolinium organ tissue deposition.<sup>42,43</sup> Although a macrocyclic gadolinium-based contrast agent was used in our study, the risk of tissue deposition could be increased in patients given a double dose of contrast material. In a previous study, 1 dose of contrast medium was suggested for the acquisition of both DSC- and DCE-MR imaging by splitting the dose, which was not considered in our MR imaging protocol.<sup>44</sup> However, our study showed the feasibility of the contrast leakage information from DSC-MR imaging, which is usually calculated from DCE-MR imaging; thus, our results can give evidence to reduce unnecessary additional contrast media injections in the future. Finally, we did not analyze the tumor tissues to find pathophysiologic evidence for why the EF parameter was associated with the prognosis in patients with glioblastoma. Thus, we believe that future studies are warranted.

## CONCLUSIONS

The EF 95th percentile value within the nonenhancing FLAIR high-signal-intensity lesions from DSC-MR imaging was the only independent parameter for prognostication in patients with glioblastoma among the contrast leakage information, which has no significant correlations with the DCE-MR imaging parameters. Application of the EF 95th percentile value can be helpful for treatment stratification in patients with glioblastoma.

Disclosures: Seung Hong Choi—RELATED: Grant: governmental grant, Comments: grants from the Korean government.\* Tae Min Kim—UNRELATED: Grants/Grants Pending: AZ-KHIDI research fund.\* Chul-Kee Park—UNRELATED: Employment: Seoul National University Hospital. \*Money paid to the institution.

## REFERENCES

- Weis SM, Cheresch DA. **Pathophysiological consequences of VEGF-induced vascular permeability.** *Nature* 2005;437:497 CrossRef Medline
- Bao S, Wu Q, Sathornsumetee S, et al. **Stem cell-like glioma cells promote tumor angiogenesis through vascular endothelial growth factor.** *Cancer Res* 2006;66:7843–48 CrossRef Medline
- Rees J. **Advances in magnetic resonance imaging of brain tumours.** *Curr Opin Neurol* 2003;16:643–50 CrossRef Medline
- Stupp R, Mason WP, Van Den Bent MJ, et al. **Radiotherapy plus concomitant and adjuvant temozolomide for glioblastoma.** *N Engl J Med* 2005;352:987–96 CrossRef Medline
- Stupp R, Hegi ME, Mason WP, et al. **Effects of radiotherapy with concomitant and adjuvant temozolomide versus radiotherapy alone on survival in glioblastoma in a randomised Phase III study: 5-year analysis of the EORTC-NCIC trial.** *Lancet Oncol* 2009;10:459–66 CrossRef Medline
- Albert FK, Forsting M, Sartor K, et al. **Early postoperative magnetic resonance imaging after resection of malignant glioma: objective evaluation of residual tumor and its influence on regrowth and prognosis.** *Neurosurgery* 1994;34:45–61 CrossRef Medline
- Lacroix M, Abi-Said D, Fourney DR, et al. **A multivariate analysis of 416 patients with glioblastoma multiforme: prognosis, extent of resection, and survival.** *J Neurosurg* 2001;95:190–98 CrossRef Medline
- Kim R, Choi SH, Yun TJ, et al. **Prognosis prediction of non-enhancing T2 high signal intensity lesions in patients with glioblastoma after standard treatment: application of dynamic contrast-enhanced MR imaging.** *Eur Radiol* 2017;27:1176–85 CrossRef Medline
- Jung SC, Yeom J, Kim J-H, et al. **Glioma: application of histogram analysis of pharmacokinetic parameters from T1-weighted dynamic contrast-enhanced MR imaging to tumor grading.** *AJNR Am J Neuroradiol* 2014;35:1103–10 CrossRef Medline
- Cao Y, Nagesh V, Hamstra D, et al. **The extent and severity of vascular leakage as evidence of tumor aggressiveness in high-grade gliomas.** *Cancer Res* 2006;66:8912–17 CrossRef Medline
- Jia Z, Geng D, Xie T, et al. **Quantitative analysis of neovascular permeability in glioma by dynamic contrast-enhanced MR imaging.** *J Clin Neurosci* 2012;19:820–23 CrossRef Medline
- Jain R. **Measurements of tumor vascular leakiness using DCE in brain tumors: clinical applications.** *NMR Biomed* 2013;26:1042–49 CrossRef Medline
- Bjornerud A, Sorensen AG, Mouridsen K, et al. **T1- and T2\*-dominant extravasation correction in DSC-MRI, Part I: theoretical considerations and implications for assessment of tumor hemodynamic properties.** *J Cereb Blood Flow Metab* 2011;31:2041–53 CrossRef Medline
- Wen PY, Macdonald DR, Reardon DA, et al. **Updated response assessment criteria for high-grade gliomas: Response Assessment in Neuro-Oncology working group.** *J Clin Oncol* 2010;28:1963–72 CrossRef Medline
- Tofts PS, Kermode AG. **Measurement of the blood-brain barrier permeability and leakage space using dynamic MR imaging, I: fundamental concepts.** *Magn Reson Med* 1991;17:357–67 CrossRef Medline
- Haacke EM, Filletti CL, Gattu R, et al. **New algorithm for quantifying vascular changes in dynamic contrast-enhanced MRI independent of absolute T1 values.** *Magn Reson Med* 2007;58:463–72 CrossRef Medline
- Emblem KE, Bjornerud A, Mouridsen K, et al. **T(1)- and T(2) (\*)-dominant extravasation correction in DSC-MRI, Part II: predicting patient outcome after a single dose of cediranib in recurrent patients with glioblastoma.** *J Cereb Blood Flow Metab* 2011; 31:2054–64 CrossRef Medline
- Boxerman J, Schmainda K, Weisskoff R. **Relative cerebral blood volume maps corrected for contrast agent extravasation significantly correlate with glioma tumor grade, whereas uncorrected maps do not.** *AJNR Am J Neuroradiol* 2006;27:859–67 Medline
- Østergaard L, Weisskoff RM, Chesler DA, et al. **High resolution measurement of cerebral blood flow using intravascular tracer bolus passages, Part I: mathematical approach and statistical analysis.** *Magn Reson Med* 1996;36:715–25 CrossRef Medline
- Sourbron S, Ingrisch M, Siefert A, et al. **Quantification of cerebral blood flow, cerebral blood volume, and blood-brain-barrier leakage with DCE-MRI.** *Magn Reson Med* 2009;62:205–17 CrossRef Medline
- Skinner JT, Moots PL, Ayers GD, et al. **On the use of DSC-MRI for measuring vascular permeability.** *AJNR Am J Neuroradiol* 2016; 37:80–87 CrossRef Medline
- Pluim JP, Maintz JA, Viergever MA. **Mutual-information-based registration of medical images: a survey.** *IEEE Trans Med Imaging* 2003;22:986–1004 CrossRef Medline
- Sundar H, Shen D, Biros G, et al. **Robust computation of mutual information using spatially adaptive meshes.** In: Ayache N. *International*

- Conference on Medical Image Computing and Computer-Assisted Intervention. Berlin: Springer-Verlag; 2007:950–58
24. Jain R, Griffith B, Alotaibi F, et al. **Glioma angiogenesis and perfusion imaging: understanding the relationship between tumor blood volume and leakiness with increasing glioma grade.** *AJNR Am J Neuroradiol* 2015;36:2030–35 CrossRef Medline
  25. Heye AK, Culling RD, Valdés Hernández MC, et al. **Assessment of blood–brain barrier disruption using dynamic contrast-enhanced MRI: a systematic review.** *Neuroimage: Clinical* 2014;6:262–74 CrossRef Medline
  26. Law M, Yang S, Babb JS, et al. **Comparison of cerebral blood volume and vascular permeability from dynamic susceptibility contrast-enhanced perfusion MR imaging with glioma grade.** *AJNR Am J Neuroradiol* 2004;25:746–75 Medline
  27. Lüdemann L, Grieger W, Wurm R, et al. **Comparison of dynamic contrast-enhanced MRI with WHO tumor grading for gliomas.** *Eur Radiol* 2001;11:1231–41 CrossRef Medline
  28. Law M, Yang S, Wang H, et al. **Glioma grading: sensitivity, specificity, and predictive values of perfusion MR imaging and proton MR spectroscopic imaging compared with conventional MR imaging.** *AJNR Am J Neuroradiol* 2003;24:1989–98 Medline
  29. Aronen HJ, Gazit IE, Louis DN, et al. **Cerebral blood volume maps of gliomas: comparison with tumor grade and histologic findings.** *Radiology* 1994;191:41–51 CrossRef Medline
  30. Sugahara T, Korogi Y, Kochi M, et al. **Correlation of MR imaging-determined cerebral blood volume maps with histologic and angiographic determination of vascularity of gliomas.** *AJR Am J Roentgenol* 1998;171:1479–86 CrossRef Medline
  31. Juillerat-Jeanneret L. **The targeted delivery of cancer drugs across the blood–brain barrier: chemical modifications of drugs or drug-nanoparticles?** *Drug Discov Today* 2008;13:1099–1106 CrossRef Medline
  32. Deeken JF, Löscher W. **The blood-brain barrier and cancer: transporters, treatment, and Trojan horses.** *Clin Cancer Res* 2007; 13:1663–74 CrossRef Medline
  33. Régina A, Demeule M, Laplante A, et al. **Multidrug resistance in brain tumors: roles of the blood–brain barrier.** *Canc Cancer Metastasis Rev* 2001;20:13–25 CrossRef Medline
  34. Muldoon LL, Soussain C, Jahnke K, et al. **Chemotherapy delivery issues in central nervous system malignancy: a reality check.** *J Clin Oncol* 2007;25:2295–2305 CrossRef Medline
  35. Park HJ, Griffin RJ, Hui S, et al. **Radiation-induced vascular damage in tumors: implications of vascular damage in ablative hypofractionated radiotherapy (SBRT and SRS).** *Radiat Red* 2012;177:311–27 CrossRef Medline
  36. Pegg AE. **Repair of O6-alkylguanine by alkyltransferases.** *Mutat Res* 2000;462:83–100 CrossRef Medline
  37. Ludlum DB. **DNA alkylation by the haloethylnitrosoureas: nature of modifications produced and their enzymatic repair or removal.** *Mutat Res* 1990;233:117–26 CrossRef Medline
  38. Hegi ME, Diserens A-C, Gorlia T, et al. **MGMT gene silencing and benefit from temozolomide in glioblastoma.** *N Engl J Med* 2005;352:997–1003 CrossRef Medline
  39. Hartmann C, Meyer J, Balss J, et al. **Type and frequency of IDH1 and IDH2 mutations are related to astrocytic and oligodendroglial differentiation and age: a study of 1,010 diffuse gliomas.** *Acta Neuropathol* 2009;118:469–74 CrossRef Medline
  40. Capper D, Weissert S, Balss J, et al. **Characterization of R132H mutation-specific IDH1 antibody binding in brain tumors.** *Brain Pathol* 2010;20:245–54 CrossRef Medline
  41. Verhoeff JJ, van Tellingen O, Claes A, et al. **Concerns about anti-angiogenic treatment in patients with glioblastoma multiforme.** *BMC Cancer* 2009;9:444 CrossRef Medline
  42. Yang L, Krefting I, Gorovets A, et al. **Nephrogenic systemic fibrosis and class labeling of gadolinium-based contrast agents by the Food and Drug Administration.** *Radiology* 2012;265:248–53 CrossRef Medline
  43. McDonald RJ, McDonald JS, Dai D, et al. **Comparison of gadolinium concentrations within multiple rat organs after intravenous administration of linear versus macrocyclic gadolinium chelates.** *Radiology* 2017;285:536–45 CrossRef Medline
  44. McGehee BE, Pollock JM, Maldjian JA. **Brain perfusion imaging: how does it work and what should I use?** *J Magn Reson Imaging* 2012;36:1257–72 CrossRef Medline

# Quantification of Iodine Leakage on Dual-Energy CT as a Marker of Blood-Brain Barrier Permeability in Traumatic Hemorrhagic Contusions: Prediction of Surgical Intervention for Intracranial Pressure Management

 U.K. Bodanapally,  K. Shanmuganathan,  Y.P. Gunjan,  G. Schwartzbauer,  R. Kondaveti, and  T.R. Feiter



## ABSTRACT

**BACKGROUND AND PURPOSE:** Hemorrhagic contusions are associated with iodine leakage. We aimed to identify quantitative iodine-based dual-energy CT variables that correlate with the type of intracranial pressure management.

**MATERIALS AND METHODS:** Consecutive patients with contusions from May 2016 through January 2017 were retrospectively analyzed. Radiologists, blinded to the outcomes, evaluated CT variables from unenhanced admission and short-term follow-up head dual-energy CT scans obtained after contrast-enhanced whole-body CT. Treatment intensity of intracranial pressure was broadly divided into 2 groups: those managed medically and those managed surgically. Univariable analysis followed by logistic regression was used to develop a prediction model.

**RESULTS:** The study included 65 patients (50 men; median age, 48 years;  $Q_1$  to  $Q_3$ , 25–65.5 years). Twenty-one patients were managed surgically (14 by CSF drainage, 7 by craniectomy). Iodine-based variables that correlated with surgical management were higher iodine concentration, pseudohematoma volume, iodine quantity in pseudohematoma, and iodine quantity in contusions. The regression model developed after inclusion of clinical variables identified 3 predictor variables: postresuscitation Glasgow Coma Scale (adjusted OR = 0.55; 95% CI, 0.38–0.79;  $P = .001$ ), age (adjusted OR = 0.9; 95% CI, 0.85–0.97;  $P = .003$ ), and pseudohematoma volume (adjusted OR = 2.05; 95% CI, 1.1–3.77;  $P = .02$ ), which yielded an area under the curve of 0.96 in predicting surgical intracranial pressure management. The 2 predictors for craniectomy were age (adjusted OR = 0.89; 95% CI, 0.81–0.99;  $P = .03$ ) and pseudohematoma volume (adjusted OR = 1.23; 95% CI, 1.03–1.45;  $P = .02$ ), which yielded an area under the curve of 0.89.

**CONCLUSIONS:** Quantitative iodine-based parameters derived from follow-up dual-energy CT may predict the intensity of intracranial pressure management in patients with hemorrhagic contusions.

**ABBREVIATIONS:** AOR = adjusted OR; DECT = dual-energy CT; HPC = hemorrhagic progression of contusion; ICP = intracranial pressure; P-GCS = postresuscitation Glasgow Coma Scale; SECT = single-energy CT; TBI = traumatic brain injury; WBCT = whole-body CT

One of the most severe pathoanatomic types of traumatic brain injury (TBI) is hemorrhagic contusion, usually complicated by secondary injury, resulting in cerebral edema leading

to increased intracranial pressure (ICP).<sup>1–3</sup> Vasogenic edema caused by BBB disruption in contusions is an important contributing factor for ICP elevation.<sup>4</sup> An uncontrolled increase in ICP is a poor prognostic factor in closed-head injuries.<sup>5–7</sup> An optimal approach to managing patients with TBI is to anticipate the onset of increased ICP, appropriately monitor it, and manage it when there are clinical manifestations of an impending increase in ICP.<sup>8</sup> Level II evidence supports ICP monitoring in patients with severe head trauma (Glasgow Coma Scale, <9) and abnormal head CT findings.<sup>9</sup> However, there are no guidelines for patients with mild and moderate TBI with abnormal CT findings. Symptoms of increased ICP in awake patients may be vague and nonspecific, such as confusion, headache, and drowsiness.<sup>6</sup> CT is the primary investigation in such patients because clinically non-obvious abnormalities of cerebral mass effect are manifested as midline shift, effacement of sulci, and compression of basal

Received June 26, 2019; accepted after revision September 30.

From the Departments of Diagnostic Radiology and Nuclear Medicine (U.K.B., K.S., T.R.F.), Neurology (Y.P.G.), and Neurosurgery (G.S.), R Adams Cowley Shock Trauma Center, University of Maryland School of Medicine, Baltimore, Maryland; and Kasturba Medical College (R.K.), Mangaluru, India.

Portions of this work previously presented in abstract form at: Annual Meeting of the Radiological Society of North America, November 25–29, 2018; Chicago, Illinois.

Please address correspondence to Uttam K. Bodanapally, MD, 22 S. Greene Street, Department of Radiology and Nuclear Medicine, University of Maryland Medical Center, Baltimore, MD 21201; e-mail: ubodanapally@umm.edu

 Indicates article with supplemental on-line table.

 Indicates article with supplemental on-line photo.

<http://dx.doi.org/10.3174/ajnr.A6316>

cisterns and ventricles, which are evaluated by the Marshall CT score; however, there are no definitive CT features that determine increased ICP or identify patients who are at increased risk of subsequent ICP elevation.<sup>6,10</sup> Hence, determination of imaging predictors of the intensity of ICP management would help identify patients at risk of increased ICP and those likely to fail medical management, helping clinicians initiate early monitoring and treatment to limit secondary injury.

There are reports of CT identification of contrast leakage caused by BBB disruption in cerebral contusions that depend on qualitative assessment of iodine leakage following CTA of the brain.<sup>11-14</sup> These studies performed on single-energy CT (SECT) showed a correlation between iodine leakage and hemorrhagic progression of contusions (HPC).<sup>11-14</sup> Although CTA for evaluating TBI is not an accepted standard of care, contrast-enhanced whole-body CT (WBCT) is widely used in the work-up of patients with polytrauma.<sup>15</sup> The contrast bolus administered during the admission WBCT leaks into and is retained in the epicenter and penumbra of hemorrhagic contusion due to capillary fragmentation and BBB disruption.<sup>2</sup> Dual-energy CT (DECT) has proved helpful in differentiating and quantifying the iodine leakage from hemorrhages in cerebral infarctions, subdural spaces, and spontaneous hemorrhages.<sup>2,16,17</sup>

Using both unenhanced admission and short-term follow-up head DECTs obtained after WBCT, we aimed to identify imaging variables and clinical parameters that correlate with surgical intervention for ICP management.

## MATERIALS AND METHODS

### Study Design

This retrospective cohort study was Health Insurance Portability and Accountability Act-compliant, and permission was obtained from University of Maryland School of Medicine review board. Informed consent was waived. Consecutive patients referred to a Level I trauma center from May 2016 through January 2017 were eligible. The inclusion criteria were the following: 1) a history of blunt trauma with acquisition of head CT as a part of WBCT performed on either a DECT or SECT scanner within 6 hours after traumatic impact, with a confirmed diagnosis of hemorrhagic contusions; 2) acquisition of follow-up head DECT within 10 hours of admission CT, to evaluate the progression of TBI; and 3) patients 18 years of age and older. The exclusion criteria were the following conditions: 1) decompressive craniectomy or CSF drainage was initiated before the follow-up CT; 2) nonfocal extraparenchymal hematomas extended over >1 lobe, with a width of >2 mm, and all holohemispheric subdural hematomas, irrespective of the width, to select pure hemorrhagic contusions; and 3) punctate or petechial hemorrhages (<10 mm in diameter) in subcortical white matter concomitant with diffuse axonal injury. At the study institution, most patients with blunt trauma are evaluated with admission WBCT. Patients with traumatic lesions on initial CT, patients with persistent altered mental status without traumatic lesions, patients for whom CT fails to explain neurologic status, and patients on anticoagulation without traumatic lesions tend to be evaluated by 6- to 8-hour follow-up head CT. We selected only patients with hemorrhagic contusions

as a predominant injury type to limit the confounding effects of noncontusional lesions on ICP.

### Study Population

A search of the radiology information system from the designated time period yielded 219 patients with a follow-up study performed on a DECT scanner within 10 hours of WBCT. A radiologist (reviewer 1, U.K.B.) with 10 years of experience reviewed the initial and follow-up studies to select all the patients with pure hemorrhagic contusions ( $n=65$ ). They constituted the study group.

Clinical information regarding the mechanism of injury, time from traumatic impact to WBCT, time to follow-up DECT, postresuscitation Glasgow Coma Scale (P-GCS) score, admission blood pressure, blood coagulation parameters, ICP monitoring, opening pressure, hyperosmolar therapy, CSF drainage, and decompressive craniectomy was obtained from the electronic medical records. In intubated patients, a verbal score for P-GCS was derived.<sup>18</sup>

### Imaging

Admission WBCT examinations were performed on a DECT (Somatom Force; Siemens, Erlangen, Germany) or 64-channel SECT (Brilliance 64-channel; Philips Healthcare, Best, the Netherlands). WBCT involves a noncontrast head CT followed by contrast-enhanced CT of the neck, chest, abdomen, and pelvis. The studies were performed after injection of 100 mL of iodinated contrast media (iohexol, Omnipaque 350; GE Healthcare, Piscataway, New Jersey).

DECT head images were obtained with the x-ray tubes at 80 kV and Sn150 kV (150 kV + Tin filter). Scan parameters were as follows: rotation time, 0.5 seconds; pitch, 0.55. The reference milliampere-second was 273 for the Sn150kV and 410 for the 80-kV tube. Original dual-energy datasets were reconstructed with an increment of 1 mm and a section thickness of 1 mm. Automatic reconstruction of 120-kV equivalent mixed DECT images at 5-mm section thickness and 5-mm intervals using an adaptive iterative reconstruction algorithm (ADMIRE; Siemens) with a strength value of 3 was performed and sent to the PACS at the time of study.

### Image Analysis of DECT and Definitions

DECT data from follow-up head CTs were processed to derive 190-keV image sets at 5-mm section thickness and 5-mm intervals on a workstation (syngo.via, Version VB10B; Siemens) and sent to the PACS for the study purpose. A total of 3 image sets were used for volume measurements in each patient: 120-kV DECT or SECT images acquired with 120 kV(peak) (from the admission study) and 120-kV and 190-keV image sets (from the follow-up study). Reviewer 1 annotated all the hemorrhagic contusions that were meant for volume measurements, and admission CT images were evaluated for Marshall CT scores. Volumes were measured using semiautomated 3D segmentation on a thin-client server (Intellispace Portal; Philips Healthcare). Measurements were randomly performed with regard to patient order and the order of the image sets to avoid potential preconceived bias.

**Table 1: Unadjusted associations among predictor variables, surgical management of intracranial pressure, and decompressive craniectomy**

Variables	Unadjusted Odds Ratios (95% CI) (Surgical Management)	P Value	Unadjusted Odds Ratios (95% CI) (Craniectomy)	P Value
Age (yr)	0.96 (0.93–0.98)	.004 <sup>a</sup>	0.94 (0.88–0.99)	.04 <sup>a</sup>
Sex, men vs women	0.94 (0.27–3.2)	.92 <sup>b</sup>	0.35 (0.07–1.77)	.34 <sup>c</sup>
P-GCS	0.63 (0.5, 0.8)	<.001 <sup>a</sup>	0.78 (0.6–1)	.05
Motor score	0.43 (0.25–0.76)	.003 <sup>a</sup>	0.7 (0.44–1.14)	.15
Systolic BP (mm Hg)	0.99 (0.97–1)	.15	1.01 (0.98,1.04)	.46
Diastolic BP (mm Hg)	0.99 (0.97–1.03)	.84	1 (0.96–1.05)	.72
PT (seconds)	0.98 (0.84–1.14)	.78	0.93 (0.67–1.3)	.64
aPTT (seconds)	1.03 (0.92–1.15)	.57	1 (0.85–1.18)	.93
Fibrinogen (mg/dL)	0.98 (0.97–0.99)	.002 <sup>a</sup>	0.99 (0.98–1)	.06
Platelets (10 <sup>3</sup> /μL)	1 (0.99–1.01)	.81	1 (0.99–1.01)	.4
Marshall CT score				
DI II	1		3.46 (0.55–21.9)	.2 <sup>c</sup>
DI III and IV	4.27 (0.9–20)	.06 <sup>c</sup>		
Hemorrhagic progression	1.12 (0.35–3.54)	.85 <sup>b</sup>	2.84 (0.32–25.4)	.31 <sup>c</sup>
Fraction of hemorrhagic progression	1.02 (0.96–1.11)	.49	1 (0.91–1)	.88
Iodine concentration (mg/mL)	44 (3.03–641)	.005 <sup>a</sup>	16 (0.58–442)	.1
Hematoma volume on admission CT (cm <sup>3</sup> )	1.05 (0.97–1.13)	.21	1.04 (0.95–1.14)	.4
Hematoma volume on follow-up CT (cm <sup>3</sup> )	1.06 (1–1.12)	.04 <sup>a</sup>	1.04 (0.99–1.1)	.1
Total pseudohematoma from all contusions (cm <sup>3</sup> )	1.32 (1.06–1.64)	.01 <sup>a</sup>	1.1 (0.99–1.23)	.06
Fractional pseudohematoma to true hematoma	2.66 (0.6–11.8)	.19	2.43 (0.3–18.9)	.39
Iodine quantity in all pseudohematomas (mg)	1.48 (1.04–2.11)	.03 <sup>a</sup>	1.04 (0.96–1.13)	.3
Iodine quantity in all contusions (mg)	1.1 (1.01–1.21)	.02 <sup>a</sup>	1.03 (0.98–1.08)	.15

**Note**—BP indicates blood pressure; DI, diffuse injury; PT, prothrombin time; aPTT, activated partial thromboplastin time.

<sup>a</sup> Significant.

<sup>b</sup> Pearson.

<sup>c</sup> Fisher exact test.

For measuring the iodine concentration in the contusion, DECT data from follow-up head CT studies were used with the modified Brain Hemorrhage application on the postprocessing workstation (syngo.via).<sup>2</sup> In patients with >1 follow-up head CT, measurements were also obtained from the second follow-up study to facilitate the calculation of the fractional rate of iodine washout from the contusions. Average iodine concentration was measured by drawing an ROI around each contusion. For every contusion, 3 ROIs were drawn, each in axial, coronal, and sagittal sections at the level of the maximum diameter. The average of the 3 ROIs was obtained. The mean values obtained by the 2 reviewers (reviewer 1 and reviewer 2 [K.S.] with 25 years of experience) were used for analysis.

### Variable Construction

We analyzed the relationship of 20 study variables derived from clinical, laboratory, and CT data (Table 1 and On-line Table).

### Study Term Definitions

**Initial and Follow-Up Hematoma Volumes.** Initial hematoma volume was measured on 120 kV or SECT images and labeled as (A) (Fig 1A); volume measurements on follow-up DECT were obtained on both 120-kV images (B) (Fig 1B) and on 190-keV (Fig 1C) images (C).

**Pseudohematoma and Fraction of Pseudohematoma.** Pseudohematoma is defined as enhancing penumbra caused by an iodine leak on follow-up 120-kV images.<sup>2</sup> The attenuation contribution of iodine tends to be negligible at 190 keV, therefore demonstrating attenuation only from the hematoma, allowing measurement of true hematoma volume.<sup>2</sup> Hence, with the

availability of hematoma volume on 120 kV- (true hematoma + enhancing penumbra) and true hematoma volume on 190-keV images, the pseudohematoma volume can be calculated as the following: Pseudohematoma Volume = (B – C), where B is the volume on 120-kV and C is volume on 190-keV images. Fraction of pseudohematoma = (B – C)/C.

**Iodine Concentration.** The average iodine concentration (milligram/milliliter) was measured on iodine maps (Fig 1D). The normalized iodine concentration was not analyzed because the quantification was performed hours after contrast administration with complete washout from blood vessels.

**Iodine Quantity in Pseudohematoma and Contusion.** Iodine quantity in pseudohematoma = [(B – C) × Iodine Concentration]. Iodine quantity in total contusion = (B × Iodine Concentration).

**Hemorrhagic Progression of Contusion and Fraction of Hemorrhagic Progression of Contusion.** Hemorrhagic progression of contusion is designated as enlargement of the existing hemorrhagic contusion (30% volume increase) or the appearance of a new lesion.<sup>2</sup> Fraction of HPC = (C – A)/(A).

**Fractional Rate of Iodine Washout.** The fractional rate of iodine washout from the contusions was calculated using the following formula:

$$WR_F = I_{c(1)} - I_{c(2)} / I_{c(1)} \times 100 / \Delta T,$$

Where  $WR_F$  represents the fractional rate of washout,  $I_{C(1)}$  and  $I_{C(2)}$  are the iodine concentrations in the first and second follow-

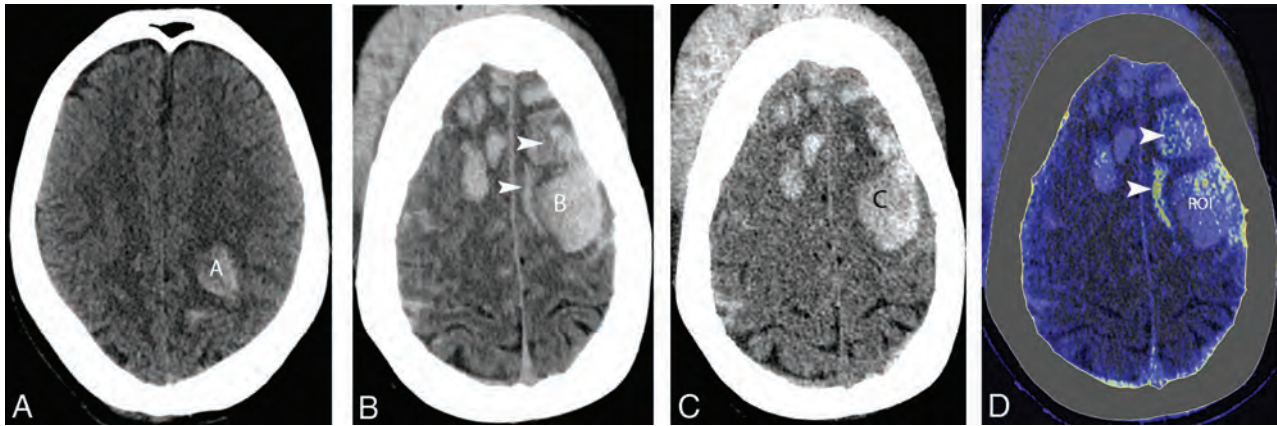


**FIG. 4.** A 65-year-old man with traumatic brain injury sustained after a motor vehicle collision. **A**, Admission 120-kV image shows a hemorrhagic contusion in the left frontoparietal lobe and measured volume ( $A = 11.4 \text{ cm}^3$ ). **B**, Follow-up axial 120-kV image shows hemorrhagic progression of contusions with increased volume of the existing hematoma ( $B = 38.3 \text{ cm}^3$ ) with multiple new hemorrhagic contusions. The image also shows areas of contrast leakage (*arrowheads*). **C**, Virtual high-monochromatic image (190 kV) shows smaller hemorrhagic contusion volume ( $C = 27.9 \text{ cm}^3$ ), compared with 120-kV images due to a negligible attenuation contribution from leaked iodinated contrast. **D**, Iodine overlay image shows contrast staining of the penumbra and paratenumbra of hemorrhagic contusions (*arrowheads*). An ROI is drawn around the largest hematoma to measure the iodine concentration ( $0.8 \text{ mg/mL}$ ).

up studies, respectively, and  $\Delta T$  represents the duration (hours) between the 2 studies.

#### **Outcome Assessment: Therapeutic Intensity of ICP Management**

Increased ICP is managed by a stepwise increase in the intensity of treatment starting with medical management and escalating to surgical intervention of CSF drainage in refractory cases and craniectomy as a last surgical option for severe refractory ICP elevation.<sup>6,8,19</sup> For this study, treatment levels were broadly divided into 2 groups: those managed medically and those managed surgically by CSF drainage or craniectomy. Medical management at the study institution includes head elevation, adequate oxygenation, fluid resuscitation, sedation, muscle relaxation, and mild hyperventilation, with or without hyperosmolar therapy.

#### **Statistical Analysis**

Statistical analysis was performed using commercially available statistical software (JMP 12 software; SAS Institute, Cary, North Carolina). Data from continuous variables are summarized as mean  $\pm$  SD for normally distributed variables and median (first quartile [ $Q_1$ ], third quartile [ $Q_3$ ]) for non-normally distributed variables. Categorical variables are summarized as counts and percentages. The association between each predictor of interest and outcomes was examined using the  $\chi^2$  test or Fisher exact test for categorical predictors and simple logistic regression for continuous predictors. The effect of each predictor of interest on surgical ICP management and craniectomy without adjusting for other predictors and the unadjusted odds ratio and corresponding 95% confidence intervals were calculated. For both categorical outcomes, predictors with  $P < .1$  on unadjusted analysis were incorporated into the logistic regression analysis. The independent predictors for each outcome were developed using the backward-elimination method. The final predictors for each outcome of

interest were selected on the basis of the Akaike information criterion. A  $P$  value of .05 indicated significance. For the prediction model for each outcome, receiver operating characteristic analysis was performed to assess the overall predictive ability of the model using the area under the receiver operating characteristic curve.

#### **RESULTS**

Baseline clinical characteristics of the cohort ( $n = 65$ ) are shown in the On-line Table. Of the 65 patients in the study cohort, 44 patients were medically managed, including hyperosmolar therapy in 20 patients. There were 21 patients managed surgically (14 by CSF drainage, 7 by craniectomy); all 21 patients had a trial of hyperosmolar therapy before escalating treatment to an operation. The median time from impact to WBCT was 1 hour 30 minutes ( $Q_1 = 1.12$  hours,  $Q_3 = 2$  hours), and the median time to follow-up head DECT was 6 hours ( $Q_1 = 4$  hours,  $Q_3 = 7.25$  hours). All contusions showed iodine leakage, with a concentration ranging from 0.1 to 1 mg/mL (median = 0.43 mg/mL,  $Q_1, Q_3 = 0.23$ –0.53 mg/mL). The correlation between the 2 reviewers' measurements of iodine concentration was very strong ( $r = 0.923$ ). The correlation between predictors is shown in the On-line Figure. In patients with multiple contusions ( $n = 28$ ), there was a strong correlation between the iodine concentration in the largest contusion with the mean concentration in smaller contusions ( $r = 0.94$ ). The median fraction of pseudo-hematoma to the true hematoma was 0.31 or 31% ( $Q_1 = 0.11, Q_3 = 0.58$ ).

#### **Surgical Management**

Twenty-one patients were managed surgically (14 by CSF drainage, 7 by craniectomy). DECT variables that correlated with surgical ICP management were higher iodine concentration (OR = 44; 95% CI, 3.03–641;  $P = .005$ ), pseudo-hematoma volume (OR = 1.32; 95% CI, 1.06–1.64;  $P = .01$ ), iodine quantity in

**Table 2: Adjusted associations among predictor variables, surgical management of intracranial pressure, and decompressive craniectomy**

Variables	Adjusted Odds Ratios (95% CI) (Surgical Management)	P Value	Adjusted Odds Ratios (95% CI) (Craniectomy)	P Value
Age (yr)	0.9 (0.85–0.97)	.003 <sup>a</sup>	0.89 (0.81–0.99)	.03 <sup>a</sup>
Total pseudohematoma from all contusions (cm <sup>3</sup> )	2.05 (1.11–3.77)	.02 <sup>a</sup>	1.23 (1.03–1.45)	.02 <sup>a</sup>
P-GCS	0.55 (0.38–0.79)	.001 <sup>a</sup>		

<sup>a</sup>Significant.

pseudohematoma (OR = 1.48; 95% CI, 1.04–2.11;  $P = .03$ ), and iodine quantity in contusion (OR = 1.1; 95% CI, 1.01–1.21;  $P = .02$ ). The conventional CT variable that correlated was hematoma volume on follow-up CT (OR = 1.06; 95% CI, 1–1.12;  $P = .04$ ). Clinical variables that correlated were younger age (OR = 0.96; 95% CI, 0.93–0.98;  $P = .004$ ), lower P-GCS (OR = 0.63; 95% CI, 0.5–0.8;  $P < .001$ ), lower motor score (OR = 0.43; 95% CI, 0.25–0.76;  $P = .003$ ), and lower fibrinogen (OR = 0.98; 95% CI, 0.97–0.99;  $P = .002$ ). Complete details are provided in Table 1. The regression model developed after combining the clinical variables and CT variables identified 3 predictors with significance in the determination of surgical ICP management (Table 2): P-GCS (adjusted odds ratio [AOR] = 0.55; 95% CI, 0.38–0.79;  $P = .001$ ), age (AOR = 0.9; 95% CI, 0.85–0.97;  $P = .003$ ), and pseudohematoma volume (AOR = 2.05; 95% CI, 1.1–3.77;  $P = .02$ ). The 3 variables resulted in an  $R^2$  of 0.6 ( $P < .001$ ) (Table 2). On average, a 1-unit (cubic centimeter) increase in pseudohematoma volume increased the odds of surgical ICP management by 105%. Receiver operating characteristic analysis of the regression model in predicting surgical ICP management yielded an area under the curve of 0.96.

### Decompressive Craniectomy

The variables that correlated with decompressive craniectomy on univariable analysis were young age and lower P-GCS. Complete details are provided in Table 1. The regression model developed after inclusion of variables with  $P < .1$  on unadjusted analysis identified 2 predictors with significance: age (AOR = 0.89; 95% CI, 0.81–0.99;  $P = .03$ ) and pseudohematoma volume (AOR = 1.23; 95% CI, 1.03–1.45;  $P = .02$ ), with an  $R^2$  of 0.32 ( $P < .001$ ) (Table 2). On average, a 1-unit (cubic centimeter) increase in pseudohematoma volume increased the odds of craniectomy by 23% (AOR = 1.23; 95% CI, 1.03–1.45;  $P = .02$ ). Receiver operating characteristic analysis of the regression model in predicting craniectomy yielded an area under the curve of 0.89.

Iodine quantity either in pseudohematoma or the contusion showed a strong linear correlation (0.95) with pseudohematoma volume; hence, these factors can be interchangeable in the regression model.

### Iodine Washout Rates

A second follow-up DECT was available in 37 patients. In these patients, there was a slow and gradual decrease in the iodine concentrations with a median of 2.22% ( $Q_1 = 0$ ,  $Q_3 = 9.6$ ). There was no correlation between the iodine concentration and washout rates (Spearman  $\rho = 0.25$ ,  $P = .13$ ). Serial iodine concentrations

measured in patients with  $>2$  follow-up studies ( $n = 22$ ) demonstrated that the complete washout of iodine was seen as soon as 56 hours and contrast was retained in the contusion for as long as 147 hours after injection. Analysis performed by adjusting the iodine concentration to the median time to follow-up CT of 6 hours showed identical predictors for surgical ICP management and decompressive craniectomy.

## DISCUSSION

Our cohort included predominantly a specific type of pathoanatomic injury (ie, contusions) with the most commonly used CT classification scheme (the Marshall CT score) as well as contusion volumes on admission and follow-up CT studies and compared them with the quantitative iodine-based DECT variables. We excluded large extraparenchymal hematomas because those pathoanatomic injury types do not share a common pathophysiologic mechanism of primary and secondary damage that influences the ICP.<sup>20</sup> The major findings from our study are the following: In traumatic cerebral contusions with a short-term follow-up head DECT after admission WBCT, quantitative iodine-based DECT variables correlated with surgical ICP management; pseudohematoma volume derived from DECT was the only imaging predictor of both surgical ICP management and craniectomy; and the clinical variables P-GCS and age were additional predictors of surgical ICP management, while age was the only clinical predictor of craniectomy.

Studies have shown a correlation between the presence of iodine leak with HPC and craniectomies after TBI.<sup>11–14</sup> In contrast to previous studies, our results did not show a correlation between leaked iodine concentration and craniectomy, but they correlated with surgical ICP management. This difference might be due to qualitative assessment of images on SECT and by using various threshold levels of Hounsfield units to confirm leaks. However, we identified pseudohematoma volume derived from DECT as the best imaging predictor of surgical ICP management and craniectomy. Pseudohematoma that constitutes approximately 30% ( $Q_1 = 10$ ,  $Q_3 = 57$ ) (On-line Table) of the median value of the contusion represents the volume of enhancing penumbra. The predictive ability of pseudohematoma is because it represents the volume of parenchyma that shows BBB disruption, hence a higher volume correlating with the magnitude of ICP elevation according to Monro-Kellie hypothesis.<sup>8</sup> Animal models have demonstrated the concept of progressive microvascular failure associated with contusions, in which the peak kinetic energy delivered to the epicenter resulted in immediate capillary fragmentation and hemorrhage. However, the energy deposited in the penumbra is not enough to fracture capillaries but is enough to activate mechanosensitive molecular processes. This upregulates sulfonylurea receptor 1, implicated in delayed microvascular dysfunction resulting in a permeable endothelium.<sup>2,21</sup> Iodine leaks through the same permeable endothelium manifest as enhancing penumbra. SECT fails to assess the volume of enhancing penumbra, while DECT enables the measurement of

the volume, thus proving to be superior to the commonly used Marshall CT score in predicting elevated ICP requiring surgical management.

Age and P-GCS were clinical predictors of surgical ICP management and age for craniectomy. The predictive ability of younger age might be due to the lack of involuntal changes of cerebral volume loss; thus, younger patients are prone to ICP elevation by milder forms of cerebral edema compared with older patients. Use of the ratio of parenchymal volume to CSF volume as a measure of the degree of brain involution as a predictor variable may yield more accurate results. However, age may be used as an effective surrogate for the magnitude of brain atrophy until a robust validated automated volume-quantification software becomes widely available. Finally, a low P-GCS that represents more severe TBI as a predictor of surgical ICP may be related to the high mechanical force at impact that propagates through a large volume of parenchyma, causing diffuse edema contributing to ICP, as opposed to more localized injury.

The current TBI classification relies on the primary presentation (Glasgow Coma Scale) without considering the second phase that includes the role of BBB permeability.<sup>22,23</sup> Establishing a routine, inexpensive, and minimally invasive technique to measure the degree of BBB disruption might improve the TBI classification and also would streamline patients for ICP monitoring and the treatment approach for increased ICP.<sup>24</sup> CT perfusion and contrast-enhanced MR imaging are the currently available imaging techniques for detection of BBB breakdown that rely on detection of the retained contrast agent in the interstitium. However, these techniques are not widely accepted for patients with TBI due to additional cost, time, and potential for additional radiation (class IIb recommendations).<sup>25</sup> Animal studies have shown that extravasation through the BBB occurs immediately after shock loading, reaches maximum intensity by 4 hours, and gradually resolves in 4 days after impact.<sup>26-28</sup> CT contrast (iohexol, with a low molecular weight [ $<2$  kDa]) can be used for measuring this transient increase in permeability. The ability to quantify iodine using increasingly available DECT technology in major academic and Level I trauma centers provides a good alternate imaging technique to assess BBB disruption.

### Strengths and Limitations

The strength of our study derives from its unique ability to assess BBB disruption and the prediction of surgical ICP management in a subset of patients with TBI with hemorrhagic contusions using the current standard of care admission WBCT and follow-up DECT data, without any additional penalty of cost, time, and radiation. Limitations include its retrospective, single-center design, which introduces selection and institutional bias. Additionally, the cohort comprised hemorrhagic contusions as the major form of injury. Therefore, these data cannot be generalized to all patients with TBI, especially those with major extraparenchymal bleeds. Finally, this study does not evaluate the optimum temporal window to obtain the follow-up studies (though most follow-up scans [75%] were performed within 7 hours 15 minutes).

## CONCLUSIONS

Quantitative iodine-based parameters derived from follow-up DECT after admission contrast-enhanced WBCT can be used to predict surgical ICP management and craniectomy in patients with hemorrhagic contusions. The identified predictors can help discriminate patients who would fail medical management and can help clinicians initiate early ICP monitoring and treatment.

Disclosures: Uttam K. Bodanapally—UNRELATED: Grants/Grants Pending: Siemens, Comments: artificial intelligence for detecting traumatic brain injuries\*; Payment for Lectures Including Service on Speakers Bureaus: Siemens, Comments: symposium; Travel/Accommodations/Meeting Expenses Unrelated to Activities Listed: Siemens, Comments: travel to the symposium. \*Money paid to the institution.

## ACKNOWLEDGMENT

The authors thank Brigitte Pocta for editing the manuscript.

## REFERENCES

1. Stiell IG, Clement CM, Grimshaw JM, et al. **A prospective cluster-randomized trial to implement the Canadian CT Head Rule in emergency departments.** *CMAJ* 2010;182:1527–32 CrossRef Medline
2. Bodanapally UK, Shanmuganathan K, Issa G, et al. **Dual-energy CT in hemorrhagic progression of cerebral contusion: overestimation of hematoma volumes on standard 120-kV images and rectification with virtual high-energy monochromatic images after contrast-enhanced whole-body imaging.** *AJNR Am J Neuroradiol* 2018; 39:658–62 CrossRef Medline
3. Smith M. **Monitoring intracranial pressure in traumatic brain injury.** *Anesth Analg* 2008;106:240–48 CrossRef Medline
4. Unterberg AW, Stover J, Kress B, et al. **Edema and brain trauma.** *Neuroscience* 2004;129:1019–27 CrossRef
5. Marshall LF, Smith RW, Shapiro HM. **The outcome with aggressive treatment in severe head injuries, Part II: acute and chronic barbiturate administration in the management of head injury.** *J Neurosurg* 1979;50:26–30 CrossRef Medline
6. Li LM, Timofeev I, Czosnyka M, et al. **The surgical approach to the management of increased intracranial pressure after traumatic brain injury.** *Anesth Analg* 2010;111:736–48 CrossRef Medline
7. Juul N, Morris GF, Marshall SB, et al; Executive Committee of the International Selfotel Trial. **Intracranial hypertension and cerebral perfusion pressure: influence on neurological deterioration and outcome in severe head injury.** *J Neurosurg* 2000;92:1–6 CrossRef Medline
8. Jantzen J. **Prevention and treatment of intracranial hypertension.** *Best Pract Res Clin Anaesthesiol* 2007;21:517–38 CrossRef Medline
9. Bratton SL, Chestnut RM, Ghajar J, et al; Brain Trauma Foundation; American Association of Neurological Surgeons; Congress of Neurological Surgeons; Joint Section on Neurotrauma and Critical Care, AANS/CNS. **Guidelines for the management of severe traumatic brain injury, VI: indications for intracranial pressure monitoring.** *J Neurotrauma* 2007;24(Suppl 1):S37–44 CrossRef Medline
10. Miller MT, Pasquale M, Kurek S, et al. **Initial head computed tomographic scan characteristics have a linear relationship with initial intracranial pressure after trauma.** *J Trauma* 2004;56:967–73 CrossRef Medline
11. Rosa M Jr, da Rocha AJ, Maia AC Jr, et al. **Contusion contrast extravasation depicted on multidetector computed tomography angiography predicts growth and mortality in traumatic brain contusion.** *J Neurotrauma* 2016;33:1015–22 CrossRef Medline
12. Letourneau-Guillon L, Huynh T, Jakobovic R, et al. **Traumatic intracranial hematomas: prognostic value of contrast extravasation.** *AJNR Am J Neuroradiol* 2013;34:773–79 CrossRef Medline
13. Huang AP, Lee CW, Hsieh HJ, et al. **Early parenchymal contrast extravasation predicts subsequent hemorrhage progression, clinical**

- deterioration, and need for surgery in patients with traumatic cerebral contusion. *J Trauma* 2011;71:1593–99 CrossRef Medline
14. Orito K, Hirohata M, Nakamura Y, et al. **Predictive value of leakage signs for pure brain contusional hematoma expansion.** *J Neurotrauma* 2018;35:760–66 CrossRef Medline
  15. Huber-Wagner S, Lefering R, Qvick LM, et al; Working Group on Polytrauma of the German Trauma Society. **Effect of whole-body CT during trauma resuscitation on survival: a retrospective, multi-centre study.** *Lancet* 2009;373:1455–61 CrossRef Medline
  16. Bodanapally UK, Dreizin D, Issa G, et al. **Dual-energy CT in enhancing subdural effusions that masquerade as subdural hematomas: diagnosis with virtual high-monochromatic (190-keV) images.** *AJNR Am J Neuroradiol* 2017;38:1946–52 CrossRef Medline
  17. Bonatti M, Lombardo F, Zamboni GA, et al. **Iodine extravasation quantification on dual-energy CT of the brain performed after mechanical thrombectomy for acute ischemic stroke can predict hemorrhagic complications.** *AJNR Am J Neuroradiol* 2018;39:441–47 CrossRef Medline
  18. Meredith W, Rutledge R, Fakhry SM, et al. **The conundrum of the Glasgow Coma Scale in intubated patients: a linear regression prediction of the Glasgow verbal score from the Glasgow eye and motor scores.** *J Trauma* 1998;44:839–45 CrossRef Medline
  19. Rangel-Castilla L, Rangel-Castillo L, Gopinath S, et al. **Management of intracranial hypertension.** *Neurol Clin* 2008;26:521–41 CrossRef Medline
  20. Saatman KE, Duhaime AC, Bullock R, et al. **Classification of traumatic brain injury for targeted therapies.** *J Neurotrauma* 2008;25:719–38 CrossRef Medline
  21. Simard JM, Chen M, Tarasov KV, et al. **Newly expressed SUR1-regulated NC(Ca-ATP) channel mediates cerebral edema after ischemic stroke.** *Nat Med* 2006;12:433–40 CrossRef Medline
  22. Jacobs B, Beems T, van der Vliet TM, et al. **Computed tomography and outcome in moderate and severe traumatic brain injury: hematoma volume and midline shift revisited.** *J Neurotrauma* 2011;28:203–15 CrossRef Medline
  23. Bodanapally UK, Sours C, Zhuo J, et al. **Imaging of traumatic brain injury.** *Radiology Clin North Am* 2015;53:695–715 CrossRef Medline
  24. Shlosberg D, Benifla M, Kaufer D, et al. **Blood-brain barrier breakdown as a therapeutic target in traumatic brain injury.** *Nat Rev Neurol* 2010;6:393 CrossRef Medline
  25. Wintermark M, Sanelli PC, Anzai Y, et al. **Imaging evidence and recommendations for traumatic brain injury: advanced neuro- and neurovascular imaging techniques.** *AJNR Am J Neuroradiol* 2015;36:E1–11 CrossRef Medline
  26. Habgood MD, Bye N, Dziegielewska KM, et al. **Changes in blood-brain barrier permeability to large and small molecules following traumatic brain injury in mice.** *Eur J Neurosci* 2007;25:231–38 CrossRef Medline
  27. Bharadwaj VN, Lifshitz J, Adelson PD, et al. **Temporal assessment of nanoparticle accumulation after experimental brain injury: effect of particle size.** *Sci Rep* 2016;6:29988 CrossRef Medline
  28. Kuriakose M, Rao KV, Younger D, et al. **Temporal and spatial effects of blast overpressure on blood-brain barrier permeability in traumatic brain injury.** *Sci Rep* 2018;8:8681 CrossRef Medline

# Angiographic Analysis of Natural Anastomoses between the Posterior and Anterior Cerebral Arteries in Moyamoya Disease and Syndrome

S. Bonasia, G. Ciccio, S. Smajda, A.G. Weil, C. Chaalala, R. Blanc, M. Reinert, M. Piotin, M. Bojanowski, and T. Robert

## ABSTRACT

**BACKGROUND AND PURPOSE:** Moyamoya disease is a chronic neurovascular steno-occlusive disease of the internal carotid artery and its main branches, associated with the development of compensatory vascular collaterals. Literature is lacking about the precise description of these compensatory vascular systems. Usually, the posterior circulation is less affected, and its vascular flow could compensate the hypoperfusion of the ICA territories. The aim of this study was to describe these natural connections between the posterior cerebral artery and the anterior cerebral artery necessary to compensate the lack of perfusion of the anterior cerebral artery territories in the Moyamoya population.

**MATERIALS AND METHODS:** All patients treated for Moyamoya disease from 2004 to 2018 in 4 neurosurgical centers with available cerebral digital subtraction angiography were included. Forty patients (80 hemispheres) with the diagnosis of Moyamoya disease were evaluated. The presence of anastomoses between the posterior cerebral artery and the anterior cerebral artery was found in 31 hemispheres (38.7%).

**RESULTS:** Among these 31 hemispheres presenting with posterior cerebral artery–anterior cerebral artery anastomoses, the most frequently encountered collaterals were branches from the posterior callosal artery (20%) and the posterior choroidal arteries (20%). Another possible connection found was pial anastomosis between cortical branches of the posterior cerebral artery and the anterior cerebral artery (15%). We also proposed a 4-grade classification based on the competence of these anastomoses to supply retrogradely the territories of the anterior cerebral artery.

**CONCLUSIONS:** We found 3 different types of anastomoses between the anterior and posterior circulations, with different abilities to compensate the anterior circulation. Their development depends on the perfusion needs of the territories of the anterior cerebral artery and can provide the retrograde refilling of the anterior cerebral artery branches.

**ABBREVIATIONS:** ACA = anterior cerebral artery; PCA = posterior cerebral artery

Moyamoya disease is a neurovascular pathology characterized by the progressive stenosis of the supraclinoid portion of the ICA and its 2 main branches: the anterior cerebral artery (ACA) and MCA in their proximal segments.<sup>1-3</sup> During the evolution of the pathology, the development of natural collaterals allows maintaining a minimal perfusion to the cerebral parenchyma and, in particular, the ACA territories.<sup>2,4,5</sup> The knowledge

of the collateral circles and the specific connections that the patient develops during the natural history of this disease is still not well-known, and just a few studies in the literature are dedicated to their analysis.<sup>6-9</sup> In a recent study,<sup>8</sup> we described the role of collaterals from the ophthalmic artery in supplying the ACA territory. However, the other collateral circles are still not known in detail. Due to this important absence in the literature, we proposed to analyze the other collateral circles in Moyamoya disease. This study aimed to describe angiographically the anastomotic circulation between the posterior cerebral artery (PCA) and the ACA, which maintains correct perfusion of the ACA territory.

## MATERIALS AND METHODS

### Patient Selection

On the basis of a prospective data base from 2004 to 2018, fifty-six patients with the diagnosis of Moyamoya disease or syndrome

Received August 9, 2019; accepted after revision September 10.

From the Department of Neurosurgery (S.B., M.R., T.R.), Neurocenter of the Southern Switzerland, Lugano, Switzerland; Department of Interventional Neuroradiology (G.C., S.S., R.B., M.P.), Rothschild Foundation Hospital, Paris, France; Department of Pediatric Neurosurgery (A.G.W.), Sainte-Justine Hospital, Montreal, Quebec, Canada; Department of Neurosurgery (C.C., M.B.), Centre Hospitalier de l'Université de Montréal, Montreal, Quebec, Canada; and Faculty of Medicine (M.R., T.R.), University of the Southern Switzerland, Lugano, Switzerland.

Please address correspondence to Sara Bonasia, MD, Regional Hospital of Lugano, Department of Neurosurgery, Neurocenter of the Southern Switzerland, Via Tesserete 46, CH-6903 Lugano, Switzerland; e-mail: sara.bonasia@gmail.com  
<http://dx.doi.org/10.3174/ajnr.A6291>

have been evaluated in our institutions (Sainte Justine Hospital, Montreal; Notre-Dame Hospital, Montreal; Rothschild Foundation Hospital, Paris; Regional Hospital, Lugano). The patients had Moyamoya syndrome with characteristic Moyamoya vasculopathy and the following associated conditions: unilateral vascular changes, sickle cell disease, neurofibromatosis type 1, and cranial therapeutic irradiation. All patients who underwent at least 1 DSA were included in our study (40 patients). The other 16 patients with Moyamoya disease who were only evaluated by MR imaging were excluded. Therefore, a retrospective angiographic study of anastomoses between the posterior and anterior circulations was possible in 80 hemispheres (40 patients). We looked for the presence of an etiology, the duration of symptoms, the type of clinical sign (ischemic or hemorrhagic), and the clinical outcome.

### Analysis of the Posterior Circulation Collateral Anatomy

A 6-vessel DSA with the patient under local anesthesia with 3D reconstruction was performed on all patients of this study. All DSA interpretation was performed by the same 2 senior neuroradiologists, and in case of disagreement, a third neuroradiologist was consulted. The Suzuki grading system<sup>10</sup> was applied to each cerebral hemisphere. As suggested by Baltsavias et al,<sup>6,7</sup> different arterial collaterals were categorized into leptomeningeal (pio-pial), duro-pial, and periventricular collaterals. For each hemisphere evaluated, careful attention was paid to the following: the presence of an anastomotic connection between the posterior cerebral artery and the anterior cerebral artery, the number of vessels involved, their exact anatomy, and the competence of the anastomosis to supply by retrograde flow the ACA territories.

### Treatment and Clinical Evolution

Modalities of medical and surgical treatments were recorded. Follow-up started at the time of the first clinical sign and ended with the last clinical visit. A neurologic examination with evaluation of the mRS was systematically performed for each visit. Most patients underwent only 1 DSA for the diagnostic radiologic assessment of the pathology and then were followed with cerebral MR imaging.

### Data Availability

The data cannot be shared for ethical reasons because patients involved were mostly younger than 18 years of age and gave no consent for data sharing.

### Statistical Analysis

A complex statistical analysis is not required for this kind of study. Percentage calculations were performed by Sara Bonasia, MD (Neurocenter of Southern Switzerland), and the detailed data are summarized in Tables 1–3.

## RESULTS

### Clinical Presentation

Between 2004 and 2018, forty patients fulfilled the inclusion criteria for this study. Patient baseline data and clinical signs are summarized in Tables 1–3. The mean age was 40.9 years

**Table 1: Demographic and clinical data**

Variable	Patients (n = 40)
Female	29 (72.5%)
Sex ratio, F/M	2.6:1
Median age (yr)	40.9 (1–64)
Clinical presentation	
Ischemic	23 (57.5%)
Hemorrhagic	13 (32.5%)
SAH	9 (22.5%)
Intraparenchymal	4 (10%)
Baseline mRS	
0	1 (2.5%)
1	12 (30%)
2	15 (37.5%)
3	5 (12.5%)
4	1 (2.5%)
5	6 (15%)

**Table 2: Suzuki stage of the population**

Suzuki Stage	Hemispheres (n = 80)
0	10 (12.5%)
I	10 (12.5%)
II	10 (12.5%)
III	14 (17.5%)
IV	16 (20%)
V	7 (8.8%)
VI	11 (13.8%)
NA (Cervical ICA occlusion)	2 (2.5%)

**Note:**—NA indicates not applicable.

**Table 3: Results**

Origin of the Collaterals	Hemispheres (n = 80)
Collaterals from posterior callosal artery (type I)	16 (20%)
Collaterals from posterior choroidal arteries (type II)	16 (20%)
Pio-pial connections (type III)	12 (15%)
Competence	
Type I	7 (8.7%)
Type II	12 (15%)
Type III	9 (11.3%)
Type IV	5 (6.3%)
Correlation between Suzuki score and posterior collaterals	
0	1 (1.3%)
I	1 (1.3%)
II	4 (5%)
III	4 (5%)
IV	8 (10%)
V	4 (5%)
VI	8 (10%)
Cervical occlusion of the ICA	1 (1.3%)

(range, 1–64 years) with a female preponderance (female/male ratio, 2.6:1). The most common clinical sign was an ischemic stroke in 23 patients (57.5%). Other patients presented with hemorrhage (13 patients, 32.5%). Among them, 4 patients had intraparenchymal bleeding; and 9 patients, a subarachnoid hemorrhage. The initial mRS score was 0 in 1 patient (2.5%), 1 in 12 patients (30%), 2 in 15 (37.5%), 3 in 5 (12.5%), 4 in 1 (2.5%), and 5 in 6 (15%).

### **Angiographic Analysis of Moyamoya Disease**

We analyzed the presence of collaterals between the PCA and the ACA for each of the 80 cerebral hemispheres. The Suzuki stage was 0 in 10 hemispheres (12.5%), I in 10 (12.5%), II in 10 (12.5%), III in 14 hemispheres (17.5%), IV in 16 (20%), V in 7 (8.75%), and VI in 11 hemispheres (13.75%). Two patients (2.5%) had a cervical occlusion of the ICA; thus, the Suzuki classification was not applicable. Among the hemispheres studied, the posterior communicating artery had a normal configuration (P1 segment larger than posterior communicating artery) in 56 cases (70%) and a fetal configuration (posterior communicating artery larger than P1 segment) in 24 cases (30%).

The observation of angiographies led us to identify different types of connections between the anterior and posterior circulations. We classified the different anastomoses observed into 3 types: In type I, the posterior pericallosal or splenial artery has anastomosis with the terminal branches of the anterior pericallosal artery; in type II, the medial posterior choroidal artery has posterior anastomosis with terminal branches of the anterior pericallosal artery; in type III, cortical branches of the PCA create pto-pial (leptomeningeal) connections to cortical ACA branches. Figure 1 shows some examples of the 3 types of PCA-ACA anastomoses.

The presence of collaterals from the posterior circulation was noted in 34 hemispheres, but 3 of them were excluded from our analysis because they had a connection between the PCA and the MCA and not with the ACA. Angiographic results of our study are summarized in Table 3. Among the 31 hemispheres (38.7% of the total) included, we found collaterals to the ACA from the posterior pericallosal or splenial artery (type I) in 16 hemispheres (20%), from the medial posterior choroidal artery (type II) in 16 hemispheres (20%), and a pto-pial connection (type III) in 12 hemispheres (15%). Figure 2 shows the Suzuki score and the presence of each type of PCA-ACA anastomosis in the different age groups of our population. Patients younger than 20 years of age and older than 50 years of age are the 2 groups in whom the presence of PCA-ACA anastomosis was the most frequent.

The presence of natural collaterals between branches of the ophthalmic artery and branches of the ACA was noted in 35 hemispheres (43.8%). There is no numerical difference among the different groups. Twenty-one hemispheres presented with ophthalmic artery-ACA anastomosis without PCA-ACA anastomosis, 5 presented with ophthalmic artery-ACA concomitantly with a PCA-ACA type I anastomosis; 5 others, ophthalmic artery-ACA and PCA-ACA type II anastomosis; and 4 hemispheres presented with ophthalmic artery-ACA concomitantly with a PCA-ACA type III anastomosis.

We also analyzed the competence of each anastomosis in supplying the ACA vascular territories. According to the importance of retrograde supply of the ACA territories, we proposed a 4-grade classification that is illustrated in Fig 3. Grade I corresponds to anastomosis allowing the visualization of the first part of the posterior pericallosal artery without seeing any cortical ACA branch (7 hemispheres, 8.7%). The grade II is noted when the retrograde flow in the ACA is important enough to see 1 cortical branch (12 hemispheres, 15%). Grade III corresponds to an anastomosis important enough to visualize  $\geq 2$  cortical branches

of the posterior pericallosal artery (9 hemispheres, 11.25%). Grade IV consists of the complete retrograde refilling of the ACA (5 hemispheres, 6.25%).

### **Collaterals from the Posterior Pericallosal (Splenial) Artery**

The most frequently encountered anastomosis between the posterior cerebral artery and the anterior cerebral artery comes from a branch of the posterior pericallosal artery or splenial artery. This connection was found in 20% of cases (16 hemispheres), and one of these cases is shown in Fig 1A. The posterior pericallosal artery normally arises from the PCA or its branches and supplies the splenium of the corpus callosum.<sup>11</sup> It can anastomose with the anterior pericallosal artery, a branch of the ACA, to fill retrogradely the latter artery.

### **Collaterals from Posterior Choroidal Arteries**

The other frequent collaterals we found are those from the medial posterior choroidal artery. The choroidal arteries could be divided into a medial and lateral system (medial posterior choroidal artery and lateral posterior choroidal artery), with the former arising from the P1 segment or at the junction of the P1-P2 segment and the latter originating from the P2 segment.<sup>12</sup> They anastomose with the branches of the anterior choroidal artery and the anterior cerebral artery to supply the choroidal plexus.<sup>11</sup> In detail, the medial posterior choroidal artery divides into a lateral branch, which anastomoses into the lateral ventricle with branches of the anterior choroidal artery or with the lateral posterior choroidal artery and into a medial branch, which anastomoses on the roof of the third ventricle with the contralateral medial posterior choroidal artery. The lateral posterior choroidal artery enters the lateral ventricle in the temporal horn or in the atrium, and here it anastomoses with anterior choroidal artery contribution.<sup>12</sup> In our series, we mostly found anastomosis between the medial posterior choroidal arteries and the ACA (16 hemispheres, 20% of cases), as illustrated in Fig 1B.

### **Pto-Pial (Leptomeningeal) Connections between PCA and ACA**

In 12 hemispheres (15%), we also found collaterals between cortical branches of the PCA and cortical branches of the ACA. These are end-to-end anastomoses between cortical branches of the PCA, such as the parieto-occipital artery, and terminal branches of the ACA, which usually develop at the watershed zones, as illustrated in the Fig 1C.

### **Treatment and Clinical Follow-Up**

Among the 56 patients, 23 were treated with antiplatelet therapy. Aspirin was always the first-line treatment. Three of them presented with a recurrent ischemic stroke and were placed under dual antiplatelet therapy. No hemorrhagic stroke was noted under surgical treatment. One patient had a bilateral superficial direct temporal artery-middle cerebral artery anastomosis; 4 others also had a superficial direct temporal artery-MCA bypass, but only at 1 side; and for the last patient, a myo-synangiosis was performed. One patient presented with an ischemic stroke as a complication of the operation, which was contralateral to the operated hemisphere and was imputed to a hypoperfusion during



**FIG 1.** The 3 types of PCA-ACA collaterals are shown by angiograms with corresponding graphic illustrations. The *blue triangles* (A and B) indicate the anastomosis between the posterior pericallosal artery and the anterior pericallosal artery (type I). The *red arrows* indicate the contribution of pto-pial connections to the anastomosis. C and D, Type II collateral, between the medial posterior choroidal artery (MPChoA) and the anterior pericallosal artery (APA) (*blue triangles*). The MPChoA turns first anteriorly and then backward around the splenium of the corpus callosum to reach the APA. Pto-pial connections are also visible in the angiogram (*red arrows*). Type III collaterals are visible (E and F), where the *dark blue arrows* indicate pto-pial or leptomeningeal connections between cortical branches from the PCA (*red arrows*) and cortical branches from the ACA (*light blue arrows*). The *green triangles* show the adjunctive presence of posterior pericallosal artery (PPA)-APA connections. POA indicates parieto-occipital artery; CMA, callosal-marginal artery; BA, basilar artery.

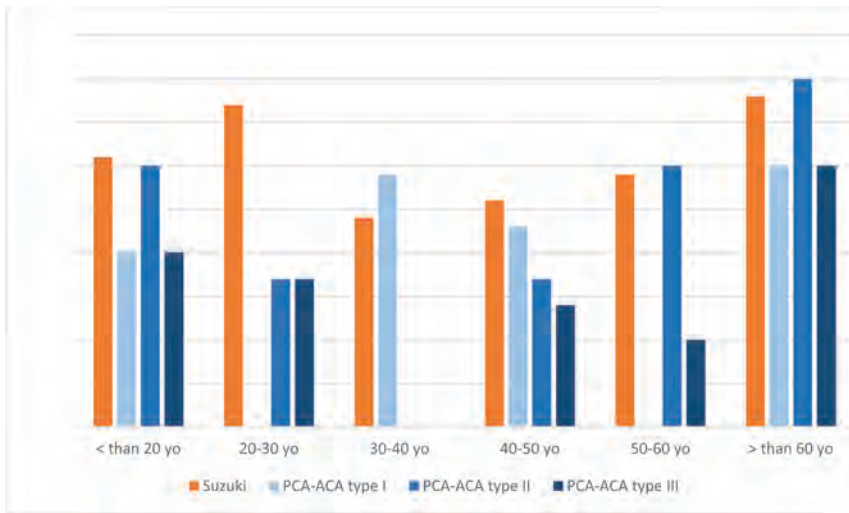


**FIG 2.** Diagram representation of the distribution of Suzuki scores and PCA-ACA anastomosis depending on the age group.

the anesthetic induction. The mean follow-up period was 58 months (range, 3–146 months). At the last visit, 14 patients (25%) presented with a poor clinical outcome (mRS  $\geq 3$ ). It was directly correlated with the clinical presentation of the patient before the treatment and also with the age at diagnosis of the patient (the older the patient is at diagnosis, the worse the clinical outcome). Among the 14 patients with a poor clinical outcome, the median age was 41 years with only 2 patients younger than 20 years of age.

## DISCUSSION

Moyamoya disease is a progressive neurovascular pathology defined by stenosis of the distal internal carotid artery and middle and anterior cerebral arteries associated with the development of vascular collaterals.<sup>1,2,10</sup> The progressive stenosis of the internal carotid artery often causes a lack of flow in the vascular territories of the ACA and the MCA.<sup>5,7</sup> The anastomosis between the posterior and the anterior circulations can provide to refill the territories pertaining to the ACA, especially when the occlusion is proximal to the ophthalmic artery.<sup>6,7</sup>

The scientific literature regarding this pathology is limited because of the rarity of Moyamoya disease,<sup>4</sup> and most articles are dedicated to the description of the surgical techniques and their outcomes. Only a few authors<sup>6-9</sup> have provided detailed angiographic descriptions of the different types of collaterals that naturally develop. Thus, many questions related to the frequency, presence of repeatable patterns, and associations of collaterals with specific phases of the pathology still remain open.

A great contribution to our knowledge was by Baltasvias et al,<sup>6,7</sup> who classified the different anastomoses into 2 superficial-meningeal systems (leptomeningeal or pio-pial and duro-pial) and 2 deep parenchymal systems (subependymal and thalamic). Among these systems, we decided to analyze the one between the posterior cerebral artery and the anterior cerebral artery. Although it is known that the posterior circulation may provide

collaterals that supply the ACA vascular territories, as described by Baltasvias et al,<sup>6</sup> a detailed analysis of the involved vessels is not available in the literature.

The first ACA-PCA collaterals found in our series came from branches of the posterior pericallosal artery or splenial artery. This anastomosis between the anterior and posterior circulations is often present in normal hemispheres;<sup>13</sup> however, it can acquire an important role in Moyamoya disease. In fact, these collaterals could supply, through retrograde flow, the territory of the anterior cerebral artery in case of proximal occlusion of the ICA or if there is poor development of collaterals from the anterior circulation. This posterior pericallosal artery is considered a cortical branch of the parieto-occipital artery, which gives an anastomosis to the anterior pericallosal artery (from the ACA) dorsal to the splenium of the corpus callosum.<sup>12</sup> Zeal and Rhoton<sup>14</sup> showed that this posterior pericallosal artery could also arise from the calcarine (12%), choroidal (12%), or posterior temporal (6%) branches of the PCA. This direct anastomosis between anterior and posterior pericallosal arteries contributes to the pial network around the splenium of the corpus callosum, which could be interpreted as one of the remnants of the embryonic limbic arch.<sup>15</sup>

The other frequent ACA-PCA anastomosis we found in our series is the connection between the posterior choroidal arteries and the anterior pericallosal artery. The posterior choroidal arteries, first described by Abbie in 1934,<sup>16</sup> are usually connected to the anterior circulation within the choroid plexus. In fact, the latter is usually supplied anteriorly by the anterior choroidal artery and the ACA and posteriorly by the posterior choroidal arteries. Our hypothesis to explain the development of these collaterals comes from the analysis of the embryologic stage of arterial development. In the early choroidal stage, the choroidal plexus is principally supplied by choroidal branches of the anterior cerebral and anterior choroidal arteries that anastomose near the interventricular foramen.<sup>17</sup> Then, the posterior choroidal arteries develop from the caudal division of the internal carotid artery (future posterior cerebral artery) and also supply the choroidal plexus of the lateral and third ventricles, creating other anastomoses to branches of the ACA and anterior choroidal artery. At this telencephalic stage (before the complete development and closure of the corpus callosum), the choroidal plexus of the lateral and third ventricles is consequently supplied by choroidal branches from 3 different systems (the anterior cerebral, anterior choroidal, and posterior choroidal arteries) and the interventricular foramen is an important place of anastomosis between these branches. During the progressive closure of the corpus callosum, choroidal branches of the ACA are elongated at the dorsal aspect of the splenium, and this elongation contributes to the regression of these choroidal branches.

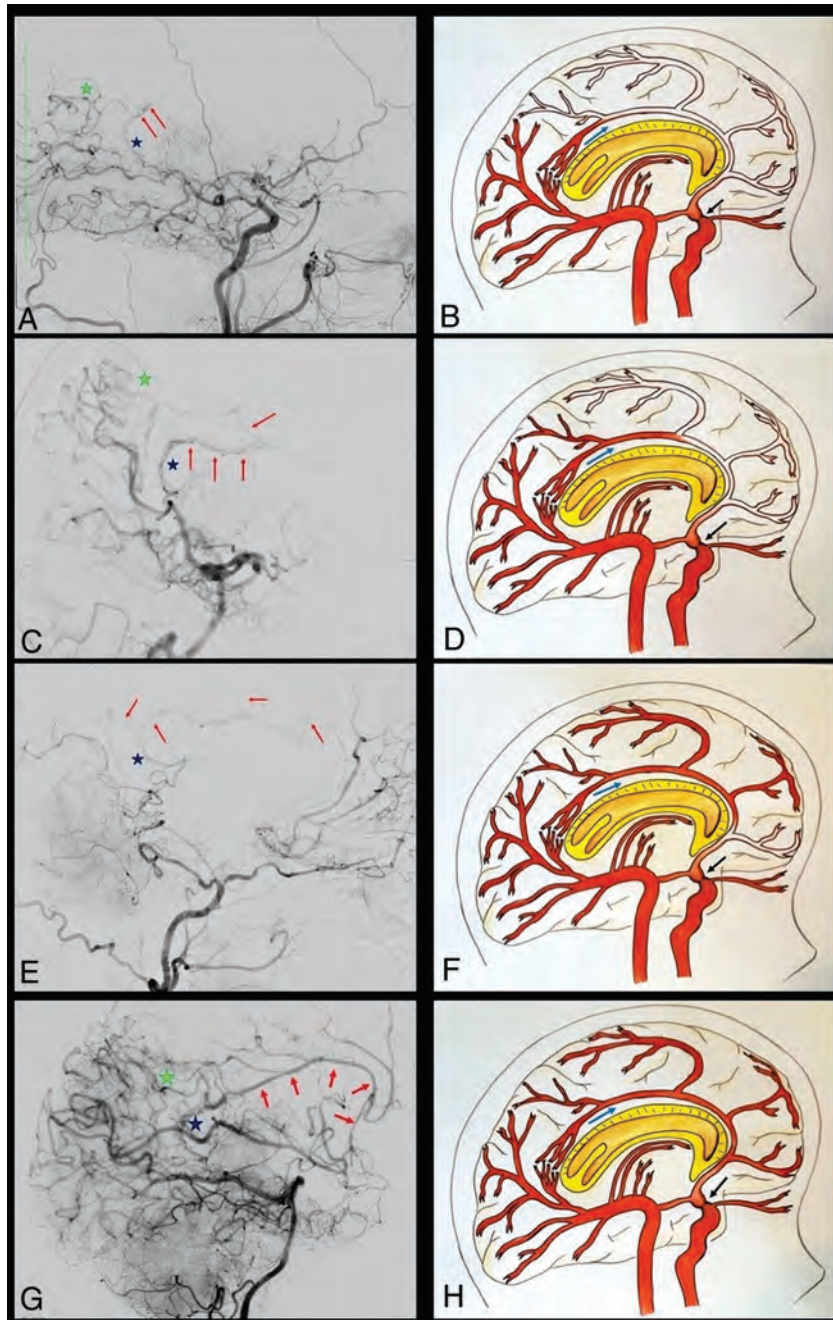


**FIG 3.** A–D, The angiograms and graphic illustrations show the capacity to compensate the ACA territories by the PCA-ACA anastomoses in case of proximal ICA stenosis (black arrow), through a 4-grade classification. In grade I (A and B), the collaterals refill just the first part of the ACA, without seeing any cortical branch. The angiogram on the left shows that the contribution to the refilling is made by the posterior pericallosal artery (blue star) and by pio-pial connections (green star). C and D, The retrograde flow reaches a larger part of the ACA, also highlighting a cortical branch of the ACA (grade II). A double contribution from the pio-pial connection (green star) and medial posterior choroidal artery (blue star) is visible in the angiogram. Grade III (E and F) consists of the retrograde refilling of 2 or 3 ACA branches (red arrows in E), which, in this case, are supported by a medial posterior choroidal artery–anterior pericallosal artery anastomosis. In grade IV, almost all the ACA territory is retrogradely refilled (G and H). The green and blue stars indicate the 2 main connections that compensate the ACA territories hypoperfusion.

Simultaneously, the choroidal territory of the ACA branches is competitively supplied by branches of the posterior choroidal arteries.

The fact that the choroidal plexus is initially served mainly by branches of the ACA and that these are progressively replaced by branches of the PCA explains the possibility of finding this type of ACA-PCA anastomosis in the adult configuration. The anastomotic system between these 2 arteries is under the control of an embryonic arterial arcade or its remnants, known as the “limbic arterial arch.” This arch was first described by Moffat<sup>18</sup> in 1961 and usually represents a transient stage during ontogenesis; however, sometimes it can also persist in adults. Lasjaunias et al<sup>12</sup> described 2 types of persisting limbic arch: the first or “true” limbic arch links the anterior choroidal artery to the ACA around the limbic structures; in the second one, the PCA takes over the anterior choroidal artery role and is linked to the ACA. In this latter case, the arch supplies the corpus callosum and multiple connections are present between the ACA and posterior choroidal artery passing around the splenium of the corpus callosum. Our impression is that the choroidal collaterals we found are linked to the ACA through the limbic arterial arch (type II). This arch could persist as described by Lasjaunias et al<sup>12</sup> or could be restored after a chronic ischemic stimulus.

Another type of collateral described in our series is a pio-pial or leptomeningeal connection between the parenchymal branches of the posterior cerebral artery and posterior branches of the anterior cerebral artery. This kind of anastomosis has already been described by Baltasvias et al<sup>6,7</sup> and mostly consists of the anastomosis between PCA and ACA parietal branches or between PCA and MCA parietal or temporal branches at the watershed zones.

Another possible anastomosis between the ACA and PCA is a choroidal anastomosis located at the level of the interventricular foramen. No case presenting this anastomosis was found in our series, probably only due to the absence of selective DSA. This is a possible anastomosis between the posterior choroidal arteries and hypothalamic branches of the anterior communicating artery. This anastomosis could also be explained by the embryologic vascularization of the choroidal plexus and the remnant of the fornix-choroidal

perforators.<sup>16,17</sup> Such branches and anastomosis have been described in other pathologies such as choroidal arteriovenous malformations or vein of Galen malformations.<sup>12</sup>

Our hypothesis is that after an ischemic stimulus from these regions, the vascular system responds by using a pre-existing anastomosis, whose flow could be improved by neovascularization, to refill retrogradely the ACA territories.

We also observed that most of these collaterals from the posterior circulation were present in advanced stages of the disease. It may suggest the necessity of supplying the ACA territories when the ICA stenosis becomes more severe and does not allow the ophthalmic artery to sufficiently supply the ACA territories through its collaterals.

The analysis of our results shows that the anastomotic circles were present in 10% of cases in Suzuki stage IV (8 hemispheres) and in 10% in Suzuki<sup>13</sup> stage VI (8 hemispheres). These connections were less common in stage 0 (1 hemisphere, 1.25%), stage I (1 hemisphere, 1.25%), stage II (4 hemispheres, 5%), stage III (4 hemispheres, 5%) and stage V (4 hemispheres, 5%).

Our impression is that the lack of blood supply in the ischemic areas stimulates the development of collaterals in patients affected by Moyamoya disease. The aim of this study was to give a more detailed view of the possible anastomoses between the posterior and the anterior cerebral circulations, to understand the evolution of these collaterals to better manage these patients.

### Limitations

Our study is retrospective, based on conventional cerebral DSA, without selective injection to evaluate the anastomosis between the posterior cerebral artery and the anterior cerebral artery. The other important limitation is that most of our patients had only 1 conventional diagnostic DSA and thereafter were followed by MR imaging. Consequently, it is not possible to evaluate the development of the collateral circles during the evolution of Moyamoya disease.

### CONCLUSIONS

We found 3 different types of anastomoses between the posterior and the anterior circulations, with different abilities to compensate retrogradely the anterior circulation. These collaterals are frequent in Moyamoya disease, particularly in advanced Suzuki stages IV to VI. Their development depends on the lack of blood supply to the ACA territories and on the ability to compensate the other 3 collateral systems (ophthalmic-ACA anastomosis, duro-pial anastomosis, and leptomeningeal anastomosis). The analysis of these collateral circles through selective contrast injection into the posterior cerebral artery and detailed analysis of the other anastomotic circles would be helpful to understand the

natural history of the disease and to better select patients who need bypass surgery.

Disclosures: Alexander G. Weil—UNRELATED: Employment: Dr. A. G. Weil, Inc. Michael Reinert—UNRELATED: Grants/Grants Pending: Neuro-oncology. \*Michel Bojanowski—UNRELATED: Employment: Center Hospitalier de l'Université de Montréal. \*Money paid to the Institution.

### REFERENCES

1. Bang OY, Fujimura M, Kim SK. **The pathophysiology of Moyamoya disease: an update.** *J Stroke* 2016;18:12–20 CrossRef Medline
2. Burke GM, Burke AM, Sherma AK. **Moyamoya disease: a summary.** *Neurosurg Focus* 2009;26:E11 CrossRef Medline
3. Scott RM, Smith ER. **Moyamoya disease and moyamoya syndrome.** *N Engl J Med* 2009;360:1226–37 CrossRef Medline
4. Kim JS. **Moyamoya disease: epidemiology, clinical features, and diagnosis.** *J Stroke* 2016;18:2–11 CrossRef Medline
5. Kwag HJ, Jeong DW, Lee SH, et al. **Intracranial hemodynamic changes during adult moyamoya disease progression.** *J Clin Neurol* 2008;4:67–74 CrossRef Medline
6. Baltasavias G, Khan N, Filipce V, et al. **Selective and superselective angiography of pediatric moyamoya disease angioarchitecture in the posterior circulation.** *Interv Neuroradiol* 2014;20:403–12 CrossRef Medline
7. Baltasavias G, Khan N, Valavanis A. **The collateral circulation in pediatric moyamoya disease.** *Childs Nerv Syst* 2015;31:389–98 CrossRef Medline
8. Robert T, Ciccio G, Sylvestre P, et al. **Anatomic and angiographic analyses of ophthalmic artery collaterals in Moyamoya disease.** *AJNR Am J Neuroradiol* 2018;39:1121–26 CrossRef Medline
9. Matsushima Y, Inaba Y. **The specificity of the collaterals to the brain through the study and surgical treatment of moyamoya disease.** *Stroke* 1986;17:117–22 CrossRef Medline
10. Suzuki J, Takaku A. **Cerebrovascular “moyamoya” disease: disease showing abnormal net-like vessels in base of brain.** *Arch Neurol* 1969;20:288–99 CrossRef Medline
11. Rhoton AL Jr. **The supratentorial arteries.** *Neurosurgery* 2002;51:S1–53–20 CrossRef Medline
12. Lasjaunias P, Brugge KG, Berenstein A. *Surgical Neuroangiography.* New York: Springer-Verlag; 2006
13. Kahilogullari G, Comert A, Ozdemir M, et al. **Arterial vascularization patterns of the splenium: an anatomical study.** *Clin Anat* 2013;26:675–81 CrossRef Medline
14. Zeal AA, Rhoton AL Jr. **Microsurgical anatomy of the posterior cerebral artery.** *J Neurosurg* 1978;48:534–59 CrossRef Medline
15. Ture U, Yasargil MG, Krisht AF. **The arteries of the corpus callosum: a microsurgical anatomic study.** *Neurosurgery* 1996;39:1075–84; discussion 1084–85 CrossRef Medline
16. Abbie AA. **The morphology of the fore-brain arteries, with especial reference to the evolution of the basal ganglia.** *J Anat* 1934;68:433–70 Medline
17. Padgett DH. **The development of the cranial arteries in the human embryo.** *Contributions to Embryology* 1948;32:205–06
18. Moffat DB. **The development of the posterior cerebral artery.** *J Anat* 1961;95:485–94 Medline

# Validation of Highly Accelerated Wave–CAIPI SWI Compared with Conventional SWI and T2\*-Weighted Gradient Recalled-Echo for Routine Clinical Brain MRI at 3T

J. Conklin, M.G.F. Longo, S.F. Cauley, K. Setsompop, R.G. González, P.W. Schaefer, J.E. Kirsch, O. Rapalino, and S.Y. Huang



## ABSTRACT

**BACKGROUND AND PURPOSE:** SWI is valuable for characterization of intracranial hemorrhage and mineralization but has long acquisition times. We compared a highly accelerated wave–controlled aliasing in parallel imaging (CAIPI) SWI sequence with 2 commonly used alternatives, standard SWI and T2\*-weighted gradient recalled-echo (T2\*W GRE), for routine clinical brain imaging at 3T.

**MATERIALS AND METHODS:** A total of 246 consecutive adult patients were prospectively evaluated using a conventional SWI or T2\*W GRE sequence and an optimized wave–CAIPI SWI sequence, which was 3–5 times faster than the standard sequence. Two blinded radiologists scored each sequence for the presence of hemorrhage, the number of microhemorrhages, and severity of motion artifacts. Wave–CAIPI SWI was then evaluated in head-to-head comparison with the conventional sequences for visualization of pathology, artifacts, and overall diagnostic quality. Forced-choice comparisons were used for all scores. Wave–CAIPI SWI was tested for superiority relative to T2\*W GRE and for noninferiority relative to standard SWI using a 15% noninferiority margin.

**RESULTS:** Compared with T2\*W GRE, wave–CAIPI SWI detected hemorrhages in more cases ( $P < .001$ ) and detected more microhemorrhages ( $P < .001$ ). Wave–CAIPI SWI was superior to T2\*W GRE for visualization of pathology, artifacts, and overall diagnostic quality (all  $P < .001$ ). Compared with standard SWI, wave–CAIPI SWI showed no difference in the presence or number of hemorrhages identified. Wave–CAIPI SWI was noninferior to standard SWI for the visualization of pathology ( $P < .001$ ), artifacts ( $P < .01$ ), and overall diagnostic quality ( $P < .01$ ). Motion was less severe with wave–CAIPI SWI than with standard SWI ( $P < .01$ ).

**CONCLUSIONS:** Wave–CAIPI SWI provided superior visualization of pathology and overall diagnostic quality compared with T2\*W GRE and was noninferior to standard SWI with reduced scan times and reduced motion artifacts.

**ABBREVIATIONS:** CAIPI = controlled aliasing in parallel imaging; GRE = gradient recalled-echo; MARS = Microbleed Anatomical Rating Scale

SWI is widely applied for clinical brain imaging due to its exquisite sensitivity for the detection and characterization of blood products, superior to that of conventional T2\*-weighted gradient recalled-echo (T2\*W GRE) imaging.<sup>1</sup> SWI is useful in the evaluation of a broad range of pathology including vascular malformations, hemorrhagic or calcified neoplasms, vasculopathies, and neurodegenerative disorders associated with

mineralization or brain iron accumulation.<sup>2,3</sup> However, conventional SWI is associated with long acquisition times (typically  $\geq 5$  minutes),<sup>1</sup> which may contribute to motion artifacts<sup>4</sup> and patient anxiety.<sup>5</sup>

Wave–controlled aliasing in parallel imaging (CAIPI) is a rapid acquisition approach that combines a corkscrew gradient trajectory with CAIPI shifts in the  $k_y$  and  $k_z$  directions to efficiently encode  $k$ -space and uniformly spread the voxel aliasing,

Received March 5, 2019; accepted after revision September 9.

From the Department of Radiology (J.C., M.G.F.L., S.F.C., K.S., R.G.G., P.W.S., J.E.K., O.R., S.Y.H.), Massachusetts General Hospital, Boston, Massachusetts; Athinoula A. Martinos Center for Biomedical Imaging (S.F.C., K.S., S.Y.H.), Boston, Massachusetts; and Harvard-MIT Division of Health Sciences and Technology (K.S., S.Y.H.), Massachusetts Institute of Technology, Cambridge, Massachusetts.

J. Conklin and M.G.F. Longo contributed equally to this work.

This work was supported by the National Institutes of Health (P41 EB015896, R01 EB020613, UL ITR002541), a Radiological Society of North America Research Resident Grant (S.Y.H.), and Siemens Healthineers. This work was conducted with support from Harvard Catalyst, Harvard Clinical and Translational Science Center (National Center for Advancing Translational Sciences, National Institutes of Health Award UL ITR002541), and financial contributions from Harvard University and its affiliated academic health care centers.

The content is solely the responsibility of the authors and does not necessarily represent the official views of Harvard Catalyst, Harvard University and its affiliated academic healthcare centers, or the National Institutes of Health.

Please address correspondence to J. Conklin, MD, MSc, Division of Neuroradiology, Department of Radiology, Massachusetts General Hospital, 55 Fruit St, GRB-273A, Boston, MA, 02114; e-mail: jconklin1@mg.harvard.edu

Indicates open access to non-subscribers at www.ajnr.org

Indicates article with supplemental on-line tables.

Indicates article with supplemental on-line photo.

<http://dx.doi.org/10.3174/ajnr.A6295>

taking full advantage of the 3D coil sensitivity information to provide high acceleration factors with negligible artifacts and g-factor penalty.<sup>6,7</sup> SWI is well-suited for this aggressive acceleration strategy due to the intrinsically high contrast between the pathology of interest (which manifests as a signal void) and background brain tissue. The resulting decrease in acquisition time may facilitate broader clinical application of SWI, especially in motion-prone populations (eg, children, elderly, and acutely ill patients). Wave-CAIPI has shown the potential to accelerate susceptibility-weighted acquisitions in healthy volunteers<sup>8,9</sup> but has not been systematically evaluated in a clinical setting.

The goal of this study was to compare a highly accelerated SWI sequence based on wave-CAIPI (wave-SWI) with 2 commonly used alternatives, conventional 3D-SWI and 2D T2\*W GRE. We hypothesized that wave-SWI would be superior to T2\*W GRE for visualization of pathology and overall diagnostic quality in a similar scan time and noninferior to the standard SWI sequence with a 3- to 5-fold reduction in scan time.

## MATERIALS AND METHODS

### **Subjects and Study Design**

A prospective comparative study was performed at a single institution (Massachusetts General Hospital, Boston, MA). Consecutive adult patients (older than 19 years of age;  $n = 246$ ) undergoing clinical brain MR imaging were prospectively evaluated, including both inpatient and outpatient examinations. Imaging was performed on a 3T Magnetom Prisma scanner from March to June 2018 and on a 3T Magnetom Skyra MR imaging scanner from May to June 2018 (Siemens, Erlangen, Germany). There were no exclusion criteria beyond those for routine clinical MR imaging. The study was Health Insurance Portability and Accountability Act-compliant and approved by our institutional review board. Verbal consent was obtained before MR imaging. Written consent was waived by the institutional review board. Demographics of the study subjects and clinical indications for MR imaging are shown in On-line Table 1.

### **Wave-CAIPI SWI Pulse Sequence and Reconstruction**

Wave-SWI was implemented using a work-in-progress dual-echo 3D gradient-echo pulse sequence<sup>6</sup> (WIP1058C; Siemens). On-line reconstruction was performed using an autocalibrated procedure for simultaneous estimation of the parallel imaging reconstruction and true  $k$ -space trajectory (which accounts for potential gradient hardware imperfections),<sup>7</sup> with a reconstruction time of approximately 60 seconds. This included phase unwrapping of the reconstructed multiecho data and a weighted combination that accounted for the TE phase evolution. The standard vendor SWI processing was then performed to produce high-pass-filtered phase images and associated SWI. Pulse sequence parameters could not be exactly matched between the wave-SWI and standard SWI sequences due to vendor constraints on the available parameter options, but they were approximated as closely as possible within the allowable range of parameter values (On-line Table 2).

### **MR Imaging Protocol**

Each patient underwent brain MR imaging on 1 of two 3T MR imaging scanners using commercially available 20- and 32-channel receiver coil arrays (Siemens). Standard institutional brain MR imaging protocols were selected by the radiologist on the basis of the provided clinical indication. Each scan included a conventional magnetic susceptibility-weighted sequence (either standard SWI or T2\*W GRE, decided at the discretion of the protocoling radiologist based on the clinical indication) and a highly accelerated wave-SWI sequence performed immediately before or after the conventional susceptibility-weighted sequence. Acceleration factors of  $R = 3 \times 2$  and  $R = 3 \times 3$  were chosen on the 20-channel and 32-channel coils, respectively, to balance scan time with an acceptable SNR for each coil configuration.<sup>10</sup> The acquisition order alternated on a weekly basis to control for the possible effect of increased patient motion on the later sequence. A summary of the magnetic susceptibility-weighted sequence parameters is provided in On-line Table 2.

### **Image Evaluation**

A semiquantitative grading system based on predetermined criteria was used to compare wave-SWI with the conventional susceptibility-weighted sequence acquired for each patient (standard SWI or T2\*W GRE). The DICOM datasets were anonymized and transferred to an independent workstation. Blinded to patient information and protocol type, 2 neuroradiologists (O.R. and S.Y.H.) with 17 and 7 years of experience, respectively, independently reviewed all images in randomized order. To obtain optimal visualization, adjustments of window widths and levels were allowed. Only the magnetic susceptibility-weighted sequences were evaluated.

To provide a comprehensive assessment of the diagnostic performance of the wave-SWI and conventional susceptibility-weighted sequences, we divided the review sessions into an individual image series analysis ("individual analysis"), in which images obtained using each sequence were presented in isolation, and a head-to-head image series analysis ("head-to-head analysis"), in which images obtained using the wave-SWI and standard magnetic susceptibility-weighted sequence were presented side-by-side with randomly selected left and right screen positions. The individual analysis was conducted in 2 sessions so that only 1 sequence per patient was presented to the reviewer in each session. The individual analysis sessions were separated by at least 2 weeks to minimize memory bias.

In the individual analysis, reviewers evaluated the following: the presence of hemorrhage, the number and location of the cerebral microhemorrhages (if present), the degree of motion, and whether the images were of diagnostic quality (yes or no). Motion was scored on a predefined 4-point scale. To minimize subjectivity, representative images of each motion score were available to reviewers during the evaluation (On-line Figure). Microhemorrhages were defined according to the Microbleed Anatomical Rating Scale (MARS)<sup>11</sup> and were counted by a single reviewer, excluding cases with gross structural lesions (eg, large parenchymal hematoma, infarct, or surgical cavity) that may limit the reliability of the microhemorrhage counts. A subset of 20

randomly selected cases was evaluated by a second reviewer to determine interrater reliability of the microhemorrhage counts.

In the head-to-head analysis, all cases in which either reviewer identified an abnormality on either of the 2 conventional susceptibility sequences in the individual analysis were presented to the reviewers in a separate blinded review, with the wave-SWI and conventional susceptibility-weighted sequence simultaneously displayed on the left and right halves of the screen, labeled image A and image B. The order of the cases and the screen position of the sequences were randomized. The raters compared and scored the 2 sequences for each of the following variables: visualization of pathology (primary outcome), the presence of artifacts (including motion, signal drop-out, and parallel imaging artifacts), and overall diagnostic quality. A predefined 5-point scale was used, in which positive numbers favored the sequence on the right and negative numbers favored the sequence on the left side of the screen (On-line Table 3). Disagreements between readers were adjudicated by a third neuroradiologist (P.W.S.) with >20 years of experience.

### Statistical Analysis

In the individual analysis, we used the McNemar test for comparison of dichotomous variables and the Wilcoxon signed rank test for comparison of ordinal variables between sequences. For motion grading, scores of 0 and 1 (ie, “no motion” and “mild motion that is not clinically relevant”) were combined in a single category, because this distinction was not clinically meaningful. In the head-to-head analysis, we tested for superiority of wave-SWI compared with T2\*WI GRE and for noninferiority of wave-SWI compared with standard SWI. This approach was selected a priori on the basis of our hypothesis that the wave-SWI was comparable with the standard SWI but superior to the T2\*-weighted GRE images. For superiority testing, we compared the ordinal radiologists’ scores using the Wilcoxon signed rank test with the null hypothesis ( $H_0$ ) of no difference between sequences. For noninferiority testing,<sup>12</sup> a noninferiority margin ( $\Delta$ ) of 15% was chosen, with the null hypothesis ( $H_0$ ) that the proportion of cases in which standard SWI was preferred over wave-SWI was >15%. We used the  $z$  statistic to calculate the probability of the standard sequence being preferred over the wave-SWI sequence in >15% of cases ( $H_0 > \Delta$ ), with a type I error rate ( $\alpha$ ) of 0.05. We also calculated the upper bound of the 95% confidence interval for the proportion of cases in which the standard SWI was preferred over wave-SWI (ie, the critical value,  $P_{\text{critical}}$ ).<sup>13</sup> The required sample size was estimated as described by Cohen<sup>14</sup> for a single proportion (the proportion of cases in which visualization of pathology was preferred on standard SWI over wave-SWI), for an effect size of 0.15, a type I error rate ( $\alpha$ ) of 0.05, and a power ( $1-\beta$ ) of 0.90. According to this calculation, a minimum of 63 cases with abnormal findings was required. For dichotomous variables, interrater agreement was evaluated using the unweighted Cohen  $\kappa$  coefficient.

For ordinal variables, interrater agreement was reported using the quadratically weighted Cohen  $\kappa$ , to disproportionately penalize larger disagreements. For the numeric microhemorrhage counts, interrater agreement was reported using the intraclass correlation coefficient. Agreement was interpreted according to

Landis and Koch.<sup>15</sup> We applied a Bonferroni correction for 5 comparisons (the presence of hemorrhage, motion artifacts, visualization of pathology, artifacts, and overall diagnostic quality), with a corrected threshold for a statistical significance of .05/5 = .01. We also performed exploratory univariate testing evaluation for the possible effect of age and study indication on motion scores. For age, we calculated the Pearson correlation coefficient between patient age and the motion score. For indication, we performed a multinomial logistic regression with the indication as the independent variable and motion score as the dependent variable. All statistical calculations were performed using R statistical and computing software, Version 3.4.3 (<http://www.r-project.org/>).

### RESULTS

Wave-SWI was successfully acquired, reconstructed, and evaluated in all 246 cases, including 139 (56.5%) with comparison with T2\*W GRE (Fig 1) and 107 (43.5%) with comparison with standard SWI (Fig 2). Abnormalities were identified in 85 cases with comparison with T2\*W GRE and 65 cases with comparison with standard SWI, which were included in the head-to-head analysis. In the individual analysis, interrater agreement ranged from moderate to almost perfect ( $\kappa = 0.85$  [95% CI, 0.80–0.89] for presence of hemorrhage, 0.52 for motion [95% CI, 0.13–0.90], and 0.49 [95% CI, 0.35–0.63] for diagnostic quality). Interrater agreement for microhemorrhage counts according to the MARS was almost perfect (intraclass correlation coefficient = 0.84 [95% CI, 0.64–0.93] for infratentorial, 0.95 [95% CI, 0.89–0.98] for deep, and 0.98 [95% CI, 0.96–0.99] for lobar microhemorrhages). In the head-to-head analysis, interrater agreement ranged from moderate to substantial ( $\kappa = 0.73$  [95% CI, 0.44–1.00] for evaluation of pathology, 0.63 [95% CI, 0.37–0.93] for artifacts, 0.47 [95% CI, 0.01–1.00] for diagnostic quality). There was a weak positive correlation between patient age and motion score ( $r = 0.289$ ,  $P < .01$ ). There was no significant effect of clinical indication on motion scores.

#### T2\*W GRE × Wave-SWI Comparison

In the individual analysis, hemorrhage was detected more frequently using wave-SWI than T2\*W GRE ( $P < .001$ , On-line Table 4). In 21 cases (15.1%), hemorrhage was identified only on the wave-SWI sequence. These cases included 15 cases of microhemorrhage, 3 cases of parenchymal hemorrhage (>10 mm), 2 cases of postoperative extra-axial hemorrhage, and 1 case of intraventricular hemorrhage. More microhemorrhages were detected using wave-SWI compared with T2\*W GRE ( $P < .01$  for infratentorial,  $P = .01$  for deep, and  $P < .001$  for lobar microhemorrhages; On-line Table 4). Motion artifacts were rated less severe on T2\*W GRE compared with wave-SWI ( $P < .001$ , On-line Table 4); however, there was no significant difference in the number of cases that were rated as nondiagnostic (7 cases with T2\*W GRE versus 6 cases with wave-SWI).

The results of the head-to-head comparison of wave-SWI and T2\*W GRE are shown in Fig 3. Wave-SWI was rated superior to T2\*W GRE for visualization of pathology, the presence of artifacts, overall diagnostic quality, and visualization of normal anatomic structures (all  $P < .001$ ).

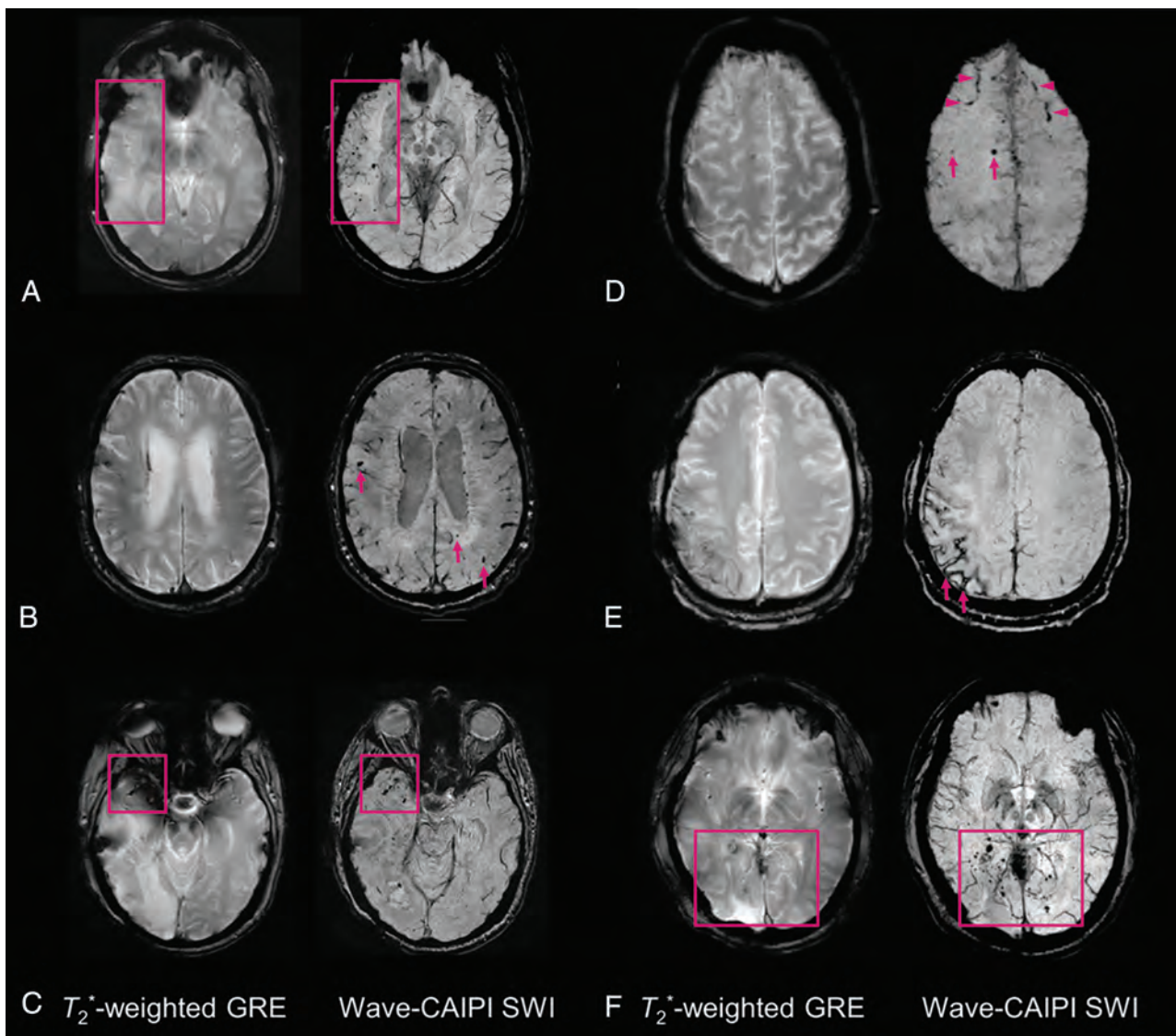


**FIG 1.** Representative images comparing T2\*W GRE and wave-SWI. *A*, Small hemorrhagic foci in the right temporal lobe are clearly seen on wave-SWI but are not well-visualized on T2\*W GRE. These abnormalities fall within the radiation field of a treated right temporal lobe oligoastrocytoma and are presumed to reflect sequelae of radiation-induced vasculopathy. *B*, Multiple cerebral microhemorrhages in a 72-year-old man with history of cardiopulmonary bypass for aortic valve replacement and ascending aortic aneurysm repair, some of which are better seen on wave-SWI and some of which are seen only on wave-SWI (arrows). *C*, Hemorrhagic foci within a right anterior temporal lobe glioblastoma are clearly visualized on wave-SWI but obscured on T2\*W GRE due to signal drop-out artifacts on the GRE sequence. *D*, Scattered foci of parenchymal (arrows) and subarachnoid (arrowheads) hemorrhage in the bilateral frontal lobes are better visualized on wave-SWI than T2\*W GRE. *E*, Superficial hemosiderosis in the right frontoparietal region is better visualized on wave-SWI than T2\*W GRE (arrows) in a patient with a history of multiple craniotomies for a recurrent anaplastic astrocytoma. *F*, Scattered foci of posterior predominant susceptibility effect are well-visualized on wave-SWI and not well-seen on T2\*W GRE (box), in a 58-year-old man with remote radiation therapy to a posterior fossa atypical meningioma. The findings were presumed to reflect postradiation changes (microhemorrhages and/or small cavernous malformations).

### Standard SWI × Wave-SWI Comparison

In the individual analysis, there was no significant difference in the presence or number of hemorrhages identified on the wave-SWI and standard SWI sequences (On-line Table 4). Motion artifacts were rated less severe with wave-SWI compared with standard SWI ( $P < .01$ ), with twice as many cases receiving a motion score of 3 (severe motion that may obscure major findings) on the standard SWI sequence (21 cases, 19.6%) compared with the wave-SWI sequence (9 cases, 9.3%). More cases were rated nondiagnostic on standard SWI (9 cases, 8.4%) than wave-SWI (3

cases, 2.8%); however, the difference was not statistically significant ( $P = .08$ ).

The results of the head-to-head comparison and the associated noninferiority testing are shown in Fig 4. Wave-SWI was noninferior to standard SWI for visualization of pathology ( $P < .001$ ), artifacts ( $P < .01$ ), and overall diagnostic quality ( $P < .01$ ) with a 15% noninferiority margin. The critical value for each noninferiority test is shown in Fig 4, corresponding to the upper bound of a 95% confidence interval on the proportion of cases in which standard SWI is preferred over wave-SWI. This

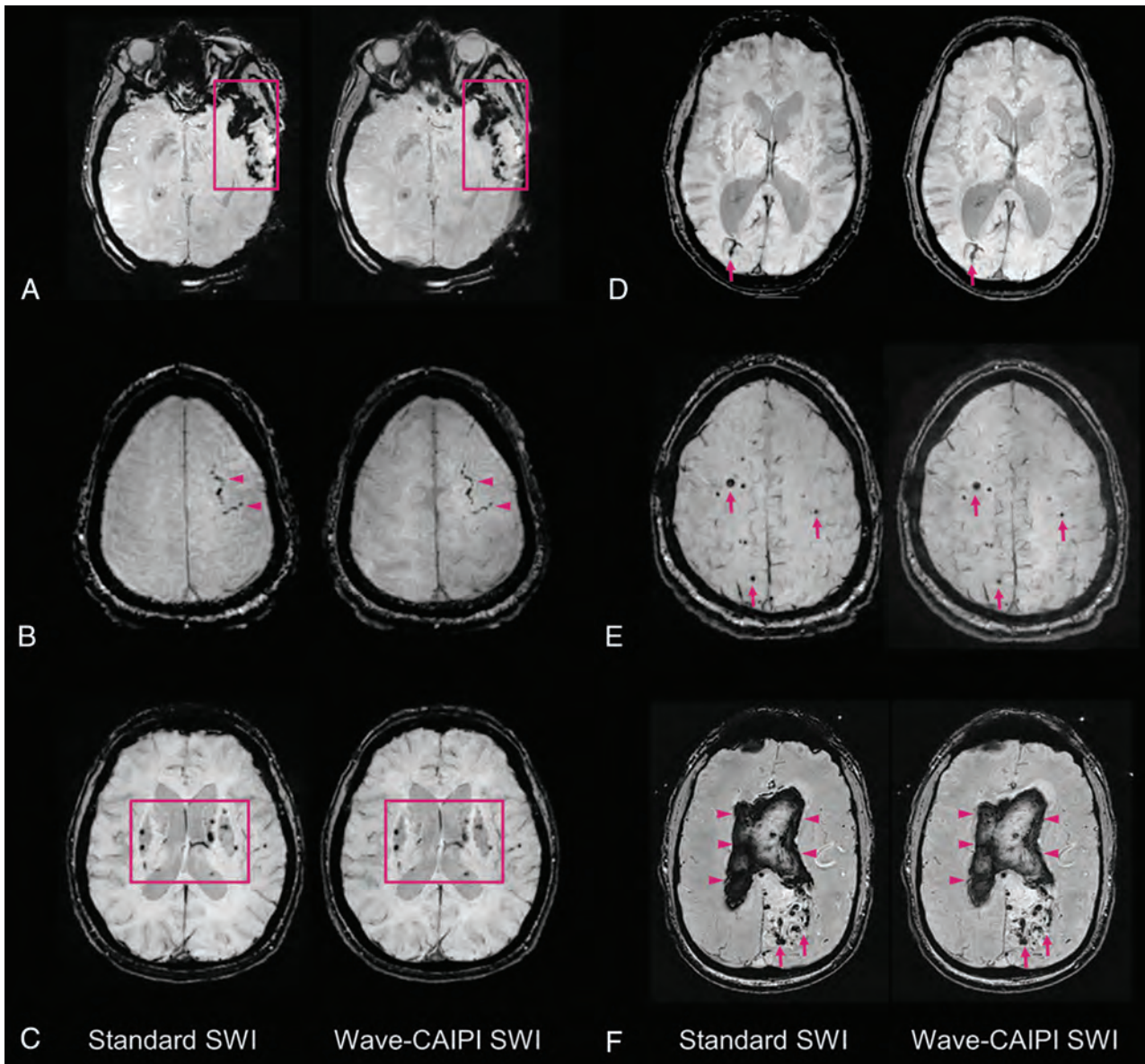


**FIG 2.** Representative images comparing standard SWI and wave-SWI. *A*, Extensive susceptibility effect in the left temporal region in a 33-year-old woman with a history of trauma, corresponding to a combination of parenchymal contusion and subdural and subarachnoid hemorrhage. *B*, Focal subarachnoid hemorrhage in the left superior frontal sulcus (*arrowheads*). *C*, Scattered microhemorrhages throughout the bilateral basal ganglia in a patient with chronic poorly controlled hypertension. *D*, Incidental finding of a right occipital lobe developmental venous anomaly (*arrows*). *E*, Scattered foci of susceptibility effect in a patient with familial multiple cavernous malformations (*arrows*). *F*, Serpiginous foci of susceptibility effect in the left occipital region corresponding to an arteriovenous malformation (*arrows*), with associated rupture and extensive diffuse intraventricular hemorrhage (*arrowheads*). In all cases, visualization of the pathology was rated equivalent (score of 0, On-line Table 3) by both interpreting radiologists.

upper bound ranged from 4% for visualization of pathology to 11% for artifacts and overall diagnostic quality.

## DISCUSSION

This study compared a highly accelerated wave-SWI sequence with 2 commonly used alternative sequences in terms of technical feasibility, visualization of pathology including hemorrhage, and overall diagnostic quality. We included consecutive MR imaging examinations obtained for a wide range of indications to understand the implications of adopting this sequence for routine clinical brain imaging.

Compared with standard T2\*W GRE, wave-SWI provided superior visualization of pathology and overall diagnostic quality, with acquisition times that were approximately 1.5 times faster than standard T2\*W GRE when the 20-channel coil was used and 2 times faster when the 32-channel coil was used. The differences in diagnostic quality were clinically relevant, including 21 cases (15.1%) in which hemorrhage was seen only on wave-SWI. With increasing use of MR imaging in the emergency setting,<sup>16</sup> the ability to rapidly detect acute pathology including hemorrhage is particularly desirable. Detection of even a small number of microhemorrhages is often clinically important. For example,

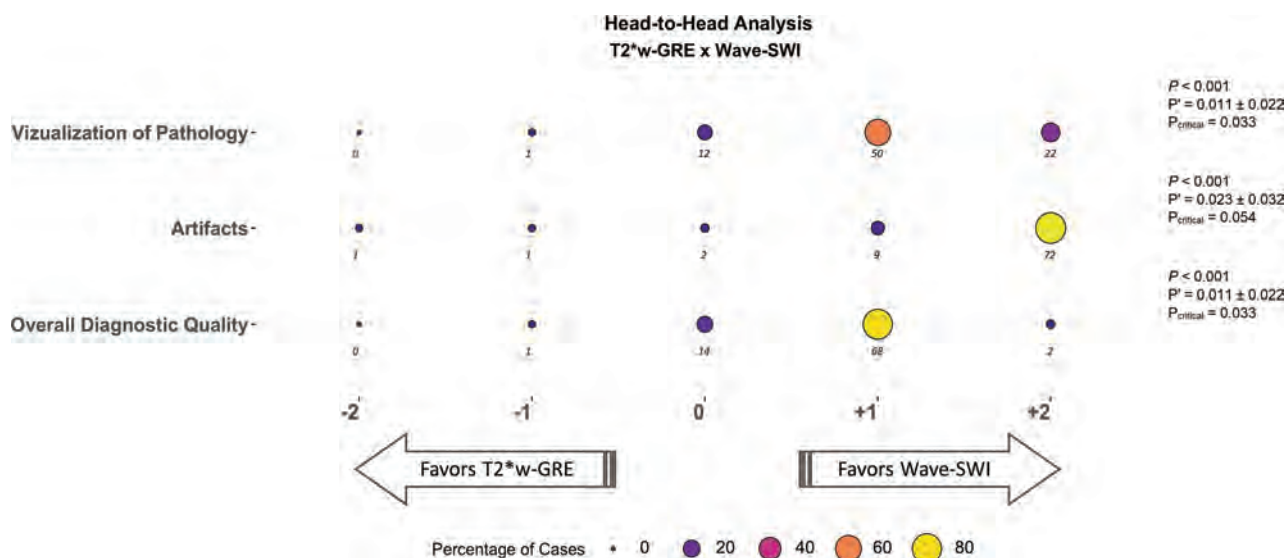


**FIG 3.** Balloonplot showing the results of the head-to-head comparison of T2\*W GRE and wave-SWI. The size and color of each *circle* represent the percentage of cases that were assigned a given score, from a total of 85 cases with abnormal findings. The actual number of cases receiving a given score is indicated below each *circle*. Negative scores (*left*) favor T2\*WI GRE, and positive scores (*right*) favor wave-SWI. The proportion of cases in which T2\*W GRE was preferred over wave-SWI ( $P'$ ) and the 95% confidence interval for this proportion are indicated at the right of the figure. The critical value ( $P_{critical}$ ) is also provided, corresponding to the upper bound of the 95% confidence interval for  $P'$ . Superiority testing was performed as described in the Materials and Methods, and the corresponding  $P$  values are shown in the figure. Wave-SWI was superior to T2\*W GRE for the 3 variables evaluated.

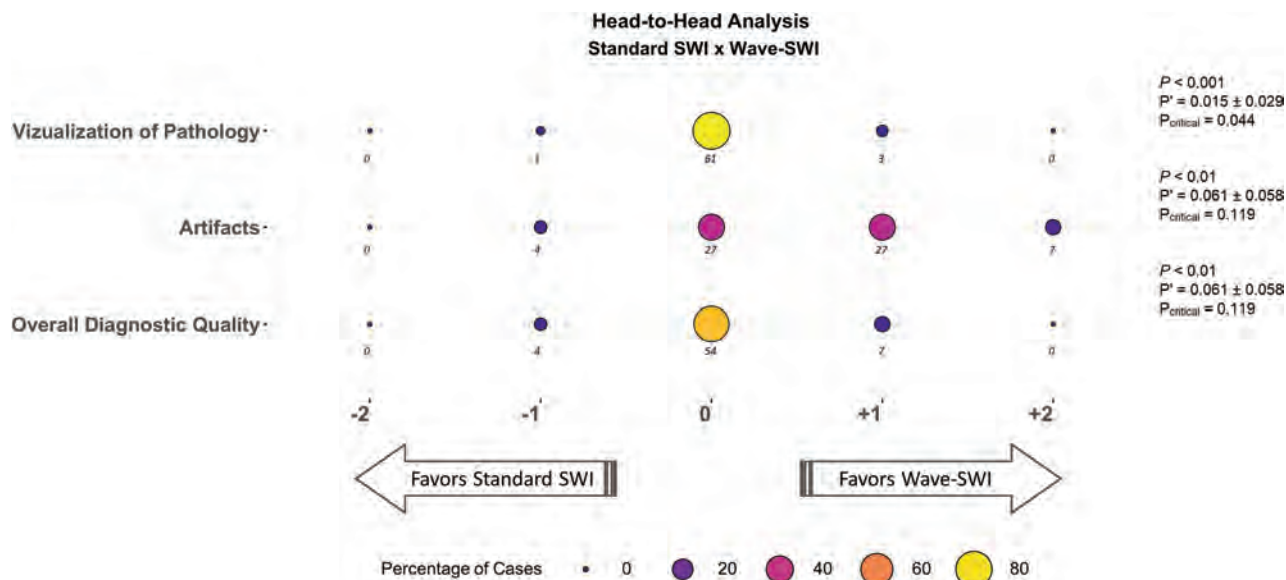


**FIG 4.** Balloonplot showing the results of the head-to-head comparison of standard SWI and wave-SWI. The size and the color of each *circle* represent the percentage of cases that were assigned a given score, from a total of 65 cases with abnormal findings. The actual number of cases receiving a given score is indicated below each *circle*. Negative scores (*left*) favor standard SWI, and positive scores (*right*) favor wave-SWI. The proportion of cases in which T2\*WI GRE was preferred over wave-SWI ( $P'$ ) and the 95% confidence interval for this proportion are indicated at the right of the figure. The critical value ( $P_{critical}$ ) is also provided, corresponding to the upper bound of the 95% confidence interval for  $P'$ . Noninferiority testing was performed as described in the Materials and Methods, and the corresponding  $P$  values are shown in the figure. Wave-SWI was noninferior to standard SWI for the 3 variables evaluated.

in patients who have undergone anticoagulation with a history of atrial fibrillation and recent stroke, the presence of microhemorrhages is associated with intracranial hemorrhage risk and may inform anticoagulation decisions.<sup>17</sup> Artifacts were rated more severe on T2\*W GRE, likely due to thicker slices resulting in

greater through-plane dephasing and signal drop-out near the skull base (Fig 1C). Motion was rated as less severe on T2\*W GRE, likely due to the intrinsically lower motion sensitivity of multisection 2D versus 3D sequences.<sup>18</sup> Thus, the reduced motion sensitivity of T2\*W GRE (and the even faster echo-planar

imaging-based GRE sequences) may provide advantages over wave-SWI in the setting of extreme motion. Our findings suggest that wave-SWI could replace T2\*W GRE for most indications, providing superior visualization of pathology with a 1.5- to 2-fold decrease in scan time, encouraging greater adoption of SWI across clinical brain imaging protocols. Wave-SWI also provides additional information over T2\*W GRE in the form of filtered-phase maps, which can be useful in distinguishing blood products from mineralization.<sup>19</sup>

Wave-SWI was noninferior to standard SWI for visualization of pathology, artifacts, and overall diagnostic quality, with reduced scan time (approximately 3 times faster than standard SWI on the 20-channel coil and 5 times faster on the 32-channel coil) and reduced motion artifacts. Twice as many scans received a motion score of 3 (severe motion that may obscure major findings) using standard SWI, likely a direct consequence of the longer acquisition time. Motion is a common source of image degradation in MR imaging, especially in emergency and inpatient settings, and is associated with substantial institutional cost.<sup>20</sup> Our findings suggest that wave-SWI could replace standard SWI for most indications, improving the use of MR imaging resources while reducing motion artifacts and cost associated with repeat sequence attempts or repeat examinations. The decreased scan time of wave-CAIPI may provide synergistic benefits with other prospective<sup>21</sup> and retrospective<sup>22</sup> motion-correction strategies. For example, the recently proposed Targeted Motion Estimation and Reduction algorithm uses a joint optimization similar to the autocalibrated wave-CAIPI reconstruction,<sup>22</sup> and future work incorporating Targeted Motion Estimation and Reduction directly into the joint reconstruction may provide even further reduction in the motion sensitivity of wave-SWI. Comparison of wave-CAIPI with other acceleration strategies based on compressed sensing<sup>23</sup> and exploiting possible synergies between these approaches would be a valuable area for future study. Further evaluation of multiecho approaches, including the optimal number and spacing of echoes for R2\* mapping and quantitative susceptibility mapping, would also be a valuable extension of this work.

Our study has several limitations. First, it is not possible to compare the diagnostic accuracy of wave-SWI and standard SWI in vivo due to the absence of a reference standard. Because of the similar contrast and image quality of these sequences and the variable nature of patient motion and other image artifacts, detection of a small hemorrhage on wave-SWI but not standard SWI does not necessarily imply a false-positive and could alternatively reflect motion artifacts obscuring the hemorrhage on the standard sequence. To validate wave-SWI as an index test in the absence of a reference standard, we followed the approach described by Reitsma et al<sup>24</sup> by relating the result of the index test to other clinically relevant characteristics—in our case, the impact on the final clinical diagnosis determined by the interpreting radiologist (On-line Table 3). Under this framework, we demonstrated noninferiority of the wave-SWI sequence with respect to the major factors relevant to the interpreting radiologist in rendering a clinical diagnosis.

Although we used a standardized image-based definition of microhemorrhages,<sup>11</sup> we did not have CT correlation to confirm the presence of calcification or follow-up imaging to confirm persistence or expansion of hemorrhage, and it is possible that some

of the microhemorrhages we identified were, in fact, calcifications or other mimics. Second, the selection of a suitable noninferiority margin for imaging studies is often challenging. Our selection was informed by a review of similar imaging-based noninferiority studies<sup>25,26</sup> and consensus among our group of neuroradiologists that the new sequence could be considered noninferior if the standard sequence was preferred in fewer than 15% of cases. Because this threshold is inherently subjective, we also reported the critical value ( $P_{critical}$ ), equivalent to the upper bound on a 95% confidence interval for the proportion of cases in which the standard sequence was preferred. The critical value allows us to understand how selection of a different noninferiority margin would impact the results. For example, with a 25% noninferiority margin, wave-SWI would be deemed noninferior to standard SWI for all of the variables considered ( $P_{critical} < 25\%$  in all cases; Fig 4). With a 5% noninferiority margin, wave-SWI would be deemed noninferior for visualization of pathology (the primary outcome), but not the remaining variables. Third, although readers were blinded to the acquisition protocol, some features of the images may allow the readers to identify the pulse sequence being evaluated. In the case of wave-SWI versus T2\*W GRE, the difference is visibly apparent. In the case of wave-SWI versus standard SWI, we minimized this possibility by matching the most important parameters that determine image quality and image contrast (including nominal voxel dimensions, section thickness, and effective echo time) as closely as possible within the range of allowable parameter values.

## CONCLUSIONS

Wave-SWI provided superior visualization of pathology and overall diagnostic quality compared with T2\*W GRE and was noninferior to standard SWI with reduced scan time and reduced motion artifacts. Broader clinical application of the wave-CAIPI approach may result in more efficient use of MR imaging resources without the loss of clinically important information.

Disclosures: Maria Gabriela F. Longo—RELATED: Other: Siemens Healthineers, Comments: scholarship for postdoctoral program.\* Kawin Setsompop—RELATED: Grant: National Institutes of Health, Comments: R01EB020613.\* Susie Y. Huang—RELATED: Grant: Siemens Healthineers, Comments: received a research grant from Siemens to support a research fellow to carry out clinical validation of wave-controlled aliasing in parallel imaging technology.\* Stephen F. Cauley—RELATED: Grant: National Institutes of Health, Comments: 1R01EB020613-01A1, 1U01HD087211-01, 5P41EB015896-18, 2R01EB006847-09A1\*; UNRELATED: Grants/Grants Pending: Siemens, Comments: Artificial Intelligence fast imaging grant.\* \*Money paid to the institution.

## REFERENCES

1. Nandigam RN, Viswanathan A, Delgado P, et al. **MR imaging detection of cerebral microbleeds: effect of susceptibility-weighted imaging, section thickness, and field strength.** *AJNR Am J Neuroradiol* 2009;30:338–43 CrossRef Medline
2. Haacke EM, Mittal S, Wu Z, et al. **Susceptibility-weighted imaging: technical aspects and clinical applications, Part 1.** *AJNR Am J Neuroradiol* 2009;30:19–30 CrossRef Medline
3. Mittal S, Wu Z, Neelavalli J, et al. **Susceptibility-weighted imaging: technical aspects and clinical applications, Part 2.** *AJNR Am J Neuroradiol* 2009;30:232–52 CrossRef Medline
4. Havsteen I, Ohlhues A, Madsen KH, et al. **Are movement artifacts in magnetic resonance imaging a real problem? A narrative review.** *Front Neurol* 2017;8:1–8 CrossRef Medline

5. Munn Z, Pearson A, Jordan Z, et al. **Patient anxiety and satisfaction in a magnetic resonance imaging department: initial results from an action research study.** *J Med Imaging Radiat Sci* 2015;46:23–29 CrossRef Medline
6. Bilgic B, Gagoski BA, Cauley SF, et al. **Wave-CAIPI for highly accelerated 3D imaging.** *Magn Reson Med* 2015;73:2152–62 CrossRef Medline
7. Cauley SF, Setsompop K, Bilgic B, et al. **Autocalibrated wave-CAIPI reconstruction; joint optimization of k-space trajectory and parallel imaging reconstruction.** *Magn Reson Med* 2017;78:1093–99 CrossRef Medline
8. Bilgic B, Xie L, Dibb R, et al. **Rapid multi-orientation quantitative susceptibility mapping.** *Neuroimage* 2016;125:1131–41 CrossRef Medline
9. Bilgic B, Ye H, Wald LL, et al. **Simultaneous time interleaved multi-slice (STIMS) for rapid susceptibility weighted acquisition.** *Neuroimage* 2017;155:577–86 CrossRef Medline
10. Conklin J, Cauley S, Setsompop K, et al. **Optimization and Clinical Evaluation of Wave-CAIPI Susceptibility-Weighted Imaging (SWI) for Detection of Intracranial Hemorrhage.** In: *Proceedings of the Annual Meeting of the Radiological Society of North America*, Chicago, Illinois. November 25–30, 2018; SSE24-04
11. Gregoire SM, Chaudhary UJ, Brown MM, et al. **The Microbleed Anatomical Rating Scale (MARS): reliability of a tool to map brain microbleeds.** *Neurology* 2009;73:1759–66 CrossRef Medline
12. Ahn S, Park SH, Lee KH. **How to demonstrate similarity by using noninferiority and equivalence statistical testing in radiology research.** *Radiology* 2013;267:328–38 CrossRef Medline
13. Lakens D, Scheel AM, Isager PM. **Equivalence testing for psychological research: a tutorial.** *Adv Advances in Methods and Practices in Psychological Science* 2018;1:259–69 CrossRef
14. Cohen J. *Statistical Power Analysis for the Behavioral Sciences*. 2nd ed. Hillsdale: L. Erlbaum Associates; 1988
15. Landis JR, Koch GG. **The measurement of observer agreement for categorical data.** *Biometrics* 1977;33:159–74 CrossRef Medline
16. Redd V, Levin S, Toerper M, et al. **Effects of fully accessible magnetic resonance imaging in the emergency department.** *Acad Emerg Med* 2015;22:741–49 CrossRef Medline
17. Wilson D, Ambler G, Shakeshaft C, et al. **Cerebral microbleeds and intracranial haemorrhage risk in patients anticoagulated for atrial fibrillation after acute ischaemic stroke or transient ischaemic attack (CROMIS-2): a multicentre observational cohort study.** *Lancet Neurol* 2018;17:539–47 CrossRef Medline
18. Runge VM, Wood ML, Kaufman DM, et al. **FLASH: clinical three-dimensional magnetic resonance imaging.** *Radiographics* 1988;8:947–65 CrossRef Medline
19. Yamada N, Imakita S, Sakuma T, et al. **Intracranial calcification on gradient-echo phase image: depiction of diamagnetic susceptibility.** *Radiology* 1996;198:171–78 CrossRef Medline
20. Andre JB, Bresnahan BW, Mossa-Basha M, et al. **Toward quantifying the prevalence, severity, and cost associated with patient motion during clinical MR examinations.** *J Am Coll Radiology* 2015;12:689–95 CrossRef Medline
21. Callaghan MF, Josephs O, Herbst M, et al. **An evaluation of prospective motion correction (PMC) for high resolution quantitative MRI.** *Front Neurosci* 2015;9:97 CrossRef Medline
22. Haskell MW, Cauley SF, Wald LL. **TARGETED Motion Estimation and Reduction (TAMER): Data consistency based motion mitigation for MRI using a reduced model joint optimization.** *IEEE Trans Med Imaging* 2018;37:1253–65 CrossRef Medline
23. Wu B, Li W, Guidon A, et al. **Whole brain susceptibility mapping using compressed sensing.** *Magn Reson Med* 2012;67:137–47 CrossRef Medline
24. Reitsma JB, Rutjes AWS, Khan KS, et al. **A review of solutions for diagnostic accuracy studies with an imperfect or missing reference standard.** *J Clin Epidemiol* 2009;62:797–806 CrossRef Medline
25. Lee SJ, Park SH, Kim AY, et al. **A prospective comparison of standard-dose CT enterography and 50% reduced-dose CT enterography with and without noise reduction for evaluating Crohn disease.** *AJR Am J Roentgenol* 2011;197:50–57 CrossRef Medline
26. Schaefer PJ, Boudghene FP, Brambs HJ, et al. **Abdominal and iliac arterial stenoses: comparative double-blinded randomized study of diagnostic accuracy of 3D MR angiography with gadodiamide or gadopentetate dimeglumine.** *Radiology* 2006; 238:827–40 CrossRef Medline

# Volumetry of Mesiotemporal Structures Reflects Serostatus in Patients with Limbic Encephalitis

L. Ernst, B. David, J. Gaubatz, I. Domínguez-Narciso, G. Lüchters, A.J. Becker, B. Weber, E. Hattingen, C.E. Elger, and T. Rüber



## ABSTRACT

**BACKGROUND AND PURPOSE:** Limbic encephalitis is an autoimmune disease. A variety of autoantibodies have been associated with different subtypes of limbic encephalitis, whereas its MR imaging signature is uniformly characterized by mesiotemporal abnormalities across subtypes. Here, we hypothesized that patients with limbic encephalitis would show subtype-specific mesiotemporal structural correlates, which could be classified by supervised machine learning on an individual level.

**MATERIALS AND METHODS:** T1WI MPRAGE scans from 46 patients with antibodies against glutamic acid decarboxylase and 34 patients with antibodies against the voltage-gated potassium channel complex (including 10 patients with leucine-rich glioma-inactivated 1 autoantibodies) and 48 healthy controls were retrospectively ascertained. Parcellation of the amygdala, hippocampus, and hippocampal subfields was performed using FreeSurfer. Volumes were extracted and compared between groups using unpaired, 2-tailed *t* tests. The volumes of hippocampal subfields were analyzed using a multivariate linear model and a binary decision tree classifier.

**RESULTS:** Temporomesial volume alterations were most pronounced in an early stage and in the affected hemispheric side of patients. Statistical analysis revealed antibody-specific hippocampal fingerprints with a higher volume of CA1 in patients with glutamic acid decarboxylase-associated limbic encephalitis ( $P=.02$ ), compared with controls, whereas CA1 did not differ from that in controls in patients with voltage-gated potassium channel complex autoantibodies. The classifier could successfully distinguish between patients with autoantibodies against leucine-rich glioma-inactivated 1 and glutamic acid decarboxylase with a specificity of 87% and a sensitivity of 80%.

**CONCLUSIONS:** Our results suggest stage-, side- and antibody-specific structural correlates of limbic encephalitis; thus, they create a perspective toward an MR imaging-based diagnosis.

**ABBREVIATIONS:** CASPR2 = contactin-associated proteinlike 2; EEG = electroencephalogram; GAD = glutamic acid decarboxylase; GAD-LE = limbic encephalitis with glutamic acid decarboxylase-associated autoantibodies; LE = limbic encephalitis; LGI1 = leucine-rich glioma-inactivated 1; VGKC = voltage-gated potassium channel complex; VGKC-LE = limbic encephalitis with voltage-gated potassium channel complex-associated autoantibodies

Limbic encephalitis (LE) is an autoimmune disease defined by subacute short-term memory loss and psychiatric

abnormalities often involving temporal lobe epilepsy.<sup>1–3</sup> Several autoantibodies have been associated with different subtypes of LE, sharing clinical core features like the limbic syndrome, and may be discriminated by other characteristics such as comorbidities and response to immunotherapy.<sup>4,5</sup> Autoantibodies against the voltage-gated potassium channel complex (VGKC) and glutamic acid decarboxylase (GAD) are commonly found in patients with LE with temporal lobe epilepsy.<sup>6</sup> Whereas patients with LE with autoantibodies against GAD and VGKC (GAD-LE and VGKC-LE) all display an early and prominent development of

Received June 21, 2019; accepted after revision September 11.

From the Department of Epileptology (L.E., B.D., J.G., I.D.-N., C.E.E., T.R.), Department of Neuropathology (A.J.B.), Institute for Experimental Epileptology and Cognition Research (B.W.), and Department of Radiology (E.H.), University of Bonn Medical Center, Bonn, Germany; Center for Development Research (G.L.), University of Bonn, Bonn, Germany; Department of Neuroradiology (E.H.), Goethe University Frankfurt, Frankfurt, Germany; and Epilepsy Center Frankfurt Rhine-Main (T.R.), Department of Neurology, and Center for Personalized Translational Epilepsy Research (T.R.), Goethe-University Frankfurt, Frankfurt am Main, Germany.

Leon Ernst received support from the Promotionskolleg Neuroimmunology of the University of Bonn and the Else-Kröner-Fresenius Stiftung. Christian E. Elger received grants from Deutsche Forschungsgemeinschaft, Bundesministerium für Bildung und Forschung, and Marga and Walter Boll Stiftung. Theodor Rüber is supported by the BONFOR research commission of the medical faculty of the University of Bonn.

Paper previously presented, in part, at: Annual Meeting of the German Society for Neurology, November 1–3, 2018, Berlin, Germany; the BonnBrain Conference, March 25–27, 2019, Bonn, Germany; and Annual Meeting of the Organization for Human Brain Mapping, June 9–13, 2019, Rome, Italy.

Please address correspondence to Theodor Rüber, MD, Department of Epileptology, University of Bonn Medical Center, Sigmund-Freud Str 25, 53127 Bonn, Germany; e-mail: theodor.rueber@ukbonn.de

Indicates open access to non-subscribers at [www.ajnr.org](http://www.ajnr.org)

Indicates article with supplemental on-line tables.

<http://dx.doi.org/10.3174/ajnr.A6289>

epileptic seizures, those with VGKC-LE are more responsive to immunotherapy. Recently, 2 antigenic components of the VGKC complex that are targeted by different autoantibodies have been identified: the leucine-rich glioma-inactivated 1 (LGI1) and contactin-associated proteinlike 2 (CASPR2).<sup>7,8</sup> However, 12%–33% of those with VGKC-LE are negative for both of these subantigens.<sup>8,9</sup> Furthermore, the detection of specific autoantibodies may not exclude the presence of other pathologic neuronal autoantibodies yet undiscovered. Therefore, it has been suggested that the diagnosis of LE should rely less on autoantibodies and more on clinical examinations and MR imaging.<sup>3,10</sup>

MR imaging is especially relevant when the results of antibody testing are not yet available, and follow-up scans may be helpful for assessing the response to therapy. However, MR imaging findings correlate imperfectly with the course of disease, and antibody-specific MR imaging signatures have not yet been found on an individual level, though antibody-specific imaging features of LE are increasingly recognized on a group level.<sup>11–14</sup> Thus, neuroimaging research in patients with LE may not only increase our pathophysiologic understanding of this disease but also help to define imaging biomarkers needed on clinical grounds. By harnessing modern techniques for hippocampal subfield segmentation, we sought to bridge the gap between clinical and radiologic findings. Here, we hypothesized that patients with LE would show stage-specific, side-specific, and antibody-specific mesiotemporal structure correlates, which could be classified by supervised machine learning on an individual level.

## MATERIALS AND METHODS

### Subjects

We retrospectively ascertained clinical and MR imaging data from patients with LE who were treated the Department of Epileptology at University of Bonn Medical Center between April 2006 and June 2017 and met the following inclusion criteria: 1) 18 years of age or older, 2) having a diagnosis of a limbic syndrome (with at least 1 of the following symptoms: temporal lobe seizures, episodic memory disturbance, or psychiatric symptoms with affective disturbance), 3) serologically proved autoantibodies against the VGKC complex (or, if tests were available, against its antigenic components LGI1 or CASPR2) or GAD, and 4) availability of at least one 3D T1-weighted MPRAGE MR imaging scan. Bilateral mesiotemporal T2-FLAIR hyperintensities in routine clinical imaging<sup>3</sup> were not considered an inclusion criterion, to avoid a selection bias of image analysis. Forty-six patients with GAD-LE and 34 patients with VGKC-LE were included in the study (80 patients in total, 36 men). Both GAD-LE and VGKC-LE groups were divided into 2 subgroups, respectively, depending on the time point of the MR imaging acquisition: The early group included T1WI scans acquired <24 months after the onset of the first LE-related symptom and is referred to as the early GAD group (23 patients in total, 7 men; age at MR imaging, 34.2 ± 11.2 years) or early VGKC group (25 patients in total, 16 men; age at MR imaging, 59.5 ± 15.2 years). The late group included the most recent available T1WI scans acquired at least 24 months after the onset of epilepsy and is referred to as late GAD group (33 patients in total, 10 men; age at MR imaging, 33.9 ± 12.3 years) or late VGKC group (22 patients in total, 10 men; age at

MR imaging, 57.0 ± 16.8 years).<sup>15</sup> Ten patients from the GAD group and 13 patients from the VGKC group were included in both the early and the late groups because they were scanned repeatedly less than and more than 24 months after the onset of the first LE-related symptom.

Control subjects with no history of psychiatric or neurologic disorders were ascertained and individually matched with regard to sex, age at MR imaging, and MR imaging sequence (see “Image Acquisition”). This process resulted in a total of 4 control groups for the 4 patient groups: an early GAD group, late GAD group, early VGKC group, and late VGKC group (for a summary of patient and controls groups see Table 1; for details, see supporting information in On-line Tables 1 and 2). The study was approved by the local institutional review board, and all participants had provided written informed consent (as part of previous studies).

### Antibody Testing

After 2014, screening for onconeural antibodies was performed using semiquantitative immunoblots coated with recombinant antigen or antigen fragments.

Before 2014, detection of GAD antibodies as well as of VGKC complex antibodies in serum was performed using a radioimmuno-precipitation assay. Antibodies against LGI1 and CASPR2 were detected by indirect immunofluorescence. These tests were not performed before 2010; thus, 13 patients in the early VGKC group and 14 patients in the late VGKC group have not been tested for CASPR2 or LGI1 (for details, see supporting information in On-line Appendix).

### Treatment

Immunotherapy was conducted according to guidelines set forth by the German Society for Neurology and expert opinion. It included first-line steroids, plasma exchange, and intravenous immunoglobulins, as well as second-line azathioprine, mycophenolate mofetil, rituximab, basiliximab, and cyclophosphamide.<sup>2,16,17</sup> Immunotherapy was administered in addition to antiepileptic medication (for a summary see Table 1; for details, see the supporting information in On-line Tables 1 and 2).

### Image Acquisition

Imaging data were acquired on a 3T Magnetom Trio scanner (Siemens, Erlangen, Germany) using an 8-channel receive head coil. For each scan time point, we acquired a T1WI MPRAGE sequence with the following parameters: voxel size = 1.0 × 1.0 × 1.0 mm<sup>3</sup>, TR = 1570 ms, TE = 3.42 ms, flip angle = 15°, matrix = 256 × 256 pixel. Due to a scanner update at the beginning of 2014, T1WI scans after this time point were acquired using a 32-channel head coil and the following parameters: voxel size = 0.8 × 0.8 × 0.8 mm<sup>3</sup>, TR = 1660 ms, TE = 2.54 ms, flip angle = 9°, matrix = 320 × 320 pixel. All control groups were matched with regard to sequence (see above).

### Image Analysis

Volumetric analysis of the hippocampus, hippocampal subfields, amygdala, and intracranial volume was performed using the FreeSurfer, Version 6.0.0 image analysis suite (<http://surfer.nmr.mgh.harvard.edu>).<sup>18,19</sup> The hippocampal substructures segmented by FreeSurfer, Version 6.0.0, included the following:

**Table 1: Demographic and clinical characteristics of subgroups of patients with limbic encephalitis and their corresponding control groups**

	GAD-LE	VGKC-LE	GAD-CON	VGKC-CON
Early group				
No. (men)	23 (7)	25 (16)	23 (7)	25 (16)
Age at MR imaging (mean) (yr)	34.2 ± 11.2	59.5 ± 15.2	35.4 ± 10.6	57.2 ± 13.2
Time between onset <sup>a</sup> and scan (mean) (mo)	9.5 ± 7.4	7.6 ± 6.1	NA	NA
Interictal EEG lateralization	5/12/1/5	7/8/2/8	NA	NA
(n = right/left/bilateral/unclear)				
No. of bilateral mesiotemporal FLAIR-T2-hyperintensities	2	5	NA	NA
No. of first-line immunotherapies	3	9	NA	NA
No. of second-line immunotherapies	0	1	NA	NA
Late group				
No. (men) <sup>b</sup>	33 (10)	22 (10)	33 (10)	22 (10)
Age at MR imaging (mean) (yr)	33.9 ± 12.3	57.0 ± 16.8	34.4 ± 11.9	53.2 ± 13.2
Time between onset <sup>a</sup> and scan (mean) (mo)	62.5 ± 26.2	61.5 ± 23.6	NA	NA
Interictal EEG lateralization	5/11/3/12	4/8/1/9	NA	NA
(n = right/left/bilateral/unclear)				
No. of bilateral mesiotemporal FLAIR-T2-hyperintensities	4	3	NA	NA
No. of first-line immunotherapies	14	18	NA	NA
No. of second-line immunotherapies	6	4	NA	NA

**Note:**—NA indicates not applicable; CON, matched healthy control group.

<sup>a</sup> Onset of the first limbic encephalitis–related symptom.

<sup>b</sup> Patients scanned repeatedly were included in both (early and late) study groups (repeat scans GAD-LE: n = 10; repeat scans VGKC-LE, n = 13).

CA1, CA2/3, CA4, fimbria, hippocampal tail, the hippocampus-amygdala transition area, granule cell layer of the dentate gyrus, presubiculum, parasubiculum, subiculum, molecular layer, and hippocampal fissure. The volume of the hippocampal fissure does not contribute to computation of the whole hippocampal volume and was deliberately excluded from the analysis.<sup>20</sup> Parcellation results were visually checked for accuracy and alignment by 2 independent raters (L.E. and I.D.-N.), supervised by an experienced neuroradiologist (E.H.). In case of inexact alignment, FreeSurfer parcellation was repeated with adjusted parameters. If parcellation results were again rated unsatisfactory by 1 or 2 raters, the subject was excluded. This procedure led to the exclusion of 1 subject from the VGKC group. All analyzed volumes were adjusted by the intracranial volume minus the ventricular volume. Patient-control differences in the hippocampal subfield volume were Z-transformed, color-coded, and visualized in a 3D model of a representative subject.

### Reorientation of Images

For analysis, volumes of the amygdala, hippocampus, and hippocampal subfields were regrouped according to the lateralization in the interictal electroencephalogram (EEG), thus, allowing differential analyses of the affected and unaffected hemispheres to estimate the lateralization of pathologic structural alterations. To control for the effect of a left-right bias, we also regrouped an equal number of controls. If a clear focus could not be determined in the EEG or if a bilateral pathologic pattern was observed, we used the mean values from both hemispheres for statistical analysis.

### Statistical Analysis

Statistical analysis was performed using STATA 2015, Stata Statistical Software, Release 14 (StataCorp, College Station, Texas). The volumetric data of the amygdala and the entire hippocampus were compared between groups using unpaired, 2-tailed *t* tests. The joint effect of group on all hippocampal

subfields was tested by means of a multivariate linear model. Subsequently, post hoc tests were conducted, which were protected by the Fisher least-significant difference.<sup>21</sup> Test results were considered statistically significant if *P* < .05. Visualization of analyses results was with Matlab's Statistics Toolbox (Release 2012b; MathWorks, Natick, Massachusetts).

### Supervised Machine Learning Classification

We set up a binary decision tree classifier using the Scikit-Learn toolkit<sup>22</sup> to distinguish early LE groups on the basis of the volumetry of the hippocampal subfields on the affected side. To prevent age-related brain atrophy (especially in patients with LGI1) from influencing classification results, we corrected all volumetry data for the intracranial volume of the respective subject. Only early LE groups were tested because structural between-group differences may be thought to be most clear-cut at a pretherapeutic stage when potential future clinical applications are most needed. Decision trees are a type of non-parametric supervised statistical learning method.<sup>23</sup> The generalizability of our decision tree was assessed using a leave-one-out cross-validation scheme. Hyperparameter tuning was performed using an exhaustive grid search over the best-split criteria, maximum tree depth, minimum number of samples required to split an internal node, minimum number of samples at a leaf node, and the maximum number of features considered at every split. The F1 score was used as an optimization metric. However, default parameters set by Scikit-Learn yielded the best estimator for our problem (please refer to Scikit-Learn API [<https://keras.io/scikit-learn-api/>] for a full-parameter description and default values). To statistically compare the accuracy of our classifier against chance level, we tested its performance against null distributions by randomly shuffling the group labels in our dataset. In this way, 100,000 unique permutations were tested. The Gini importance of classification features was assessed post hoc on the basis of the model fit.

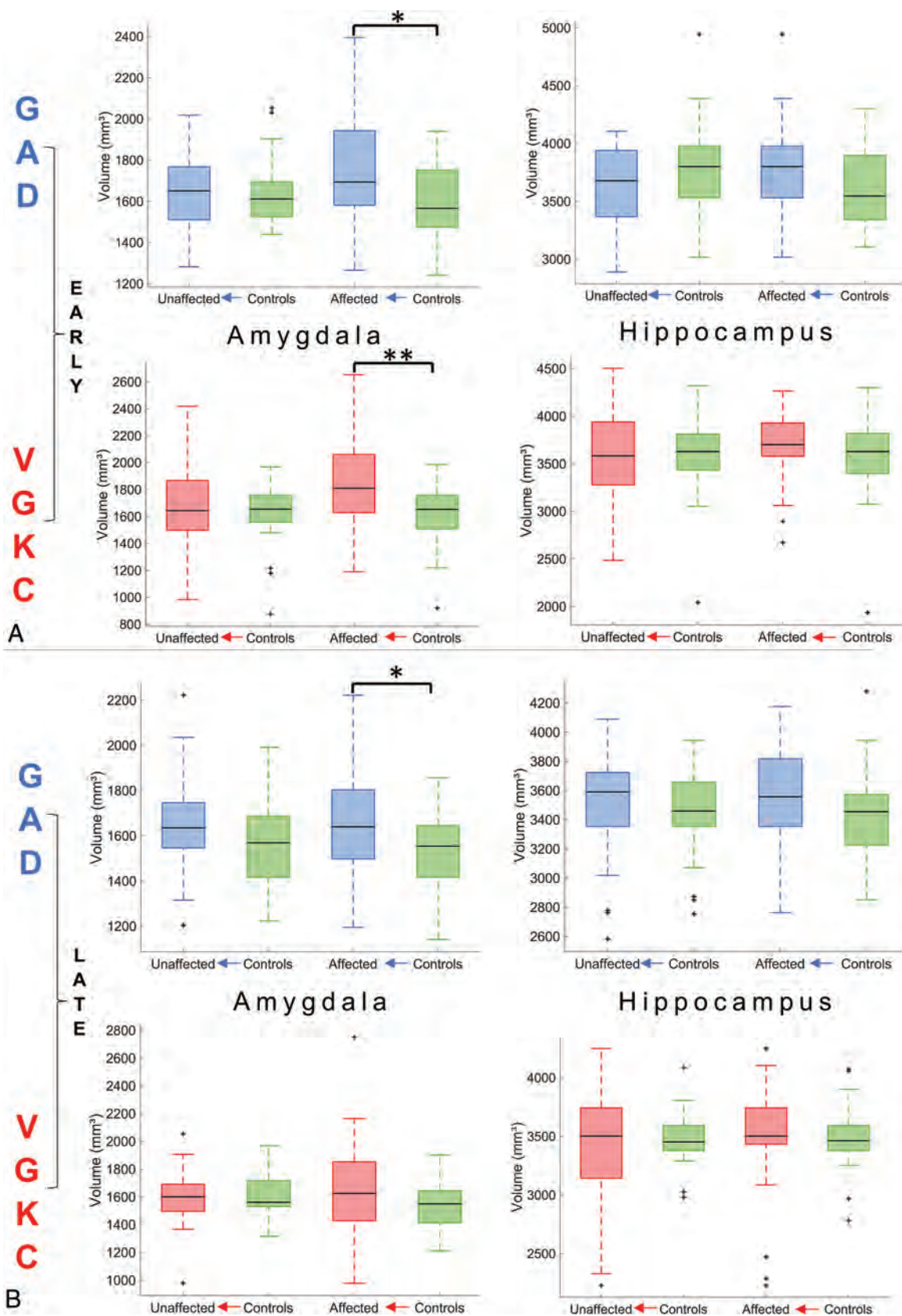


**FIG 1.** Volumetry of the amygdala and hippocampus. *A*, Volumetry in the early group. *B*, Volumetry in the late group. Asterisks represent levels of significance (single asterisk indicates .05; double asterisks, .01).

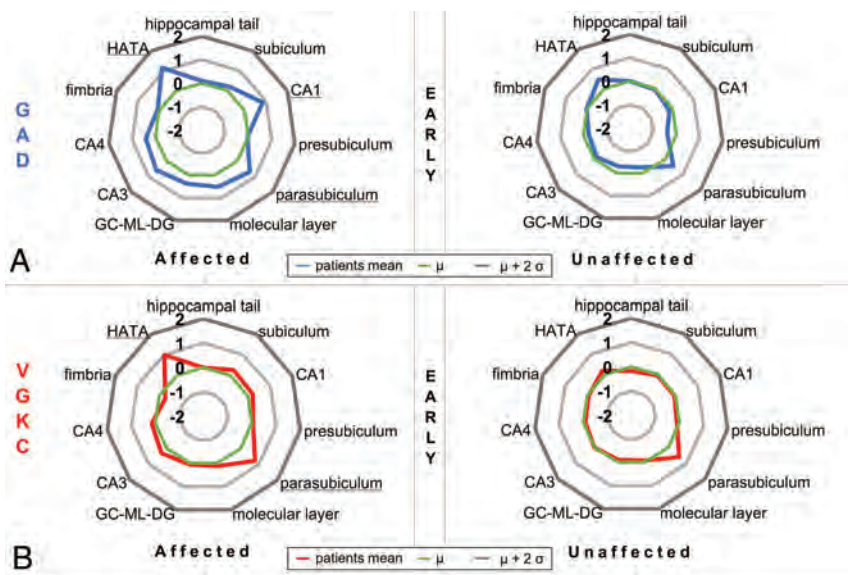


**FIG 2.** Starplots showing hippocampal subfield volume differences between patients in the early group and controls. Z values reflect the hippocampal subfield volume difference between patients in the early group and controls in the affected and the unaffected hemispheric sides. Underlined words indicate statistical significance of the respective hippocampal subfield ( $P < .05$ ) in post hoc tests between patients and controls following a multivariate linear model (see MATERIALS AND METHODS and supporting information in On-line Tables 3–8). A, Relative hippocampal subfield volumes of the affected and unaffected sides of GAD-LE. B, Relative hippocampal subfield volumes of the affected and unaffected sides of VGKC-LE. GC-ML-DG indicates granule cell layer of the dentate gyrus; HATA, hippocampus-amygdala transition area.

## RESULTS

### Volumetry of Amygdala and Hippocampus

Compared with matched controls, the amygdala showed a higher volume in early GAD-LE and late GAD-LE (both,  $P = .03$ ; Fig 1), whereas VGKC-LE showed only a higher volume in the early group ( $P = .004$ ). No group differences between early and late groups and controls were found in the volume of the hippocampus.

### Volumetry of Hippocampal Subfields

Volumetry of hippocampal subfields yielded hippocampal fingerprints specific to the serogroup and hemispheric side. Multivariate linear models indicated statistically significant volume differences between patients and controls in the affected hemisphere for the early GAD group, the late GAD group, and the early VGKC group ( $P < .02$ ), but not for the late VGKC group ( $P = .12$ ). The most noticeable subfield differences were found among the early groups: We observed that volumes of CA1, the hippocampus-amygdala transition area, and the parasubiculum were significantly higher on the affected side in patients with early GAD-LE compared with their matched controls (all,  $P < .04$ ), while in early VGKC-LE, this was the case for the hippocampus-amygdala transition area and the parasubiculum (all  $P < .01$ ; see Fig 2 and supporting information in On-line Tables 3–8). Because 10 patients in the early VGKC group were positively tested for autoantibodies against LGI1, we also compared the patients with LGI1 and the early VGKC group without LGI1 with matched controls and found significant differences ( $P < .01$ , Fig 3). Please see the supporting information in On-line Tables

3–8 and On-line Tables 9 and 10 for the full results of the statistical analyses.

The anatomic 3D visualization of results illustrates subregional volume alterations. This and the schematic plots of Z values as a function of the estimated anatomic distance from the amygdala reveal an anterior-to-posterior gradient with volume-increased hippocampal subfields in the anterior part (as opposed to the posterior part of the hippocampus) only in the early GAD group (Fig 4).

### Classification Performance

The decision tree could successfully distinguish between patients with early LGI1 and early GAD with a specificity of 87% and sensitivity of 80% (positive predictive value = 72.2%; negative predictive value = 90.9%; accuracy = 84.8%; F1 score = 0.76; Fig 3). Permutation testing further confirmed an above-chance classification performance ( $P = .002$ ). A post hoc analysis of feature selection showed the fimbria to be of the highest importance for classification (Gini = 0.49), followed by CA1 (Gini = 0.27), the presubiculum (Gini = 0.13), and the

hippocampal tail (Gini = 0.11). Differentiation between the early GAD group and the early VGKC group reached only a specificity of 59% and a sensitivity of 61% (positive predictive value = 64.1%; negative predictive value = 56.5%; accuracy = 60.4%; F1 score = 0.63), and permutation testing could not confirm an above-chance classification performance ( $P = .16$ ).

## DISCUSSION

This study yields 4 main results: Mesiotemporal volume alterations in patients with antibody-associated LE are most prominent in an early stage (stage-specificity), they primarily occur in the clinically affected hemispheric side (side-specificity), and hippocampal volume alterations are antibody-specific for GAD, VGKC, and LGI1 on a group level (autoantibody-specificity) and may discriminate between GAD and LGI1 on an individual level using a decision tree classifier (classification).

### Stage-Specificity

Between those with GAD-LE and controls, volumetry of the amygdala yields differences in the early and the late groups. Volumetry of VGKC-LE and controls in contrast shows amygdala group differences only in the early group (Fig 1, with supporting information in On-line Table 9). The results of amygdala volumetry are paralleled by results of the multivariate linear model of hippocampal-subfield volumetry (see supporting information in On-line Tables 3–8), whereas no overall differences between patients and controls were found in the entire hippocampal volume (Fig 1). The analysis of stage-specificity in a

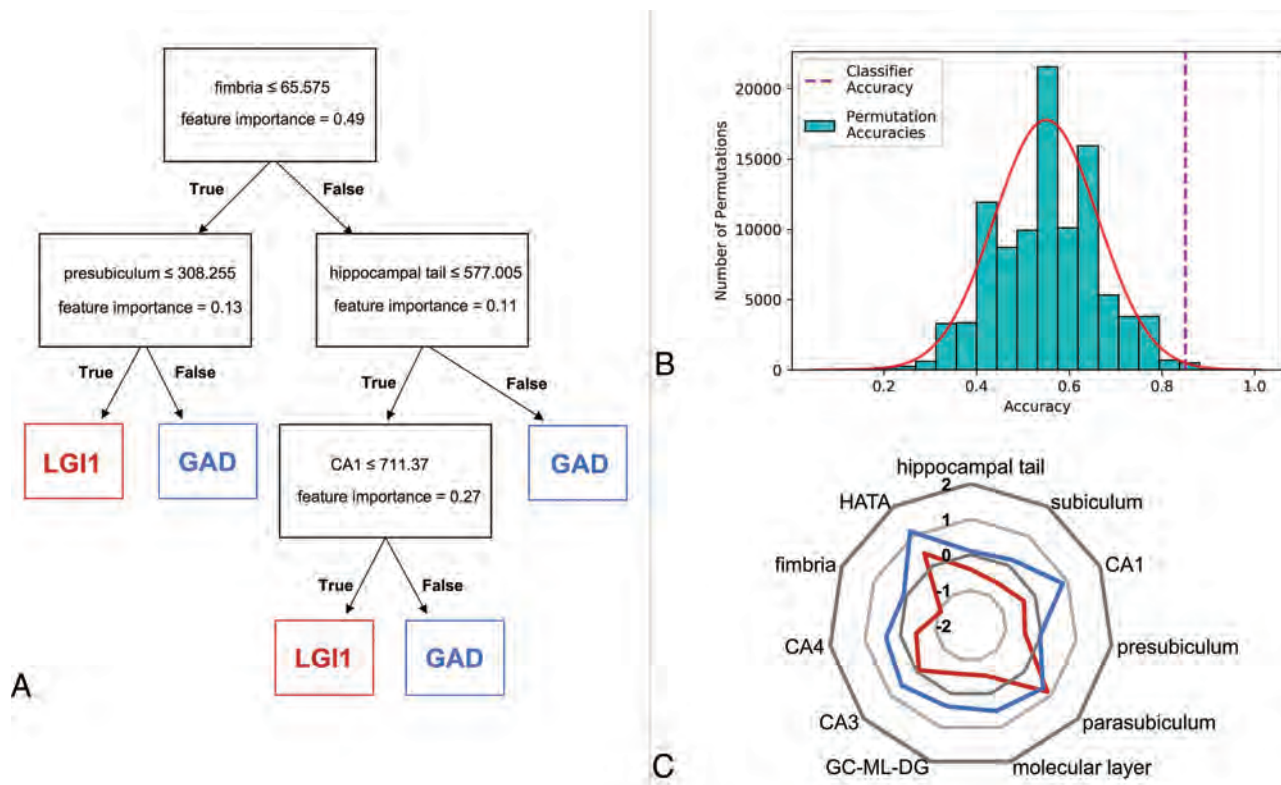


**FIG 3.** Decision tree classification. Decision tree classification between LGI1 and GAD using hippocampal subfield volumes from the hemisphere affected in the EEG in early-stage LE. *A*, Decision tree with importance of features. *B*, Histogram showing the number of label-shift permutations for each accuracy bin. The solid red line displays a fitted Gaussian curve describing the underlying probability density function. The dashed purple line marks the classifier performance on the real data. *C*, Starplot showing Z values of the hippocampal subfield volume differences between LGI1-LE and GAD-LE in the affected hemispheric side (see supporting information in On-line Tables 3 and 5 for statistics). HATA indicates hippocampus-amygdala transition area; GC-ML-DG, granule cell layer of the dentate gyrus.

retrospective clinical study like the current one is challenged by therapeutic interventions. Whereas most patients in the early group had not undergone immunotherapy, most patients in the late group had (see Table 1 and supporting information in On-line Tables 1 and 2). It is, therefore, difficult to determine whether changes observed between the early and the late groups are due to treatment or occur after treatment. Those with GAD-LE have been described as less responsive to immunotherapy compared with those with VGKC-LE, and the conspicuous persistence of mesiotemporal volume alterations in those with late GAD-LE (between-group differences also in late groups) may reflect a poor response to therapy. VGKC-LE, in turn, shows no mesiotemporal volume alterations in the late group, which may be treatment- or disease-related. There has been accruing evidence that abnormal findings on MR imaging are most prominent and specific in the early course of the disease,<sup>24,25</sup> emphasizing the idea of an MR imaging-based classification on clinical grounds, when early diagnosis is vital for the patient. Higher volumes of mesiotemporal structures in the initial phase of LE may be explained by a functional loss of energy-dependent sodium-potassium adenosine triphosphatase with consecutive cellular swelling and cytotoxic edema due to persistent neuronal damage.<sup>26,27</sup> The late course of LE, particularly LE with LGI1 autoantibodies, has been reported to result in hippocampal sclerosis as residual damage, characterized by atrophy of the hippocampus.<sup>9,25,28</sup>

Indeed, in our study, LGI1-LE shows the most prominent atrophy of the hippocampus already in an early stage compared with GAD-LE and VGKC-LE, possibly heralding the onset of hippocampal sclerosis (Fig 3C).

### Side-Specificity

Previous MR imaging studies have found biamygdalar swelling in patients with LE.<sup>15,25</sup> This study is the first to reorient MR imaging volumes according to lateralization of EEG abnormalities, and normal contralateral EEG does not preclude pathologic affection of the contralateral hemisphere. Nevertheless, volume differences between patients and controls after reorientation could be found only in the affected hemispheric amygdala. This suggests that at least in its early phase, LE might be a unihemispheric disease. This notion is corroborated by the unilateral hippocampal signal changes observed in conventional visual assessment in most patients (Table 1). Navarro et al<sup>29</sup> have suggested that LGI1-LE may initially evolve in 1 hemisphere and progress to bilateral effects before immunomodulatory treatment. Indeed, in our study, the asymmetry of amygdala volumes was more pronounced in the early group. It is open to discussion whether biamygdalar swelling found in previous studies was reported due to the inclusion of patients with LE evolving in both the left and the right hemisphere or whether it shows the consequence of bihemispheric progression. In any case, there is skepticism as to whether

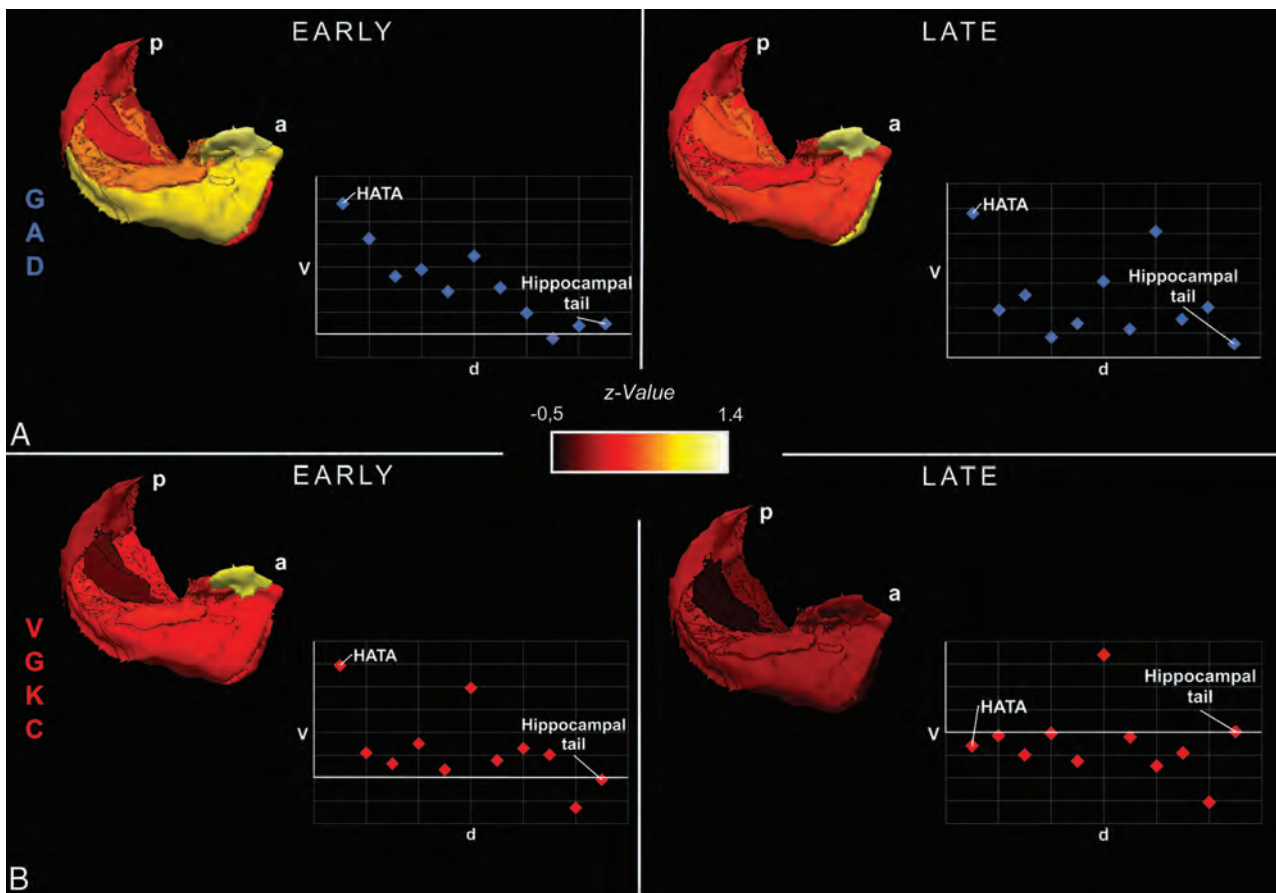


**FIG 4.** 3D visualization showing hippocampal subfield volume differences between patients and controls. 3D visualization of group differences between all GAD-LE and controls (A) as well as between VGKC-LE and controls (B) using hippocampal subfield volumes from the affected hemisphere in early and late stages. Schematic scatterplots show Z values of volumes as a function of the approximate spatial distance from the amygdala. P indicates posterior; a, anterior; d, distance; V, volume. Please note the anterior-to-posterior gradient of subfield volume alterations in early GAD-LE and how the gradient tapers off in late GAD-LE.

bilateral MR imaging abnormalities should be considered a diagnostic criterion in LE.<sup>3</sup>

### Autoantibody-Specificity

The presence of the limbic syndrome and numerous histopathologic studies confirming neuronal loss and lymphocytic infiltration mainly in the amygdala and the hippocampus<sup>30,31</sup> both lead to the understanding of LE as a mesiotemporal disease. Although autoantibody-specific imaging features have also been found in extratemporal regions, the radiologic MR imaging signature of LE is characterized by hyperintensity in T2WI and/or FLAIR images and volume alteration of the amygdala and hippocampus.<sup>12,14</sup> In the current study, we observed significantly higher volumes of CA1 and the hippocampus-amygdala transition area on the affected hemisphere in patients with early GAD-LE compared with their matched controls, whereas in early VGKC-LE, this was the case for the hippocampus-amygdala transition area and parasubiculum. Studies in patients with focal lesions limited to the CA1 region of the hippocampus attribute a crucial role in autobiographic memory retrieval, mental time travel, and auto-noetic consciousness to CA1.<sup>32,33</sup> Most interesting, these cognitive functions have been shown to be impaired in GAD-LE,<sup>34</sup> and the swollen CA1 region in GAD-

LE most likely constitutes the structural correlate of this cognitive deficit.

It is open to discussion why CA1 is selectively affected in GAD-LE. It has been shown that CA1 is particularly vulnerable to a variety of pathologic conditions such as ischemia, inflammation, or increased metabolic demand related to epileptic activity<sup>27,35</sup> and CA1 neurons express an extraordinary high density of *N*-methyl-D-aspartate NR2 subunits.<sup>36,37</sup> Neuronal death in CA1 in GAD-LE may, thus, be caused by a cytotoxic accumulation of  $Ca^{2+}$  following excessive stimulation of the *N*-methyl-D-aspartate receptor by an abnormally high accumulation of glutamic acid due to autoantibody-mediated dysfunction of GAD.

A recent study on the structure-function relationship in the healthy human hippocampus suggested an anterior-to-posterior gradient of distinctive temporolimbic connectivity.<sup>38</sup> The anterior parts of the hippocampus were shown to emphasize associations with memory- and emotion-related terms. This finding is paralleled by the anterior-to-posterior gradient with volume-increased hippocampal regions we found in early GAD-LE and emphasizes its functional relevance (Fig 4). In late GAD-LE, the anterior-to-posterior gradient is not prominent, and instead a generalized structural alteration of the hippocampus is observed. It may be most cautiously speculated that this anterior-to-posterior

gradient in early GAD-LE is indicative of an acute inflammatory process originating from the amygdala and progressing via the hippocampus-amygdala transition area<sup>39</sup> toward the hippocampal tail along the long hippocampal axis.

### Classification

Markedly, observed mesiotemporal differences were sufficiently defined so that classification was possible on an individual level between LGI1 and GAD by means of supervised machine learning. To the best of our knowledge, this is the first approach of computerized classification between serogroups in LE on the basis of postprocessed MR imaging data described. However, our classification results need to be interpreted cautiously: Despite using a leave-one-out cross-validation scheme to leverage most of our data for training, we cannot rule out possible effects of overfitting due to the low and unbalanced sample size. It has been thoroughly discussed in recent neuroimaging literature that small sample sizes inflate reported accuracies, suggesting that our results are rather over- than underestimating sensitivity and specificity.<sup>40</sup> Despite these limitations, using permutation testing, we could show that our classifier extracts useful patterns of the hippocampal profiles of the real patient distributions and does not fit random distributions. Nevertheless, due to the described limitations, our findings do not yet translate into gains for patients with LE in more than an experimental setting with a wide range of autoantibody-associated subtypes of LE, or even in those without shown autoantibody association (antibody-negative LE). The recent surge in the discovery of novel LE-associated autoantibodies implies that these patients with antibody-negative LE could quite possibly have yet-unknown autoantibodies. They might obtain a syndrome-based diagnosis only based on their clinical presentation. Thus, it would be very helpful to differentially define imaging correlates of various LE subtypes; however, larger sample sizes are needed for a reliable predictive analysis of possible imaging biomarkers.

### CONCLUSIONS

Diagnostic attention has long been focused on the serostatus of patients with LE. It only shifted to their clinical presentation when the large number of seronegative patients presenting with a limbic syndrome became evident and novel studies bolstered the importance of prompt therapy, even before the results of antibody testing are available. MR imaging is an important pillar of early diagnostics and frequently casts clinical suspicion toward autoimmune encephalitis. However, the MR imaging signature of LE, hallmarked by temporomesial abnormalities, appears to be overly simplistic in light of the current findings and with regard to the wide clinical disease spectrum of LE. The method presented here is clearly not yet applicable in a clinical setting. Instead, it may be seen as a first step toward bridging the gap between a wide clinical disease spectrum and a relatively uniform description of MR imaging findings in patients with LE. Furthermore, our results stress the existence of a multitude of pathologic entities covered by the umbrella term “limbic encephalitis.” It is our hope that this study and future imaging research will add weight to using MR imaging within the diagnostic work-

up of patients with LE and will contribute to a most detailed description of pathologic entities.

### ACKNOWLEDGMENTS

The authors are grateful for the kind support provided by the Verein zur Förderung der Epilepsieforschung e.V.

Disclosures: Theodor Rüber—RELATED: Grant: grant from BONFOR Research Commission of the Medical Faculty of the University of Bonn. Leon Ernst—RELATED: Grant: Promotionskolleg Neuroimmunology of the University of Bonn and the Else-Kröner-Fresenius Stiftung. Christian Elger—UNRELATED: Consultancy: Eisai, Desitin, Novartis, Union Chimique Belge, Medtronic; Employment: Beta Klinik, Bonn; Payment for Lectures Including Service on Speakers Bureaus: Novartis, Cyberonics, Desitin, Eisai; Payment for Development of Educational Presentations: Union Chimique Belge.

### REFERENCES

1. Bien CG, Elger CE. **Limbic encephalitis: a cause of temporal lobe epilepsy with onset in adult life.** *Epilepsy Behav* 2007;10:529–38 CrossRef Medline
2. Dalmau J, Graus F. **Antibody-mediated encephalitis.** *N Engl J Med* 2018;378:840–51 CrossRef Medline
3. Graus F, Titulaer MJ, Balu R, et al. **A clinical approach to diagnosis of autoimmune encephalitis.** *Lancet Neurol* 2016;15:391–404 CrossRef Medline
4. Malter MP, Helmstaedter C, Urbach H, et al. **Antibodies to glutamic acid decarboxylase define a form of limbic encephalitis.** *Ann Neurol* 2010;67:470–78 CrossRef Medline
5. Binks SNM, Klein CJ, Waters P, et al. **LGI1, CASPR2 and related antibodies: a molecular evolution of the phenotypes.** *J Neurol Neurosurg Psychiatry* 2018;89:526–34 CrossRef Medline
6. Dubey D, Pittock SJ, Kelly CR, et al. **Autoimmune encephalitis epidemiology and a comparison to infectious encephalitis.** *Ann Neurol* 2018;83:166–77 CrossRef Medline
7. Van Sonderen A, Ariño H, Petit-Pedrol M, et al. **The clinical spectrum of Caspr2 antibody-associated disease.** *Neurology* 2016;87:521–58 CrossRef Medline
8. Irani SR, Alexander S, Waters P, et al. **Antibodies to Kv1 potassium channel-complex proteins leucine-rich, glioma inactivated 1 protein and contactin-associated protein-2 in limbic encephalitis, Morvan’s syndrome and acquired neuromyotonia.** *Brain* 2010;133:2734–48 CrossRef Medline
9. Malter MP, Frisch C, Schoene-Bake JC, et al. **Outcome of limbic encephalitis with VGKC-complex antibodies: relation to antigenic specificity.** *J Neurol* 2014;261:1695–705 CrossRef Medline
10. Jayaweera HK, Hickie IB, Duffy SL, et al. **Episodic memory in depression: the unique contribution of the anterior caudate and hippocampus.** *Psychol Med* 2016;46:2189–99 CrossRef Medline
11. Finke C, Kopp UA, Scheel M, et al. **Functional and structural brain changes in anti-N-methyl-D-aspartate receptor encephalitis.** *Ann Neurol* 2013;74:284–96 CrossRef Medline
12. Wagner J, Schoene-Bake JC, Witt JA, et al. **Distinct white matter integrity in glutamic acid decarboxylase and voltage-gated potassium channel-complex antibody-associated limbic encephalitis.** *Epilepsia* 2016;57:475–83 CrossRef Medline
13. Heine J, Prüss H, Bartsch T, et al. **Imaging of autoimmune encephalitis; relevance for clinical practice and hippocampal function.** *Neuroscience* 2015;309:68–83 CrossRef Medline
14. Urbach H, Rauer S, Mader I, et al. **Supratentorial white matter blurring associated with voltage-gated potassium channel-complex limbic encephalitis.** *Neuroradiology* 2015;57:1203–09 CrossRef Medline
15. Wagner J, Weber B, Elger CE. **Early and chronic gray matter volume changes in limbic encephalitis revealed by voxel-based morphometry.** *Epilepsia* 2015;56:754–61 CrossRef Medline

16. Malter MP, Frisch C, Zeitler H, et al. **Treatment of immune-mediated temporal lobe epilepsy with GAD antibodies.** *Seizure* 2015;30:57–63 CrossRef Medline
17. Gastaldi M, Thouin A, Vincent A. **Antibody-mediated autoimmune encephalopathies and immunotherapies.** *Neurotherapeutics* 2016;13:147–62 CrossRef Medline
18. Fischl B, Salat DH, Busa E, et al. **Whole brain segmentation: automated labeling of neuroanatomical structures in the human brain.** *Neuron* 2002;33:341–55 CrossRef Medline
19. Fischl B, Salat DH, Van Der Kouwe AJW, et al. **Sequence-independent segmentation of magnetic resonance images.** *Neuroimage* 2004;23(Suppl 1):S69–84 CrossRef Medline
20. Iglesias JE, Augustinack JC, Nguyen K, et al. **A computational atlas of the hippocampal formation using ex vivo, ultra-high-resolution MRI: application to adaptive segmentation of in vivo MRI.** *Neuroimage* 2015;115:117–37 CrossRef Medline
21. Milliken GA, Johnson DE. *Analysis of Messy Data.* London: Chapman & Hall/CRC; 2009
22. Pedregosa F, Weiss R, Brucher M. **Scikit-Learn: machine learning in Python.** <https://scikit-learn.org/stable/index.html>. Accessed February 4, 2019
23. Quinlan JR. **Induction of decision trees.** *Mach Learning* 1986;1:81–106 CrossRef
24. Finke C, Prüss H, Heine J, et al. **Evaluation of cognitive deficits and structural hippocampal damage in encephalitis with leucine-rich, glioma-inactivated 1 antibodies.** *JAMA Neurol* 2017;74:50–59 CrossRef Medline
25. Wagner J, Witt JA, Helmstaedter C, et al. **Automated volumetry of the mesiotemporal structures in antibody-associated limbic encephalitis.** *J Neurol Neurosurg Psychiatry* 2015;86:735–42 CrossRef Medline
26. Urbach H, Soeder BM, Jeub M, et al. **Serial MRI of limbic encephalitis.** *Neuroradiology* 2006;48:380–86 CrossRef Medline
27. Bartsch T, Döhning J, Reuter S, et al. **Selective neuronal vulnerability of human hippocampal CA1 neurons: lesion evolution, temporal course, and pattern of hippocampal damage in diffusion-weighted MR imaging.** *J Cereb Blood Flow Metab* 2015;35:1836–45 CrossRef Medline
28. Irani SR, Stagg CJ, Schott JM, et al. **Faciobrachial dystonic seizures: the influence of immunotherapy on seizure control and prevention of cognitive impairment in a broadening phenotype.** *Brain* 2013;136:3151–62 CrossRef Medline
29. Navarro V, Kas A, Apartis E, et al. **Motor cortex and hippocampus are the two main cortical targets in LGI1-antibody encephalitis.** *Brain* 2016;139:1079–93 CrossRef Medline
30. Khan NL, Jeffree MA, Good C, et al. **Histopathology of VGKC antibody-associated limbic encephalitis.** *Neurology* 2009;72:1703–05 CrossRef Medline
31. Graus F, Saiz A, Lai M, et al. **Neuronal surface antigen antibodies in limbic encephalitis: clinical-immunologic associations.** *Neurology* 2008;71:930–36 CrossRef Medline
32. Bartsch T, Alfke K, Stिंगele R, et al. **Selective affection of hippocampal CA-1 neurons in patients with transient global amnesia without long-term sequelae.** *Brain* 2006;129:2874–84 CrossRef Medline
33. Bartsch T, Döhning J, Rohr A, et al. **CA1 neurons in the human hippocampus are critical for autobiographical memory, mental time travel, and autoegetic consciousness.** *Proc Natl Acad Sci U S A* 2011;108:17562–67 CrossRef Medline
34. Witt JA, Vogt VL, Widman G, et al. **Loss of autoegetic awareness of recent autobiographical episodes and accelerated long-term forgetting in a patient with previously unrecognized glutamic acid decarboxylase antibody related limbic encephalitis.** *Front Neurol* 2015;6:1–8 CrossRef Medline
35. Schmidt-Kastner R, Freund TF. **Selective vulnerability of the hippocampus in brain ischemia.** *Neuroscience* 1991;40:599–636 CrossRef Medline
36. Butler TR, Self RL, Smith KJ, et al. **Selective vulnerability of hippocampal cornu ammonis 1 pyramidal cells to excitotoxic insult is associated with the expression of polyamine-sensitive N-methyl-D-aspartate-type glutamate receptors.** *Neuroscience* 2010;165:525–34 CrossRef Medline
37. Lalonde CC, Mielke JG. **Selective vulnerability of hippocampal subfields to oxygen-glucose deprivation is a function of animal age.** *Brain Res* 2014;1543:271–79 CrossRef Medline
38. Vos de Wael R, Larivière S, Caldaïrou B, et al. **Anatomical and microstructural determinants of hippocampal subfield functional connectome embedding.** *Proc Natl Acad Sci USA* 2018;115:10154–59 CrossRef Medline
39. Zeidman P, Maguire EA. **Anterior hippocampus: the anatomy of perception, imagination and episodic memory.** *Nat Rev Neurosci* 2016;17:173–82 CrossRef Medline
40. Varoquaux G. **Cross-validation failure: small sample sizes lead to large error bars.** *Neuroimage* 2018;180:68–77 CrossRef Medline

# Prevalence of Asymptomatic Middle Cranial Fossa Floor Pits and Encephaloceles on MR Imaging

J.C. Benson, J. Lane, J.R. Geske, J.V. Gompel, and K.N. Krecke



## ABSTRACT

**BACKGROUND AND PURPOSE:** Temporal lobe encephaloceles are increasingly identified and treated as epileptogenic foci. However, there is relatively scant research on the prevalence of asymptomatic encephaloceles. This study set out to describe the frequency of incidental temporal lobe encephaloceles and middle cranial fossa pits.

**MATERIALS AND METHODS:** A retrospective review was completed of high-resolution ( $\leq 0.5$ -mm section thickness) axial T2WI for internal auditory canal protocol imaging. The presence and laterality of middle cranial fossa pits (small bony defects containing CSF) and encephaloceles (brain parenchyma protrusion through osseous defects with or without bony remodeling) were recorded. Electronic medical records of patients with encephaloceles were searched for a history of seizure.

**RESULTS:** A total of 203 patients were included in the final cohort; 106 (52.2%) women. Forty-five (22.2%) patients had middle cranial fossa pits: 14 (31.1%) unilateral on the right, 17 (37.8%) unilateral on the left, and 14 (31.1%) bilateral. Ten (5.0%) patients had  $\geq 1$  encephalocele, none of whom had a documented history of seizure in the electronic medical record. No significant difference was noted in the frequency of pits or encephaloceles based on sex ( $P = .332$  and  $P = .383$ , respectively) or age ( $P = .497$  and  $P = .914$ , respectively).

**CONCLUSIONS:** Incidental middle cranial fossa pits are common findings, and their prevalence is not related to age or sex. Temporal lobe encephaloceles, though rarer, also exist occasionally among asymptomatic patients. Such findings have diagnostic implications for encephaloceles identified during imaging work-up for epilepsy.

**ABBREVIATIONS:** BHAG = brain herniation into arachnoid granulations; MCF = middle cranial fossa

Both middle cranial fossa (MCF) pits and temporal lobe encephaloceles are subtypes of cephaloceles, intracranial content herniations through calvarial defects.<sup>1</sup> MCF pits, focal bony dehiscences containing CSF but not brain parenchyma, likely represent arachnoid granulations protruding into the overlying bone; these may also be called “small meningoceles.”<sup>2</sup> Temporal lobe encephaloceles, comparatively, are protrusions of brain through focal defects in the bone.<sup>3,4</sup> The etiologies of pits and encephaloceles are unknown, though some have posited that increased CSF pressure or volume could play a role.<sup>2,5</sup>

Temporal lobe encephaloceles are associated with a number of processes, including otorrhea, hearing loss, and recurrent

meningitis.<sup>6,7</sup> Encephaloceles are also a known rare cause of epilepsy.<sup>3,4,8-10</sup> The first reported case led to complete seizure freedom following temporal lobectomy for a patient with an MCF encephalocele.<sup>11</sup> Since then, several other authors have reported seizure freedom following partial temporal lobectomy or lesionectomy for symptomatic lesions.<sup>12-15</sup> Nevertheless, surgical resection of encephaloceles for refractory epilepsy remains nuanced because it remains uncertain whether encephaloceles can be routinely considered epileptogenic.<sup>16</sup>

The location and small size of such abnormalities have led to under-recognition on MR imaging.<sup>4</sup> However, as spatial resolution of MRI continues to advance, particularly with the emergence of high-field imaging systems, the identification of MCF pits and encephaloceles can be expected to increase with time.<sup>17,18</sup> The clinical import and prevalence of pits and encephaloceles, therefore, deserve further investigation because both findings may be a source of diagnostic confusion and consternation. This study aimed to assess the prevalence of MCF encephaloceles and pits on high-resolution MR imaging in asymptomatic patients.

Received June 20, 2019; accepted after revision September 27.

From the Department of Neuroradiology (J.C.B., J.L., K.N.K.), Division of Biomedical Statistics and Informatics (J.R.G.), and Department of Neurosurgery (J.V.G.), Mayo Clinic, Rochester, Minnesota.

Please address correspondence to John C. Benson, 200 1st St. SW, Rochester, MN 55905; e-mail: benson.john3@mayo.edu

<http://dx.doi.org/10.3174/ajnr.A6311>

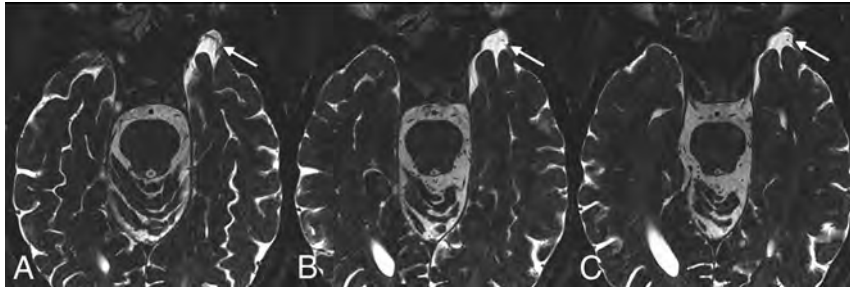


**FIG 1.** A 53-year-old man who presented with intermittent episodes of imbalance and left-greater-than-right sensorineural hearing loss. Axial T2 SPACE images (from inferior to superior, A–C) demonstrate a focal osseous defect in the greater wing of the left sphenoid bone containing CSF, consistent with an MCF pit (arrow). No herniation of brain parenchyma is present.

**Table 1: Number and frequency of MCF pits and encephaloceles based on laterality<sup>a</sup>**

	Right	Left	Bilateral
MCF pits (No.) (%)	14 (31.1%)	17 (37.8%)	14 (31.1%)
Encephaloceles (No.) (%)	4 (40%)	5 (50%)	1 (10%)

<sup>a</sup> Percentages are of the number of patients in which either pits or encephaloceles were observed.

## MATERIALS AND METHODS

### Patient Selection

Institutional review board approval was obtained for this study. A retrospective review was completed of all internal auditory canal MR imaging examinations performed between January 1, 2017, and June 30, 2018. Included patients had the following: 1) MR imaging examination including a 0.5-mm axial T2 sampling perfection with application-optimized contrasts by using different flip angle evolutions (SPACE; Siemens, Erlangen, Germany) sequence or CISS or FIESTA images, and 2) imaging FOV that encompassed the osseous walls of the MCF bilaterally, requiring craniad coverage from the floor of the fossa to the floor of the sella or higher. Axial sequences were part of the dedicated internal auditory canal protocol used in our institution. Patients were excluded if images were of suboptimal quality (eg, degraded by motion artifacts).

### Imaging and Clinical Review

Two neuroradiologists and a neuroradiology fellow reviewed MR images for the presence or absence of MCF “pits” (defined as extension of meninges and CSF through the inner table of the skull base, but not through the outer table, with or without bony remodeling) and the presence or absence of MCF “encephaloceles” (defined as extension of brain parenchyma through the aforementioned defect). Similar defects of the anterior and posterior cranial fossae were excluded from analysis. Lateralization (right versus left) was noted for encephaloceles and pits. For patients in whom  $\geq 1$  encephalocele was detected, a review of the electronic medical record was completed to assess a history of seizures. The body mass index of each patient was also assessed because elevated body mass indices are known to be associated with idiopathic intracranial hypertension; these were found via a retrospective review of the electronic medical record.

When a potential encephalocele was identified, the source thin axial T2 images were inspected in multiplanar reformatted images generated on a diagnostic radiology workstation running Visage Software, Version 7.1.12 (Visage Imaging, San Diego, California). Encephalocele was confirmed if the temporal lobe cortex extended into the inner table defect. Location of the encephalocele was assigned following the classification described by Wilkins, et al.<sup>19</sup>

### Statistical Analysis

Association of the presence or absence of MCF pits or encephaloceles with sex was examined using a  $\chi^2$  test. Differences in age by the presence or absence of MCF pits or encephaloceles was examined using *t* tests. Analyses were conducted using SAS (Version 9.4; SAS Institute, Cary, North Carolina).

## RESULTS

Of the 204 patients who met the inclusion criteria for this study, one was excluded due to incomplete visualization of the MCF. Hence, 203 patients composed the patient cohort; 106 (52.2%) were women. The mean patient age was  $53.4 \pm 10.0$  years.

Forty-five of 203 (22.2%) patients had MCF pits (Fig 1). Of the pits detected, 17/45 (37.8%) were unilateral on the left, 14/45 (31.1%) were unilateral on the right, and 14/45 (29.2%) were bilateral (Table 1).

Ten of 203 patients (5%) had 15 encephaloceles (Figs. 2 and 3). Nine of the 10 patients had single encephaloceles, 5 on the left. One patient had 6 encephaloceles, 3 on each side. Twelve encephaloceles were located in the greater wing of the sphenoid bone; the other 3, in the temporal bone. The greater sphenoid wing encephaloceles were most numerous in the anterior-inferior dural surface (10 of 12, 83%), with the remaining 2 located posteriorly, immediately lateral to the foramen spinosum and deep to the sphenoid spine. In the temporal bone, 2 of the 3 encephaloceles were located in the temporal squamosa immediately lateral to the sphenosquamosal suture; the third was located in the tegmen. Six of the 15 encephaloceles (40%) demonstrated gliosis or volume loss, compatible with encephalomalacia. The size of the observed encephaloceles ranged from 3 to 10 mm (mean, 6 mm). Six of 15 (40.0%) had some degree of associated encephalomalacia of the adjacent parenchyma. None of the patients with encephalocele had a history of seizures or epilepsy. None of the patients with encephaloceles had a known or suspected history of elevated intracranial pressure.

The prevalence of MCF pits in women was 26.4%, compared with 20.6% in men; no significant difference was noted in the prevalence of pits along sex lines ( $P = .332$ ). Similarly, no significant difference was observed between the frequency of encephaloceles and sex (5.7% for women versus 3.1% for men,  $P = .383$ ). Additionally, there was neither a significant difference in the mean age of patients with MCF pits ( $54.3 \pm 8.7$

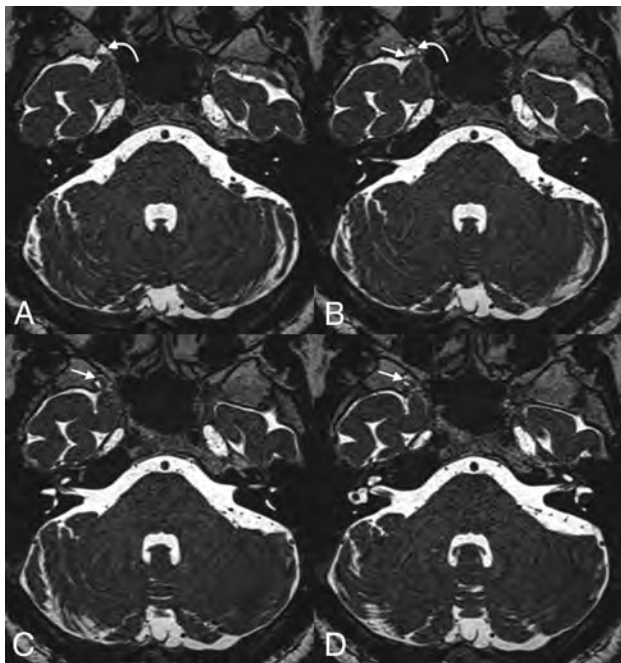


**FIG 2.** A 65-year-old man with a history of progressive bilateral sensorineural hearing loss. From superior to inferior (A–D), axial T2 SPACE images demonstrate a focal dehiscence of the medial right greater wing of the sphenoid (*curved arrows* in A and B). A small right temporal lobe encephalocele is seen protruding into the bony defect (*straight arrows* in B–D).

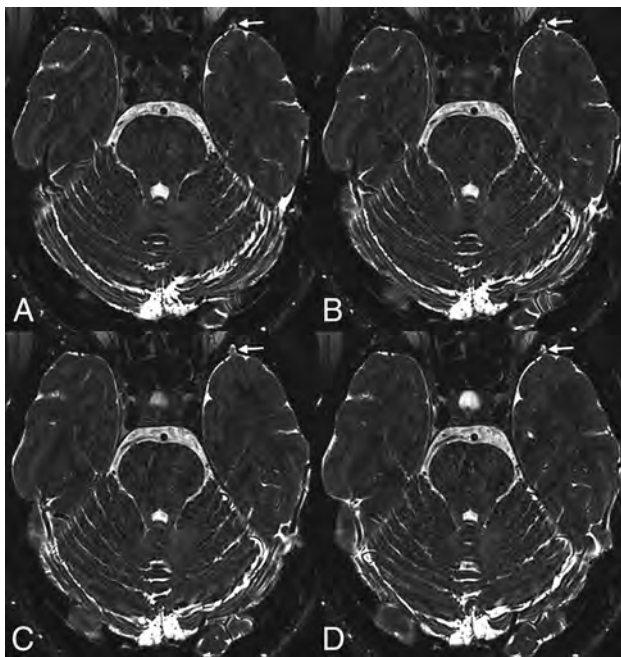


**FIG 3.** A 47-year-old woman who presented with a 2-month history of vertigo. From inferior to superior (A–D), images demonstrate a small incidental encephalocele protruding into the greater wing of the left sphenoid (*arrows*).

years) compared with those without ( $53.2 \pm 10.4$  years,  $P = .497$ ) nor a significant difference between the mean age of patients with encephaloceles ( $53.1 \pm 10.1$  years) compared with those without ( $53.5 \pm 10.1$  years,  $P = .914$ ) (Table 2).

**Table 2: Comparisons of MCF pit and encephalocele frequency with age**

	Present	Not Present	P Value
MCF pits (mean age) (yr)	$54.3 \pm 8.7$	$53.2 \pm 10.4$	.497
Encephaloceles (mean age) (yr)	$53.1 \pm 10.1$	$53.5 \pm 10.1$	.914

No association was found between patient body mass index and the presence of dural pits ( $P = .267$ ), nor was an association found between body mass index and encephaloceles ( $P = 1.000$ ).

## DISCUSSION

Most MCF pits likely arise from aberrant arachnoid granulations. Such aberrantly located arachnoid granulations expand into the calvaria but do not communicate with a venous sinus.<sup>20</sup> Protrusion of parenchyma through these defects, commonly called brain herniation into arachnoid granulations (BHAG), is a well-documented imaging finding, though it is more often described in the posterior fossa and along the larger sinuses.<sup>5,20–22</sup> BHAG can be associated with abnormal signal of the herniated, or adjacent, parenchyma, though the findings rarely seem to be symptomatic.<sup>5</sup> Some authors, such as Battal and Castillo,<sup>23</sup> have sought to differentiate BHAG from classic temporal lobe encephaloceles. However, the distinction between the entities is somewhat opaque, raising the suspicion that encephaloceles and BHAG exist on a spectrum based on the severity of osseous thinning and/or remodeling. Thus, the current study will refer to brain herniation through any osseous defect as an encephalocele.

Spontaneous encephalocele is an extension of cerebral tissue and coverings into or through a defect in the skull not caused by trauma, inflammation, neoplasm, or surgical disruption. In our cohort, 14 of the encephaloceles involved the greater wing of the sphenoid bone or immediately adjacent temporal squamosal, lateral to the cranial base neural foramina (rotundum, ovale, and spinosum) and projected anteriorly or anterior-inferiorly through the inner table. A single encephalocele was located posteriorly and inferiorly in the tegmen tympani, lateral to the otic capsule and geniculate ganglion. Wilkins et al<sup>19</sup> classified spontaneous temporal encephaloceles into 5 types, including anterior-inferior and posterior-inferior. The spontaneous anterior-inferior encephalocele is the type most commonly reported in the epilepsy literature associated with refractory temporal lobe epilepsy.<sup>24</sup> The current study did not identify clinically occult encephaloceles of the other 3 types (anterior/spheno-orbital, anterior-medial/sphenoid sinus, or lateral/pterional). This absence may be an artifact of the volume of coverage, with the thin T2 images centered on the internal auditory canals typically not spanning the full height of the middle cranial fossa; however, in the authors' experience, these latter types are rare in asymptomatic patients.

The identification and treatment of temporal lobe encephaloceles for refractory temporal lobe epilepsy have increased in recent years.<sup>25</sup> The incidence of asymptomatic encephaloceles noted in the current study underscores the potential diagnostic dilemma encountered when a temporal lobe encephalocele is discovered—that is, should a temporal lobe encephalocele, identified on otherwise normal MR imaging findings of a patient with refractory epilepsy, be targeted as the potential

epileptogenic focus? Alternatively, should an encephalocele ipsilateral to mesial temporal sclerosis be considered dual pathology? Future research may be useful to identify characteristics of encephaloceles that carry a higher risk of seizure foci, such as size, morphology, and abnormal signal. Until such data are gathered, radiologists and epileptologists may continue to take into account the clinical context as well data points from other modalities, including electroencephalography, PET MR imaging, SPECT, and magnetoencephalography.

To our knowledge, there have been no reported cases in which MCF pits were implicated as the direct cause of seizures. Still, pits are of conceivable clinical import: They are likely precursors of encephaloceles and could represent an early form of a spectrum of pathology that includes all cephaloceles, both pits and encephaloceles. Nevertheless, the incidence of such pits is likely underestimated on imaging; a study by Chen et al found many more middle cranial fossa arachnoid granulations on cadaveric dissections than were seen on NCCT.<sup>26</sup> Future studies may be useful to investigate how frequently pits progress to BHAG and encephaloceles.

Our study is limited by its retrospective nature. In addition, because the detection of MCF pits and encephaloceles was based solely on axial images, it is possible that smaller abnormalities may not have been detected. Thus, it is likely that the rate of small MCF abnormalities is underestimated in this study. A more comprehensive review using coronal and sagittal sequences may have superior sensitivity for the detection MCF abnormalities. Finally, although electronic medical records of patients with encephaloceles were reviewed for a history of seizure, it is unknown whether the observed pits and encephaloceles were truly asymptomatic.

## CONCLUSIONS

MCF pits are frequently observed incidental and presumably asymptomatic findings on high-resolution T2-weighted MR imaging. Temporal lobe encephaloceles, some with evident encephalomalacia, are also occasionally seen among asymptomatic patients. The incidence of such findings should be taken into account when identifying or treating such lesions as possible epileptogenic foci.

## REFERENCES

- Settecase F, Harnsberger HR, Michel MA, et al. **Spontaneous lateral sphenoid cephaloceles: anatomic factors contributing to pathogenesis and proposed classification.** *AJNR Am J Neuroradiol* 2014; 35:784–89 CrossRef Medline
- Lu CX, Du Y, Xu X-X, et al. **Multiple occipital defects caused by arachnoid granulations: emphasis on T2 mapping.** *World J Radiol* 2012;4:341–44 CrossRef Medline
- Morone PJ, Sweeney AD, Carlson ML, et al. **Temporal lobe encephaloceles.** *Otol Neurotol* 2015;36:1439–42 CrossRef Medline
- Abou-Hamden A, Lau M, Fabinyi G, et al. **Small temporal pole encephaloceles: a treatable cause of “lesion negative” temporal lobe epilepsy.** *Epilepsia* 2010;51:2199–202 CrossRef Medline
- Liebo GB, Lane JJ, Van Gompel JJ, et al. **Brain herniation into arachnoid granulations: clinical and neuroimaging features.** *J Neuroimaging* 2016;26:592–98 CrossRef Medline
- Roehm PC, Tint D, Chan N, et al. **Endoscope-assisted repair of CSF otorrhea and temporal lobe encephaloceles via keyhole craniotomy.** *J Neurosurg* 2018;128:1880–84 CrossRef Medline
- Van Gompel JJ, Miller JW. **How epileptogenic are temporal encephaloceles?.** *Neurology* 2015;85:1440–41 CrossRef Medline
- Byrne RW, Smith AP, Roh D, et al. **Occult middle fossa encephaloceles in patients with temporal lobe epilepsy.** *World Neurosurg* 2010;73:541–46 CrossRef Medline
- Urbach H, Jamneala G, Mader I, et al. **Temporal lobe epilepsy due to meningoencephaloceles into the greater sphenoid wing: a consequence of idiopathic intracranial hypertension?.** *Neuroradiology* 2018;60:51–60 CrossRef Medline
- Wang ZI, McBride A, Grinenko O, et al. **Utility of CISS sequence in detecting anteroinferior temporal encephalocele.** *J Neurol Sci* 2017;381:59–61 CrossRef Medline
- Ruiz Garcia F. **A case of temporal lobe epilepsy caused by an encephalocele** [in Spanish]. *Rev Esp Otoneurooftalmol Neurocir* 1971;29:216–20 Medline
- Bannout F, Harder S, Lee M, et al. **Epilepsy surgery for skull-base temporal lobe encephaloceles: should we spare the hippocampus from resection?.** *Brain Sci* 2018;8 CrossRef Medline
- Semenov MS, Belyakova-Bodina AI, Murtazina AF, et al. **Surgery for intractable epilepsy in a patient with encephalocele of the temporal lobe: a case report** [in Russian; Abstract available in Russian from the publisher]. *Zh Vopr Neurokhir Im N N Burdenko* 2017;81:99 CrossRef Medline
- Toledano R, Jiménez-Huete A, Campo P, et al. **Small temporal pole encephalocele: a hidden cause of “normal” MRI temporal lobe epilepsy.** *Epilepsia* 2016;57:841–51 CrossRef Medline
- Saavalainen T, Jutila L, Mervaala E, et al. **Temporal anteroinferior encephalocele: an underrecognized etiology of temporal lobe epilepsy?.** *Neurology* 2015;85:1467–74 CrossRef Medline
- Panov F, Li Y, Chang EF, et al. **Epilepsy with temporal encephalocele: characteristics of electrocorticography and surgical outcome.** *Epilepsia* 2016;57:e33–38 CrossRef Medline
- Pittau F, Baud MO, Jorge J, et al. **MP2RAGE and susceptibility-weighted imaging in lesional epilepsy at 7T.** *J Neuroimaging* 2018;28:365–69 CrossRef Medline
- De Ciantis A, Barba C, Tassi L, et al. **7T MRI in focal epilepsy with unrevealing conventional field strength imaging.** *Epilepsia* 2016; 57:445–54 CrossRef Medline
- Wilkins RH, Radtke RA, Burger PC. **Spontaneous temporal encephalocele: case report.** *J Neurosurg* 1993;89:492–98 CrossRef Medline
- Rodrigues JR, Santos GR. **Brain herniation into giant arachnoid granulation: an unusual case.** *Case Rep Radiol* 2017;2017:8532074 CrossRef Medline
- Malekzadehlashkariani S, Wanke I, Rüfenacht DA, et al. **Brain herniations into arachnoid granulations: about 68 cases in 38 patients and review of the literature.** *Neuroradiology* 2016;58:443–57 CrossRef Medline
- Sade R, Ogul H, Polat G, et al. **Brain herniation into the transverse sinuses’ arachnoid granulations in the pediatric population investigated with 3 T MRI.** *Acta Neurol Belg* 2019;119:225–31 CrossRef Medline
- Battal B, Castillo M. **Brain herniations into the dural venous sinuses or calvarium: MRI of a recently recognized entity.** *Neuroradiol J* 2014;27:55–62 CrossRef Medline
- Wind JJ, Caputy AJ, Roberti F. **Spontaneous encephaloceles of the temporal lobe.** *Neurosurg Focus* 2008;25:E11 CrossRef Medline
- Campbell ZM, Hyer JM, Lauzon S, et al. **Detection and characteristics of temporal encephaloceles in patients with refractory epilepsy.** *AJNR Am J Neuroradiol* 2018;39:1468–72 CrossRef Medline
- Chen F, Deng Xf, Liu B, et al. **Arachnoid granulations of middle cranial fossa: a population study between cadaveric dissection and in vivo computed tomography examination.** *Surg Radiol Anat* 2011;33(3):215–21

# Outcome Study of the Pipeline Embolization Device with Shield Technology in Unruptured Aneurysms (PEDSU)

 D. Atasoy,  N. Kandasamy,  J. Hart,  J. Lynch,  S.-H. Yang,  D. Walsh,  C. Tolia, and  T.C. Booth



## ABSTRACT

**BACKGROUND AND PURPOSE:** The recently introduced Pipeline Flex Embolization Device with Shield Technology (Pipeline Shield) is the third generation of Pipeline flow-diverter devices. It has a new stent-surface modification, which reduces thrombogenicity. We aimed to evaluate clinical and radiographic (safety and efficacy) outcomes of the Pipeline Shield.

**MATERIALS AND METHODS:** The 30-day and 1-year mortality and morbidity rates and the 6- and 18-month radiographic aneurysm occlusion outcomes for procedures performed between March 2016 and January 2018 were analyzed. 3D-TOF-MRA was used for follow-up.

**RESULTS:** Forty-four attempted Pipeline Shield procedures were performed for 41 patients with 44 target aneurysms (total of 52 aneurysms treated). A total of 88.5% of devices were inserted in the anterior circulation, and 11.5%, in the posterior circulation; 49/52 (94.2%) aneurysms were saccular; and 1/52 (1.9%) was fusiform. One (1.9%) aneurysm was an iatrogenic pseudoaneurysm, and 1 (1.9%) was a dissecting aneurysm. Seventy-one percent (35/49) of the saccular aneurysms were wide-neck (neck, >4 mm), 34.6% (18/52) were large ( $\geq 10$  mm), and 3.8% (2/52) were giant ( $\geq 25$  mm). The mean aneurysm sac maximal diameter was 9.0 mm, and the mean neck width was 5.0 mm. The cumulative mortality and morbidity rates were 2.3% and 6.8% at 1 year, respectively. The adequate occlusion rate was 78.8% at 6 months and 90.3% at 18 months.

**CONCLUSIONS:** In this pragmatic and non-industry-sponsored study, the occlusion rates and safety outcomes were similar to those seen in previously published studies with flow-diverter devices and earlier generation Pipeline Embolization Devices.

Flow-diverter devices have been used to treat cerebral aneurysms for nearly 10 years. These devices occlude aneurysms through endoluminal reconstruction and remodeling of the parent artery.<sup>1</sup> The Pipeline Embolization Device (PED; Covidien, Irvine, California) is 1 of 2 FDA-approved flow-diverter devices.<sup>2</sup> The first generation of PEDs has been used effectively and safely for many years.<sup>3-5</sup> The second generation, the Pipeline Flex

Embolization Device (Covidien), had a redesigned delivery system enabling better repositioning and redeployment of the stent.<sup>6,7</sup> Nonetheless, thromboembolic complications remain an important cause of morbidity in both generations of PEDs.<sup>3</sup> Thus, a third generation, the Pipeline Flex Embolization Device with Shield Technology (Pipeline Shield; Covidien) was recently produced (Fig 1). The second-generation delivery system remained the same; however, there is a new phosphorylcholine stent-surface modification aimed at minimizing thrombogenicity.<sup>8</sup> Because there is no difference in cost between the Pipeline Shield and earlier PED devices, the Pipeline Shield has been adopted as the default PED, though there are limited clinical data to support its use. In this study, we demonstrate clinical and radiographic (safety and efficacy) outcomes of the third-generation PED.

## MATERIALS AND METHODS

### Patient Selection

All patients who underwent Pipeline Shield placement at a single center between March 2016 and January 2018 were included in this pragmatic and retrospective cohort study. All cases were selected following a consensus decision at a neurovascular

Received June 1, 2019; accepted after revision September 20.

From Karadeniz Technical University (D.A.), Farabi Hospital, Trabzon, Turkey; Departments of Neuroradiology (N.K., J.H., J.L., T.C.B.) and Neurosurgery (D.W., C.T.), King's College Hospital National Health Service Foundation Trust, London, UK; Department of Radiology (S.-H.Y.), Wan Fang Hospital, Taipei Medical University, Taipei, Taiwan; Department of Radiology (S.-H.Y.), School of Medicine, College of Medicine, Taipei Medical University, Taipei, Taiwan; and School of Biomedical Engineering and Imaging Sciences (T.C.B.), King's College London, London, UK.

This work was supported by the Wellcome/Engineering and Physical Sciences Research Council Center for Medical Engineering (WT 203148/Z/16/Z).

Paper previously presented at: Annual Meeting of the American Society of Neuroradiology, May 18–23, 2019; Boston, Massachusetts.

Please address correspondence to Thomas C. Booth, EDiNR, DMCC, MA, MBBS, MRCP, FRCP, PhD, Department of Neuroradiology, King's College Hospital NHS Foundation Trust, London SE5 9RS, UK; e-mail: tombooth@doctors.org.uk; @ThomasCBooth

 Indicates open access to non-subscribers at [www.ajnr.org](http://www.ajnr.org)

<http://dx.doi.org/10.3174/ajnr.A6314>

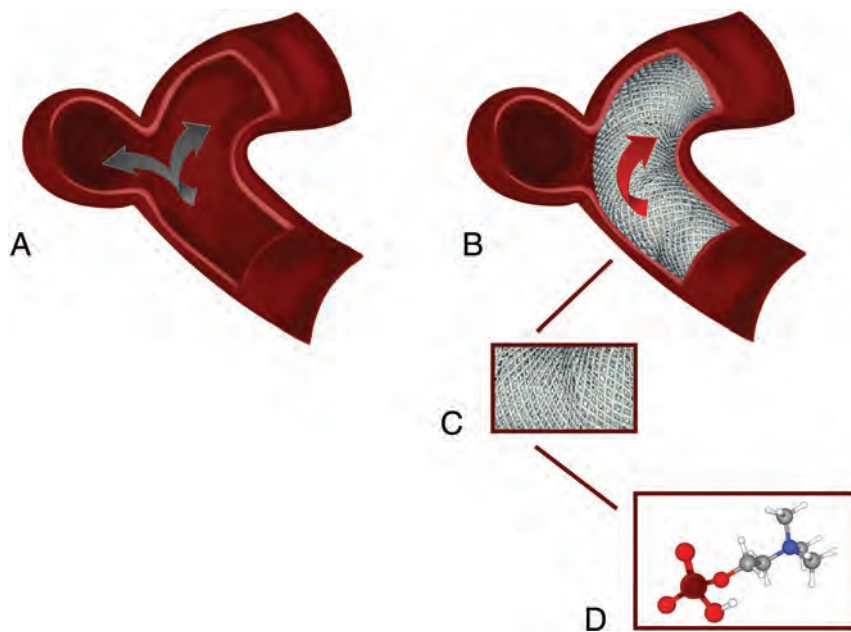


**FIG 1.** Illustration of Pipeline Shield mechanism and structure. *A*, Before Pipeline Shield deployment, the blood flow is through both the parent artery and the aneurysm. *B*, However, after device deployment, the blood flow in the aneurysm is reduced or disrupted. *C*, A schematic showing the magnified appearance of the braided wires of the Pipeline Shield. *D*, A 3D illustration of the phosphorylcholine molecule, which is covalently bound onto the bare metal wires in a polymer form, resulting in physiologic imitation of the cell membrane.

multidisciplinary team meeting, which included interventional neuroradiologists and neurovascular surgeons. A high neck-to-sac ratio, a high probability of aneurysm recurrence, and increased neurosurgical technical difficulty were the factors leading to Pipeline Shield treatment in preference to coiling, stent-assisted coiling, or neurosurgery.<sup>9</sup>

### Procedural Details

Patients started dual-antiplatelet therapy (aspirin and clopidogrel) 7 days before their procedure and continued clopidogrel once daily for 6–9 months and continued aspirin for life (all doses, 75 mg daily). Platelet-resistance testing was not performed at our center due to our interpretation of the literature indicating a lack of evidence to show a proven clinical benefit.<sup>10–13</sup>

Pipeline Shield placement procedures were performed with the patient under general anesthesia using biplane angiography (Allura Xper FD, Philips Healthcare, Amsterdam, Netherlands). All procedures were performed with a femoral arterial approach with 6F or 8F guiding-catheter systems (0.088-inch NeuronMax or 6F Benchmark, both Penumbra, Alameda, California; Shuttle guide sheath, Cook, Bloomington, Indiana), which were positioned in the cervical segment of the ICA ipsilateral to the target aneurysm or a distal V2 segment. A triaxial system, incorporating a 0.058- or 0.072-inch intracranial support catheter (Navien, Covidien, Irvine, California) was used in both the anterior and posterior circulations. The Pipeline Shield device was deployed using a 0.027-inch microcatheter (Phenom 27 or Marksman; both Covidien). Embolization catheters (Echelon, Covidien; or Excelsior SL10, Stryker, Kalamazoo, Michigan) were used for

adjunctive coil delivery in selected cases. Patients typically were discharged home the morning after the procedure.

### Data Collection

Electronic patient records (Allscripts Sunrise, Chicago, Illinois); preprocedural, procedural, and postprocedural images on the PACS; and written procedural records for patients treated with the Pipeline Shield were reviewed. Data on aneurysm size and location were acquired from DSA images (Allura Xper FD, Philips Healthcare, Amsterdam, Netherlands). As in a previous PED study,<sup>9</sup> the first posttreatment follow-up was performed typically at 6 months postprocedure using 3D-TOF-MRA (Signa 1.5 T HDX; GE Healthcare; or AERA 1.5T, Siemens, Erlangen, Germany) with respective TR = 23 or 25 ms, TE = 2.5 or 7 ms, flip angle = 20° or 25° (with ramped pulse), matrix = 320 × 224 or 241 × 256; FOV = 19 × 19 or 18 × 18 cm, section thickness = 1.4 mm

(reconstructed to 0.7 or 0.5 mm, respectively). If there were new clinical features during follow-up, an earlier MR imaging (with MRA) or CT (with CTA) was performed on a case-by-case basis. All images were reviewed in the neurovascular multidisciplinary team meeting, and further follow-up 3D-TOF-MRA was typically scheduled for 18 months postprocedure. All data were reviewed and analyzed by an independent core laboratory (D.A.).

Aneurysm occlusion status was classified using the Raymond-Roy Outcome Classification (Raymond Scale): class 1, complete occlusion; class 2, residual neck; and class 3, residual aneurysm. To compare our results with those of the largest clinical trial of PEDs to date (the International Retrospective Study of the Pipeline Embolization Device (InttrePED)<sup>3</sup>), we used the identical adverse event classification. A neurologic adverse event included rupture of the target aneurysm causing subarachnoid hemorrhage or carotid cavernous fistula, intraparenchymal hemorrhage, ischemic stroke, parent artery stenosis, and cranial neuropathy. A persistent clinical deficit at 7 days following the event was defined as a “major” adverse event. Other events that resolved within 7 days with no clinical sequelae were defined as “minor” adverse events.

### Statistical Analysis

Descriptive and comparative statistical analyses were performed using SPSS (Version 23.0; IBM, Armonk, New York). Student *t* tests or Mann-Whitney tests were used. All adverse events were reviewed on an intention-to-treat basis. Aneurysm characteristics and occlusion rates were performed on a per-aneurysm basis because some patients had >1 aneurysm treated with ≥1 PED.

**Table 1: Aneurysm characteristics**

Characteristic	No. (%) or Mean (Range)
Aneurysm location	
Anterior circulation <sup>a</sup>	46 (88.5)
ICA cavernous segment	2 (3.8)
ICA paraophthalmic segment	29 (55.7)
ICA posterior communicating segment	12 (23.1)
ICA terminal segment	2 (3.8)
M1 segment of MCA	1 (1.9)
Posterior circulation	6 (11.5)
Basilar artery	3 (5.8)
Vertebral artery	2 (3.8)
Posterior cerebral artery	1 (1.9)
Neck width (mm <sup>b</sup> )	5.0 (1.0–21.0)
Maximum aneurysm sac diameter (mm <sup>b</sup> )	9.0 (1.0–28.0)
<10	32 (60.8)
10–25	18 (34.6)
≥25	2 (3.8)
PED number (per aneurysm)	0.86 (45/52)
Adjunctive coils placed	15 (28.8)

<sup>a</sup> ICA according to the New York University classification.<sup>14</sup>

<sup>b</sup> Millimeter to the nearest 0.5.

### Ethical Statement

Written informed consent was obtained from all patients. We received written confirmation from the Research and Innovation Department at King's College Hospital that the Health Research Authority of the UK does not require review by a Research Ethics Committee, given the nature of the retrospective study using de-identified data. The study was performed in accordance with the ethical standards laid down in the 1964 Declaration of Helsinki and its later amendments.

## RESULTS

### Patient and Aneurysm Characteristics

There were 41 patients between March 2016 and January 2018 whom we intended to treat with the Pipeline Shield device. The mean age was 56 years (range, 17–82 years), and 68.3% (28/41) of patients were women.

There were no acutely ruptured aneurysms. There had been prior treatment of intracranial aneurysm with coils in 32.6% (17/52) of aneurysms. The mean aneurysm neck width was 5.0 mm, the mean sac maximal diameter was 9.0 mm, 34.6% (18/52) were large (≥10 mm), and 3.8% (2/52) were giant (≥25 mm) (Table 1). Forty-nine (94.2%) aneurysms were saccular, and 1 (1.9%) was fusiform. One (1.9%) aneurysm was an iatrogenic pseudoaneurysm, and 1 (1.9%), a dissecting aneurysm. Seventy-one percent (35/49) of the saccular aneurysms were wide-neck (neck, >4 mm). Most aneurysms were located in the anterior circulation, 46/52 (88.5%); 6/52 (11.5%) were located in the posterior circulation.

A total of 44 attempted Pipeline Shield procedures were performed for the 41 patients with 44 target aneurysms (total, 52 aneurysms treated; there were 8 cases in which the device covered additional nontarget aneurysms). Three patients who had been treated for ICA aneurysms had a second Pipeline Shield procedure for aneurysms located in the contralateral ICA within 1 month. Two patients each received 2 Pipeline Shields for 1 target aneurysm in a single procedure. Device-deployment success

**Table 2: Clinical outcomes**

Outcome	Procedure No. (%)
Periprocedural outcomes (within 30 days)	
Major adverse events <sup>a</sup>	
Death from subdural hemorrhage	1 (2.3)
Cranial nerve palsy <sup>b</sup>	1 (2.3)
Minor adverse events	
Stroke/TIA	1 (2.3)
Headache <sup>b</sup>	1 (2.3)
Postprocedure outcomes (30 days to 1 yr)	
Major adverse events <sup>a</sup>	
Pulsatile tinnitus (carotid cavernous fistula)	1 (2.3)
Mass effect causing reduced visual acuity	1 (2.3)

<sup>a</sup> An ongoing clinical event at 7 days following the event.

<sup>b</sup> Same patient.

(release of the Pipeline Shield at the target site) was achieved in 45 of 46 (97%) of the attempted Pipeline Shield deployments. It was not possible to deploy a Pipeline Shield in 1 patient who had a wide-neck saccular M1 segment aneurysm. Deployment was unsuccessful because the Pipeline Shield would not travel through the Marksman catheter, which was within a 0.058 Navien intracranial support catheter placed inside a tortuous cervical ICA. The aneurysm was subsequently treated with a LEO Baby stent (Balt Extrusion, Montmorency, France) and coils. Stable complete occlusion (Raymond scale 1) at 18-month follow-up was seen. In total, 45 devices were deployed in the 44 procedures. The mean number of deployed devices per aneurysm was 0.86 (45/52) or, if nontarget aneurysms were ignored, 1.02 (44/45). No thromboembolic or hemorrhagic events occurred during the procedures.

### Periprocedural Clinical Outcomes

The periprocedural mortality rate was 1/44 (2.3%) Pipeline Shield procedures (Table 2). This patient had a recurrent giant basilar termination aneurysm after previous coiling treatment. This aneurysm measured 27 mm in maximum dimension with a 10-mm recurrent sac diameter. He had an acute subdural hematoma 15 days after the successful Pipeline Shield deployment with adjunctive coiling and died 16 days after the procedure. There were 2 periprocedural major events including this death, 2/44 (4.6%). The second major event gave a periprocedural neurologic morbidity rate of 2.3% (1/44). This patient was treated with 2 Pipeline Shield devices for a giant (28 mm) right cavernous segment ICA aneurysm. On day 7 postprocedure, the patient was re-admitted with an ipsilateral third nerve palsy. A head CT revealed the expected appearances of a thrombosed aneurysm. The third cranial nerve palsy was attributed to the thrombosed aneurysm. At the time of presentation, the patient also experienced a headache (Universal Pain Assessment Tool for headache, 5/10). CT of the head also showed a new small remote right temporal intraparenchymal hematoma. The patient was managed symptomatically for headache, and in view of the hemorrhage, clopidogrel was stopped temporarily with the patient continuing on aspirin. Following appropriate evolution of the right temporal hemorrhage on follow-up CT, clopidogrel therapy was restarted and the patient was discharged with no headache. There were 2 periprocedural minor events, including the headache described here,

**Table 3: Image outcome<sup>a</sup>**

Outcome	Aneurysm No. (%) or Mean (Range)
Adequate occlusion/remodeling at 6 months (Raymond scale 1 and 2)	41 (78.8)
No residual neck or sac (Raymond scale 1)	36 (69.2)
Residual neck (Raymond scale 2)	5 (9.6)
Residual sac (Raymond scale 3)	11 (21.1)
Adequate occlusion/remodeling at 18 months (Raymond scale 1 and 2)	47 (90.3)
No residual neck or sac (Raymond scale 1)	43 (82.7)
Residual neck (Raymond scale 2)	4 (7.7)
Residual sac (Raymond scale 3)	5 (9.6)
Mean size of aneurysms (mm)	
Residual sac (Raymond scale 3)	11.5 (4.0–22.0)
No residual neck or sac (Raymond scale 1)	8.5 (1.0–28.0)
Mean size of neck (mm)	
Residual sac (Raymond scale 3)	8.0 (3.0–21.0)
No residual neck or sac (Raymond scale 1)	4.5 (1.0–16.0)

<sup>a</sup> Millimeter to the nearest 0.5.

with a total of 2/44 (4.6%). The second minor event yielded a 2.3% (1/44) stroke/TIA rate. This patient had a TIA with a temporary left-sided facial droop and slurred speech 6 days after right ICA PED deployment. CT, MR imaging, and MRA showed no intracranial hemorrhage or recent infarct. The patient was also known to have atrial fibrillation and was referred to the TIA clinic.

### MRA Outcomes

Follow-up MRA was performed in 38/40 patients who had undergone technically successful procedures. One patient died 16 days postprocedure, and the other patient refused imaging follow-up (the patient is clinically healthy). The mean follow-up time until the first MRA was 5.8 months (range, 1–7 months).

**Within 6 Months.** We classified 3 aneurysms as nonoccluded because the first follow-up MRA was performed after 6 months (despite the follow-up >6-month MRA showing occlusion). Similarly, we classified the aneurysm in the patient who refused follow-up imaging as nonoccluded. Therefore, within 6 months, 78.8% (41/52) of aneurysms achieved adequate occlusion (Raymond scale 1 or 2) or remodeling (1 dysplastic fusiform and 1 dissecting aneurysm) (Table 3). The complete occlusion rate (Raymond scale 1) was 69.2% (36/52). A residual aneurysm sac remnant (Raymond scale 3) was seen in 21.1% (11/52) of aneurysms at 6 months.

**Between 6 and 18 Months.** We classified the aneurysm in the patient who refused follow-up imaging as nonoccluded. The mean follow-up time until the second MRA was 17.2 months (range, 7–20 months). Six additional aneurysms were completely occluded (Raymond scale 1). The total adequate occlusion rate (Raymond scale 1 and 2) in this study was 90.3% (47/52), and the complete occlusion rate (Raymond scale 1) was 82.7% (43/52) at 18 months.

The maximum sac diameters of aneurysms with residual sac filling (Raymond scale 3) and aneurysms that showed complete occlusion (Raymond scale 1) were not significantly different ( $P = .28$ ; mean, 11.5 mm [range, 4.0–22.0 mm] versus mean, 8.5 mm

[range, 1.0–28.0 mm]). The neck width of aneurysms with residual sac filling (Raymond scale 3) was not significantly different from that of those with complete occlusion (Raymond scale 1) ( $P = .10$ ; mean, 8.0 mm [range, 3.0–21.0 mm] versus mean, 4.5 mm [range, 1.0–16.0 mm]).

No in-stent stenosis was identified at either follow-up time point.

In summary, the adequate occlusion rate and the complete occlusion rate were 78.8% (41/52) and 69.2% (36/52), respectively, at 6 months. At 18 months, the adequate occlusion rate was 90.3% (47/52) and the complete occlusion rate was 82.7% (43/52).

### Postprocedural Clinical Outcomes 30 Days to 1 Year

One patient experienced blurry vision 3 months following the procedure, and ophthalmologic examination showed papilledema (Table 2). MRA at 5 months postprocedure showed that there was residual neck filling (Raymond Scale 2; 8-mm neck remnant) in a paraophthalmic segment aneurysm (Fig 2). The stent was no longer covering the entire aneurysm neck, and the aneurysm cross-sectional diameter had increased during the 5-month interval from 17 to 32 mm. The aneurysm was re-treated with a larger diameter flow-diverter device, the Flow-Redirection Endoluminal Device (FRED; MicroVention, Tustin, California), which was deployed across the uncovered neck. The rationale was that this larger stent would give superior apposition to the parent vessel lumen distal to this segment. MRA performed 1, 2, and 6 months after the second procedure showed stability of the aneurysm cross-sectional diameter with a reduction in the neck remnant size (Raymond Scale 2; 4 mm).

There was 1 further major adverse event. This patient had a recurrent left cavernous segment ICA 9.5-mm wide-neck aneurysm after coiling. During the procedure, there was a transient iatrogenic carotid cavernous fistula, which had resolved by the end of the procedure when the Pipeline Shield was satisfactorily deployed across the neck of the aneurysm. However, the patient presented with sudden-onset pulsatile tinnitus 1 month later, and DSA showed that there was recurrent carotid cavernous fistulation (note that because our methodology used the IntraPED study adverse event classification as described above, this was classified as a postprocedural event). This fistula was treated with coil embolization. There were no further clinical sequelae.

Cumulative adverse events of any sort occurred after treatment of 4 anterior circulation aneurysms from a total of 38 (10.5%) target aneurysms. There was 1 adverse event (periprocedural subdural hematoma) that occurred after treatment of a posterior circulation aneurysm from a total of 6 (16.7%) target aneurysms.

No aneurysms ruptured periprocedurally or at 1-year follow-up.

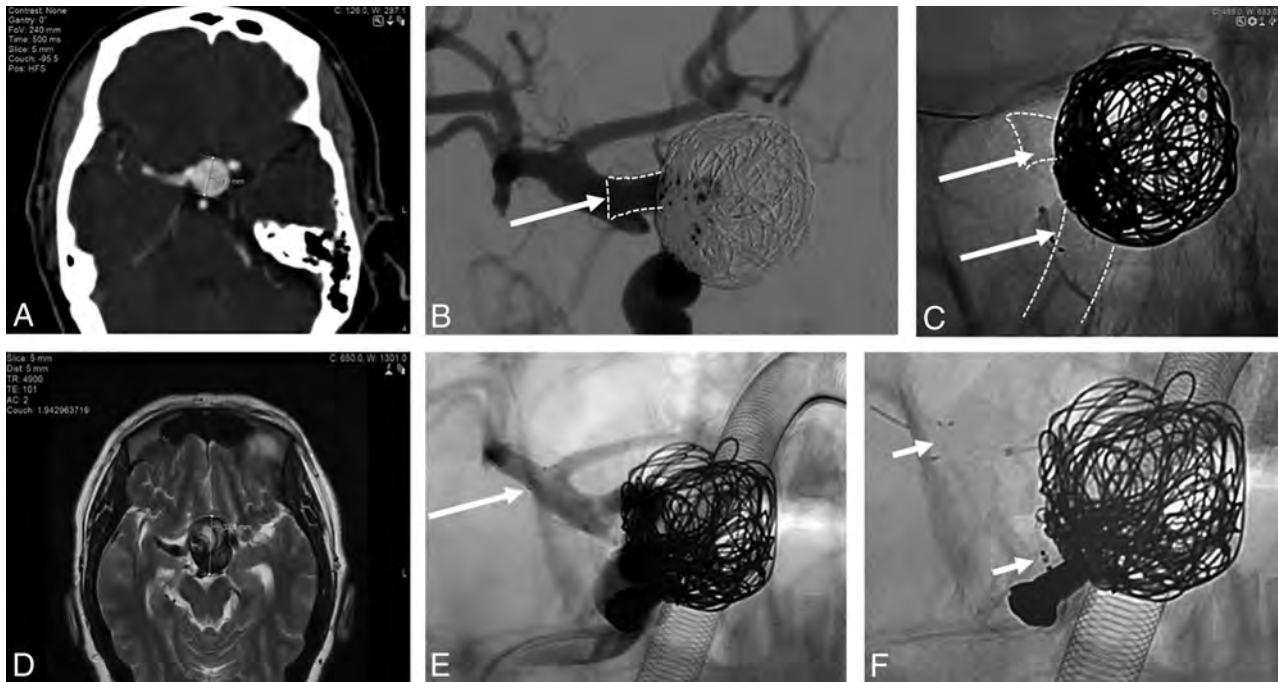


**FIG 2.** Pipeline Shield case. *A*, CTA shows a right ICA paraophthalmic segment aneurysm measuring 17 mm in maximal sac diameter before treatment. *B*, Digital subtraction angiography oblique view shows the aneurysm after treatment with a 5 × 14 mm Pipeline Shield and 7 adjunctive coils. The landing zone (arrow) was selected as shown because the ICA paraophthalmic segment lumen was 5.00 mm in diameter, the ICA posterior communicating artery segment lumen was 4.75 mm in diameter (wider at the infundibulum), and the ICA terminal segment was 5.5 mm in diameter. The nominal maximum diameter of the largest Pipeline Shield is 5.0 mm with a maximum unconstrained diameter of 5.25 mm. *C*, Different oblique view without subtraction after treatment. The Pipeline Shield (arrows) has a flared appearance as it bulges into the infundibulum of the ICA posterior communicating artery segment. *D*, MR imaging at 5 months postprocedure shows that the aneurysm cross-sectional diameter had increased during the 5-month interval from 17 to 32 mm. The stent was no longer covering the entire aneurysm neck in the ICA paraophthalmic segment. *E* and *F*, The aneurysm was re-treated by telescoping a larger-diameter flow-diverter device (FRED, MicroVention; arrows show proximal and distal markers), measuring 5.5 × 14 mm, through the Pipeline Shield, across the small segment of uncovered neck, and landing the stent in the ICA terminal segment. Anesthetic equipment is superimposed over the image.

## DISCUSSION

This pragmatic and non-industry-sponsored outcome study adds to the limited safety and efficacy outcome evidence of the third-generation Pipeline Shield. In contrast to earlier generation PEDs, which have been studied extensively,<sup>3,7,15-19</sup> there is only 1 recent industry-sponsored prospective study (Pipeline Flex Embolization Device with Shield Technology (PFLEX))<sup>16,20</sup> and several case reports<sup>21,22</sup> examining the Pipeline Shield when used to treat aneurysms that have not acutely ruptured. We analyzed the 30-day and 1-year mortality and morbidity rates, and the 6- and 18-month radiographic aneurysm occlusion outcomes.

### Clinical Outcomes

Our overall mortality rate was 2.3%, which was lower than the 3.8% seen in the IntrePED study (the largest clinical trial for previous generation PEDs)<sup>3</sup> and higher than the PFLEX study, which was 0%.<sup>20</sup> The 1 death in our study was caused by a subdural hematoma 15 days after treatment.

The overall morbidity rate of 6.8% in our study (1 periprocedural and 2 postprocedural major adverse events in 44 procedures) is similar to that in a very similar study using previous-generation devices (10.0%)<sup>9</sup> as well as the IntrePED study (7.4%).<sup>3</sup> Two of the major adverse events occurred in giant aneurysms, and 1, in a large aneurysm, again highlighting the

higher complication risk associated with PED (or any) treatment of large or giant aneurysms ( $\geq 10$  mm). Because the PFLEX study used a different outcome classification from the IntrePED study classification, which was used in the current study, a direct comparison with the PFLEX outcomes was limited. For indirect comparison, the PFLEX study showed 0% major strokes (defined as the NIHSS score increasing by 4 points) or neurologic deaths at 1 year postprocedure. However, there were 6% (3/50) procedure-related adverse events (headache, diplopia, and retroperitoneal hematoma) categorized as serious in the PFLEX study. Events including a carotid dissection and a cerebral infarction (the NIHSS score changed by  $\leq 3$  points) also occurred but were considered nonserious events.

In vitro, ex vivo, and in vivo studies have shown reduced thrombogenicity of the Pipeline Shield compared with the PED without phosphorylcholine surface modification.<sup>8,23,24</sup> There are no clinical data to prove that surface modification results in improved clinical outcomes, but the following observations suggest that surface modification does not worsen clinical outcomes. No thromboembolic events occurred during the procedure; 1 patient (2.3%), who also had atrial fibrillation, had a periprocedural thromboembolic event; and no thromboembolic events occurred during postprocedural follow-up. In the PFLEX study,

there were no procedural or periprocedural thromboembolic events; but 1 patient experienced a thromboembolic event at 1 year (2%). In comparison, the previous-generation PEDs led to a periprocedural thromboembolic event rate of 6.5% and 3.3% in the pipeline Embolization Device for the intracranial treatment of aneurysms trial (PITA)<sup>1</sup> and IntrePED<sup>3</sup> studies respectively; and in 2 large meta-analyses of flow-diverter device treatment, the rate was 3.6% and 5%.<sup>25,26</sup> At a median follow-up of 19 months, there was a cumulative 4.7% thromboembolic event rate in the IntrePED study. Although the numbers are too small for a comparative multivariate analysis, a very similar pragmatic study at our center using previous-generation PEDs yielded a cumulative 10.0% thromboembolic event rate.<sup>9</sup> Taken together, the data from these studies and the current study suggest that there is no reason to refute the *in vitro*, *ex vivo*, and *in vivo* (animal and clinical) evidence of the low thrombogenicity of the Pipeline Shield.

### Occlusion Rates

Our complete occlusion (Raymond scale 1) rate was 69.2% at 6 months and 82.7% at 18 months. Our results are not dissimilar to those of flow-diverter device studies in general (ranging between 55% and 95% during various follow-up intervals)<sup>27,28</sup> or the studies described below using the PED only. Our study of the first 2 generations of PEDs, also using 3D-TOF-MRA follow-up, yielded similar complete occlusion rates at 6 and 18 months (65.6% and 78.1%, respectively).<sup>9</sup> At the 1-year follow up of the PFLEX study,<sup>20</sup> the complete aneurysm occlusion rate was 81.8%.

We note that the pipeline for uncoilable or failed aneurysms study (PUFS)<sup>5</sup> study had a complete occlusion rate of 86.8% at 1-year follow up and the PITA<sup>1</sup> had 93.3% at 6-month follow up, which were higher than our occlusion rates. Although statistical comparison cannot be made directly among the different studies, we make the following tentative observations: First, the mean aneurysmal sac size in these studies was larger than that in our study (18.0 and 11.5 mm compared with 9.0 mm in our study), so the putative occlusion rate differences are unlikely to be caused by a difference in aneurysm size (indeed, a meta-analysis with flow-diverter devices showed no relationship between the occlusion rates and sac diameter of aneurysms<sup>5</sup>). Second, the putative occlusion rate differences are unlikely to be caused by a difference in adjunctive coiling because the PITA study adjunctive coil rate was higher (51.6%), while the PUFS rate was lower (0.9%) compared with our rate (28.8%). A lack of relationship between occlusion rates and adjunctive coil rates might be expected because there is little evidence that adjunctive coiling when using flow-diverter devices is beneficial.<sup>29</sup> Anecdotally, there is more motivation for adjunctive coiling to prevent rupture of large aneurysms during thrombosis rather than to influence occlusion rates. Third, additional overlapping PEDs are anecdotally thought to influence occlusion rates by increasing mesh density. It is plausible that the putative occlusion rate differences are caused by a difference in mesh density because the mean number of Pipeline Shields used per aneurysm was 0.9 (or if nontarget aneurysms are ignored, 1.0), whereas in PITA and PUFS, the rates were 1.5 and 3, respectively. We also note that the PFLEX study<sup>20</sup> had an

occlusion rate similar to that in our study using a similar Pipeline Shield rate of 1.1.

Aneurysm sac diameter is considered an important factor influencing the occlusion rate in endovascular treatment, especially in aneurysm coiling. However, as mentioned above, a meta-analysis with flow-diverter devices showed no relationship between the occlusion rates and sac diameter of aneurysms.<sup>5</sup> Our results also did not show that the sac diameter of the Pipeline Shield influences occlusion rates.

In contrast to the first 2 generations of PEDs studied previously,<sup>9</sup> no significant difference in neck width was seen when occluded and nonoccluded subgroups were compared following Pipeline Shield treatment.

### Strengths and Limitations

Studies such as PFLEX,<sup>20</sup> PITA,<sup>1</sup> and PUFs<sup>5</sup> used DSA as the follow-up technique for PED-treated aneurysms. There has been widespread adoption of flow-diverter devices with a range of follow-up methods and time points, and a recent meta-analysis that compared MRA and DSA concluded that both 3D-TOF-MRA and contrast-enhanced MRA can be used reliably to follow up flow-diverter devices.<sup>30</sup> The sensitivity and specificity of TOF-MRA were 86% and 95%, respectively. Contrast-enhanced MRA had a sensitivity and specificity of 90% and 92%. MRA has been chosen as a suitable follow-up imaging technique in pragmatic flow-diverter device studies including the flow diversion in the treatment of aneurysms (FIAT) randomized controlled trial, which analyzed the safety and efficacy of PEDs.<sup>31</sup> As in a study of previous-generation PEDs,<sup>9</sup> we used 3D-TOF-MRA.

Despite the data from the meta-analysis, there may be concerns that the PED can result in a marked local signal void due to a larger bimetallic surface area coverage and radiofrequency shielding,<sup>32,33</sup> which may cause false-positive detection of in-stent stenosis.<sup>34,35</sup> However, the impact of this potential overestimation of in-stent stenosis was negligible in our study because no in-stent stenosis was seen on the 3D-TOF-MRA follow-up.

A further concern using 3D-TOF-MRA as a follow-up technique may relate to false-positive detection of intra-aneurysmal residual flow, which has been recognized with TOF-MRA due to T1-weighted hyperintensity of the thrombus.<sup>36</sup> False-positive detection of intra-aneurysmal residual flow in our study is likely to be very low because other sequences (T2-weighted) and scan planes (multiplanar reformat) were routinely reviewed. In our institution, we have yet to discover a false-positive after a subsequent DSA, nor was a false-positive seen in a previous PED study using 3D-TOF-MRA when analysis of multiple MR imaging planes and sequences was also performed at follow-up.<sup>9</sup> Furthermore, cross-sectional MR imaging confirmed complete occlusion because a decrease in the size of the aneurysm sac on cross-sectional imaging appears to be the single most consistent sign of durable aneurysm occlusion (likely implying full endothelialization of the device construct and secondary exclusion of the aneurysm from the parent circulation).<sup>37,38</sup> In contrast, intra-aneurysmal thrombosis in a nonoccluded growing aneurysm can occasionally appear on DSA as an apparently occluded aneurysm (false-negative).

Although contrast-enhanced MRA may theoretically overcome some of these potential concerns, the data from the meta-analysis (particularly at 1.5T) do not support a change of practice at our institution from TOF to contrast-enhanced MRA, to obviate the potential drawbacks of TOF.<sup>36,39</sup>

Nonetheless, a limitation of this study is that DSA was not performed for follow-up, which would have allowed direct comparison of efficacy outcomes with many previous studies and provided complementary information.

Another limitation of this study is that it was performed in a single center and is retrospective; however, the results of this pragmatic study are likely to be generalizable to similar centers.<sup>9</sup> This would be other centers with a similar operator number (3 performing PEDs), operator experience (10, 9, and 4 years of interventional neuroradiology experience at the point of first deployment of the Shield), neurovascular multidisciplinary team composition (2 neurosurgeons, 4 interventional neuroradiologists, 1 stroke neurologist), and a population at risk (3.5 million in a unit treating 160–200 aneurysms per year).

A further limitation of the study is the small absolute number of cases. However, small numbers can be expected in a single-center study (we note that the National Institute of Clinical Excellence in the UK estimates that 60 PEDs are used in the entire UK per year<sup>40</sup>), and even the seminal PITA study consisted of only 31 aneurysms.<sup>1</sup> Furthermore, because PFLEX included 50 patients with 50 unruptured target aneurysms, the current study, which includes 41 patients with 44 unruptured target aneurysms, almost doubles the total number of Pipeline Shield cases studied (94 unruptured aneurysms).

The overall incidence of DWI positive foci presumably representing thromboembolic events following endovascular treatment of intracranial aneurysms is approximately 50%, with no significant difference between coiling and flow diversion.<sup>13</sup> According to some studies from the coiling and flow-diversion literature, there is no association between the presence of DWI lesions and neuropsychological examination performance.<sup>41,42</sup> Nonetheless, future studies may wish to routinely perform post-procedural DWI to investigate the rate of these foci after Pipeline Shield deployment.

## CONCLUSIONS

Our retrospective study Pipeline Embolization Device with Shield Technology in Unruptured Aneurysms (PEDSU) is a pragmatic and non-industry-sponsored study into clinical and radiographic (safety and efficacy) outcomes of the third-generation Pipeline Shield device. The study adds to the limited outcome evidence regarding the third-generation Pipeline Shield used to treat aneurysms that have not acutely ruptured. Our results demonstrated that occlusion rates and safety outcomes are similar compared with those in previously published studies using other flow-diverter devices or the first 2 generations of PEDs. Follow-up with 3D-TOF-MRA showed similar PED occlusion results compared with those acquired with MRA or DSA from other studies.

Disclosures: Naga Kandasamy—UNRELATED: Travel/Accommodations/Meeting Expenses Unrelated to Activities Listed: Medtronic, Comments: funding for

conferences and academic meetings. Jonathan Hart—UNRELATED: Travel/Accommodations/Meeting Expenses Unrelated to Activities Listed: MicroVention, Comments: Money was not paid directly to me, but costs of travel, accommodation, and course fees were covered by the company to attend the “Brainstorm” meeting in Edinburgh 2019.

## REFERENCES

1. Nelson PK, Lylyk P, Szikora I, et al. **The Pipeline Embolization Device for the intracranial treatment of aneurysms trial.** *AJNR Am J Neuroradiol* 2011;32:34–40 CrossRef Medline
2. Premarket approval. <https://www.accessdata.fda.gov/scripts/cdrh/cfdocs/cfpma/pma.cfm?ID=P100018>. Accessed June 12, 2019
3. Kallmes DF, Hanel R, Lopes D, et al. **International retrospective study of the Pipeline embolization device: a multicenter aneurysm treatment study.** *AJNR Am J Neuroradiol* 2015;36:108–115 CrossRef Medline
4. Kallmes DF, Brinjikji W, Boccardi E, et al. **Aneurysm study of Pipeline in an observational registry (ASPIRE).** *Interv Neurol* 2016;5:89–99 CrossRef Medline
5. Becske T, Kallmes DF, Saatci I, et al. **Pipeline for uncoilable or failed aneurysms: results from a multicenter clinical trial.** *Radiology* 2013;267:858–68 CrossRef Medline
6. Pereira VM, Kelly M, Vega P, et al. **New Pipeline Flex device: initial experience and technical nuances.** *J Neurointerv Surg* 2015;7:920–25 CrossRef Medline
7. Colby GP, Lin LM, Caplan JM, et al. **Immediate procedural outcomes in 44 consecutive Pipeline Flex cases: the first North American single-center series.** *J Neurointerv Surg* 2016;8:702–09 CrossRef Medline
8. Girdhar G, Li J, Kostousov L, et al. **In-vitro thrombogenicity assessment of flow diversion and aneurysm bridging devices.** *J Thromb Thrombolysis* 2015;40:437–43 CrossRef Medline
9. Yang SH, Hampton T, Kandasamy N, et al. **Outcome study of the Pipeline embolization device for treatment of intracranial aneurysms at a single UK institution.** *Br J Neurosurg* 2017;31:661–67 CrossRef Medline
10. Comin J, Kallmes DF. **Platelet-function testing in patients undergoing neurovascular procedures: caught between a rock and a hard place.** *AJNR Am J Neuroradiol* 2013;34:730–34 CrossRef Medline
11. Brinjikji W, Lanzino G, Cloft HJ, et al. **Platelet testing is associated with worse clinical outcomes for patients treated with the Pipeline Embolization Device.** *AJNR Am J Neuroradiol* 2015;36:2090–95 CrossRef Medline
12. Siller-Matula JM, Trenk D, Schrör K, et al. **Response variability to P2Y<sub>12</sub> receptor inhibitors.** *JACC Cardiovasc Interv* 2013;6:1111–28 CrossRef Medline
13. Brasiense LBC, Stanley MA, Grewal SS, et al. **Silent ischemic events after Pipeline embolization device: a prospective evaluation with MR diffusion-weighted imaging.** *J Neurointerv Surg* 2016;8:1136–39 CrossRef Medline
14. Shapiro M, Becske T, Riina HA, et al. **Toward an endovascular interlinal carotid artery classification system.** *AJNR Am J Neuroradiol* 2014;35:230–36 CrossRef Medline
15. Duckworth EAM, Nickele C, Hoit D, et al. **The first North American use of the Pipeline flex flow diverter.** *J Neurointerv Surg* 2016;8:e8 CrossRef Medline
16. Martínez-Galdámez M, Lamin SM, Lagios KG, et al. **Periprocedural outcomes and early safety with the use of the Pipeline Flex Embolization Device with Shield Technology for unruptured intracranial aneurysms: preliminary results from a prospective clinical study.** *J Neurointerv Surg* 2017;9:772–76 CrossRef Medline
17. Lylyk P, Miranda C, Ceratto R, et al. **Curative endovascular reconstruction of cerebral aneurysms with the Pipeline embolization device: the Buenos Aires experience.** *Neurosurgery* 2009;64:632–42 CrossRef Medline
18. Szikora I, Berentei Z, Kulcsar Z, et al. **Treatment of intracranial aneurysms by functional reconstruction of the parent artery: the**

- Budapest experience with the Pipeline embolization device. *AJNR Am J Neuroradiol* 2010;31:1139–47 CrossRef Medline
19. Fischer S, Vajda Z, Perez MA, et al. **Pipeline Embolization Device (PED) for neurovascular reconstruction: initial experience in the treatment of 101 intracranial aneurysms and dissections.** *Neuroradiology* 2012;54:369–82 CrossRef Medline
  20. Martínez-Galdámez M, Lamin SM, Lagios KG, et al. **Treatment of intracranial aneurysms using the Pipeline flex embolization device with shield technology: angiographic and safety outcomes at 1-year follow-up.** *J Neurointerv Surg* 2019;11:396–99 CrossRef Medline
  21. Griessenauer CJ, Goren O, Dalal SS, et al. **Pipeline Embolization Device with Shield Technology for intracranial aneurysms: an initial U.S. experience.** *World Neurosurg* 2018;119:0–14 CrossRef Medline
  22. Orlov K, Kisilitsin D, Strelnikov N, et al. **Experience using Pipeline Embolization Device with Shield Technology in a patient lacking a full postoperative dual antiplatelet therapy regimen.** *Interv Neuroradiol* 2018;24:270–73 CrossRef Medline
  23. Matsuda Y, Chung J, Lopes DK. **Analysis of neointima development in flow diverters using optical coherence tomography imaging.** *J Neurointerv Surg* 2018;10:162–67 CrossRef Medline
  24. Hagen MW, Girdhar G, Wainwright J, et al. **Thrombogenicity of flow diverters in an ex vivo shunt model: effect of phosphorylcholine surface modification.** *J Neurointerv Surg* 2017;9:1006–11 CrossRef Medline
  25. Arrese I, Sarabia R, Pintado R, et al. **Flow-diverter devices for intracranial aneurysms: systematic review and meta-analysis.** *Neurosurgery* 2013;73:193–200 CrossRef Medline
  26. Brinjikji W, Murad MH, Lanzino G, et al. **Endovascular treatment of intracranial aneurysms with flow diverters: a meta-analysis.** *Stroke* 2013;44:442–47 CrossRef Medline
  27. Byrne JV, Beltechi R, Yarnold JA, et al. **Early experience in the treatment of intra-cranial aneurysms by endovascular flow diversion: a multicentre prospective study.** *PLoS One* 2010;5:e12492–98 CrossRef
  28. Saatci I, Yavuz K, Ozer C, et al. **Treatment of intracranial aneurysms using the Pipeline Flow-Diverter Embolization Device: a single-center experience with long-term follow-up results.** *AJNR Am J Neuroradiol* 2012;33:1436–46 CrossRef Medline
  29. Sweid A, Atallah E, Herial N, et al. **Pipeline-assisted coiling versus Pipeline in flow diversion treatment of intracranial aneurysms.** *J Clin Neurosci* 2018;58:20–24 CrossRef Medline
  30. Ahmed SU, Mocco J, Zhang X, et al. **MRA versus DSA for the follow-up imaging of intracranial aneurysms treated using endovascular techniques: a meta-analysis.** *J Neurointerv Surg* 2019;11:1009–14 CrossRef Medline
  31. Raymond J, Gentric JC, Darsaut TE, et al. **Flow diversion in the treatment of aneurysms: a randomized care trial and registry.** *J Neurosurg* 2017;127:454–62 CrossRef Medline
  32. Wall A, Kugel H, Bachman R, et al. **3.0 T vs. 1.5 T MR angiography: in vitro comparison of intravascular stent artifacts.** *J Magn Reson Imaging* 2005;22:772–79 CrossRef Medline
  33. Wang Y, Truong TN, Yen C, et al. **Quantitative evaluation of susceptibility and shielding effects of nitinol, platinum, cobalt-alloy, and stainless steel stents.** *Magn Reson Med* 2003;49:972–76 CrossRef Medline
  34. Blum MB, Puchner S, Funovics MA, et al. **Quantification and detectability of in-stent stenosis with CT angiography and MR angiography in arterial stents in vitro.** *AJR Am J Roentgenol* 2007;189:1238–42 CrossRef
  35. Lettau M, Sauer A, Heiland S, et al. **Carotid artery stents: in vitro comparison of different stent designs and sizes using CT angiography and contrast-enhanced MR angiography at 1.5T and 3T.** *AJNR Am J Neuroradiol* 2009;30:1993–97 CrossRef Medline
  36. Boddu SR, Tong FC, Dehkharghani S, et al. **Contrast-enhanced time-resolved MRA for follow-up of intracranial aneurysms treated with the Pipeline Embolization Device.** *AJNR Am J Neuroradiol* 2014;35:2112–18 CrossRef Medline
  37. Slater LA, Soufan C, Holt M, et al. **Effect of flow diversion with Silk on aneurysm size: a single-center experience.** *Interv Neuroradiol* 2015;21:12–18 CrossRef Medline
  38. Shapiro M. **Neurovascular topics in the endovascular arena. SAM-vascular-audience response (AR) self-assessment module (SAM).** In: *Proceedings of the Annual Meeting of the American Society of Neuroradiology*, Long Beach, California. April 22–27, 2017
  39. Attali J, Benaissa A, Soize S, et al. **Follow-up of intracranial aneurysms treated by flow diverter: comparison of three-dimensional time-of-flight MR angiography (3D-TOF-MRA) and contrast-enhanced MR angiography (CE-MRA) sequences with digital subtraction angiography as the gold standard.** *J Neurointerv Surg* 2016;8:81–86 CrossRef Medline
  40. National Institute for Health and Care Excellence. **Medical technologies guidance [MTG10], 2012.** <https://www.nice.org.uk/guidance/mtg10/chapter/4-NHS-considerations>. Accessed May 14, 2017
  41. Kang DH, Hwang YH, Kim YS, et al. **Cognitive outcome and clinically silent thromboembolic events after coiling of asymptomatic unruptured intracranial aneurysms.** *Neurosurgery* 2013;72:638–45 CrossRef Medline
  42. Iosif C, Camilleri Y, Saleme S, et al. **Diffusion-weighted imaging-detected ischemic lesions associated with flow-diverting stents in intracranial aneurysms: safety, potential mechanisms, clinical outcome, and concerns.** *J Neurosurg* 2015;122:627–36 CrossRef Medline

# Comparing Morphology and Hemodynamics of Stable-versus-Growing and Grown Intracranial Aneurysms

E.L. Leemans, B.M.W. Cornelissen, C.H. Slump, C.B.L.M. Majoie, J.R. Cebral, and H.A. Marquering

## ABSTRACT

**BACKGROUND AND PURPOSE:** Aneurysm growth has been related to higher rupture risk. A better understanding of the characteristics related to growth may assist in the treatment decisions of unruptured intracranial aneurysms. This study aimed to identify morphologic and hemodynamic characteristics associated with aneurysm growth and to determine whether these characteristics deviate further from those of stable aneurysms after growth.

**MATERIALS AND METHODS:** We included 81 stable and 56 growing aneurysms. 3D vascular models were segmented on CTA, MRA, or 3D rotational angiographic images. With these models, we performed computational fluid dynamics simulations. Morphologic (size, size ratios, and shape) and hemodynamic (inflow, vorticity, shear stress, oscillatory shear index, flow instability) characteristics were automatically calculated. We compared the characteristics between aneurysms that were stable and those that had grown at baseline and final imaging. The significance level after Bonferroni correction was  $P < .002$ .

**RESULTS:** At baseline, no significant differences between aneurysms that were stable and those that had grown were detected ( $P > .002$ ). Significant differences between aneurysms that were stable and those that had grown were seen at the final imaging for shear rate, aneurysm velocity, vorticity, and mean wall shear stress ( $P < .002$ ). The latter was 11.5 (interquartile range, 5.4–18.8 dyne/cm<sup>2</sup>) compared with 17.5 (interquartile range, 11.2–29.9 dyne/cm<sup>2</sup>) in stable aneurysms ( $P = .001$ ). Additionally, a trend toward lower area weighted average Gaussian curvature in aneurysms that had grown was observed with a median of 6.0 (interquartile range, 3.2–10.7 cm<sup>-2</sup>) compared with 10.4 (interquartile range, 5.0–21.2 cm<sup>-2</sup>) in stable aneurysms ( $P = .004$ ).

**CONCLUSIONS:** Morphologic and hemodynamic characteristics at baseline were not associated with aneurysm growth in our population. After growth, almost all indices increase toward values associated with higher rupture risks. Therefore, we stress the importance of longitudinal imaging and repeat risk assessment in unruptured aneurysms.

**ABBREVIATIONS:** CFD = computational fluid dynamics; CLL = core-line length; EI = ellipticity index; ELAPSS = Earlier subarachnoid hemorrhage, location of the aneurysm, age, population, size, and shape of the aneurysm; GAA = area weighted average of the Gaussian curvature; IQR = interquartile range; LSA = low shear stress area; OSI = oscillatory shear index; PHASES = Population, Hypertension, Age, Size, Earlier Subarachnoid Hemorrhage, and Site; SizeR = size ratio; 3DRA = 3D rotational angiography; VO = mean vorticity; VOR = volume-to-ostium ratio; WSS = wall shear stress

Intracranial aneurysm rupture often leads to death or severe disability. This imposes a considerable clinical and socio-economic burden. Usually, aneurysms are asymptomatic until they rupture. Due to improvement in and the increased use of imaging, an increasing number of unruptured aneurysms are being detected.<sup>1</sup>

The decision to treat an unruptured aneurysm is difficult because both the treatment risk and rupture risk must be considered. Treatment risk has already been studied extensively and is dependent on the aneurysm location and size, patient age, and clinical condition; for instance, older patients have a higher risk of complications.<sup>2,3</sup> The most used determinants for rupture risk are size, location, and growth of the aneurysm.<sup>4</sup> However, many SAHs admitted to the hospital arise from small aneurysms.<sup>5,6</sup> Therefore, more characteristics are needed to improve the rupture risk assessment. Several additional characteristics can be derived from

Received June 20, 2019; accepted after revision September 23.

From the Departments of Biomedical Engineering and Physics (E.L.L., B.M.W.C., H.A.M.) and Radiology and Nuclear Medicine (E.L.L., B.M.W.C., C.B.L.M.M., H.A.M.), Amsterdam UMC, Academic Medical Center, University of Amsterdam, Amsterdam, the Netherlands; MIRA Institute for Biomedical Engineering and Technical Medicine (B.M.W.C., C.H.S.), University of Twente, Enschede, the Netherlands; and Bioengineering and Mechanical Engineering Department, (J.R.C.), Volgenau School of Engineering, George Mason University, Fairfax, Virginia.

This study was supported by a grant from the TWIN association, Hengelo, the Netherlands.

Please address correspondence to Eva L. Leemans, Departments of Biomedical Engineering and Physics, Radiology and Nuclear Medicine, Room L0-147, Amsterdam UMC, location AMC, Meibergdreef 9, 1105AZ, Amsterdam, the Netherlands; e-mail: e.l.leemans@amc.uva.nl  
<http://dx.doi.org/10.3174/ajnr.A6307>

imaging data for such an assessment. These characteristics have been based on aneurysm morphology and hemodynamics.<sup>7-9</sup> Nevertheless, the clinical applicability of these characteristics is still limited.

Approximately 10% of aneurysms grow after detection.<sup>10</sup> Studies have shown a higher rupture risk in growing aneurysms.<sup>11</sup> As a result, aneurysm growth gives a high motivation for intervention. Yet, our understanding of the association between aneurysmal growth and rupture-related characteristics is limited. Recently, the ELAPSS score (Earlier subarachnoid hemorrhage, location of the aneurysm, age, population, size, and shape of the aneurysm) has been developed to estimate the 3- and 5-year risk of aneurysm growth.<sup>12</sup> This score incorporates patient characteristics (age, population, previous SAH) and aneurysm characteristics (size and location). Only a few studies have evaluated the association of more morphologic characteristics with aneurysm growth.<sup>13-15</sup>

Several studies have examined the relation between hemodynamics and unstable (growing or symptomatic) aneurysms.<sup>16,17</sup> These studies have shown a more concentrated area of high wall shear stress (WSS) with more complex intra-aneurysmal flows in unstable aneurysms. These differences have some similarities with the differences between stable and ruptured aneurysms, which show extreme high and low WSS and complex intra-aneurysmal flow patterns with a high oscillatory shear stress in ruptured aneurysms.<sup>16,18-20</sup>

Many of the studies evaluating the relation between hemodynamics and aneurysm stability had inconclusive findings or examined a small population. As a result, it is unknown whether aneurysm growth is associated with hemodynamic characteristics. Therefore, the primary aim of this study was to identify morphologic and hemodynamic characteristics associated with aneurysm growth. Because the rupture risk seems to increase with aneurysm growth, we also evaluated the differences between morphologic and hemodynamic characteristics of aneurysms that are stable and those that have grown at last imaging, to determine whether characteristics of aneurysms that are growing become more similar to those of ruptured aneurysms.

## MATERIALS AND METHODS

### Population

We combined patients from 2 data bases. The first data base consisted of all patients who presented with an unruptured intracranial aneurysm at the Amsterdam UMC, Academic Medical Center (Amsterdam), between 2012 and 2016, who had an MRA before and after aneurysm growth.

The second data base consisted of patients from multiple hospitals in the United States with an unruptured aneurysm. This data base mostly consisted of patients from the Inova Fairfax Hospital (Virginia), Mt. Sinai Medical Center (New York), and the Mayo Clinic (Minnesota). Imaging consisted of 3D rotational angiography (3DRA) or CTA. For all cases, the imaging before and after aneurysm growth was performed with the same technique.

Aneurysm growth was primarily evaluated by the local neuro-radiologist. Growth was evaluated on the basis of the first and last available imaging (duration of follow-up was 0.5–13 years). Aneurysms were marked as growing when a change in size of at

least 0.5 mm or a change in shape was seen. Aneurysms were marked as stable when no size or shape change was seen. Aneurysms with a total follow-up of <1 year and not showing a change in size or shape were excluded from this study. For the control group, we included all the stable cases in the second data base. Imaging of the stable cases mostly consisted of 3DRA; 10 patients had undergone CTA.

All images were anonymized. The requirement for informed consent was waived by the local institutions review boards because no diagnostics other than routine clinical imaging were used in this study.

### Computational Fluid Dynamics

Computational fluid dynamics (CFD) simulations were created for all aneurysms. The first step was creating 3D vascular reconstructions. To obtain these reconstructions, we performed segmentation of the patient-specific vascular geometry and subsequently created a tetrahedral mesh. The models based on MR imaging were created with the Vascular Modeling Toolkit ([www.vmtk.org](http://www.vmtk.org); Orobix, Bergamo, Italy); the models based on CTA and 3DRA were created using in-house-developed software. The vessel segmentation extended proximally to the ICA for anterior circulation aneurysms and to the vertebral artery for posterior circulation aneurysms. In 4 cases, the vertebral artery was not present in the imaging FOV; for these cases, the segmentation started at the basilar artery.

For all cases, growth was confirmed using 3D vascular reconstructions. The models were manually aligned and evaluated for a change in size and shape. An aneurysm was definitively categorized as growing if a change of > 0.5 mm was seen between baseline and last imaging.

The aneurysm was isolated by manually identifying the aneurysm neck. The position of the neck before and after growth was compared and, if needed, was corrected to make sure the positioning was comparable in both vascular reconstructions.

No patient-specific inflow conditions were available. Therefore, we used flow profiles based on phase-contrast MR imaging of healthy subjects scaled with a power law to the area of the inflow vessel.<sup>21</sup> Outflow boundary conditions were prescribed according to the Murray Law.<sup>22</sup> The CFD simulations were subsequently performed using a previously described framework.<sup>23,24</sup> Blood was modeled as an incompressible Newtonian fluid with a viscosity of 0.04 dyne × s/cm and a density of 1.0 g/cm<sup>3</sup>. The vessel walls were assumed to be rigid with a nonslip boundary. For each simulation, 2 cardiac cycles were acquired. Only the last cardiac cycle was used to characterize the aneurysm hemodynamics.

### Aneurysm Characteristics

We analyzed 15 previously described morphologic and 12 hemodynamic characteristics (Table 1). The morphologic characteristics were related to size (size, neck diameter, volume, and parent vessel diameter), size ratios (height-width ratio, size ratio [SizeR], aspect ratio, bulge location, volume-to-ostium ratio [VOR], and isoperimetric ratio), shape (ellipticity index [EI], nonsphericity index, undulation index, and area weighted average of Gaussian curvature [GAA]). These characteristics were calculated according to previous work.<sup>25,26</sup>

**Table 1: Description of morphologic and hemodynamic characteristics**

Name	Description	Unit
Morphologic characteristics		
Aneurysm volume	Volume of the aneurysm	cm <sup>3</sup>
Aneurysm size	Maximum Euclidean distance of the aneurysm surface	cm
Neck size	Maximum Euclidean distance of the neck surface	cm
Parent vessel diameter	Diameter of the vessel nearest to the aneurysm neck	cm
AR	Aspect ratio; aneurysm height/neck size	Ratio
HWR	Height-to-width ratio; aneurysm height/aneurysm width	Ratio
BF	Bottleneck factor; aneurysm width/neck size	Ratio
BL	Bulge location; distance of plane with largest diameter from neck/aneurysm height	Ratio
SizeR	Size ratio	Ratio
VOR	Volume to ostium ratio; aneurysm volume/neck area	Ratio
IPR	Isoperimetric ratio; aneurysm area/aneurysm volume <sup>2/3</sup>	Ratio
UI	Undulation index	Index
EI	Ellipticity index	Index
NSI	Nonsphericity index	Index
GAA	Area weighted average of the Gaussian curvature	cm <sup>-2</sup>
Hemodynamic characteristics		
ICI	Inflow concentration index	Index
SR	Shear rate	1/s
VE	Mean velocity	cm/s
VO	Mean vorticity	1/s
WSS	Wall shear stress (time averaged mean and maximum)	dyne/cm <sup>2</sup>
LSA	Low shear stress area	%
SCI	Shear concentration index	Index
OSI	Oscillatory shear index (time averaged mean and maximum)	Index
CLL	Time-averaged vortex core-line length	cm
PODE	Proper orthogonal decomposition entropy	

The determined hemodynamic characteristics were related to aneurysm inflow (inflow concentration index), intrasaccular flow (maximum velocity, mean vorticity [VO], mean shear rate, and vortex core-line length [CLL]), flow instability (proper orthogonal decomposition entropy), and aneurysm wall shear stress (maximal, mean WSS, shear concentration index, low shear area [LSA], and mean and maximum oscillatory shear index [OSI]). These characteristics were calculated according to the methods described by Mut et al.<sup>27</sup>

We also calculated the Population, Hypertension, Age, Size, Earlier Subarachnoid Hemorrhage, and Site (PHASES)<sup>4</sup> and ELAPSS<sup>12</sup> scores to estimate the risk of rupture and growth in the population. The PHASES score consists of the population (Finnish, Japanese, or other), the presence of hypertension, age, aneurysm size, earlier SAH, and aneurysm location. The ELAPSS score consists of earlier SAH, aneurysm location, age, population (Finnish, Japanese, or other), and aneurysm shape and size. In most patients, no data on hypertension and population were available. In these patients, zero points were awarded for the missing values.

### Statistical Analysis

Normality of the data was tested using a Shapiro-Wilk test. Subsequently, normally distributed characteristics are reported as mean ± SD, and non-normally distributed characteristics, as median and interquartile range (IQR, 25%–75%).

We evaluated the difference in morphologic and hemodynamic characteristics between aneurysms that were stable and those that had grown at baseline and follow-up using an unpaired Student *t* test for normally distributed data. A Mann-Whitney *U* test was performed in case of non-normally distributed data. To prevent false discovery rates, we applied a Bonferroni correction

for multiple analyses on the same dependent variable. The adjusted significance level was .002 (.05/27).

We visually compared the changes in morphology and hemodynamics during growth by evaluating the ratio between stable aneurysms and those that had grown. This ratio represents the median values of the aneurysms that had grown over the median values of the stable aneurysms.

### RESULTS

We included 81 stable and 56 growing aneurysms. Patients with a growing aneurysm were more often female compared with patients with a stable aneurysm (86% compared with 65% in the stable group; *P* = .004). Patients with growing aneurysms were often younger (mean, 55 ± 14 years) compared with patients with stable aneurysms (mean, 59 ± 18 years; *P* = .13). Between the groups, there was no difference observed for aneurysm location (Table 2). Both the PHASES and ELAPSS scores did not significantly differ between aneurysms that were stable and those that had grown (*P* = .05 and .13, respectively). Growing aneurysms were significantly more frequently present in patients with a previous SAH (*P* < .001). Figure 1 shows that the basilar and posterior communicating arteries increase more in volume, compared with the MCA and ICA.

### Morphology

At baseline, there were no differences in morphologic characteristics between growing and stable aneurysms. After growth, the aneurysm size and volume were slightly larger compared with stable aneurysms (*P* = .006 and *P* = .006, respectively). The SizeR showed a trend toward higher values before growth, which was significantly higher after growth (median, 1.38 [IQR,

**Table 2: Baseline and hemodynamic characteristics for each group**

	Stable Aneurysms	Growing Aneurysms: Baseline	Grown Aneurysms: Follow-Up Imaging
No.	81	56 <sup>b</sup>	56
Sex			
Male	11 (14%)	7 (12%)	
Female	53 (65%)	48 (86%)	
Unknown	17 (21%)	1 (2%)	
Artery (%)			
ACA	5 (6%)	1 (2%)	
AcomA	8 (10%)	8 (14%)	
ICA	37 (46%)	18 (32%)	
MCA	16 (20%)	19 (34%)	
PcomA	12 (15%)	3 (5%)	
Posterior circulation	3 (3%)	7 (13%)	
Previous SAH = yes (%)	2 (2%)	14 (25%) <sup>a</sup>	
Configuration = lateral (%)	33 (41%)	18 (32%)	
Age (mean) (SD) (yr)	59 (18)	55 (14)	59 (13)
PHASES (mean) (SD)	3 (2)	4 (3) <sup>c</sup>	5 (3) <sup>a</sup>
Without hypertension and population	3 (3)	4 (3)	5 (3) <sup>c</sup>
ELAPSS (mean) (SD)	14 (6)	15 (7)	17 (6) <sup>b</sup>
Without population	14 (6)	15 (7)	17 (6) <sup>b</sup>
Hemodynamic characteristics			
ICI (median) (IQR)	0.4 (0.2–1.0)	0.5 (0.3–1.2)	0.6 (0.3–1.2)
SR (median) (IQR) (1/s)	207.3 (124.0–317.5)	190.1 (67.8–273.7)	126.3 (65.1–177.0) <sup>a</sup>
VE (median) (IQR) (cm/s)	9.4 (5.9–13.6)	8.0 (4.6–11.4)	6.6 (3.8–10.2) <sup>b</sup>
VO (median) (IQR) (l/s)	270.5 (165.5–416.2)	256.9 (93.9–384.5)	177.5 (88.3–255.0) <sup>a</sup>
Max WSS (median) (IQR) (dyne/cm <sup>2</sup> )	175.2 (126.8–239.2)	149.5 (107.6–194.5) <sup>c</sup>	146.8 (94.7–186.1) <sup>b</sup>
Mean WSS (median) (IQR) (dyne/cm <sup>2</sup> )	17.5 (11.2–29.9)	16.5 (6.5–24.2)	11.5 (5.4–18.8) <sup>a</sup>
LSA (median) (IQR) (%)	54 (29–74)	53 (31–77)	68 (50–89) <sup>c</sup>
SCI (median) (IQR)	3.2 (1.9–4.6)	2.7 (1.0–4.2)	3.2 (0.2–5.7)
Max OSI (median) (IQR)	0.3 (0.1–0.4)	0.2 (0.2–0.4)	0.3 (0.2–0.4)
Mean OSI (median) (IQR)	0.01 (0.01–0.01)	0.01 (0.0–0.01)	0.01 (0.01–0.02)
CLL (median) (IQR)	0.7 (0.2–1.4)	0.6 (0.4–1.5)	1.1 (0.5–2.0) <sup>c</sup>
PODE (median) (IQR)	0.1 (0.1–0.2)	0.1 (0.1–0.2)	0.2 (0.1–0.3)

**Note:**—ACA indicates anterior cerebral artery; AcomA, anterior communicating artery; PcomA, posterior communicating artery; Q, flow rate; ICI, inflow concentration index; SR, mean aneurysm shear rate; SCI, shear concentration index; max, maximum. *P*-value compared to stable aneurysms.

<sup>a</sup> *P* < .001.

<sup>b</sup> *P* < .02.

<sup>c</sup> *P* < .05.

1.07–2.04] for stable aneurysms versus median, 2.14 [IQR, 1.44–3.01] for aneurysms that had grown; *P* = .001). Additionally, the GAA was slightly lower after growth with a median of 6.0 (IQR, 3.2–10.7 cm<sup>-2</sup>) compared with 10.4 (IQR, 5.0–21.2 cm<sup>-2</sup>) in stable aneurysms (*P* = .003). The values of all morphologic characteristics are shown in Table 3.

### Hemodynamics

At baseline, there were no significant differences in hemodynamic characteristics between aneurysms that were stable and those that had grown. However, a trend toward a lower maximum WSS was seen (mean: 149.5; [IQR, 107.6–194.5 dyne/cm<sup>2</sup>] in growing versus mean: 175.2 [IQR, 126.8–239.2 dyne/cm<sup>2</sup>] in stable aneurysms; *P* = .03). After growth, several hemodynamic characteristics were significantly different from those in stable aneurysms: The shear rate, VO, and mean WSS were significantly lower (Table 2). For instance, median of the mean WSS was 11.5

(IQR, 5.4–18.8 dyne/cm<sup>2</sup>) compared with 17.5 (IQR, 11.2–29.9 dyne/cm<sup>2</sup>) in stable aneurysms (*P* = .001). Additionally, a trend was seen after growth toward a different mean intra-aneurysmal velocity, LSA, and maximum WSS between aneurysms that were stable and those that had grown.

As shown in Fig 2, after growth, most characteristics differ more from those of the stable aneurysms. Characteristics that are higher in growing than stable aneurysms at baseline increase, while characteristics that are lower at baseline decrease. There are a few exceptions: the CLL, maximum OSI, proper orthogonal decomposition entropy, and undulation index. While the OSI is slightly lower compared with stable aneurysms at baseline, it increases after growth. Similarly, the undulation index decreases.

The boxplots in Fig 3 show that the differences in some of the variables (LSA and CLL) depend on location; for instance, a much larger variation in CLL is seen in the locations with a higher risk of growth according to the ELAPSS score. The LSA shows increasingly higher values in grown aneurysms at high-risk locations for rupture and growth according to the PHASES score, while aneurysms at low-risk locations show smaller differences between aneurysms that are stable and those that have grown.

### DISCUSSION

In our population, we could not identify growing aneurysms on the basis of morphologic and hemodynamic characteristics at baseline because there were minimal differences between aneurysms that were stable and those that had grown. Nevertheless, after growth, the characteristics of grown aneurysms differed more from those of stable aneurysms.

The growth rates in our study were similar to previous reported growth rates.<sup>28</sup> Some researchers have assumed that growth is not a continuous process but irregular and discontinuous.<sup>29</sup> Specific triggers might initiate aneurysm growth, such as inflammation. Therefore, the baseline images might represent aneurysms still in their stable form.

In contrast to previous studies, our study showed small differences at baseline. Previous studies have shown that growing aneurysms tend to have more complex intra-aneurysmal flow patterns at baseline with larger areas of low WSS and a more concentrated inflow.<sup>16,17</sup> Although we observed differences after growth, these were not seen at baseline. The smaller aneurysm

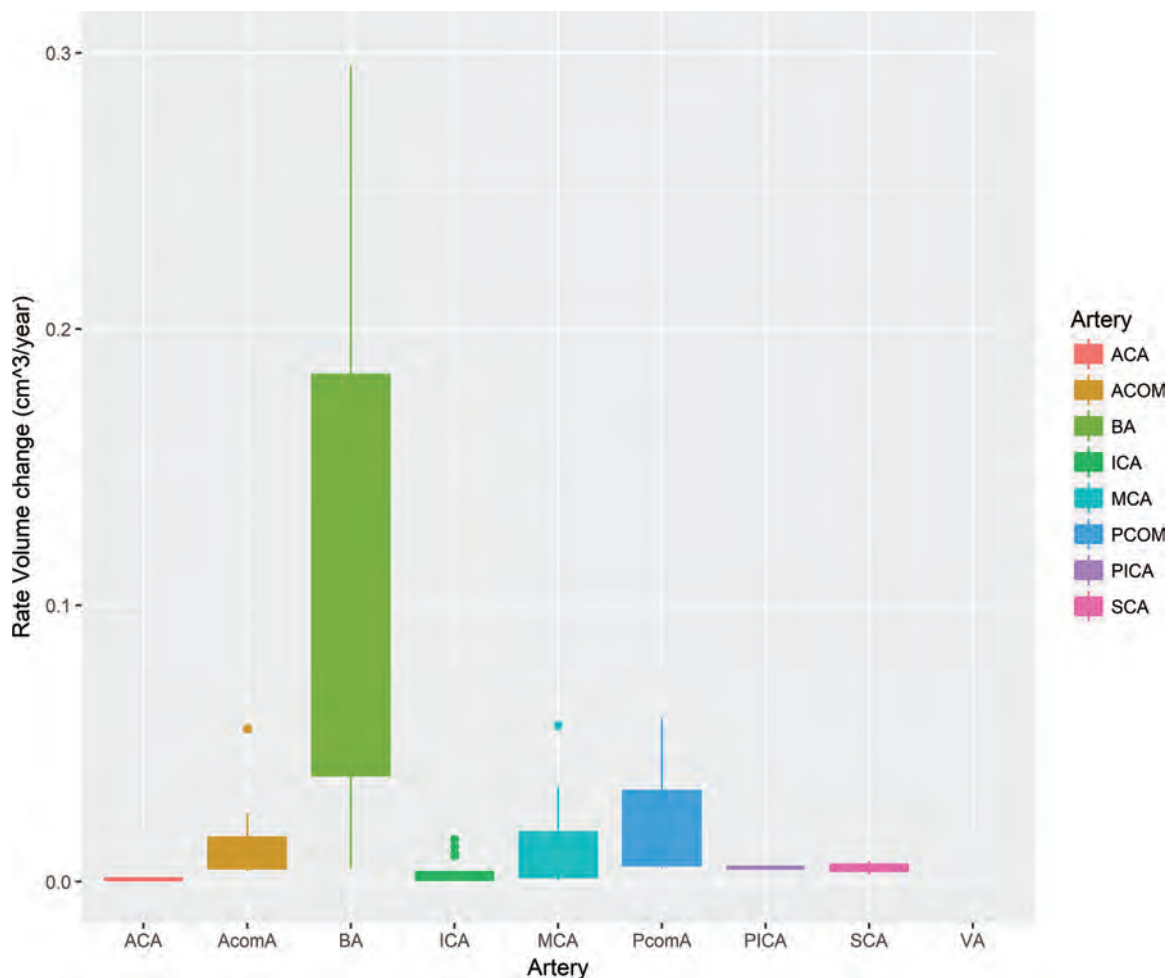


**FIG 1.** Boxplot showing the growth rate per aneurysm location. ACA indicates anterior cerebral artery; PcomA, posterior communicating artery; AcomA, anterior communicating artery; BA, basilar artery; SCA, superior cerebellar artery; VA, vertebral artery.

**Table 3: Morphologic characteristics for each group**

	Stable Aneurysms	Growing Aneurysms: Baseline	Grown Aneurysms: Follow-Up Imaging
No.	81	56	56
Aneurysm volume (median) (IQR) (cm)	0.02 (0.01–0.11)	0.03 (0.01–0.12)	0.05 (0.02–0.19) <sup>b</sup>
Aneurysm size (median) (IQR) (cm)	0.53 (0.36–0.76)	0.53 (0.41–0.81)	0.64 (0.46–0.97) <sup>b</sup>
Neck size (median) (IQR) (cm)	0.42 (0.30–0.55)	0.43 (0.33–0.62)	0.48 (0.38–0.69) <sup>b</sup>
Parent vessel diameter (median) (IQR) (cm)	0.37 (0.29–0.45)	0.33 (0.28–0.38) <sup>b</sup>	0.33 (0.28–0.38) <sup>b</sup>
AR (median) (IQR)	0.73 (0.53–1.10)	0.76 (0.56–0.95)	0.88 (0.71–1.08) <sup>c</sup>
HWR (median) (IQR)	0.82 (0.64–0.97)	0.84 (0.70–0.95)	0.90 (0.80–1.08) <sup>b</sup>
BF (median) (IQR)	1.00 (0.87–1.25)	1.03 (0.89–1.25)	1.15 (0.97–1.32) <sup>c</sup>
BL (median) (IQR)	0.30 (0.13–0.44)	0.32 (0.16–0.45)	0.39 (0.26–0.48) <sup>b</sup>
SizeR (median) (IQR)	0.37 (0.29–0.45)	1.82 (1.12–2.49)	2.14 (1.44–3.01) <sup>a</sup>
VOR (median) (IQR)	1.38 (1.07–2.04)	0.25 (0.14–0.59)	0.35 (0.20–0.89) <sup>b</sup>
IPR (median) (IQR)	0.22 (0.10–0.67)	4.71 (4.60–4.85)	4.71 (4.61–4.93)
UI (median) (IQR)	4.74 (4.61–4.90)	0.23 (0.14–0.36)	0.19 (0.13–0.27)
EI (median) (IQR)	0.21 (0.14–0.35)	0.26 (0.25–0.28)	0.26 (0.24–0.27)
NSI (median) (IQR)	0.26 (0.25–0.29)	0.19 (0.17–0.21)	0.19 (0.17–0.22)
GAA (median) (IQR) (cm <sup>-2</sup> )	10.4 (5.0–21.2)	8.7 (4.4–15.9)	6.0 (3.2–10.7) <sup>b</sup>

**Note:**—*P*-value compared with stable aneurysms.

<sup>a</sup> *P* < .001.

<sup>b</sup> *P* < .02.

<sup>c</sup> *P* < .05.

sizes and size ratios in our population likely result in fewer vortices and complex flow patterns.<sup>30</sup> Additionally, Chung et al<sup>16</sup> controlled for location, sex, and age. Although these did not significantly differ within our study, the location might play an important role because anterior communicating artery aneurysms might be influenced differently by the hemodynamic environment compared with MCA aneurysms. A multivariable analysis could further elucidate these differences. However, a larger sample size is needed because according to recommendations, 10–20 cases per independent variable are needed to acquire a reliable result.<sup>31</sup> Combining the most relevant population characteristics, the variables with a *P* value < .05, would lead to 20 independent variables, needing at least 200 patients per group. Similarly, due to the number

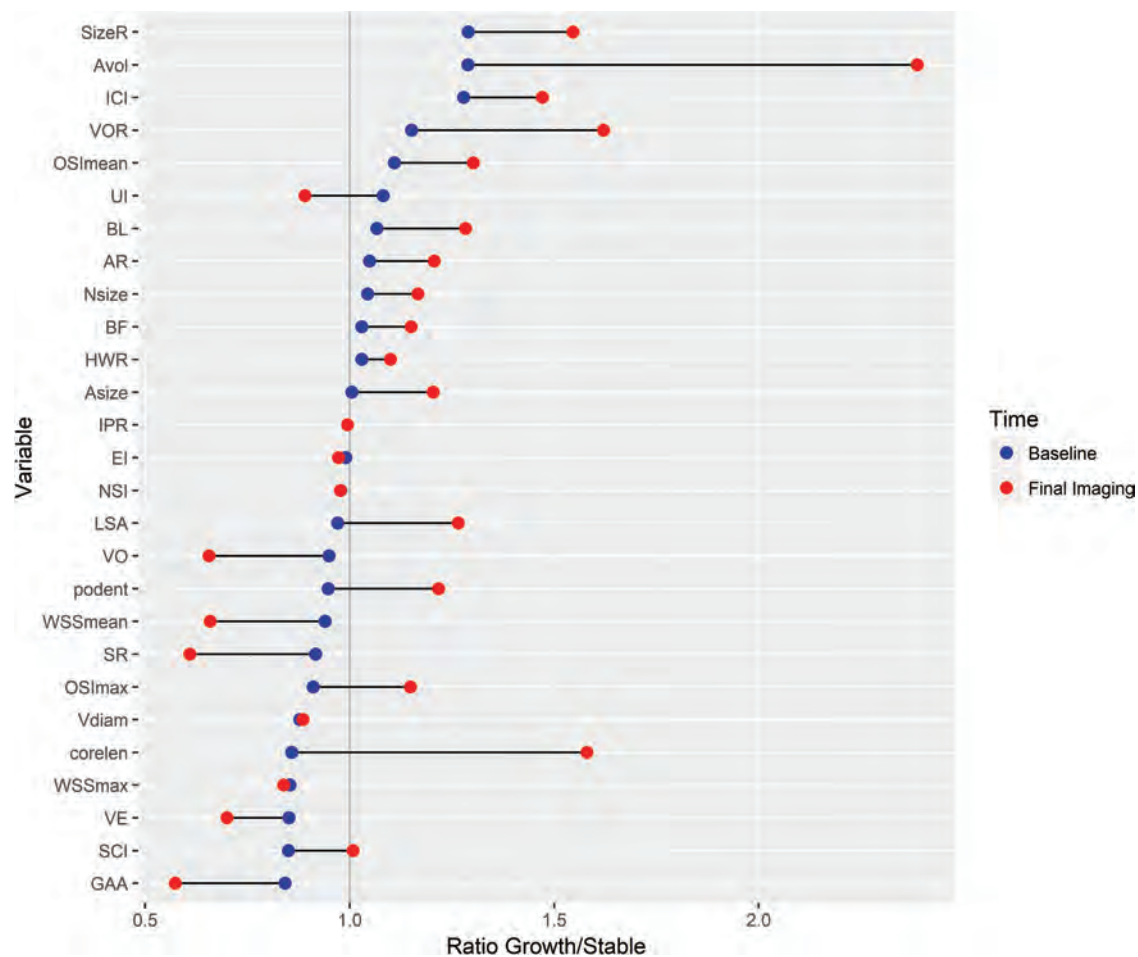


**FIG 2.** Dumbbell plot depicting the ratio between the median value of growing and stable aneurysms at baseline (blue) and last imaging (red). Characteristics are sorted according to baseline size. ICI indicates inflow concentration index; SR, mean aneurysm shear rate; VE, mean aneurysm velocity; SCI, shear concentration index; AR, aspect ratio; BF, bottleneck factor; BL, bulge location; IPR, isoperimetric ratio; UI, undulation index; NSI, nonsphericity index; Avol, aneurysm Volume; Nsize, Neck Size; HWR, height-to-width ratio; Asize, Aneurysm Size; podent, *proper orthogonal decomposition entropy*; max, maximum; Vdiam, Vessel diameter; corelen, core line length.

of characteristics, this study required correction for multiple testing. Larger sample sizes increase the ability to detect the differences and thus would not require such a correction.

After growth, almost all characteristics deviated further from those in stable aneurysms, indicating an association between these characteristics and instability. Additionally, several characteristics coincided with rupture-related characteristics, such as more complex flows, a lower mean WSS, a larger LSA, and viscous energy loss.<sup>7,16,17,20,32,33</sup> Because the hemodynamic environment is more similar to ruptured intracranial aneurysms after growth, this feature might indicate why growing aneurysms have a higher rupture risk.<sup>11</sup> Ruptured aneurysms have also been related to a higher maximum WSS and OSI, a trend that was not seen on follow-up imaging of the aneurysms that grew in our population. Sforza et al<sup>17</sup> also did not observe a significantly higher WSS and OSI in aneurysms that had grown. Therefore, it has been proposed that aneurysm growth occurs at regions of low WSS.<sup>18,34</sup> We observed a trend toward larger areas of low WSS after growth; however, this trend seems significant in high-risk locations for growth and rupture (communicating arteries and posterior circulation). Therefore, although

similarities in the hemodynamic environment exist between aneurysms that have ruptured and those that have grown, the differences might show different underlying mechanisms between growth and rupture. A low wall shear stress is associated with inflammation and atherosclerosis, while high shear stresses are associated with mural cell destruction and flow impingement.<sup>18</sup> Thus low shear stresses likely cause aneurysms to remodel and repair, while high shear stresses causes the wall to degenerate and rupture.

The PHASES score has been developed to predict rupture,<sup>4</sup> and more recently, it has also been shown to be associated with aneurysm growth.<sup>35</sup> Consistent with these studies, the growing aneurysms in our study showed higher PHASES scores at baseline. Nevertheless, the baseline ELAPSS scores—developed to predict growth<sup>12</sup>—did not significantly differ between growing and stable aneurysms in our study. The main differences between these scores is that the ELAPSS includes irregularity and has different weights for the prediction model for location and size. Our presented population had similar sizes, ages, and irregularity at baseline for growing and stable aneurysms, which likely resulted in similar ELAPSS scores.

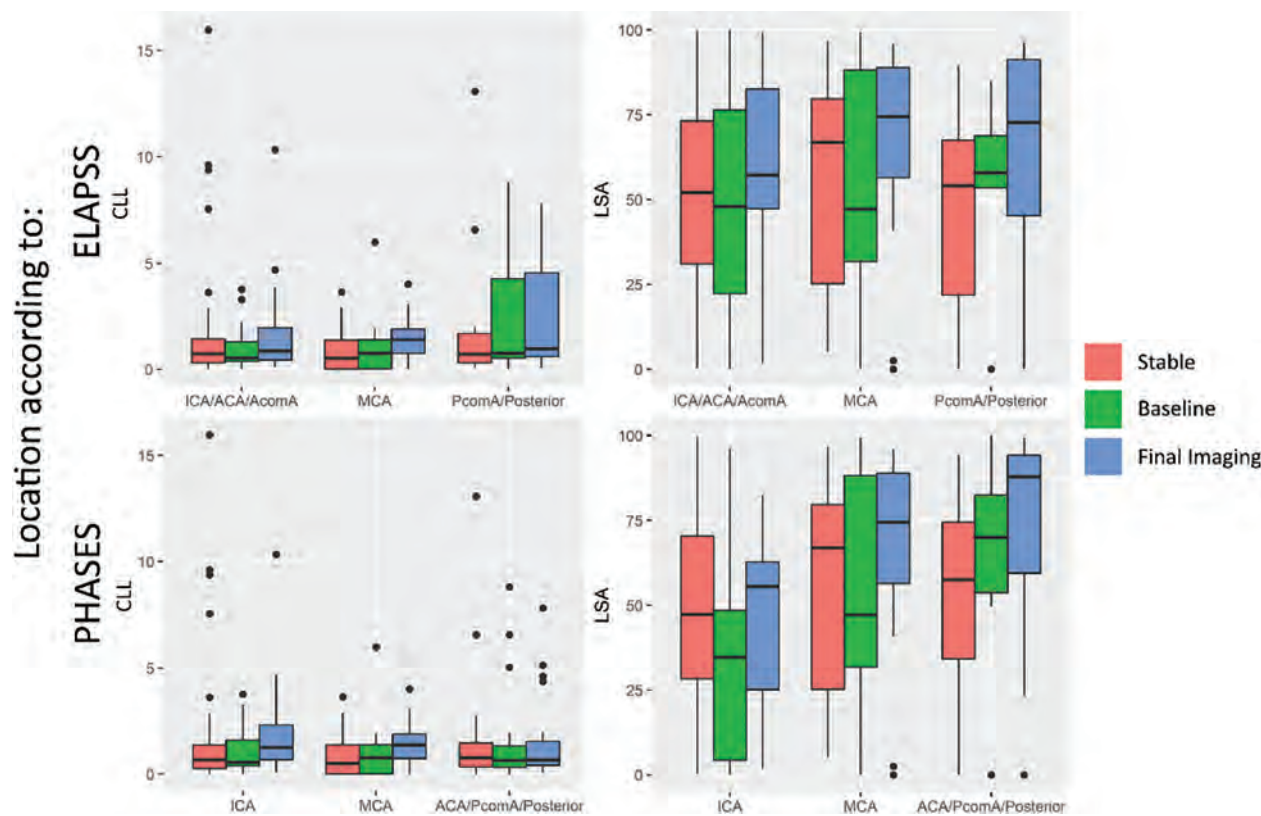


**FIG 3.** Boxplot comparing core-line length (*left*) and low shear area (*right*) in the different location categories according to the ELAPSS (*upper row*) and PHASES (*lower row*) scores. ACA indicates anterior cerebral artery; PcomA, posterior communicating artery; AcomA, anterior communicating artery.

This study has several limitations. First, a selection bias is present because this study only included aneurysms with longitudinal data. Therefore, the aneurysms in this study likely had a low rupture risk because aneurysms considered to be at high risk are treated at a short notice. However, the presented cases do give information on the course of untreated aneurysms. Additionally, due to the limited resolution of the CTA and MRA images (approximately 0.5 mm), some cases with little growth (<0.5 mm) might be missed. Most studies of aneurysm growth only assess growth >0.5 or 1 mm.<sup>12,15</sup> Therefore, this study also had 0.5 mm as a lower limit for growth.

Second, the accuracy of the CFD model is highly dependent on the segmentations. This study used multiple imaging methods to acquire all the patient-specific segmentations. To optimize the comparability between baseline and follow-up imaging of growing aneurysms, the same imaging technique was used for both time points. All segmentations were visually inspected and corrected to make sure inflow and outflow vessels were similar in size at both time points. The vascular models of stable cases were mostly based on 3DRA, while CTA and MRA were used for growing aneurysms. Because 3DRA is an invasive method, it is not often used in follow-up imaging, resulting in the differences among groups. Every imaging technique has some systematic errors;<sup>36</sup> as a result, each segmentation method was tailored to the imaging technique. Differences between techniques were minimized by manually checking and correcting each segmentation. However, we observed slight-but-insignificant lower parent

vessel diameters in growing aneurysms, especially in the MRA images. These differences could reflect actual size differences but are more likely due to the different imaging resolutions and methods. Previous studies have reported similar differences between imaging modalities; comparing time-of-flight MRA with digital subtraction angiography has shown smaller diameters in the MRA images.<sup>37-39</sup> This systematic error could influence differences between aneurysms that were stable and those that had grown, leading to lower flow conditions in growing aneurysms because these were mostly imaged with MRA.

Additionally, the CFD models are based on several assumptions and approximations about intra-aneurysmal flow and resulting hemodynamic characteristics. For instance, because no patient-specific flow conditions were available, we used typical flow waveforms derived from healthy volunteers. Previous studies have shown that the patient-specific inflows and the completeness of the circle of Willis could significantly influence the inflow rates.<sup>40,41</sup> For instance, lower basilar flow rates were observed with hypoplastic or absent P1 arteries. For anterior communicating artery aneurysms, we imposed flow conditions at both ICAs; thus, the effect of a hypoplastic or absent A1 segment was included into the model. However, we did not take into account the influence of a hypoplastic or absent P1. Only a small proportion of the patients in our dataset had a posterior aneurysm, and because the P1 was missing in only some patients, it is expected that the change in inflow had a minor influence on the presented results.

## CONCLUSIONS

No association was found between morphologic and hemodynamic characteristics and aneurysm growth at baseline. However, after growth, the differences in morphology and hemodynamics between aneurysms that have grown and those that are stable increased. Therefore, aneurysms that have grown likely have a higher rupture risk.

Disclosures: Eva L. Leemans—RELATED: Grant/Grants Pending: TWIN association, Comments: This study was supported by a grant from the TWIN association, Hengelo, the Netherlands.\* Bart M.W. Cornelissen—RELATED: Grant/Grants Pending: TWIN association.\* Charles B.L.M. Majoie—RELATED: Grant/Grants Pending: TWIN association,\* the Dutch Heart Foundation,\* and Stryker.\* OTHER: cofounder of and shareholder in Nico-lab. Juan R. Cebral—RELATED: Grant/Grants Pending: National Institutes of Health,\* UNRELATED: Grant/Grants Pending: National Institutes of Health/Philips, Comments: research grants.\* Henk A. Marquering—RELATED: Grant/Grants Pending: TWIN association; OTHER: cofounder of and shareholder in Nico-lab. Cornelis H. Slump—RELATED: Grant/Grants Pending: TWIN association. \*Money paid to the institution.

## REFERENCES

- Gabriel RA, Kim H, Sidney S, et al. **Ten-year detection rate of brain arteriovenous malformations in a large, multiethnic, defined population.** *Stroke* 2010;41:21–26 CrossRef Medline
- Lecler A, Raymond J, Rodriguez-Régent C, et al. **Intracranial aneurysms: recurrences more than 10 years after endovascular treatment: a prospective cohort study.** *Radiology* 2015;277:173–80 CrossRef Medline
- Molyneux AJ, Birks J, Clarke A, et al. **The durability of endovascular coiling versus neurosurgical clipping of ruptured cerebral aneurysms: 18-year follow-up of the UK cohort of the International Subarachnoid Aneurysm Trial (ISAT).** *Lancet* 2015;385:691–97 CrossRef Medline
- Greving JP, Wermer MJH, Brown RD, et al. **Development of the PHASES score for prediction of risk of rupture of intracranial aneurysms: a pooled analysis of six prospective cohort studies.** *Lancet Neurol* 2014;13:59–66 CrossRef Medline
- Weir B, Disney L, Karrison T. **Sizes of ruptured and unruptured aneurysms in relation to their sites and the ages of patients.** *J Neurosurg* 2002;96:64–70 CrossRef Medline
- Korja M, Kaprio J. **Controversies in epidemiology of intracranial aneurysms and SAH.** *Nat Rev Neurol* 2016;12:50–55 CrossRef Medline
- Xiang J, Natarajan SK, Tremmel M, et al. **Hemodynamic-morphologic discriminants for intracranial aneurysm rupture.** *Stroke* 2011;42:144–152 CrossRef Medline
- Cebral JR, Mut F, Weir J, et al. **Quantitative characterization of the hemodynamic environment in ruptured and unruptured brain aneurysms.** *AJNR Am J Neuroradiol* 2011;32:145–51 CrossRef Medline
- Dhar S, Tremmel M, Mocco J, et al. **Morphology parameters for intracranial aneurysm rupture risk assessment.** *Neurosurgery* 2008;63:185–97 CrossRef Medline
- Etminan N, Rinkel GJ. **Unruptured intracranial aneurysms: development, rupture and preventive management.** *Nat Rev Neurol* 2016;12:699 CrossRef Medline
- Villablanca JP, Duckwiler GR, Jahan R, et al. **Natural history of asymptomatic unruptured cerebral aneurysms evaluated at CT angiography: growth and rupture incidence and correlation with epidemiologic risk factors.** *Radiology* 2013;269:258–65 CrossRef Medline
- Backes D, Rinkel GJE, Greving JP, et al. **ELAPSS score for prediction of risk of growth of unruptured intracranial aneurysms.** *Neurology* 2017;88:1600–06 CrossRef Medline
- Chien A, Xu M, Yokota H, et al. **Nonsphericity index and size ratio identify morphologic differences between growing and stable aneurysms in a longitudinal study of 93 cases.** *AJNR Am J Neuroradiol* 2018;39:500–06 CrossRef Medline
- Ramachandran M, Raghavan ML. **On the Role of Intracranial Aneurysm Morphology in Stable versus Unstable Lesions.** Iowa City: University of Iowa; 2012
- Backes D, Rinkel GJ, Laban KG, et al. **Patient- and aneurysm-specific risk factors for intracranial aneurysm growth: a systematic review and meta-analysis.** *Stroke* 2016;47:951–57 CrossRef Medline
- Chung BJ, Mut F, Putman CM, et al. **Identification of hostile hemodynamics and geometries of cerebral aneurysms: a case-control study.** *AJNR Am J Neuroradiol* 2018;39:1860–66 CrossRef Medline
- Sforza DM, Kono K, Tateshima S, et al. **Hemodynamics in growing and stable cerebral aneurysms.** *J Neurointerv Surg* 2016;8:407–12 CrossRef Medline
- Meng H, Tutino VM, Xiang J, et al. **High WSS or low WSS? Complex interactions of hemodynamics with intracranial aneurysm initiation, growth, and rupture: toward a unifying hypothesis.** *AJNR Am J Neuroradiol* 2014;35:1254–62 CrossRef Medline
- Fan J, Wang Y, Liu J, et al. **Morphological-hemodynamic characteristics of intracranial bifurcation mirror aneurysms.** *World Neurosurg* 2015;84:114–120.e2 CrossRef Medline
- Doddasamayajula R, Chung BJ, Mut F, et al. **Hemodynamic characteristics of ruptured and unruptured multiple aneurysms at mirror and ipsilateral locations.** *AJNR Am J Neuroradiol* 2017;38:2301–07 CrossRef Medline
- Cebral JR, Castro MA, Putman CM, et al. **Flow-area relationship in internal carotid and vertebral arteries.** *Physiol Meas* 2008;29:585–94 CrossRef Medline
- Murray CD. **The physiological principle of minimum work, I: the vascular system and the cost of blood volume.** *Proc Natl Acad Sci U S A* 1926;12:207–14 CrossRef Medline
- Cebral JR, Castro M, Burgess JE, et al. **Characterization of cerebral aneurysms for assessing risk of rupture by using patient-specific computational hemodynamics models.** *AJNR Am J Neuroradiol* 2005;26:2550–59 Medline
- Cebral JR, Mut F, Sforza D, et al. **Clinical application of image-based CFD for cerebral aneurysms.** *Int J Numer Method Biomed Eng* 2011;27:977–92 CrossRef Medline
- Raghavan ML, Ma B, Harbaugh RE. **Quantified aneurysm shape and rupture risk.** *J Neurosurg* 2005;102:355–62 CrossRef Medline
- Ma B, Harbaugh RE, Raghavan ML. **Three-dimensional geometrical characterization of cerebral aneurysms.** *Ann Biomed Eng* 2004;32:264–73 CrossRef Medline
- Mut F, Löhner R, Chien A, et al. **Computational hemodynamics method for the analysis of cerebral aneurysms.** *Int J Numer Method Biomed Eng* 2011;27:822–39 CrossRef Medline
- Jou LD, Mawad ME. **Growth rate and rupture rate of unruptured intracranial aneurysms: a population approach.** *Biomed Eng Online* 2009;8:1–9 CrossRef Medline
- Koffijberg H, Buskens E, Algra A, et al. **Growth rates of intracranial aneurysms: exploring constancy.** *J Neurosurg* 2008;109:176–85 CrossRef Medline
- Tremmel M, Dhar S, Levy EI, et al. **Influence of intracranial aneurysm-to-parent vessel size ratio on hemodynamics and implication for rupture: results from a virtual experimental study.** *Neurosurgery* 2009;64:622–30; discussion 630–31 CrossRef Medline
- Tabachnick BG, Fidell LS. *Using Multivariate Statistics.* 6th ed. New York: Pearson; 2013
- Varble N, Rajabzadeh-Oghaz H, Wang J, et al. **Differences in morphologic and hemodynamic characteristics for “PHASES-based” intracranial aneurysm locations.** *AJNR Am J Neuroradiol* 2017;38:2105–10 CrossRef Medline
- Xu J, Yu Y, Wu X, et al. **Morphological and hemodynamic analysis of mirror posterior communicating artery aneurysms.** *PLoS One* 2013;8:e55413 CrossRef Medline
- Boussel L, Rayz V, McCulloch C, et al. **Aneurysm growth occurs at region of low wall shear stress: patient-specific correlation of**

- hemodynamics and growth in a longitudinal study. *Stroke* 2008; 39:2997–3002 CrossRef Medline
35. Backes D, Vergouwen MD, Groenestege AT, et al. **PHASES score for prediction of intracranial aneurysm growth.** *Stroke* 2015;46:1221–27 CrossRef Medline
36. Schneiders JJ, Marquering HA, Antiga L, et al. **Intracranial aneurysm neck size overestimation with 3D rotational angiography: the impact on intra-aneurysmal hemodynamics simulated with computational fluid dynamics.** *AJNR Am J Neuroradiol* 2013;34:121–28 CrossRef Medline
37. Behme D, Amelung N, Khakzad T, et al. **How to size intracranial aneurysms: a phantom study of invasive and noninvasive methods.** *AJNR Am J Neuroradiol* 2018; 39:2291–96 CrossRef Medline
38. Lauric A, Hippelheuser JE, Malek AM. **Critical role of angiographic acquisition modality and reconstruction on morphometric and haemodynamic analysis of intracranial aneurysms.** *J Neurointerv Surg* 2018;10:911–15 CrossRef Medline
39. Millán RD, Dempere-Marco L, Pozo JM, et al. **Morphological characterization of intracranial aneurysms using 3-D moment invariants.** *IEEE Trans Med Imaging* 2007;26:1270–82 CrossRef Medline
40. Cornelissen BMW, Schneiders JJ, Sprengers ME, et al. **Aneurysmal parent artery-specific inflow conditions for complete and incomplete circle of Willis configurations.** *AJNR Am J Neuroradiol* 2018;39:910–15 CrossRef Medline
41. Jansen IG, Schneiders JJ, Potters WV, et al. **Generalized versus patient-specific inflow boundary conditions in computational fluid dynamics simulations of cerebral aneurysmal hemodynamics.** *AJNR Am J Neuroradiol* 2014;35:1543–48 CrossRef Medline

# Identification of Vortex Cores in Cerebral Aneurysms on 4D Flow MRI

 K. Futami,  T. Uno,  K. Misaki,  S. Tamai,  I. Nambu,  N. Uchiyama, and  M. Nakada



## ABSTRACT

**BACKGROUND AND PURPOSE:** The complexity and instability of the vortex flow in aneurysms are factors related to the rupture risk of unruptured cerebral aneurysms. We identified aneurysm vortex cores on 4D flow MR imaging and examined the relationship of these factors with the characteristics of cerebral aneurysms.

**MATERIALS AND METHODS:** We subjected 40 aneurysms (37 unruptured, 3 ruptured) to 4D flow MR imaging. We visualized streamlines with velocities below the threshold—that is, a percentage value of the aneurysm maximum inflow velocity—and progressively decreased the threshold to identify vortex cores as thin, streamline bundles with minimum velocities. Complexity and stability were compared in aneurysms with a smooth surface and those with blebs or daughter sacs.

**RESULTS:** The threshold for visualizing vortex cores ranged from 3% to 13% of the maximum inflow velocity. Vortex cores could be visualized in 38 aneurysms; in 2, they were not visualized through the cardiac cycle. A simple flow pattern (single vortex core) was identified in 27 aneurysms; the other 13 exhibited a complex flow pattern. The cores were stable in 32 and unstable in 8 aneurysms. Significantly more aneurysms with than without blebs or daughter sacs had a complex flow pattern ( $P = .006$ ). Of the 3 ruptured aneurysms, 1 aneurysm had an unstable vortex core; in the other 2, the vortex core was not visualized.

**CONCLUSIONS:** The identification of vortex cores on 4D flow MR imaging may help to stratify the rupture risk of unruptured cerebral aneurysms.

**ABBREVIATION:** CFD = computational fluid dynamics

Rupture-risk stratification is crucial to decide appropriate treatments for unruptured cerebral aneurysms to avoid profound complications elicited by invasive treatments. The complexity and instability of the intra-aneurysmal vortical flow have been correlated with the rupture risk of unruptured cerebral aneurysms.<sup>1-4</sup> The vortex core line, a skeleton of the vortical flow and defined on the basis of various mathematic definitions,<sup>5,6</sup> facilitates the qualitative and quantitative evaluation of the complexity and instability of the intra-aneurysmal flow of aneurysm models using computational fluid dynamic (CFD) simulations.<sup>1-4,7,8</sup> However, CFD analysis is based on assumptions and approximations regarding blood properties, vessel wall compliance, and flow conditions,<sup>1-4</sup> and the location of the vortex core line depends on mathematic

definitions.<sup>8</sup> Although 4D flow MR imaging, based on time-resolved 3D cine phase-contrast MR imaging techniques, has been used to evaluate the hemodynamics in human cerebral aneurysms,<sup>9-12</sup> the visualization of aneurysm vortex cores with this imaging technique has not been reported. Identification of vortex cores on 4D flow MR imaging may be an alternative to CFD analysis of aneurysm models and may lead to new insights into the role of vortex cores in aneurysm behavior.

In this study, we identified vortex cores by showing streamlines with minimum flow velocities in cerebral aneurysms and examined the relationship between the complexity and stability of the vortex core and the characteristics of cerebral aneurysms.

## MATERIALS AND METHODS

The institutional review board of Hokuriku Central Hospital approved this study; prior informed consent was obtained from all patients.

This study included 35 patients (13 men, 22 women; mean age,  $68.2 \pm 10.8$  years; range, 41–89 years) with 40 aneurysms (37 unruptured, 3 ruptured). They were located on the cavernous

Received June 6, 2019; accepted after revision August 13.

From the Department of Neurosurgery (K.F.), Hokuriku Central Hospital, Toyama, Japan; and Department of Neurosurgery (T.U., K.M., S.T., I.N., N.U., M.N.), Kanazawa University School of Medicine, Ishikawa, Japan.

Please address correspondence to Kazuya Futami, MD, Department of Neurosurgery, Hokuriku Central Hospital, 1-2-3 Nodera, Oyabe, 932-8503 Toyama, Japan; e-mail: k-futami@h-c-h.jp

<http://dx.doi.org/10.3174/ajnr.A6322>

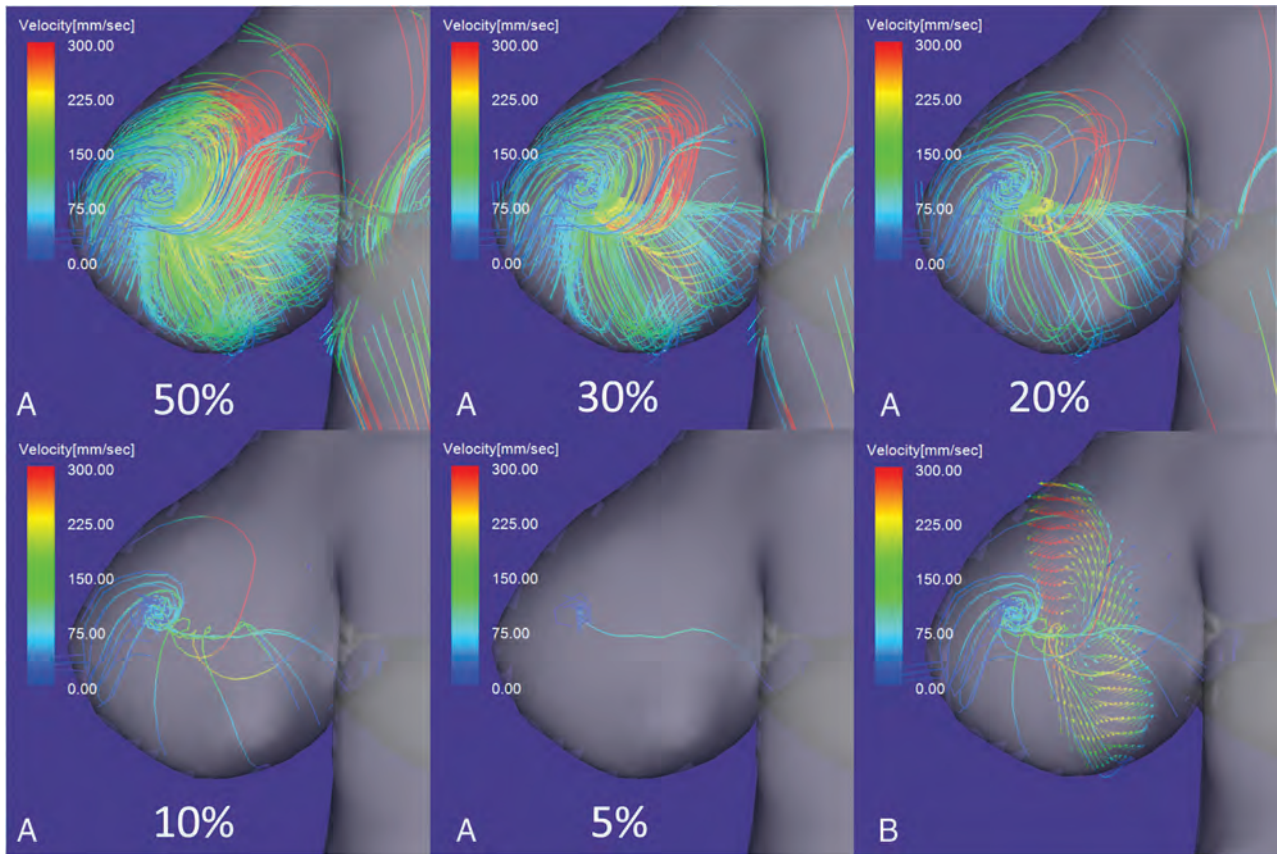


**FIG 1.** 4D flow MR images of flow streamlines with velocities below the threshold determined by the percentage value of the maximum inflow velocity. *A*, When the threshold was decreased from 30% to 10% of the maximum inflow velocity, a single vortex core was visualized as a thin, streamline bundle. At a threshold of 5%, the vortex core was a single line. *B*, A thin, streamline bundle passed through the center of vortical flow vectors on a cutting plane of the aneurysm dome.

segment ( $n = 1$ ), the paraclinoid segment ( $n = 10$ ), and the communicating segment ( $n = 5$ ) of the ICA; the ICA bifurcation ( $n = 1$ ); the MCA bifurcation ( $n = 12$ ); the A1 segment of the anterior cerebral artery ( $n = 1$ ); the anterior communicating artery ( $n = 5$ ); and the tip of the basilar artery ( $n = 5$ ). The maximum diameter and neck size were  $6.5 \pm 2.8$  mm (range, 4.0–15.0 mm) and  $5.0 \pm 2.1$  mm (range, 2.5–11.3 mm), respectively. Their sizes exceeded the spatial resolution of 4D flow MR imaging.<sup>11,12</sup>

### MRI

We used a 1.5T MR imaging scanner (Magnetom Avanto; Siemens, Erlangen, Germany) with a slew rate of 125 T/m/s and an 8-channel head array coil. Contrast-enhanced MRA was performed after the injection of 0.2 mL/kg of gadodiamide delivered via an 18- or 20-ga cannula at a rate of 1 mL/s into the antecubital vein. The scanning parameters were the following: TR/TE/NEX, 4.65/1.74 ms/average 1; flip angle, 20°; band width, 330 Hz/pixel; FOV, 180 × 180 mm; section thickness, 0.7 mm; 1 slab; 60 sections/slab; voxel size, 0.6 × 0.6 × 0.7 mm; transaxial direction.

The parameters for phase-contrast MR imaging were the following: TR/TE/NEX, 33.05/5.63 ms/average 1; flip angle, 22°; band width, 434 Hz/pixel; FOV, 200 × 200 mm; section thickness, 0.8 mm; 1 slab; 24–26 sections/slab; z-coverage, 19.2 mm; matrix, 192 × 192; no interpolation processing; voxel size, 1.04 × 1.04 × 0.8 mm; velocity encoding, 40–60 cm/s; parallel imaging

with reduction factor, 2; imaging time, 20–30 minutes depending on the patient's heart rate; transaxial direction; retrospective gating with an electrocardiogram; temporal resolution, 0.0333 seconds.

Commercially available software (Flova II, Version 2.10.7.0; R<sup>2</sup>Tech, Hamamatsu, Japan) was used to visualize flow vectors and streamlines on the basis of 3D blood flow information obtained by 4D flow MR imaging. The vascular wall was reconstructed with region-growing<sup>13</sup> and marching cubes<sup>14</sup> methods applied to datasets obtained by contrast-enhanced MRA. The 3D datasets acquired by phase-contrast MR imaging were converted to voxel datasets at a spatial resolution of 0.5 × 0.5 × 0.5 mm using a vander-provided function.

By means of the Runge-Kutta method,<sup>15</sup> streamlines were constructed by integrating flow vectors in the whole intra-aneurysmal region and in close parent arteries. They were visualized at a density of 16 lines/mm<sup>2</sup>. Because streamlines constructed with forward integration tended to conceal flow structures inside the vortices, we used backward-integration exclusively to visualize the vortex cores.

### Data Analysis

By means of a Flova II function, an arbitrary percentage value of the maximum inflow velocity in the aneurysm orifice can be selected as the visualization threshold of flow streamlines in the aneurysm. Byrne et al<sup>3</sup> reported that a vortex core line can be

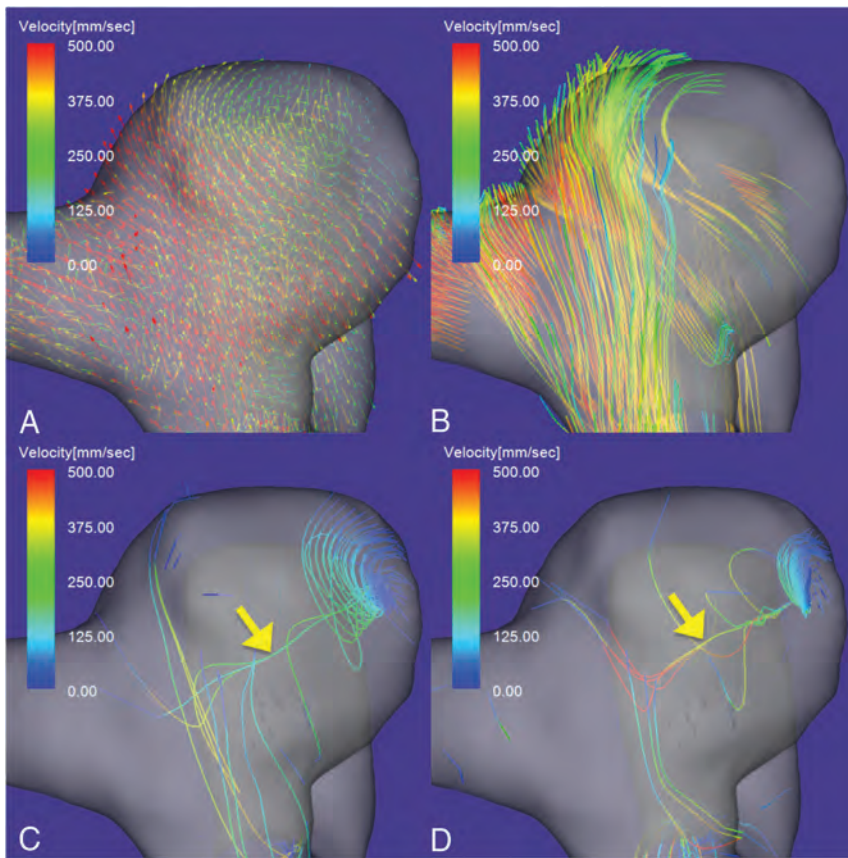


**FIG 2.** 4D flow MR images of an unruptured aneurysm on the paraclinoid segment of the right ICA. *A*, Flow vector map. *B*, The inflow jet is visualized as a layer of streamlines with high velocities. A single stable vortex core (yellow arrow) is visualized in the diastolic (*C*) and systolic (*D*) phases of the cardiac cycle. The vortex core is visualized as a bundle of streamlines with velocities below 7% (*C*) and 10% (*D*) of the maximum inflow velocity. The aneurysm flow pattern is simple and stable.

**Table: Complexity and stability of vortex cores in cerebral aneurysms<sup>a</sup>**

Aneurysm	Complexity Simple/Complex	Stability Stable/Unstable
Smooth wall ( <i>n</i> = 25)	21 (84.0%)/4 (16.0%)	22 (88.0%)/3 (12.0%)
Irregular wall ( <i>n</i> = 15)	6 (40.0%)/9 (60.0%)	10 (66.7%)/5 (33.3%)
<i>P</i> value	.006 (S)	.126 (NS)

**Note:**—NS indicates not significant; S, significant on the Fisher exact test.

<sup>a</sup>Simple and complex flow patterns were defined as exhibiting a single vortex core or multiple or nonvisualized vortex cores through the cardiac cycle, respectively. Stable and unstable flow patterns were defined as exhibiting persistent vortex cores or moving or nonvisualized vortex cores, respectively. The designation of “irregular wall” was recorded when the wall had protruding blebs or daughter sacs. Differences of *P* < .05 were considered significant.

constructed by connecting the points along the faces containing the zeros of the reduced velocity in cerebral aneurysms. We visualized the vortex cores as thin, streamline bundles composed of streamlines with velocities below the threshold, which was determined by progressively decreasing the percentage value of the maximum inflow velocity in each aneurysm. The maximum inflow velocity was measured on the aneurysm orifice plane using 4D flow MR imaging as the maximum value during the cardiac cycle.

We defined simple flow patterns as those with a single vortex core and complex flow patterns as those with multiple or

nonvisualized vortex cores through the cardiac cycle. Stable flow patterns were defined as those with persistent vortex cores; unstable flow patterns, as those with moving or nonvisualized vortex cores. Because aneurysms with no visualized vortex cores through the cardiac cycle had multiple small vortices beneath the aneurysm surface and irregular streamlines, we attributed this observation to the presence of an extremely complex and unstable intra-aneurysmal flow and recorded them as exhibiting a complex and unstable flow pattern.

We compared the complexity and stability of aneurysms with a smooth surface and those with an irregular wall characterized by blebs or daughter sacs. Three observers (K.F., T.U., and K.M.) independently recorded the number and location of vortex cores. Disagreements were settled by consensus.

For statistical analysis we used the Fisher exact test for categorical variables. Differences of *P* value < .05 were considered significant.

## RESULTS

Figure 1A shows aneurysm flow streamlines with velocities below the threshold determined by progressively decreased percentage values of the maximum inflow velocity of the aneurysm. A single

vortex core was observed as a thin, streamline bundle when the threshold was decreased from 30% to 10% of the maximum inflow velocity; at the 5% threshold, the vortex core was a single line. A thin, streamline bundle passed through the center of vortical flow vectors on a cutting plane of the aneurysm dome (Fig 1B). On en face views of the inflow jet of aneurysms, most vortex cores were orthogonal to the inflow jet (Fig 2B). Because the threshold value appropriate for visualizing the vortex cores of individual aneurysms depended on the systolic or diastolic phase of the cardiac cycle and on the vortex core per se, we progressively decreased the threshold by 1% for each aneurysm. Consequently, the threshold for assessing the vortex cores ranged from 3% to 13% of the maximum inflow velocity.

Vortex cores could be identified in 38 of the 40 aneurysms; in the other 2, they were not visualized through the cardiac cycle. As shown in the Table, a simple flow pattern (single vortex core) was visualized in 27 aneurysms; the other 13 exhibited a complex flow pattern. The vortex core was stable in 32 aneurysms and unstable in the other 8. There were 15 aneurysms with an irregular wall: Six manifested a simple pattern, and 9, a complex pattern. The vortex core was stable in 10 and unstable in 5 of these aneurysms (*P* = .126). The incidence of a complex flow pattern was significantly higher in aneurysms with an irregular wall

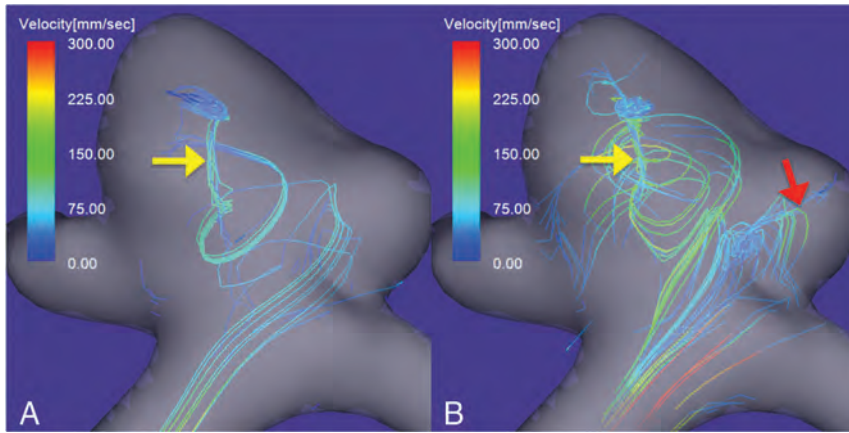


**FIG 3.** An unruptured right MCA bifurcation aneurysm with a daughter sac. Vortex cores in the diastolic (A) and systolic (B) phases of the cardiac cycle. A single vortex core is visualized in the diastolic phase (A, yellow arrow), and another, in the systolic phase (B, red arrow). The vortex cores are visualized as bundles of streamlines with velocities below 4% and 7% values of the maximum inflow velocity in the diastolic and systolic phases, respectively. The flow pattern was recorded as complex.

**Case 2.** A 52-year-old man presented with an unruptured right MCA bifurcation aneurysm with a daughter sac (Fig 3). The maximum aneurysm diameter and neck size were 6.5 and 4.1 mm, respectively. The maximum inflow velocity was 580 mm/s. During the diastolic phase of the cardiac cycle, only 1 vortex core could be visualized (yellow arrow in Fig 3A). However, during the systolic phase, another vortex core was observed; it was directed toward the tip of the daughter sac (red arrow in Fig 3B). These vortex cores were visualized as bundles of streamlines with velocities below the 4% and 7% values of the maximum inflow velocity in the diastolic and systolic phases, respectively. The flow pattern was recorded as complex.

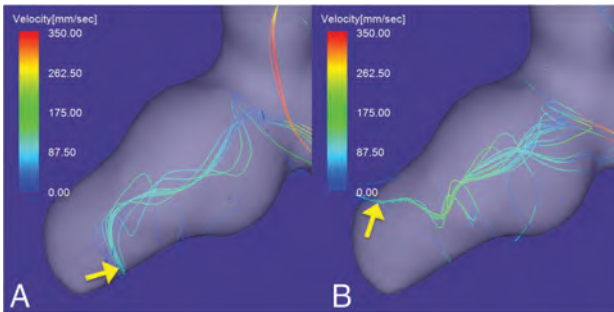


**FIG 4.** A ruptured right ICA aneurysm with a daughter sac. The vortex core in the diastolic (A) and systolic (B) phases of the cardiac cycle. The vortex core in both phases is visualized as a bundle of streamlines with velocities below 4% of the maximum inflow velocity. The direction of the tip of the vortex core markedly changes during the cardiac cycle (yellow arrows). The flow pattern was recorded as unstable.

**Case 3.** A 53-year-old man presented with a ruptured right ICA aneurysm with a daughter sac on the tip of the aneurysm (Fig 4). The maximum aneurysm diameter and neck size were 8.7 and 3.5 mm, respectively. The maximum inflow velocity was 620 mm/s. In the diastolic (Fig 4A) and systolic phases (Fig 4B), a vortex core was visualized as a bundle of streamlines with velocities below 4% of the maximum inflow velocity. The vortex core was directed from the aneurysm neck to the daughter sac. The direction of the tip of the vortex core was markedly different during the diastolic and systolic phases (yellow arrows in Fig 4A, -B). The flow pattern was recorded as unstable.

( $P = .006$ ). Of the 3 ruptured aneurysms, 1 aneurysm exhibited an unstable vortex core; in the other 2, multiple small vortices beneath the aneurysm surface and irregular streamlines were visualized, while no vortex cores were visualized through the cardiac cycle.

### Case Presentation

**Case 1.** A 61-year-old woman presented with an unruptured aneurysm on the paraclinoid segment of the right ICA (Fig 2). The maximum aneurysm diameter and neck size were 7.3 and 5.5 mm, respectively. The maximum inflow velocity was 710 mm/s. A vortex core was visualized as a bundle of streamlines with velocities below the 7% value and below the 10% value of the maximum inflow velocity in the diastolic and systolic phases, respectively (Fig 2C, -D). The vortex core was single and stable through the cardiac cycle. The vortex core was orthogonal to the inflow jet in the aneurysm (Fig 2B). This aneurysm flow pattern was recorded as simple and stable.

**Case 4.** A 73-year-old man presented with a large ruptured aneurysm on the tip of the basilar artery (Fig 5). The maximum aneurysm diameter and neck size were 15.0 and 11.3 mm, respectively. The maximum inflow velocity was 820 mm/s. 4D flow MR imaging acquired through the cardiac cycle revealed multiple small vortices beneath the aneurysm surface and irregular streamlines in the aneurysm (Fig 5B, -C). No vortex cores were visualized.

### DISCUSSION

We first report that vortex cores in cerebral aneurysms can be identified and evaluated on 4D flow MR imaging, and we document that the incidence of complex flow patterns was significantly higher in aneurysms with blebs or daughter sacs.

A complex and unstable flow pattern is a rupture risk for cerebral aneurysms.<sup>1-4</sup> Xiang et al,<sup>2</sup> who performed CFD analysis in 38 ruptured and 81 unruptured aneurysms, found that rupture was strongly correlated with a complex flow pattern characterized by multiple vortices. Byrne et al<sup>3</sup> evaluated the hemodynamics of 210 aneurysms, including 83 ruptured aneurysms; their CFD analysis showed that ruptured aneurysms manifested a more complex and more unstable flow pattern than unruptured aneurysms. However, Cornelissen et al<sup>16</sup> reported that morphologic changes of aneurysms on rupture might affect the results of hemodynamic analysis of ruptured aneurysms. Risk factors

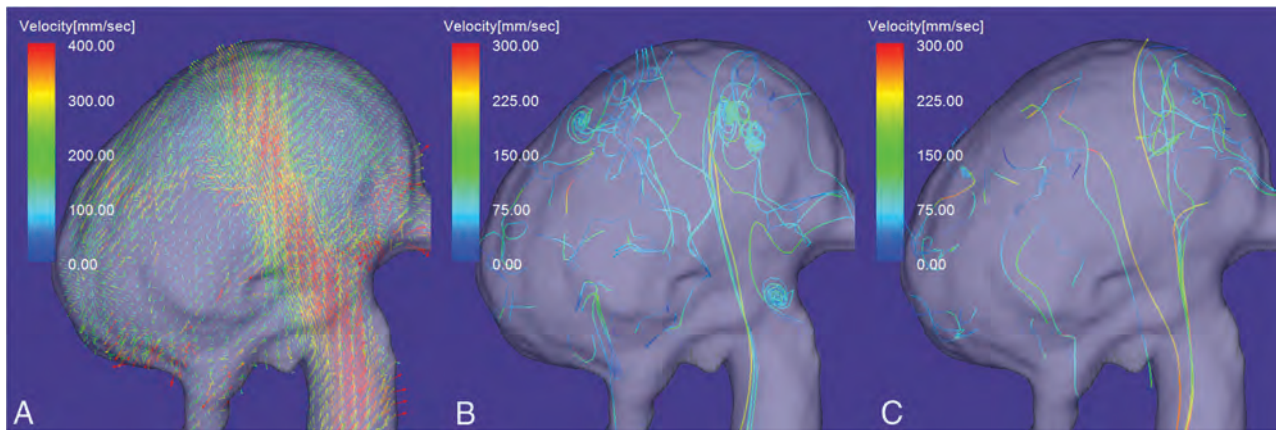


**FIG 5.** A large ruptured aneurysm on the tip of the basilar artery. A, Flow vector map. Streamlines with velocities below 7% of the maximum inflow velocity in the diastolic (B) and systolic (C) phases. Although multiple small vortices beneath the aneurysm surface and irregular streamlines are visualized, no vortex cores are visualized through the cardiac cycle.

obtained by comparing the hemodynamics of ruptured and unruptured cerebral aneurysms should be interpreted with caution. According to Cebal et al,<sup>17</sup> the complexity and instability of the intra-aneurysmal flow were related to the aneurysm wall property. Therefore, the complexity and instability of the intra-aneurysmal flow should be considered in the evaluation of the rupture risk of unruptured cerebral aneurysms. Although the vortex core line visualized by CFD analysis facilitates the evaluation of the complexity and instability of vortical flows, aneurysm vortex cores have not been identified on 4D flow MR imaging.

Although vortex cores have been extracted on the basis of a variety of mathematic algorithms,<sup>5,6</sup> there is no formal definition.<sup>8</sup> The most widely used algorithm is based on reduced velocity<sup>3</sup> or the velocity gradient tensor, eg, the Q-Criterion or the  $\lambda_2$ -Criterion method.<sup>7,18</sup> Köhler et al<sup>18</sup> compared the vortical structures semiautomatically extracted using different local vortex criteria on 4D flow MR imaging of the aorta and pulmonary artery. They found that the  $\lambda_2$ -Criterion method was most suitable for the extraction of vortices. However, a reliable method to accurately extract the vortex cores of cerebral aneurysms remains to be established. Although Marquering et al<sup>19</sup> and Feliciani et al<sup>20</sup> quantified vortical structures using scale-space techniques on the basis of 4D flow MR imaging of an aneurysm phantom, they did not apply their method to detect and quantify the vortex cores of human cerebral aneurysms. For the extraction of vortex cores, Byrne et al<sup>3</sup> constructed a vortex core line using an algorithm that connects the points along faces containing the zero value of the reduced velocity of intra-aneurysmal vortices. Because Flova II does not feature a mathematic algorithm to extract the vortex cores, we attempted to visualize them by demonstrating the streamlines with minimum velocities. By progressively decreasing the threshold (ie, the percentage value of the maximum inflow velocity), we were able to visualize vortex cores at a range from 3% to 13% of the maximum inflow velocity. Our method is simple and allows visual evaluation of the characteristics of vortex cores in aneurysms.

Blebs or daughter sacs are a risk factor for aneurysm rupture.<sup>21-23</sup> In a prospective study, UCAS Japan investigators<sup>21</sup> followed up 6697 unruptured aneurysms conservatively. They

documented that 18.9% featured daughter sacs and that their presence was a risk factor for rupture. Murayama et al<sup>22</sup> performed a prospective 10-year cohort study with a mean follow-up duration of 7388 follow-up years; they also found that daughter sacs were a significant independent predictor of rupture. Additionally, Tsukahara et al<sup>23</sup> reported that the rupture rate during the first year of their observation of all unruptured aneurysms was 3.42%; it was 28.3% for aneurysms with blebs. We found that aneurysms with blebs or daughter sacs had a complex flow pattern at a significantly higher rate than the other aneurysms ( $P = .006$ ). Of our 3 ruptured aneurysms, 1 aneurysm had an unstable vortex core. In the other 2, we noted multiple small vortices and irregular streamlines that were attributable to an extremely complex and unstable flow; no vortex cores were identified. Corresponding to earlier reports,<sup>1-4</sup> our observations suggest that a complex and unstable intra-aneurysm vortical flow raises the risk for rupture. Moreover, the nonvisualization of vortex cores on 4D flow MR imaging may be related to aneurysm rupture. Therefore, evaluation of vortex cores on 4D flow MR imaging may be useful for the rupture-risk stratification of unruptured cerebral aneurysms.

Our study has some limitations. Flova II is not available for the quantitative evaluation of vortex cores in cerebral aneurysms on 4D flow MR imaging. More sophisticated algorithms are needed to quantify the vortex cores of these aneurysms. Due to the limited spatial and temporal resolution of our 1.5T MR imaging scanner, we may have overlooked small vortex cores that present in a very short time; high-resolution imaging techniques may solve this problem. In addition, the lower signal-to-noise ratio of our MR imaging scanner may have affected the stability of vortex cores; a 3T MR imaging scanner with a head array coil for increasing the signal-to-noise ratio may reduce this effect. In this study, the velocity-encoding value for phase-contrast MR imaging was 40–60 cm/s; it may have compromised our ability to visualize streamlines with minimum velocities on our scans. Studies are underway to identify the optimal velocity-encoding value for the assessment of vortex cores and for determining the aneurysm rupture risk. Our study included only 3 ruptured aneurysms. Large-scale studies may facilitate validation of the role of 4D flow

MR imaging for the assessment of the rupture risk of unruptured cerebral aneurysms. Information on ruptured aneurysms subjected to 4D flow MR imaging studies during the observation period must be collected to determine the role of the complexity and instability of vortex cores in the rupture risk. Because such studies are not prone to the effect of morphologic changes on aneurysm rupture,<sup>16</sup> hemodynamic studies on 4D flow MR imaging may yield the required information.

## CONCLUSIONS

Vortex cores in cerebral aneurysms can be identified and evaluated on 4D flow MR imaging. Significantly more aneurysms with-than-without blebs or daughter sacs had a complex flow pattern. Vortex cores of ruptured aneurysms may not be visualized on 4D flow MR imaging. The evaluation of vortex cores on 4D flow MR imaging may help stratify the rupture risk of unruptured cerebral aneurysms.

## REFERENCES

- Cebral JR, Mut F, Weir J, et al. **Association of hemodynamic characteristics and cerebral aneurysm rupture.** *AJNR Am J Neuroradiol* 2011;32:264–70 CrossRef Medline
- Xiang J, Natarajan SK, Tremmel M, et al. **Hemodynamic-morphologic discriminants for intracranial aneurysm rupture.** *Stroke* 2011;42:144–52 CrossRef Medline
- Byrne G, Mut F, Cebral J. **Quantifying the large-scale hemodynamics of intracranial aneurysms.** *AJNR Am J Neuroradiol* 2014;35:333–38 CrossRef Medline
- Jing L, Fan J, Wang Y, et al. **Morphologic and hemodynamic analysis in the patients with multiple intracranial aneurysms: ruptured versus unruptured.** *PLoS ONE* 2015;10:e0132494 CrossRef Medline
- Jiang M, Machiraju R, Thompson DS, et al. Detection and visualization of vortices. In: Hansen CD, ed. *Visualization Handbook*. Amsterdam: Elsevier Butterworth-Heinemann; 2005:295–309
- Rütten M, Alrutz T, Wendland H. **A vortex axis and vortex core border grid adaptation algorithm.** *Int J Numer Methods Fluids* 2008;58:1299–326 CrossRef
- Le TB, Troolin DR, Amatya D, et al. **Vortex phenomena in sidewall aneurysm hemodynamics: experiment and numerical simulation.** *Ann Biomed Eng* 2013;41:2157–70 CrossRef Medline
- Oeltze-Jafra S, Cebral JR, Janiga G, et al. **Cluster analysis of vortical flow in simulations of cerebral aneurysm hemodynamics.** *IEEE Trans Vis Comput Graph* 2016;22:757–66 CrossRef Medline
- Meckel S, Stalder AF, Santini F, et al. **In vivo visualization and analysis of 3-D hemodynamics in cerebral aneurysms with flow sensitized 4-D MR imaging at 3 T.** *Neuroradiology* 2008;50:473–84 CrossRef Medline
- Boussel L, Rayz V, Martin A, et al. **Phase-contrast magnetic resonance imaging measurements in intracranial aneurysms in vivo of flow patterns, velocity fields, and wall shear stress: comparisons with computational fluid dynamics.** *Magn Reson Med* 2009;61:409–17 CrossRef Medline
- Futami K, Kitabayashi T, Sano H, et al. **Inflow jet patterns of unruptured cerebral aneurysms based on the flow velocity in the parent artery: evaluation using 4D flow MRI.** *AJNR Am J Neuroradiol* 2016;37:1318–23 CrossRef Medline
- Futami K, Nambu I, Kitabayashi T, et al. **Inflow hemodynamics evaluated by using four-dimensional flow magnetic resonance imaging and size ratio of unruptured cerebral aneurysms.** *Neuroradiology* 2017;59:411–18 CrossRef Medline
- Lorensen WE, Cline HE. **Marching cubes: a high-resolution 3D surface construction algorithm.** *SIGGRAPH Comput Graph* 1987;21:163–69 CrossRef
- Shimai H, Yokota H, Nakamura S, et al. **Extraction from biological volume data of a region of interest with nonuniform intensity.** In: *Proceedings of the Society of Photo-Optical Instrumentation Engineers 6051, Optomechatronic Machine Vision*. Kazuhiko Sumi, Japan. December 5–7, 2005; 6051:605115
- Dormand JR, Prince PJ. **A family of embedded Runge-Kutta formulae.** *J Comput Appl Math* 1980;6:19–26 CrossRef
- Cornelissen BMW, Schneiders JJ, Potters WV, et al. **Hemodynamic differences in intracranial aneurysms before and after rupture.** *AJNR Am J Neuroradiol* 2015;36:1927–33 CrossRef Medline
- Cebral JR, Duan X, Chung BJ, et al. **Wall mechanical properties and hemodynamics of unruptured intracranial aneurysms.** *AJNR Am J Neuroradiol* 2015;36:1695–703 CrossRef Medline
- Köhler B, Gasteiger R, Preim U, et al. **Semi-automatic vortex extraction in 4D PC-MRI cardiac blood flow data using line predicates.** *IEEE Trans Vis Comput Graph* 2013;19:2773–82 CrossRef Medline
- Marquering HA, van Ooij P, Streekstra GJ, et al. **Multiscale flow patterns within an intracranial aneurysm phantom.** *IEEE Trans Biomed Eng* 2011;58:3447–50 CrossRef Medline
- Feliciani G, Potters W, van Ooij P, et al. **Multi-scale 3D+t intracranial aneurysmal flow vortex detection.** *IEEE Trans Biomed Eng* 2015;9294:1–8 CrossRef Medline
- Morita A, Kirino T, Hashi K; UCAS Japan Investigators. **The natural course of unruptured cerebral aneurysms in a Japanese cohort.** *N Engl J Med* 2012;366:2474–82 CrossRef Medline
- Murayama Y, Takao H, Ishibashi T, et al. **Risk analysis of unruptured intracranial aneurysms: prospective 10-year cohort study.** *Stroke* 2016;47:365–71 CrossRef Medline
- Tsukahara T, Murakami N, Sakurai Y, et al. **Treatment of unruptured cerebral aneurysms: multi-center study at Japanese national hospital.** *Acta Neurochir Suppl* 2005;94:77–85 CrossRef Medline

# How Flow Reduction Influences the Intracranial Aneurysm Occlusion: A Prospective 4D Phase-Contrast MRI Study

 O. Brina,  P. Bouillot,  P. Reymond,  A.S. Luthman,  C. Santarosa,  M. Fahrat,  K.O. Lovblad,  P. Machi,  B.M.A. Delattre,  V.M. Pereira, and  M.I. Vargas



## ABSTRACT

**BACKGROUND AND PURPOSE:** Flow-diverter stents are widely used for the treatment of wide-neck intracranial aneurysms. Various parameters may influence intracranial aneurysm thrombosis, including the flow reduction induced by flow-diverter stent implantation, which is assumed to play a leading role. However, its actual impact remains unclear due to the lack of detailed intra-aneurysmal flow measurements. This study aimed to clarify this relationship by quantitatively measuring the intra-aneurysmal flow using 4D phase-contrast MR imaging.

**MATERIALS AND METHODS:** We acquired prospective pre- and post-stent implantation 4D phase-contrast MR imaging data of a consecutive series of 23 patients treated with flow-diverter stents. Velocity field data were combined with the intraprocedural 3D angiogram vessel geometries for precise intracranial aneurysm extraction and partial volume correction. Intra-aneurysmal hemodynamic modifications were compared with occlusion outcomes at 6 and 12 months.

**RESULTS:** The averaged velocities at systole were lower after flow-diverter stent implantation for all patients and ranged from  $21.7 \pm 7.1$  cm/s before to  $7.2 \pm 2.9$  cm/s after stent placement. The velocity reduction was more important for the group of patients with aneurysm thrombosis at 6 months (68.8%) and decreased gradually from 66.2% to 55% for 12-month thrombosis and no thrombosis, respectively ( $P = .08$ ).

**CONCLUSIONS:** We propose an innovative approach to measure intracranial flow changes after flow-diverter stent implantation. We identified a trend between flow reduction and thrombosis outcome that brings a new insight into current understanding of the flow-diversion treatment response.

**ABBREVIATIONS:** CFD = computational fluid dynamics; 3DRA = 3D rotational angiography; FDS = flow-diverter stent; IA = intracranial aneurysm; PCMR = phase-contrast MRI; PVRR = proportional velocity-reduction ratio;  $Q_{ICA}$  = ICA systolic flow rates ratio;  $\bar{Q}_{ICA}$  = ICA mean flow rates;  $Vel_{an}$  = intra-aneurysmal velocity; VENC = velocity encoding

Flow-diverter stents (FDSs) are a widely used option for the endovascular treatment of large-neck intracranial aneurysms (IAs).<sup>1-4</sup> The high density of stent struts across the IA neck dampens the intrasaccular flow and promotes a progressive thrombosis of the cavity to ultimately exclude the aneurysm from the circulation.<sup>5,6</sup> FDSs also have other advantages such as vessel wall remodeling of the parent artery, often altered in large-neck ICA aneurysms,<sup>7</sup> as well as the improvement of outcomes for

symptomatic lesions due to the progressive decompression of surrounding tissues as the aneurysm shrinks.<sup>8</sup> In addition, compared with other endovascular procedures, FDS implantation yields a higher rate of complete and permanent aneurysm exclusion, considering both residual and complete recanalization.<sup>2,9,10</sup> Furthermore, from an interventional point of view, FDS implantation procedures are rapid and avoid the risky penetration of the aneurysm sac with embolization material, though the delivery of the device requires appropriate training.<sup>11</sup> However, the physiologic mechanisms leading to aneurysmal occlusion are

Received May 21, 2019; accepted after revision September 20.

From the Divisions of Neuroradiology (O.B., P.R., A.S.L., C.S., K.O.L., P.M., V.M.P., M.I.V.) and Radiology (B.M.A.D.), Geneva University Hospitals, University of Geneva, Geneva, Switzerland; Department of Quantum Matter Physics (P.B.), University of Geneva, Geneva, Switzerland; Laboratory for Hydraulic Machines (M.F.), Ecole Polytechnique Fédérale de Lausanne, Lausanne, Switzerland; Division of Neuroradiology (V.M.P.), Department of Medical Imaging (V.M.P.), and Division of Neurosurgery (V.M.P.), Department of Surgery, Toronto Western Hospital, University Health Network, Toronto, Ontario, Canada.

This work was supported by Swiss National Science Foundation grants (SNF 32003B 160222 and SNF 320030 156813).

Please address correspondence to Maria Isabel Vargas, MD, Geneva University Hospitals, Division of Diagnostic and Interventional Neuroradiology, Rue Gabrielle-Perret-Gentil 4, 1211 Genève 14; e-mail: maria.i.vargas@hcuge.ch

 Indicates open access to non-subscribers at [www.ajnr.org](http://www.ajnr.org)

 Indicates article with supplemental on-line appendix and table.

 Indicates article with supplemental on-line photos.

<http://dx.doi.org/10.3174/ajnr.A6312>

complex, and many factors such as hemodynamics, antiaggregation therapy individual responses, and biologic factors are associated with them. This complexity may translate into posttreatment rupture<sup>12,13</sup> and delayed aneurysm occlusion, thus resulting in patients with a suboptimally treated lesion.<sup>9,10</sup> It is hypothesized that the flow reduction after FDS implantation has a strong impact on occlusion likelihood and may play a role in delayed rupture, but this relationship is yet to be established.

At present, the quantitative assessment of aneurysmal flow changes relies on 3 main methods: 1) video densitometry based on DSA time-series,<sup>14,15</sup> 2) blood flow modeling using computational fluid dynamics (CFD),<sup>16-18</sup> and 3) 2D and 4D phase-contrast MR imaging (4D-PCMR). The latter presents the major advantage of being the only quantitative method for the in vivo measurement of 3D velocity fields over time, and some neurovascular disorders have been addressed with this technique, such as arteriovenous malformation hemodynamics.<sup>19</sup> Regarding IAs treated with FDSs, only a limited number of in vitro studies<sup>20</sup> have been performed, and even fewer in vivo studies have included a maximum of 10 patients. This lack of data has prevented determination of any correlation with the resultant treatment outcomes.<sup>21,22</sup>

The sparse literature available may be due to the stent-induced metallic artifacts, which do not make 4D-PCMR intuitively indicated for post-treatment acquisitions. However, we have shown that these metallic artifacts are limited to the lumen of the stent without extension to the aneurysm bulge, which guarantees the accuracy of the velocities measured in the aneurysm volume.<sup>23</sup> On the basis of these results, we aimed to measure pre- and post-FDS velocity fields with 4D-PCMR in a prospective patient cohort and to correlate hemodynamic changes with aneurysm occlusion outcomes at 6 and 12 months.

## MATERIALS AND METHODS

### Patient Selection

We prospectively included patients with unruptured saccular ICA aneurysms treated with FDS only. We excluded patients with partly thrombosed aneurysms. Our treatment strategy consisted of placing a single layer of flow diverter, without coil association. The study was approved by Geneva University Hospitals institutional ethics committee (NEC 07-056). All patients provided written informed consent.

### MR Imaging Acquisition

MR imaging examinations were performed the day before and within 48 hours following the stent implantation procedure with an Ingenuity TF PET/MR (Achieva 3 T TX series MR imaging system; Philips Healthcare, Best, the Netherlands) and an 8-channel head coil. The circle of Willis was imaged using a 3D-TOF sequence on which the 4D-PCMR slices were positioned in a sagittal/oblique orientation to cover both the aneurysm and its adjacent parent vessel. The acquisition parameters are detailed in the On-line Appendix.<sup>22,23</sup>

### Endovascular Procedure

Procedures were performed with a biplane angiosuite (Allura FD20; Philips Healthcare). 3D rotational angiography (3DRA) was systematically acquired as part of the preimplantation work-

up for device sizing and to determine the working projection views. Given its high spatial resolution and enhanced contrast, 3DRA was also used during postprocessing to segment the vessel geometry and separate the aneurysm from the parent vessel. At the end of the procedure, a contrast-enhanced conebeam CT was performed to verify the apposition of the device to the vessel wall.

### Data Postprocessing

Although 4D-PCMR provides the 3D velocity vector field over time in the entire acquisition volume, preliminary postprocessing steps are required to prepare the raw datasets for the calculation of the velocity field within the vessel lumen. Thus, we combined the 4D-PCMR velocities with the vessel geometric information provided by the 3DRA. More details are provided in the On-line Appendix and Bouillot et al.<sup>24</sup>

### Proportional Velocity-Reduction Ratio Calculation

Aneurysmal flow modification induced by the FDS implantation was quantified with the proportional velocity-reduction ratio (PVRR).<sup>22</sup> We focused on the systolic phase with the highest velocity range, minimizing the impact of the measurement uncertainties affecting low velocities. The PVRR expresses the rate of intra-aneurysmal velocity reduction normalized with the ICA flow rate as follows:

$$PVRR = 1 - \frac{Vel_{an}}{Vel_{an}} \times \frac{Q_{ICA,Pre}}{Q_{ICA,Post}}$$

Where  $Vel_{an,Pre}$  and  $Vel_{an,Post}$  are intra-aneurysmal velocities averaged spatially at the systolic time-step before and after FDS implantation, respectively. The normalization with the ICA systolic flow rates ratio,  $Q_{ICA,Pre}/Q_{ICA,Post}$ , aimed to correct for the potential differences in physiologic conditions between the 2 MR imaging examinations. The PVRR was calculated using the following methodology for aneurysm velocity  $Vel_{an}$  and ICA flow-rate extraction  $Q_{ICA}$ :

**Aneurysm Velocities (VELAN).** The aneurysm was disconnected from the parent vessel by removing the mesh cells of the circulating volume located within a diameter of 1 mm larger than the actual parent vessel diameter. This exclusion criterion defined from the vessel center line (Fig 1A.2) aimed to include the outer bounds of the stent struts covering the neck. When an artery originated from the aneurysm, elements were interactively removed to disconnect the vessel from its origin. Once extracted, the velocities of the aneurysm volume at the systolic phase were averaged spatially to compute the  $Vel_{an}$ . We excluded patients with aneurysms presenting more than half of their volume with unreliable velocities with  $Vel_{an} < 7.7$  cm/s before FDS implantation. This threshold corresponds to the measurement error previously identified and reported in Pereira et al<sup>22</sup> and Bouillot et al.<sup>23</sup>

**Flow Rates (QICA).** As described in Bouillot et al,<sup>24</sup> measurement planes, each separated by 2 mm, were automatically placed orthogonal to the vessel center line within a user-selected distance corresponding to the C2-3 segment (Fig 1C.1). In each plane, the 3D-PCMR data velocities were interpolated within the boundaries of the vessel provided by the 3DRA (Fig 1C.2). The instantaneous flow rate was computed after partial volume

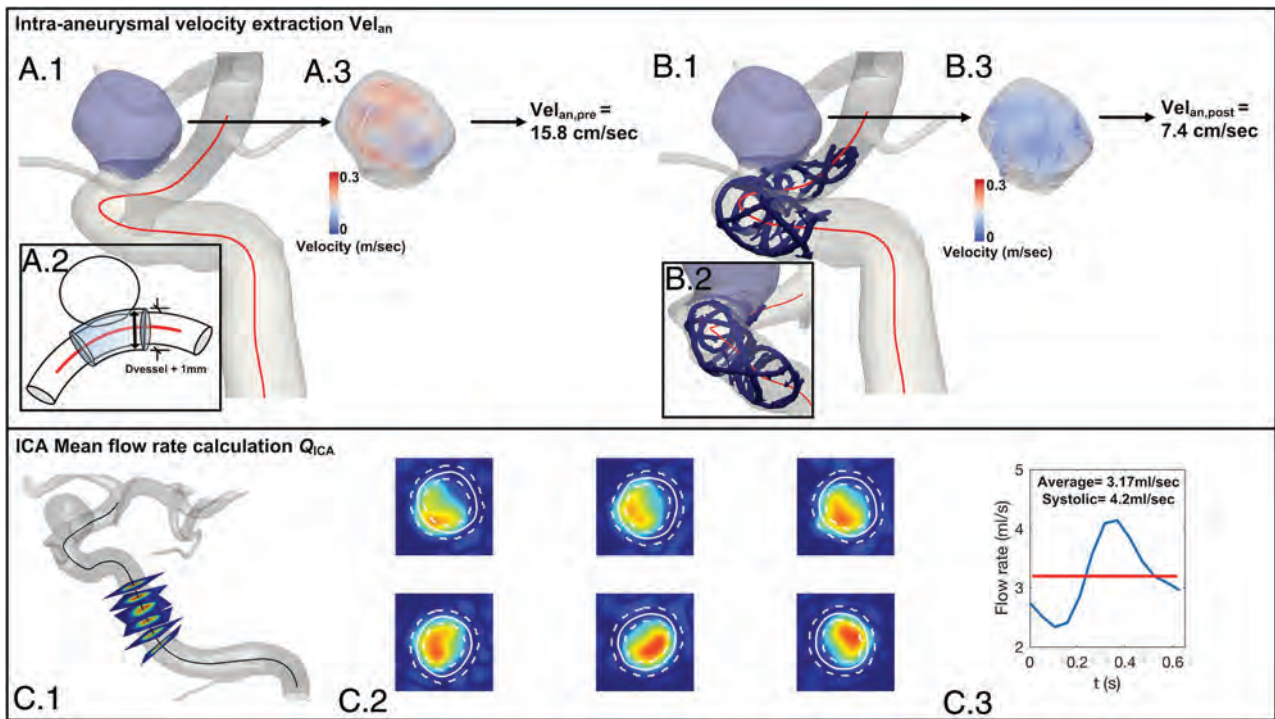


**FIG 1.** Upper row, Aneurysm extraction for pre- and poststent acquisitions (A.1 and B.1), their 3D velocity fields (A.3 and B.3), and their systolic  $Vel_{an}$  values, respectively. The extraction method is illustrated in A.2, where the aneurysm bulge is isolated from the parent artery by removing all the mesh cells within a diameter  $D_{vessel} + 1\text{mm}$  around the center line. B.1 and B.2, The conebeam CT of the implanted Silk (radio-opaque markers segmented in blue) is registered with the 3DRA geometry to show its clear separation from the extracted aneurysm. Lower row, QICAs (C.3) measured on orthogonal planes positioned along the vessel center line (C.1), with partial volume correction (C.2) as described in Bouillot et al.<sup>24</sup>

correction and subsequently averaged over the measurement planes (Fig 1C.3).

#### Qualitative Evaluation of the Intra-Aneurysmal Velocities

Pre- and poststent flow patterns of each patient were qualitatively evaluated by means of streamlines using Paraview software (<http://paraview.org>).

#### Follow-Up and Statistical Analysis

Patient follow-up was performed by MR imaging examinations at 6 and 12 months after FDS implantation. At 12 months, an angiogram was obtained to either confirm the complete thrombosis of the aneurysm or assess the need for retreatment in the case of absent or incomplete thrombosis. Imaging records were reviewed by an experienced neuroradiologist (M.I.V.). Outcomes were labeled as follows: complete thrombosis at 6 months, complete thrombosis at 12 months, and no or partial thrombosis at 12 months. Differences between PVRR and thrombosis outcomes for the 3 groups were evaluated using the Kruskal-Wallis test. Statistical results are presented as mean  $\pm$  SD. Statistical analysis was performed in Matlab R2017A (MathWorks, Natick, Massachusetts). Finally, we analyzed the potential relationships between geometric characteristics of the aneurysm and PVRR by measuring the volume, maximum size, aspect ratio, and neck size on 3DRA data.

## RESULTS

We included 28 consecutive patients from January 2012 to December 2017. All patients were successfully treated with the following FDSs: Silk (Balt Extrusion, Montmorency, France) ( $n=7$ ); Pipeline Embolization Device (PED; Covidien, Irvine, California) ( $n=17$ ); and the Flow-Redirection Endoluminal Device (FRED; MicroVention, Tustin, California) ( $n=4$ ). Five patients received 2 devices to either extend the coverage length or improve the wall apposition of the stent at the landing zone. Pre- and post-4D-PCMR sequences were successfully acquired for all patients, representing 56 MR imaging examinations. Two patients were excluded from the study because follow-up imaging was not complete at 6 or 12 months. Three patients presenting with  $>50\%$  of their aneurysmal volumes with  $Vel_{an}$  below  $7.7\text{ cm/s}$  were excluded, including 1 patient with a double stent. For the remaining 23 patients, the rate of aneurysm occlusion increased from  $60.9\%$  ( $n=14$ ) at 6 months to  $82.6\%$  ( $n=19$ ) at 12-month follow-up. Four aneurysms remained patent at 12 months. These results are slightly lower than the reported occlusion rates of  $73.6\%$  and  $86.8\%$  for 6-month and 1-year follow-up, respectively.<sup>1</sup>

#### Flow-Reduction and Thrombosis Outcomes

On average, the ICA mean flow rates ( $\bar{Q}_{ICA}$ ) were not significantly different before and after the procedure (Fig 2A;  $\bar{Q}_{ICA,Pre} = 3.54 \pm 0.7\text{ mL/s}$  and  $\bar{Q}_{ICA,Post} = 3.64 \pm 0.7\text{ mL/s}$ ;  $P = .66$ ). By contrast, the intra-aneurysmal systolic velocities,  $Vel_{an}$ , were reduced

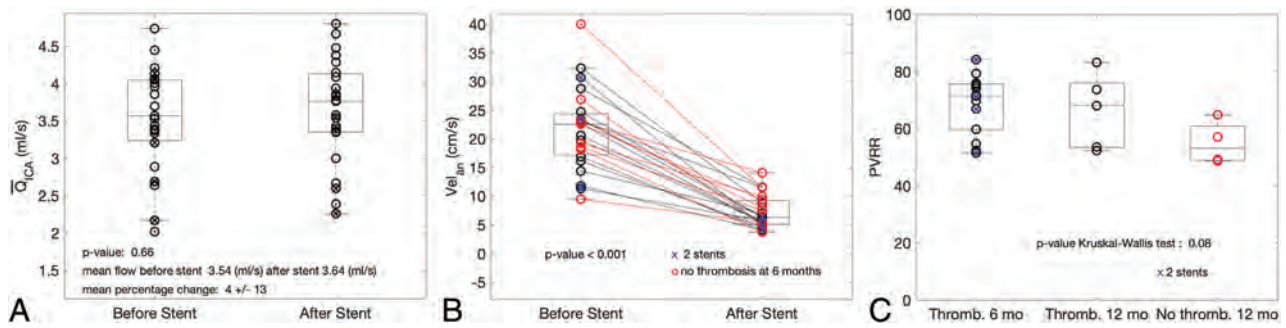


**FIG 2.** Descriptive statistics. *A*, ICA mean flow rates with no significant differences between pre- and poststent MR imaging acquisitions. *B*, Intra-aneurysmal systolic velocities show a wide range before stent placement and converging toward a narrower range after flow diversion. *C*, The PVRR for patients thrombosed at 6 and 12 months and not thrombosed at 12 months. *Blue cross dots* represent patients implanted with 2 stents. *Thromb* indicates thrombosis.

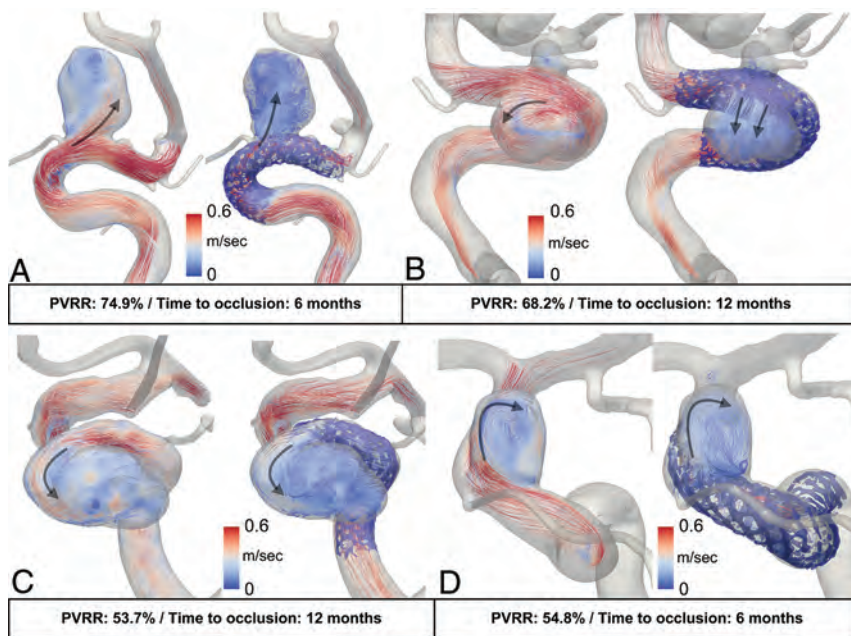


**FIG 3.** Pre-/post-FDS implantation streamlines at the systolic phase within the 3DRA geometries (in transparent rendering) of 4 illustrative patients. The deployed stents imaged with vasoCT (Philips Healthcare) are added on the poststent data. The *upper row* shows 2 patients (*A* and *B*) both with strong modifications of the velocity patterns and flow reduction (PVRR  $\approx$  70%), leading to different thrombosis outcomes. The *lower row* shows 2 other patients (*C* and *D*) with unchanged velocity patterns and lower flow reduction (PVRR  $\approx$  55%), leading to different thrombosis outcomes.

for all patients, on average, from  $21.7 \pm 7.1$  cm/s before to  $7.2 \pm 2.9$  cm/s after FDS placement (Fig 2B). Of note, a wide range of pretreatment intra-aneurysmal systolic velocities converged toward a much narrower range after flow diversion.

On average, PVRR gradually decreased from 68.8%, 66.2%, and 55% for 6- and 12-month thrombosis times and no thrombosis at 12 months, respectively. This finding is consistent with a lower flow reduction when the occlusion is delayed. Although not statistically significant ( $P = .08$ ), a trend was identified between PVRR and these 3 groups of different occlusion times (Fig 2C).

In addition, all IAs treated with 2 stents were occluded at 6 months but were spread into the bulk of PVRR, including the lowest value. This finding indicates that the decrease of porosity,

though not quantified, appears to be not necessarily associated with higher PVRRs as could be expected. No correlations between the geometric characteristics and flow reduction or occlusion outcomes were observed ( $R^2 = 0.24, 0.27, 0.02, 0.06$  for volume, maximum size, aspect ratio, and neck size, respectively). More details are provided in the On-line Appendix.

### Qualitative Analysis of the Velocity Vector Fields

Intra-aneurysmal velocity patterns were modified by the stent either in magnitude and/or direction. However, these modifications were not related to the thrombosis outcome as illustrated for 2 pairs of patients in Fig 3. In each pair, the patients presented with close PVRRs and flow-pattern behaviors, but with 6- and 12-month thrombosis times, respectively. For patients *A* and *B*, flow patterns were strongly modified by the stent, namely, the location of the aneurysm inflow and the more diffuse aspect of the jet (PVRRs  $\approx$  70%). On the other hand, patients *C* and *D* showed similar pre- and poststent flow patterns, but with a lower velocity magnitude (PVRRs  $\approx$  54%).

## DISCUSSION

This study presents quantitative PCMR measurements of FDS-induced flow changes performed in a cohort of patients. To our knowledge, this is the largest study comparing in vivo flow-reduction measurements and IA thrombosis outcomes.

### Flow Reduction and Thrombosis Outcomes

On average, the measured intra-aneurysmal velocities,  $Vel_{an,pre} = 21.7 \pm 7.1$  cm/s and  $Vel_{an,post} = 7.2 \pm 2.9$  cm/s, were in agreement with those in previous studies. On the basis of CFD

simulations performed on 8 patients, Kulcsar et al<sup>16</sup> reported time-averaged velocities reduced from 6 cm/s (pre-FDS) to 3 cm/s (post-FDS) for large aneurysms (diameter, >10 mm) and from 14.5 to 8 cm/s for small aneurysms (diameter, <10 mm). Consistent with our findings, Sindeev et al<sup>20</sup> showed a wide range of systolic  $Vel_{an,pre} = 44\text{--}7$  cm/s before stent placement, with in vitro 4D-PCMR measurements, which converged to a narrower range after stent placement ( $Vel_{an,post} = 7.6\text{--}4$  cm/s).

Various CFD studies have reported correlations between flow changes and aneurysm thrombosis, but there has been disagreement regarding the hemodynamic criteria associated with fast aneurysm occlusion. For example, Mut et al<sup>17</sup> found that an absolute threshold of mean aneurysm velocity (1.3 cm/s), mean aneurysm inflow rate (0.37 mL/s), and mean shear rate (16.3 seconds<sup>-1</sup>) discriminated between fast and slow occlusion times in a group of 23 aneurysms. By contrast, Kulcsar et al<sup>16</sup> suggested a relative aneurysm-specific velocity and wall shear stress reduction threshold associated with thrombosis. Similarly, Ouared et al<sup>25</sup> found that a relative velocity reduction of at least one-third was associated with durable thrombosis. The hemodynamic component is widely accepted as the driving factor in aneurysm healing. This has led to a trend by manufacturers toward decreasing stent porosity by increasing the mesh density, while keeping reasonable navigation features and from the operator's side, by adding stent layers to achieve "sufficient" contrast agent stagnation following subjective indicators considered prone to thrombosis patterns.<sup>26</sup>

In this study, the PVRR was gradually lower in the 6- to 12-month thrombosis and no-thrombosis groups. This finding is consistent with a diminished flow reduction for delayed occlusions. However, the small PVRR differences among the 3 groups put in perspective the role of flow reduction as a driving parameter in the long-term occlusion of aneurysms treated by FDS. Other parameters should be also considered for a comprehensive understanding of IA thrombosis as suggested by the following studies: Paliwal et al<sup>18</sup> showed that the average velocity reduction was not different between successful (52.4%) and unsuccessful (49.2%) treatments in 15 patients. Similarly, Berg et al<sup>27</sup> studied 2 morphologically equivalent carotid-ophthalmic aneurysms presenting with completely different outcomes (3-month occlusion for one and 3 additional layers required for the other) and found opposite hemodynamic changes. Furthermore, histologic studies suggest that neck endothelialization plays an important role in the healing process, highlighting the importance of stent wall apposition to promote the tissue growing across the neck.<sup>28</sup> Nevertheless, it remains unclear whether the aneurysm thrombosis, the neck endothelialization, or both are dominant factors for occlusion. Most interesting, Kadirvel et al<sup>29</sup> suggested that long-term occlusion occurred only as a result of neck covering, characterized by a contiguous layer of endothelial cells overlying a smooth-muscle cell substrate. This suggestion could bring new insights for manufacturers, researchers, and clinicians with implications for device development (Marosfoi et al<sup>30</sup> showed that temporal and spatial endothelial growth was related to stent design), adjunctive medications (Li et al<sup>31</sup> showed that intravenous injection of recombinant human SDF-1- $\alpha$  accelerated re-endothelialization of the stent), and dual-antiplatelet therapy.

### **PCMR Measurements and Flow Diversion**

This study was made possible due to prior investigations on intracranial stent-related artifacts.<sup>23</sup> In particular, we showed that these artifacts were mainly related to the shielding effect and were therefore restricted to the stent lumen. Furthermore, the following recent technical developments<sup>24</sup> were assembled in a postprocessing pipeline to obtain consistent and reliable PVRR and  $Vel_{an}$  assessment from 4D-PCMR data: 1) the combination of 4D-PCMR data with 3DRA geometry for a precise delineation of the circulating domain; 2) the partial volume correction allowing unbiased ICA mean flow-rate quantification; and 3) the semiautomatic aneurysm extraction, thus ensuring a systematic and user-independent selection of the volume of interest and the consistent inclusion of the relevant aneurysm inflow velocities close to the neck.<sup>32</sup> In the context of flow-diversion treatment, only a few PCMR investigations have been reported. The hemodynamic changes in the parent vessel were measured in patients with 2D-PCMR by Eker et al<sup>7</sup> and MacDonald et al.<sup>33</sup> Sindeev et al<sup>20</sup> used 4D-PCMR in 3 patient-specific models and found flow reductions of 89% and 30%–50% for fast and delayed thrombosis outcomes, respectively. Karmonik et al<sup>21</sup> used a combination of in vitro experiments and the measurements of 3 patients, but these were not associated with occlusion times, findings similar to those of Pereira et al.<sup>22</sup>

This limited literature can probably be attributed to the inherent limitations of 4D-PCMR related to data acquisition: long scan duration; coarse spatial resolution regarding the size of the IA; the unique velocity encoding (VENC) that cannot cover the large range of involved velocities; and the low temporal resolution, which smooths out the peak systolic velocities. Additionally, 4D-PCMR cannot provide mechanical loads, such as wall shear stress obtained with CFD simulations. However, simulations have their own restrictions: The patient flow conditions are usually unknown; the non-Newtonian behavior of the flow is rarely taken into account, though non-negligible for low velocities and recirculation areas as in flow diversion<sup>34</sup>; and the virtual stent hardly replicates the actual procedure deployment and its related vessel-geometry modifications.<sup>35</sup> In comparison, 4D-PCMR has the great advantage of providing direct in vivo flow measurement readily available in clinical settings and already routinely applied for the hemodynamic assessment of cardiac disorders.<sup>36</sup> In the context of intracranial measurements, further improvements are needed to address the spatial resolution issues, while reducing the scanning time.

### **Clinical Relevance**

The PVRRs of patients implanted with 2 stents were homogeneously distributed along the PVRR range (Fig 2C), with 1 having even the lowest value. Even if all the patients with double layers had occlusion at 6 months, the absence of a relationship between multilayer implantations and higher PVRRs suggests that the placement of additional devices does not necessarily increase the flow diversion. These results are in line with those of Chalouhi et al,<sup>37</sup> who demonstrated similar occlusion rates for single and multiple PED FDSs. Moreover, they showed that the placement of additional stent layers added only morbidity with a 3-fold

complication rate. In our study, the wide range of velocities before stent placement (probably related to the wide range of aneurysm sizes and shapes) was dampened in a narrower range after stent implantation, independent of the initial conditions. From a clinical point of view, this is relevant information for interventionalists to potentially avoid adding unnecessary stent layers.

### Limitations

Our study has some limitations. First, whereas a range of VENC values has been used in the literature, we chose a VENC of 80 cm/s in accordance with Markl et al<sup>38</sup> for intracranial vessel measurements. Other 4D-PCMR studies used, VENCs of 120 cm/s,<sup>39</sup> 100 cm/s,<sup>20</sup> and a range of 60–80 cm/s<sup>21</sup> for pre- and poststent acquisitions. Our main limitation, with a potential impact on the results, was the choice of the poststent VENC, which led us to decrease this parameter from 80 cm/s (the first 17 patients) to 40 cm/s (in the remaining 6 patients) to capture the low velocities more accurately at the expense of aliasing artifacts. Furthermore, to rely on the aneurysmal velocities presented in this study, we used the cutoff published in Pereira et al<sup>22</sup> and Bouillot et al<sup>23</sup> to exclude patients with >50% of their prestent velocities below this value, assuming that poststent measurements would be severely biased. For some patients, the proportion of aneurysm volume below this threshold could have been larger than 50% after stent placement, thus reflecting very low velocities or nearly stagnant flows. This sensitive acquisition parameter would need to be refined by using in vitro ground truth measurements, such as particle imaging velocimetry, especially for poststent measurements.

Second, poststent MR imaging measurements were performed shortly after the procedure and did not reflect the entire IA thrombosis evolution influencing both the flow conditions and the neck endothelialization as shown in vitro by Gester et al.<sup>40</sup> Consequently, our statements should be weighed carefully, and further studies should be considered to monitor aneurysmal velocity modification during follow-up imaging. Third, our results presented here (based on systolic velocity reduction) are limited among other relevant flow parameters in flow diversion, such as wall shear stress, the stagnation zone, and residence time. The inherent limitations of the PCMR technique (spatial and temporal resolution) must be considered to accurately resolve near-wall velocities and low velocity ranges. Further research is needed to improve PCMR measurements to allow a reliable computation of these hemodynamic parameters. Finally, the small number of patients, especially for 12-month thrombosis time and thrombosis absence, may have limited the emergence of a significant relationship between PVRR and thrombosis time. The inaccuracy of low-velocity measurements could have also affected the low PVRRs. A study with a larger sample size would help in confirming the PVRR as a potential predictor for fast and delayed thrombosis.

### CONCLUSIONS

This study showed a trend between IA occlusion time and velocity reductions measured with 4D-PCMR among a cohort of patients treated with FDSs. Thanks to previous research on the

FDS and 4D-PCMR we confirmed that this is a valid technique to characterize IA flow changes with regard to clinical outcomes following FDS implantation. PVRR is a promising indicator for a more comprehensive understanding of the FDS treatment response.

Disclosures: Vitor Mendes Pereira—UNRELATED: Consulting Fee or Honorarium: Medtronic and Stryker, Comments: Proctor and Steering Committee for the PREMIER and EVOLVE studies.\* \*Money paid to the institution.

### REFERENCES

1. Becks T, Kallmes DF, Saatci I, et al. **Pipeline for uncoilable or failed aneurysms: results from a multicenter clinical trial.** *Radiology* 2013;267:858–68 CrossRef Medline
2. Briganti F, Leone G, Marseglia M, et al. **Endovascular treatment of cerebral aneurysms using flow-diverter devices: a systematic review.** *Neuroradiol J* 2015;28:365–75 CrossRef Medline
3. Brijnijkji W, Murad MH, Lanzino G, et al. **Endovascular treatment of intracranial aneurysms with flow diverters: a meta-analysis.** *Stroke* 2013;44:442–47 CrossRef Medline
4. Walcott BP, Stapleton CJ, Choudhri O, et al. **Flow diversion for the treatment of intracranial aneurysms.** *JAMA Neurol* 2016;73:1002–08 CrossRef Medline
5. Bouillot P, Brina O, Ouared R, et al. **Particle imaging velocimetry evaluation of intracranial stents in sidewall aneurysm: hemodynamic transition related to the stent design.** *PLoS One* 2014;9:e113762 CrossRef Medline
6. Bouillot P, Brina O, Ouared R, et al. **Hemodynamic transition driven by stent porosity in sidewall aneurysms.** *J Biomech* 2015; 48:1300–09 CrossRef
7. Eker OF, Boudjeltia KZ, Jerez RA, et al. **MR derived volumetric flow rate waveforms of internal carotid artery in patients treated for unruptured intracranial aneurysms by flow diversion technique.** *J Cereb Blood Flow Metab* 2015;35:2070–79 CrossRef Medline
8. Szikora I, Marosfoi M, Salomvary B, et al. **Resolution of mass effect and compression symptoms following endoluminal flow diversion for the treatment of intracranial aneurysms.** *AJNR Am J Neuroradiol* 2013;34:935–39 CrossRef Medline
9. Chalouhi N, Tjoumakaris S, Starke RM, et al. **Comparison of flow diversion and coiling in large unruptured intracranial saccular aneurysms.** *Stroke* 2013;44:2150–54 CrossRef Medline
10. Di Maria F, Pistocchi S, Clarencon F, et al. **Flow diversion versus standard endovascular techniques for the treatment of unruptured carotid-ophthalmic aneurysms.** *AJNR Am J Neuroradiol* 2015;36: 2325–30 CrossRef Medline
11. Delgado Almandoz JE, Kayan Y, Tenreiro A, et al. **Clinical and angiographic outcomes in patients with intracranial aneurysms treated with the Pipeline embolization device: intra-procedural technical difficulties, major morbidity, and neurological mortality decrease significantly with increased operator experience in device deployment and patient management.** *Neuroradiology* 2017;59: 1291–99 CrossRef Medline
12. Ikeda H, Ishii A, Kikuchi T, et al. **Delayed aneurysm rupture due to residual blood flow at the inflow zone of the intracranial paraclinoid internal carotid aneurysm treated with the Pipeline Embolization Device: histopathological investigation.** *Interv Neuroradiol* 2015;21: 674–83 CrossRef Medline
13. Kulcsar Z, Houdart E, Bonafe A, et al. **Intra-aneurysmal thrombosis as a possible cause of delayed aneurysm rupture after flow-diversion treatment.** *AJNR Am J Neuroradiol* 2011;32:20–25 CrossRef Medline
14. Pereira VM, Bonnefous O, Ouared R, et al. **A DSA-based method using contrast-motion estimation for the assessment of the intra-aneurysmal flow changes induced by flow-diverter stents.** *AJNR Am J Neuroradiol* 2013;34:808–15 CrossRef Medline
15. Chien A, Vinuela F. **IS FlowMap, a novel tool to examine blood flow changes induced by flow diverter stent treatment: initial**

- experiences with Pipeline cases. *J Neurointerv Surg* 2013;5(Suppl 3):iii43–47 CrossRef Medline
16. Kulcsar Z, Augsburg L, Reymond P, et al. **Flow diversion treatment: intra-aneurysmal blood flow velocity and WSS reduction are parameters to predict aneurysm thrombosis.** *Acta Neurochir (Wien)* 2012;154:1827–34 CrossRef Medline
  17. Mut F, Raschi M, Scrivano E, et al. **Association between hemodynamic conditions and occlusion times after flow diversion in cerebral aneurysms.** *J Neurointerv Surg* 2015;7:286–90 CrossRef Medline
  18. Paliwal N, Damiano RJ, Davies JM, et al. **Association between hemodynamic modifications and clinical outcome of intracranial aneurysms treated using flow diverters.** *Proc SPIE Int Soc Opt Eng* 2017;10135 CrossRef Medline
  19. Wu C, Ansari SA, Honarmand AR, et al. **Evaluation of 4D vascular flow and tissue perfusion in cerebral arteriovenous malformations: influence of Spetzler-Martin grade, clinical presentation, and AVM risk factors.** *AJNR Am J Neuroradiol* 2015;36:1142–49 CrossRef Medline
  20. Sindeev S, Arnold PG, Frolov S, et al. **Phase-contrast MRI versus numerical simulation to quantify hemodynamical changes in cerebral aneurysms after flow diverter treatment.** *PLoS One* 2018;13:e0190696 CrossRef Medline
  21. Karmonik C, Anderson JR, Elias S, et al. **Four-dimensional phase contrast magnetic resonance imaging protocol optimization using patient-specific 3-dimensional printed replicas for in vivo imaging before and after flow diverter placement.** *World Neurosurg* 2017;105:775–82 CrossRef Medline
  22. Pereira VM, Brina O, Delattre BM, et al. **Assessment of intra-aneurysmal flow modification after flow diverter stent placement with four-dimensional flow MRI: a feasibility study.** *J Neurointerv Surg* 2015;7:913–19 CrossRef Medline
  23. Bouillot P, Brina O, Delattre BMA, et al. **Neurovascular stent artifacts in 3D-TOF and 3D-PCMR: influence of stent design on flow measurement.** *Magn Reson Med* 2019;81:560–72 CrossRef Medline
  24. Bouillot P, Delattre BMA, Brina O, et al. **3D phase contrast MRI: partial volume correction for robust blood flow quantification in small intracranial vessels.** *Magn Reson Med* 2018;79:129–40 CrossRef Medline
  25. Ouared R, Larrabide I, Brina O, et al. **Computational fluid dynamics analysis of flow reduction induced by flow-diverting stents in intracranial aneurysms: a patient-unspecific hemodynamics change perspective.** *J Neurointerv Surg* 2016;8:1288–93 CrossRef Medline
  26. O'Kelly CJ, Krings T, Fiorella D, et al. **A novel grading scale for the angiographic assessment of intracranial aneurysms treated using flow diverting stents.** *Interv Neuroradiol* 2010;16:133–37 CrossRef Medline
  27. Berg P, Saalfeld S, Janiga G, et al. **Virtual stenting of intracranial aneurysms: a pilot study for the prediction of treatment success based on hemodynamic simulations.** *Int J Artif Organs* 2018;41:698–705 CrossRef Medline
  28. Rouchaud A, Ramana C, Brinjikji W, et al. **Wall apposition is a key factor for aneurysm occlusion after flow diversion: a histologic evaluation in 41 rabbits.** *AJNR Am J Neuroradiol* 2016;37:2087–91 CrossRef Medline
  29. Kadirvel R, Ding YH, Dai D, et al. **Cellular mechanisms of aneurysm occlusion after treatment with a flow diverter.** *Radiology* 2014;270:394–99 CrossRef Medline
  30. Marosfoi M, Langan ET, Strittmatter L, et al. **In situ tissue engineering: endothelial growth patterns as a function of flow diverter design.** *J Neurointerv Surg* 2017;9:994–98 CrossRef Medline
  31. Li Z, Zhao R, Fang X, et al. **Recombinant human SDF-1alpha administration accelerates aneurysm neck reendothelialization in rabbit saccular aneurysm after flow diverter treatment.** *Acta Biochim Biophys Sin (Shanghai)* 2017;49:246–53 CrossRef Medline
  32. Qiu T, Jin G, Bao W, et al. **Intercorrelations of morphology with hemodynamics in intracranial aneurysms in computational fluid dynamics.** *Neurosciences (Riyadh)* 2017;22:205–12 CrossRef Medline
  33. MacDonald ME, Dolati P, Mitha AP, et al. **Hemodynamic alterations measured with phase-contrast MRI in a giant cerebral aneurysm treated with a flow-diverting stent.** *Radiol Case Rep* 2015;10:1109 CrossRef Medline
  34. Frolov SV, Sindeev SV, Liepsch D, et al. **Experimental and CFD flow studies in an intracranial aneurysm model with Newtonian and non-Newtonian fluids.** *Technol Health Care* 2016;24:317–33 CrossRef Medline
  35. Bouillot P, Brina O, Yilmaz H, et al. **Virtual-versus-real implantation of flow diverters: clinical potential and influence of vascular geometry.** *AJNR Am J Neuroradiol* 2016;37:2079–86 CrossRef Medline
  36. Stankovic Z, Allen BD, Garcia J, et al. **4D flow imaging with MRI.** *Cardiovasc Diagn Ther* 2014;4:173–92 CrossRef Medline
  37. Chalouhi N, Tjoumakaris S, Phillips JL, et al. **A single Pipeline embolization device is sufficient for treatment of intracranial aneurysms.** *AJNR Am J Neuroradiol* 2014;35:1562–66 CrossRef Medline
  38. Markl M, Frydrychowicz A, Kozerke S, et al. **4D flow MRI.** *J Magn Reson Imaging* 2012;36:1015–36 CrossRef Medline
  39. Anderson JR, Klucznik R, Diaz O, et al. **Quantification of velocity reduction after flow diverter placement in intracranial aneurysm: an ex vivo study with 3D printed replicas.** *Conf Proc IEEE Eng Med Biol Soc* 2015;2015:7300–03 CrossRef Medline
  40. Gester K, Luchtefeld I, Busen M, et al. **In vitro evaluation of intra-aneurysmal, flow-diverter-induced thrombus formation: a feasibility study.** *AJNR Am J Neuroradiol* 2016;37:490–96 CrossRef Medline

# Optimizing the Quality of 4D-DSA Temporal Information

 K.L. Ruedinger,  E.C. Harvey,  S. Schafer,  M.A. Speidel, and  C.M. Strother

## ABSTRACT

**BACKGROUND AND PURPOSE:** Quantification of blood flow using a 4D-DSA would be useful in the diagnosis and treatment of cerebrovascular diseases. A protocol optimizing identification of density variations in the time-density curves of a 4D-DSA has not been defined. Our purpose was to determine the contrast injection protocol most likely to result in the optimal pulsatility signal strength.

**MATERIALS AND METHODS:** Two 3D-printed patient-specific models were used and connected to a pulsatile pump and flow system, which delivered 250–260 mL/min to the model. Contrast medium (Iovue, 370 mg I/mL, 75% dilution) was injected through a 6F catheter positioned upstream from the inlet of the model. 4D-DSA acquisitions were performed for the following injection rates: 1.5, 2.0, 2.5, 3.0 and 3.5 mL/s for 8 seconds. To determine pulsatility, we analyzed the time-density curve at the inlets using the oscillation amplitude and a previously described numeric metric, the sideband ratio. Vascular geometry from 4D-DSA reconstructions was compared with ground truth and micro-CT measurements of the model. Dimensionless numbers that characterize hemodynamics, Reynolds and Craya-Curtet, were calculated for each injection rate.

**RESULTS:** The strongest pulsatility signal occurred with the 2.5 mL/s injections. The largest oscillation amplitudes were found with 2.0- and 2.5-mL/s injections. Geometric accuracy was best preserved with injection rates of >1.5 mL/s.

**CONCLUSIONS:** An injection rate of 2.5 mL/s provided the strongest pulsatility signal in the 4D-DSA time-density curve. Geometric accuracy was best preserved with injection rates above 1.5 mL/s. These results may be useful in future in vivo studies of blood flow quantification.

**ABBREVIATIONS:** Ct = Craya-Curtet number; SBR = sideband ratio; TDC = time-density curve

Quantification of blood flow with invasive techniques using pressure and flow-sensing guidewires and catheters is routinely performed as a part of diagnostic and therapeutic procedures involving the heart and peripheral vasculature. Measurement of velocity and flow using MRA or Doppler techniques is also widely available. None of these methods have, however, shown satisfactory utility as a part of diagnostic or interventional procedures of the CNS vasculature. After the discovery of DSA by Mistretta et al in the 1970s, almost immediately, investigators began to use the density of a contrast bolus, as it passed between 2 points, to determine the velocity of blood flow.<sup>1</sup> In a comprehensive review, these techniques, along with

their potential benefits and limitations, were described by Shpilfoygel et al.<sup>2</sup> More recent reports have described using the combination of 2D- and 3D-DSA to quantify blood flow.<sup>3–6</sup>

In 2013, Davis et al<sup>7</sup> reported a technique for reconstructing time-resolved vascular volumes (4D-DSA) from conventional 3D-DSA acquisitions. 4D-DSA provides both the temporal and spatial information required to calculate velocity and flow.<sup>8–10</sup> The velocity and flow calculations depend on the following: 1) visualizing the cardiac-induced rhythmic changes in contrast bolus density occurring between systole and diastole, 2) quantifying the arrival time of the time-varying bolus between 2 points along a vessel, and 3) quantifying the vessel cross-sectional area. The method exploits a naturally occurring image signal in 4D-DSA acquired with arterial injection. During injection, a contrast bolus rapidly mixes with blood flowing downstream from the injection site. Rhythmic changes in the rate of nonopacified blood coflowing with the contrast medium result in a time-varying contrast density.

Studies documenting the feasibility of using the data from a 4D-DSA reconstruction to quantify velocity and flow were

Received July 20, 2019; accepted after revision September 3.

From the Department of Biomedical Engineering (K.L.R.), School of Medicine and Public Health (K.L.R.), Department of Medical Physics (E.C.H., M.A.S.), and Department of Radiology (C.M.S.), University of Wisconsin-Madison, Madison, Wisconsin; and Siemens Healthineers Forchheim Germany (S.S.), Hoffman Estates, Illinois.

Please address correspondence to Katrina L. Ruedinger, MS, c/o Charles Strother, Department of Radiology, University of Wisconsin-Madison, WIMR, 1111 Highland Ave, Madison WI 53705; e-mail: klruedinger@wisc.edu  
<http://dx.doi.org/10.3174/ajnr.A6290>

recently published by Shaughnessy et al.<sup>8</sup> and by Wu et al.<sup>9</sup> In both reports, calculation of velocity and flow was found to be dependent on accurate identification of a pulsatility signal in the time-density curves (TDCs) of a reconstruction; this requirement was noted to be a potential limitation of both methods used for quantification. The pulsatility signal is defined as the change in bolus density between systole and diastole as seen in a TDC for a given point in the volume as a function of time. The pulsatility signal strength (ie, amplitude) is largely dependent on the ratio between nonopacified blood and the blood-contrast mixture causing x-ray attenuation changes that are clearly apparent in the TDCs of a reconstruction.

By defining an injection protocol that optimizes this signal strength, our study aimed to increase the utility of the temporal information in a 4D-DSA reconstruction. The goal was to quantitatively evaluate a variety of injection protocols using patient-specific 3D-printed vascular models. From this, an optimal protocol, which provided reconstructions preserving the dimensional accuracy of the vasculature while also optimizing the pulsatility signal strength, was defined. The capacity to quantify blood flow in the angiography suite would enhance treatment planning, evaluation of treatment results, and diagnostic accuracy for a variety of cerebrovascular diseases such as occlusive diseases, AVMs, and aneurysms. Because most patients undergoing studies in the angiography suite will already have an arterial catheter in place, acquiring 4D-DSA data will not necessitate any increase in invasiveness of the angiographic evaluation.

## MATERIALS AND METHODS

### Vascular Models

Two patient-specific vascular models were created using angiographic data from an institutional review board (UW-Madison School of Medicine and Public Health)-approved data base. The models were 3D-printed out of a rigid photopolymer using a stereolithographic process (Form 2; Formlabs, Somerville, Massachusetts). Details of the 3D printing protocol were recently described by Ruedinger et al.<sup>10</sup> Both models included the ICA and M1 and A1 segments of the MCA and the anterior cerebral artery. The model had ICA inlets of sufficient length to allow full development of flow.<sup>11</sup>

### Flow System

The models were connected to a closed-loop flow system driven by a positive-displacement pulsatile pump (Bdc PD-1100; Bdc Laboratories, Wheat Ridge, Colorado) (Fig 1). Contrast medium was injected through a catheter (6F, Penumbra 5MAX ACE; Penumbra, Alameda, California), which was inserted through an introducer sheath positioned upstream from the ICA inlet. Contrast medium (iopamidol, Isovue 370 mg I/mL, 75% concentration; Bracco, Princeton, New Jersey) was injected with a dual-head power injector (Press Duo Kemoto Kyorindo co., Ltd Nemoto, Kyoto, Japan). A mixture of 40% glycerol and 60% de-ionized water was used as blood-mimicking fluid (density = 1111kg/m<sup>3</sup>, viscosity = 3.79 cP) to match physiologic parameters. To establish fluid flow rates that simulated physiologic flow hemodynamics, we set total flow to

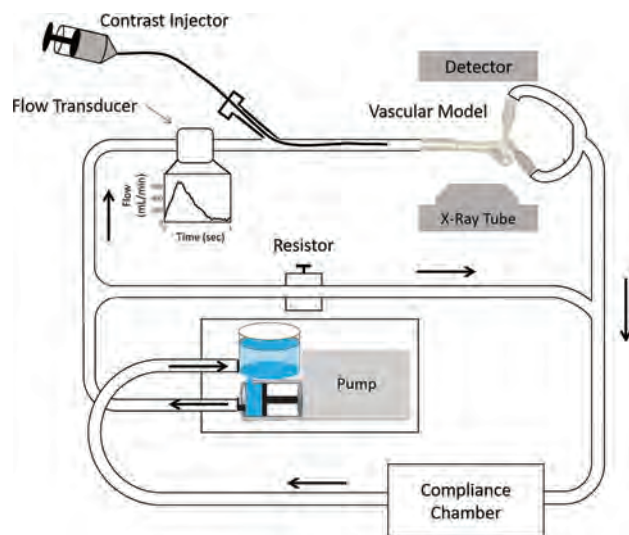


**FIG 1.** Closed-loop flow system. Setup includes a pulsatile pump, flow transducer, power injector, patient-specific vascular model, flow-diverting loop to simulate systemic vasculature, a compliance chamber, and location of the x-ray detector.

match a cardiac output averaging 5.5 L/min at a frequency of 60 beats per minute. Over each cardiac cycle, the flow varied between 0 and 7 L/min. A bypass loop was used to simulate the systemic circulation so that the average flow delivered to the model inlet (ICA) was between 250 and 260 mL/min. Flow rates were measured using an ultrasonic flow probe (16PXL-MS25; Transonic, Ithaca, New York).

### Data Acquisition

A commercially available C-arm angiographic system was used for x-ray imaging. (Artis zee; Siemens, Erlangen, Germany). Rotational angiographic data for each of the models were acquired using a vendor-approved protocol for 4D-DSA (70 kV, 0.36  $\mu$ Gy/frame, 260° rotation, 304 projections/rotation). Each 4D-DSA acquisition consisted of a noncontrast (“mask”) rotation followed by a contrast-enhanced (“fill”) rotation. Contrast medium was injected at rates of 1.5, 2.0, 2.5, 3.0, 3.5 mL/s for 8 seconds with no x-ray delay. Two datasets (trials) were acquired for each of the 2 models at each injection rate ( $n = 10$ ). The mask runs were assessed to ensure that the interval between injections was sufficient for the contrast not to accumulate in the fluid to a degree that would reduce the pulsatility signal strength in the fill rotation. The fluid was renewed if necessary.

### Image Postprocessing

Each dataset was reconstructed using a 4D-DSA prototype reconstruction, not commercially available, on a vendor-supplied research workstation (X-Workplace; Siemens). These reconstructions comprised temporal series of 512  $\times$  512  $\times$  384 voxel volumes with a homogeneous voxel size of 0.46 mm. The reconstructions contained temporal and spatial information as voxel-specific TDCs.

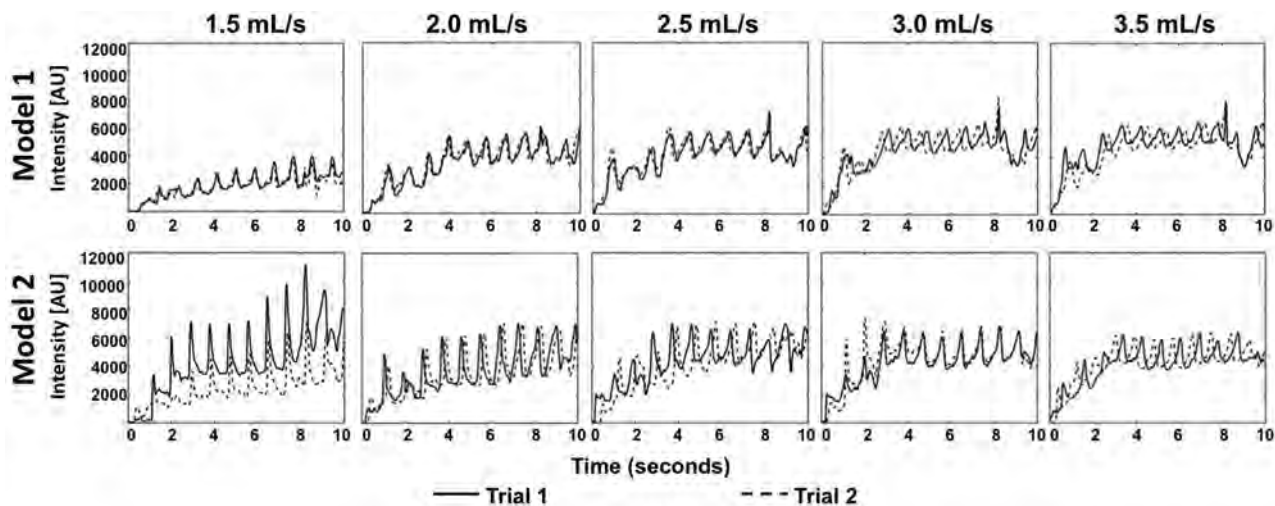


**FIG 2.** TDCs from both trials of the 5 different injection rates, 1.5, 2.0, 2.5, 3.0, 3.5 mL/s. TDCs show differences in contrast intensity from varying injection rates. Variation at the 1.5-mL/s injection rate in model 2 stems from contrast layering.

### Sideband Ratio and Amplitude Calculation

The inlet of each model was manually segmented from the rest of the model vasculature, resulting in approximately 20,000 voxels and their corresponding TDCs. A previously described numeric metric, the sideband ratio (SBR), was used to determine pulsatility signal strength from a TDC.<sup>8</sup> If a given TDC exhibits strong pulsatility signal strength, a large peak will be prominent in the Fourier transform; therefore, a large ratio between the peak and the nearby neighboring frequency signals (high SBR) will be present. The SBR values for the largest pulsatile signal within each TDC were used to analyze overall pulsatility signal strength within the inlet section. The median SBR value within the entire inlet section was then used as the final metric for determining pulsatility strength in the 4D-DSA reconstruction. Each of the 2 trials for both of the models was included in the SBR cohort, and the median was determined. The median estimator was chosen instead of the mean because it is less sensitive to outlier SBR values resulting from the noise and artifacts in the 4D-DSA image sets.

The amplitude of the pulsatility signals was quantified for each of the 4D-DSA reconstructions as a secondary metric. The analysis of pulsatility signal amplitude was made within voxels defined by 2 cubes ( $5 \times 5 \times 5$  voxels) placed at the proximal and distal extents of the inlet. Voxels that were positioned fully outside the vessel did not show a TDC and were not included in the analysis. The average of the median pulsatility signal was calculated for each of the 2 trials.

### Hemodynamic Analysis

A change in the injection rate of contrast results in changes in the hemodynamics of the contrast bolus. To characterize this feature, 2 dimensionless numbers (Reynolds [Re] and Craya-Curtet [Ct]) were calculated for each of the injection rates. The Reynolds number describes the ratio of inertial-to-viscous forces within the fluid. It was calculated for both the blood-mimicking fluid (base fluid) and the contrast medium using Equation 1, where  $\rho$  = density,  $v$  = velocity,  $D$  = diameter,  $\mu$  is the viscosity of the base fluid ( $f$ ) or contrast ( $c$ ).

1)

$$Re = \frac{\rho v D}{\mu}$$

The Ct number describes the ratio of momentums of the base fluid to the contrast. This number is an indicator of the type of flow patterns that will occur during an injection.<sup>11</sup> In turn, this determines how well mixing of contrast with the base fluid will occur.<sup>11</sup>

2)

$$Ct = \left(\frac{\rho_f}{\rho_c}\right)^{\frac{1}{2}} \left(\frac{Q_f}{Q_c}\right) \left[\frac{ID_c}{(ID_a^2 - OD_a^2)^{\frac{1}{2}}}\right]$$

$\rho_b$  and  $Q_b$  and  $\rho_c$  and  $Q_c$  are the densities and mean flow rates of blood and contrast, respectively,  $ID_c$  and  $OD_c$  represent the inner and outer diameters of the catheter, and  $ID_a$  is the lumen diameter of the artery.

### Geometry Comparison

Ground truth geometries of both vascular models were determined using results from previously acquired micro-CT scans.<sup>10</sup> Measurement of the inlet diameters of each model was performed using a geometry-analysis tool available on a vendor-provided workstation (syngo Neuro Aneurysm Analysis; Siemens). The inlet of each model was measured 3 times, resulting in a total of 12 (2 models  $\times$  2 trials  $\times$  3 measurements) measurements for each injection rate. The mean absolute difference between the measured inlet diameter and the ground truth diameter (model 1 = 4.60 mm, model 2 = 4.96 mm) and the SD was calculated for each dataset.

## RESULTS

### 4D-DSA Reconstructions

Except for 1 acquisition, at an injection rate of 1.5 mL/s in model 2, the TDCs showed an appropriate increase in density immediately after contrast injection with clearly defined oscillations in bolus density between systole and diastole. The outlier was due to contrast layering with slow washout with time, which created a higher-than-expected overall intensity (Fig 2, model 2).

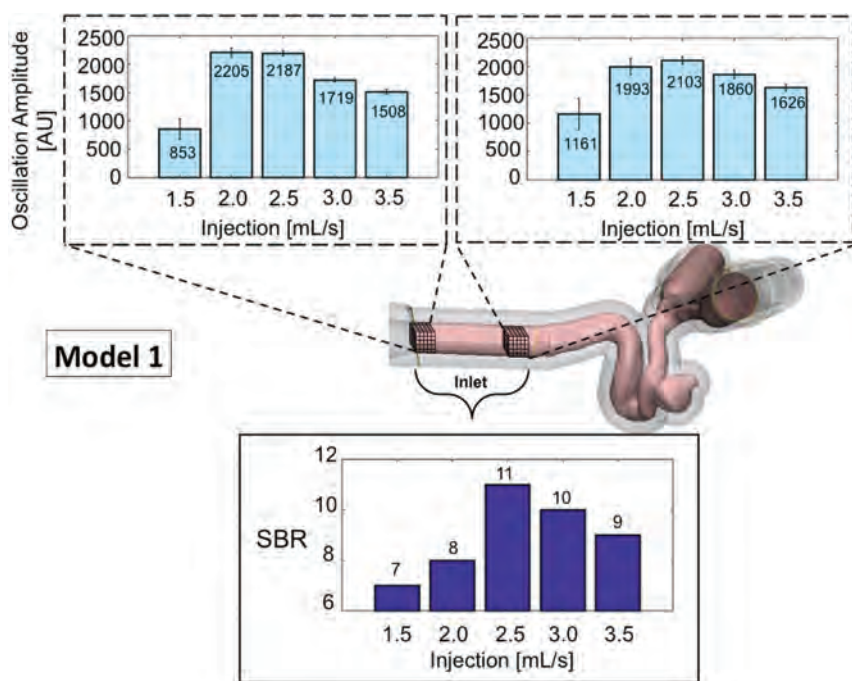


**FIG 3.** SBR and amplitude of oscillation within the TDC for model 1. The median SBR at different injection rates is presented for the entire inlet section for the combination of trials (*lower bar graph*). A higher SBR corresponds to stronger contrast pulsatility, with an injection rate of 2.5 mL/s producing the highest SBR. The median oscillation amplitude between systole and diastole was highest in the acquisitions with 2.0- and 2.5-mL/s injection rates (Fig 3). Details of the median SBR and oscillation amplitudes for trials 1 and 2 in this model are shown in Fig 3. AU indicates Arbitrary Units, and the error bars show SBR variance from the voxels within the 2 cubes.

### SBR and Amplitude

In model 1, the median SBR at the inlet was highest (11) with the 2.5 mL/s injection (Fig 3). The median oscillation amplitude between systole and diastole was highest in the acquisitions with 2.0- and 2.5-mL/s injection rates (Fig 3). Details of the median SBR and oscillation amplitudes for trials 1 and 2 in this model are shown in Fig 3.

In model 2, excluding the acquisition at 1.5 mL/s in which contrast layering and stasis were observed, the 2.5-mL/s injection rate also provided the highest SBR (18) and the second highest amplitude in the proximal section and the highest in the distal section of the inlet. Details of the median SBR and oscillation amplitudes for both trials in model 2 are shown in Fig 4.

### Geometric Analysis

The largest absolute differences in inlet diameter measurements from the 4D-DSA reconstructions to the ground truth micro-CT measurements were  $0.66 \pm 0.08$  mm in model 1 and  $1.0 \pm 0.3$  mm in model 2 at the lowest injection rate, 1.5 mL/s (Fig 5). The 1.5-mL/s injection rate also had the largest SD in inlet measurements from the 4D-DSA reconstruction in both model 1 (0.08 mm) and model 2 (0.3 mm). Figure 5 also illustrates a smaller difference in geometry with injection rates at 2.0 mL/s and above.

### Hemodynamic Analysis

Achieving a ratio between the contrast blood mixture and the nonopacified blood comprising an injection bolus is dependent

on the type of mixing flows created at the injection site. Because the inner diameter of an injection catheter is typically much smaller than that of the artery into which contrast is injected, the velocity of the contrast medium is considerably higher than that of blood flow. The dimensionless Ct number is an indicator of the characteristics of these flows and thus of the degree to which mixing occurs during an injection. In a previous study, optimal mixing, as desired for temporal signal encoding through contrast-density changes, was seen when the Ct number was in the range of 0.4–0.9.<sup>11</sup> The Table illustrates hemodynamic parameters of both the base and contrast flow and velocity, as well as the governing dimensionless numbers of Reynolds and Ct or model 1 (upper half) and model 2 (lower half). Changes in hemodynamic parameters were consistent with those expected (Table).

### DISCUSSION

Using 2 patient-specific 3D printed vascular models and a closed-loop pulsatile flow system, we demonstrated that the pulsatility signal strength in TDCs from a 4D-DSA reconstruction is sensitive to

small changes in the rate of contrast medium injection. An injection protocol was found that optimized the quality of the temporal data while also maintaining the fidelity of the spatial data. These results could be helpful in clinical studies aimed at assessing the utility of 4D-DSA for measuring blood flow.

Since Tenjin's original description of using TDC analysis for the evaluation of blood velocity, additional studies using variations on his method have been reported for the analysis of flow under a variety of conditions.<sup>12–15</sup> The feasibility of measuring some parameters of flow (eg, time to peak, inflow, outflow) was shown in studies of aneurysms and AVMs both before and after treatment.<sup>13–15</sup> In 2 of these, contrast was manually injected intra-arterially, and analysis was based on placement of an ROI on projections of the vasculature chosen to eliminate or minimize vessel overlap. The use of manual injection of contrast and the lack of information regarding the length of time for the DSA acquisitions reduce the utility of the temporal data acquired from these studies.

Another study reported the use of parametric processing of 2D-DSA to provide color-coded images of hemispheric blood flow in 18 patients with chronic ischemic disease. Contrast medium was injected into the aortic arch using a power injector. All patients also had conventional PET perfusion imaging; the mean interval between the x-ray and PET studies was  $2.05 \pm 1.75$  days. Strong correlation was found between relative perfusion parameters measured with PET and flow parameters determined from

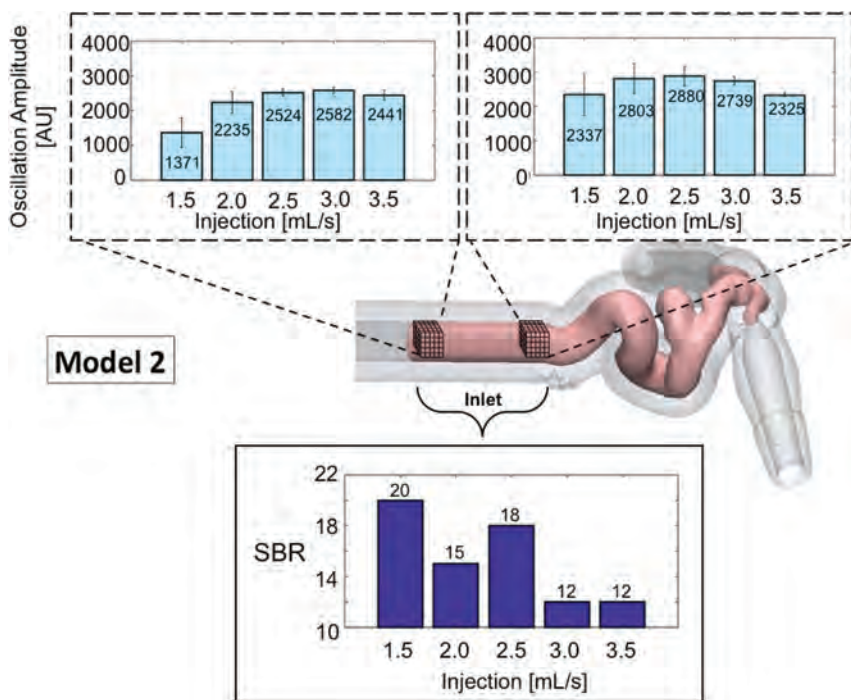


**FIG 4.** SBR and amplitude of oscillation within the TDC for model 2. The median SBR at different injection rates is presented for the entire inlet section for the combination of trials (*lower bar graph*). A high SBR represents strong contrast pulsatility; 1.5 mL/s is abnormally high due to contrast layering causing an erroneous signal in the 4D-DSA reconstruction. The amplitude of oscillation is studied in 2 cubes that transect the vessel diameter at 2 locations within the inlet of model 2. The median of the oscillation amplitude and median absolute derivation within each cube of voxels are presented for each trial (*upper bar graphs*). AU indicates Arbitrary Units, and the error bars show SBR variance from the voxels within the 2 cubes.

the 2D x-ray angiographic perfusion technique. The combination of a lack of any details of the software and the inability to measure anything more than global blood flow (ie, hemispheric with a 2D technique and the long interval between the x-ray and PET studies) makes it difficult to assess the validity of the reported results. Lin et al<sup>14</sup> evaluated the ability to measure flow velocity in the angiographic suite using data from 4D-DSAs in a study consisting of healthy control, ruptured AVM, and unruptured AVM groups. In measurements made from ROIs placed on the ICA and MCA, they reported that the amplitude of pulsatile waveforms in patients with AVMs was greater than that of the controls, with pulsatile waveforms not seen in some 20% of the control group as well as in the ruptured AVM group. Lin et al commented on the need for a better understanding of how the injection protocol may impact pulsatility waveforms; therefore, it directly relates to our study.

Blood flow, bolus volume, injection rate, downstream resistance, and artery size all influence the amplitudes of TDCs. These are intrinsically less in small vessels compared with larger ones. Downstream amplitudes are similar to ones measured upstream when resistance downstream is lower (eg, in the nidus of an AVM as in healthy controls).<sup>15</sup> Image quality (SNR) is less when nonopacified blood enters the vessel of interest downstream from the injection site or when the contrast injection does not result in either adequate mixing of contrast with blood or causes mixing to a degree in which variations in bolus density between systole and diastole are much reduced (ie, the bolus becomes homogeneous). Of these variables, the only one controllable in clinical studies is the injection protocol.

Our study defined 1 way for evaluating how variations in injection rates may influence the amplitudes of the pulsatility waveforms. The ability to achieve optimal pulsatility strength would increase the accuracy and utility of velocity and flow measurements using a 4D-DSA reconstruction. Having this ability in the angiography suite could result in increased ability to identify

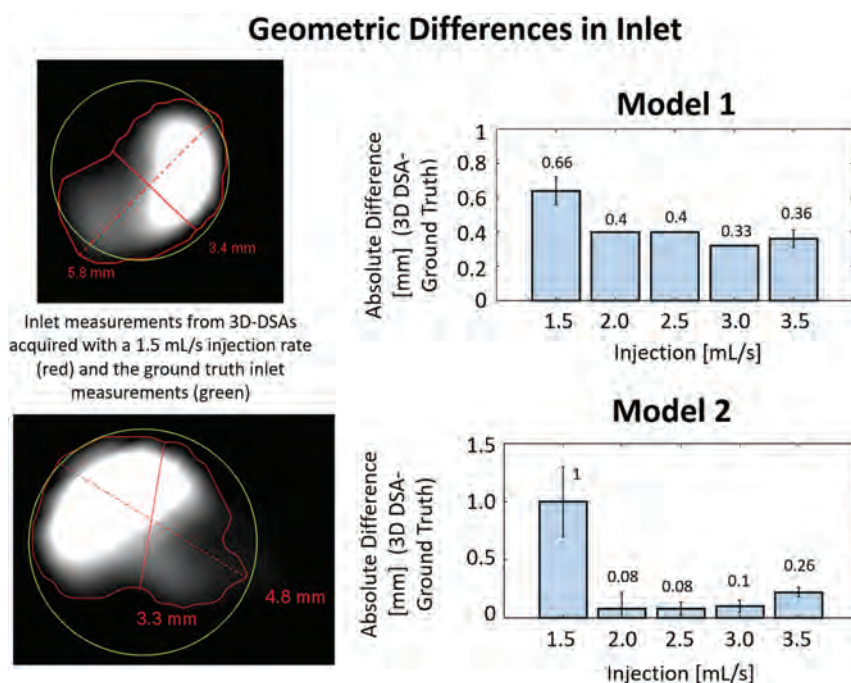


**FIG 5.** *Left*, effect of contrast layering on volumetric reconstruction. The absolute difference (millimeters) between the inlet diameter measurement using the workstation tool and the ground truth inlet diameter from micro-CT measurements is shown in the bar graphs (*right*). The greatest geometric difference in both models occurs with the 1.5-mL/s injection rate. Error bars represent variance in absolute differences based on multiple measurements.

### Hemodynamic parameters characterizing flow profiles achieved from various injection rates within the closed-loop flow setup<sup>a</sup>

Injection Rate	Q <sub>f</sub> (mL/min)	V <sub>f</sub> (cm/s)	V <sub>c</sub> (cm/s)	Re <sub>f</sub>	Re <sub>c</sub>	Ct
1.5	252	22.27	120.30	328.72	101.6	0.69
2			160.40		135.5	0.52
2.5			200.50		169.3	0.41
3			240.60		203.2	0.35
3.5			280.70		237.0	0.30
1.5	260	22.43	120.30	335.05	101.6	0.70
2			160.40		135.5	0.52
2.5			200.50		169.3	0.42
3			240.60		203.2	0.35
3.5			280.70		237.0	0.30

**Note:**—Significant figures varied depending on the hemodynamic parameter. Q<sub>f</sub> indicates flow rate of working fluid; V<sub>f</sub>, velocity of working fluid; V<sub>c</sub>, velocity contrast; Re<sub>f</sub> = Reynolds number of working fluid; Re<sub>c</sub>, Reynolds number of contrast.

<sup>a</sup> Upper half refers to model 1, and bottom half refers to model 2.

those arteries that have increased or decreased velocity and flow (eg, AVMs and steno-occlusive disease), compared with those with normal velocity and flow. This, in turn, could allow a more accurate selection of target arteries for embolization in AVMs and for stent placement or thrombectomy. The ability to compare velocity and flow before and after an intervention would also likely add value to assessing the effectiveness of said intervention.

Limitations of our study include the inability to transfer the results to acquisitions with catheters and vessels of different sizes. Just as the Reynolds and Ct numbers changed dramatically with small (ie, 0.5 mL/s) changes in the injection rate, these parameters may also change considerably with small changes in the internal diameter of the injection catheter and vessel size. Our results also directly apply only to situations when blood flow is in the range of that used for our experiments. These limitations may be reduced by studies of amplitude changes performed with other commonly used catheters and a range of physiologically realistic flow rates.

### CONCLUSIONS

The availability of blood flow quantification in the angiography suite would add to the ability to understand the significance of flow abnormalities that are either too slow or too fast. It would also improve the ability to measure the degree to which interventions to augment or reduce flow are effective. The reliability of blood flow quantification using the temporal information from a 4D-DSA reconstruction depends on the ability to consistently and accurately detect the cardiac-induced pulsatility in the time-density curves. The greatest pulsatility signal strength while maintaining geometric accuracy in the 4D-DSA reconstruction was provided with the contrast injection rate of 2.5 mL/s. The definition of an optimal contrast injection protocol for 1 catheter size and flow rate is 1 step in creating a tool that would provide guidance regarding a patient-specific injection protocol.

Disclosures: Sebastian Schafer—UNRELATED; Other: Siemens Healthineers Forchheim Germany, Comments: employee. Michael A. Speidel—UNRELATED; Grant: Siemens Healthineers Forchheim Germany, Comments: Partial financial support was received through a research contract between Siemens Healthineers Forchheim Germany and the University of Wisconsin-Madison\*. \*Money paid to the institution.

### REFERENCES

1. Kruger RA, Mistretta CA, Houck TL, et al. **Computerized fluoroscopy in real time for noninvasive visualization of the cardiovas-**

**cular system.** Preliminary studies. *Radiology* 1979;130:49–57 CrossRef Medline

2. Shpilfoylgel SD, Close RA, Valentino DJ, et al. **A critical review of literature.** *Med Phys* 2000;27:2008–23 CrossRef Medline
3. Pereira VM, Ouared R, Brina O, et al. **Quantification of internal carotid artery flow with digital subtraction angiography: validation of an optical flow approach with Doppler ultrasound.** *AJNR Am J Neuroradiol* 2014;35:156–63 CrossRef Medline
4. Copeland AD, Mangoubi RS, Desai MN, et al. **Spatio-temporal data fusion for 3D+T image reconstruction in cerebral angiography.** *IEEE Trans Med Imaging* 2010;29:1238–51 CrossRef Medline
5. Schmitt H, Grass M, Suurmond R, et al. **Reconstruction of blood propagation in three-dimensional rotational X-ray angiography (3D-RA).** *Comput Med Imaging Graph* 2005;29:507–20 CrossRef Medline
6. Wiesent K, Barth K, Navab N, et al. **Enhanced 3-D reconstruction algorithm for C-arm systems suitable for interventional procedures.** *IEEE Trans Med Imaging* 2000;19:391–403 CrossRef Medline
7. Davis B, Royalty K, Kowarschik M, et al. **4D digital subtraction angiography: implementation and demonstration of feasibility.** *AJNR Am J Neuroradiol* 2013;34:1914–21 CrossRef Medline
8. Shaughnessy G, Schafer S, Speidel MA, et al. **Measuring blood velocity using 4D-DSA: a feasibility study.** *Med Phys* 2018;45:4510–18 CrossRef Medline
9. Wu XY, Shaughnessy XG, Hoffman CA, et al. **Quantification of blood velocity with 4D digital subtraction angiography using the shifted least-squares method.** *AJNR Am J Neuroradiol* 2018;39:1871–77 CrossRef Medline
10. Ruedinger KL, Rutkowski DR, Schafer S, et al. **Impact of image reconstruction parameters when using 3D DSA reconstructions to measure intracranial aneurysms.** *J Neurointerv Surg* 2018;10:285–89 CrossRef Medline
11. Lieber BB, Sadasivan C, Hao Q, et al. **The mixability of angiographic contrast with arterial blood.** *Med Phys* 2009;36:5064–78 CrossRef Medline
12. Tenjin H, Asakura F, Nakahara Y, et al. **Evaluation of intraaneurysmal blood velocity by time-density curve analysis and digital subtraction angiography.** *AJNR Am J Neuroradiol* 1998;19:1303–07 Medline
13. Göltz P, Struffert T, Hoelter P, et al. **Flow-diverting stents allow efficient treatment of unruptured, intradural dissecting aneurysms of the vertebral artery: an explanatory approach using in vivo flow analysis.** *Interv Neuroradiol* 2016;22:76–83 CrossRef Medline
14. Lin CJ, Yang HC, Chien AC, et al. **In-room assessment of intravascular velocity from time-resolved rotational angiography in patients with arteriovenous malformation: a pilot study.** *J Neurointerv Surg* 2018;10:583–88 CrossRef Medline
15. Asai K, Nakamura H, Watabe T, et al. **X-ray angiography perfusion imaging with an intra-arterial injection: comparative study with 15 O-gas/water positron emission tomography.** *J Neurointerv Surg* 2018;10:780–83 CrossRef Medline

# The Influence of Angioarchitectural Features on the Success of Endovascular Embolization of Cranial Dural Arteriovenous Fistulas with Onyx

D.F. Vollherbst, C. Herweh, S. Schönenberger, F. Seker, S. Nagel, P.A. Ringleb, M. Bendszus, and M.A. Möhlenbruch

## ABSTRACT

**BACKGROUND AND PURPOSE:** Endovascular embolization can be an effective treatment for cranial dural arteriovenous fistulas. However, a considerable number of dural arteriovenous fistulas still cannot be treated sufficiently. The purpose of this study was to report our single-center experience of endovascular embolization of dural arteriovenous fistulas with Onyx, including the investigation of the influence of angioarchitectural features on the treatment success.

**MATERIALS AND METHODS:** Clinical data, angioarchitectural features, complications, treatment success (defined as complete symptom remission for low-grade dural arteriovenous fistulas and complete occlusion for high-grade dural arteriovenous fistulas), and occlusion rates were assessed. The influence of various angioarchitectural features (including location, pattern of venous drainage, and quantity and origin of feeding arteries) was investigated using multivariable backward logistic regression.

**RESULTS:** One hundred four patients with 110 dural arteriovenous fistulas were treated in 132 treatment procedures. Treatment success and complete occlusion rates were 81.8% and 90.9%, respectively. After a mean follow-up of 23.6 months, 95.5% of the patients showed complete symptom remission or symptom relief. The overall complication rate was 8.3% (4.5% asymptomatic, 2.3% transient, and 1.5% permanent complications). Logistic regression showed that  $\geq 10$  feeding arteries ( $P = .041$ ) and involvement of the ascending pharyngeal artery ( $P = .039$ ) significantly lowered the probability of treatment success. Treatment success tended to be lower for low-grade dural arteriovenous fistulas, Cognard type I dural arteriovenous fistulas, and dural arteriovenous fistulas with involvement of dural branches of the internal carotid artery, however without reaching statistical significance in the multivariable model.

**CONCLUSIONS:** The presence of multiple feeding arteries and involvement of the pharyngeal artery negatively influence the treatment success of endovascular embolization of cranial dural arteriovenous fistulas with Onyx.

**ABBREVIATION:** DAVF = dural arteriovenous fistula

Cranial dural arteriovenous fistulas (DAVFs) are pathologic arteriovenous connections between the dural arteries and dural sinuses or cortical veins. According to the risk of hemorrhage, DAVFs can be divided into low-grade DAVFs without an increased risk of hemorrhage and high-grade DAVFs, which are accompanied by an annual risk of hemorrhage of up to 20%.<sup>1</sup> The most important risk factors for hemorrhage are cortical venous reflux and ectasia of these cortical veins.<sup>2,3</sup> Therapy is indicated for low-grade DAVFs in cases of intolerable symptoms, mostly pulsatile tinnitus. For high-grade

DAVFs, therapy is always indicated because of the increased risk of hemorrhage.

Endovascular treatment has become the first-line treatment for most DAVFs.<sup>4,5</sup> One of the most frequently used techniques is endovascular embolization using liquid embolic agents; Onyx (Medtronic Neurovascular, Irvine, California), a liquid, precipitating, and nonadhesive material, is one of the most commonly used agents. Even though, currently, most patients can be treated successfully by endovascular embolization, a considerable number of DAVFs cannot be treated sufficiently in terms of complete symptom remission for low-grade DAVFs or complete occlusion for high-grade DAVFs.<sup>1,6-8</sup>

The aim of this study was to report our consecutive single-center experiences in patients with DAVFs who were treated with endovascular liquid embolization using Onyx, including the assessment of the rates of occlusion, treatment success, and

Received July 24, 2019; accepted after revision September 26.

From the Departments of Neuroradiology (D.F.V., C.H., F.S., M.B., M.A.M.) and Neurology (S.S., S.N., P.A.R.), Heidelberg University Hospital, Heidelberg, Germany.

Please address correspondence to Markus A. Möhlenbruch, MD, Department of Neuroradiology, Heidelberg University Hospital, INF 400, 69120 Heidelberg, Germany; e-mail: markus.moehlenbruch@med.uni-heidelberg.de

<http://dx.doi.org/10.3174/ajnr.A6326>

complications, and to investigate the influence of angioarchitectural features on the treatment success.

## MATERIALS AND METHODS

### Clinical and Angiographic Analysis

Approval and informed consent for data collection for this case series were provided by the local ethics committee and by the patients, respectively (registry number: S-247/2009). A retrospective analysis of a prospectively maintained patient data base was performed to identify all subsequent patients with a diagnosis of intracranial DAVFs who were treated at our institution with endovascular embolization using Onyx from October 2008 to June 2019.

Patient demographics, clinical presentation, and clinical follow-up were assessed and recorded. The preinterventional mRS score on the day of the intervention and the postinterventional mRS score at discharge and after 6 months were assessed by a board-certified neurologist. The following angioarchitectural features of the treated DAVFs were extracted by 2 experienced neuroradiologists (D.F.V. and M.A.M. with 6 and 13 years of experience, respectively): location, type (according to the Cognard and Borden classifications<sup>2,3</sup>), pattern of venous drainage, number and origin of feeding arteries, and the presence of bilateral feeders and pial artery supply. The documented procedural parameters included the selected feeder for embolization, the number of embolization positions, and the embolization technique. Intra- and postprocedural complications were assessed and graded as asymptomatic, transient, or permanent complications. The initial complete angiographic occlusion was assessed after the last treatment procedure. Overall complete angiographic occlusion was defined as complete occlusion at the last follow-up examination, diagnosed with DSA, which was performed 6 months after the last treatment, and/or MR imaging, which was performed before discharge and during the follow-up period. Treatment success was defined differently for low-grade DAVFs (no cortical venous reflux/Cognard I-IIa) and high-grade DAVFs (presence of cortical venous reflux/Cognard IIa+b to IV). For low-grade DAVFs, treatment success was defined as complete symptom remission; for high-grade DAVFs, treatment success was defined as complete occlusion.

### Interventional Procedure

All interventions were performed with the patient under general anesthesia on a biplane angiography suite (Artis Q or Artis zee; Siemens, Erlangen, Germany). Preinterventional bilateral diagnostic angiographies of the internal and external carotid arteries and of the vertebral arteries were performed. Afterward, endovascular embolization was performed with a dimethyl-sulfoxide-compatible microcatheter (Marathon or Apollo, Medtronic Neurovascular; or Sonic, Balt, Montmorency, France) using Onyx 18, 20, or 34 under the roadmap technique. In selected cases, mostly in patients with DAVFs of the transverse and sigmoid sinus, transarterial liquid embolization in combination with transvenous balloon-assisted protection of the venous sinus was performed using a compliant, dimethyl-sulfoxide-compatible venous remodeling balloon (Copernic RC, 8 × 80 or 10 × 80 mm; Balt) as previously described by Vollherbst et al.<sup>9</sup> In cases in

which the microcatheter could not be navigated close enough to the fistula point or in DAVFs with large fistula networks, a dual-lumen balloon catheter (Scepter XC; MicroVention, Aliso Viejo, California) was used to prevent reflux and to enhance penetration of Onyx into the DAVF. After we terminated the embolization procedure, diagnostic angiographies were performed via the feeder territories for treatment control.

### Influence of Angioarchitectural Features on the Treatment Success

We assessed the influence of the following angioarchitectural factors on the treatment success: location, DAVF type according to the Cognard and Borden classifications,<sup>2,3</sup> type of venous drainage (into the dural venous sinuses or directly into the cortical veins), the presence of cortical venous reflux (low-grade versus high-grade DAVFs), the number of feeding arteries (DAVFs with <10 feeding arteries versus DAVFs with ≥10 feeding arteries, defined as arteries with a length of ≥10 mm, measured from the fistula point), the presence of bilateral feeders, the presence of pial artery supply, and involvement of the following feeder territories: middle meningeal artery, occipital artery, internal carotid artery (dural branches), vertebral artery (dural branches), superficial temporal artery, and ascending pharyngeal artery.

### Statistics

SPSS Statistics, Version 25.0 (IBM, Armonk, New York) was used for data analysis. Quantitative data are presented as number (relative frequency) or mean ± SD. To investigate the influence of angioarchitectural features on the treatment success, we analyzed all selected variables using univariate logistic regression models, with “treatment success” as the outcome variable. Afterward, only the significant variables ( $P < .05$ ) of this analysis were used in an interim multivariable logistic regression model. This model was adjusted with a variable selection based on the  $P$  value with a backward stepwise approach based on the Wald test, resulting in the final multivariable logistic regression model.  $P$  values of .05 were defined as the threshold for statistical significance and were not adjusted for multiple testing because this was a hypothesis-generating study. Hence, the  $P$  values should be interpreted descriptively. For odds ratios, 95% confidence intervals were calculated.

## RESULTS

### Patient Characteristics

A total of 190 patients diagnosed with intracranial DAVFs were treated with endovascular therapies between October 2008 and June 2019. Of this population, 104 patients with 110 DAVFs who were treated with endovascular embolization using Onyx in 132 treatment procedures were included in this study. Eighty-six patients were not included for the following reasons: treatment with coiling only ( $n = 48$ , mainly carotid cavernous fistulas), embolization with other liquid embolic agents ( $n = 24$ ), particle embolization ( $n = 7$ ), and outstanding treatments ( $n = 7$ ). Of the study population, 89 (80.9%), 17 (15.5%), and 3 (2.7%) patients were treated in 1, 2, and 3 treatment procedures, respectively. The mean age was  $57.4 \pm 13.0$  years, and the male/female ratio was 2:5. Most patients (93.3%) were symptomatic: Thirty-eight

(36.5%) had headache, 34 (32.7%) had tinnitus, and 13 (12.5%) had ocular symptoms. Twenty-eight patients (26.9%) presented with intracerebral hemorrhage, and 21 patients (20.2%), with cerebral venous congestion.

### Angioarchitectural Features of the Treated DAVFs

Angioarchitectural features of the treated DAVFs are summarized in Table 1. Most of the DAVFs were located at the transverse

**Table 1: Angioarchitectural features**

Feature	No. (relative frequency)
<b>Location</b>	
Transverse and/or sigmoid sinus	46 (41.8%)
Tentorial/petrosal	25 (22.7%)
Superior sagittal sinus	20 (18.2%)
Torcular	7 (6.4%)
Anterior cranial fossa	6 (5.5%)
Sphenoparietal sinus	4 (3.6%)
Others	2 (1.8%)
<b>Cognard and Borden type</b>	
Cognard I	12 (10.9%)
Cognard IIa	7 (6.4%)
Cognard IIb	2 (1.8%)
Cognard IIa+b	10 (9.1%)
Cognard III	28 (25.5%)
Cognard IV	51 (46.4%)
Borden I	19 (17.3%)
Borden II	11 (10.9%)
Borden III	79 (71.8%)
<b>Feeder territories</b>	
Middle meningeal artery	96 (87.3%)
Occipital artery	83 (75.5%)
Internal carotid artery (dural branches)	41 (37.3%)
Vertebral artery (dural branches)	41 (37.3%)
Superficial temporal artery	32 (29.1%)
Ascending pharyngeal artery	27 (24.5%)
<b>Other features</b>	
DAVFs with <10 arterial feeders	56 (50.9%)
DAVFs with ≥10 arterial feeders	54 (49.1%)
Bilateral feeders	56 (50.9%)
Pial artery supply	41 (37.3%)

and/or sigmoid sinus (41.8%), followed by a tentorial/petrosal location (22.7%), and the superior sagittal sinus (18.2%). Most DAVFs were high-grade fistulas (Cognard III–IV/Borden III, 71.9%). The ascending pharyngeal artery was involved in 27 (24.5%) DAVFs. DAVFs with ascending pharyngeal artery supply were located at the transverse and/or sigmoid sinus (59.3% of the DAVFs with involvement of the ascending pharyngeal artery), at the tentorium (33.3%), and at the marginal sinus (7.4%). The number of arterial feeders was <10 in 50.9% and ≥10 in 49.1% of the cases. Bilateral feeders were present in 50.9%, and pial artery supply, in 37.3% of DAVFs. The predominant feeder territories were the middle meningeal artery (87.3%) and the occipital artery (75.5%).

### Treatment Characteristics

Two sample cases are presented in Figs 1 and 2. Procedural parameters, complications, follow-up and outcome are summarized in Table 2. Most DAVFs were embolized via the middle meningeal artery (65.2%) or the occipital artery (23.5%). The most frequent embolization technique was conventional transarterial embolization (57.6%), followed by transarterial embolization combined with venous balloon protection (21.2%) and transarterial embolization with a dual-lumen balloon catheter (14.4%).

### Complications

The overall complication rate was 8.3%, of which 6 (4.5%) were asymptomatic, 3 (2.3%) were transient, and 2 (1.5%) were permanent. The asymptomatic and transient complications included small intracranial hemorrhages, most likely caused by vessel perforation, material-related complications such as catheter occlusion, rupture, or retention, as well as small venous infarctions. Both of the permanent complications were fatal large intracerebral hemorrhages of Cognard type IV/Borden type III DAVFs. The first patient initially presented with severe sinus thrombosis, venous congestion, and obstructive hydrocephalus. In this patient, only subtotal embolization of the DAVF could be

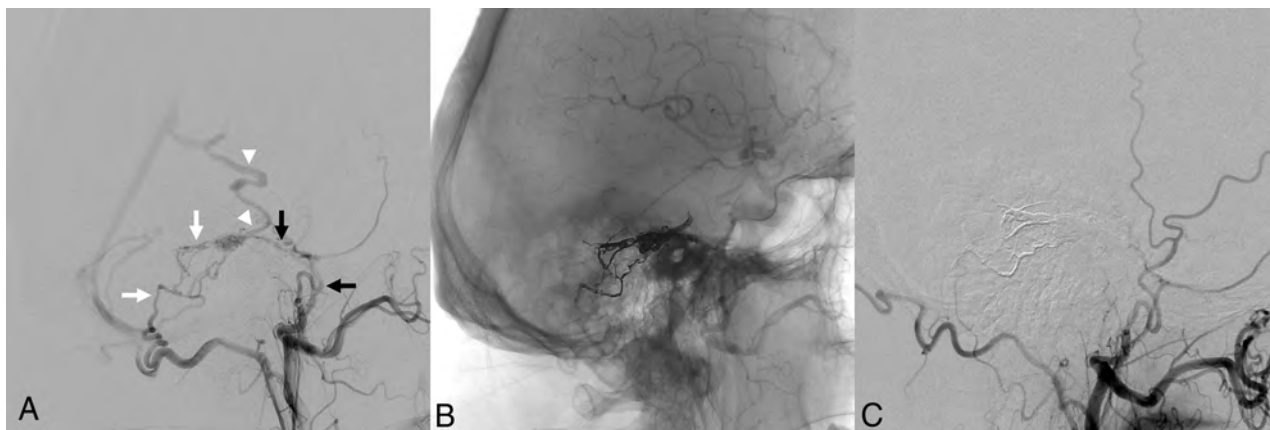


**FIG 1.** Sample case of a DAVF without angioarchitectural features with a negative influence on the treatment success. A DAVF with direct cortical venous drainage (Cognard type III), located at the tentorium in a 65-year-old man with headaches (A). Involved feeding arteries are the middle meningeal artery (black arrows in A) and the occipital artery (white arrows in A), which shunt directly into a cortical vein (white arrowheads). There were <10 feeding arteries, and the ascending pharyngeal artery was not involved. The DAVF could be occluded completely by transarterial embolization with Onyx (B). DSA 6 months after embolization shows stable occlusion of the DAVF (C).

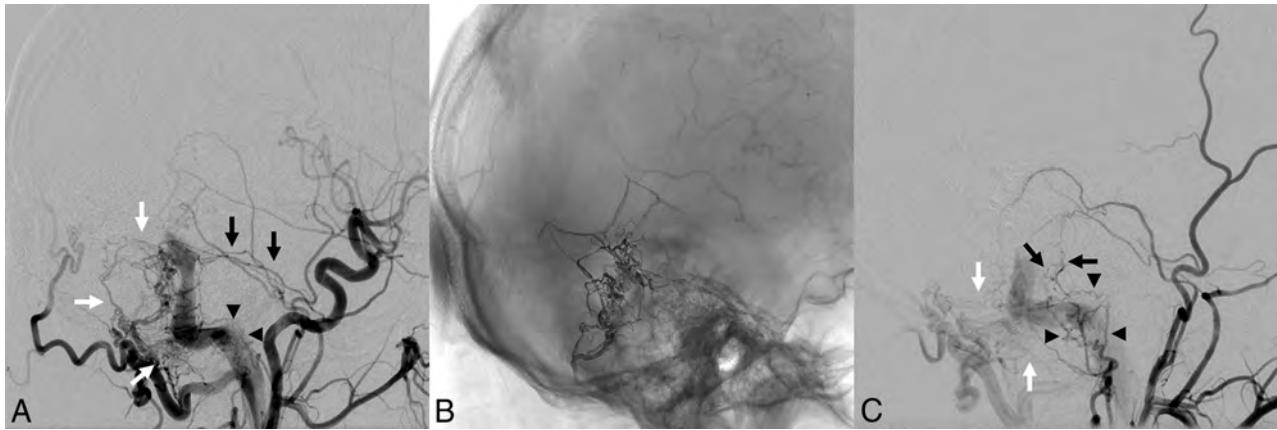


**FIG 2.** Sample case of a DAVF presenting with angioarchitectural features with a negative influence on the treatment success. A DAVF is located at the transverse and sigmoid sinus with antegrade flow in the sinus (Cognard type I) in a 46-year-old man who presented with severe pulsatile tinnitus (A). Multiple feeders supply the DAVF, including the middle meningeal artery (black arrows in A), the occipital artery (white arrows in A), and the ascending pharyngeal artery (black arrowheads in A). The DAVF was treated by transarterial Onyx embolization in combination with transvenous balloon-assisted protection of the venous sinus (B). The DAVF could not be occluded completely, due to small branches of the middle meningeal artery (black arrows in C) and of the occipital artery (white arrows in C), and particularly because of multiple persistent feeders from the ascending pharyngeal artery (black arrowheads in C), which could not be catheterized distal enough because of their small size and their tortuosity. The patient's symptoms were declining but still persistent at the latest follow-up.

achieved due to the small caliber and the tortuosity of the feeding arteries. Immediately after extubation, the patient developed a large intracerebral hemorrhage, most likely caused by venous congestion. In the second patient, complete angiographic occlusion was achieved in 2 treatment procedures. This patient was asymptomatic after extubation until he experienced increasing headache 3 hours after the second treatment procedure. The subsequent CT scan showed a large intracerebral hemorrhage causing the patient's death on the day of the second treatment procedure. For this patient, no specific cause of the intracerebral hemorrhage could be found.

#### **Occlusion, Success, and Recurrence Rates**

The initial complete angiographic occlusion rate was 78.2%. There was spontaneous occlusion after subtotal initial occlusion in 14 patients (12.7%) after a mean time of 6.6 months, resulting in a complete angiographic occlusion rate of 90.9%. After a mean follow-up of 23.6 months, 66.4% of patients were free of symptoms, 29.1% showed symptom relief, 2.7% showed stable symptoms, and 1.8% showed worsening of symptoms after treatment. Treatment success was achieved in 90 patients (81.8%). Recurrence after complete angiographic occlusion (diagnosed with DSA) was observed in 4 cases (3.6%): Three DAVFs were successfully re-treated with endovascular Onyx embolization and 1 DAVF was successfully treated by neurosurgical ligation of the fistula.

#### **Influence of Angioarchitectural Features on the Treatment Success**

The analysis of the influence of angioarchitectural features on the treatment success is summarized in Table 3. The results of the final multivariable logistic regression model are presented in Table 4. Two of the investigated parameters showed a significant negative influence on the treatment success in the multivariable model:  $\geq 10$  feeding arteries ( $P = .041$ ; OR, 0.278; 95% CI, 0.081–

0.949) and involvement of the ascending pharyngeal artery ( $P = .039$ ; OR, 0.319; 95% CI, 0.107–0.945). Treatment success tended to be lower for low-grade DAVFs, Cognard type I DAVFs, and DAVFs with involvement of dural branches of the internal carotid artery ( $P < .05$  in the univariate models), however without reaching statistical significance in the multivariable model.

#### **DISCUSSION**

The results of this study demonstrate the effectiveness and safety of endovascular embolization of DAVFs using Onyx. On the basis of a comparatively large number of patients with DAVFs treated with endovascular Onyx embolization, the influence of angioarchitectural features on the treatment success was assessed.

Numerous studies in the literature have investigated the efficacy and safety of endovascular embolization of DAVFs or have compared different treatment techniques; however, the influence of angioarchitectural features on the treatment success has not yet been the focus of research.<sup>4,6-8,10-12</sup> We assessed various angioarchitectural features and analyzed their influence on the treatment success. Of the investigated features, a large number of feeding arteries and involvement of the ascending pharyngeal artery showed a significant negative influence. Treatment success tended to be lower for low-grade DAVFs, Cognard type I DAVFs, and DAVFs with involvement of dural branches of the internal carotid artery without reaching statistical significance. Also, other angioarchitectural features, such as location and Borden type or pial artery supply, did not show significant influence on the treatment success.

Multiple feeding arteries represent a challenge in the treatment of DAVFs.<sup>13-16</sup> Complete occlusion of DAVFs with multiple feeding arteries can generally be achieved in 3 ways: 1) transarterial embolization of parts of the fistula point and of the proximal draining veins or the sinus with subsequent reflux of

**Table 2: Procedural parameters, complications, follow-up, and outcome**

Parameter	No. (relative frequency) / Mean $\pm$ SD
Selected feeder for embolization	
Middle meningeal artery	86 (65.2%)
Occipital artery	31 (23.5%)
Others	14 (10.6%)
No. of embolization positions	
1	103 (78.0%)
2	24 (18.2%)
3	4 (3.0%)
Embolization technique	
Onyx transarterial	76 (57.6%)
Onyx transarterial combined with venous balloon protection	28 (21.2%)
Onyx transarterial with a dual-lumen balloon catheter	19 (14.4%)
Onyx transvenous combined with coiling	3 (2.3%)
Others	7 (5.3%)
Complications	
Overall complications	11 (8.3%)
Asymptomatic complications	6 (4.5%)
Transient symptomatic complications	3 (2.3%)
Permanent complications <sup>a</sup>	2 (1.5%)
Follow-up	
Follow-up period (mo)	23.6 $\pm$ 23.5
Total follow-up time (patient yr)	216.3
Angiographic outcome	
Initial complete angiographic occlusion	86 (78.2%)
Spontaneous occlusion after subtotal endovascular occlusion	14 (12.7%)
Time period from last treatment to diagnosis of spontaneous occlusion (months)	6.6 $\pm$ 8.1
Overall complete occlusion at last examination	100 (90.9%)
Recurrence	4 (3.6%)
Clinical outcome	
Preinterventional mRS score	0.8 $\pm$ 0.9
Postinterventional mRS score at discharge	0.7 $\pm$ 1.1
Postinterventional mRS score at 6 mo after treatment	0.4 $\pm$ 0.9
Complete symptom remission after treatment	73 (66.4%)
Symptom relief after treatment	32 (29.1%)
Stable symptoms after treatment	3 (2.7%)
Worsening of symptoms after treatment	2 (1.8%)
Treatment success <sup>b</sup>	90 (81.8%)

<sup>a</sup> Both permanent complications were lethal intracerebral hemorrhages.

<sup>b</sup> Defined as complete symptom remission for low-grade DAVFs (no cortical venous reflux/Cognard I–IIa) and complete angiographic occlusion for high-grade DAVFs (to presence of cortical venous reflux/Cognard IIa+b to IV).

embolic agent into the fistula point and the other multiple arterial feeders; 2) transarterial embolization in combination with transvenous balloon protection of the draining veins or the sinus, the latter facilitating retrograde embolization of the whole fistula network; or 3) transvenous coiling of the draining veins or the sinus with or without subsequent transarterial and/or transvenous embolization of the complete DAVF. These embolization techniques are often complex and are not always successful. In this context, it is obvious that the higher the number of feeding arteries, the higher is the chance of incomplete embolization of the DAVF.

In DAVF embolization, particular importance is attributed to the ascending pharyngeal artery, which is regularly involved in the arterial supply of DAVFs (25% in our study). Embolization of this artery is often avoided because of its potential anastomoses to the internal carotid artery and vertebral arteries as well as its supply to the vasa nervorum of the lower cranial nerves.<sup>17</sup> In our study, an ascending pharyngeal artery supply was most frequently observed in DAVFs located at the transverse and/or sigmoid sinus and in tentorial DAVFs. Even though treatment success was not significantly different for DAVF locations, the ascending pharyngeal artery supply often contributed to the angioarchitectural complexity of difficult-to-treat DAVFs of these 2 locations. Especially for tentorial DAVFs, which are rare and have a high risk of hemorrhage, involvement of the ascending pharyngeal artery increases the complexity of the angioarchitecture, which can make the endovascular treatment of these difficult-to-treat lesions even more difficult.<sup>18</sup> These factors are possible explanations for the lower treatment success rate for DAVFs with involvement of this artery in our study.

A possible explanation for the tendency toward a lower treatment success rate for DAVFs without cortical venous reflux (low-grade DAVFs; Borden I/Cognard I–IIa) can be related to their complex angioarchitecture: multiple arteries shunting into the wall of a venous sinus, which is usually functioning and thus mostly essential for the venous drainage of the brain, forming a large fistula plate rather than a circumscribed fistula point. In most cases, for complete occlusion of the fistula, assistive techniques such as balloon protection of the venous sinus are indispensable, while sacrificing the sinus is accompanied by an increased risk of complications.<sup>6,9,13,19</sup> These complicating factors result in a greater difficulty of complete embolization of the DAVF and thus make symptom remission less probable.

The special significance and the impact of indirect cortical venous drainage and of pial artery supply on the natural course and on the therapeutic regimen were investigated and discussed in recent studies.<sup>7,20</sup> However, the presence of these factors did not show a significant influence on the treatment success in our study. With regard to pial artery supply, the number of DAVFs with pial artery supply was relatively high in our study (37%) compared with research results in the literature. The largest and most recent study with a focus on a pial artery supply of DAVFs is the work of Osada and Krings,<sup>20</sup> who reported a rate of pial artery supply of 11% in 204 patients.

For high-grade DAVFs (presence of cortical venous reflux), the primary aim of treatment is complete occlusion of the fistula, to eliminate the risk of hemorrhage. However, for low-grade DAVFs (absence of cortical venous reflux), which are not accompanied by an increased risk of hemorrhage, complete symptom remission is the primary goal of treatment. The rate of symptom remission or relief after endovascular embolization of DAVFs is rarely and heterogeneously reported in the literature and is between 20% and 80%.<sup>4,6–8,10,11</sup> To combine complete angiographic occlusion, as the primary goal for high-grade DAVFs, and complete symptom remission, as the primary goal for low-grade DAVFs, we defined the treatment success differently for low-grade and high-grade DAVFs: Complete symptom remission was defined as treatment success for low-grade DAVFs, whereas

**Table 3: Influence of angioarchitectural features on the treatment success—summary and univariate models**

Angioarchitectural Feature, Treatment Success Rate							P Value (Univariate Analysis)
Location	Transverse/Sigmoid Sinus, 80.4%	Tentorial/Petrosal, 72.0%	Superior Sagittal Sinus, 95.0%	Torcular, 100%	Anterior Cranial Fossa, 83.3%	Sphenoparietal Sinus, 75.0%	.084
Cognard type	I, 60.0%	Ila, 75.0%	Ilb, 100%	Ila+b, 70.0%	III, 96.4%	IV, 80.4%	.047 <sup>a</sup>
Borden type	I, 66.7%		II, 76.9%		III, 86.1%		.144
Venous drainage		Into dural venous sinus, 71.4%			Directly into cortical veins, 85.4%		.099
Presence of cortical venous reflux		Yes, 85.9%			No, 61.1%		.013
No. of feeding arteries		<10, 92.6%			≥10, 71.4%		.004 <sup>a</sup>
Bilateral feeders		Yes, 83.3%			No, 80.4%		.686
Pial artery supply		Yes, 77.8%			No, 83.1%		.531
Involvement of the middle meningeal artery		Yes, 80.2%			No, 92.9%		.252
Involvement of the occipital artery		Yes, 80.7%			No, 85.2%		.602
Involvement of the internal carotid artery <sup>b</sup>		Yes, 70.7%			No, 88.4%		.020 <sup>a</sup>
Involvement of the vertebral artery <sup>b</sup>		Yes, 75.6%			No, 85.5%		.193
Involvement of the superficial temporal artery		Yes, 81.3%			No, 82.1%		.921
Involvement of the ascending pharyngeal artery		Yes, 61.5%			No, 88.1%		.002 <sup>a</sup>

<sup>a</sup> Statistically significant.

<sup>b</sup> Dural branches.

**Table 4: Influence of angioarchitectural features on the treatment success—final multivariable logistic regression model**

Angioarchitectural Feature	P Value	Odds Ratio (95% Confidence Interval)
No. of feeding arteries	.041	0.278 (0.081–0.949)
Involvement of the ascending pharyngeal artery	.039	0.319 (0.107–0.945)

complete angiographic occlusion was defined as treatment success for high-grade DAVFs.

The overall occlusion rate of 90.9% in this study is in line with results of studies in the current literature. For a relatively large series of 251 patients treated with different endovascular techniques (not only Onyx embolization), Gross et al<sup>4</sup> reported an initial angiographic occlusion rate of 70% and a rate of spontaneous occlusion after partial treatment of 8%, resulting in an overall complete occlusion rate of 78%. For studies reporting DAVF embolization with Onyx as the only embolic agent, the pooled initial angiographic occlusion rate was 82% in a recent meta-analysis.<sup>21</sup> The overall complete occlusion rate for embolization with Onyx only ranges between 83.3% and 100% in the most recent studies.<sup>7,8,11</sup>

Recent studies in the literature on endovascular Onyx embolization of DAVFs reported overall complication rates between 8% and 24%.<sup>4,6-8,11</sup> The complication rate of 8.3% in our study is thus comparable with that in these studies. In our study, no case of cranial nerve palsy was observed. However, cranial nerve palsy is a rare but regularly observed complication after endovascular embolization of DAVFs. The rate of cranial nerve palsy lies between 0% and 6%<sup>4,7,8,10,11,21</sup> in the latest studies, with a pooled rate of 2% according to the above-mentioned meta-analysis of

Sadeh-Gonike et al.<sup>22</sup> Both of the 2 fatal complications in our study were large intracranial hemorrhages. One of these cases occurred after subtotal embolization of a high-grade DAVF, which should be avoided in any case, if possible. For the second patient, no specific reason for the lethal intracerebral hemorrhage could be found.

A potential limitation of this study is the relatively low number of patients. However, to the best of our knowledge, this is the largest known population sample for a study reporting DAVF embolization with Onyx as the only embolic agent. Furthermore, this was a single-center study with retrospective analysis of prospectively maintained data, potentially limiting the study findings. A further limitation with regard to the analysis of the angioarchitectural features is that some of the analyzed angioarchitectural features influence each other (eg, number of feeding arteries and the individual feeder territories).

## CONCLUSIONS

Endovascular embolization of cranial DAVFs with Onyx is safe and offers high rates of occlusion and of symptom remission. The presence of multiple feeding arteries and involvement of

the pharyngeal artery negatively influence the treatment success of endovascular embolization of cranial DAVFs with Onyx.

Disclosures: Dominik F. Vollherbst—UNRELATED: Travel/Accommodations/Meeting Expenses Unrelated to Activities Listed: MicroVention and Stryker, Comments: travel support outside this work.\* Christian Herweh—UNRELATED: Consultancy: Brainomix, Oxford UK. Simon Nagel—UNRELATED: Board Membership: Brainomix; Grants/Grants Pending: Cerenovus\*; Payment for Lectures Including Service on Speakers Bureaus: Pfizer, Boehringer Ingelheim. Peter Ringleb—UNRELATED: Consultancy: Advisory Board for Boehringer Ingelheim; Grants/Grants Pending: German Research Foundation; Payment for Lectures Including Service on Speakers Bureaus: Bayer AG, Boehringer Bristol-Myers Squibb, Pfizer, Daiichi Sankyo, Comments: lecture fee. Martin Bendszus—UNRELATED: Board Membership: Vascular Dynamics, Boehringer, Guerbet, Roche; Consultancy: B. Braun Medical, Roche, Guerbet; Grants/Grants Pending: German Research Foundation, European Union, Hopp Foundation, Novartis, Siemens, Stryker, Medtronic, Guerbet\*; Payment for Lectures Including Service on Speakers Bureaus: Novartis, Teva Pharmaceutical Industries, Guerbet, Merck & Co, Grifols. Markus A. Möhlenbruch—UNRELATED: Consultancy: MicroVention, Medtronic, Stryker; Grants/Grants Pending: Balt Extrusion, MicroVention\*; Payment for Lectures Including Service on Speakers Bureaus: Medtronic, MicroVention, Stryker. \*Money paid to the institution.

## REFERENCES

1. Gross BA, Du R. **The natural history of cerebral dural arteriovenous fistulae.** *Neurosurgery* 2012;71:594–602; discussion 602–03 CrossRef Medline
2. Borden JA, Wu JK, Shucart WA. **A proposed classification for spinal and cranial dural arteriovenous fistulous malformations and implications for treatment.** *J Neurosurg* 1995;82:166–79 CrossRef Medline
3. Cognard C, Gobin YP, Pierot L, et al. **Cerebral dural arteriovenous fistulas: clinical and angiographic correlation with a revised classification of venous drainage.** *Radiology* 1995;194:671–80 CrossRef Medline
4. Gross BA, Albuquerque FC, Moon K, et al. **Evolution of treatment and a detailed analysis of occlusion, recurrence, and clinical outcomes in an endovascular library of 260 dural arteriovenous fistulas.** *J Neurosurg* 2017;126:1884–93 CrossRef Medline
5. Rammos S, Bortolotti C, Lanzino G. **Endovascular management of intracranial dural arteriovenous fistulae.** *Neurosurg Clin N Am* 2014;25:539–49 CrossRef Medline
6. Ertl L, Bruckmann H, Kunz M, et al. **Endovascular therapy of low- and intermediate-grade intracranial lateral dural arteriovenous fistulas: a detailed analysis of primary success rates, complication rates, and long-term follow-up of different technical approaches.** *J Neurosurg* 2017;126:360–67 CrossRef Medline
7. Mantilla D, Le Corre M, Cagnazzo F, et al. **Outcome of transarterial treatment of dural arteriovenous fistulas with direct or indirect cortical venous drainage.** *J Neurointerv Surg* 2018;10:958–63 CrossRef Medline
8. Rangel-Castilla L, Barber SM, Klucznik R, et al. **Mid- and long-term outcomes of dural arteriovenous fistula endovascular management with Onyx: experience of a single tertiary center.** *J Neurointerv Surg* 2014;6:607–13 CrossRef Medline
9. Vollherbst DF, Ulfert C, Neuberger U, et al. **Endovascular treatment of dural arteriovenous fistulas using transarterial liquid embolization in combination with transvenous balloon-assisted protection of the venous sinus.** *AJNR Am J Neuroradiol* 2018;39:1296–1302 CrossRef Medline
10. Baltasavias G, Valavanis A. **Endovascular treatment of 170 consecutive cranial dural arteriovenous fistulae: results and complications.** *Neurosurg Rev* 2014;37:63–71 CrossRef Medline
11. Chandra RV, Leslie-Mazwi TM, Mehta BP, et al. **Transarterial Onyx embolization of cranial dural arteriovenous fistulas: long-term follow-up.** *AJNR Am J Neuroradiol* 2014;35:1793–97 CrossRef Medline
12. Piippo A, Niemela M, van Popta J, et al. **Characteristics and long-term outcome of 251 patients with dural arteriovenous fistulas in a defined population.** *J Neurosurg* 2013;118:923–34 CrossRef Medline
13. Abud TG, Nguyen A, Saint-Maurice JP, et al. **The use of Onyx in different types of intracranial dural arteriovenous fistula.** *AJNR Am J Neuroradiol* 2011;32:2185–91 CrossRef Medline
14. Cognard C, Januel AC, Silva NA Jr, et al. **Endovascular treatment of intracranial dural arteriovenous fistulas with cortical venous drainage: new management using Onyx.** *AJNR Am J Neuroradiol* 2008;29:235–41 CrossRef Medline
15. Gandhi D, Chen J, Pearl M, et al. **Intracranial dural arteriovenous fistulas: classification, imaging findings, and treatment.** *AJNR Am J Neuroradiol* 2012;33:1007–13 CrossRef Medline
16. Roy D, Raymond J. **The role of transvenous embolization in the treatment of intracranial dural arteriovenous fistulas.** *Neurosurgery* 1997;40:1133–41; discussion 1141–44 Medline
17. Gross BA, Albuquerque FC, Moon K, et al. **The road less traveled: transarterial embolization of dural arteriovenous fistulas via the ascending pharyngeal artery.** *J Neurointerv Surg* 2017;9:97–101 CrossRef Medline
18. Lawton MT, Sanchez-Mejia RO, Pham D, et al. **Tentorial dural arteriovenous fistulae: operative strategies and microsurgical results for six types.** *Neurosurgery* 2008;62:110–24; discussion 124–25 Medline
19. Piechowiak E, Zibold F, Dobrocky T, et al. **Endovascular treatment of dural arteriovenous fistulas of the transverse and sigmoid sinuses using transarterial balloon-assisted embolization combined with transvenous balloon protection of the venous sinus.** *AJNR Am J Neuroradiol* 2017;38:1984–89 CrossRef Medline
20. Osada T, Krings T. **Intracranial dural arteriovenous fistulas with pial arterial supply.** *Neurosurgery* 2019;84:104–15 CrossRef Medline
21. Sadeh-Gonike U, Magand N, Armoiry X, et al. **Transarterial Onyx embolization of intracranial dural fistulas: a prospective cohort, systematic review, and meta-analysis.** *Neurosurgery* 2018;82:854–63 CrossRef Medline
22. Johnson CS, Chiu A, Cheung A, et al. **Embolization of cranial dural arteriovenous fistulas in the liquid embolic era: a Sydney experience.** *J Clin Neurosci* 2018;49:62–70 CrossRef Medline

# Ultra-High-Field Targeted Imaging of Focal Cortical Dysplasia: The Intracortical Black Line Sign in Type IIb

E. Bartolini, M. Cosottini, M. Costagli, C. Barba, L. Tassi, R. Spreafico, R. Garbelli, L. Biagi, A. Buccoliero, F. Giordano, and R. Guerrini



## ABSTRACT

**BACKGROUND AND PURPOSE:** Conventional MR imaging has limitations in detecting focal cortical dysplasia. We assessed the added value of 7T in patients with histologically proved focal cortical dysplasia to highlight correlations between neuropathology and ultra-high-field imaging.

**MATERIALS AND METHODS:** Between 2013 and 2019, we performed a standardized 7T MR imaging protocol in patients with drug-resistant focal epilepsy. We focused on 12 patients in whom postsurgical histopathology revealed focal cortical dysplasia and explored the diagnostic yield of preoperative 7T versus 1.5/3T MR imaging and the correlations of imaging findings with histopathology. We also assessed the relationship between epilepsy surgery outcome and the completeness of surgical removal of the MR imaging-visible structural abnormality.

**RESULTS:** We observed clear abnormalities in 10/12 patients using 7T versus 9/12 revealed by 1.5/3T MR imaging. In patients with focal cortical dysplasia I, 7T MR imaging did not disclose morphologic abnormalities ( $n=0/2$ ). In patients with focal cortical dysplasia II, 7T uncovered morphologic signs that were not visible on clinical imaging in 1 patient with focal cortical dysplasia IIa ( $n=1/4$ ) and in all those with focal cortical dysplasia IIb ( $n=6/6$ ). T2\*WI provided the highest added value, disclosing a peculiar intracortical hypointense band (black line) in 5/6 patients with focal cortical dysplasia IIb. The complete removal of the black line was associated with good postsurgical outcome ( $n=4/5$ ), while its incomplete removal yielded unsatisfactory results ( $n=1/5$ ).

**CONCLUSIONS:** The high sensitivity of 7T T2\*-weighted images provides an additional tool in defining potential morphologic markers of high epileptogenicity within the dysplastic tissue of focal cortical dysplasia IIb and will likely help to more precisely plan epilepsy surgery and explain surgical failures.

**ABBREVIATIONS:** EEG = electroencephalography; FCD = focal cortical dysplasia; SWAN = susceptibility-weighted angiography

Focal cortical dysplasia (FCD) is among the most common structural brain lesions observed in patients who have undergone an operation for drug-resistant epilepsy,<sup>1</sup> reaching up to 78% of neuropathologic findings in pediatric series.<sup>2,3</sup> The neuropathologic spectrum of FCD includes different cytoarchitectural subtypes.<sup>4</sup>

Abnormal cortical layering, affecting either the radial (FCD type Ia) or tangential organization (FCD type Ib) of the cortex,

characterizes FCD type I. Specific cytologic abnormalities within a disrupted cortical lamination separate FCD type II, into IIa (cortical dyslamination + dysmorphic neurons) and IIb (cortical dyslamination + dysmorphic neurons + balloon cells). In FCD type III, lamination abnormalities are associated with different principal brain lesions, namely hippocampal sclerosis (type IIIa),

This work was supported by Projects 133/11 "Ultra-high field MRI targeted imaging of dysplastic cortical lesions and dysembryoplastic tumors" and "Development and Epilepsy: Strategies for Innovative Research to improve diagnosis, prevention and treatment in children with difficult to treat Epilepsy (DESIRE)" and the European Union Seventh Framework Program FP7/2007–2013, grant agreement 602531.

Please address correspondence to Renzo Guerrini, MD, Neuroscience Department, Meyer Children's Hospital, University of Florence, Viale Pieraccini 24, 50139 Firenze, Italy; e-mail: r.guerrini@meyer.it

Indicates open access to non-subscribers at [www.ajnr.org](http://www.ajnr.org)

Indicates article with supplemental on-line appendix and tables.

Indicates article with supplemental on-line photos.

<http://dx.doi.org/10.3174/ajnr.A6298>

Received June 20, 2019; accepted after revision September 18.

From the Department of Pediatric Neurology (E.B., C.B., A.B., R. Guerrini), Neurogenetics and Neurobiology Unit and Laboratories, and Pediatric Neurosurgery Unit (F.G.), Children's Hospital A. Meyer-University of Florence, Florence, Italy; Neurology Unit (E.B.), USL Centro Toscana, Nuovo Ospedale Santo Stefano, Prato, Italy; Department of Translational Research and New Technologies in Medicine and Surgery (M. Cosottini), University of Pisa, Pisa, Italy; IMAGO7 Research Foundation (M. Costagli), Pisa, Italy; Epilepsy Surgery Centre C. Munari (L.T.), Ospedale Niguarda, Milano, Italy; Clinical Epileptology and Experimental Neurophysiology Unit (R.S., R. Garbelli), Fondazione Istituto di Ricovero e Cura a Carattere Scientifico, Istituto Neurologico C. Besta, Milano, Italy; and Istituto Di Ricovero e Cura a Carattere Scientifico Fondazione Stella Maris (L.B., R. Guerrini), Pisa, Italy.

tumors (type IIIb), vascular malformations (type IIIc), or any other principal lesions (FCD type IIIId).<sup>4</sup>

FCD type I is a heterogeneous entity deriving from late postmigrational insults to the developing brain, while FCD type II is a more homogeneous malformation, thought to result from early perturbation of cell proliferation and specification.<sup>5</sup> Activating brain somatic mutations in genes of the mTOR pathway are recognized at increasing rates in FCD IIa and IIb and hemimegalencephaly.<sup>4,6,7</sup> Although type I FCD can, at times, be widespread, involving multiple lobes, neuroimaging may be unrevealing. Otherwise, different combinations of imaging signs of FCD have been described, including blurring of the gray/white matter junction, T2-weighted hyperintensity and T1-weighted hypointensity in the subcortical WM, regional hypoplasia/atrophy,<sup>8,9</sup> and cortical thinning.<sup>8,10</sup>

MR imaging signs associated with FCD type II include cortical thickening, increased T2-weighted signal within the cortex or the underlying WM tapering toward the ventricle (ie, transmantle sign), blurring of the GM/WM junction, T2-weighted hyperintensity, and T1-weighted hypointensity in the subcortical WM.<sup>9,11</sup>

However, none of these signs is completely reliable, and the capability of disclosing regions of cortical dysplasia even at 3T MR imaging is suboptimal, especially for FCD types I and IIa.<sup>9,11-13</sup>

In addition, even in patients with MR imaging positive for structural abnormalities the lesion boundaries often escape proper recognition, limiting the possibility of performing tailored surgical resections that reliably include the whole lesion. Although invasive electroencephalographic (EEG) recordings help to identify the seizure-onset zone, histologic abnormalities can extend beyond the electrographic margin,<sup>14</sup> making it problematic to properly define the epileptogenic zone. Poor delimitation of the lesion by MR imaging represents a major drawback because completeness of the surgical resection is a key element for a favorable seizure outcome after the operation.<sup>15-20</sup> Improving the detection rate of FCD and reliably identifying the malformation boundaries are therefore crucial for optimizing surgical planning.

Ultra-high-field MR imaging offers an enhanced spatial resolution reaching microscopic values due to its high signal-to-noise ratio, allowing the different components within the cortex to be visualized, especially through sequences weighted in T2\* and magnetic susceptibility.<sup>21-23</sup> The 7T MR imaging has the capability of disclosing areas of polymicrogyric cortex in brain regions previously considered normal using 3T MR imaging<sup>24</sup> and of uncovering cryptic regions of cortical dysplasia in patients with MR imaging negative for focal epilepsy.<sup>25</sup> The 7T MR imaging has also proved superior to conventional neuroimaging in disclosing radiologic signs of FCD.<sup>26</sup>

We studied 12 patients with FCD using 7T MR imaging and correlated imaging characteristics with neuropathology findings and postoperative epilepsy outcome.

## MATERIALS AND METHODS

Between 2013 and 2019, we performed a 7T MR imaging protocol of investigation with no sedation in patients with drug-resistant focal epilepsy (8 years of age or older).

We performed a retrospective analysis of a suitable surgical series focusing on 12 of these patients who fulfilled the following

inclusion criteria: 1) clinical and EEG findings suggestive of a focal, single seizure-onset zone; 2) previous preoperative 1.5/3T brain MR imaging performed with an optimized protocol for focal epilepsy, including at least 3D T1-weighted (maximum section thickness, 1 mm), coronal/axial T2-weighted, and FLAIR sequences (maximum section thickness, 3 mm); 3) high-quality preoperative 7T brain MR imaging; 4) ablative brain operation with a histopathologic diagnosis of FCD; and 5) availability of postsurgical 1.5/3T MR imaging.

We sought to explore the structural characteristics of FCD using ultra-high-field MR imaging with respect to the specific histologic subtype and to correlate morphologic data with postoperative epilepsy outcome, as defined by the Engel criteria.<sup>27</sup> The study protocol received approval of the Italian Ministry of Health and the Pediatric Ethics Committee of the Tuscany Region. Written informed consent was obtained from all patients or their representatives.

### MR Imaging Acquisitions

All patients had preliminarily undergone diagnostic 1.5/3T studies with dedicated protocols for focal epilepsy (On-line Appendix).

We performed the 7T brain MR study at the IMAGO7 Foundation, Pisa, Italy, on a Discovery MR 950 MR imaging scanner (GE Healthcare; Chicago, Illinois) equipped with a 2-channel quadrature transmit/32-channel receive head coil (Model NM008-32-7GE-MR950, Nova Medical, Wilmington, Massachusetts).

The research study protocol was developed for the investigation of focal epilepsy and consisted of the following sequences: 3D T1-weighted fast-spoiled gradient recalled or 3D T1-weighted Silent<sup>28</sup> with spatial resolution of  $1 \times 1 \times 1 \text{ mm}^3$ , 3D magnetization-prepared FLAIR sequence<sup>29</sup> with spatial resolution of  $0.7 \times 0.7 \times 0.7 \text{ mm}^3$ , 3D susceptibility-weighted angiography (SWAN) with spatial resolution of  $0.328 \times 0.438 \times 1.2 \text{ mm}^3$ , targeted 3D-SWAN with spatial resolution of  $0.6 \times 0.6 \times 0.6 \text{ mm}^3$  used to also produce quantitative susceptibility maps (On-line Appendix), 2D T2\*WI targeted dual echo gradient recalled echo and 2D T2-weighted FSE, both with in-plane resolution of  $0.313 \times 0.313 \text{ mm}^2$  and section thickness of 2 mm, and 2D targeted gray-white matter tissue border enhancement FSE-inversion recovery<sup>30</sup> with in-plane resolution of  $0.5 \times 0.5 \text{ mm}^2$  and section thickness of 2 mm. We chose the localization of targeted sequences according to the seizure-onset zone, as defined by clinical and EEG findings.

Postsurgical brain MRIs were obtained either on the 1.5T (ACS-NT and Achieva) or 3T (Achieva; Philips Healthcare, Best, the Netherlands) MR imaging systems, with minimum sequence requirements of 3D T1-weighted (maximum section thickness, 1 mm), coronal/axial T2-weighted, and FLAIR sequences (maximum section thickness, 3 mm).

### Brain MR Imaging Analysis and Interpretation

One experienced neuroradiologist and 1 neurologist with expertise in advanced neuroimaging, blinded to the histopathologic diagnosis and to the epilepsy outcome, evaluated both the preoperative 1.5/3T and 7T examinations for signs of FCD (increased

cortical thickness, cortical thinning, abnormal sulcation, regional hypoplasia/atrophy, transmantle sign, blurring of the GM/WM junction, T2-weighted hyperintensity, and T1-weighted hypointensity in subcortical WM). The analysis was performed in a joint session on a dedicated workstation (Advantage Workstation 4.6; GE Healthcare).

To optimize assessment of the extent of surgical resection, we aligned images of the postsurgery clinical MR imaging with those acquired with the 7T system using the FMRIB Linear Image Registration Tool (FLIRT; <http://www.fmrib.ox.ac.uk/fsl/fslwiki/FLIRT>).<sup>31</sup>

### **Surgical Procedure and Histopathologic Assessment**

We planned the surgical resections on the basis of the epileptogenic zone, as defined according to each patient's clinical, imaging, and EEG characteristics.

The histopathologic review of resected brain tissue was performed at Children's Hospital Anna Meyer, Florence, and at the Istituto Neurologico Carlo Besta, Milan, by 3 experienced neuropathologists (On-line Appendix). Histopathologic interpretation was based on the international league against epilepsy (ILAE) classification of focal cortical dysplasia.<sup>4</sup> To explore the histopathologic counterpart of the radiologically defined black line (see below), we relied on macroscopic anatomic landmarks on the surgical specimen, limited to patients who had stereo-EEG recordings (patients 3 and 7), on electrode traces.

### **RESULTS**

Demographic and clinical information of the study population is shown in the On-line Table. Neuropathologic assessment revealed FCD Ib in 2 patients (patients 5 and 6), FCD IIa in 4 (patients 4, 8, 9, and 12), and FCD IIb in 6 (patients 1–3, 7, 10, and 11).

Preoperative 1.5/3T MR imaging revealed abnormal findings in 9/12 (75%) patients. In detail, in the 2 patients with FCD Ib, 1.5/3T MR imaging was unrevealing; in the 4 patients with FCD IIa, there was blurring of the GM/WM junction, which was associated with lobar hypoplasia, abnormal gyral contouring, and, in 1 patient, increased cortical thickness. Patients with FCD IIb had either unrevealing 1.5/3T MR imaging findings (Patient 10) or exhibited variably combined signs of FCD, namely abnormal sulcal/gyral contouring (patients 2, 3, 7, and 11), increased cortical thickness (patients 3, 7, and 11), increased T2-weighted intracortical signal (patients 1, 3, and 7), blurring of the GM/WM junction (patients 1–3 and 11), a T2-weighted hyperintense transmantle sign (patients 1–3, 7, and 11), T2-weighted hyperintensity in the subcortical WM (patients 1–3, 7, and 11), and T1-weighted hypointensity in the subcortical WM (patients 2, 3, 7, and 11).

The 7T MR imaging examination demonstrated clear morphologic or signal abnormalities in 10/12 (83%) patients. In both patients with FCD Ib, we considered 7T MR imaging to be unrevealing, though we observed a nonspecific granular and blurry appearance of the subcortical WM, which was not visible on previous examinations (On-line Fig 1). In all 10 patients with FCD II, the 7T MR imaging examination confirmed the 1.5/3T findings but revealed additional subtle signs in one of the patients with FCD IIa (patient 12) and in all those with FCD IIb (patients

1–3, 7, 10, and 11). The elevated spatial resolution allowed a better visualization of the abnormal gyral contouring in all patients with FCD IIb and in 1 with FCD IIa (patient 12), resolving the anatomic details of a single gyrus, which yielded an apparent increased cortical thickness on conventional imaging due to partial volume effects.

The transmantle sign and the WM signal alterations were clearly defined due to the high 7T SNR in 5/5 patients with such radiologic features. Susceptibility-weighted images revealed an abnormal venous drainage undisclosed by conventional angiogram venography in 1 patient (patient 2) and depicted a peculiar intracortical hypointense band (black line) with high susceptibility on quantitative susceptibility maps in 5/6 patients with FCD IIb (patients 1–3, 7, and 10, whose 1.5/3T T2\*-weighted images were unrevealing) (Figs 1 and 2).

Postsurgical histopathology demonstrated widespread dysmorphic neurons and balloon cells over the cortical regions having such a T2\*WI hypointense band (black line) (patients 1–3, 7, and 10) (On-line Fig 2). On the contrary, dysmorphic neurons and balloon cells spared the cerebral cortex and were atypically limited to subcortical WM in the single patient with FCD IIb who did not exhibit the T2\*WI hypointense black line on 7T imaging (patient 11).

Postsurgical outcome was unsatisfactory in both patients with FCD Ib (patients 5 and 6), while it was favorable in 8/10 (80%) of those with FCD II (Engel class I, patients 1–4, 8–10 and 12). In patients with FCD IIb, by analyzing the coregistration between the 7T examination and the postsurgical MR imaging, we could assess whether the surgical procedure had completely removed the WM/GM blurring ( $n = 3/4$ ), the transmantle sign ( $n = 0/4$ ), the subcortical T2-weighted hyperintense region ( $n = 1/3$ ), and the intracortical black line ( $n = 4/5$ ) (On-line Table 2).

We found that incomplete removal of subcortical regions corresponding to the transmantle sign (patients 1–3) or to T2-weighted hyperintensity (patient 1) did not hamper a favorable epilepsy outcome (ie, Engel class I). Conversely, cortical resections with either incomplete removal of the underlying area of GM/WM blurring seen in FCD IIa ( $n = 1/4$ , patient 8) or of the intracortical T2\*WI black line typical of FCD IIb ( $n = 1/5$ , patient 7) yielded an unfavorable postsurgical outcome (ie, Engel classes II–IV). In patients 3 and 7, we also acquired postoperative 7T scans. In patient 7, who still experienced drug-resistant seizures during follow-up, a residual intracortical hypointense black line persisted next to the surgical crater in the SWAN images of the postoperative 7T scan (Fig 1). Conversely, the black line had completely disappeared in patient 3, who was seizure-free after the operation (Fig 2).

### **DISCUSSION**

In our series of 12 surgically treated patients with histologically proved FCD, 7T MR imaging acquisition yielded positive results in 10 of them, identifying FCD type II in 10/10 exhibiting this histopathologic subtype. From a neuroimaging perspective, the capability of conventional MR imaging to detect signs of cortical dysplasia has been demonstrated to be suboptimal because about half of patients with FCD type I,<sup>9</sup> 10% of those with type IIb,<sup>32</sup> and up to 49% of those with type IIa<sup>11</sup> are reported to exhibit nonspecific MR imaging findings.

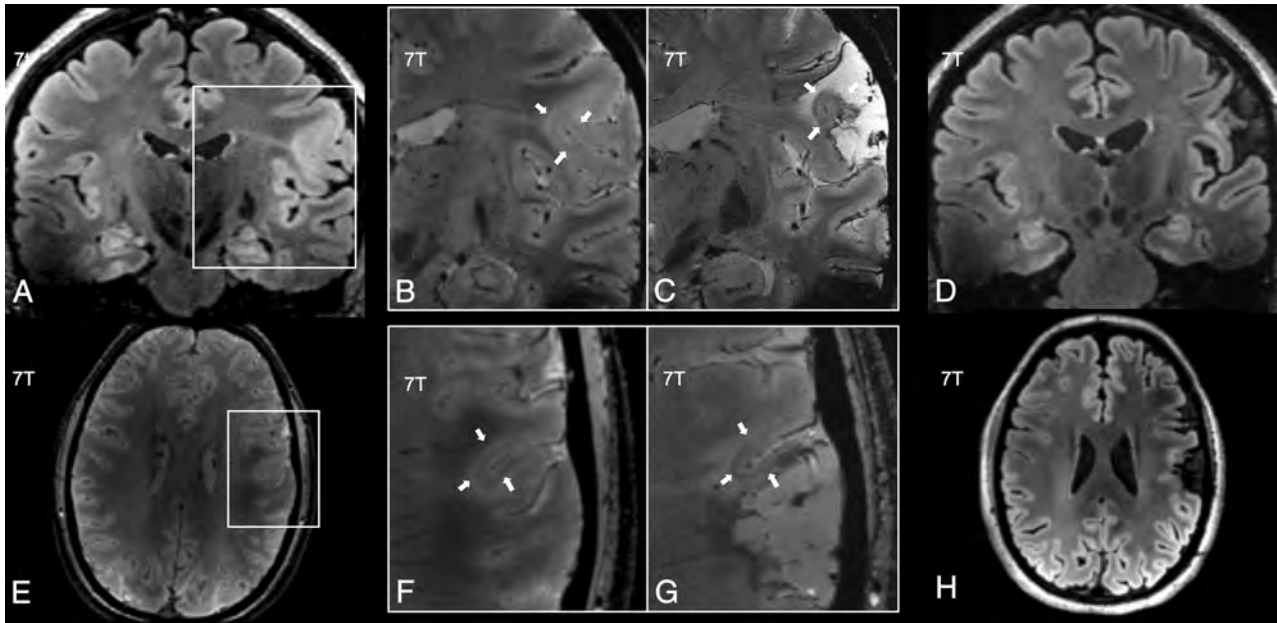


**FIG 1.** A 7T brain imaging of patient 7 (FCD IIb) with unsatisfactory postoperative outcome (Engel class III). A 7T preoperative FLAIR (A), magnified preoperative (B) and postoperative (C) coronal gradient recalled-echo images, postoperative coronal FLAIR (D), preoperative axial SWAN image (E), magnified preoperative (F) and postoperative (G) axial SWAN images, and postoperative axial FLAIR (H). Before the operation, FLAIR images show the transmantle sign, while T2\*WI reveals an intracortical hypointense layer (black line) (white arrows in B and F). Postoperative T2\*WI highlights the persistence of the intracortical hypointense layer black line, next to the postsurgical crater (white arrows in C and G). Postoperative FLAIR images (D and H) show that the transmantle sign and the white matter hyperintensity were not surgically removed.

As observed in previous studies,<sup>25,26</sup> 7T may uncover structural abnormalities that are not apparent using conventional imaging.

However, in this series, the diagnostic gain was confined to FCD type II, while only minor features could be identified with hindsight in FCD type I (On-line Fig 1).

Ultra-high field imaging revealed with higher resolution the MR imaging signs previously observed by 1.5/3T exams and also detected additional subtle findings in FCD IIb. In particular, we identified a new imaging marker of FCD IIb, consisting of an intracortical band of hypointense signal, visible using SWAN sequences, which we termed “black line,” located in the deep layers beneath seemingly preserved upper cortical layers. We first observed this intracortical signal change in a patient (included here as patient 10) with FCD type IIb, belonging to a clinical series of focal epilepsies studied at 7T,<sup>25</sup> and have now confirmed it in all patients with pathologically proved type IIb FCD (patients 1–3, 7, and 10), except patient 11, who atypically exhibited balloon cells and dysmorphic neurons only in the subcortical WM but not within the cortex.

In a study matching ex vivo 7T imaging with histopathology, T2-weighted imaging disclosed an inhomogeneous intracortical signal intensity in the core of FCD IIb lesions, corresponding to disorganized myelinated fibers and numerous clustered dysmorphic neurons and balloon cells.<sup>33</sup> In view of the similarities our in vivo images have with these ex vivo findings, it is possible that the clustering of abnormal cells and disorganized intracortical fibers of type IIb FCD represent the pathologic substrate of the intracortical black line layer.

Overall, T2\*WI signal decreases with reduced fiber and neuronal cell density, as reported in both the normal and dysplastic cerebral cortex of FCD type I and IIa.<sup>34,35</sup> FCD type IIb features hypomyelination and neuronal rarefaction,<sup>36</sup> yet the contribution

of intracortical dysmorphic neurons and balloon cells in generating the in vivo T2\*WI signal is still unclear. T2\*WI signal intensity might also be modulated by the amount of intracortical iron, but clear evidence of increased microglia<sup>35</sup> or abnormal iron concentration is still lacking.<sup>34</sup> Quantitative histopathology would be essential for a comprehensive understanding of the relationship between tissue microstructure and MR imaging signal changes in FCD subtypes.<sup>37</sup> From a clinical perspective, although our series is too small to draw firm conclusions, we are inclined to consider the black line as sensitive and specific for FCD II since we never observed it in association with other subtypes of dysplasia and in healthy controls (published in part in Cosottini et al<sup>38</sup>).

About 80% of patients with FCD IIb also exhibited the transmantle sign, which both conventional and ultra-high-field imaging clearly revealed. This sign is more frequently observed in type IIb FCD<sup>11</sup> and reflects a reduction of myelinated fibers, with high density of balloon cells and reduced oligodendrocytes with abnormal nuclei.<sup>36</sup> Defective myelination is likely the consequence of an exuberant balloon cell proliferation in early proliferation corticogenesis, likewise observed in tuberous sclerosis complex.<sup>39</sup> In 5/6 patients with FCD IIb, 7T imaging also revealed signal changes in the subcortical white matter. In 4 of these patients, all exhibiting both white matter hyperintensity and the intracortical black line (4/6 patients with FCD IIb), T2\*WI bears a resemblance to the flaglike appearance described by Colon et al<sup>26</sup> using 7T in FCD. In a single patient, we also uncovered a venous drainage abnormality (patient 2), which may sometimes be located next to the dysplastic cortex in malformations of cortical development.<sup>40</sup>

To quantify the completeness of surgical excision and correlate it with clinical outcome in patients with FCD IIb, we

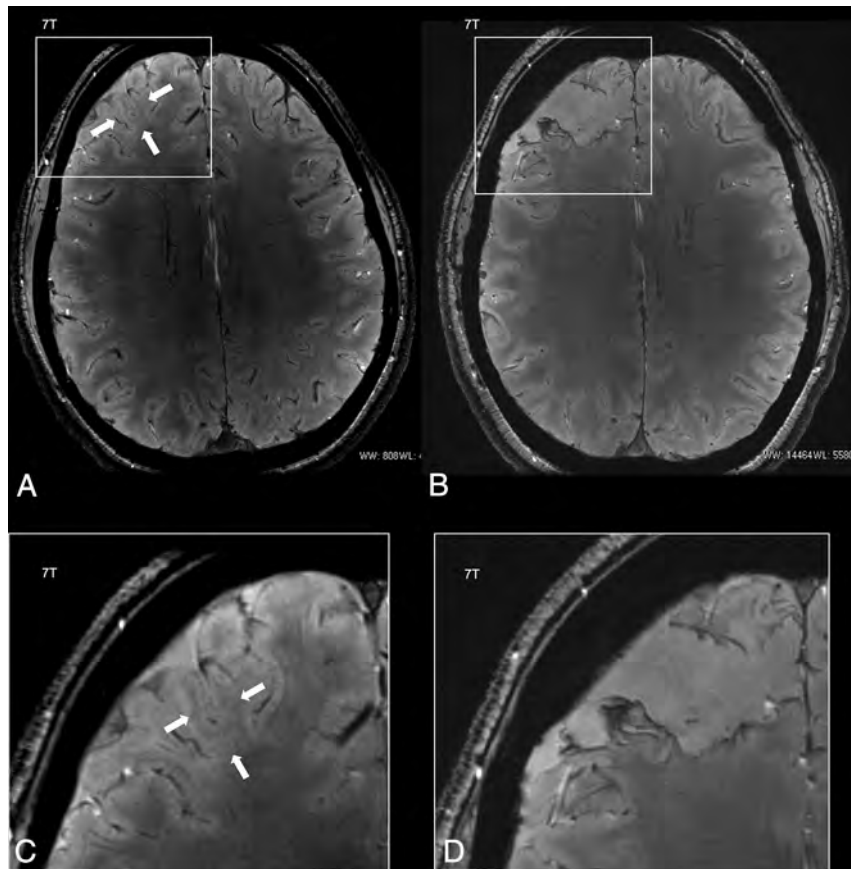


**FIG 2.** A 7T brain imaging of patient 3 (FCD IIb), with favorable postoperative outcome (Engel class I); 7T axial preoperative (A and C) and postoperative (B and D) SWAN images. Preoperative T2\*WI (A) shows an intracortical hypointense layer (black line, white arrows, magnified in C). Postoperative T2\*WI (B, magnified in D) demonstrates the complete removal of the intracortical hypointense layer (black line).

compared the preoperative and postoperative MR imaging. For this purpose, we coregistered ultra-high-field SWAN imaging with preoperative high-resolution anatomic T1-weighted images. Coregistration with postoperative anatomic T1-weighted images was then obtained to establish the relationship between the spatial coordinates of FCD and the postsurgical crater. Rigid coregistration of pre- and postoperative images did not guarantee an optimal comparison in 2/6 patients (patients 2 and 3) because the postresection brain was largely distorted. To obviate this limitation, we used anatomic landmarks to visually assess removed-versus-spared FCD tissue.

We found that in patients with FCD IIb, clinical outcome correlated with the complete removal of the intracortical black line because its complete excision was accompanied by the best post-surgery outcomes (patients 1–3, 10, and 11), while the only patient with incomplete removal still experienced disabling seizures during follow-up (patient 7).

Persistence of the transmantle sign after the operation did not hamper a good seizure outcome (patients 1, 2, and 3), confirming that the demyelinated white matter underlying the dysplastic cortex is not necessarily and directly related to epileptogenesis.<sup>41</sup>

## CONCLUSIONS

We compared conventional brain MR imaging studies performed with different magnet strengths with a standardized 7T MR imaging protocol of investigation. In particular, half of the patients had undergone a preliminary 1.5T scan optimized for epilepsy, and one-fourth of the patients did not have T2\*WI included in conventional MR imaging studies. These limitations hamper a head-to-head comparison with ultra-high-field imaging and limit the generalization of our findings, which should be considered preliminary and exploratory. In addition, we could not focus on a point-by-point correspondence between macroscopic imaging characteristics and histologic findings. Such a drawback could be partially overcome by also studying ex vivo 7T scans of the surgical specimen and including only patients studied by stereo-EEG to use the electrode tracks as landmarks, but technical limitations in coregistration between presurgical and postsurgical brain images are still to be solved. Preoperative investigations of FCD combine electroclinical data, MR imaging, and, in selected patients, [<sup>18</sup>F] FDG-PET and invasive electrophysiologic monitoring.<sup>42</sup> The

sensitivity of SWAN images at ultra-high-field strengths in detecting the intracortical component of FCD IIb, which we designated as the black line, represents a potential adjunctive tool for characterizing the epileptogenic dysplastic cortex and defining its extent, thereby improving surgical planning and prognostication, and weighting the indications for a re-operation in case of failure. A study specifically addressing the presence of the black line sign on standardized 3T MR imaging would provide further information on the clinical value of such findings in clinical practice.

Disclosures: Renzo Guerrini—RELATED: Grant: European Union, Comments: Projects 133/11 “Ultra-high field MRI targeted imaging of dysplastic cortical lesions and dysembryoplastic tumors” and “Development and Epilepsy: Strategies for Innovative Research to improve diagnosis, prevention and treatment in children with difficult to treat Epilepsy (DESIRE)” and European Union Seventh Framework Program FP7/2007–2013, grant agreement 602531.\* \*Money paid to the institution.

## REFERENCES

1. Blumcke I, Spreafico R, Haaker G, et al. **Histopathological findings in brain tissue obtained during epilepsy surgery.** *N Engl J Med* 2017;377:1648–56 CrossRef Medline
2. Spencer S, Huh L. **Outcomes of epilepsy surgery in adults and children.** *Lancet Neurol* 2008;7:525–37 CrossRef Medline

3. Palmieri A, Holthausen H. **Focal malformations of cortical development: a most relevant etiology of epilepsy in children.** *Handb Clin Neurol* 2013;111:549–65 CrossRef Medline
4. Blümcke I, Thom M, Aronica E, et al. **The clinicopathologic spectrum of focal cortical dysplasias: a consensus classification proposed by an ad hoc Task Force of the ILAE Diagnostic Methods Commission.** *Epilepsia* 2011;52:158–74 CrossRef Medline
5. Barkovich AJ, Guerrini R, Kuzniecky RI, et al. **A developmental and genetic classification for malformations of cortical development: update 2012.** *Brain* 2012;135:1348–69 CrossRef Medline
6. Mirzaa GM, Campbell CD, Solovieff N, et al. **Association of *MTOR* mutations with developmental brain disorders, including megalencephaly, focal cortical dysplasia, and pigmented mosaicism.** *JAMA Neurol* 2016;73:836–45 CrossRef Medline
7. Conti V, Pantaleo M, Barba C, et al. **Focal dysplasia of the cerebral cortex and infantile spasms associated with somatic 1q21.1-q44 duplication including the *AKT3* gene: *AKT3* duplication and FCD.** *Clin Genet* 2015;88:241–47 CrossRef Medline
8. Blümcke I, Pieper T, Pauli E, et al. **A distinct variant of focal cortical dysplasia type I characterised by magnetic resonance imaging and neuropathological examination in children with severe epilepsies.** *Epileptic Disord* 2010;12:172–80 CrossRef Medline
9. Tassi L, Colombo N, Garbelli R, et al. **Focal cortical dysplasia: neuropathological subtypes, EEG, neuroimaging and surgical outcome.** *Brain* 2002;125:1719–32 CrossRef Medline
10. Hong S-J, Bernhardt BC, Schrader DS, et al. **Whole-brain MRI phenotyping in dysplasia-related frontal lobe epilepsy.** *Neurology* 2016;86:643–50 CrossRef Medline
11. Colombo N, Tassi L, Deleo F, et al. **Focal cortical dysplasia type IIa and IIb: MRI aspects in 118 cases proven by histopathology.** *Neuroradiology* 2012;54:1065–77 CrossRef Medline
12. Colombo N, Salamon N, Raybaud C, et al. **Imaging of malformations of cortical development.** *Epileptic Disord* 2009;11:194–205 CrossRef Medline
13. Leach JL, Miles L, Henkel DM, et al. **Magnetic resonance imaging abnormalities in the resection region correlate with histopathological type, gliosis extent, and postoperative outcome in pediatric cortical dysplasia.** *J Neurosurg Pediatr* 2014;14:68–80 CrossRef Medline
14. Cohen-Gadol AA, Özdoğan K, Bronen RA, et al. **Long-term outcome after epilepsy surgery for focal cortical dysplasia.** *J Neurosurg* 2004;101:55–65 CrossRef Medline
15. Kim DW, Lee SK, Chu K, et al. **Predictors of surgical outcome and pathologic considerations in focal cortical dysplasia.** *Neurology* 2009;72:211–16 CrossRef Medline
16. Krsek P, Maton B, Jayakar P, et al. **Incomplete resection of focal cortical dysplasia is the main predictor of poor postsurgical outcome.** *Neurology* 2009;72:217–23 CrossRef Medline
17. Phi JH, Cho BK, Wang KC, et al. **Longitudinal analyses of the surgical outcomes of pediatric epilepsy patients with focal cortical dysplasia.** *J Neurosurg Pediatr* 2010;6:49–56 CrossRef Medline
18. Chang EF, Potts MB, Keles GE, et al. **Seizure characteristics and control following resection in 332 patients with low-grade gliomas.** *J Neurosurg* 2008;108:227–35 CrossRef Medline
19. Rowland NC, Englot DJ, Cage TA, et al. **A meta-analysis of predictors of seizure freedom in the surgical management of focal cortical dysplasia.** *J Neurosurg* 2012;116:1035–41 CrossRef Medline
20. Oluigbo CO, Wang J, Whitehead MT, et al. **The influence of lesion volume, perilesion resection volume, and completeness of resection on seizure outcome after respective epilepsy surgery for cortical dysplasia in children.** *J Neurosurg Pediatr* 2015;15:644–650 CrossRef Medline
21. Kwan JY, Jeong SY, Gelderen PV, et al. **Iron accumulation in deep cortical layers accounts for MRI signal abnormalities in ALS: correlating 7 Tesla MRI and pathology.** *PLoS One* 2012;7:e35241. CrossRef Medline
22. Cosottini M, Donatelli G, Costagli M, et al. **High-resolution 7T MR imaging of the motor cortex in amyotrophic lateral sclerosis.** *AJNR Am J Neuroradiol* 2016;37:455–61 CrossRef Medline
23. Costagli M, Donatelli G, Biagi L, et al. **Magnetic susceptibility in the deep layers of the primary motor cortex in amyotrophic lateral sclerosis.** *Neuroimage Clin* 2016;12:965–69 CrossRef Medline
24. De Ciantis A, Barkovich AJ, Cosottini M, et al. **Ultra-high field MR imaging in polymicrogyria and epilepsy.** *AJNR Am J Neuroradiol* 2015;36:309–16 CrossRef Medline
25. De Ciantis A, Barba C, Tassi L, et al. **7T MRI in focal epilepsy with unrevealing conventional field strength imaging.** *Epilepsia* 2016; 57:445–54 CrossRef Medline
26. Colon AJ, van Osch MJ, Buijs M, et al. **Detection superiority of 7 T MRI protocol in patients with epilepsy and suspected focal cortical dysplasia.** *Acta Neurol Belg* 2016;116:259–69 CrossRef Medline
27. Engel J. **Update on surgical treatment of the epilepsies. Summary of the Second International Palm Desert Conference on the Surgical Treatment of the Epilepsies (1992).** *Neurology* 1993;43 1612–7
28. Costagli M, Symms MR, Angeli L, et al. **Assessment of Silent T1-weighted head imaging at 7 T.** *Eur Radiol* 2016;26:1879–88 CrossRef Medline
29. Saranathan M, Tourdias T, Kerr AB, et al. **Optimization of magnetization-prepared 3-dimensional fluid attenuated inversion recovery imaging for lesion detection at 7 T.** *Invest Radiol* 2014;49:290–98 CrossRef Medline
30. Costagli M, Kelley DAC, Symms MR, et al. **Tissue border enhancement by inversion recovery MRI at 7.0 Tesla.** *Neuroradiology* 2014;56:517–23 CrossRef Medline
31. Jenkinson M, Bannister P, Brady M, et al. **Improved optimization for the robust and accurate linear registration and motion correction of brain images.** *Neuroimage* 2002;17:825–41 CrossRef Medline
32. Lerner JT, Salamon N, Hauptman JS, et al. **Assessment and surgical outcomes for mild type I and severe type II cortical dysplasia: a critical review and the UCLA experience.** *Epilepsia* 2009;50:1310–35 CrossRef Medline
33. Zucca I, Milesi G, Medici V, et al. **Type II focal cortical dysplasia: ex vivo 7T magnetic resonance imaging abnormalities and histopathological comparisons.** *Ann Neurol* 2016;79:42–58 CrossRef Medline
34. Garbelli R, Zucca I, Milesi G, et al. **Combined 7-T MRI and histopathologic study of normal and dysplastic samples from patients with TLE.** *Neurology* 2011;76:1177–85 CrossRef Medline
35. Reeves C, Tachrount M, Thomas D, et al. **Combined ex vivo 9.4T MRI and quantitative histopathological study in normal and pathological neocortical resections in focal epilepsy.** *Brain Pathol* 2016;26:319–33 CrossRef Medline
36. Mühlbner A, Coras R, Kobow K, et al. **Neuropathologic measurements in focal cortical dysplasias: validation of the ILAE 2011 classification system and diagnostic implications for MRI.** *Acta Neuropathol* 2012;123:259–72 CrossRef Medline
37. Adler S, Lorio S, Jacques TS, et al. **Towards in vivo focal cortical dysplasia phenotyping using quantitative MRI.** *Neuroimage Clin* 2017;15:95–105 CrossRef Medline
38. Cosottini M, Frosini D, Biagi L, et al. **Short-term side-effects of brain MR examination at 7T: a single-centre experience.** *Eur Radiol* 2014;24:1923–28 CrossRef Medline
39. Prabowo AS, Anink JJ, Lammens M, et al. **Fetal brain lesions in tuberous sclerosis complex: TORC1 activation and inflammation.** *Brain Pathol* 2013;23:45–59 CrossRef Medline
40. Cui Z, Luan G. **A venous malformation accompanying focal cortical dysplasia resulting in a reorganization of language-eloquent areas.** *J Clin Neurosci* 2011;18:404–06 CrossRef Medline
41. Wagner J, Urbach H, Niehusmann P, et al. **Focal cortical dysplasia type IIb: completeness of cortical, not subcortical, resection is necessary for seizure freedom.** *Epilepsia* 2011;52:1418–24 CrossRef Medline
42. Guerrini R, Duchowny M, Jayakar P, et al. **Diagnostic methods and treatment options for focal cortical dysplasia.** *Epilepsia* 2015; 56:1669–86 CrossRef Medline

# Cost and Utility of Routine Contrast-Enhanced Neck MRA in a Pediatric MRI Stroke Evaluation Protocol

 A. Baltensperger,  D. Mirsky,  J. Maloney,  I. Neuberger,  L. Fenton,  T. Bernard,  J. Borgstede, and  N. Stence



## ABSTRACT

**BACKGROUND AND PURPOSE:** Cervical arterial dissection is one of the frequent causes of pediatric arterial ischemic stroke. Out of concern for missing cervical arterial dissection in patients in whom pediatric stroke is suspected, our tertiary children's hospital added contrast-enhanced 3D neck MR angiography to every pediatric stroke work-up. This research investigated whether the routine use of contrast-enhanced neck MRA in our MR imaging stroke protocol ever detected a cervical arterial abnormality when the DWI, SWI/gradient recalled-echo, or circle of Willis MRA findings from the brain MR imaging were reported as normal.

**MATERIALS AND METHODS:** The institutional PACS data base was searched for stroke protocol MRIs that included DWI, gradient recalled-echo or SWI, circle of Willis MRA, and 3D contrast-enhanced neck MRA in patients younger than 18 years of age with examinations performed between September 2010 and June 2017.

**RESULTS:** In only a single case (0.15%) were the DWI, SWI/gradient recalled-echo, or circle of Willis MRA findings all separately reported as normal and the contrast-enhanced neck MRA findings reported as abnormal. To reach these findings, we screened 681 patients, which would have resulted in an estimated >\$200,000 in Medicare charges and \$80,000 in out-of-pocket cost to patients.

**CONCLUSIONS:** In our large series, the addition of a routine contrast-enhanced neck MRA to our pediatric stroke MR imaging protocol was of extremely low yield. We believe the use of neck MRA should reasonably be limited to cases in which abnormalities are initially detected on standard brain sequences or to patients with atypical presentation or recurrent pathology.

**ABBREVIATIONS:** AIS = arterial ischemic stroke; CAD = cervical arterial dissection; CE = contrast-enhanced; CoW = circle of Willis; GRE = gradient recalled-echo; VEN\_BOLD = venous blood oxygen level-dependent

Acute ischemic stroke (AIS) accounts for about half of all strokes in children,<sup>1</sup> and most survivors have life-long disability.<sup>2</sup> Cervical arterial dissection (CAD) is a major cause of pediatric AIS, occurring in 2.5 children per 100,000 per year and accounting for 5%–25% of childhood-onset AIS.<sup>3</sup> Furthermore,

children with AIS secondary to CAD have a significant recurrence risk, estimated at 19%–20%, and a diagnosis of CAD has the potential to change management.<sup>4,5</sup>

Children with acute-onset focal neurologic deficits present a unique clinical challenge. AIS is the most common diagnosis for an adult presenting with an acute-onset focal neurologic deficit, occurring in 73% of cases. However, AIS accounts for only 7% of children presenting emergently with neurologic deficits, with migraines, seizures, and Bell palsy occurring more frequently.<sup>6</sup> Therefore, while AIS is an important, treatable, and common etiology of this presentation in children, imaging protocols in this setting should also evaluate other etiologies.

In most pediatric stroke centers, MR imaging/MRA has become the first-line imaging technique for pediatric patients with suspected AIS because it is noninvasive and free of radiation, while effectively evaluating AIS, dissection, and other neurologic diseases. MR imaging protocols usually include diffusion-weighted, FLAIR, and T1 images of the brain and T1 or T2 fat-saturated axial imaging through the neck. MRA typically includes

Received June 17, 2019; accepted after revision September 18.

From the Department of Pediatrics (A.B., T.B.), Section of Child Neurology, Department of Radiology (D.M., J.M., I.N., L.F., N.S.), Section of Pediatric Radiology, and Department of Radiology (J.B.), University of Colorado School of Medicine, Aurora, Colorado.

T.B.'s work on this project was supported by the Health Resources and Services Administration of the US Department of Health and Human Services under No. 2H30MC24049, Mountain States Hemophilia Network.

This information or content and conclusions are those of the authors and should not be construed as the official position or policy of nor should any endorsements be inferred by Health Resources and Services Administration, US Department of Health and Human Services, or the US Government.

Please address correspondence to Nicholas Stence, MD, Department of Radiology, Children's Hospital Colorado, 13123 E 16th Ave, Aurora, CO 80045; e-mail: nicholas.stence@ucdenver.edu

 Indicates open access to non-subscribers at [www.ajnr.org](http://www.ajnr.org)

<http://dx.doi.org/10.3174/ajnr.A6315>

3D time-of-flight MRA of the head and neck (from the aortic arch through the circle of Willis).<sup>7</sup>

Recent guidelines regarding the urgent management of stroke in children include recommendations for MR imaging with axial DWI, fluid-attenuated inversion recovery, susceptibility-weighted imaging, and time-of-flight MR angiography of the head and neck.<sup>2</sup> More recently in 2017, the International Pediatric Stroke Study Neuroimaging Consortium and the Pediatric Stroke Neuroimaging Consortium published recommendations on imaging pathways for children presenting with stroke, endeavoring to further standardize the practice. The publication argues that because some arteriopathies in childhood affect the cervical vessels while others, the intracranial vasculature, vascular imaging of the head and neck ought to be performed in most cases, specifically including at the time of initial MR imaging, an MRA of the head and neck to evaluate arteriopathy, thrombus, or findings that require independent prompt treatment (ie, cervical artery dissection).<sup>8</sup>

However, equipoise remains on institutional practices for imaging patients with suspected stroke, with an unclear prevalence of abnormal neck imaging findings in the setting of normal brain imaging findings to bolster such practices. There is no comprehensive evaluation of the rates of abnormal neck vessel imaging findings in all-comers pediatric patients to stroke protocol imaging. The Vascular effects of Infection in Pediatric Stroke (VIPS) study identified only one-half of the 355 patients as having undergone cervical imaging at stroke ictus.<sup>9</sup> More data are needed to drive an effective determination of the clinical utility of neck-vessel imaging in pediatric stroke and further standardize our current practices. An appreciated low utility could realistically minimize a potentially unnecessary (as routine) diagnostic component of stroke protocol that would benefit resource use within the institution as well as expedition of appropriate patient care.

Out of concern for missing CAD in children when AIS is suspected, in 2010, our tertiary children's hospital (Children's Hospital Colorado, Aurora, Colorado) added contrast-enhanced neck MR angiography (CE-MRA) to every MR imaging ordered for a pediatric stroke work-up, with the option to limit the examination to DWI, gradient recalled-echo (GRE)/VEN\_BOLD, and circle of Willis (CoW) MRA only if an acute stroke was seen and administration of tPA was considered. CE-MRA was chosen because it was much faster than 2D or 3D time-of-flight noncontrast MRA (30 seconds versus 5–10 minutes). Since the adoption of this MR imaging pediatric stroke protocol, the newly discovered issue of gadolinium deposition has caused us to re-evaluate our neuroimaging protocols that use gadolinium contrast agents. For this reason and to ensure best practices, we undertook a retrospective quality-improvement project to determine whether the routine use of a neck CE-MRA in our MR imaging stroke protocol was indeed necessary, specifically in the subset of children in whom the DWI, GRE/VEN\_BOLD, or CoW MRA findings from the brain MR imaging were reported as normal.

## MATERIALS AND METHODS

### Patients

The study was a local institutional review board–approved retrospective assessment of MR imaging stroke protocol performed

at our hospital between September 2010 and June 2017. The institutional PACS database at Children's Hospital Colorado was searched using Montage (Montage Healthcare Solutions, Philadelphia, Pennsylvania) for stroke protocol MRIs that included DWI, GRE, or VEN\_BOLD; circle of Willis MRA; and neck CE-MRA in patients younger than 18 years of age.

We reviewed reports and collected the following data: accession number, patient age, examination date, any abnormal findings on examinations; abnormal findings on DWI (stroke or other); stroke location if applicable (anterior cerebral artery, MCA, posterior cerebral artery, cerebellum, brain stem); abnormal findings on CoW MRA (stenosis or occlusion or other), GRE or VEN\_BOLD (bleeding or venous distension or other), neck MRA (stenosis or occlusion or other), or those identified on different pulse sequences; and eventual clinical diagnosis.

### CE-MRA Protocol

The neck CE-MRA sequences were acquired on either a 1.5T scanner (Avanto; Siemens, Erlangen, Germany) or a 3T scanner (Ingenia; Philips Healthcare, Best, the Netherlands). The 1.5T neck CE-MRA sequence used TR/TE, 3.17/1.1 ms; acquisition matrix, 110 × 384; 72 slices; 1.2-mm section thickness with no gap. The 3T neck CE-MRA sequence used TR/TE, 4/1.4 ms; acquisition matrix, 251 × 300; 70 slices; 1.8-mm section thickness with –0.9 mm gap. Neck CE-MRA was performed with bolus tracking after the administration of 0.1 mmol/kg body weight of gadolinium-based contrast agent (MultiHance, 0.5 mmol/mL, gadobenate dimeglumine; Bracco Diagnostics, Princeton, New Jersey) at a rate of 2 mL/s.

### Cost-Effectiveness Analysis

The Medicare Physician Fee Schedule global charge for a post-contrast cervical MRA (CPT 70548) is \$311.80 (for 2019), which underestimates private payer reimbursement and generally overestimates Medicaid reimbursement. Given that most commercial payer subscribers pay, on average, 20% coinsurance after the deductible and because a typical commercial contract can be up to twice Medicare rates, our estimates for out-of-pocket expenses for these families range from approximately \$62 to \$125.

## RESULTS

The search result yielded 1147 examinations. Following exclusion of 10 examinations for excessive artifacts or incomplete documentation, there were 1137 examinations in 888 unique patients (522 males; average age, 10.8 years).

In only a single case (a 15-year-old girl with an unusual history of episodic cervical ICA vasospasm) were the DWI, SWI/GRE, or CoW MRA findings all separately reported as normal and the neck CE-MRA findings reported as abnormal for a cervical arterial abnormality. With a total of 681 studies without any identified abnormalities on brain imaging, this case represented 0.15% of those total studies. In comparison, 456 cases reported abnormal findings on DWI, GRE/VEN\_BOLD, or CoW MRA, with 130 (28.5%) of those cases having abnormal neck vessel imaging findings (absolute proportion difference, 28.35; 95% CI, 24.34–32.66;  $P < .001$ ).

By means of our estimates of cost, the routine neck CE-MRA imaging performed in the 681 brain studies that were reported as having normal findings would have resulted in an estimated \$212,335.80 in Medicare payments and potentially from \$42,222 to \$85,125 in patient out-of-pocket costs.

## DISCUSSION

In our large series of >660 children with strokelike symptoms, the addition of a routine neck CE-MRA to our pediatric stroke MR imaging protocol was of extremely low yield when DWI, GRE/VEN\_BOLD, and MRA CoW findings were all normal, revealing only a single case of carotid pathology (0.15%). Our number of 681 needed to screen patients, using a conservative Medicare cost estimate, would result in >\$200,000 of charges and \$80,000 of out of pocket cost to patients.

Additionally, when our protocol was initially devised in 2010, our use of neck CE-MRA in these patients was predicated on its relatively fast acquisition time of ~30 seconds. However, given the recently discovered and ongoing concerns over findings of gadolinium deposition in children,<sup>10</sup> many pediatric centers are not administering contrast whenever possible. Substituting a noncontrast time-of-flight neck MRA could add 5–10 minutes of imaging time to an examination in which speed of imaging is often critical.

Since conducting this study, we have significantly limited the routine use of neck CE-MRA in our stroke imaging work-ups. However, in certain clinical circumstances, we believe it is still important to evaluate the cervical vessels, even when brain imaging findings are normal, particularly when symptoms may point to pathology in the posterior circulation, given the increased prevalence of vertebral dissection in these patients.<sup>4,7</sup>

## CONCLUSIONS

On the basis of the extremely low yield of routine neck CE-MRA in a pediatric stroke MR imaging protocol when DWI, GRE/VENOUS\_BOLD, and CoW MRA findings are normal, we believe the use of a neck CE-MRA in the evaluation of pediatric

stroke should reasonably be limited to cases in which abnormalities are initially detected on routine brain sequences or in patients with atypical presentations or recurrent pathology.

Disclosures: Austin Baltensperger—UNRELATED: Employment: United States Air Force. Laura Fenton—UNRELATED: Board Membership: Society for Pediatric Radiology, Board of Directors, Comments: No money was paid to me or the institution.

## REFERENCES

1. Lynch JK, Hirtz DG, DeVeber G, et al. **Report of the National Institute of Neurological Disorders and Stroke workshop on perinatal and childhood stroke.** *Pediatrics* 2002;109:116–23 CrossRef Medline
2. Rivkin MJ, Bernard TJ, Dowling MM, et al. **Guidelines for urgent management of stroke in children.** *Pediatr Neurol* 2016;56:8–17 CrossRef Medline
3. Mackay MT, Wiznitzer M, Benedict SL, et al. **Arterial ischemic stroke risk factors: the International Pediatric Stroke Study.** *Ann Neurol* 2011;69:130–40 CrossRef Medline
4. Uohara MY, Beslow LA, Billingham L, et al. **Incidence of recurrence in posterior circulation childhood arterial ischemic stroke.** *JAMA Neurol* 2017;74:316–23 CrossRef Medline
5. Fullerton HJ, Wintermark M, Hills NK, et al. **Risk of recurrent arterial ischemic stroke in childhood: a prospective international study.** *Stroke* 2016;47:53–59 CrossRef Medline
6. Mackay MT, Chua ZK, Lee M, et al. **Stroke and nonstroke brain attacks in children.** *Neurology* 2014;82:1434–40 CrossRef Medline
7. Stence NV, Fenton LZ, Goldenberg NA, et al. **Cranio-cervical arterial dissection in children: diagnosis and treatment.** *Curr Treat Options Neurol* 2011;13:636 CrossRef Medline
8. Mirsky DM, Beslow LA, Amlie-Lefond C, et al. **Pathways for neuroimaging of childhood stroke.** *Pediatr Neurol* 2017;69:11–23 CrossRef Medline
9. Wintermark M, Hills NK, DeVeber GA, et al. **Clinical and imaging characteristics of arteriopathy subtypes in children with arterial ischemic stroke: results of the VIPS study.** *AJNR Am J Neuroradiol* 2017;38:2172–79 CrossRef Medline
10. Flood TF, Stence NV, Maloney JA, et al. **Pediatric brain: repeated exposure to linear gadolinium-based contrast material is associated with increased signal intensity at unenhanced T1-weighted MR imaging.** *Radiology* 2017;282:222–28 CrossRef Medline

# Topological Alterations of the Structural Brain Connectivity Network in Children with Juvenile Neuronal Ceroid Lipofuscinosis

T. Roine, U. Roine, A. Tokola, M.H. Balk, M. Mannerkoski, L. Åberg, T. Lönnqvist, and T. Autti



## ABSTRACT

**BACKGROUND AND PURPOSE:** We used diffusion MR imaging to investigate the structural brain connectivity networks in juvenile neuronal ceroid lipofuscinosis, a neurodegenerative lysosomal storage disease of childhood. Although changes in conventional MR imaging are typically not visually apparent in children aged <10 years, we previously found significant microstructural abnormalities by using diffusion MR imaging. Therefore, we hypothesized that the structural connectivity networks would also be affected in the disease.

**MATERIALS AND METHODS:** We acquired diffusion MR imaging data from 14 children with juvenile neuronal ceroid lipofuscinosis (mean  $\pm$  SD age, 9.6  $\pm$  3.4 years; 10 boys) and 14 control subjects (mean  $\pm$  SD age, 11.2  $\pm$  2.3 years; 7 boys). A follow-up MR imaging was performed for 12 of the patients (mean  $\pm$  SD age, 11.4  $\pm$  3.2 years; 8 boys). We used graph theoretical analysis to investigate the global and local properties of the structural brain connectivity networks reconstructed with constrained spherical deconvolution-based whole-brain probabilistic tractography.

**RESULTS:** We found significantly increased characteristic path length ( $P = .003$ ) and decreased degree ( $P = .003$ ), which indicated decreased network integration and centrality in children with juvenile neuronal ceroid lipofuscinosis. The findings were similar for the follow-up MR imaging, and there were no significant differences between the two acquisitions of the patients. In addition, we found that the disease severity correlated negatively ( $P < .007$ ) with integration, segregation, centrality, and small-worldness of the networks. Moreover, we found significantly ( $P < .0003$ ) decreased local efficiency in the left supramarginal gyrus and temporal plane, and decreased strength in the right lingual gyrus.

**CONCLUSIONS:** We found significant global and local network alterations in juvenile neuronal ceroid lipofuscinosis that correlated with the disease severity and in areas related to the symptomatology.

**ABBREVIATIONS:** CLN3 = juvenile neuronal ceroid lipofuscinosis; CSD = constrained spherical deconvolution; LSD = lysosomal storage disease; UPDRS = Unified Parkinson's Disease Rating Scale

Diffusion-weighted MR imaging has enabled the in vivo investigation of white matter tracts in the brain.<sup>1</sup> Different kinds of approaches have been applied, such as analyzing specific regions of interest or investigating the white matter tract skeleton of the brain.<sup>2</sup> However, a large part of the white matter remains outside of these analyses.<sup>3,4</sup> Recently, graph theoretical analysis

has been applied to investigate structural brain connectivity networks.<sup>5,6</sup> In this approach, whole-brain tractography is first performed to reconstruct the white matter pathways of the brain,<sup>7</sup> which are then used to weight connections between segmented gray matter areas.<sup>8</sup> Graph theoretical metrics can then be used to investigate both global and local properties of these networks.<sup>9</sup> This approach has been shown to be reproducible<sup>10</sup> and has been used in several diseases, for example, schizophrenia,<sup>11</sup> autism spectrum disorder,<sup>12</sup> and Alzheimer disease.<sup>13</sup>

Received July 19, 2019; accepted after revision September 18.

From the Hospital District of Helsinki and Uusimaa Medical Imaging Center (T.R., U.R., A.T., M.H.B., T.A.), Radiology, Child Psychiatry (M.M.), Department of Psychiatry (L.Å.), University of Helsinki and Helsinki University Hospital, Helsinki, Finland; Turku Brain and Mind Center (T.R.), University of Turku, Turku, Finland; Department of Neuroscience and Biomedical Engineering (T.R.), Aalto University School of Science, Espoo, Finland; and Department of Child Neurology (T.L.), Children's Hospital, University of Helsinki and Helsinki University, Helsinki, Finland.

This study was supported by a grant from Noah's Hope/Hope 4 Bridget, Thisbe and Noah Scott Foundation, and the Batten Disease Support and Research Association, Finnish Medical Foundation, Pehr Oscar Klingendahl Fund, Arvo and Lea Ylppö Foundation, Finnish Cultural Foundation, and Emil Aaltonen Foundation.

Please address correspondence to Timo Roine, PhD, Hospital District of Helsinki and Uusimaa Medical Imaging Center, Radiology, University of Helsinki and Helsinki University Hospital, PL 22 (Haartmaninkatu 4), FI-00014 Helsingin Yliopisto, Finland; e-mail: timo.roine@iki.fi; @TimoRoine

Indicates open access to non-subscribers at www.ajnr.org

Indicates article with supplemental on-line table.

Indicates article with supplemental on-line photos.

<http://dx.doi.org/10.3174/ajnr.A6306>

Lysosomal storage diseases (LSDs) are often inherited in an autosomal recessive manner and are caused by mutations in genes encoding for enzymes involved in the degradation of macromolecules.<sup>14</sup> This results in excessive storage of cellular material in lysosomes, which eventually leads to cell death and dysfunction of several organs.<sup>14</sup> However, the CNS seems to be especially vulnerable to the storage of cellular material, and neurologic symptoms are common or, in some cases, even the only symptoms, in these disorders.<sup>14</sup> The neuropathology of LSDs has been reviewed before<sup>14</sup> and includes several mechanisms that lead to neurologic dysfunction, depending on the disease. However, in many of these diseases, the pathology is poorly understood.

The classification of LSDs also includes neuronal ceroid lipofuscinoses,<sup>14</sup> a group of inherited, progressive, neurodegenerative disorders, in which autofluorescent ceroid lipopigments are accumulated in the lysosomes. Juvenile neuronal ceroid lipofuscinosis (CLN3) is caused by mutations in the *CLN3* gene encoding a membrane protein, whose dysfunction leads to severe symptoms: progressive visual failure, which leads to blindness around the ages of 4 to 10 years<sup>15-17</sup>; deterioration in cognitive and motor functions; epileptic seizures; and neuropsychiatric symptoms.<sup>15</sup> Also, the disease leads to death in the second or third decade of life.<sup>18</sup> The exact mechanism of the disease is poorly understood, although several functions of the protein have been proposed: membrane fusion, vesicular transport, cytoskeletal linked function, lysosomal acidification, lysosomal arginine import, autophagy, apoptosis, and proteolipid modification.<sup>18</sup>

Previous MR imaging studies in patients with CLN3 reported cerebral and cerebellar atrophy, progressive hippocampal atrophy, alterations of the thalami, and decreased white matter volume in the corona radiata.<sup>19-21</sup> In a postmortem study, higher MR imaging signal intensity of the periventricular white matter was reported, together with histologically observed severe periventricular loss of myelin and gliosis.<sup>22</sup> We recently investigated the white matter microstructure of the brain in children with CLN3<sup>23</sup> and found significant global and widespread local differences by using tract-based spatial statistics<sup>2</sup> and whole-brain tractography,<sup>7</sup> even though conventional MR imaging is usually visually normal in patients aged <10 years.<sup>19</sup>

In this study, we analyzed the topological organization of the structural brain connectivity networks with graph theoretical methods.<sup>6</sup> To our knowledge, these networks have not been investigated before in LSDs. We hypothesized that there would be 1) global topological alterations; and 2) local connectivity abnormalities in the structural brain connectivity networks in CLN3, and that they would be related to the severity of the symptoms. We used constrained spherical deconvolution (CSD)-based tractography<sup>7,24</sup> instead of the more traditional DTI<sup>25</sup> because the latter is unable to characterize crossing fibers, present in 60%-90% of the white matter.<sup>26</sup> Most of the patients underwent follow-up MR imaging after 2 years, which allowed us to investigate longitudinal changes in the structural brain connectivity networks. Furthermore, we analyzed the correlations between the network properties and the scores from the Unified Parkinson's Disease Rating Scale (UPDRS) Part III Motor Examination.<sup>27</sup>

**Table 1: Description of the symptoms of the patients with CLN3 during the first acquisition**

Symptoms	None, n (%)	Mild, n (%)	Severe, n (%)
Visual impairment	1 (7)	9 (64)	4 (29)
Psychiatric symptoms	9 (64)	4 (29)	1 (7)
Epilepsy	9 (64)	3 (21)	2 (14)
Intellectual disability	9 (64)	4 (29)	1 (7)
Motor impairment	9 (64)	5 (36)	0 (0)

## MATERIALS AND METHODS

### Participants

We acquired diffusion-weighted MR imaging data from 14 patients with CLN3 (age, mean  $\pm$  SD 9.3  $\pm$  3.1 years; 10 boys) and 14 age-matched control subjects (age, mean  $\pm$  SD 11.3  $\pm$  2.3 years; 7 boys). The control subjects were healthy volunteers recruited through the personnel mailing list of the Helsinki University Hospital. They were attending conventional elementary school education and did not have regular medication, brain diseases, or long-term diagnoses. One of the control subjects had to be excluded due to image artifacts. A follow-up MR imaging was performed for 12 of the patients (age mean  $\pm$  SD 11.2  $\pm$  3.1 years; 8 boys). The differences in age were not statistically significant between the patients and the controls. The motor performance of the patients was clinically evaluated with UPDRS Part III before the first (score, mean  $\pm$  SD 5.5  $\pm$  8.6 [range, 0-23]) and second (score, mean  $\pm$  SD 7.6  $\pm$  13.8 [range, 0-38]) MR imaging acquisition.

The patients were diagnosed based on their clinical symptoms, including the deterioration of vision and typical ophthalmologic findings. The symptoms of each patient are described in more detail in Table 1. The diagnoses were confirmed by a DNA analysis.<sup>23</sup> Symptomatic medication typical to the disease was in use. The ethics committee for Gynaecology and Obstetrics, Pediatrics and Psychiatry of the Hospital District of Helsinki and Uusimaa approved the research protocol, and a guardian of all the participants signed a written informed consent form before the study.

### Data Acquisition

The MR imaging data were acquired with an (Philips Medical Systems, Best, Netherlands) Achieva 3T scanner (Phillips Healthcare, Best, the Netherlands) and an 8-channel head coil by using a 2 mm  $\times$  2 mm  $\times$  2 mm voxel size and 32 gradient orientations with a diffusion weighting of 1000 s/mm<sup>2</sup>. In addition, 1 non-DWI was acquired. The field of view was 224 mm  $\times$  224 mm  $\times$  160 mm, and 80 axial slices were acquired. Echo time was 59.5 ms, and repetition time was 10.809 seconds. T1-weighted anatomic 3D images were acquired with a resolution of 1 mm  $\times$  1 mm  $\times$  1 mm. The field of view was 256 mm  $\times$  256 mm  $\times$  170 mm, repetition time was 8.3 ms, echo time was 3.8 ms, and the flip angle was 8°. T2WIs were acquired, with a resolution of 0.5 mm  $\times$  0.5 mm  $\times$  4.4 mm and for 8 of the 12 patients in the second acquisition, fluid-attenuated inversion recovery images were acquired, with a resolution of 0.4 mm  $\times$  0.4 mm  $\times$  4.4 mm.

### Reconstruction of the Structural Brain Connectivity Networks

We first corrected the diffusion-weighted data for subject motion<sup>28</sup> and eddy current-induced distortions in ExploreDTI

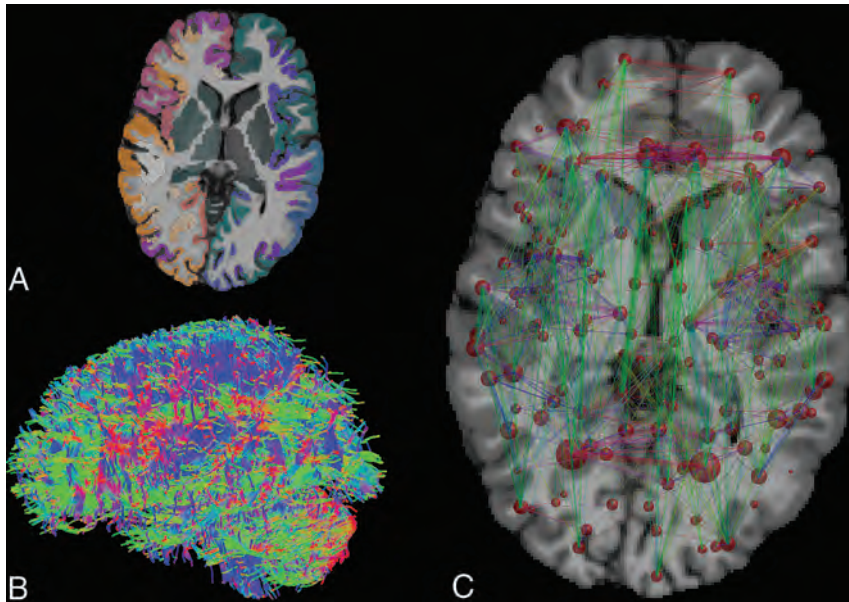


**FIG 1.** Reconstruction of the structural brain connectivity networks. A, Cortical and subcortical parcellation of the T1WI results in 164 gray matter regions. B, Whole-brain probabilistic streamlines tractography based on the corrected DWI can be used to reconstruct structural connectivity pathways of the brain. C, The structural brain connectivity network, in which the nodes represent the gray matter areas and the edges are weighted by the number of streamlines that connect the nodes. The size of the nodes corresponds to the volume of the gray matter area. The width of the edges corresponds to the number of streamlines, and the color of the edges corresponds to the direction of the connection (red: left-right, green: anterior-posterior, blue: superior-inferior).

(version 4.8.6; <http://exploredti.com/>).<sup>29</sup> Because no reverse phase-encoding data were available, we used nonlinear registration with cubic splines to the T1-weighted data to correct for the echo-planar imaging distortions.<sup>30</sup> We then estimated fiber orientation distributions with CSD<sup>24</sup> by using up to fourth-order spherical harmonics. We performed probabilistic CSD-based tractography<sup>7</sup> in ExploreDTI<sup>29</sup> with a seed point resolution of 1.0 mm × 1.0 mm × 1.0 mm within the brain mask, step size of 1 mm, fiber orientation distribution threshold of 0.1, angle threshold of 45°, and fiber length range of 50 to 500 mm. Cortical and subcortical gray matter parcellation of the T1WI was performed in FreeSurfer<sup>8</sup> (<http://surfer.nmr.mgh.harvard.edu>) by using the Destrieux atlas.<sup>31</sup> Also, the 2 ends of each reconstructed streamline were assigned to gray matter areas based on the parcellation, including the cerebellum, as described in Fig 1. In the structural brain connectivity networks, the nodes represent the gray matter areas, and the edges represent the reconstructed streamlines between the nodes, which resulted in a 164 × 164 connectivity matrix weighted by the number of streamlines. The networks were visualized in MRtrix3 (<http://neuro.debian.net/pkgs/mrtrix.html>),<sup>32</sup> and the whole-brain tractography was performed (Fig 1B) in ExploreDTI.<sup>29</sup>

### Graph Theoretical Analysis of the Brain Network Properties

We investigated global and local properties of the structural brain connectivity networks weighted by the number of streamlines by using graph theoretical analysis.<sup>6,9</sup> Based on a study in 2019 by

Civier et al,<sup>33</sup> we did not apply a threshold based on the number of streamlines to the networks. The graph theoretical analyses were performed in Matlab (MathWorks, Natick, Massachusetts) by using the Brain Connectivity Toolbox.<sup>9</sup> In the global analysis, we investigated degree, strength, clustering coefficient,<sup>34</sup> characteristic path length,<sup>35</sup> global efficiency,<sup>36</sup> betweenness centrality,<sup>37</sup> and small-worldness.<sup>35</sup> Local node-level analyses were performed for strength, local efficiency, and betweenness centrality. The measures are presented in more detail in the On-line Table.

### Statistical Analyses

Statistical analyses were performed with the general linear model in SPSS Statistics version 25 (IBM, Armonk, New York) by using age and sex as covariates. The results were corrected for multiple comparisons with the Bonferroni correction. The partial correlations with the UPDRS Part III scores were calculated by using age and sex as covariates.

## RESULTS

### Global Graph Theoretical Properties

We found global differences in the topological organization of the structural brain connectivity networks between the patients with CLN3 and the healthy control subjects. The characteristic path length was significantly increased ( $P = .003$ ) and the degree was significantly decreased in patients with CLN3 ( $P = .003$ ), as shown in Table 2. In addition, clustering coefficient, global efficiency, small-worldness, and strength were decreased in patients with CLN3 ( $P < .05$ ) but did not endure the Bonferroni correction for multiple comparisons.

The results were similar for the first and the second acquisitions of the patients compared with the control subjects, as shown in Table 2. However, small-worldness was not decreased ( $P > .05$ ) during the second acquisition of the patients with CLN3 compared with the control subjects, and betweenness centrality was increased ( $P < .05$ ). No significant differences were found in any of the global network properties between the 2 acquisitions of the patients with CLN3 on the group level or by using a pair-wise  $t$  test ( $P > .05$ ). The global results are further visualized in On-line Figure 1.

We found significant correlations between several global network properties and the UPDRS Part III scores in patients with CLN3, including the data from both the first and second acquisitions, as shown in Fig 2. Clustering coefficient, global efficiency, small-worldness, and strength correlated negatively, and characteristic path length correlated positively with the UPDRS Part III

**Table 2: Global differences in the network properties between the patients with CLN3 and the control subjects, with age and sex used as covariates**

Network Property	CLN3 <sup>a</sup>		Control Subjects <sup>a</sup>	P	
	First Acquisition	Second Acquisition		CLN3 First Acquisition vs. Control Subjects	CLN3 Second Acquisition vs. Control Subjects
Betweenness centrality	288 ± 22	294 ± 17	278 ± 11	.084	.008
Characteristic path length	0.118 ± 0.062	0.130 ± 0.073	0.074 ± 0.014	.003 <sup>b</sup>	.003 <sup>b</sup>
Clustering coefficient	5.27 ± 1.57	5.32 ± 2.12	6.45 ± 0.77	.011	.017
Degree	25.9 ± 4.6	25.3 ± 5.0	29.5 ± 1.79	.003 <sup>b</sup>	.002 <sup>b</sup>
Global efficiency	22.6 ± 8.6	22.8 ± 11.6	28.5 ± 4.5	.014	.030
Small-worldness	5.03 ± 0.85	5.24 ± 1.19	5.78 ± 0.80	.009	.126
Strength	511 ± 191	506 ± 255	645 ± 105	.012	.020

<sup>a</sup> Data are mean ± standard deviation.

<sup>b</sup> Indicates significant differences after the Bonferroni correction for multiple comparisons.

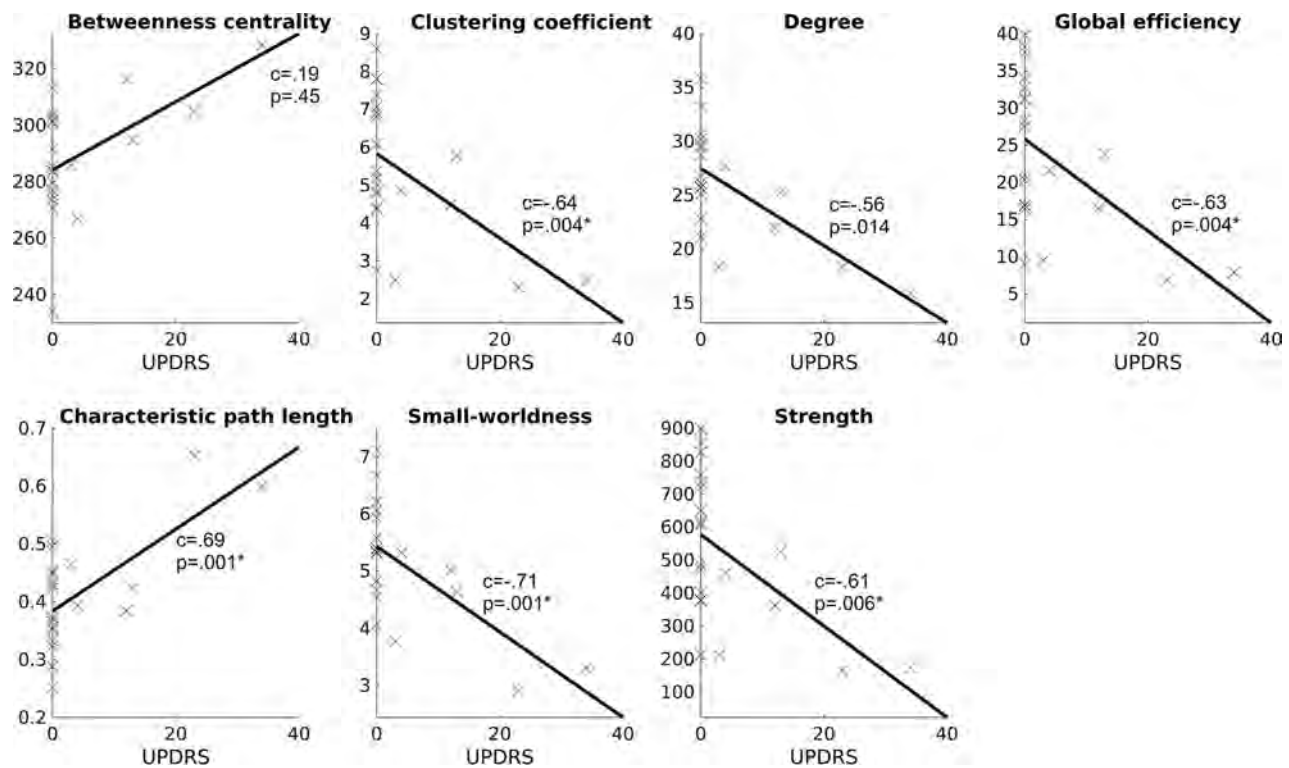


**FIG 2.** Scatterplots and the fitted lines, describing the correlation between the global network properties and UPDRS Part III: motor examination scores. Statistically significant (Bonferroni corrected) correlation coefficients (c) are marked with an asterisk.

scores. The correlations were similar for the first and second acquisitions separately but did not endure the Bonferroni correction for multiple comparisons.

### Local Graph Theoretical Properties

We investigated 3 local network properties: betweenness centrality, local efficiency, and strength. In the first acquisition of the patients with CLN3 compared with the control subjects, we found increased betweenness centrality in 1 region ( $P < .01$ ), decreased local efficiency in 27 regions ( $P < .01$ ), and decreased strength in 9 regions ( $P < .01$ ) in CLN3. These results are presented in more detail in the On-line Figure 2 and On-line Figure 3. However, none of these results endured the Bonferroni correction for multiple comparisons.

In the second acquisition of the patients with CLN3 compared with the control subjects, we found increased betweenness

centrality in the left thalamus ( $P = .002$ ) and in the left middle frontal gyrus ( $P = .004$ ), decreased local efficiency in 48 regions ( $P < .01$ ), and decreased strength in 7 regions ( $P < .01$ ), as shown in On-line Figure 3. These results are illustrated in Fig 3. Of these results, the decreased local efficiency of the left supramarginal gyrus in the inferior parietal lobe and left temporal plane of the superior temporal gyrus, and the decreased strength of the right lingual gyrus in the medial occipitotemporal gyrus remained significant after the Bonferroni correction for multiple comparisons ( $P < .0003$ ). These results are emphasized with red circles in Fig 3.

Between the first and the second acquisitions of the patients with CLN3, we found differences ( $P < .01$ ) in 2 regions: increased betweenness centrality in the orbital part of the right inferior frontal gyrus; and increased strength in the area, including the right lingual gyrus and the right medial occipito-

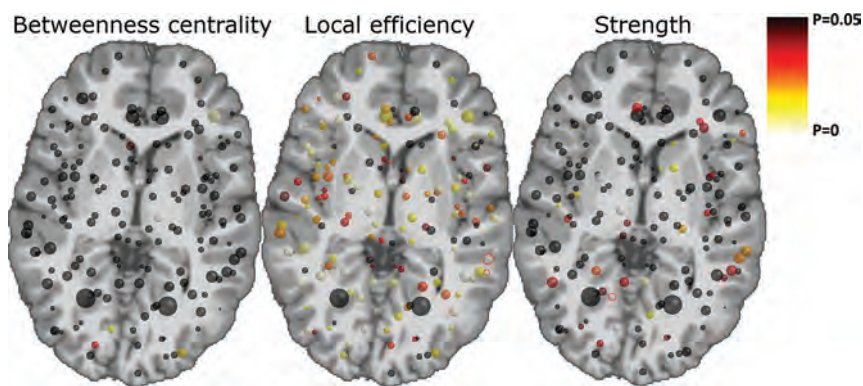


**FIG 3.** Local differences in betweenness centrality, local efficiency, and strength between the second acquisition of the patients with CLN3 and the control subjects. The size of the nodes illustrates the volume of the gray matter region, and the color indicates the statistical significance of the differences ( $P$  values). Significant differences ( $P < .0003$ ) after a Bonferroni correction for multiple comparisons are highlighted with red circles. Local efficiency was decreased in the left supramarginal gyrus and the left temporal plane, and strength was decreased in the right lingual gyrus.

temporal sulcus. These results were not significant after the Bonferroni correction.

## DISCUSSION

In this study, we compared both global and local structural brain network properties between children with CLN3 and age-matched controls. Twelve of 14 patients underwent a follow-up MR imaging after 2 years, which allowed us to investigate longitudinal changes. Moreover, we investigated whether the global network properties correlated with motor impairment.

The comparison of the global graph theoretical properties between the children with CLN3 and the control subjects revealed a significantly increased characteristic path length and decreased degree in CLN3. Characteristic path length<sup>35</sup> is a measure of integration of the network, and it describes how easily the different nodes, in this case, gray matter areas, can communicate with each other.<sup>9</sup> An increased characteristic path length suggests that the integration of the structural brain networks in children with CLN3 is decreased, which may indicate that the networks in CLN3 are more lattice, with a lower number of interconnecting links.<sup>6</sup> The decreased degree indicates decreased centrality of the networks in CLN3.

However, there were no significant differences in the global or local network properties between the 2 acquisitions of the patients with CLN3, similar to our previous results with concern to the white matter microstructure.<sup>23</sup> This suggests that neither the microstructural nor the connectivity properties change rapidly at this age and that the alterations are present already before the age of 10 years.

Moreover, we investigated the correlation between the global network measures and UPDRS Part III scores. The characteristic path length was positively correlated and global efficiency was negatively correlated with UPDRS Part III scores, which suggests an increase in motor impairment, with a decrease of the integration of structural brain networks. The small-worldness and clustering coefficient correlated negatively with the scores, which indicates that the segregation decreases when the motor

impairment increases. Strength correlated negatively with the UPDRS Part III scores, but the correlation of degree was not significant after the correction for multiple comparisons.

We investigated 3 local network properties: betweenness centrality, local efficiency, and strength. Local efficiency and strength were decreased in 20%–30% of the nodes in children with CLN3. However, only 3 nodes remained significant after the Bonferroni correction for multiple comparisons, and thus, other results should be interpreted with caution. The 3 significant differences were the decreased local efficiency in the left supramarginal gyrus and the left temporal plane,

and decreased strength in the right lingual gyrus in patients with CLN3, which indicate that the structural connectivity of these areas would be impaired in CLN3.

The temporal plane forms a major part of the Wernicke area, and is thought to be involved in early phonological and nonword auditory processing.<sup>38,39</sup> Lesions near or including the area might lead to auditory discrimination and speech comprehension deficits, and the area is assumed to be involved in Wernicke aphasia.<sup>38</sup> The left temporal plane is typically larger in healthy subjects, and reduced asymmetry has been linked to schizophrenia and dyslexia.<sup>38</sup> Some of the patients with CLN3 experience hallucinations, and some might also produce jargon, which is also a symptom of Wernicke aphasia. However, in our experience, it is more common for the patients with CLN3 to have problems in speech production than the content of the speech.

The supramarginal gyrus belongs to the inferior parietal lobe, together with the angular gyrus.<sup>40,41</sup> Based on a classic neurobiological model of language, the inferior parietal lobe is involved in the recognition of visual word forms,<sup>42</sup> which are then linked to auditory word forms in the Wernicke area, and motor patterns in the Broca area.<sup>40</sup> Increased activation of the supramarginal gyrus has been reported when focusing on the sound of the words in contrast to their meaning.<sup>43</sup> The supramarginal gyrus is connected to auditory association areas in the posterior supratemporal plane and posterior inferior frontal gyrus,<sup>44</sup> both of which are involved in phonological processing.<sup>45</sup> Difficulties related to phonological word decisions are typically related to damage in the left hemisphere<sup>46</sup> and might lead to conduction aphasia<sup>44,47</sup> or Wernicke aphasia.<sup>48</sup> In CLN3, the speech difficulties increase as the disease progresses and include, for instance, difficulties in starting to speak and festinating stuttering.<sup>49</sup>

The lingual gyrus, a region in the occipital lobe, has been linked to vision, especially related to processing of letters,<sup>50–52</sup> encoding of complex images,<sup>53</sup> impairment of visual memories,<sup>54</sup> and logical order of events.<sup>55</sup> The lingual gyrus has also been related to semantic processing during a task with repeating stimuli during a variety of aphasia tests in subjects with aphasia.<sup>56</sup> In

addition, possible links to the hippocampal regions (related to recollection of facts)<sup>57</sup> and the amygdala (related to high-emotion words and images) have been reported.<sup>58</sup> Also, the occipitotemporal region is involved in perception of colors<sup>59,60</sup> and faces,<sup>61,62</sup> and especially the right lingual gyrus has been related to prosopagnosia<sup>63,64</sup> and to topographagnosia,<sup>65</sup> the inability to recognize faces and landmarks, respectively. In CLN3, the first symptom is usually an impairment in vision that leads rapidly to blindness. Decreased strength in the right lingual gyrus indicates that patients with CLN3 have fewer connections from the lingual gyrus to other nodes than do the control subjects.

Previous MR imaging findings indicate that there are thalamic alterations in LSDs.<sup>66</sup> In CLN3, decreased gray matter volume in the dorsomedial part of the thalamus has been reported.<sup>67</sup> We found decreased local efficiency and strength in the right thalamus and increased betweenness centrality in the left thalamus. However, the results that concern the thalamus did not endure correction for multiple comparisons.

Limitations of this study include a relatively small sample size, which is common in rare diseases, for example, CLN3. In addition, the acquisition was suboptimal for CSD-based tractography because the diffusion weighting and the number of gradient orientations and non-DWIs were relatively low,<sup>68</sup> and reverse-phase encoding data were not available. However, fiber crossings can be reliably identified with CSD.<sup>69</sup> In the future, multi-shell diffusion-weighted MR imaging acquisition may be used to enable more advanced models, such as neurite orientation dispersion and attenuation imaging,<sup>70</sup> and improve tractography within the gray matter.<sup>71,72</sup>

## CONCLUSIONS

We found increased characteristic path length and decreased degree, which indicate decreased global integration and centrality of the structural brain connectivity networks in CLN3. Local analyses revealed differences in the left supramarginal gyrus, the left temporal plane, and the right lingual gyrus. In addition, although not significant after correction for multiple comparisons, the changes in the right thalamus are interesting because thalamic alteration have been reported consistently in LSDs. No significant differences were observed between the 2 acquisitions of the patients in the network properties. Our previous study, together with the current study, indicate that, in patients with CLN3, the microstructural white matter abnormalities and changes in the structural brain network properties are present already before the age of 10 years and do not progress rapidly in the prepubertal stage.

## ACKNOWLEDGMENT

We acknowledge the computational resources provided by the Aalto Science-IT project.

Disclosures: T. Roine—RELATED: Grant: Noah's Hope/Hope 4 Bridget, Thisbe and Noah Scott Foundation, Batten Disease Support and Research Association.\* Comments: Money was paid to University of Helsinki, of which salary for 3 months was paid to me; Other: Emil Aaltonen Foundation, Finnish Cultural Foundation, Comments: Personal research grants (a total of 24 months). U. Roine—RELATED: Grant: Noah's Hope/Hope 4 Bridget, Thisbe and Noah Scott Foundation, and the Batten Disease Support and Research Association.\*

Comments: Money paid to University of Helsinki, and of these funds, salary for 5 months was paid to me; Support for Travel to Meetings for the Study or Other Purposes: Arvo and Lea Ylppö Foundation, Comments: Travel grant to attend Annual Meeting of the Organization for Human Brain Mapping 2018 conference; Other: Finnish Medical Foundation, Pehr Oscar Klingendahl Fund, and Arvo and Lea Ylppö Foundation, Comments: Personal research grants partially granted for this research project. L. Åberg—UNRELATED: Employment: Normal clinical work at the clinic for the intellectually impaired, City of Helsinki. T. Autti—RELATED: Grant: Batten Disease Support and Research Association, Comments: Grant \$60,000. \*Money paid to the institution.

## REFERENCES

1. Tournier JD, Mori S, Leemans A. **Diffusion tensor imaging and beyond.** *Magn Reson Med* 2011;65:1532–56 CrossRef Medline
2. Smith SM, Jenkinson M, Johansen-Berg H. **Tract-based spatial statistics: voxelwise analysis of multi-subject diffusion data.** *Neuroimage* 2006;31:1487–505 CrossRef Medline
3. Jones DK, Knösche TR, Turner R. **White matter integrity, fiber count, and other fallacies: The do's and don'ts of diffusion MRI.** *Neuroimage* 2013;73:239–54 CrossRef Medline
4. Bach M, Laun FB, Leemans A, et al. **Methodological considerations on tract-based spatial statistics (TBSS).** *Neuroimage* 2014;100:358–69 CrossRef Medline
5. Hagmann P, Cammoun L, Gigandet X, et al. **Mapping the structural core of human cerebral cortex.** *PLoS Biol* 2008;6:e159 CrossRef
6. Bullmore ET, Sporns O. **Complex brain networks: graph theoretical analysis of structural and functional systems.** *Nat Rev Neurosci* 2009;10:186–98 CrossRef Medline
7. Jeurissen B, Leemans A, Jones DK, et al. **Probabilistic fiber tracking using the residual bootstrap with constrained spherical deconvolution.** *Hum Brain Mapp* 2011;32:461–79 CrossRef Medline
8. Fischl B, van der Kouwe A, Destrieux C, et al. **Automatically parcellating the human cerebral cortex.** *Cereb Cortex* 2004;14:11–22 CrossRef Medline
9. Rubinov M, Sporns O. **Complex network measures of brain connectivity: uses and interpretations.** *Neuroimage* 2010;52:1059–69 CrossRef Medline
10. Roine T, Jeurissen B, Perrone D, et al. **Reproducibility and intercorrelation of graph theoretical measures in structural brain connectivity networks.** *Med Image Anal* 2019;52:56–67 CrossRef Medline
11. van den Heuvel MP, Mandl RCW, Stam CJ, et al. **Aberrant frontal and temporal complex network structure in schizophrenia: A graph theoretical analysis.** *J Neurosci* 2010;30:15915–26 CrossRef Medline
12. Roine U, Roine T, Salmi J, et al. **Abnormal wiring of the connectome in adults with high-functioning autism spectrum disorder.** *Mol Autism* 2015;6:65. CrossRef Medline
13. Lo CY, Wang PN, Chou KH, et al. **Diffusion tensor tractography reveals abnormal topological organization in structural cortical networks in Alzheimer's disease.** *J Neurosci* 2010;30:16876–85 CrossRef Medline
14. Boustany RM. **Lysosomal storage diseases—the horizon expands.** *Nat Rev Neurol* 2013;9:583 CrossRef Medline
15. Santavuori P, Lauronen L, Kirveskari K, et al. **Neuronal ceroid lipofuscinoses in childhood.** *Suppl Clin Neurophysiol* 2000;53:443–51 CrossRef Medline
16. Collins J, Holder GE, Herbert H, et al. **Batten disease: features to facilitate early diagnosis.** *Br J Ophthalmol* 2006;90:1119–24 CrossRef Medline
17. Spalton DJ, Taylor DS, Sanders MD. **Batten's disease: an ophthalmological assessment of 26 patients.** *Br J Ophthalmol* 1980;64:726–32 CrossRef Medline
18. Jalanko A, Braulke T. **Neuronal ceroid lipofuscinoses.** *Biochim Biophys Acta* 2009;1793:697–709 CrossRef Medline
19. Autti T, Raininko R, Vanhanen SL. **MRI of neuronal ceroid lipofuscinoses: I. Cranial MRI of 30 patients with juvenile neuronal ceroid lipofuscinoses.** *Neuroradiology* 1996;38:476–82 CrossRef Medline

20. Tokola AM, Salli EK, Åberg LE, et al. **Hippocampal volumes in juvenile neuronal ceroid lipofuscinosis: a longitudinal magnetic resonance imaging study.** *Pediatr Neurol* 2014;50:158–63 CrossRef Medline
21. Autti T, Joensuu R, Åberg L. **Decreased T2 signal in the thalami may be a sign of lysosomal storage disease.** *Neuroradiology* 2007;49:571–78 CrossRef Medline
22. Autti T, Raininko R, Santavuori P, et al. **MRI of neuronal ceroid lipofuscinosis. II. Postmortem MRI and histopathological study of the brain in 16 cases of neuronal ceroid lipofuscinosis of juvenile or late infantile type.** *Neuroradiology* 1997;39:371–77 CrossRef Medline
23. Roine U, Roine TJ, Hakkarainen A, et al. **Global and widespread local white matter abnormalities in juvenile neuronal ceroid lipofuscinosis.** *AJNR Am J Neuroradiol* 2018;39:1349–54 CrossRef Medline
24. Tournier J-D, Calamante F, Connelly A. **Robust determination of the fibre orientation distribution in diffusion MRI: non-negativity constrained super-resolved spherical deconvolution.** *Neuroimage* 2007;35:1459–72 CrossRef Medline
25. Basser PJ, Mattiello J, LeBihan D. **MR diffusion tensor spectroscopy and imaging.** *Biophys J* 1994;66:259–67 CrossRef Medline
26. Jeurissen B, Leemans A, Tournier JD, et al. **Investigating the prevalence of complex fiber configurations in white matter tissue with diffusion magnetic resonance imaging.** *Hum Brain Mapp* 2013;34:2747–66 CrossRef Medline
27. **Movement Disorder Society Task Force on Rating Scales for Parkinson's Disease. The Unified Parkinson's disease rating scale (UPDRS): status and recommendations.** *Mov Disord* 2003;18:738–50 CrossRef Medline
28. Leemans A, Jones DK. **The B-matrix must be rotated when correcting for subject motion in DTI data.** *Magn Reson Med* 2009;61:1336–49 CrossRef Medline
29. Leemans A, Jeurissen B, Sijbers J, et al. **ExploreDTI: a graphical toolbox for processing, analyzing, and visualizing diffusion MR data.** *Proc 17th Sci Meet Int Soc Magn Reson Med* 2009;17:3537
30. Irfanoglu MO, Walker L, Sarlls J, et al. **Effects of image distortions originating from susceptibility variations and concomitant fields on diffusion MRI tractography results.** *Neuroimage* 2012;61:275–88 CrossRef Medline
31. Destrieux C, Fischl B, Dale A, et al. **Automatic parcellation of human cortical gyri and sulci using standard anatomical nomenclature.** *Neuroimage* 2010;53:1–15 CrossRef Medline
32. Tournier JD, Calamante F, Connelly A. **MRtrix: Diffusion tractography in crossing fiber regions.** *Int J Imaging Syst Technol* 2012;22:53–66 CrossRef
33. Civier O, Smith RE, Yeh C, et al. **Is removal of weak connections necessary for graph-theoretical analysis of dense weighted structural connectomes from diffusion MRI?** *Neuroimage* 2019;194:68–81 CrossRef Medline
34. Saramäki J, Kivela M, Onnela JP, et al. **Generalizations of the clustering coefficient to weighted complex networks.** *Phys Rev E Stat Nonlinear Soft Matter Phys* 2007;75(Pt 2):027105
35. Watts DJ, Strogatz SH. **Collective dynamics of “small-world” networks.** *Nature* 1998;393:440–42 CrossRef Medline
36. Latora V, Marchiori M. **Efficient behavior of small-world networks.** *Phys Rev Lett* 2001;87:198701 CrossRef Medline
37. Freeman LC. **Centrality in social networks conceptual clarification.** *Soc Netw* 1978;1:215–39 CrossRef
38. Shapleske J, Rossell SL, Woodruff PW, et al. **The planum temporale: a systematic, quantitative review of its structural, functional and clinical significance.** *Brain Res Brain Res Rev* 1999;29:26–49 CrossRef Medline
39. Binder JR, Frost JA, Hammeke TA, et al. **Function of the left planum temporale in auditory and linguistic processing.** *Brain* 1996;119:1239–47 CrossRef Medline
40. Stoeckel C, Gough PM, Watkins KE, et al. **Supramarginal gyrus involvement in visual word recognition.** *Cortex* 2009;45:1091–96 CrossRef Medline
41. Rushworth MF, Behrens TE, Johansen-Berg H. **Connection patterns distinguish 3 regions of human parietal cortex.** *Cereb Cortex* 2006;16:1418–30 CrossRef Medline
42. Déjerine J. **Sur un cas de cécité verbale avec agraphie suivi d'autopsie [On a case of verbal blindness with agraphia, followed by autopsy].** *Mémoires Société Biol* 1891;3:197–201.
43. Devlin JT, Matthews PM, Rushworth M. **Semantic processing in the left inferior prefrontal cortex: a combined functional magnetic resonance imaging and transcranial magnetic stimulation study.** *J Cogn Neurosci* 2003;15:71–84 CrossRef Medline
44. Catani M, Jones DK, Ffytche DH. **Perisylvian language networks of the human brain.** *Ann Neurol* 2005;57:8–16 CrossRef Medline
45. Poldrack RA, Wagner AD, Prull MW, et al. **Functional specialization for semantic and phonological processing in the left inferior prefrontal cortex I.** *Neuroimage* 1999;35:15–35 CrossRef
46. Hartwigsen G, Baumgaertner A, Price CJ, et al. **Phonological decisions require both the left and right supramarginal gyri.** *Proc Natl Acad Sci U S A* 2010;107:16494–99 CrossRef Medline
47. Arnett PA, Swanson SJ, Hammeke TA. **Conduction aphasia in multiple sclerosis: a case report with MRI findings.** *Neurology* 1996;47:576–78 CrossRef Medline
48. Kertesz A, Lau WK, Polk M. **The structural determinants of recovery in Wernicke's aphasia.** *Brain Lang* 1993;44:153–64 CrossRef Medline
49. Mole SE, Williams RE. **Neuronal ceroid-lipofuscinoses.** In: Adam M, Ardinger H, Pagon R, et al. eds. *GeneReviews*. Seattle: University of Washington, 2001
50. Patterson K, Brown WD, Wise R, et al. **The cortical localization of the lexicons: positron emission tomography evidence.** *Brain* 1992;115:1769–82 CrossRef Medline
51. Price CJ, Wise RJS, Watson JDG, et al. **Brain activity during reading. The effects of exposure duration and task.** *Brain* 1994;117(Pt 6):1255–69 CrossRef Medline
52. Bookheimer SY, Zeffiro TA, Blaxton T, et al. **Regional cerebral blood flow during object naming and word reading.** *Hum Brain Mapp* 1995;3:93–106 CrossRef
53. Machielsen WC, Rombouts SA, Barkhof F, et al. **fMRI of visual encoding: reproducibility of activation.** *Hum Brain Mapp* 2000;9:156–64 CrossRef Medline
54. Bogousslavsky J, Miklossy J, Deruaz J-P, et al. **Lingual and fusiform gyri in visual processing: a clinico-pathologic study of superior altitudinal hemianopia.** *J Neurol Neurosurg Psychiatry* 1987;50:607–14 CrossRef Medline
55. Brunet E, Sarfati Y, Hardy-Baylé MC, et al. **A PET investigation of the attribution of intentions with a nonverbal task.** *Neuroimage* 2000;11:157–66 CrossRef Medline
56. Heath S, McMahon KL, Nickels L, et al. **Neural mechanisms underlying the facilitation of naming in aphasia using a semantic task: an fMRI study.** *BMC Neurosci* 2012;13:98 CrossRef Medline
57. Cho S, Metcalfe AWS, Young CB, et al. **Hippocampal – prefrontal engagement and dynamic causal interactions in the maturation of children's fact retrieval.** *J Cogn Neurosci* 2012;24:1849–66 CrossRef Medline
58. Isenberg N, Silbersweig D, Engelen A, et al. **Linguistic threat activates the human amygdala.** *Proc Natl Acad Sci U S A* 1999;96:10456–59 CrossRef Medline
59. Damasio A, Yamada T, Damasio H, et al. **Central achromatopsia: behavioral, anatomic, and physiologic aspects.** *Neurology* 1980;30:1064. CrossRef Medline
60. Meadows JC. **Disturbed perception of colours associated with localized cerebral lesions.** *Brain* 1974;97:615–32 CrossRef Medline
61. Kanwisher N. **Domain specificity in face perception.** *Nat Neurosci* 2000;3:759–63 CrossRef Medline
62. Meadows JC. **The anatomical basis of prosopagnosia.** *J Neurol Neurosurg Psychiatry* 1974;37:489–501 CrossRef Medline
63. Damasio AR, Damasio H, Van Hoesen GW. **Prosopagnosia: anatomic basis and behavioral mechanisms.** *Neurology* 1982;32:331 CrossRef Medline

64. Barton JJS, Press DZ, Keenan JP, et al. **Lesions of the fusiform face area impair perception of facial configuration in prosopagnosia.** *Neurology* 2002;58:71–78 CrossRef Medline
65. Takahashi N, Kawamura M. **Pure topographical disorientation - the anatomical basis of landmark agnosia.** *Cortex* 2002;38:717–25 CrossRef Medline
66. Tokola AM, Åberg LE, Autti TH. **Brain MRI findings in aspartylglucosaminuria.** *J Neuroradiol* 2015;42:345–57 CrossRef Medline
67. Autti T, Hämäläinen J, Åberg L, et al. **Thalami and corona radiata in juvenile NCL (CLN3): A voxel-based morphometric study.** *Eur J Neurol* 2007;14:447–50 CrossRef Medline
68. Tournier JD, Calamante F, Connelly A. **Determination of the appropriate b value and number of gradient directions for high-angular-resolution diffusion-weighted imaging.** *NMR Biomed* 2013;26:1775–86 CrossRef Medline
69. Farquharson S, Tournier JD, Calamante F, et al. **White matter fiber tractography: why we need to move beyond DTI.** *J Neurosurg* 2013;118:1367–77 CrossRef Medline
70. Zhang H, Schneider T, Wheeler-Kingshott CA, et al. **NODDI: practical in vivo neurite orientation dispersion and density imaging of the human brain.** *Neuroimage* 2012;61:1000–16 CrossRef Medline
71. Jeurissen B, Tournier JD, Dhollander T, et al. **Multi-tissue constrained spherical deconvolution for improved analysis of multi-shell diffusion MRI data.** *Neuroimage* 2014;103:411–26 CrossRef Medline
72. Roine T, Jeurissen B, Perrone D, et al. **Informed constrained spherical deconvolution (iCSD).** *Med Image Anal* 2015;24:269–81

# Cerebellar Heterotopias: Expanding the Phenotype of Cerebellar Dysgenesis in CHARGE Syndrome

J.N. Wright, J. Rutledge, D. Doherty, and F. Perez



## ABSTRACT

**BACKGROUND AND PURPOSE:** Coloboma of the eye, Heart defects, Atresia of the choanae, Retardation of growth and/or development, Genital and/or urinary abnormalities, and Ear abnormalities and deafness (CHARGE) syndrome is a multisystem developmental disorder associated with a number of well-described clinical and imaging findings, including cerebellar hypoplasia. We observed cerebellar heterotopias on MR imaging in 2 patients with CHARGE, confirmed by postmortem examination. We sought to determine the prevalence and define the characteristics of similar findings on MR imaging for a cohort of patients with CHARGE syndrome.

**MATERIALS AND METHODS:** We performed a retrospective, observational, cross-sectional study to assess the prevalence and characteristic features of cerebellar heterotopias in 35 patients with CHARGE syndrome with available brain MR imaging studies, as well as to evaluate additional features of cerebellar dysgenesis.

**RESULTS:** Cerebellar heterotopias were identified in 27/35 (77%) patients with CHARGE, characteristic in both location and appearance. Additional features of cerebellar dysgenesis were present in 31/34 evaluable patients (91%), including inferior vermian hypoplasia (90%), anteromedial rotation of the inferior tonsils (90%), and disorganized foliation of the cerebellar hemispheres (74%) or superior vermis (16%).

**CONCLUSIONS:** Patients with CHARGE syndrome have a high prevalence of characteristic cerebellar heterotopias and disorganized foliation and abnormal cerebellar morphology, thereby expanding the phenotype of cerebellar dysgenesis in this syndrome.

**ABBREVIATION:** CHARGE = Coloboma of the eye, Heart defects, Atresia of the choanae, Retardation of growth and/or development, Genital and/or urinary abnormalities, and Ear abnormalities and deafness

Coloboma of the eye, Heart defects, Atresia of the choanae, Retardation of growth and/or development, Genital and/or urinary abnormalities, and Ear abnormalities and deafness (CHARGE) syndrome (Online Mendelian Inheritance in Man, 214800) is a multisystem developmental disorder most commonly caused by heterozygous pathogenic variants in the *chromodomain helicase DNA binding protein 7 (CHD7)* gene encoding chromodomain helicase DNA-binding protein 7.<sup>1</sup> Cardinal features include colobomata, congenital heart disease, choanal atresia, growth retardation and developmental delay, genitourinary abnormalities, and characteristic ear anomalies or

sensorineural hearing loss. Diagnostic criteria as initially proposed by Blake et al<sup>2</sup> and modified by Amiel et al<sup>3</sup> and Verloes<sup>4</sup> include the combination of major and minor criteria based on both clinical and radiologic analyses (Table).

More recently, several additional radiologic features characteristic of CHARGE syndrome have been reported that may serve to improve the performance of future iterations of diagnostic criteria. Among these, posterior fossa anomalies, including cerebellar hypoplasia<sup>5,6</sup> and skull base malformations,<sup>7-12</sup> have recently been reported, highlighting increasing recognition of CNS manifestations of the disease.

We noted unusual paired foci of signal abnormality on MR imaging in the cerebellar hemispheres of children with CHARGE syndrome, corresponding to neuronal heterotopias on histopathologic analysis in 2 patients who underwent postmortem examination. Imaging-apparent cerebellar heterotopias have not been previously reported in CHARGE syndrome. We subsequently performed a retrospective investigation of the prevalence of cerebellar heterotopias on MR imaging in a larger cohort of children with clinically and/or genetically confirmed CHARGE syndrome.

Received June 21, 2019; accepted after revision September 3.

From the Departments of Radiology (J.N.W., F.P.) and Pediatrics, Divisions of Developmental and Genetic Medicine (D.D.), University of Washington and Seattle Children's Hospital, Seattle, Washington; and Department of Pathology (J.R.), Seattle Children's Hospital, Seattle, Washington

Please address correspondence to J.N. Wright, M/S MA.7.220, PO Box 5371, Seattle, WA 98105-5371; e-mail: jnixon@uw.edu; @JNixonWright

Indicates article with supplemental on-line table.

<http://dx.doi.org/10.3174/ajnr.A6280>

## Diagnostic criteria for CHARGE syndrome

Diagnostic Characteristics	Manifestations
Major criteria	
Ocular coloboma	Coloboma of the iris, retina, choroid, disc; microphthalmos
Choanal atresia or stenosis	Unilateral or bilateral, bony or membranous, atresia or stenosis
Cranial nerve dysfunction or anomaly	I, Hyposmia or anosmia VII, Facial palsy (unilateral or bilateral) VIII, Hypoplasia of auditory nerve IX/X, Swallowing problems with aspiration
CHARGE syndrome ear	Outer ear: short, wide ear with little or no lobe, “snipped off” helix, prominent antihelix that is often discontinuous with tragus, triangular concha, decreased cartilage; often protruding and usually asymmetric Middle ear: ossicular malformations Cochlea: incomplete partition Vestibular apparatus: absent or hypoplastic semicircular canals
Minor criteria	
Genital hypoplasia	Males: micropenis, cryptorchidism Females: hypoplastic labia
Developmental delay	Delayed milestones, hypotonia
Cardiovascular malformation	Conotruncal defects (eg, tetralogy of Fallot), atrioventricular canal defects, aortic arch anomalies
Growth deficiency	Short stature, usually postnatal with or without growth hormone deficiency
Orofacial cleft	Cleft lip and/or palate
Tracheoesophageal fistula	Tracheoesophageal defects of all types
Distinctive facial features	Square face with broad prominent forehead, prominent nasal bridge and columella, flat midface

We further sought to correlate the presence of heterotopias with other findings of cerebellar dysgenesis.

## MATERIALS AND METHODS

The study was performed with approval from Seattle Children’s Hospital’s institutional review board. From an institutional data base of 43 patients with a clinical and/or genetic diagnosis of CHARGE syndrome, we identified 35 patients 0–18 years of age who had at least 1 brain MR imaging available for analysis. Details regarding the clinical and/or genetic basis for diagnosis were extracted from the medical record by chart review (On-line Table). Clinical diagnoses were subcategorized as “definite CHARGE syndrome” or “probable/possible CHARGE syndrome” as outlined by Lalani et al.<sup>13</sup>

Using a diagnostic PACS viewer, 2 board-certified pediatric neuroradiologists, with 8 (J.N.W.) and 7 (F.P.) years’ experience, independently reviewed the MR imaging studies and resolved discrepancies by consensus. All available anatomic sequences were evaluated for cerebellar white matter heterotopias, with reviewers noting the presence, location, bilaterality, and signal characteristics. We further evaluated this cohort for additional signs of cerebellar dysgenesis. Based on a prior report of cerebellar abnormalities<sup>5,6</sup> and an initial preliminary review of our patient cohort, specific features chosen for analysis included inferior vermian hypoplasia, abnormal rotation of the inferior cerebellar hemispheres, and disorganized cerebellar foliation.

We correlated the presence of cerebellar heterotopias as well as presence of any features of cerebellar dysgenesis with both a definite-versus-probable/possible clinical diagnosis and a clinical-versus-genetic diagnosis of CHARGE syndrome using the Fisher exact test. We correlated the presence or absence of the heterotopias with patient age, magnetic field strength, section thickness,

and examination quality using the Fisher exact test for categorical variables and point-biserial correlation for continuous variables.

## RESULTS

The cohort of 35 patients with an available MR imaging for analysis included 24 patients with definite CHARGE syndrome, 10 patients with probable/possible CHARGE syndrome, and 1 patient with a negative clinical assessment for CHARGE syndrome but a known pathogenic *CHD7* variant (the patient died at 8 months of age, limiting the sensitivity of the clinical criteria for diagnosis). Twenty-two patients underwent genetic analysis for *CHD7* variants. Of these, 17 had known or predicted pathogenic variants, 4 were negative for them (2 were definite and 2 were probable/possible CHARGE syndrome based on clinical criteria), and 1 returned a variant of unknown significance (clinically categorized as probable/possible CHARGE syndrome). Among the *CHD7* gene variations, 4 were stop-gain mutations; 3, frameshift; 3, canonical splice-site; 2, interstitial deletions; 2, missense (1 known pathogenic and 1 of unknown significance); and 3 were reported pathogenic in the medical records without specific genetic results available for review.

We identified cerebellar white matter heterotopias in 27/35 (77%) patients with CHARGE, with histopathologic correlation in 2 patients on postmortem examination. Histologic analysis in both cases demonstrated neuronal heterotopias, corresponding on gross pathologic sections to the foci of abnormality on MR imaging (Fig 1). The cell rests comprised loose clusters of morphologically normal granular cell neurons admixed with large Purkinje cells in a background of mixed glial cells (Fig 2).

The heterotopias were relatively stereotyped in their MR imaging appearance and location, occurring symmetrically in the immediate subcortical white matter of the bilateral inferior

cerebellar hemispheres, distinct from the inferior dentate nuclei (Fig 3). They typically comprised a single ellipsoid cellular conglomeration per hemisphere, though occasionally  $\geq 2$  clustered heterotopias were noted on a given side (Fig 4B, -D). Signal intensity was similar or identical to that of adjacent gray matter structures, standing out as hyperintense on T1 and hypointense on T2 relative to surrounding unmyelinated white matter, and hypointense on T1 and hyperintense on T2 relative to myelinated white matter (Fig 4). Heterotopias were isointense to the cortex on diffusion-weighted imaging when visible, though conspicuity was limited due to low spatial resolution and axial imaging plane.

Additional findings of cerebellar dysgenesis were identified in a total of 31/34 (91%) patients in our series, with 28/31 (90%) demonstrating multiple features. One patient who was status post medulloblastoma resection was excluded from analysis for features of dysgenesis. Among patients with dysgenesis, the most common findings were abnormal anteromedial rotation of the cerebellar tonsils (28/31, 90%), frequently but not invariably associated with inferior vermian hypoplasia (28/31, 90%) (Figs 5 and 6). Fewer patients demonstrated disorganized foliation of the cerebellar hemispheres (23/31, 74%) or superior vermis (5/31, 16%) (Fig 7). A single patient (1/35, 3%) had a Chiari I malformation. Most (25/26, 96%) patients with identifiable heterotopias had  $\geq 1$  additional finding of cerebellar dysgenesis.

The presence of heterotopias did not correlate with definite-versus-probable/possible clinical categorization (19/24 [79%] vs 6/10 [60%];  $P = .40$ ), or clinical-versus-genetic diagnosis (11/17 [65%] vs 15/18 [83%];  $P = .80$ ) of CHARGE syndrome. The presence of cerebellar dysgenesis correlated with definite-versus-probable/possible clinical categorization (23/23 [100%] vs 7/10 [70%];  $P = .02$ ), but the correlation did not hold after correction for multiple comparisons. There was no correlation between cerebellar dysgenesis and a clinical-versus-genetic diagnosis (15/17 [88%] vs 16/17 [94%];  $P = 1.00$ ) of CHARGE syndrome. Neither the presence of heterotopias nor the presence of cerebellar dysgenesis was more generally correlated with MR imaging field strength ( $P = .62$  for heterotopias,  $P = 1.00$  for dysgenesis), MR imaging section thickness ( $r = -0.29/P = .11$  for heterotopias;  $r = -0.34/P = .06$  for dysgenesis), or age at the time of MR imaging ( $r = -0.02/P = .920$  for heterotopias;  $r = 0.06/P = .75$  for dysgenesis).

## DISCUSSION

Microscopic cerebellar heterotopias are relatively common in children on histologic evaluation and are well-described in the pathology literature. Rorke et al<sup>14</sup> described 4 histologic subtypes of microscopic heterotopias identified in the cerebella of infants, most (147/200, 74%) of which were found in children without associated somatic or neural malformations. The only reported consistent syndromic association was with Trisomy 13.

Legendre et al<sup>15</sup> reported on the neuropathology of 40 aborted fetuses with an antenatal diagnosis of CHARGE syndrome and found “massive Purkinje cell heterotopias” in a minority (8/40, 20%). Lin et al<sup>16</sup> also reported a patient with CHARGE syndrome who had a “neuronal heterotopia” on pathologic examination. Neither publication provided specific histopathologic details. Identification of macroscopic cerebellar heterotopias on routine clinical MR imaging has only rarely been reported<sup>17-19</sup> and never previously in CHARGE syndrome, to our knowledge.

Histologic analysis in 2 of our patients who underwent postmortem

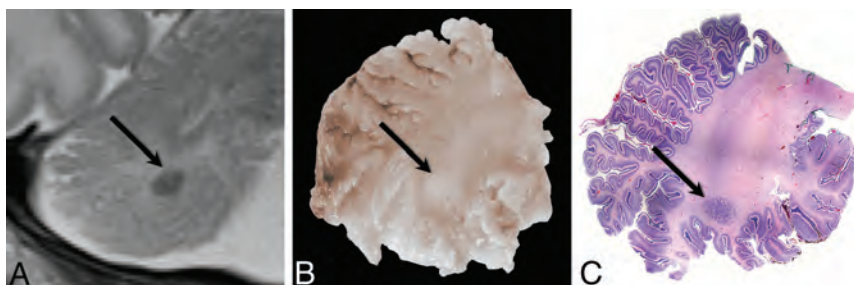


**FIG 1.** Radiologic-pathologic correlation in patient 7. Cropped coronal T2-weighted MR image of the right cerebellar hemisphere (A) obtained at 5 days of age shows the subcortical heterotopia (black arrow). Corresponding gross pathologic specimen (B) demonstrates the lesion as a white nodule (black arrow). Whole-mount hematoxylin-eosin-stained microscopic pathologic specimen (C) demonstrates the corresponding neuronal heterotopia (black arrow) (original magnification  $\times 1$ ).

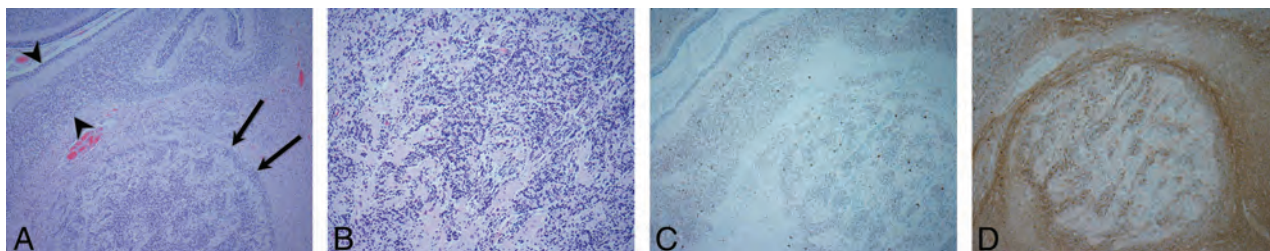


**FIG 2.** Photomicrographs demonstrate the histopathology of the heterotopia in patient 7. A, A cluster of disorganized neurons (black arrows) is juxtaposed to an adjacent normal-layered foliar cortex (bracketed by black arrowheads) (hematoxylin-eosin stain, original magnification  $\times 4$ ). B, Heterotopia comprises a dominant population of morphologically normal granular cell neurons in a background of mixed glial cells (hematoxylin-eosin stain, original magnification  $\times 20$ ). C, Purkinje cells (darkly staining cells) are scattered within the granular cell neurons as well as within the adjacent cortex (HuC stain, original magnification  $\times 4$ ). D, Nerve fibers (darkly staining material) surround and traverse the cluster of heterotopic neurons (calretinin stain, original magnification  $\times 4$ ).

examination confirmed the presence of large neuronal heterotopias, corresponding to the foci of abnormality on MR imaging. The cell rests comprised loose, disorganized clusters of morphologically normal granular cell neurons admixed with normal Purkinje cells in a background of mixed glial cells and neuronal processes. Histologically, these cell rests correspond to the “heterotaxia” subtype described by Rorke et al<sup>14</sup> according to the earlier classification of Brun.<sup>20</sup>

This study demonstrates that macroscopic cerebellar heterotopias are a frequent neuroimaging finding in CHARGE syndrome, present in at least 77% of patients in our series. They were most commonly and easily identified on the T2 sequence in the coronal plane, less commonly on the coronal T1 sequences. Of the 9 patients in whom the finding was not identified, substantial motion artifacts were present on one of the scans, 3 others lacked any sequences obtained in the coronal plane, and severe cerebellar architectural distortion related to Chiari I malformation was present on an additional scan, suggesting that the prevalence of 77% may be an underestimation. Indeed, one of the patients characterized on initial review as being negative for heterotopias with a motion-degraded examination had a subsequent follow-up examination that well-demonstrated bilateral heterotopias.

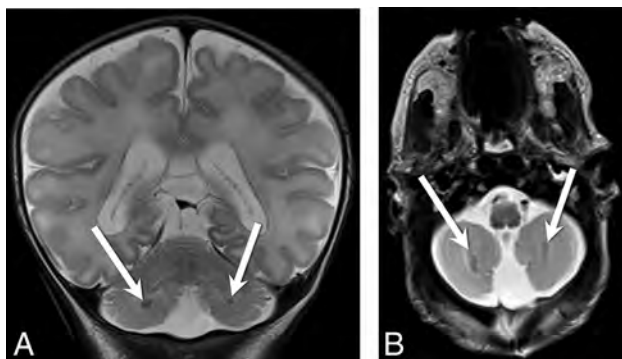


**FIG 3.** Coronal (A) and axial (B) T2-weighted images from patient 7 demonstrate bilateral cerebellar heterotopias (white arrows, A and B) with characteristic ellipsoid morphology and subcortical location in the bilateral inferior cerebellar hemispheres.

These cerebellar heterotopias are stereotyped in their MR imaging appearance and location. As expected, signal intensity relative to surrounding white matter evolved with progressive cerebellar myelination. Furthermore, they were consistently noted symmetrically within the immediate subcortical white matter of the bilateral inferior cerebellar hemispheres. Thus, they may prove useful as one of the more objective imaging findings of cerebellar dysgenesis in CHARGE syndrome.

Identification of these heterotopias was not associated with age at scanning, magnet strength, or scan parameters. These findings suggest that lack of awareness of this easily overlooked imaging finding is the primary driver behind lack of identification. In 1 case, however, heterotopias that were clearly identifiable on an MR imaging obtained at 3 days of age were substantially decreased in conspicuity on repeat imaging at 3 months of age, suggesting that transitional myelination in the deep cerebellar white matter that peaks at 3–4 postnatal months may limit detection in some cases.

Cerebellar heterotopias in our series largely occurred in the context of more widespread findings of cerebellar dysgenesis. Recent reports have described inferior vermian hypoplasia and generally disordered foliation in patients with CHARGE syndrome.<sup>5,6</sup> Our study both reinforces and expands this assertion. A greater proportion of patients in our series had cerebellar abnormalities than previously reported by Yu et al<sup>5</sup> or Sohn et al<sup>6</sup> (91% vs 55% vs 29%, respectively). Furthermore, we report a wider diversity of imaging findings of cerebellar maldevelopment. Although vermian hypoplasia was a common finding, we also noted relatively characteristic abnormalities in cerebellar fissuration and foliation, most notable in the inferior cerebellar hemispheres. These included anteromedial rotation of the inferior cerebellar tonsils, which was commonly but not invariably found in association with inferior vermian hypoplasia and therefore treated as a primary morphologic abnormality, as well as a diffusely disorganized foliar pattern. These findings extend and refine the phenotype of cerebellar dysgenesis seen in patients with CHARGE syndrome.

On the basis of mouse models, Yu et al<sup>5</sup> suggested that homeotic transformation of the dorsal first rhombomere related to altered *Fgf8* gene expression might be responsible for the cerebellar findings of CHARGE syndrome. The high

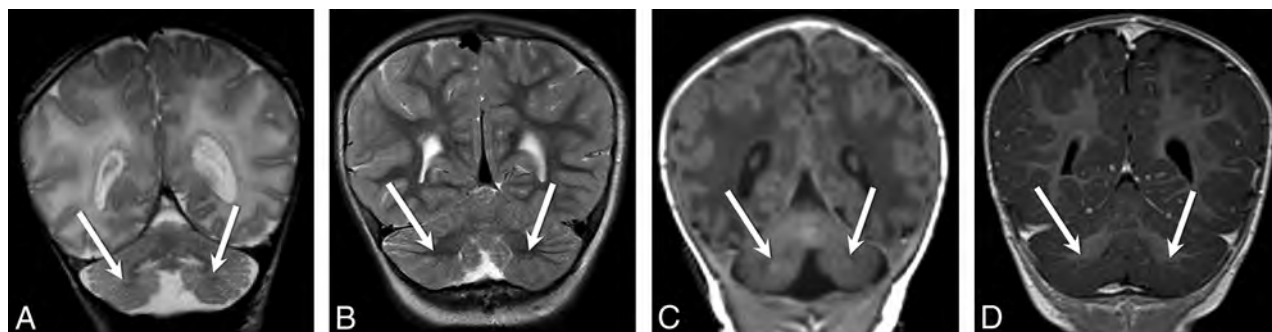


**FIG 4.** Coronal T2-weighted images from patient 15 at 3 days (A) and again at 3 years (B) of age demonstrate the expected evolution of the signal intensity of the heterotopias—hypointense relative to surrounding unmyelinated white matter (white arrows, A), becoming hyperintense relative to surrounding myelinated white matter (white arrows, B). Coronal T1-weighted images from patient 7 at 3 days of age (C) and patient 17 at 13 months of age (D) demonstrate similar isointensity of the heterotopias (white arrows, C and D) to gray matter.

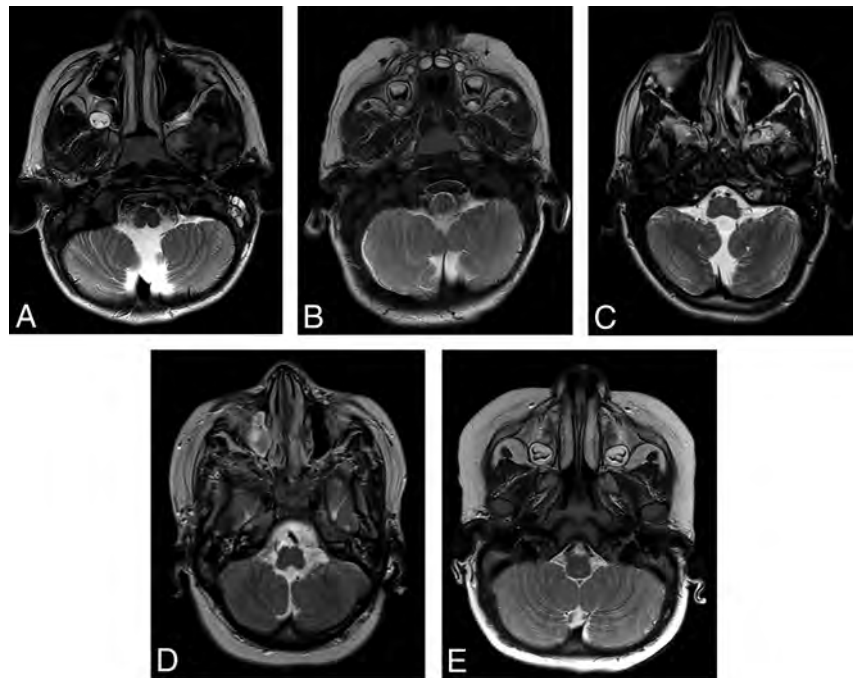


**FIG 5.** Axial T2-weighted images from patient 22 (A), patient 33 (B), patient 13 (C), and patient 1 (D) demonstrate anteromedial rotation of the inferior cerebellar tonsils. Axial T2-weighted image from a 10-month-old control patient is included for comparison (E).

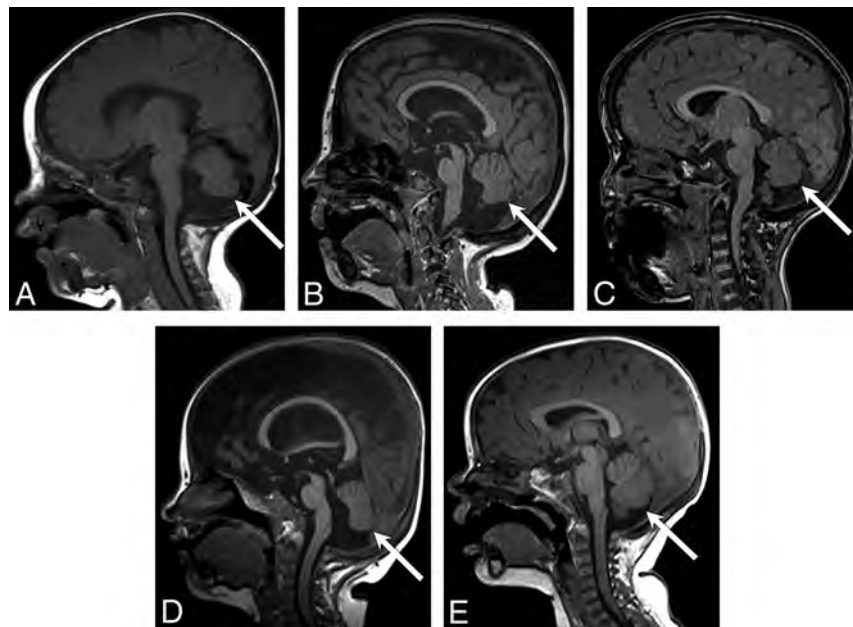


**FIG 6.** Sagittal T1-weighted images in patient 25 (A), patient 19 (B), patient 16 (C), and patient 12 (D) demonstrate a spectrum of inferior vermian hypoplasia. Axial T2-weighted image from a 10-month-old control patient is included for comparison (E).

prevalence of heterotopias in patients with CHARGE syndrome suggests that secondary or unrelated derangements in gene products related to cerebellar cellular migration may also be relevant. The foliation abnormalities we report are consistent with type 2 abnormalities in the classification of cerebellar malformations by Demareel,<sup>21</sup> which he suggested implicated a broader defect in cellular migration and organization.

The close association of cerebellar heterotopias and aberrant foliation is predicted by the classification system of cerebellar malformations proposed by Barkovich et al.<sup>18</sup> It is known that cerebellar neuronal migration and proliferation act as a trigger for normal foliation and fissuration.<sup>22,23</sup> Mice with pathogenic mutations in genes encoding cellular guidance proteins may demonstrate a phenotype that includes a deficient vermis, cerebellar heterotopias, and dysplastic foliation.<sup>24,25</sup> It is likely that

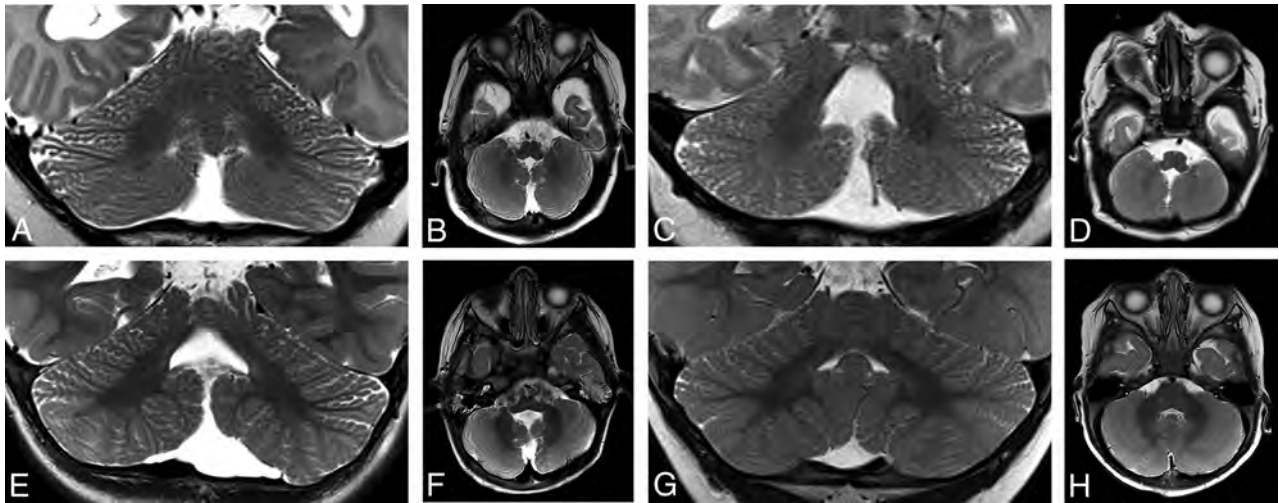


**FIG 7.** Coronal and axial T2-weighted images from patient 11 (A and B), patient 30 (C and D), and patient 22 (E and F) demonstrate a diffusely disorganized pattern of cerebellar foliation of the bilateral cerebellar hemispheres. Coronal (G) and axial (H) T2-weighted images from a 10-month-old control patient are included for comparison.

varied patterns of expression in multiple genes secondary to the underlying *CHD7* mutation, including those contributory to cerebellar cellular migration, are responsible for the cerebellar dysgenesis in CHARGE syndrome.

## CONCLUSIONS

We present the novel imaging finding of characteristic cerebellar neuronal heterotopias in patients with CHARGE syndrome, commonly associated with disordered foliation and abnormal inferior cerebellar morphology, thereby expanding the phenotype of cerebellar dysgenesis in this syndrome. The heterotopias are symmetrically located in the subcortical white matter of the bilateral inferior cerebellar hemispheres and were common in our cohort. Recognition of these findings should prompt consideration of CHARGE syndrome in the undiagnosed patient, and they can serve as supportive neuroimaging markers for the condition in patients for whom the diagnosis is being considered.

Disclosures: Joe Rutledge—UNRELATED: Travel/Accommodations/Meeting Expenses Unrelated to Activities Listed: College of American Pathologists, Comments: reimbursement of travel to committee meetings (3 times a year).

## REFERENCES

- Vissers LE, van Ravenswaaij CM, Admiraal R, et al. Mutations in a new member of the chromodomain gene family cause CHARGE syndrome. *Nat Genet* 2004;36:955–57 CrossRef Medline
- Blake KD, Davenport SL, Hall BD, et al. CHARGE association: an update and review for the primary pediatrician. *Clin Pediatr (Phila)* 1998;37:159–73 CrossRef Medline
- Amiel J, Attiéé-Bitach T, Marianowski R, et al. Temporal bone anomaly proposed as a major criteria for diagnosis of CHARGE syndrome. *Am J Med Genet* 2001;99:124–27 CrossRef Medline
- Verloes A. Updated diagnostic criteria for CHARGE syndrome: a proposal. *Am J Med Genet A* 2005;133A:306–08 Medline
- Yu T, Meiners LC, Danielsen K, et al. Deregulated FGF and homeotic gene expression underlies cerebellar vermis hypoplasia in CHARGE syndrome. *Elife* 2013;2:e01305 CrossRef Medline
- Sohn YB, Ko JM, Shin CH, et al. Cerebellar vermis hypoplasia in CHARGE syndrome: clinical and molecular characterization of 18 unrelated Korean patients. *J Hum Genet* 2016;61:235–39 CrossRef Medline
- Fujita K, Aida N, Asakura Y, et al. Abnormal basioccipital development in CHARGE syndrome. *AJNR Am J Neuroradiol* 2009;30:629–34 CrossRef Medline
- Natung T, Goyal A, Handique A, et al. Symmetrical chorioretinal colobomata with craniovertebral junction anomalies in CHARGE syndrome: a case report with review of literature. *J Clin Imaging Sci* 2014;4:5 CrossRef Medline
- Hoch MJ, Patel SH, Jethanamest D, et al. Head and neck MRI findings in CHARGE syndrome. *AJNR Am J Neuroradiol* 2017;38:2357–63 CrossRef Medline
- Mahdi E, Whitehead MT. Coronal clival cleft in CHARGE syndrome. *Neuroradiol J* 2017;30:574–77 CrossRef Medline
- Mahdi ES, Whitehead MT. Clival malformations in CHARGE syndrome. *AJNR Am J Neuroradiol* 2018;39:1153–56 CrossRef Medline
- de Geus CM, Bergman JEH, van Ravenswaaij-Arts CM, et al. Imaging of clival hypoplasia in CHARGE syndrome and hypothesis for development: a case-control study. *AJNR Am J Neuroradiol* 2018;39:1938–42 CrossRef Medline
- Lalani SR, Hefner MA, Belmont JW, et al. CHARGE syndrome. In: Adam MP, Pagon RA, Ardinger HH, et al, eds. *GeneReviews*. Seattle: University of Washington; 2012
- Rorke LB, Fogelson MH, Riggs HE. Cerebellar heterotopia in infancy. *Dev Med Child Neurol* 1968;10:644–50 CrossRef Medline
- Legendre M, Gonzales M, Goudefroye G, et al. Antenatal spectrum of CHARGE syndrome in 40 fetuses with CHD7 mutations. *J Med Genet* 2012;49:698–707 CrossRef Medline
- Lin AE, Chin AJ, Devine W, et al. The pattern of cardiovascular malformation in the CHARGE association. *Am J Dis Child* 1987;141:1010–13 CrossRef Medline
- Patel S, Barkovich AJ. Analysis and classification of cerebellar malformations. *AJNR Am J Neuroradiol* 2002;23:1074–87 Medline
- Barkovich AJ, Millen KJ, Dobyns WB. A developmental and genetic classification for midbrain-hindbrain malformations. *Brain* 2009;132:3199–230 CrossRef Medline
- Salvati A, Dicuonzo F, Carella A, et al. A case of isolated focal cerebellar heterotopia in a patient affected by HHT: MR and

- MR spectroscopy findings.** *J Neurol Neurophysiol* 2010;01:107 CrossRef
20. Brun A. **Zur Kenntnis der Bildungsfehler des Kleinhirns; Epikritische Bemerkungen zur Entwicklungspathologie, Morphologie und Klinik der umschriebenen Entwicklung-shemmungen des Neocerebellums.** *Schweiz Arch Neurol Psych* 1917;1:48–105
21. Demaerel P. **Abnormalities of cerebellar foliation and fissuration: classification, neurogenetics and clinicoradiological correlations.** *Neuroradiology* 2002;44:639–46 CrossRef Medline
22. Millen KJ, Millonig JH, Wingate RJ, et al. **Neurogenetics of the cerebellar system.** *J Child Neurol* 1999;14:574–82 CrossRef Medline
23. Sudarov A, Joyner AL. **Cerebellum morphogenesis: the foliation pattern is orchestrated by multi-cellular anchoring centers.** *Neural Dev* 2007;2:26 CrossRef Medline
24. Kuwamura M, Shirota A, Yamate J, et al. **Analysis of aberrant neuronal migrations in the hereditary cerebellar vermis defect (CVD) rat using bromodeoxyuridine immunohistochemistry.** *Acta Neuropathol* 1998;95:143–48 CrossRef Medline
25. Kuramoto T, Kuwamura M, Serikawa T. **Rat neurological mutations cerebellar vermis defect and hobble are caused by mutations in the netrin-1 receptor gene Unc5h3.** *Brain Res Mol Brain Res* 2004; 122:103–08 CrossRef Medline

# White Matter Injury and Structural Anomalies in Infants with Prenatal Opioid Exposure

S.L. Merhar, N.A. Parikh, A. Braimah, B.B. Poindexter, J. Tkach, and B. Kline-Fath



## ABSTRACT

**SUMMARY:** Previous studies have not found structural injury or brain malformations in infants and children with prenatal opioid exposure. As part of an ongoing study evaluating neuroimaging in infants with prenatal opioid exposure, we reviewed structural brain MR imaging in 20 term infants with prenatal opioid exposure and 20 term controls at 4–8 weeks of age. We found that 8 of the 20 opioid-exposed infants had punctate white matter lesions or white matter signal abnormality on structural MR imaging, and 2 of the opioid-exposed infants had a septopreoptic fusion anomaly. No controls had white matter injury or structural malformations. Our findings underscore the importance of clinical neurodevelopmental follow-up and the need for more comprehensive imaging and long-term outcomes research following prenatal opioid exposure.

Due to the ongoing opioid epidemic, >40,000 infants are now born exposed to opioids each year in the United States. The few previous studies evaluating structural neuroimaging in infants with prenatal opioid exposure have found no increase in the incidence of macrostructural injury or malformations.<sup>1,2</sup> More recent studies have shown decreased head circumference,<sup>3</sup> decreased brain volumes,<sup>4,5</sup> and altered white matter microstructure<sup>6</sup> in infants with prenatal opioid exposure compared with controls. Prior studies may have been confounded by coexposures because most opioid-exposed infants are also exposed to tobacco in utero,<sup>7</sup> and a large proportion are also exposed to hepatitis C.<sup>8</sup> Prenatal tobacco exposure is also associated with decreased head circumference<sup>9</sup> and brain volumes.<sup>10–12</sup> There are no reports of neuroimaging after prenatal hepatitis C exposure in infants or children, but adults with active hepatitis C infection are known to have white matter changes.<sup>13</sup> As part of a larger prospective study, we acquired structural brain MRIs in infants with prenatal opioid exposure and controls. Here we report our findings of white matter injury and congenital structural malformations in infants with prenatal opioid exposure, all of whom also

had tobacco exposure and all of whom except one had hepatitis C exposure.

## MATERIALS AND METHODS

As part of an ongoing prospective cohort study on functional brain connectivity in infants with opioid exposure, we acquired structural MR imaging in 4- to 8-week-old infants with confirmed prenatal opioid exposure and unexposed healthy term controls. Inclusion criteria for the opioid-exposed group included infants  $\geq 37$  weeks' gestation with known exposure to maternal buprenorphine or methadone during pregnancy and no known prenatal alcohol exposure. Inclusion criteria for controls were infants of  $\geq 37$  weeks' gestation with no opioid, alcohol, or illicit drug exposure during pregnancy confirmed by maternal urine toxicology screen and maternal history. Exclusion criteria for both groups included a 5-minute Apgar score of  $< 7$ , any need for positive pressure ventilation at any time after birth, head trauma, and known chromosomal or congenital anomalies potentially affecting the central nervous system. Opioid-exposed infants were recruited from surrounding birth hospitals and the Cincinnati Children's opioid-exposed follow-up clinic. Controls were recruited from surrounding birth hospitals, flyers in surrounding pediatric offices, and e-mails sent to all hospital employees.

The study was approved by the Cincinnati Children's Hospital Medical Center Institutional Review Board, and written informed consent was obtained from parents/guardians. Images were acquired on a 3T Ingenia scanner (Philips Healthcare, Best, the Netherlands) with a 32-channel head coil during natural sleep using the feed-and-swaddle method. MR imaging included a

Received July 1, 2019; accepted after revision September 3.

From the Perinatal Institute, Division of Neonatology (S.L.M., N.A.P., B.B.P.), Pediatric Neuroimaging Research Consortium (A.B.), and Department of Radiology (J.T., B.K.-F.), Cincinnati Children's Hospital Medical Center, Cincinnati, Ohio; and Department of Pediatrics (S.L.M., N.A.P., B.B.P.), University of Cincinnati College of Medicine, Cincinnati, Ohio.

Dr Merhar was supported by National Institutes of Health KL2 TR1426.

Please address correspondence to Stephanie L. Merhar, MD, MS, Cincinnati Children's Hospital, Division of Neonatology, 3333 Burnet Ave ML 7009, Cincinnati OH 45229; e-mail: Stephanie.merhar@cchmc.org

Indicates open access to non-subscribers at [www.ajnr.org](http://www.ajnr.org)

<http://dx.doi.org/10.3174/ajnr.A6282>

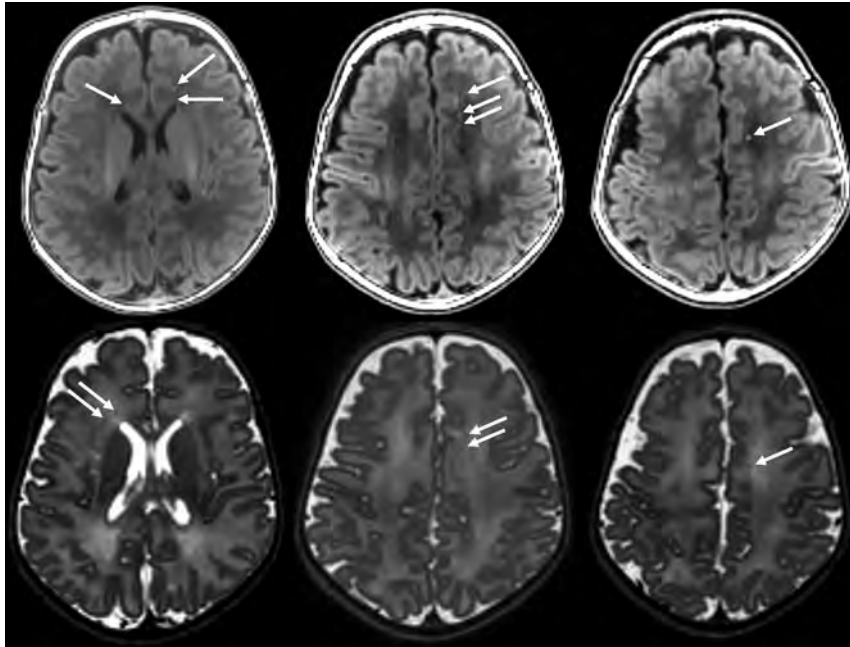


**FIG 1.** Example of punctate white matter injury seen in an infant with prenatal opioid exposure. Arrows show punctate white matter lesions. Upper row, T1-weighted images. Lower row, T2-weighted images.

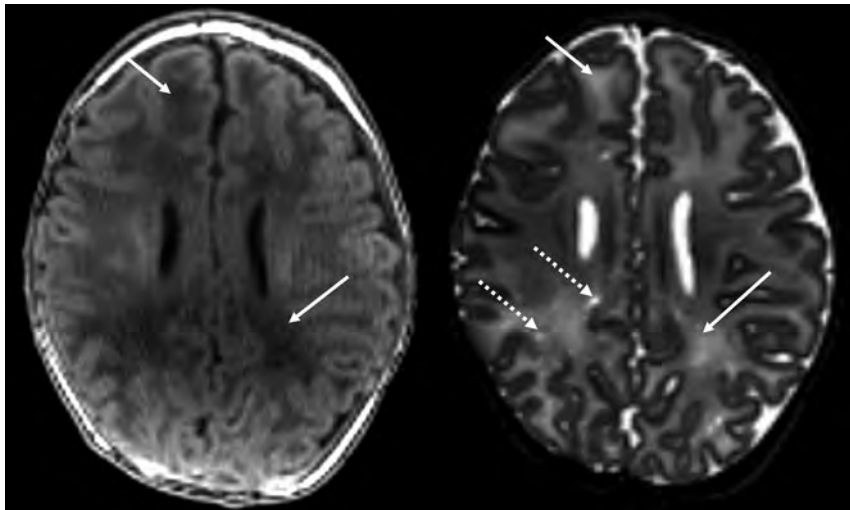


**FIG 2.** Example of diffuse white matter injury in infants with prenatal opioid exposure. Solid arrows denote abnormal T1 and T2 prolongation (which is bilateral but only denoted on the right). Dotted arrow demonstrates an example of perivascular space enlargement. Left, T1-weighted image. Right, T2-weighted image.

sagittal 3D T1-weighted gradient-echo sequence (voxel size =  $1 \times 1 \times 1$  mm; scan time 3 minutes 6 seconds), an axial T2-weighted fast spin-echo sequence (voxel size =  $1 \times 1.11 \times 1$  mm; scan time 3 minutes 19 seconds), an axial 6-direction single-shot echo-planar DWI sequence (b-value = 800; voxel size =  $2 \times 2 \times 2$  mm; scan time = 1:47 minutes), and an axial 3D-SWI sequence (voxel size =  $0.6 \times 0.6 \times 2$  mm; scan time 4 minutes 3 seconds).

We reviewed electronic medical records from the infant's birth hospitalization for information including gestational age,

birth weight/length/head circumference, sex, Apgar scores, results of maternal urine toxicology screen (done universally at the time of delivery at our surrounding birth hospitals), maternal medications and medical problems during pregnancy, maternal hepatitis C status, and length of hospital stay. Additional information reviewed for infants with opioid exposure included the results of neonate toxicology screen, the need for and type of treatment for neonatal abstinence syndrome, and the length of opioid treatment for neonatal abstinence syndrome, if necessary. At the time of the MR imaging visit, mothers filled out a questionnaire with self-reported information about their use of prescription medications, illicit drugs, alcohol, and tobacco during pregnancy.

MR images were reviewed by a single pediatric neuroradiologist blinded to clinical history. Initially a clinical read was reported to rule out structural injury, and then MRIs were scored in detail using a scoring system based on Kidokoro et al,<sup>14</sup> which included white matter abnormalities (cystic white matter lesions, focal signal abnormality, corpus callosum thinning, dilated lateral ventricles), cortical gray matter abnormalities, and deep gray matter and cerebellar abnormalities. The MR imaging scores were based on all 4 sequences (T1, T2, DWI, and SWI).

## RESULTS

We included 40 infants, 20 with prenatal opioid exposure and 20 controls. Eight of the 20 infants (40%) with prenatal opioid exposure had punctate foci of white matter injury or more diffuse white matter injury seen on the initial clinical read by the radiologist.

Two of the opioid-exposed infants were also incidentally found to have septo-optic fusion, a very mild form of holoprosencephaly. One of these 2 infants also had punctate white matter lesions. An example of the punctate white matter injury is shown in Fig 1. An example of the diffuse white matter injury is shown in Fig 2. No white matter injury or congenital structural malformations were observed in any of the control infants. One control infant had mildly enlarged extra-axial fluid spaces, one had a borderline small cerebellar vermis, and one had germinolytic cysts at the caudothalamic grooves bilaterally. One infant in each group (opioid-exposed and controls) had

### Characteristics of prenatal opioid-exposed and healthy term control study cohorts

	WMI (n = 8)	No WMI (n = 12)	Control (n = 20)
Gestational age at birth (weeks) <sup>a</sup>	38.9 (0.74)	38.9 (0.93)	39.0 (0.80)
Day of life at scan <sup>a</sup>	40.6 (9.5)	43.0 (8.5)	39.3 (6.1)
Birth weight (g) <sup>a</sup>	3172 (302)	2982 (321)	3201 (460)
Birth head circumference (cm) <sup>a</sup>	34.4 (1.2)	33.9 (1.4)	34.0 (1.5)
Mom methadone <sup>b</sup>	4 (50%)	4 (33%)	0 (0%)
Mom buprenorphine <sup>b</sup>	4 (50%)	8 (67%)	0 (0%)
Mom street drugs <sup>b</sup>	3 (38%)	3 (25%)	0 (0%)
Mom alcohol <sup>b</sup>	0 (0%)	0 (0%)	0 (0%)
Mom smoking <sup>b</sup>	8 (100%)	11 (92%)	0 (0%)
Mom hepatitis C <sup>b</sup>	7 (88%)	9 (75%)	0 (0%)
Baby treated for NAS <sup>b</sup>	5 (63%)	7 (58%)	0 (0%)

**Note:**—NAS indicates neonatal abstinence syndrome; WMI, WM injury; Mom, mother.

<sup>a</sup> Values are mean (SD).

<sup>b</sup> Values are No. (%).

a small cerebellar germinal matrix hemorrhage. No other infants in either group had cortical gray matter, deep gray matter, or cerebellar abnormalities. Demographics and exposures for the 3 groups (prenatal opioid exposure with WM injury, prenatal opioid exposure without WM injury, and unexposed controls) are shown in the Table. As shown in the Table, all 8 infants with white matter injury also had tobacco exposure and 7 of the 8 also had hepatitis C exposure. No infant in any group was exposed to alcohol prenatally per parental report.

### DISCUSSION

White matter injury is described most commonly in infants born preterm, but it can also occur in full-term infants who sustain in utero insults during a susceptible period of white matter development.<sup>15</sup> Both diffuse and punctate white matter lesions are thought to be related to the selective vulnerability of preoligodendrocytes.<sup>15</sup> Punctate white matter lesions are small patches of increased signal intensity seen on T1-weighted imaging corresponding to areas of either small necroses, glial scars, or microhemorrhage.<sup>16</sup> Punctate white matter lesions have also been reported in term and late-preterm infants with congenital heart disease, hypoxic-ischemic encephalopathy, and genetic disorders, and following neonatal surgery.<sup>17</sup> In term infants with congenital heart disease, punctate white matter lesions are thought to be due to abnormal brain maturation due to disrupted blood flow and hypoxia from the cardiac lesion,<sup>18</sup> leading to a delay in the maturation of preoligodendrocytes.<sup>19</sup> Neurodevelopmental sequelae of punctate white matter lesions are variable, with some preterm infants with small isolated lesions (as in our cohort) reported as healthy, while others with more extensive lesion burden displaying motor and cognitive delays.<sup>20,21</sup> Diffuse non-necrotic white matter injury is also commonly seen in preterm infants and also reflects disruption of the normal maturation of preoligodendrocytes.<sup>15,16,22</sup> Outcomes after this diffuse mild injury are also variable. Studies that used qualitative diagnosis of diffuse signal abnormalities report normal developmental outcomes,<sup>23-25</sup> while studies that quantify it objectively or follow children with extensive hyperintensity report later cognitive and language delays.<sup>26,27</sup>

In our cohort of infants with prenatal opioid exposure, the etiology of the white matter injury is unclear. All 8 mothers were on medication-assisted therapy (in methadone treatment programs

and 4 in buprenorphine treatment programs) throughout pregnancy, and 3 mothers had used street drugs early in pregnancy per maternal report and review of maternal urine toxicology. All of the mothers smoked during this pregnancy, and all except 1 of the mothers were positive for hepatitis C. WM injury has not been previously reported in the literature in association with prenatal opioid, tobacco, or hepatitis C exposure.

Two of the infants with prenatal opioid exposure were also incidentally found to have a septopreoptic fusion anomaly. This anomaly has been

described in a single case series in the literature as the mildest form of holoprosencephaly, in which the septal and preoptic regions are fused and the rest of the brain undergoes normal cleavage.<sup>28</sup> Cleavage of the prosencephalon normally occurs between days 18 and 28 of gestation.<sup>29</sup> Holoprosencephaly has been associated with various genes and also environmental factors such as maternal diabetes, maternal alcohol use, and maternal infections.<sup>30</sup> One of the 2 infants with this malformation had a mother with “borderline gestational diabetes” during her pregnancy, but the other had no record of diabetes in the maternal or infant chart. We could not find any literature describing an association between prenatal opioid exposure and holoprosencephaly in animal models. This finding in 2 of our 20 patients could very well be coincidental because there are no other reported cases of this association in either the human or animal literature.

The few studies evaluating structural brain MR imaging in infants with prenatal opioid exposure have concluded that there is no increase in macrostructural injury compared with controls.<sup>1,2</sup> One of these studies used a 1.5T MR imaging scanner with thicker slices (4 mm), which could explain the lack of findings,<sup>2</sup> but the other used a 3T scanner with 1-mm slices,<sup>1</sup> similar to our protocol. Studies using more advanced MR imaging techniques have documented smaller brain volumes,<sup>4,5,31,32</sup> altered white matter microstructure,<sup>6,33,34</sup> and decreased cortical surface area and thickness<sup>5</sup> in opioid-exposed infants and children compared with controls. None of these studies controlled for maternal smoking, and many included mothers with polysubstance use during pregnancy. However, animal studies have consistently shown the effects of prenatal methadone and buprenorphine on neurotransmitter biosynthesis,<sup>35,36</sup> neurogenesis,<sup>37</sup> and white matter development,<sup>38,39</sup> providing evidence that opioids themselves likely affect brain development.

Overt brain injury has not been reported in infants exposed to tobacco during pregnancy. However, studies have shown an association between prenatal tobacco exposure and smaller brain volumes<sup>10</sup> and decreased cortical thickness.<sup>10,12,40</sup> There is no information in the literature about perinatal hepatitis C exposure and the developing brain, especially in the large majority of infants who are exposed to the virus but do not acquire the infection. However, hepatitis C is known to invade the central nervous

system and lead to neurotoxicity, including altered white matter integrity in adults.<sup>13</sup>

## CONCLUSIONS

We found that 8 of 20 infants with prenatal opioid exposure, all of whom also had coexposure to tobacco and all except 1 who had exposure to hepatitis C, had mild white matter injury seen on structural MR imaging at 4–8 weeks of age, and 2 of the 20 opioid-exposed infants had a septopreoptic fusion anomaly. Our study was limited by small sample size, and further studies must explore these associations in a much larger population.

Disclosures: Stephanie L. Merhar—RELATED: Grant: National Institutes of Health, Comments: KL2 TR 1426\*; UNRELATED: Employment: Children's Hospital Medical Center (Cincinnati). Brenda B. Poindexter—RELATED: Grant: National Institutes of Health, Comments: National Institutes of Health/Eunice Kennedy Shriver National Institute of Child Health and Human Development UGI HD027853-2751 Clinical Research Investigator Supplement Award\*; UNRELATED: Employment: Cincinnati Children's Hospital. \*Money paid to institution.

## REFERENCES

1. Sirnes E, Elgen IB, Chong WK, et al. **Cerebral magnetic resonance imaging in children with prenatal drug exposure.** *Clin Pediatr (Phila)* 2017;56:326–32 CrossRef Medline
2. Kahila H, Kivittie-Kallio S, Halmesmaki E, et al. **Brain magnetic resonance imaging of infants exposed prenatally to buprenorphine.** *Acta Radiol* 2007;48:228–31 CrossRef Medline
3. Towers CV, Hyatt BW, Visconti KC, et al. **Neonatal head circumference in newborns with neonatal abstinence syndrome.** *Pediatrics* 2019;143:e20180541 CrossRef Medline
4. Sirnes E, Olstedal L, Bartsch H, et al. **Brain morphology in school-aged children with prenatal opioid exposure: a structural MRI study.** *Early Hum Dev* 2017;106-107:33–39 CrossRef Medline
5. Nygaard E, Slinning K, Moe V, et al. **Neuroanatomical characteristics of youths with prenatal opioid and poly-drug exposure.** *Neurotoxicol Teratol* 2018;68:13–26 CrossRef Medline
6. Monnelly VJ, Anblagan D, Quigley A, et al. **Prenatal methadone exposure is associated with altered neonatal brain development.** *Neuroimage Clin* 2018;18:9–14 CrossRef Medline
7. Chisolm MS, Fitzsimons H, Leoutsakos JM, et al. **A comparison of cigarette smoking profiles in opioid-dependent pregnant patients receiving methadone or buprenorphine.** *Nicotine Tob Res* 2013;15:1297–1304 CrossRef Medline
8. Epstein RL, Sabharwal V, Wachman EM, et al. **Perinatal transmission of hepatitis C virus: defining the cascade of care.** *J Pediatr* 2018;203:34–40.e31 CrossRef Medline
9. Ekblad M, Korkeila J, Lehtonen L. **Smoking during pregnancy affects foetal brain development.** *Acta Paediatr* 2015;104:12–18 CrossRef Medline
10. El Marroun H, Schmidt MN, Franken IH, et al. **Prenatal tobacco exposure and brain morphology: a prospective study in young children.** *Neuropsychopharmacol* 2014;39:792–800 CrossRef Medline
11. Roza SJ, Verburg BO, Jaddoe VW, et al. **Effects of maternal smoking in pregnancy on prenatal brain development: the Generation R Study.** *Eur J Neurosci* 2007;25:611–17 CrossRef Medline
12. Anblagan D, Jones NW, Costigan C, et al. **Maternal smoking during pregnancy and fetal organ growth: a magnetic resonance imaging study.** *PLoS One* 2013;8:e67223 CrossRef Medline
13. Bladowska J, Zimny A, Knysz B, et al. **Evaluation of early cerebral metabolic, perfusion and microstructural changes in HCV-positive patients: a pilot study.** *J Hepatol* 2013;59:651–57 CrossRef Medline
14. Kidokoro H, Neil JJ, Inder TE. **New MR imaging assessment tool to define brain abnormalities in very preterm infants at term.** *AJNR Am J Neuroradiol* 2013;34:2208–14 CrossRef Medline
15. Back SA. **White matter injury in the preterm infant: pathology and mechanisms.** *Acta Neuropathol* 2017;134:331–49 CrossRef Medline
16. Volpe JJ. **Confusions in nomenclature: “periventricular leukomalacia” and “white matter injury”—identical, distinct, or overlapping?** *Pediatr Neurol* 2017;73:3–6 CrossRef Medline
17. Hayman M, van Wezel-Meijler G, van Straaten H, et al. **Punctate white-matter lesions in the full-term newborn: underlying aetiology and outcome.** *Eur J Paediatr Neurol* 2019;23:280–87 CrossRef Medline
18. Marelli A, Miller SP, Marino BS, et al. **Brain in congenital heart disease across the lifespan: the cumulative burden of injury.** *Circulation* 2016;133:1951–62 CrossRef Medline
19. Guo T, Chau V, Peyvandi S, et al. **White matter injury in term neonates with congenital heart diseases: topology and comparison with preterm newborns.** *Neuroimage* 2019;185:742–49 CrossRef Medline
20. Cornette LG, Tanner SF, Ramenghi LA, et al. **Magnetic resonance imaging of the infant brain: anatomical characteristics and clinical significance of punctate lesions.** *Arch Dis Child Fetal Neonatal Ed* 2002;86:F171–77 CrossRef Medline
21. Tumor N, Benders MJ, Counsell SJ, et al. **Punctate white matter lesions associated with altered brain development and adverse motor outcome in preterm infants.** *Sci Rep* 2017;7:13250 CrossRef Medline
22. Parikh NA, Pierson CR, Rusin JA. **Neuropathology associated with diffuse excessive high signal intensity abnormalities on magnetic resonance imaging in very preterm infants.** *Pediatr Neurol* 2016;65:78–85 CrossRef Medline
23. de Bruine FT, van den Berg-Huysmans AA, Leijser LM, et al. **Clinical implications of MR imaging findings in the white matter in very preterm infants: a 2-year follow-up study.** *Radiology* 2011;261:899–906 CrossRef Medline
24. Jeon TY, Kim JH, Yoo SY, et al. **Neurodevelopmental outcomes in preterm infants: comparison of infants with and without diffuse excessive high signal intensity on MR images at near-term-equivalent age.** *Radiology* 2012;263:518–26 CrossRef Medline
25. Broström L, Bolk J, Padilla N, et al. **Clinical implications of diffuse excessive high signal intensity (DEHSI) on neonatal MRI in school age children born extremely preterm.** *PLoS One* 2016;11:e0149578 CrossRef Medline
26. Parikh NA, He L, Bonfante-Mejia E, et al. **Automatically quantified diffuse excessive high signal intensity on MRI predicts cognitive development in preterm infants.** *Pediatr Neurol* 2013;49:424–30 CrossRef Medline
27. Mürner-Lavanchy IM, Kidokoro H, Thompson DK, et al. **Thirteen-year outcomes in very preterm children associated with diffuse excessive high signal intensity on neonatal magnetic resonance imaging.** *J Pediatr* 2019;206:66–71.e61 CrossRef Medline
28. Hahn JS, Barnes PD, Clegg NJ, et al. **Septopreoptic holoprosencephaly: a mild subtype associated with midline craniofacial anomalies.** *AJNR Am J Neuroradiol* 2010;31:1596–1601 CrossRef Medline
29. Dubourg C, Bendavid C, Pasquier L, et al. **Holoprosencephaly.** *Orphanet J Rare Dis* 2007;2:8 CrossRef Medline
30. Johnson CY, Rasmussen SA. **Non-genetic risk factors for holoprosencephaly.** *Am J Med Genet C Semin Med Genet* 2010;154C:73–85 CrossRef Medline
31. Yuan Q, Rubic M, Seah J, et al. **Do maternal opioids reduce neonatal regional brain volumes? A pilot study.** *J Perinatol* 2014;34:909–13 CrossRef Medline
32. Wallhovd KB, Moe V, Slinning K, et al. **Volumetric cerebral characteristics of children exposed to opiates and other substances in utero.** *Neuroimage* 2007;36:1331–44 CrossRef Medline
33. Wallhovd KB, Watts R, Amlien I, et al. **Neural tract development of infants born to methadone-maintained mothers.** *Pediatr Neurol* 2012;47:1–6 CrossRef Medline
34. Wallhovd KB, Westlye LT, Moe V, et al. **White matter characteristics and cognition in prenatally opiate- and polysubstance-exposed children: a diffusion tensor imaging study.** *AJNR Am J Neuroradiol* 2010;31:894–900 CrossRef Medline

35. Robinson SE, Maher JR, Wallace MJ, et al. **Perinatal methadone exposure affects dopamine, norepinephrine, and serotonin in the weanling rat.** *Neurotoxicol Teratol* 1997;19:295–303 CrossRef Medline
36. Wu VW, Mo Q, Yabe T, et al. **Perinatal opioids reduce striatal nerve growth factor content in rat striatum.** *Eur J Pharmacol* 2001; 414:211–14 CrossRef Medline
37. Wu CC, Hung CJ, Shen CH, et al. **Prenatal buprenorphine exposure decreases neurogenesis in rats.** *Toxicol Lett* 2014;225:92–101 CrossRef Medline
38. Vestal-Laborde AA, Eschenroeder AC, Bigbee JW, et al. **The opioid system and brain development: effects of methadone on the oligodendrocyte lineage and the early stages of myelination.** *Dev Neurosci* 2014;36:409–21 CrossRef Medline
39. Sanchez ES, Bigbee JW, Fobbs W, et al. **Opioid addiction and pregnancy: perinatal exposure to buprenorphine affects myelination in the developing brain.** *Glia* 2008;56:1017–27 CrossRef Medline
40. Toro R, Leonard G, Lerner JV, et al. **Prenatal exposure to maternal cigarette smoking and the adolescent cerebral cortex.** *Neuropsychopharmacol* 2008;33:1019–27 CrossRef Medline

# Intraspinal Paragonimiasis in Children: MRI Findings and Suggestions for Pathogenesis

Y. Qin, J. Cai, W. Ji, X. Chen, L. Tian, S. Jun, L. Wang, and X. He

## ABSTRACT

**BACKGROUND AND PURPOSE:** Intraspinal paragonimiasis is a rare entity for which imaging findings have seldom been described. The present study investigated the MR imaging features of spinal paragonimiasis, thus providing diagnostic imaging evidence and exploring the possible pathogenesis of intraspinal paragonimiasis.

**MATERIALS AND METHODS:** The clinical and imaging findings of spinal paragonimiasis in 6 children were analyzed retrospectively. Spinal MR imaging was performed in all patients, 5 of whom also underwent enhanced MR imaging. The diagnosis was confirmed by enzyme-linked immunosorbent assay in all cases and postoperative pathology in 4 cases.

**RESULTS:** All cases manifested as fusiform-shaped or beanlike masses in the extradural space in the thoracic spine. The extradural masses were connected with pleural lesions through the intervertebral foramen. The plain MR imaging scan showed mixed signals with predominant isointensity on T1WI and hyperintensity on T2WI, among which 5 (5/6) masses presented as patchy hemorrhage with hyperintensity on T1WI. On enhanced scans, all masses (5/5) showed heterogeneous marked enhancement, with thickening and enhancement in the adjacent spinal meninges (5/5). Various degrees of spinal cord compression and edema were found in 5 cases (5/6).

**CONCLUSIONS:** MR imaging is sensitive for detecting and characterizing spinal paragonimiasis. The MR imaging features of intraspinal granulomas included localization to the extradural space and thoracic segment, connections between intraspinal lesions and pleural lesions through the intervertebral foramen, and hemorrhagic foci within the mass. These findings support an intraspinal mode of paragonimiasis pathogenesis: The *Paragonimus* larvae migrate from the chest into the extradural space through the intervertebral foramen.

Paragonimiasis is an infestation caused by a lung fluke of the genus *Paragonimus*.<sup>1</sup> Human infection is usually caused by eating raw or undercooked crayfish that harbor these parasites or drinking infested fresh water. The metacercariae of the *Paragonimus* excyst in the small intestine penetrate through the intestinal wall into the peritoneal cavity, then migrate through the diaphragm to the pleural space and into the lungs, and finally become adult organisms. For some species, the lung flukes cannot develop into adults in humans, and the larvae can migrate into other sites from the lung or pleural spaces.<sup>1</sup> The CNS is the most common site of extrapulmonary paragonimiasis.<sup>2</sup> Intracranial paragonimiasis has been comprehensively reported, and some imaging features have been summarized and regarded as

important diagnostic evidence.<sup>3,4</sup> However, only a few isolated cases with occurrence in the spinal canal have been reported.<sup>5-8</sup>

In a review of the literature, most of these cases were reported in the 1950s and 1960s, without any description of CT and/or MR imaging findings<sup>5-7</sup> because no modern imaging device was available at that time. Because neuroimaging, especially MR imaging, can accurately localize and comprehensively demonstrate lesions, this technique plays an important role in the diagnosis and differential diagnosis of intraspinal diseases<sup>9,10</sup>; it is crucial to summarize and analyze the imaging features of intraspinal paragonimiasis. Here, we report 6 cases of intraspinal extradural paragonimiasis, with a detailed description of the clinical and MR imaging findings. Then, we discuss the possible pathogenesis of spinal paragonimiasis based on imaging evidence.

Received June 8, 2019; accepted after revision September 3.

From the Departments of Radiology (Y.Q., J.C., L.T., S.J., L.W., X.H.), Outpatient Surgery (X.C.), and Neurosurgery (W.J.), Children's Hospital of Chongqing Medical University, Chongqing, China.

Please address correspondence to Jinhua Cai, MD, Children's Hospital of Chongqing Medical University, 136 Zhongshan 2nd Rd, Yuzhong District, Chongqing, China 400014; e-mail: cai\_jinhua@126.com

<http://dx.doi.org/10.3174/ajnr.A6296>

## MATERIALS AND METHODS

### General Patient Information

This study was approved by the Research Ethics Committee of the Children's Hospital of Chongqing Medical University.

Informed consent was obtained from all patients included in the study. Six patients with spinal paragonimiasis (5 boys and 1 girl; ranging from 5 to 12 years of age, with a mean of 8.2 years) were selected from 83 patients with CNS involvement in a total of 723 patients with paragonimiasis diagnosed in our hospital during the past 10 years (January 2008 to January 2018). All cases were from southwest China, the epidemic area of lung flukes, including Chongqing ( $n=4$ ), Sichuan ( $n=1$ ), and Guizhou ( $n=1$ ) provinces. The most common chief symptom of these patients was weak lower limbs and back pain. The diagnosis was confirmed by an enzyme-linked immunosorbent assay for *Paragonimus*-specific antibody (immunoglobulin G) in serum (6/6) and postoperative pathology (4/6).

### **Clinical Symptoms and History**

The main clinical manifestations were lower extremity weakness ( $n=4$ ) and thoracolumbar pain ( $n=2$ ), of which 1 case was complicated by sensory disorders. All 6 patients were complicated by pleural lesions, and among these patients, 2 patients were complicated by pulmonary paragonimiasis. Regarding their life history, 3 patients reported a history of eating raw or undercooked crabs, one reported a history of drinking fresh water, and 2 patients had an unknown history of infection.

### **Laboratory Examination**

The blood examinations of the 6 patients with spinal paragonimiasis all showed eosinophil counts that were increased to varying degrees, ranging from 8% to 47%. Lumbar puncture for CSF analysis was performed in 4 patients. The CSF appeared colorless and transparent in all patients. In 1 patient, the CSF pressure increased to 215 mm H<sub>2</sub>O, with the eosinophil counts increasing to 19%, while in the other patients, the CSF pressure (80–180 mm H<sub>2</sub>O) and eosinophil counts were normal. Enzyme-linked immunosorbent assays in serum were performed, and the results were positive for *Paragonimus* antibody in all cases.

### **Therapy and Prognosis**

Two patients were treated with oral administration of praziquantel alone at a dose of 25 mg/kg administered 3 times per day for 3 consecutive days, followed by an intermission of 4 days, after which this course was repeated for 9 weeks. Subsequently, the clinical manifestations disappeared, and the physical examination revealed no abnormalities. The other 4 patients underwent surgical removal of the masses under general anesthesia, and then praziquantel was orally administered. The dosage and duration of the treatment were the same as for those receiving oral administration alone. No dysfunction of movement or sensation was found in the 3–6 months of follow-up.

### **MR Imaging Examination**

All 6 patients underwent plain MR imaging, and 5 patients underwent enhanced imaging. The shortest length of time from onset to the imaging examination was 2 days, while the longest was 30 days, with a mean duration of 7 days. The follow-up MR imaging was performed 1 week after surgical removal or after 10 courses of medical treatment. All MR imaging examinations were performed using a 1.5T MR imaging scanner (Signa Excite HD; GE Healthcare, Milwaukee, Wisconsin) or a 3T MR imaging

scanner (Achieva; Philips Healthcare, Best, the Netherlands) with a spine coil. The scan sequences included sagittal and axial spin-echo T1WI and T2WI. The scan parameters were as follows—T1WI: TR of 400–460 ms, TE of 8–12 ms; T2WI: TR of 3000–6000 ms, TE of 90–120 ms; thickness of 3–6 mm, distance of 2–3 mm, matrix of 266 × 266, and 2–4 excitations. A contrast-enhanced T1WI scan was obtained after intravenous injection of GD-DTPA at a dose of 0.2 mL/kg.

## **RESULTS**

### **Lesion Location**

Five lesions were located within the thoracic spine (Figs 1A, -B), while 1 lesion was located in the junction of thoracolumbar segments (Figs 2A, -B). In the axial direction of the spine, all 6 lesions involved the intraspinal extradural space; additionally, the 6 lesions were all connected with the pleural lesions through the intervertebral foramen (Figs 1C, -D and 2C, -D).

### **Lesion Morphology**

The sagittal view showed fusiform-shaped (5/6) or bean-shaped (1/6) masses in the extradural space, and the longitudinal diameter passed 4–10 vertebral bodies, with a length ranging from 5.9 to 16.7 cm. The axial view showed that the granulomatous lesions of the 6 patients were all connected to pleural lesions (including pleural thickening in 6, pleural effusion in 4, and subpleural nodules in 4) through the intervertebral foramen, similar to the dumbbell-like sign (Figs 1C, -D and 2C, -D).

### **MR Imaging Signal**

The plain MR imaging scan of the 6 granulomatous lesions showed mixed signals with predominant isointensity on T1WI (Figs 1A, -C and 2A, -C) and hyperintensity on T2WI (Figs 1B, -D and 2B, -D), of which 5 fusiform-shaped lesions presented with multiple patchlike or irregular hemorrhagic foci with hyperintensity on T1WI within the masses (Figs 1A, -C and 2A, -C). The 5 patients undergoing the enhanced MR image showed heterogeneous and marked enhancement in the granulomatous masses (Figs 1E, -F and 2E, -F). The lesions in the intervertebral foramen and the pleura showed an enhancement pattern that was similar to that in the intraspinal lesions (Figs 1F and 2F). Furthermore, there was enhancement in the adjacent spinal meninges (Figs 1E and 2E).

### **Spinal Cord**

In 5 of the 6 patients, the corresponding segment of the spinal cord exhibited various degrees of compression and edema, which was visible as hyperintensity on T2WI (Fig 1B, -D).

### **Combined Lesions**

All 6 spinal paragonimiasis cases were complicated by pleural lesions, including 6 cases of pleural thickening, 4 cases with a small amount of pleural effusion, and 4 cases of subpleural nodules. The chest CT of 2 patients showed pulmonary nodules and stripe-shaped small cavity lesions. However, no clinical or imaging evidence of cerebral paragonimiasis was found in the 6 spinal paragonimiasis cases.

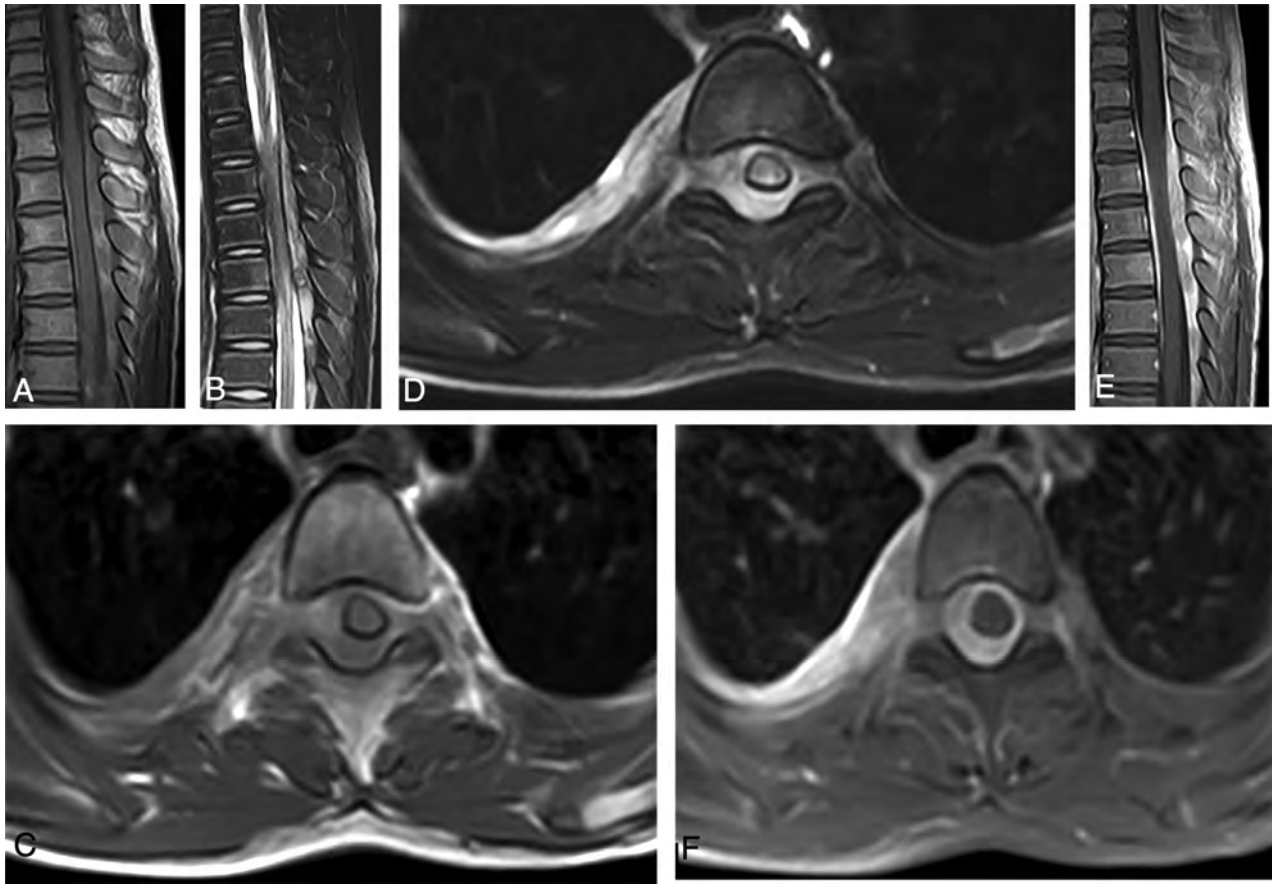


**FIG 1.** MR imaging of intraspinal paragonimiasis in a 6-year-old patient. Sagittal TIWI (A) and T2WI (B) show a longitudinal fusiform-shaped mass located in the intraspinal extradural space parallel to the level of T2–T11, with predominant isointensity on TIWI and hyperintensity on T2WI, and there are multiple patchlike hemorrhagic areas with hyperintensity on TIWI and hypointensity on T2WI within the mass. Axial TIWI (C) and T2WI (D) show that the mass is located in the extradural space and extends to the right intervertebral foramen, connecting to the irregularly thickened pleural lesions on the right, accompanied by a small amount of pleural effusion. The compressed spinal cord moves slightly to the left front, and there is edema with hyperintensity on T2WI. The sagittal (E) and axial (F) views of the contrast-enhanced images indicate that the mass is obviously enhanced, and there are scattered nonenhancement areas within it. Additionally, the adjacent spinal meninges show obvious enhancement.

### Follow-Up MR Imaging

After treatment with oral medication or surgical removal, the follow-up MR imaging showed that the masses were reduced or had disappeared. The spinal cord compression was completely relieved, and the edema with hyperintensity on T2WI had disappeared.

### Pathologic Findings

The macroscopic observation of the pathologic specimens showed grayish-white tissue with a soft and loose texture, and hemorrhage and necrosis were found on the cut surface. The microscopic observation showed tunnels within the granulomas, and a large number of eosinophils and lymphocytes invaded the granulomatous tissue around the tunnel. Furthermore, a large number of erythrocytes were found in some regions.

## DISCUSSION

*Paragonimus* infection can invade various parenchymal organs and tissues, including the lungs, pleura, brain, liver, and sub-

cutaneous tissue.<sup>3,11–17</sup> The infection involving the CNS is rare and constitutes approximately 0.8%–31.0% of all active paragonimiasis.<sup>3</sup> Spinal involvement is even more uncommonly encountered, with the occurrence ranging from 2% to 10% among CNS paragonimiasis.<sup>5</sup> In our series, only 6 cases of spinal involvement occurred among 83 patients with CNS paragonimiasis (7.2%, 6/83), which is similar to that in previous reports.

The pathogenesis of the formation of spinal paragonimiasis is still uncertain.<sup>1,5–8,18</sup> Several theories have been proposed in previous reports. The first is that the *Paragonimus* larvae may directly migrate from the lung and/or pleura to the spinal canal through the paravertebral soft tissue.<sup>5</sup> A second theory was suggested by Diaconita and Nagy<sup>18</sup> in 1957, which stated that paragonimiasis involvement in the spinal canal could result from hematogenous extension. Another theory was that the infection of the spinal canal was caused by the direct downward movement of cerebral paragonimiasis.<sup>5</sup> The above theories regarding the spinal involvement of paragonimiasis are conflicting, and none of these notions have been confirmed by any clear imaging or other evidence. In this study, the imaging findings of the 6 extradural

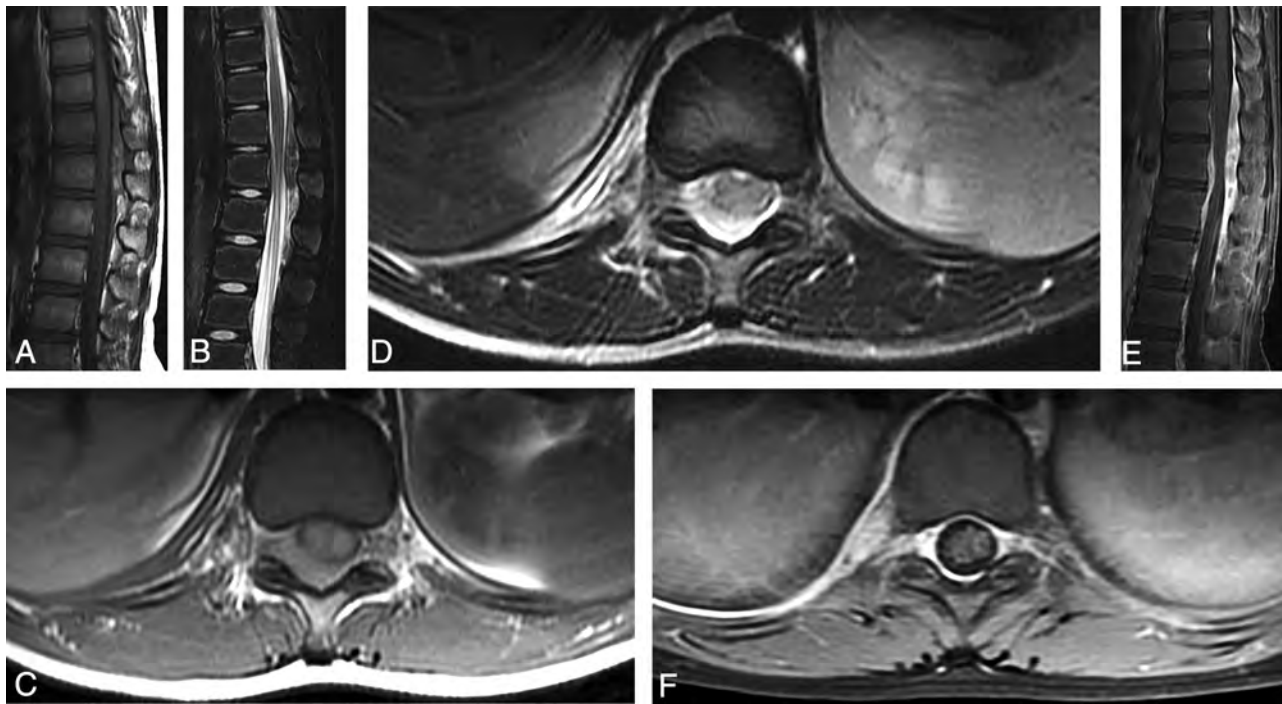


**FIG 2.** MR imaging of intraspinal paragonimiasis in a 12-year-old patient. Sagittal T1WI (A) and T2WI (B) show a fusiform-shaped mass located in the intraspinal extradural space at the junction of the thoracolumbar spine (T10–L2). The mass shows a heterogeneous signal with multiple patchy hemorrhage foci. Axial T1WI (C) and T2WI (D) show that the mass is located in the extradural space and connects with the irregular pleural lesions through the right intervertebral foramen. The spinal cord is compressed, but there is no edema. The sagittal view of the contrast imaging (E) shows a heterogeneous and significant enhancement in the extradural masses, and the axial view (F) also shows significant enhancement in the intervertebral foramen and pleural lesions. Meanwhile, the adjacent spinal meninges show thickening and enhancement.

spinal paragonimiasis cases provided strong evidence for a mechanism of pathogenesis in which the lung flukes directly invade the spinal canal from the pleural lesions through the intervertebral foramen. First, all the intraspinal granulomatous masses in this series occurred in thoracic segments, also consistent with the report from Moon et al<sup>5</sup> showing that thoracic spines were involved in all 8 patients with spinal paragonimiasis examined in that study. Second, all the lesions located in the extradural space were connected to the pleural lesions through the intervertebral foramen. This physical connection indicated that the intraspinal extradural lesions were from the adjacent pleural (or pulmonary) lesions. Third, no imaging evidence of either cervical paragonimiasis or cerebral paragonimiasis was found in this group of patients; therefore, the possibility that extradural spinal paragonimiasis was caused by the downward movement of cerebral paragonimiasis could be excluded. In addition, no imaging or laboratory data in our cases supported the theory of hematogenous extension.

On the basis of the mode of invasion of paragonimiasis from the pleura to the spinal canal, the extradural space could be inevitably invaded. This has been confirmed in our cases and in most previously reported cases.<sup>5-7</sup> However, in the previous reports, there were a few cases complicated by intradural or/and spinal cord involvement except for extradural invasion. There has been no reasonable explanation for this phenomenon. We speculate that the intradural or/and spinal cord lesions could be a result of migration from the extradural space. Because the *Paragonimus* larvae habitually migrate, they can penetrate the intestinal wall,

pleura, and meninges. In this mode, they can also penetrate the dura mater and the soft spinal membrane, resulting in intraspinal or/and spinal lesion formation. Whether the intradural or/and spinal cord lesions occur could be determined by the progression of the disease. In our series, the lesions in all cases were limited in the extradural space. This could be attributed to the early detection achieved via the application of modern imaging technology.

As with cerebral paragonimiasis, hemorrhage is also considered a very important imaging feature in the diagnosis of spinal paragonimiasis. In this group of patients, 83.3% (5/6) had hemorrhage, which showed patchy hyperintensity on T1WI and hypointensity on T2WI. The hemorrhagic tendency of paragonimiasis could be attributed to the biologic behavior of the parasite.<sup>19-21</sup> When the worm entered the epidural space through the intervertebral foramen, it formed granulomatous lesions; additionally, the migration of worms can cause hyperemia, vasculitis, and broken capillaries, resulting in hemorrhage.<sup>1,19</sup> In addition, hemorrhage is more likely to occur in children because their blood vessels are more vulnerable than those of adults. In this study, the granuloma of 1 patient did not show hemorrhage with obvious hyperintensity on T1WI, which may be due to the small size of the granulomatous lesion or the different maturity grades of the granuloma.<sup>20,22</sup>

The laboratory tests, including the eosinophil counts, the dot-immunogold filtration assay, and enzyme-linked immunosorbent assay, have high specificity and sensitivity to detect paragonimiasis.<sup>1,23</sup> These methods, however, are unable to locate or characterize the lesions. Although myelography was also used for the

detection of spinal paragonimiasis lesions by Moon et al,<sup>5</sup> it is an invasive method and the imaging results are nonspecific, with a low positive rate; thus, this technique is now rarely used. Compared with myelography, MR imaging has the advantage of multiplane imaging and excellent contrast of the soft tissue, which is especially suitable for displaying spinal lesions. In this study, MR imaging not only clearly revealed the location, range, and size of lesions but also found the signal features of the hemorrhage in spinal paragonimiasis, as well as its relationship with the spinal cord, thus providing useful information for the early diagnosis of spinal paragonimiasis and surgical treatment.

Because of some similarities in their imaging manifestations, extradural spinal paragonimiasis needs to be differentiated from the following diseases:

1) Neurogenic tumors: because the intraspinal soft-tissue masses of spinal paragonimiasis are connected to the paravertebral and pleural lesions through the intervertebral foramen, the lesions appear to be distributed along the spinal nerves, similar to the dumbbell-like sign, and they are easily misdiagnosed as neurogenic tumors.<sup>24</sup> However, they can be differentiated on the basis of the following features: First, in most cases, the dumbbell-like mass formed by neurogenic tumors has a well-defined boundary, with an enlarged intervertebral foramen and even bone absorption and destruction, while spinal paragonimiasis presents with the exact opposite features. Second, the mass of spinal paragonimiasis is closely related to the pleura with thickening, pleural nodularity, and enhancement. However, in neurogenic tumors, only a few cases showed adjacent slightly pleural responses. Third, paragonimiasis has a tendency to produce hemorrhage, while neurogenic tumors have no such tendency.

2) Tuberculoma or bacterial abscess: tuberculoma is often encountered in the intraspinal extradural space. It shares a similar lesion location and enhancement patterns with paragonimiasis and is also frequently accompanied by pleural and intrapulmonary lesions. However, hemorrhage with hyperintensity on T1WI is seldom observed in intraspinal extradural tuberculoma. In addition, intraspinal tuberculomas are usually accompanied by vertebral or intracranial invasion.<sup>9</sup> Bacterial abscess is another infectious disease that can form a mass in the intraspinal extradural space. For this disease, enhanced MR imaging usually shows a ring-shaped enhancement, which is different from the substantial enhancement pattern of paragonimiasis granuloma.

3) Intraspinal hematoma: because hemorrhage in granulomas is common in spinal paragonimiasis, it must be differentiated from intraspinal hematoma. In the early stages, intraspinal hematoma usually presents with uniform hyperintensity on T1WI and does not extend to the subpleural space through the intervertebral foramen. Moreover, intraspinal hematoma could change the signal features on follow-up MR imaging.<sup>25</sup>

4) Lymphomas: most extradural lymphomas usually present with uniform signals on plain and enhanced scans<sup>26</sup>; however, intraspinal paragonimiasis granulomas often present with heterogeneous signals because of internal hemorrhage.

5) Angiomyolipomas: this tumor occasionally occurs in the epidural space and needs to be considered in the differential diagnosis.<sup>27</sup> The fat composition in angiomyolipomas can be easily detected by MR imaging; this feature could be helpful in

differentiating it from paragonimiasis. In addition to the differences in imaging features, the *Paragonimus* endemic areas (especially in East Asia), the increased eosinophil counts in laboratory examinations, and the antibody test by enzyme-linked immunosorbent assay are also strong evidence for the diagnosis of spinal paragonimiasis and the exclusion of all the aforementioned diseases.

## CONCLUSIONS

Spinal paragonimiasis is a very rare entity and can be sensitively detected by MR imaging. On MR imaging, the intraspinal granulomas often present as a longitudinal fusiform-shaped or beanlike mass located in the thoracic segment and the extradural space and connect to pleural lesions through the intervertebral foramen. Hemorrhagic foci within the mass are a significant imaging feature, which is consistent with the imaging features of cerebral paragonimiasis. These MR imaging findings provide strong evidence for the following mode of pathogenesis for extradural spinal paragonimiasis: The *Paragonimus* larvae migrate from the primary chest lesions into the intraspinal extradural space through the intervertebral foramen instead of by hematogenous extension or by downward movement of cerebral paragonimiasis.

## REFERENCES

1. Chai JY. **Paragonimiasis.** *Handb Clin Neurol* 2013;114:283–96 CrossRef Medline
2. Nawa Y. **Re-emergence of paragonimiasis.** *Intern Med* 2000;39:353–54 CrossRef Medline
3. Chen J, Chen Z, Lin J, et al. **Cerebral paragonimiasis: a retrospective analysis of 89 cases.** *Clin Neurol Neurosurg* 2013;115:546–51 CrossRef Medline
4. Xia Y, Chen J, Ju Y, et al. **Characteristic CT and MR imaging findings of cerebral paragonimiasis.** *J Neuroradiol* 2016;43:200–06 CrossRef Medline
5. Moon TJ, Yoon BY, Hahn YS. **Spinal paragonimiasis.** *Yonsei Med J* 1964;5:55–61 CrossRef Medline
6. Oh SJ. **Spinal paragonimiasis.** *J Neurol Sci* 1968;6:125–40 CrossRef Medline
7. Oh SJ. **Cerebral and spinal paragonimiasis: a histopathological study.** *J Neurol Sci* 1969;9:205–36 CrossRef Medline
8. Qin Y, Cai J. **MRI findings of intraspinal extradural paragonimiasis granuloma in a child.** *Pediatr Radiol* 2012;42:1250–03 CrossRef Medline
9. Gupta RK, Gupta S, Kumar S, et al. **MRI in intraspinal tuberculosis.** *Neuroradiology* 1994;36:39–43 CrossRef Medline
10. Kumar S, Jain AK, Dhammi IK, et al. **Treatment of intraspinal tuberculoma.** *Clin Orthop Relat Res* 2007;460:62–66 CrossRef Medline
11. Lee CH, Kim JH, Moon WS, et al. **Paragonimiasis in the abdominal cavity and subcutaneous tissue: report of 3 cases.** *Korean J Parasitol* 2012;50:345–47 CrossRef Medline
12. Park CW, Chung WJ, Kwon YL, et al. **Consecutive extrapulmonary paragonimiasis involving liver and colon.** *J Dig Dis* 2012;13:186–89 CrossRef Medline
13. Scharhoff T. **Paragonimiasis of the lung** [in German]. *Z Erkr Atmungsorgane* 1987;168:265–72 Medline
14. Choi DW. **Paragonimus and paragonimiasis in Korea.** *Kisaengchungghak Chapchi* 1990;28(Suppl):79–102 Medline
15. Yokogawa M. **Paragonimus and paragonimiasis.** *Adv Parasitol* 1965;3:99–158 CrossRef Medline

16. Peng X, Zhang J, Zhang J, et al. **Incidence of paragonimiasis in Chongqing China: a 6-year retrospective case review.** *Parasitology* 2018;145:792–96 CrossRef Medline
17. Diaz JH. **Paragonimiasis acquired in the United States: native and nonnative species.** *Clin Microbiol Rev* 2013;26:493–504 CrossRef Medline
18. Diaconita G, Nagy P. **Contributions to the study of intrarachidian localisation of distoma (paragonimiasis).** *Acta Med Scand* 1957;159:151–54 Medline
19. Xia Y, Ju Y, Chen J, et al. **Hemorrhagic stroke and cerebral paragonimiasis.** *Stroke* 2014;45:3420–42 CrossRef Medline
20. Zhang JS, Huan Y, Sun LJ, et al. **MRI features of pediatric cerebral paragonimiasis in the active stage.** *J Magn Reson Imaging* 2006;23:569–73 CrossRef Medline
21. Chang KH, Han MH. **MRI of CNS parasitic diseases.** *J Magn Reson Imaging* 1998;8:297–307 CrossRef Medline
22. Nomura M, Nitta H, Nakada M, et al. **MRI findings of cerebral paragonimiasis in chronic stage.** *Clin Radiol* 1999;54:622–64 CrossRef Medline
23. Cho SY, Hong ST, Rho YH, et al. **Application of micro-ELISA in serodiagnosis of human paragonimiasis.** *Kisaengchunghak Chapchi* 1981;19:151–56 Medline
24. Ozawa H, Kokubun S, Aizawa T, et al. **Spinal dumbbell tumors: an analysis of a series of 118 cases.** *J Neurosurg Spine* 2007;7:587–93 CrossRef Medline
25. Hetland S, Berg-Johnsen J, Heier T, et al. **Intraspinal hematoma after thoracic epidural analgesia** [in Norwegian]. *Tidsskr Nor Laegeforen* 1998;118:241–44 Medline
26. Colosimo C, Moschini M, Fileni A, et al. **Diagnostic imaging of intracranial and spinal lymphomas.** *Rays* 1994;19:490–510 Medline
27. Sakaida H, Waga S, Kojima T, et al. **Thoracic spinal angiomyolipoma with extracanal extension to the thoracic cavity: a case report.** *Spine (Phila Pa 1976)* 1998;23:391–94 CrossRef Medline

## Methodologic Concerns on the Reported Values for Assessing Permeability of the Blood-Brain Barrier in the Hippocampus

**W**e read with great interest the article by Ivanidze et al<sup>1</sup> in the March issue of the *American Journal of Neuroradiol*.

In this article, the authors suggested a normative value for assessing the permeability of the blood-brain barrier (BBB) in the hippocampus, the volume transfer constant ( $K^{\text{trans}}$ ), which is potentially valuable to researchers and neuroradiologists.

We are concerned, however, about the methods used by the authors of this article and about the results presented.

First, the authors used the extended Tofts model to generate hippocampal  $K^{\text{trans}}$  values in their study. However, expert consensus is that the Patlak model is better than other models such as the extended Tofts model to measure very small changes in BBB permeability ( $K^{\text{trans}}$ ).<sup>2,3</sup> According to Barnes et al,<sup>2</sup> the highest contrast-to-noise ratio for  $K^{\text{trans}}$  was obtained when the analysis by the Patlak model was combined with long scan times (10–30 minutes), modest temporal resolution (<60 s/image), and long baseline scans (1–4 minutes). Therefore, the documented  $K^{\text{trans}}$  value of the hippocampus obtained using the extended Tofts model may not be as useful as expected.

Second, the authors did not provide the full details of the dynamic contrast-enhanced MR imaging (DCE-MR imaging) sequence used in their study. Recently, a consensus recommendation on the imaging of BBB permeability in small-vessel disease was published.<sup>3</sup> The recommendation would be applicable to all diseases with small changes in BBB permeability. It suggests that reporting of imaging results of BBB permeability should include full details of DCE- and T1-weighted MR imaging measurements, image preprocessing, selection of vessel input function, model fitting, formulas, generation of region and tissue mask, and post-processing and statistical analysis of data. Especially, one should document the following MR imaging acquisition parameters: the pulse sequence used for DCE- and T1-weighted MR imaging, flip angle mapping, field strength, inversion-/saturation-recovery delay, TR, TE, flip angle,  $k$ -space sampling scheme, acceleration technique, bandwidth, orientation, acquisition matrix, FOV, acquired spatial resolution, temporal resolution, and acquisition time and signal drift.<sup>3</sup> Among them, the flip angle and acquisition

time are very important for accurate calculation of  $K^{\text{trans}}$  values in the brain.<sup>4,5</sup>

Third, the spatial resolution and section thickness of the DCE-MR imaging sequence used were not optimal. Measurement of BBB leakage is essentially the leakage of fluid through capillaries, and not through medium- and small-sized vessels. Thus, the presence of a marginally large vascular component within the voxel might contaminate the results. As seen in Fig 1 of Ivanidze et al,<sup>1</sup> the ROI drawn on axial MR images with a thick section (5 mm in this study) almost always includes the hippocampal artery and its branches. This might inevitably lead to abnormally high  $K^{\text{trans}}$  values of the voxels. Furthermore, contamination by CSF could alter the value of BBB permeability of the voxels. ROIs of the hippocampus in the study of Ivanidze et al covered the choroidal fissure as well as the hippocampus. Therefore, an unknown amount of CSF, contained within the choroidal fissure, could have contributed to the measurement of BBB permeability; moreover, in their case, the signal contributed by the CSF did not appear to be removed accurately by the analysis software.

Fourth, we suspect that some systemic error might have contributed to the unusually high  $K^{\text{trans}}$  values reported with the Olea software (Olea Medical, La Ciotat, France). The reported  $K^{\text{trans}}$  values in the study deviate considerably from those reported in the recent literature, which is approximately 0.001 minutes<sup>-1</sup> in an animal study<sup>6</sup> and  $<2.5 \times 10^{-3} \times$  minutes<sup>-1</sup> (0.0025 minutes<sup>-1</sup>) in human subjects.<sup>7</sup>

In our hospital, we evaluated and compared the results of the  $K^{\text{trans}}$  map obtained by DCE-MR imaging of 1 healthy subject, using both the nordicICE (NordicNeuroLab, Bergen, Norway) and Olea software. We chose the same mathematic model (extended Tofts model) used in the study of Ivanidze et al.<sup>1</sup> Most interesting, we found that the Olea-derived  $K^{\text{trans}}$  value was 100 times larger than that derived by the nordicICE software. We compared the 2 software products using the exact same options (without selecting an additional option).

Finally, the unit for the  $K^{\text{trans}}$  reported might be confusing to some readers. The commonly used unit for expressing the  $K^{\text{trans}}$  value is minutes<sup>-1</sup>.<sup>4</sup> The authors have stated that  $K^{\text{trans}}$  is expressed in milliliters/minute/100 mg.<sup>1</sup> In the literature, the unit

of  $K^{\text{trans}}$  is expressed in milliliters/minute/milliliter or milliliters/minute/ $g^4$  or milliliters/minute/100 mL.<sup>8</sup> The unit volume of tissue is expressed per 100 mL rather than in grams because imaging devices measuring cross-sectional areas provide the data of tissue volume.  $K^{\text{trans}}$  is a volume transfer constant between the blood plasma and extravascular extracellular space. Thus, reduced permeability is equivalent to the product of permeability surface area per unit volume of tissue. It would be preferable to use the commonly used unit of minutes<sup>-1</sup> for expressing  $K^{\text{trans}}$ .<sup>2</sup>

Precise methodology for imaging BBB permeability is extremely important. Chronic neurodegenerative disease could result in minimal BBB leakage, whereas a brain tumor causes massive BBB leakage with very high  $K^{\text{trans}}$  values. A minimal change in chronic neurodegenerative disease, in terms of  $K^{\text{trans}}$  values, may present difficulties in discriminating the normal and targeted neurodegenerative condition.<sup>3</sup> Hence, neuroradiologists and clinical researchers should be aware of the potential problems when dealing with imaging results of BBB permeability.

## REFERENCES

- Ivanidze J, Mackay M, Hoang A, et al. **Dynamic contrast-enhanced MRI reveals unique blood-brain barrier permeability characteristics in the hippocampus in the normal brain.** *AJNR Am J Neuroradiol* 2019;40:408–11 CrossRef Medline
- Barnes SR, Ng TS, Montagne A, et al. **Optimal acquisition and modeling parameters for accurate assessment of low Ktrans blood-brain barrier permeability using dynamic contrast-enhanced MRI.** *Magn Reson Med* 2016;75:1967–77 CrossRef Medline
- Thrippleton MJ, Backes WH, Sourbron S, et al. **Quantifying blood-brain barrier leakage in small-vessel disease: review and consensus recommendations.** *Alzheimers Dement* 2019;15:840–58 CrossRef Medline
- Tofts PS, Brix G, Buckley DL, et al. **Estimating kinetic parameters from dynamic contrast-enhanced T(1)-weighted MRI of a diffusible tracer: standardized quantities and symbols.** *J Magn Reson Imaging* 1999;10:223–32 Medline
- Haar HJ, Jansen JFA, Jeukens CRLPN, et al. **Subtle blood-brain barrier leakage rate and spatial extent: considerations for dynamic contrast-enhanced MRI.** *Med Phys* 2017;44:4112–25 CrossRef Medline
- Arena F, Bardini P, Blasi F, et al. **Gadolinium presence, MRI hyperintensities, and glucose uptake in the hypoperfused rat brain after repeated administrations of gadodiamide.** *Neuroradiology* 2019; 61:163–73 CrossRef Medline
- Montagne A, Barnes SR, Sweeney MD, et al. **Blood-brain barrier breakdown in the aging human hippocampus.** *Neuron* 2015;85:296–302 CrossRef Medline
- Cuenod CA, Balvay D. **Perfusion and vascular permeability: basic concepts and measurement in DCE-CT and DCE-MRI.** *Diagn Interv Imaging* 2013;94:1187–1204 CrossRef Medline

 C.M. Lim

 W.-J. Moon

Department of Radiology

Konkuk University Medical Center, Konkuk University School of Medicine

Seoul, Republic of Korea

REPLY:

We appreciate the comments from Drs Lim and Moon on our article entitled, "Dynamic Contrast-Enhanced MRI Reveals Unique Blood-Brain Barrier Permeability Characteristics in the Hippocampus in the Normal Brain," and appreciate the opportunity to respond.

The first comment is focused on the permeability model used in dynamic contrast-enhanced (DCE)-MR imaging postprocessing. In our study, we used a commercially available software, Olea Sphere (Olea Medical, La Ciotat, France), using the extended Tofts permeability model to postprocess the acquired DCE-MR imaging data into blood-brain barrier permeability (BBBP) parameters of  $K^{\text{trans}}$  and VE. The authors suggest the use of the Patlak model combined with long scan times of 10–30 minutes<sup>1</sup> to improve the contrast-to-noise ratio for  $K^{\text{trans}}$ , thereby improving the detectability of subtle BBB permeability changes.

Different theoretic models have been proposed for DCE-MR imaging data analysis, including the Tofts and extended Tofts models, the adiabatic tissue homogeneity model, the 2CX model, the distributed capillary adiabatic tissue homogeneity model, and the gamma capillary transit time model.<sup>2</sup> The model used in our study, while less robust as indicated by the authors, is readily integrated in the clinical setting and is thus more practical from a clinical standpoint compared with the other aforementioned models. The Tofts model and other models have previously been shown to overestimate  $K^{\text{trans}}$ , and variability in  $K^{\text{trans}}$  values across different models is a known issue affecting all models.<sup>2,3</sup> Most important, even if absolute  $K^{\text{trans}}$  values may have been overestimated in our study, all subjects were analyzed with the same model conditions; therefore, our conclusions regarding relative region-based changes in  $K^{\text{trans}}$  remain valid.

While there are certain inherent disadvantages to the Tofts and Kermode model in detecting subtle BBBP changes, our study nevertheless revealed statistically significant region-specific BBBP differences in healthy subjects. Most important, the purpose of our study was to compare the BBBP in different brain regions in healthy subjects and not to optimize permeability models or parameters. We used a commonly used commercial software and found statistically significant results on an intraindividual level.

Although we mentioned in our Materials and Methods section that 80 cine phases were performed, we did not explicitly state that the acquisition time was 11 minutes 14 seconds. The benefits of extending the acquisition time in clinical practice may be limited by considerations such as patient tolerability, cost, and renal clearance of gadolinium-based contrast agents.<sup>4</sup> The authors additionally requested details of the acquisition protocol based on a consensus recommendation on BBB permeability imaging in small-vessel disease.<sup>4</sup> Given that our findings are specific to young healthy volunteers without small-vessel disease, we did not consider that the referenced consensus guideline applied in this study; however, in our Materials and Methods section, we do state specific pertinent DCE-MR imaging acquisition

parameters. Our aim was to apply DCE-MR imaging protocol and postprocessing methods, which can be readily implemented into clinical workflows.

We would next like to address the authors' comments on spatial resolution and section thickness and concerns regarding contamination of the hippocampal measurements by the hippocampal artery and choroid plexus. We acknowledge that caution must be exercised when interpreting our results, given the small sample size in our study and the challenge in avoiding choroid plexus contamination in the ROI sampling of the hippocampus, and we mention these important points in the limitations section of our article. We would also like to emphasize that we used rigorous methods when placing the ROIs in the hippocampal region using trained research personnel closely supervised by an experienced neuroradiologist. Our research team has >15 years' experience in performing these methods of ROI placement in the brain while minimizing contamination from other structures (such as vascular structures, choroid plexus, ventricles, CSF, and skull) in our prior publications. As visualized in Fig 1, meticulous care was taken to minimize the possibility of choroid plexus contamination when placing the hippocampal ROI. As an added precaution, ROIs with CBF values >100 mL/100 g/min were excluded from the statistical analysis to further avoid possible contamination of the data from any vascular input, particularly the choroid plexus. Our findings were consistent across subjects, as evidenced by the individual-subject DCE curves supporting our data being robust using these methods. Furthermore, our data are also concordant with other previously published animal model data,<sup>5</sup> and DCE-MR imaging–based human studies demonstrating increased hippocampal BBB permeability,<sup>6</sup> providing additional support from the literature.

We do not have personal experience with the nordicICE software (NordicNeuroLab, Bergen, Norway) mentioned by the authors; however, we use the Olea software on a daily basis in a clinical setting at both the first and senior authors' institutions (Weill Cornell Medical College and Northwell Health, respectively). Typical  $K^{\text{trans}}$  values in normal-appearing brain parenchyma using our clinical acquisition and analysis protocol (with Olea software) are approximately 0.01, with slightly higher values typically seen in the hippocampus, concordant with the findings in our study.

We would like to clarify that the measurement unit for  $K^{\text{trans}}$  (milliliters/minute/100 mg) is mathematically equivalent to the units mentioned by the authors ( $\text{minute}^{-1} \times 10^{-2}$ ) because milligrams and milliliters are equivalent, assuming a density of 1 kg/m<sup>3</sup>. The  $10^{-2}$  factor (and variability of inclusion thereof in different perfusion-analysis software packages) may have contributed to the difference between nordicICE and Olea data observed by the authors and to the difference pointed out by the authors regarding published studies.<sup>6</sup>

We agree with the authors that precise methodology in BBB permeability imaging is extremely important. We recognize that our study reveals initial proof-of-concept findings that warrant further investigation. As we stated in our Conclusions, "This work may help further our understanding of specific brain regions susceptible to neurologic diseases affecting the BBB.

Larger scale prospective studies evaluating hippocampal BBB characteristics are needed to confirm these findings and potentially incorporate them into diagnostic and therapeutic strategies.”

We appreciate the authors' interest in our study and hope our reply clarifies their questions.

Thank you.

## REFERENCES

1. Barnes SR, Ng TS, Montagne A, et al. **Optimal acquisition and modeling parameters for accurate assessment of low Ktrans blood-brain barrier permeability using dynamic contrast-enhanced MRI.** *Magn Reson Med* 2016;75:1967–77 CrossRef Medline
2. Sourbron SP, Buckley DL. **On the scope and interpretation of the Tofts models for DCE-MRI.** *Magn Reson Med* 2011;66:735–45 CrossRef Medline
3. Bergamino M, Saitta L, Barletta L, et al. **Measurement of blood-brain barrier permeability with T1-weighted dynamic contrast-enhanced MRI in brain tumors: a comparative study with two different algorithms.** *ISRN Neurosci* 2013;2013:905279 CrossRef Medline
4. Thrippleton MJ, Backes WH, Sourbron S, et al. **Quantifying blood-brain barrier leakage in small vessel disease: review and consensus recommendations.** *Alzheimers Dement* 2019;15:840–58 CrossRef Medline
5. Weidman EK, Foley CP, Kallas O, et al. **Evaluating permeability surface-area product as a measure of blood-brain barrier permeability in a murine model.** *AJNR Am J Neuroradiol* 2016;37:1267–74 CrossRef Medline
6. Montagne A, Barnes SR, Sweeney MD, et al. **Blood-brain barrier breakdown in the aging human hippocampus.** *Neuron* 2015;85:296–302 CrossRef Medline

 **J. Ivanidze**

Department of Radiology  
Weill Cornell Medicine  
New York, New York

 **M. Mackay**

The Center for Autoimmune, Musculoskeletal and Hematopoietic Diseases

 **A. Hoang**

 **J.M. Chi**

 **K. Cheng**

Department of Radiology, Northwell Health

 **C. Aranow**

The Center for Autoimmune, Musculoskeletal and Hematopoietic Diseases

 **B. Volpe**

The Center for Biomedical Science, Feinstein Institute for Medical Research

 **B. Diamond**

The Center for Autoimmune, Musculoskeletal and Hematopoietic Diseases

Donald and Barbara Zucker School of Medicine at Hofstra/Northwell

Manhasset, New York

 **P.C. Sanelli**

Feinstein Institute for Medical Research, The Center for Health Innovations and

Outcomes Research

Donald and Barbara Zucker School of Medicine at Hofstra/Northwell

Manhasset, New York

Department of Radiology, Northwell Health

Imaging Clinical Effectiveness and Outcomes Research Program

Manhasset, New York

## Multinodular and Vacuolating Neuronal Tumor of the Cerebrum: Does the Name Require Review?

**M**ultinodular and vacuolating neuronal tumor (MVNT) of the cerebrum is a relatively novel entity added to the revised 2016 World Health Organization classification,<sup>1</sup> though first described in 2013.<sup>2</sup> It is characterized by a cluster of intra-axial nodules with mixed neuro-glial cells demonstrating internal vacuolating architecture. The lesions are benign and nonprogressive and, given their innocence, are a potential “no touch” or “leave-me-alone” lesion.<sup>3</sup> All published cases have been described in the supratentorium. So far, there are no published cases of MVNT of the cerebellum. We have seen at least 3 cases with imaging characteristics identical to those of MVNT of the cerebrum that were observed in the cerebellum.

We had 3 patients between 23 and 39 years of age presenting with headaches (2 cases) and vertigo (1 case). The neurologic examination findings were unremarkable in all cases. MR imaging of the brain showed a cluster of nodules, 1–3 mm each, located in the superior vermis and within the surrounding superior cerebellar hemisphere (Figs 1–3). In all cases, the nodules were hypointense to gray matter on T1-weighted imaging, hyperintense on T2, and did not suppress completely on FLAIR imaging. There was no enhancement, susceptibility, or diffusion restriction. There was no surrounding edema or mass effect. The imaging features were consistent with the imaging descriptions of MVNT. A 12-month follow-up MR imaging showed no interval change.

We have no histopathologic evidence because these are “no touch” lesions.<sup>3,4</sup> However, their exact imaging similarities to supratentorial MVNT and stability across time suggesting a benign natural history support that these likely represent the same histopathologic entity involving the cerebellum. We propose that the name of the entity be expanded to “MVNT of the brain” to include cerebellar lesions in the phenotypic spectrum of this newly described entity.

<http://dx.doi.org/10.3174/ajnr.A6284>

Disclosures: Aanchal Agarwal—UNRELATED: Employment: Sir Charles Gairdner Hospital.

### REFERENCES

1. Louis DN, Perry A, Reifenberger G, et al. **The 2016 World Health Organization Classification of Tumors of the Central Nervous System: a summary.** *Acta Neuropathol* 2016;131:803–20 CrossRef Medline
2. Huse JT, Edgar M, Halliday J, et al. **Multinodular and vacuolating neuronal tumors of the cerebrum: 10 cases of a distinctive seizure-associated lesion.** *Brain Pathol* 2013;23:515–24 CrossRef Medline
3. Nunes RH, Hsu CC, da Rocha AJ, et al. **Multinodular and vacuolating neuronal tumor of the cerebrum: a new “leave me alone” lesion with a characteristic imaging pattern.** *AJNR Am J Neuroradiol* 2017; 38:1899–904 CrossRef Medline
4. Alsufayan R, Alcaide-Leon P, de Tilly LN, et al. **Natural history of lesions with the MR imaging appearance of multinodular and vacuolating neuronal tumor.** *Neuroradiology* 2017;59:873–83 CrossRef Medline

**A. Agarwal**

Neurointervention and Imaging Services of Western Australia  
Sir Charles Gairdner Hospital  
Nedlands, Western Australia

**R. Lakshmanan**

Princess Margaret Hospital  
Subiaco, Western Australia  
University College of London Foundation Trust  
National Hospital for Neurology and Neurosurgery, London  
London, UK

**I. Devagnanam**

University College of London Foundation Trust  
National Hospital for Neurology and Neurosurgery, London  
London, UK

**M. Bynevelt**

Neurointervention and Imaging Services of Western Australia  
Sir Charles Gairdner Hospital  
Nedlands, Western Australia  
Princess Margaret Hospital  
Subiaco, Western Australia

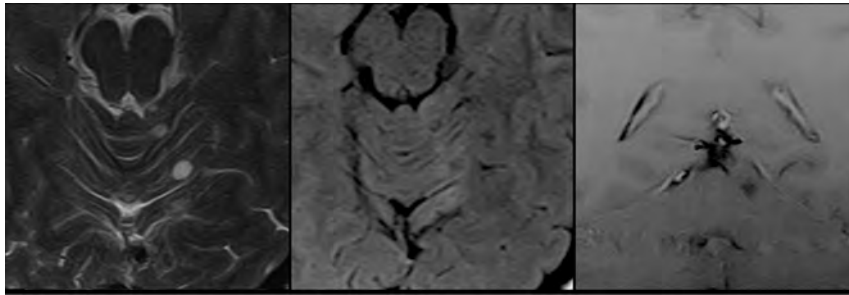


**FIG 1.** Montage of images (axial T2, axial FLAIR, coronal T1 fat-saturated postcontrast) shows at least 2 T2 hyperintense nodules of 3 and 5 mm each to the left of the superior vermis. These are hyperintense to CSF on T2, show incomplete suppression on FLAIR, and do not enhance.

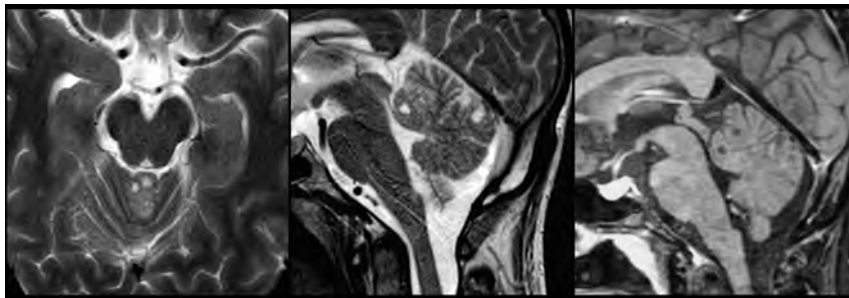


**FIG 2.** Montage of images (axial T2, sagittal T2, and sagittal T1 postcontrast) shows small T2 hyperintense nodules in the superior vermis. They do not enhance.

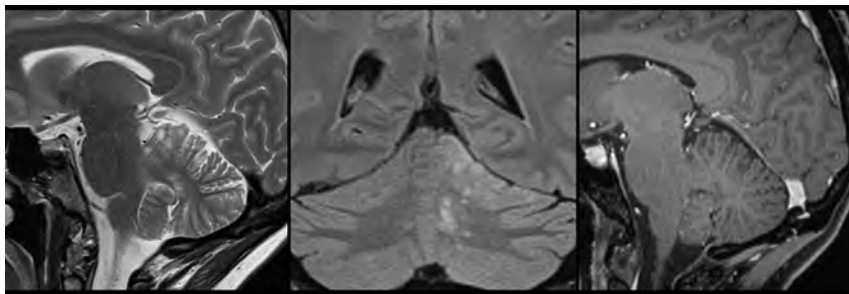


**FIG 3.** Montage of images (sagittal T2, coronal FLAIR, and sagittal T1 fat-saturated postcontrast) shows a cluster of small nodules of similar size within the left paravermian and cerebellar hemisphere.

In the article commentary “Impact of Vessel Wall MR Imaging in the Work-Up for Ischemic Stroke” (Song JW. *AJNR Am J Neuroradiol* 2019;40:1707–08. 10.3174/ajnr.A6241), the author omitted a citation for the article discussed. The referenced article is “Diagnostic Impact of Intracranial Vessel Wall MRI in 205 Patients with Ischemic Stroke or TIA” (Schaafsma JD, Rawal S, Coutinho JM, et al. *AJNR Am J Neuroradiol* 2019;40:1701–06. 10.3174/ajnr.A6202).

<http://dx.doi.org/10.3174/ajnr.A6353>

**On-line Table 1: Vascular risk factors in study sample (n = 130)<sup>a</sup>**

Risk Factors	
BMI (kg/m <sup>2</sup> )	27.3 ± 3.7
Current smoker	15%
Hypertension	90%
Hyperlipidemia	93%
Diabetes	19%
Metabolic syndrome	52%

Note—BMI indicates body mass index.

<sup>a</sup> Values are presented as mean ± SD or %.

**On-line Table 2: Sensitivity analysis of the association between carotid atherosclerosis and ICAS burden**

	ICAS Burden (b-value) <sup>a</sup> (95% CI)
cIMT, per +0.1 mm	0.50 (0.04 to 0.97)
cIMT quartiles	
Quartile 1	0 (Reference)
Quartile 2	0.93 (−1.98–3.83)
Quartile 3	0.35 (−2.62–3.33)
Quartile 4	2.85 (−0.02–5.72)
Carotid stenosis	
No stenosis	0 (Reference)
1%–49% stenosis	2.06 (−0.37–4.50)
50%–100% stenosis	6.23 (1.94–10.52)

<sup>a</sup> B-values are unstandardized linear regression coefficients adjusted for age, sex, and time interval between carotid sonography and 7T MR imaging.

**On-line Table 3: Sensitivity analysis of the association between ABI and ICAS burden**

	ICAS Burden (b-value) <sup>a</sup> (95% CI)
ABI, per +0.1 in ratio	−0.34 (−0.89–0.2)
ABI > 0.9	0 (Reference)
ABI ≤ 0.9	5.08 (2.00–8.16)

<sup>a</sup> B-values are unstandardized linear regression coefficients adjusted for age, sex, and time interval between ABI measurement and 7T MR imaging.

**On-line Table 4: Sensitivity analysis of the association between renal function and ICAS burden**

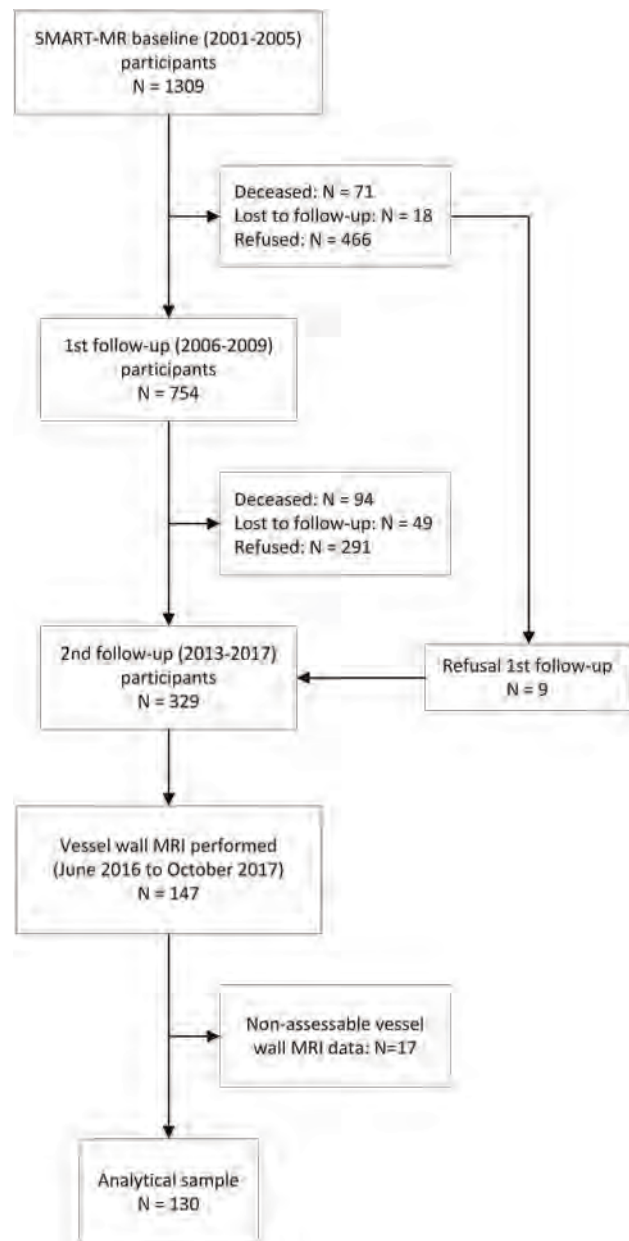
	ICAS Burden (b-value) <sup>a</sup> (95% CI)
eGFR, per +10 mL/min	−0.78 (−1.50 to −0.06)
eGFR ≥60 mL/min	0 (Reference)
eGFR <60 mL/min	3.02 (0.31–5.72)

<sup>a</sup> B-values are unstandardized linear regression coefficients adjusted for age, sex, and time interval between eGFR measurement and 7T MR imaging.

**On-line Table 5: Sensitivity analysis of the association between history of vascular disease and ICAS burden**

	ICAS Burden (b-value) <sup>a</sup> (95% CI)
Coronary artery disease	0 (Reference)
Peripheral artery disease	0.09 (−3.66–3.84)
Cerebrovascular disease	0.55 (−2.94–4.04)
Multivascular disease	1.93 (−0.73–4.59)

<sup>a</sup> B-values are unstandardized linear regression coefficients adjusted for age, sex, and time interval between ECAS and ICAS measurement. Categories are mutually exclusive.



**ON-LINE FIG.** Flowchart of the study sample.

## REFERENCES

1. Abraham P, Scott Pannell J, Santiago-Dieppa D, et al. **Vessel wall signal enhancement on 3-T MRI in acute stroke patients after stent retriever thrombectomy.** *Neurosurg Focus* 2017;42:E20 CrossRef Medline
2. Ahn S, Lee J, Kim Y, et al. **Isolated MCA disease in patients without significant atherosclerotic risk factors: a high-resolution magnetic resonance imaging study.** *Stroke* 2015;46:697–703 CrossRef Medline
3. Aoki S, Shirouzu I, Sasaki Y, et al. **Enhancement of the intracranial arterial wall at MR imaging: relationship to cerebral atherosclerosis.** *Radiology* 1995;194:477–81 CrossRef Medline
4. Aoki S, Hayashi N, Abe O, et al. **Radiation-induced arteritis: thickened wall with prominent enhancement on cranial MR images report of five cases and comparison with 18 cases of Moyamoya disease.** *Radiology* 2002;223:683–88 CrossRef Medline
5. Bae YJ, Choi BS, Jung C, et al. **Differentiation of deep subcortical infarction using high-resolution vessel wall MR imaging of middle cerebral artery.** *Korean J Radiol* 2017;18:964–72 CrossRef Medline
6. Berkefeld J, Enzensberger W, Lanfermann H. **MRI in human immunodeficiency virus-associated cerebral vasculitis.** *Neuroradiology* 2000;42:526–28 CrossRef Medline
7. Blankena R, Kleinloog R, Verweij BH, et al. **Thinner regions of intracranial aneurysm wall correlate with regions of higher wall shear stress: a 7T MRI study.** *AJNR Am J Neuroradiol* 2016;37:1310–17 CrossRef Medline
8. Boussel L, Wintermark M, Martin A, et al. **Monitoring serial change in the lumen and outer wall of vertebrobasilar aneurysms.** *AJNR Am J Neuroradiol* 2008;29:259–64 CrossRef Medline
9. Chen C, Chen S, Fuh J, et al. **Vascular wall imaging in reversible cerebral vasoconstriction syndrome: a 3-T contrast-enhanced MRI study.** *J Headache Pain* 2018;19:74 CrossRef Medline
10. Chen Z, Liu A, Chen H, et al. **Evaluation of basilar artery atherosclerotic plaque distribution by 3D MR vessel wall imaging.** *J Magn Reson Imaging* 2016;44:1592–99 CrossRef Medline
11. Cheng-Ching E, Jones S, Hui FK, et al. **High-resolution MRI vessel wall imaging in varicella zoster virus vasculopathy.** *J Neurol Sci* 2015;351:168–73 CrossRef Medline
12. Choi JW, Han M, Hong JM, et al. **Feasibility of improved motion-sensitized driven-equilibrium (IMSDE) prepared 3D T1-weighted imaging in the diagnosis of vertebrobasilar artery dissection.** *J Neuroradiol* 2018;45:186–91 CrossRef Medline
13. Chung GH, Kwak HS, Hwang SB, et al. **High resolution MR imaging in patients with symptomatic middle cerebral artery stenosis.** *Eur J Radiol* 2012;81:4069–74 CrossRef Medline
14. Chung J, Bang OY, Lee MJ, et al. **Echoing plaque activity of the coronary and intracranial arteries in patients with stroke.** *Stroke* 2016;47:1527–33 CrossRef Medline
15. Coutinho JM, Sacho RH, Schaafsma JD, et al. **High-resolution vessel wall magnetic resonance imaging in angiogram-negative non-perimesencephalic subarachnoid hemorrhage.** *Clin Neuroradiol* 2017;27:175–83 CrossRef Medline
16. Dieleman N, van der Kolk AG, van Veluw SJ, et al. **Patterns of intracranial vessel wall changes in relation to ischemic infarcts.** *Neurology* 2014;83:1316–20 CrossRef Medline
17. Dieleman N, Yang W, Abrigo JM, et al. **Magnetic resonance imaging of plaque morphology, burden, and distribution in patients with symptomatic middle cerebral artery stenosis.** *Stroke* 2016;47:1797–802 CrossRef Medline
18. Dieleman N, Yang W, van der Kolk AG, et al. **Qualitative evaluation of a high-resolution 3D multi-sequence intracranial vessel wall protocol at 3 Tesla MRI.** *PLoS One* 2016;11:e0160781 CrossRef Medline
19. Edjlali M, Gentric J, Régent-Rodriguez C, et al. **Does aneurysmal wall enhancement on vessel wall MRI help to distinguish stable from unstable intracranial aneurysms?** *Stroke* 2014;45:3704–06 CrossRef Medline
20. Feng C, Xu Y, Bai X, et al. **Basilar artery atherosclerosis and hypertensive small vessel disease in isolated pontine infarctions: a study based on high-resolution MRI.** *Eur Neurol* 2013;70:16–21 CrossRef Medline
21. Han C, Li M, Xu Y, et al. **Adult Moyamoya-atherosclerosis syndrome: clinical and vessel wall imaging features.** *J Neurol Sci* 2016;369:181–84 CrossRef Medline
22. Hartevelde AA, Denswil NP, Siero JCW, et al. **Quantitative intracranial atherosclerotic plaque characterization at 7T MRI: an ex vivo study with histologic validation.** *AJNR Am J Neuroradiol* 2016;37:802–10 CrossRef Medline
23. Hartevelde AA, Denswil NP, Van HW, et al. **Ex vivo vessel wall thickness measurements of the human circle of Willis using 7T MRI.** *Atherosclerosis* 2018;273:106–14 CrossRef Medline
24. Hartevelde AA, van der Kolk AG, van der Worp HB, et al. **High-resolution intracranial vessel wall MRI in an elderly asymptomatic population: comparison of 3T and 7T.** *Eur Radiol* 2017;27:1585–95 CrossRef Medline
25. Hartevelde AA, van der Kolk AG, van der Worp HB, et al. **Detecting intracranial vessel wall lesions with 7T-magnetic resonance imaging: patients with posterior circulation ischemia versus healthy controls.** *Stroke* 2017;48:2601–04 CrossRef Medline
26. Hirai T, Korogi Y, Murata Y, et al. **Transcranial artery dissections: serial evaluation with MR imaging, MR angiography, and source images of MR angiography.** *Radiat Med* 2003;21:86–93 Medline
27. Huang B, Yang W, Liu X, et al. **Basilar artery atherosclerotic plaques distribution in symptomatic patients: a 3.0 T high-resolution MRI study.** *Eur J Radiol* 2013;82:e203 CrossRef Medline
28. Ide S, Kakeda S, Miyata M, et al. **Intracranial vessel wall lesions in patients with systematic lupus erythematosus: vessel wall lesions in SLE patients.** *J Magn Reson Imaging* 2018;48:1237–46 CrossRef Medline
29. Ishitsuka K, Sakaki Y, Sakai S, et al. **Diagnosis and follow-up of posterior inferior cerebellar artery dissection complicated with ischemic stroke assisted by T1-VISTA: a report of two cases.** *BMC Neurol* 2016;16:121 CrossRef Medline
30. Jang J, Kim T, Hwang E, et al. **Assessment of arterial wall enhancement for differentiation of parent artery disease from small artery disease: comparison between histogram analysis and visual analysis on 3-dimensional contrast-enhanced T1-weighted turbo spin echo MR images at 3T.** *Korean J Radiol* 2017;18:383–91 CrossRef Medline
31. Jiang W, Yu W, Ma N, et al. **High-resolution MRI guided endovascular intervention of basilar artery disease.** *J Neurointerv Surg* 2011;3:375–78 CrossRef Medline
32. Jiang Y, Zhu C, Peng W, et al. **Ex-vivo imaging and plaque type classification of intracranial atherosclerotic plaque using high resolution MRI.** *Atherosclerosis* 2016;249:10–16 CrossRef Medline
33. Jung SC, Kim HS, Choi C, et al. **Spontaneous and unruptured chronic intracranial artery dissection: high-resolution magnetic resonance imaging findings.** *Clin Neuroradiol* 2018;28:171–81 CrossRef Medline
34. Katchanov J, Siebert E, Klingebiel R, et al. **Infectious vasculopathy of intracranial large- and medium-sized vessels in neurological intensive care unit: a clinico-radiological study.** *Neurocrit Care* 2010;12:369–74 CrossRef Medline
35. Kim J, Jung K, Sohn C, et al. **Middle cerebral artery plaque and prediction of the infarction pattern.** *Arch Neurol* 2012;69:1470–75 CrossRef Medline
36. Kim J, Jung K Sohn C, et al. **Intracranial plaque enhancement from high resolution vessel wall magnetic resonance imaging predicts stroke recurrence.** *Int J Stroke* 2016;11:171–79 CrossRef Medline

37. Kim TH, Choi JW, Roh HG, et al. **Atherosclerotic arterial wall change of non-stenotic intracranial arteries on high-resolution MRI at 3.0 T: correlation with cerebrovascular risk factors and white matter hyperintensity.** *Clin Neurol Neurosurg* 2014;126:1–6 CrossRef Medline
38. Kim T, Choi HS, Koo J, et al. **Intramural hematoma detection by susceptibility-weighted imaging in intracranial vertebral artery dissection.** *Cerebrovasc Dis* 2013;36:292–98 CrossRef Medline
39. Kim YJ, Lee DH, Kwon JY, et al. **High resolution MRI difference between Moyamoya disease and intracranial atherosclerosis.** *Eur J Neurol* 2013;20:1311–18 CrossRef Medline
40. Kim YS, Lim S, Oh K, et al. **The advantage of high-resolution MRI in evaluating basilar plaques: a comparison study with MRA.** *Atherosclerosis* 2012;224:411–16 CrossRef Medline
41. Kitanaka C, Tanaka J, Kuwahara M, et al. **Magnetic resonance imaging study of intracranial vertebrobasilar artery dissections.** *Stroke* 1994;25:571–75 CrossRef Medline
42. Klein IF, Lavallée PC, Mazighi M, et al. **Basilar artery atherosclerotic plaques in paramedian and lacunar pontine infarctions: a high-resolution MRI study.** *Stroke* 2010;41:1405–09 CrossRef Medline
43. Klein IF, Lavallée PC, Schouman-Claeys E, et al. **High-resolution MRI identifies basilar artery plaques in paramedian pontine infarct.** *Neurology* 2005;64:551–52 CrossRef Medline
44. Klein IF, Lavallée PC, Touboul PJ, et al. **In vivo middle cerebral artery plaque imaging by high-resolution MRI.** *Neurology* 2006;67:327–29 CrossRef Medline
45. Kleinloog R, Korkmaz E, Zwanenburg JJM, et al. **Visualization of the aneurysm wall: a 7.0-Tesla magnetic resonance imaging study.** *Neurosurgery* 2014;75:614–22 CrossRef Medline
46. Kwon JY, Kim N, Suh DC, et al. **Intracranial and extracranial arterial dissection presenting with ischemic stroke: lesion location and stroke mechanism.** *J Neurol Sci* 2015;358:371–76 CrossRef Medline
47. Küker W, Gaertner S, Nagele T, et al. **Vessel wall contrast enhancement: a diagnostic sign of cerebral vasculitis.** *Cerebrovasc Dis* 2008;26:23–29 CrossRef Medline
48. Lam WW, Wong KS, So NM, et al. **Plaque volume measurement by magnetic resonance imaging as an index of remodeling of middle cerebral artery: correlation with transcranial color Doppler and magnetic resonance angiography.** *Cerebrovasc Dis* 2004;17:166–69 CrossRef Medline
49. Li F, Chen Q, Chen Z, et al. **Magnetic resonance imaging of plaque burden in vascular walls of the middle cerebral artery correlates with cerebral infarction.** *Curr Neurovasc Res* 2016;13:263–70 CrossRef Medline
50. Li M, Xu W, Song L, et al. **Atherosclerosis of middle cerebral artery: evaluation with high-resolution MR imaging at 3 T.** *Atherosclerosis* 2009;204:447–52 CrossRef Medline
51. Li M, Xu W, Feng F, et al. **Clinical use of magnetic resonance plaque imaging for intracranial arteries.** *Zhongguo Yi Xue Ke Xue Yuan Xue Bao* 2012;34:443–49 Medline
52. Li M, Xu W, Song L, et al. **High-resolution MRI diagnosis of atherosclerosis of intracranial artery.** *Chinese Journal of Medical Imaging Technology* 2010;26:1009–12
53. Li M, Xu Y, Hou B, et al. **High-resolution intracranial vessel wall imaging using 3D CUBE T1 weighted sequence.** *Eur J Radiol* 2016;85:803–07 CrossRef Medline
54. Lou X, Ma N, Ma L, et al. **Contrast-enhanced 3T high-resolution MR imaging in symptomatic atherosclerotic basilar artery stenosis.** *AJNR Am J Neuroradiol* 2013;34:513–17 CrossRef Medline
55. Lou X, Jiang W, Ma L, et al. **In vivo high-resolution magnetic resonance imaging in severe intracranial stenosis [in Chinese].** *Zhonghua Nei Ke Za Zhi* 2008;47:478–81 Medline
56. Lou X, Ma N, Shen H, et al. **Noninvasive visualization of the basilar artery wall and branch ostia with high-resolution three-dimensional black-blood sequence at 3 Tesla.** *J Magn Reson Imaging* 2014;39:911–16 CrossRef Medline
57. Ma N, Jiang WJ, Lou X, et al. **Arterial remodeling of advanced basilar atherosclerosis: a 3-Tesla MRI study.** *Neurology* 2010;75:253–58 CrossRef Medline
58. Ma N, Lou X, Zhao T, et al. **Intraobserver and interobserver variability for measuring the wall area of the basilar artery at the level of the trigeminal ganglion on high-resolution MR images.** *AJNR Am J Neuroradiol* 2011;32:E29–32 CrossRef Medline
59. Madokoro Y, Sakurai K, Kato D, et al. **Utility of T1- and T2-weighted high-resolution vessel wall imaging for the diagnosis and follow up of isolated posterior inferior cerebellar artery dissection with ischemic stroke: report of 4 cases and review of the literature.** *J Stroke Cerebrovasc Dis* 2017;26:2645–51 CrossRef Medline
60. Majidi S, Sein J, Watanabe M, et al. **Intracranial-derived atherosclerosis assessment: an in vitro comparison between virtual histology by intravascular ultrasonography, 7T MRI, and histopathologic findings.** *AJNR Am J Neuroradiol* 2013;34:2259–64 CrossRef Medline
61. Mandell DM, Matouk CC, Farb RI, et al. **Vessel wall MRI to differentiate between reversible cerebral vasoconstriction syndrome and central nervous system vasculitis: preliminary results.** *Stroke* 2012;43:860–62 CrossRef Medline
62. Martin AJ, Hetsch SW, Dillon WP, et al. **MR imaging of partially thrombosed cerebral aneurysms: characteristics and evolution.** *AJNR Am J Neuroradiol* 2011;32:346–51 CrossRef Medline
63. Mascacchi M, Bianchi MC, Mangiafico S, et al. **MRI and MR angiography of vertebral artery dissection.** *Neuroradiology* 1997;39:329–40 CrossRef Medline
64. Matouk CC, Mandell DM, Günel M, et al. **Vessel wall magnetic resonance imaging identifies the site of rupture in patients with multiple intracranial aneurysms: proof of principle.** *Neurosurgery* 2013;72:492–96 CrossRef Medline
65. Mizutani T. **A fatal, chronically growing basilar artery: a new type of dissecting aneurysm.** *J Neurosurg* 1996;84:962–71 CrossRef Medline
66. Mossa-Basha M, Hwang WD, De HA, et al. **Multicontrast high-resolution vessel wall magnetic resonance imaging and its value in differentiating intracranial vasculopathic processes.** *Stroke* 2015;46:1567–73 CrossRef Medline
67. Mossa-Basha M, Shibata DK, Hallam DK, et al. **Added value of vessel wall magnetic resonance imaging for differentiation of nonocclusive intracranial vasculopathies.** *Stroke* 2017;48:3026–33 CrossRef Medline
68. Mossa-Basha M, de Havenon A, Becker KJ, et al. **Added value of vessel wall magnetic resonance imaging in the differentiation of Moyamoya vasculopathies in a non-Asian cohort.** *Stroke* 2016;47:1782–88 CrossRef Medline
69. Muraoka S, Araki Y, Taoka T, et al. **Prediction of intracranial arterial stenosis progression in patients with Moyamoya vasculopathy: contrast-enhanced high-resolution magnetic resonance vessel wall imaging.** *World Neurosurg* 2018;116:e1114–21 CrossRef Medline
70. Nagahata S, Nagahata M, Obara M, et al. **Wall enhancement of the intracranial aneurysms revealed by magnetic resonance vessel wall imaging using three-dimensional turbo spin-echo sequence with motion-sensitized driven-equilibrium: a sign of ruptured aneurysm?** *Clin Neuroradiol* 2016;26:277–83 CrossRef Medline
71. Natori T, Sasaki M, Miyoshi M, et al. **Intracranial plaque characterization in patients with acute ischemic stroke using pre- and post-contrast three-dimensional magnetic resonance vessel wall imaging.** *J Stroke Cerebrovasc Dis* 2016;25:1425–30 CrossRef Medline
72. Natori T, Sasaki M, Miyoshi M, et al. **Evaluating middle cerebral artery atherosclerotic lesions in acute ischemic stroke using magnetic resonance T1-weighted 3-dimensional vessel wall imaging.** *J Stroke Cerebrovasc Dis* 2014;23:706–11 CrossRef Medline
73. Natori T, Sasaki M, Miyoshi M, et al. **Detection of vessel wall lesions in spontaneous symptomatic vertebrobasilar artery**

- dissection using T1-weighted 3-dimensional imaging. *J Stroke Cerebrovasc Dis* 2014;23:2419–24 CrossRef Medline
74. Niizuma K, Shimizu H, Takada S, et al. **Middle cerebral artery plaque imaging using 3-Tesla high-resolution MRI.** *J Clin Neurosci* 2008;15:1137–41 CrossRef Medline
  75. Niu P, Yu Y, Zhou H, et al. **Vessel wall differences between middle cerebral artery and basilar artery plaques on magnetic resonance imaging.** *Sci Rep* 2016;6:38534 CrossRef Medline
  76. Obusez EC, Hui F, Hajj-Ali R, et al. **High-resolution MRI vessel wall imaging: spatial and temporal patterns of reversible cerebral vasoconstriction syndrome and central nervous system vasculitis.** *AJNR Am J Neuroradiol* 2014;35:1527–32 CrossRef Medline
  77. Omodaka S, Endo H, Niizuma K, et al. **Quantitative assessment of circumferential enhancement along the wall of cerebral aneurysms using MR imaging.** *AJNR Am J Neuroradiol* 2016;37:1262–66 CrossRef Medline
  78. Park JK, Lee CS, Sim KB, et al. **Imaging of the walls of saccular cerebral aneurysms with double inversion recovery black-blood sequence.** *J Magn Reson Imaging* 2009;30:1179–83 CrossRef Medline
  79. Park KJ, Jung SC, Kim HS, et al. **Multi-contrast high-resolution magnetic resonance findings of spontaneous and unruptured intracranial vertebral artery dissection: qualitative and quantitative analysis according to stages.** *Cerebrovasc Dis* 2016;42:23–31 CrossRef Medline
  80. Pfefferkorn T, Linn J, Habs M, et al. **Black blood MRI in suspected large artery primary angiitis of the central nervous system.** *J Neuroimaging* 2013;23:379–83 CrossRef Medline
  81. Power S, Matouk C, Casaubon LK, et al. **Vessel wall magnetic resonance imaging in acute ischemic stroke: effects of embolism and mechanical thrombectomy on the arterial wall.** *Stroke* 2014;45:2330–34 CrossRef Medline
  82. Qiao Y, Zeiler SR, Mirbagheri S, et al. **Intracranial plaque enhancement in patients with cerebrovascular events on high-spatial-resolution MR images.** *Radiology* 2014;271:534–42 CrossRef Medline
  83. Qiao Y, Anwar Z, Intrapromkul J, et al. **Patterns and implications of intracranial arterial remodeling in stroke patients.** *Stroke* 2016;47:434–40 CrossRef Medline
  84. Qiao Y, Steinman DA, Qin Q, et al. **Intracranial arterial wall imaging using three-dimensional high isotropic resolution black blood MRI at 3.0 Tesla.** *J Magn Reson Imaging* 2011;34:22–30 CrossRef Medline
  85. Ryoo S, Cha J, Kim SJ, et al. **High-resolution magnetic resonance wall imaging findings of Moyamoya disease.** *Stroke* 2014;45:2457–60 CrossRef Medline
  86. Ryu C, Jahng G, Shin HS. **Gadolinium enhancement of atherosclerotic plaque in the middle cerebral artery: relation to symptoms and degree of stenosis.** *AJNR Am J Neuroradiol* 2014;35:2306–10 CrossRef Medline
  87. Sakurai K, Miura T, Sagisaka T, et al. **Evaluation of luminal and vessel wall abnormalities in subacute and other stages of intracranial vertebrobasilar artery dissections using the volume isotropic turbo-spin-echo acquisition (VISTA) sequence: a preliminary study.** *J Neuroradiol* 2013;40:19–28 CrossRef Medline
  88. Schuster S, Bachmann H, Thom V, et al. **Subtypes of primary angiitis of the CNS identified by MRI patterns reflect the size of affected vessels.** *J Neurol Neurosurg Psychiatry* 2017;88:749–55 CrossRef Medline
  89. Seo W, Oh K, Suh S, et al. **Clinical significance of wall changes after recanalization therapy in acute stroke: high-resolution vessel wall imaging.** *Stroke* 2017;48:1077–80 CrossRef Medline
  90. Shen M, Gao P, Zhang Q, et al. **Middle cerebral artery atherosclerosis and deep subcortical infarction: a 3T magnetic resonance vessel wall imaging study.** *J Stroke Cerebrovasc Dis* 2018;27:3387–92 CrossRef Medline
  91. Shi M, Wang S, Zhou H, et al. **Compensatory remodeling in symptomatic middle cerebral artery atherosclerotic stenosis: a high-resolution MRI and microemboli monitoring study.** *Neurol Res* 2012;34:153–58 CrossRef Medline
  92. Skarpathiotakis M, Mandell DM, Swartz RH, et al. **Intracranial atherosclerotic plaque enhancement in patients with ischemic stroke.** *AJNR Am J Neuroradiol* 2013;34:299–304 CrossRef Medline
  93. Sun L, Li Z, Tang W, et al. **High resolution magnetic resonance imaging in pathogenesis diagnosis of single lenticulostriate infarction with nonstenotic middle cerebral artery, a retrospective study.** *BMC Neurol* 2018;18:51 CrossRef Medline
  94. Swartz RH, Bhuta SS, Farb RI, et al. **Intracranial arterial wall imaging using high-resolution 3-Tesla contrast-enhanced MRI.** *Neurology* 2009;72:627–34 CrossRef Medline
  95. Takano K, Yamashita S, Takemoto K, et al. **MRI of intracranial vertebral artery dissection: evaluation of intramural haematoma using a black blood, variable-flip-angle 3D turbo spin-echo sequence.** *Neuroradiology* 2013;55:845–51 CrossRef Medline
  96. Takano K, Hida K, Kuwabara Y, et al. **Intracranial arterial wall enhancement using gadolinium-enhanced 3D black-blood T1-weighted imaging.** *Eur J Radiol* 2017;86:13–19 CrossRef Medline
  97. Teng Z, Peng W, Zhan Q, et al. **An assessment on the incremental value of high-resolution magnetic resonance imaging to identify culprit plaques in atherosclerotic disease of the middle cerebral artery.** *Eur Radiol* 2016;26:2206–14 CrossRef Medline
  98. Thaler C, Kaufmann-Bühler A, Gansukh T, et al. **Neuroradiologic characteristics of primary angiitis of the central nervous system according to the affected vessel size.** *Clin Neuroradiol* 2019;29:37–44 CrossRef Medline
  99. Urbach H, Meyer-Lindenberg A, Bendszus M, et al. **Dissections of the basilar artery [in German].** *Rofo* 1998;169:170–74 CrossRef Medline
  100. Vakil P, Vranic J, Hurley MC, et al. **T1 gadolinium enhancement of intracranial atherosclerotic plaques associated with symptomatic ischemic presentations.** *AJNR Am J Neuroradiol* 2013;34:2252–58 CrossRef Medline
  101. van der Kolk AG, Zwanenburg JJM, Brundel M, et al. **Distribution and natural course of intracranial vessel wall lesions in patients with ischemic stroke or TIA at 7.0 Tesla MRI.** *Eur Radiol* 2015;25:1692–700 CrossRef Medline
  102. van der Kolk AG, Zwanenburg JJM, Brundel M, et al. **Intracranial vessel wall imaging at 7.0-T MRI.** *Stroke* 2011;42:2478–84 CrossRef Medline
  103. Wang M, Yang Y, Zhou F, et al. **The contrast enhancement of intracranial arterial wall on high-resolution MRI and its clinical relevance in patients with Moyamoya vasculopathy.** *Sci Rep* 2017;7:44264 CrossRef Medline
  104. Wang Y, Lou X, Li Y, et al. **Imaging investigation of intracranial arterial dissecting aneurysms by using 3 T high-resolution MRI and DSA: from the interventional neuroradiologists' view.** *Acta Neurochir (Wien)* 2014;156:515–25 CrossRef Medline
  105. Wu F, Ma Q, Song H, et al. **Differential features of culprit intracranial atherosclerotic lesions: a whole-brain vessel wall imaging study in patients with acute ischemic stroke.** *J Am Heart Assoc* 2018;7 CrossRef Medline
  106. Wu F, Song H, Ma Q, et al. **Hyperintense plaque on intracranial vessel wall magnetic resonance imaging as a predictor of artery-to-artery embolic infarction.** *Stroke* 2018;49:905–11 CrossRef Medline
  107. Xu W, Li M, Gao S, et al. **Middle cerebral artery intraplaque hemorrhage: prevalence and clinical relevance.** *Ann Neurol* 2012;71:195–98 CrossRef Medline
  108. Xu W, Li M, Gao S, et al. **Plaque distribution of stenotic middle cerebral artery and its clinical relevance.** *Stroke* 2011;42:2957–59 CrossRef Medline
  109. Xu W, Li M, Gao S, et al. **In vivo high-resolution MR imaging of symptomatic and asymptomatic middle cerebral artery atherosclerotic stenosis.** *Atherosclerosis* 2010;212:507–11 CrossRef Medline

110. Xu W, Li M, Niu J, et al. **Intracranial artery atherosclerosis and lumen dilation in cerebral small-vessel diseases: a high-resolution MRI study.** *CNS Neurosci Ther* 2014;20:364–67 CrossRef Medline
111. Xu X, Wei Y, Zhang X, et al. **Value of higher-resolution MRI in assessing middle cerebral atherosclerosis and predicting capsular warning syndrome.** *J Magn Reson Imaging* 2016;44:1277–83 CrossRef Medline
112. Xu Y, Li M, Gao S, et al. **Etiology of intracranial stenosis in young patients: a high-resolution magnetic resonance imaging study.** *Ann Transl Med* 2017;5:319 CrossRef Medline
113. Xu Y, Li D, Yuan C, et al. **Association of severity between carotid and intracranial artery atherosclerosis.** *Ann Clin Transl Neurol* 2018;5:843–49 CrossRef Medline
114. Xu Y, Yuan C, Zhou Z, et al. **Co-existing intracranial and extracranial carotid artery atherosclerotic plaques and recurrent stroke risk: a three-dimensional multicontrast cardiovascular magnetic resonance study.** *J Cardiovasc Magn Reson* 2016;18:90 CrossRef Medline
115. Yang Q, Deng Z, Bi X, et al. **Whole-brain vessel wall MRI: A parameter tune-up solution to improve the scan efficiency of three-dimensional variable flip-angle turbo spin-echo.** *J Magn Reson Imaging* 2017;46:751–57 CrossRef Medline
116. Yang W, Chen X, Zhao H, et al. **In vitro assessment of histology verified intracranial atherosclerotic disease by 1.5T magnetic resonance imaging: concentric or eccentric?** *Stroke* 2016;47:527–30 CrossRef Medline
117. Yang W, Huang B, Liu X, et al. **Reproducibility of high-resolution MRI for the middle cerebral artery plaque at 3T.** *Eur J Radiol* 2014;83:49 CrossRef Medline
118. Yu JH, Kwak HS, Chung GH, et al. **Association of intraplaque hemorrhage and acute infarction in patients with basilar artery plaque.** *Stroke* 2015;46:2768–72 CrossRef Medline
119. Yu J, Li M, Xu Y, et al. **Plaque distribution of low-grade basilar artery atherosclerosis and its clinical relevance.** *BMC Neurology* 2017;17:8 CrossRef Medline
120. Yu L He H, Zhao J, et al. **More precise imaging analysis and diagnosis of Moyamoya disease and Moyamoya syndrome using high-resolution magnetic resonance imaging.** *World Neurosurg* 2016; 96:252–60 CrossRef Medline
121. Yun SY, Heo YJ, Jeong HW, et al. **Spontaneous intracranial vertebral artery dissection with acute ischemic stroke: high-resolution magnetic resonance imaging findings.** *Neuroradiol J* 2018;31:262–69 CrossRef Medline
122. Zhang L, Zhang N, Wu J, et al. **High resolution three dimensional intracranial arterial wall imaging at 3 T using T1 weighted SPACE.** *Magn Reson Imaging* 2015;33:1026–34 CrossRef Medline
123. Zhang X, Zhu C, Peng W, et al. **Scan-rescan reproducibility of high resolution magnetic resonance imaging of atherosclerotic plaque in the middle cerebral artery.** *PLoS One* 2015;10:e0134913 CrossRef Medline
124. Zhao D, Deng G, Xie B, et al. **Wall characteristics and mechanisms of ischaemic stroke in patients with atherosclerotic middle cerebral artery stenosis: a high-resolution MRI study.** *Neurol Res* 2016;38:606–13 CrossRef Medline
125. Zhao D, Deng G, Xie B, et al. **High-resolution MRI of the vessel wall in patients with symptomatic atherosclerotic stenosis of the middle cerebral artery.** *J Clin Neurosci* 2015;22:700–04 CrossRef Medline
126. Zhou Z, Li R, Zhao X, et al. **Evaluation of 3D multi-contrast joint intra- and extracranial vessel wall cardiovascular magnetic resonance.** *J Cardiovasc Magn Reson* 2015;17:41 CrossRef Medline
127. Zhu C, Haraldsson H, Tian B, et al. **High resolution imaging of the intracranial vessel wall at 3 and 7 T using 3D fast spin echo MRI.** *MAGMA* 2016;29:559–70 CrossRef Medline
128. Zou X, Chung Y, Zhang L, et al. **Middle cerebral artery atherosclerotic plaques in recent small subcortical infarction: a three-dimensional high-resolution MR study.** *BioMed Res Int* 2015;2015: 540217 CrossRef Medline

**On-line Table 1: Search terms for data base search**

Search Terms	
Imaging related terms:	
Imaging	("imaging"[All Fields])
MR imaging/magnetic resonance imaging	(MR imaging[MeSH Terms] OR ("magnetic"[All Fields] AND "resonance"[All Fields] AND "imaging"[All Fields]) OR "MR imaging"[All Fields] OR "mri"[All Fields] OR "MR imaging"[All Fields])
Neuroimaging	(neuroimaging[MeSH Terms] OR "neuroimaging"[All Fields])
Gadolinium contrast	("gadolinium"[MeSH Terms] OR "gadolinium"[All Fields]) AND ("contrast media"[Pharmacological Action] OR "contrast media"[MeSH Terms] OR ("contrast"[All Fields] AND "media"[All Fields]) OR "contrast media"[All Fields] OR "contrast"[All Fields])
AND	
Vessel wall imaging-related terms:	
Vessel wall imaging	((("blood vessels"[MeSH Terms] OR ("blood"[All Fields] AND "vessels"[All Fields]) OR "blood vessels"[All Fields]) OR "vessel"[All Fields]) AND wall[All Fields] AND "imaging"[All Fields] AND "blood vessels"[MeSH Terms])
Vessel wall MR imaging	(vessel[All Fields] AND wall[All Fields] AND MR[All Fields] AND imaging[All Fields])
High-resolution vessel wall MR imaging	(high[All Fields] AND resolution[All Fields] AND ("blood vessels"[MeSH Terms] OR "blood"[All Fields] AND "vessels"[All Fields]) OR "blood vessels"[All Fields] OR "vessel"[All Fields] AND wall[All Fields] AND MR[All Fields] AND imaging[All Fields])
Vessel wall	((("blood vessels"[MeSH Terms] OR ("blood"[All Fields] AND "vessels"[All Fields]) OR "blood vessels"[All Fields]) OR "vessel"[All Fields]) AND wall[All Fields])
AND	
Intracranial circulation-related terms:	
Basilar artery	("basilar artery"[MeSH Terms] OR ("basilar"[All Fields] AND "artery"[All Fields]) OR "basilar artery"[All Fields])
Carotid artery	("carotid artery, common"[MeSH Terms] OR ("carotid"[All Fields] AND "artery"[All Fields] AND "common"[All Fields]) OR "common carotid artery"[All Fields] OR ("carotid"[All Fields] AND "artery"[All Fields]) OR "carotid artery"[All Fields] OR "carotid arteries"[MeSH Terms] OR ("carotid"[All Fields] AND "arteries"[All Fields]) OR "carotid arteries"[All Fields] OR ("carotid"[All Fields] AND "artery"[All Fields]))
Carotid artery internal	(carotid artery, internal[MeSH Terms] OR ("carotid"[All Fields] AND "artery"[All Fields] AND "internal"[All Fields]) OR "internal carotid artery"[All Fields] OR ("carotid"[All Fields] AND "artery"[All Fields] AND "internal"[All Fields]) OR "carotid artery internal"[All Fields])
Cerebral artery	("cerebral arteries"[MeSH Terms] OR ("cerebral"[All Fields] AND "arteries"[All Fields]) OR "cerebral arteries"[All Fields] OR ("cerebral"[All Fields] AND "artery"[All Fields]) OR "cerebral artery"[All Fields])
Cerebrovascular	(cerebrovascular[All Fields])
Circle of Willis	(circle of willis[MeSH Terms] OR ("circle"[All Fields] AND "willis"[All Fields]) OR "circle of willis"[All Fields])
Middle cerebral artery	(middle cerebral artery[MeSH Terms] OR ("middle"[All Fields] AND "cerebral"[All Fields] AND "artery"[All Fields]) OR "middle cerebral artery"[All Fields])
Anterior cerebral artery	(anterior cerebral artery[MeSH Terms] OR ("anterior"[All Fields] AND "cerebral"[All Fields] AND "artery"[All Fields]) OR "anterior cerebral artery"[All Fields])
Posterior cerebral artery	(posterior cerebral artery[MeSH Terms] OR ("posterior"[All Fields] AND "cerebral"[All Fields] AND "artery"[All Fields]) OR "posterior cerebral artery"[All Fields])
Vertebral artery	("vertebral artery"[MeSH Terms] OR ("vertebral"[All Fields] AND "artery"[All Fields]) OR "vertebral artery"[All Fields])
Wall of the blood vessel	(wall[All Fields] AND ("blood vessels"[MeSH Terms] OR ("blood"[All Fields] AND "vessels"[All Fields]) OR "blood vessels"[All Fields] OR ("blood"[All Fields] AND "vessel"[All Fields]) OR "blood vessel"[All Fields]))
Wall of artery	(wall[All Fields] AND ("arteries"[MeSH Terms] OR "arteries"[All Fields] OR "artery"[All Fields]))
Lumen	(lumen[All Fields])
Vertebrobasilar	(Vertebrobasilar[All Fields])
Intracranial	(intracranial[All Fields])
Cerebral/brain	(cerebrum[MeSH Terms] OR "cerebrum"[All Fields] OR "cerebral"[All Fields] OR "brain"[MeSH Terms] OR "brain"[All Fields])
AND	
Vascular disease-related terms:	
Cerebral arterial disease	("cerebral arterial diseases"[MeSH Terms] OR ("cerebral"[All Fields] AND "arterial"[All Fields] AND "diseases"[All Fields]) OR "cerebral arterial diseases"[All Fields] OR ("cerebral"[All Fields] AND "arterial"[All Fields] AND "disease"[All Fields]) OR "cerebral arterial disease"[All Fields])

*Continued on next page*

**On-line Table 1: Continued**

Search Terms	
Cerebrovascular disorders	(cerebrovascular disorders[MeSH Terms] OR (“cerebrovascular”[All Fields] AND “disorders”[All Fields]) OR “cerebrovascular disorders”[All Fields])
Thrombosis	(thrombosis[MeSH Terms] OR “thrombosis”[All Fields])
Stenosis	(constriction, pathologic[MeSH Terms] OR (“constriction”[All Fields] AND “pathologic”[All Fields]) OR “pathologic constriction”[All Fields] OR “stenosis”[All Fields])
Infarction/infarct	(infarction[MeSH Terms] OR “infarction”[All Fields] OR “infarct”[All Fields])
Small-vessel disease	(small[All Fields] AND (“blood vessels”[MeSH Terms] OR (“blood”[All Fields] AND “vessels”[All Fields]) OR “blood vessels”[All Fields] OR “vessel”[All Fields]) AND (“disease”[MeSH Terms] OR “disease”[All Fields]))
Arterial occlusive diseases	(arterial occlusive diseases[MeSH Terms] OR (“arterial”[All Fields] AND “occlusive”[All Fields] AND “diseases”[All Fields]) OR “arterial occlusive diseases”[All Fields])
Aneurysm	(aneurysm[MeSH Terms] OR “aneurysm”[All Fields])
Arteriosclerosis	(arteriosclerosis[MeSH Terms] OR “arteriosclerosis”[All Fields])
Embolism	(embolism[MeSH Terms] OR “embolism”[All Fields])
Hypertension	(hypertension[MeSH Terms] OR “hypertension”[All Fields])
Stroke	(stroke[MeSH Terms] OR “stroke”[All Fields])
Lacunar	(lacunar[All Fields])
Lacunar stroke	(stroke, lacunar[MeSH Terms] OR (“stroke”[All Fields] AND “lacunar”[All Fields]) OR “lacunar stroke”[All Fields] OR (“lacunar”[All Fields] AND “stroke”[All Fields]))
Lacune	(lacunae[All Fields])
Transient ischemic attack	(transient ischemic attack[All Fields] OR “ischemic attack, transient”[MeSH Terms] OR (“ischemic”[All Fields] AND “attack”[All Fields] AND “transient”[All Fields]) OR “transient ischemic attack”[All Fields] OR (“transient”[All Fields] AND “ischemic”[All Fields] AND “attack”[All Fields]) OR TIA[All Fields])
Vasospasm	(vasoconstriction[MeSH Terms] OR “vasoconstriction”[All Fields] OR “vasospasm”[All Fields])
Cerebral vasospasm	(vasospasm, intracranial[MeSH Terms] OR (“vasospasm”[All Fields] AND “intracranial”[All Fields]) OR “intracranial vasospasm”[All Fields] OR (“cerebral”[All Fields] AND “vasospasm”[All Fields]) OR “cerebral vasospasm”[All Fields])
Vasculitis	(vasculitis[MeSH Terms] OR “vasculitis”[All Fields])
CNS vasculitis	(vasculitis, central nervous system[MeSH Terms] OR (“vasculitis”[All Fields] AND “central”[All Fields] AND “nervous”[All Fields] AND “system”[All Fields]) OR “central nervous system vasculitis”[All Fields] OR (“central”[All Fields] AND “nervous”[All Fields] AND “system”[All Fields] AND “vasculitis”[All Fields]))
Plaque, atherosclerotic/atheroma	(plaque, atherosclerotic[MeSH Terms] OR (“plaque”[All Fields] AND “atherosclerotic”[All Fields]) OR “atherosclerotic plaque”[All Fields] OR “atheroma”[All Fields])
Remodeling (index, positive, negative)	(remodeling[All Fields] OR (“remodeling” AND “index”[All Fields]) OR “remodeling index”[All Fields] OR (“positive” AND “remodeling”[All Fields]) OR “positive remodeling” OR (“negative” AND “remodeling”[All Fields]) OR “negative remodeling”[All Fields])
ICAD	(intracranial[All Fields] AND atherosclerotic[All Fields] AND (“disease”[MeSH Terms] OR “disease”[All Fields]) OR “ICAD”[All Fields])
ICAS	(intracranial arteriosclerosis[MeSH Terms] OR (“intracranial”[All Fields] AND “arteriosclerosis”[All Fields]) OR “intracranial arteriosclerosis”[All Fields] OR (“intracranial”[All Fields] AND “atherosclerosis”[All Fields]) OR “intracranial atherosclerosis”[All Fields] OR ICAS[All Fields])
Ischemia/ischemic	(ischemia[All Fields] OR “ischemia”[MeSH Terms] OR “ischemia”[All Fields] OR “ischemic”[All Fields])
Brain ischemia	(brain ischemia[All Fields] OR “brain ischemia”[MeSH Terms] OR (“brain”[All Fields] AND “ischemia”[All Fields]) OR “brain ischemia”[All Fields])

**Note:**—ICAS indicates intracranial atherosclerosis.

**On-line Table 2: Assessment of publication bias—distribution of vasculopathies of included publications versus excluded conference abstracts<sup>a</sup>**

Vasculopathy Type	Included Publications	Conference Abstracts
Intracranial atherosclerotic disease	62	30
Aneurysm	10	3
Vasculitis	6	2
Dissection	16	6
Moyamoya disease	4	2
Reversible cerebral vasoconstriction syndrome	1	1
Post-endovascular treatment	3	3
Multiple, specific vasculopathies	11	1
Vessel lesions	8	10
Multiple vasculopathies with healthy volunteers as a comparator group	6	0
Healthy volunteers	0	3

<sup>a</sup> Likelihood ratio  $\chi^2$  test,  $P = .95$ .

**On-line Table 3: Sensitivity analysis of CRS**

	CRS <sub>All</sub> <sup>a</sup>	
	STROBE Items Reported in Any Part of the Article (Footnotes, Bylines) ( $P = .30$ )	Partially Reported Items Considered Fully Reported ( $P = .27$ )
All ( $n = 62$ )	0.66 (0.16)	0.77 (0.16)
North America ( $n = 11$ )	0.62 (0.10)	0.74 (0.12)
Asia ( $n = 40$ )	0.66 (0.15)	0.82 (0.14)
Europe ( $n = 6$ )	0.58 (0.19)	0.70 (0.10)
Transcontinental collaborations ( $n = 5$ )	0.68 (0.06)	0.79 (0.05)

<sup>a</sup> CRS measures reported in means (SD) or medians (interquartile range) based on normality test.

**On-line Table 4: STROBE item descriptions and scores<sup>a</sup>**

Items	Description	Mean Score (SD)
1	a) Indicate the design of the study with a commonly used term in the title or the abstract b) Provide in the abstract an informative and balanced summary of what was done and what was found	0.52 (0.14)
Introduction		
2	Explain the scientific background and rationale for the investigation being reported	0.98 (0.14)
3	State specific objectives, including any prespecified hypotheses	1.00 (0)
Methods		
4	Present key elements of study design early in the article	0.08 (0.24)
5	Describe the setting, locations, and relevant dates, including periods of recruitment, exposure, follow-up, and data collection	0.57 (0.31)
6	Give the eligibility criteria and the sources and methods of selection of participants; describe methods of follow-up	0.85 (0.23)
7	Clearly define all outcomes, exposures, predictors, potential confounders, and effect modifiers; give diagnostic criteria if applicable	0.34 (0.32)
8	For each variable of interest, give sources of data and details of methods of assessment (measurement); describe comparability of assessment methods if there is >1 group	0.94 (0.21)
9	Describe any effort to address potential sources of bias	0.75 (0.43)
10	Explain how the study size was determined	0
11	Explain how quantitative variables were handled in the analyses; if applicable, describe which groupings were chosen and why	0.54 (0.46)
12	a) Describe all statistical methods, including those used to control for confounding b) Describe any methods used to examine subgroups and interactions c) Explain how missing data were addressed	0.85 (0.36)
Results		
13	a) Report numbers of individuals at each stage of study—eg, numbers potentially eligible, examined for eligibility, confirmed eligible, included in the study, completing follow-up, and analyzed b) Give reasons for nonparticipation at each stage c) Consider use of a flow diagram	0.59 (0.35)
14	Give characteristics of study participants (eg, demographic, clinical, social) and information on exposures and potential confounders	0.46 (0.19)
15	Report numbers of outcome events or summary measures across time	0.91 (0.27)
16	a) Give unadjusted estimates and, if applicable, confounder-adjusted estimates and their precision (eg, 95% confidence interval). Make clear which confounders were adjusted for and why they were included b) Report category boundaries when continuous variables were categorized	0.50 (0.37)
17	Report other analyses—eg, analyses of subgroups and interactions, and sensitivity analyses	0.57 (0.50)
Discussion		
18	Summarize key results with reference to study objectives	1.00 (0)
19	Discuss limitations of the study, taking into account sources of potential bias or imprecision; discuss both direction and magnitude of any potential bias	0.55 (0.24)
20	Give a cautious overall interpretation of results, considering objectives, limitations, multiplicity of analyses, results from similar studies, and other relevant evidence	0.77 (0.31)
21	Discuss the generalizability of the study results	0.26 (0.44)
Funding		
22	Give the source of funding and the role of the funders for the present study	0.72 (0.45)

<sup>a</sup>Please see STROBE guidelines and checklist for full description (<https://www.strobe-statement.org/index.php?id=strobe-home>).

## ON-LINE APPENDIX

### MATERIALS AND METHODS

#### Image Acquisition

MR imaging of all patients was performed using 1 of two 3T MR imaging scanners (Magnetom Verio or Magnetom Skyra; Siemens, Erlangen, Germany) with a 32-channel head coil. The MR imaging protocol included pre- and postcontrast 3D-MPRAGE sequences with multiplanar reconstructions for T1WI in the axial, coronal, and sagittal planes; an axial T2 FLAIR sequence; and an axial T2WI with turbo spin-echo sequences. The specific parameters for the sequences were as follows: 1) for 3D-MPRAGE: TR, 1370–1600 ms; TE, 1.9–2.8 ms; flip angle, 9°; matrix, 256 × 232; FOV, 250 × 250; section thickness, 1 mm; and NEX, 1; 2) for the axial T2 FLAIR sequence: TR, 8000–9000 ms; TE, 90–97 ms; TI, 2300–2500 ms; flip angle, 130°–150°; matrix, 384 × 209–278; FOV, 199 × 220; section thickness, 5 mm; and NEX, 1–2; and 3) for the axial T2WI sequence: TR, 5100 ms; TE, 89 ms; flip angle, 150°; matrix, 640 × 348; FOV, 199 × 220; section thickness, 5 mm; and NEX, 3.

For the DCE-MR imaging, 3D gradient-echo T1WI was acquired. Forty images were obtained at intervals equal to the TR for each section. The specific imaging parameters were as follows: TR, 2.8 ms; TE, 1.0 ms; flip angle, 10°; matrix, 192 × 192; FOV, 240 × 240 mm; section thickness, 3 mm; voxel size, 1.25 × 1.25 × 3 mm<sup>3</sup>; and total acquisition time, 5 minutes 8 seconds.

Afterwards, the DSC-MR imaging was performed with a single-shot, gradient-echo, echo-planar imaging sequence. Sixty images were obtained at intervals equal to the TR for

each section. The imaging parameters of the DSC-MR imaging were as follows: TR, 1600 ms; TE, 30 ms; flip angle, 90°; matrix, 128 × 128; FOV, 240 × 240 mm; section thickness, 6 mm; inter-section gap, 6.9 mm; voxel size, 1.86 × 1.86 × 5 mm; and total acquisition time, 1 minute 36 seconds.

The DCE-MR imaging was performed after intravenous administration of gadobutrol (Gadovist; Bayer Schering Pharma, Berlin, Germany; at a dose of 0.1 mmol/kg of body weight), followed by a 30-mL saline bolus at a rate of 4 mL/s using a power injector (Spectris; MedRad, Indianola, Pennsylvania). Then, the DSC-MR imaging was acquired after an intravenous injection of the same contrast agent using the same dose and method.

### RESULTS

#### Correlation Analysis

The Pearson correlation analysis was performed and the intraclass correlation coefficients were calculated to evaluate whether the EF from DSC-MR imaging was correlated with contrast leakage information from DCE-MR imaging, including the  $K^{trans}$ ,  $V_e$ , and  $V_p$ . The Pearson correlation analysis showed a weak correlation only between the mean EF and  $V_p$  values, whereas no significant correlation was found for the other cases. The correlation coefficient  $r$  and  $P$  value of each case are shown in On-line Fig 3. For the intraclass correlation coefficients, no significant agreement was found between the EF and the  $K^{trans}$ ,  $V_e$ , and  $V_p$ . The intraclass correlation coefficient values and 95% CIs are shown in On-line Table 1.

**On-line Table 1: Intraclass correlation coefficients between the EF from DSC-MR imaging and the  $K^{trans}$ ,  $V_e$ , and  $V_p$  from DCE-MR imaging**

Lesion/Parameters	ICC <sup>a</sup>	95% CI	Agreement
Enhancing area on contrast-enhanced T1WI			
EF mean vs $K^{trans}$ mean	-0.032	-0.225–0.162	Negative
EF mean vs $V_e$ mean	-0.002	-0.195–0.192	Negative
EF mean vs $V_p$ mean	-0.105	-0.293–0.090	Negative
Nonenhancing FLAIR high-signal-intensity area			
EF mean vs $K^{trans}$ mean	-0.001	-0.195–0.193	Negative
EF mean vs $V_e$ mean	0.018	-0.177–0.211	Positive but poor
EF mean vs $V_p$ mean	-0.196	-0.376 to -0.003	Negative
EF 95th PV vs $K^{trans}$ 95th PV	-0.001	-0.195–0.192	Negative
EF 95th PV vs $V_e$ 95th PV	0.015	-0.180–0.208	Positive but poor
EF 95th PV vs $V_p$ 95th PV	-0.166	-0.349–0.029	Negative

**Note:**—ICC indicates intraclass correlation coefficient; PV, percentile value.

<sup>a</sup>ICC values are <0 (negative), 0–0.20 (positive but poor), 0.21–0.40 (fair), 0.41–0.60 (moderate), 0.61–0.80 (good), or >0.81 (excellent).

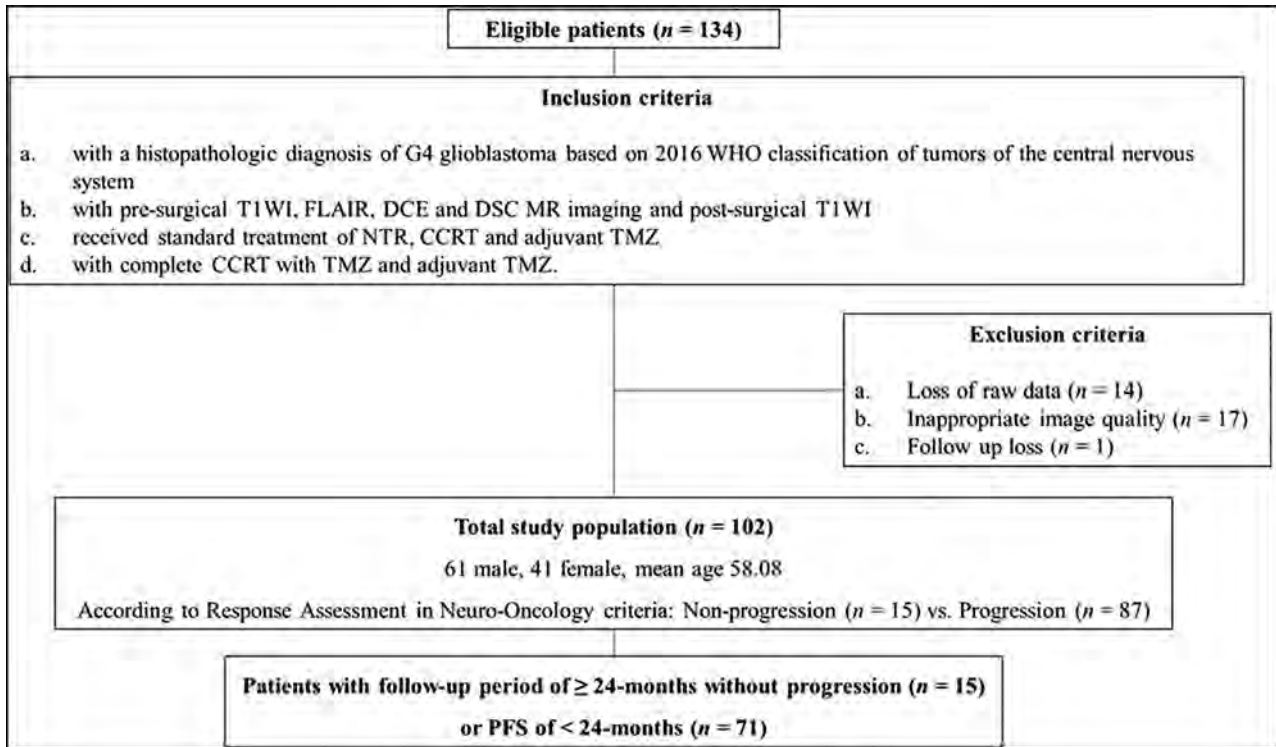
**On-line Table 2: Cox proportional hazards regression<sup>a</sup>**

	EF 95th PV	IDH1/2	MGMT	Age
<i>P</i> value <sup>b</sup>	.01	.30	.12	.36

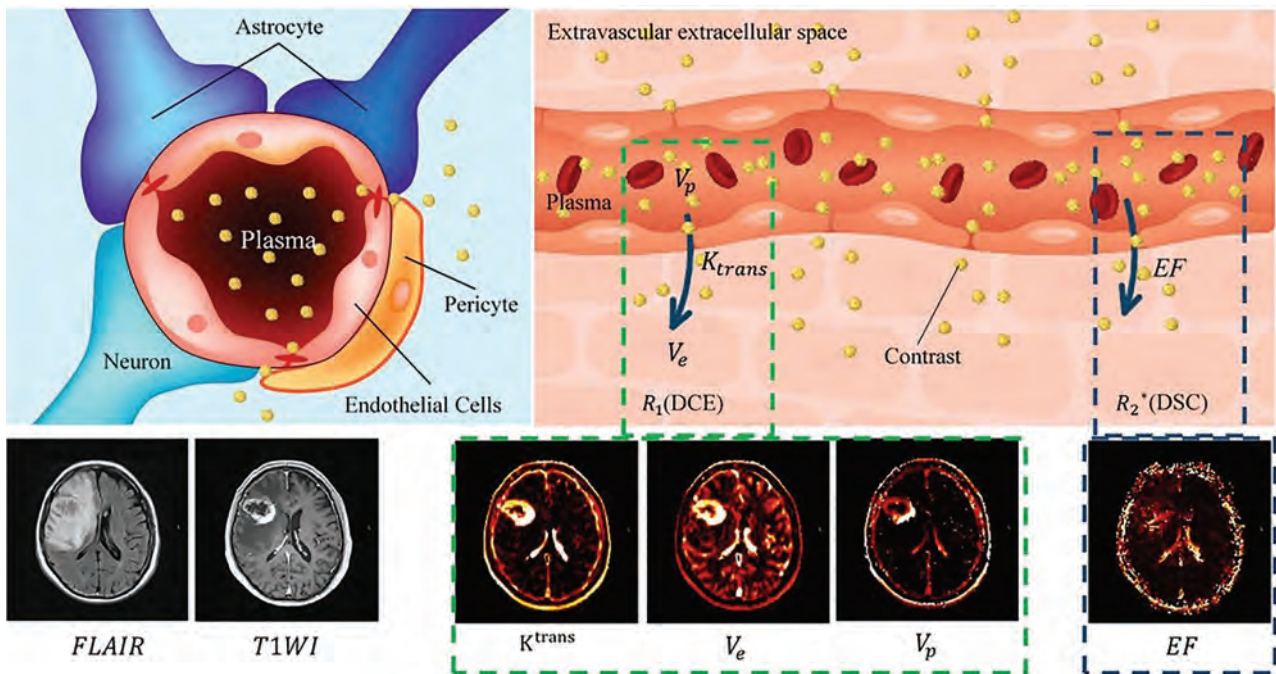
Note:—PV indicates percentile value.

<sup>a</sup> The study population (*n* = 102) was analyzed.

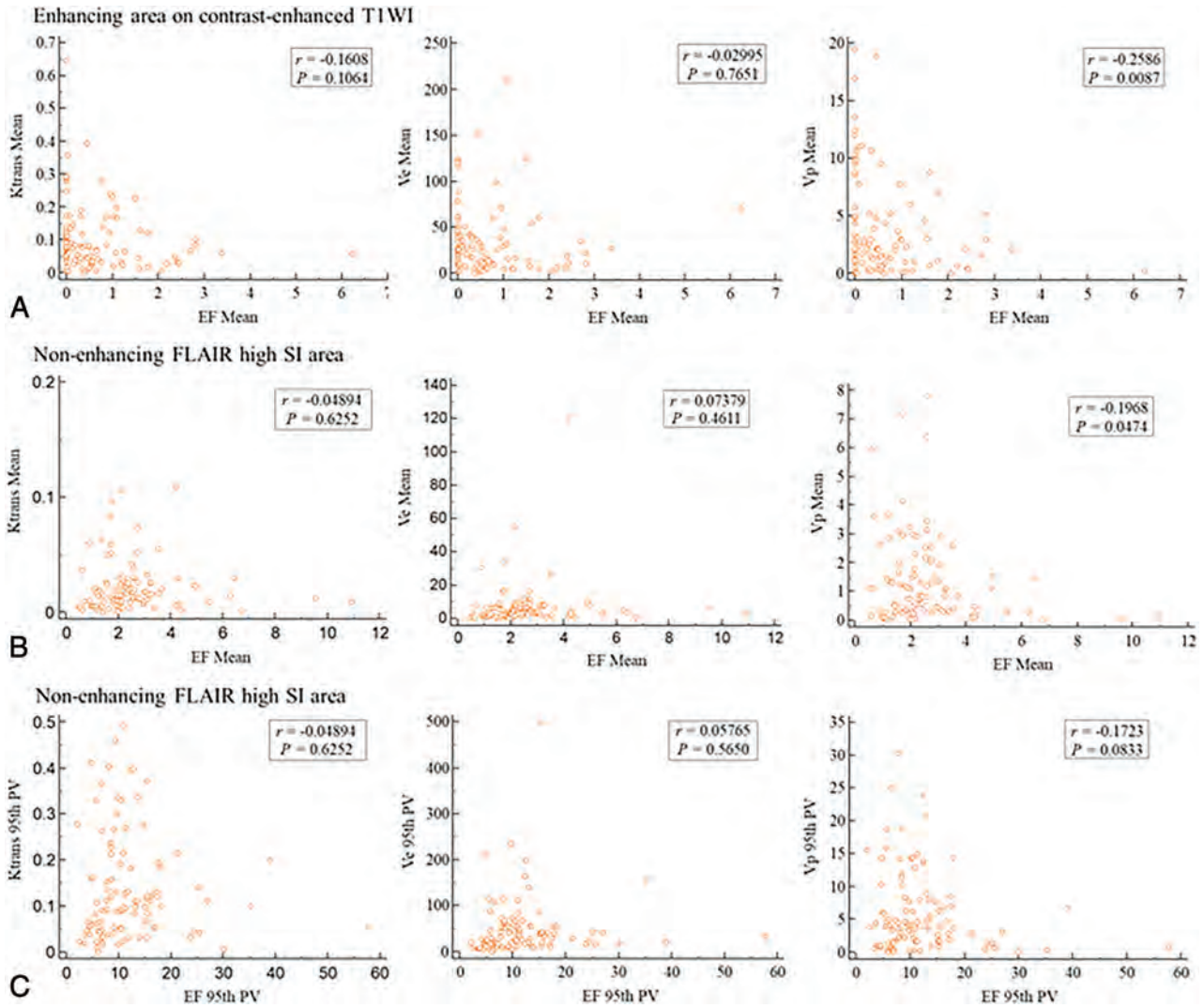
<sup>b</sup> Calculated with Cox proportional hazards model analysis.



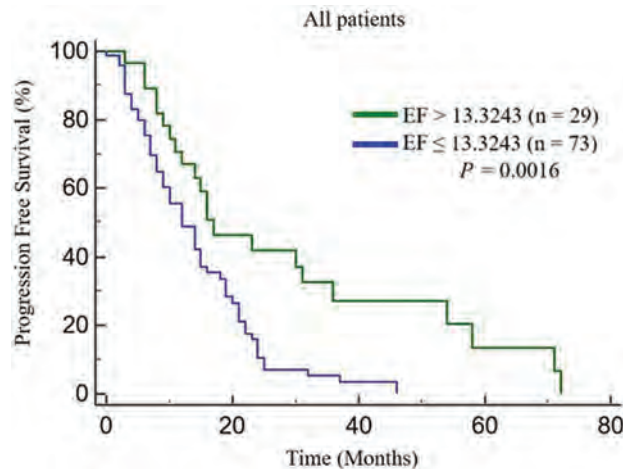
**ON-LINE FIG 1.** Study design flow chart.



**ON-LINE FIG 2.** Schematic diagram of the contrast leakage information based on DCE- and DSC-MR imaging. DSC-MR imaging uses T2\* shortening effects, whereas DCE-MR imaging uses T1 shortening effects. EF is a parameter from DSC-MR imaging, and  $K^{trans}$ ,  $V_e$ , and  $V_p$  are parameters from DCE-MR imaging for contrast leakage information.



**ON-LINE FIG 3.** The Pearson correlation analysis between the EF from DSC-MR imaging and  $K^{trans}$ , Ve, and Vp from DCE-MR imaging. The Pearson correlation analysis between the mean EF value and the  $K^{trans}$ , Ve, and Vp based on T1 enhancing lesions (A). The Pearson correlation analysis between the mean value (B) or 95th percentile value (C) of EF and the  $K^{trans}$ , Ve, and Vp based on nonenhancing FLAIR high-signal-intensity lesions. Except for a weak correlation between the mean EF and Vp values, there were no significant results.

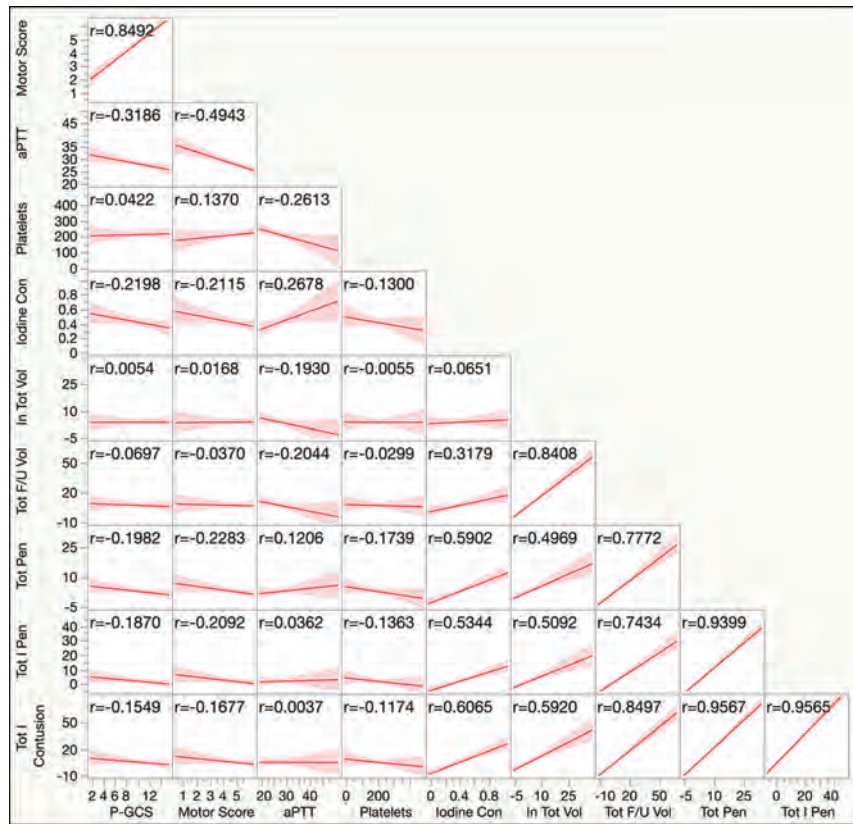


**ON-LINE FIG 4.** Kaplan-Meier survival analysis according to the EF value. The high EF 95th percentile value patient group showed significantly longer PFS than the low EF 95th percentile value patient group. The median survival of the high and low EF 95th percentile value patient groups was 17.0 months (95% CI, 12.0–36.0 months) versus 12.0 months (95% CI, 9.0–15.0 months), respectively ( $P = .02$ ).

**On-line Table: Independent variables from clinical, laboratory, and CT data**

Variables	Total (n = 65)	Medical Management (n = 44)	Surgical Management (n = 21)	Craniectomy (-) (n = 58)	Craniectomy (+) (n = 7)
Age (median) (Q <sub>1</sub> to Q <sub>3</sub> ) (yr)	48 (25–65.5)	54 (32.2–74)	26 (21–50.5)	50.5 (26.5–67.3)	21 (19–26)
Sex					
Men (%)	50 (76.9)	34 (52.3)	16 (24.6)	46 (70.8)	4 (6.2)
Women (%)	15 (23)	10 (15.4)	5 (7.7)	12 (18.5)	3 (4.6)
P-GCS (median) (Q <sub>1</sub> to Q <sub>3</sub> )	11 (7–14)	14 (10–14)	7 (7–9)	13 (7.8–14)	9 (7–9)
Motor score (median) (Q <sub>1</sub> to Q <sub>3</sub> )	5 (4.25–6)	6 (5–6)	4.5 (4–5)	6 (5–6)	5 (4–5)
Systolic BP (mean) (SD) (mm Hg)	149.6 (29.9)	153.3 (30.2)	141.9 (28.5)	148.6 (31)	157.3 (17.9)
Diastolic BP (mean) (SD) (mm Hg)	87.3 (17.3)	87.6 (17.2)	86.7 (17.9)	87 (17.8)	89.4 (13.9)
PT (median) (Q <sub>1</sub> to Q <sub>3</sub> ) (seconds)	14.3 (13.6–15.7)	14.4 (13.5–15.8)	14 (13.7–15.4)	14.4 (13.5–15.7)	13.8 (13.6–15.8)
aPTT (median) (Q <sub>1</sub> to Q <sub>3</sub> ) (seconds)	28 (26–30)	27 (25–30)	28 (26–30)	28 (25.5–30)	28 (26–31)
Fibrinogen (mean) (SD) (mg/dL)	295.2 (97.3)	325.4 (94.4)	234.8 (73.1)	303 (97)	228.6 (76.9)
Platelets (median) (Q <sub>1</sub> to Q <sub>3</sub> ) (10 <sup>3</sup> /μL)	210 (172–250)	212.5 (181.3–250)	192 (144.5–251.5)	210 (171–252.8)	210 (174–243)
Marshall CT score (%)					
DI II	57 (87.7)	41 (63.1)	16 (24.6)	52 (80)	5 (7.7)
DI III	7 (10.8)	2 (3.1)	5 (7.7)	5 (7.7)	2 (3.1)
DI IV	1 (1.5)	1 (1.5)	0	1 (1.5)	0
Multiple contusions (%)	28 (43.1)	14 (21.5)	14 (21.5)	24 (36.9)	4 (6.2)
Hemorrhagic progression (%)	44 (69.8)	29 (46)	15 (23.8)	38 (60.3)	6 (9.5)
Fraction of hemorrhagic progression (median) (Q <sub>1</sub> to Q <sub>3</sub> )	1.33 (0.12–3.8)	1.29 (0.1–3.56)	1.45 (0.27–4)	1.2 (0.1–3.73)	2.8 (0.5–9)
Iodine concentration (median) (Q <sub>1</sub> to Q <sub>3</sub> ) (mg/mL)	0.43 (0.23–0.53)	0.35 (0.23–0.49)	0.5 (0.32–0.78)	0.42 (0.23–0.5)	0.5 (0.3–0.9)
Hematoma volume on admission CT (median) (Q <sub>1</sub> to Q <sub>3</sub> ) (cm <sup>3</sup> )	1.52 (0.4–5.1)	0.97 (0.34–2.89)	2.2 (0.75–7.2)	1.2 (0.4–3.75)	3.48 (1.9–8.45)
Hematoma volume on follow-up CT (median) (Q <sub>1</sub> to Q <sub>3</sub> ) (cm <sup>3</sup> )	3.2 (1–9)	2.04 (0.93–7.3)	6.9 (2.8–16.8)	2.55 (0.98–7.95)	8.7 (7.2–23)
Total pseudo-hematoma from all contusions (median) (Q <sub>1</sub> to Q <sub>3</sub> ) (cm <sup>3</sup> )	1.02 (0.2–3.1)	0.75 (0.13–1.9)	3.2 (0.66–8.9)	0.97 (0.18–2.8)	4.3 (1.9–15)
Fractional pseudo-hematoma to true hematoma (median) (Q <sub>1</sub> to Q <sub>3</sub> )	0.3 (0.1–0.57)	0.3 (0.1–0.46)	0.38 (0.12–0.66)	0.3 (0.1–0.54)	0.44 (0.23–0.68)
Iodine quantity in all pseudo-hematomas (median) (Q <sub>1</sub> to Q <sub>3</sub> ) (mg)	0.34 (0.08–1.12)	0.28 (0.04–0.6)	0.96 (0.17–5.4)	0.33 (0.04–0.74)	3.17 (0.2–6.9)
Iodine quantity in all contusions (median) (Q <sub>1</sub> to Q <sub>3</sub> ) (mg)	1.33 (0.46–6)	1.1 (0.33–2.8)	3.35 (1.2–16.4)	1.24 (0.39–4.5)	7.85 (2.2–22.5)

**Note:**—BP indicates blood pressure; DI, diffuse injury; PT, prothrombin time; aPTT, activated partial thromboplastin time.



**ON-LINE FIGURE.** Correlations between predictor variables. The variables are on the horizontal axis with corresponding correlation values ( $r$ ) against each variable on the vertical axis. aPTT indicates activated partial thromboplastin time; Tot, total; F/U, follow-up; Con, concentration; Pen, penumbra.

**On-line Table 1: Clinical characteristics of the patients**

Characteristics	Whole Cohort (n = 246)	Wave-SWI vs Standard SWI (n = 107)	Wave-SWI vs T2*WI GRE (n = 139)
Male (%)	115 (46.7%)	58 (54.2%)	57 (41.0%)
Age (mean) (yr)	58.6 ± 17.0	60.1 ± 16.7	57.5 ± 17.3
Clinical indication for MR imaging (%)			
Tumor	93 (37.8%)	32 (29.9%)	61 (43.9%)
Stroke	40 (16.3%)	10 (9.3%)	30 (21.6%)
AMS	25 (10.2%)	13 (12.1%)	12 (8.6%)
Hemorrhage	18 (7.3%)	13 (12.1%)	5 (3.6%)
TBI	11 (4.5%)	9 (8.4%)	2 (1.4%)
Headache	11 (4.5%)	3 (2.8%)	8 (5.8%)
Dementia	8 (3.3%)	7 (6.5%)	1 (0.7%)
Infection	8 (3.3%)	3 (2.8%)	5 (3.6%)
AVM	4 (1.6%)	4 (3.7%)	0 (0%)
Seizure	2 (0.8%)	0 (0%)	2 (1.4%)
Other	26 (10.6%)	13 (12.1%)	13 (9.4%)

**Note:**—AMS indicates altered mental status; TBI, traumatic brain injury; AVM, arteriovenous malformation.

**On-line Table 2: Acquisition parameters for magnetic susceptibility sequences**

Parameter	T2*W GRE	Standard SWI	Wave-SWI
FOV read (mm)	250	240	240
FOV phase (%)	87.5	75.0	87.5
Matrix	256 × 190	256 × 182	288 × 189
Section thickness (mm)	5	1.8	1.8
TR/TE (ms)	694/20	30/20	40/(13 and 30; effective TE. 21.5)
Flip angle	20°	12°	15°
Acceleration factor <i>R</i>			
20-channel	1	GRAPPA, <i>R</i> = 2	Wave-CAIPI, <i>R</i> = 6
32-channel	1	GRAPPA, <i>R</i> = 2	Wave-CAIPI, <i>R</i> = 9
Bandwidth (Hz/pixel)	200	120	100
Scan time (min) (sec)			
20-channel	2, 21	5, 21	1, 40
32-channel	2, 21	5, 21	1, 6

**Note:**—GRAPPA indicates generalized autocalibrating partially parallel acquisition.

**On-line Table 3: Semiquantitative scoring criteria used for head-to-head comparison of wave-SWI versus standard susceptibility sequence (standard SWI or T2\*WI GRE)**

Parameter	Favors Image A <sup>a</sup>				Favors Image B <sup>a</sup>	
	Score -2	Score -1	0	Score +1	Score +2	
Visualization of pathology	Visualization of pathology is superior on image A; lesions are not visualized on image B	Visualization of pathology is preferred on image A, but lesions are still visualized on image B	Equivalent	Visualization of pathology is preferred on image B, but lesions are still visualized on image A	Visualization of pathology is superior on image B; lesions are not visualized on image A	
Artifacts	Image B has more artifacts that may obscure small lesions	Image B has more artifacts, but small lesions are not obscured	Equivalent	Image A has more artifacts, but small lesions are not obscured	Image A has more artifacts that may obscure small lesions	
Overall diagnostic quality	Image B is of lower quality, and the difference alters the clinical diagnosis	Image B is of lower quality, but the difference does not alter the clinical diagnosis	Equivalent	Image A is of lower quality, but the difference does not alter the clinical diagnosis	Image A is of lower quality, and the difference alters the clinical diagnosis	

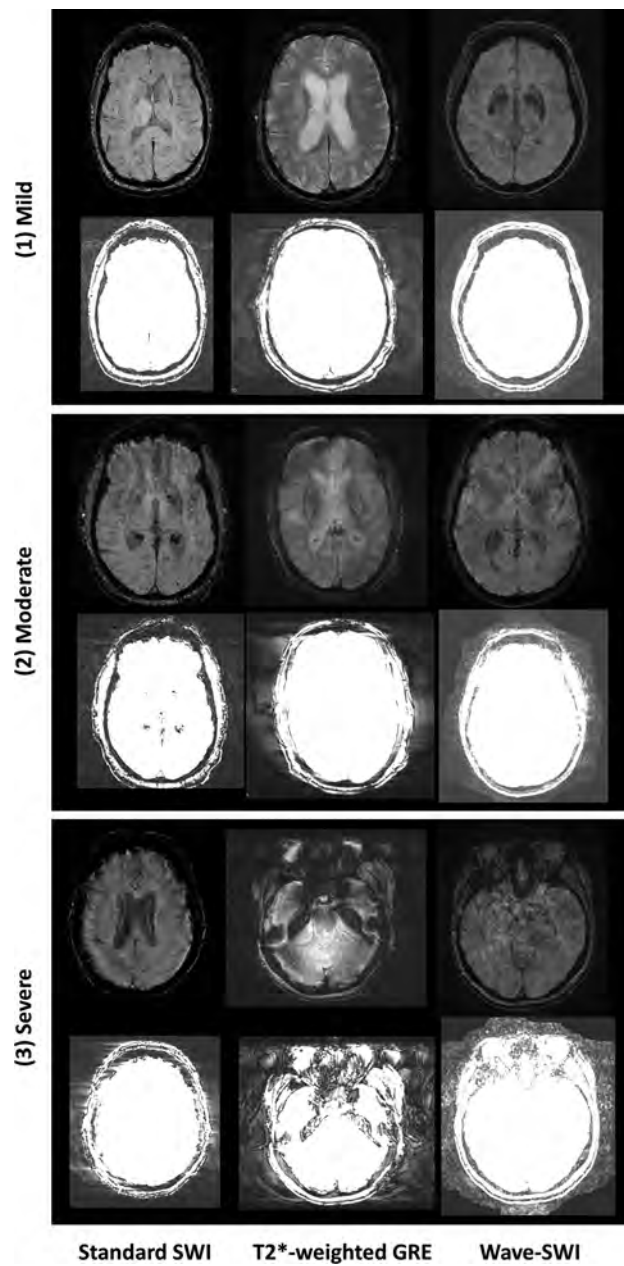
<sup>a</sup> The wave-SWI and standard susceptibility sequences were randomly positioned on either the right or left side of the screen, labeled image A and image B.

**On-line Table 4: Results of individual image series analysis**

Variable	T2*WI GRE (n = 139)	Wave-SWI (n = 139)	P <sup>a</sup>	Standard SWI (n = 107)	Wave-SWI (n = 107)	P <sup>a</sup>	
Presence of hemorrhage							
Yes	76 (54.7%)	95 (68.3%)	<.001	62 (57.9%)	61 (57.0%)	1	
No	63 (45.3%)	44 (31.7%)		45 (42.1%)	46 (43.0%)		
No. of micro-hemorrhages <sup>b</sup> (total) (range)							
Infratentorial	22 (0–6)	45 (0–10)	<.01	105 (0–49)	91 (0–42)	.21	
Deep	16 (0–2)	42 (0–7)		83 (0–27)	73 (0–29)		.47
Lobar	33 (0–5)	245 (0–72)		<.001	385 (0–146)		387 (0–141)
Motion artifacts							
No/mild	115 (82.7%)	84 (60.4%)	<.001	55 (51.4%)	59 (55.1%)	.01	
Moderate	15 (10.8%)	38 (27.3%)		31 (29.0%)	38 (35.5%)		
Severe	9 (6.5%)	17 (12.2%)		21 (19.6%)	10 (9.3%)		
Diagnostic?							
Yes	132 (95.0%)	133 (95.7%)	1	98 (91.6%)	104 (97.2%)	.08	
No	7 (5.0%)	6 (4.3%)		9 (8.4%)	3 (2.8%)		

<sup>a</sup> McNemar test for dichotomous variables; Wilcoxon signed rank test for ordinal variables.

<sup>b</sup> Total number of microhemorrhages according to MARS.<sup>11</sup>



**ON-LINE FIGURE.** Reference images available to readers during the image review, illustrating representative images for the grading of motion artifacts. Motion was graded according to the following scale: 0, none; 1, mild (motion is perceptible but not clinically relevant); 2, moderate (motion is present and may obscure subtle findings); and 3, severe (motion is present and may obscure major findings).

## ON-LINE APPENDIX

### **Antibody Testing**

After 2014, screening for onco-neuronal antibodies was performed using semiquantitative immunoblots (EUROLINE PNS 12; DL 1111–1601–7 G; Euroimmun, Lübeck, Germany) coated with recombinant antigen or antigen fragments (dilution: serum, 1:100; cerebrospinal liquor, 1:1). In parallel, immunocytochemistry was performed using Human Embryonic Kidney 293-cells with expression of antigens on the cell surface (IIFT: Auto-immune Enzephalitis Mosaik1, Euroimmun; FA 1120–1005-1; GAD65-IIFT, Euroimmun; FA 1022–1005-50) for NMDAR, CASPR, LGI1, GABAA, GABAB, AMPAR, and GAD65 autoantibodies (dilution, serum 1:10; cerebrospinal liquor, 1:1). Before

2014, detection of GAD antibodies in serum was performed using an anti-<sup>125</sup>I-GAD radioimmunoprecipitation assay (normal values,  $\leq 1$  U/mL; Wetherall Institute of Molecular Medicine, Oxford, UK; or Euroimmun). VGKC-complex antibodies were also examined by radioimmunoprecipitation assay (normal values,  $< 100$  picomolar; Wetherall Institute of Molecular Medicine or Euroimmun). Antibodies against LGI1 and CASPR2 were detected by indirect immunofluorescence using formalin-fixed human Embryonic Kidney 293-cells containing membrane bound LGI1 or CASPR2 (normal values,  $< 1:10$ ; all tests performed by Euroimmun). These tests were not performed before 2010, which is why 13 patients in the early VGKC group and 14 patients in the late VGKC group have not been tested for CASPR2 or LGI1.

**On-line Table 1: Patient characteristics and antibody testing—early groups<sup>a</sup>**

Study Group	ID	Sex	Age at MR Imaging (yr)	Time between Onset and Scan (mo)	Lateralization EEG	Immunotherapy before MR Imaging Acquisition	Antibody Status (at the Time of MR Imaging Acquisition)	Clinical Imaging
Early GAD	1	F	48	23	Left temporal	—	Neg. (S. and L.)	—
Early GAD	2	F	17	11	Right temporal	—	—	—
Early GAD	3	F	25	16	Left temporal	Steroids	Pos. (S. and L.)	—
Early GAD	4	M	26	3	Left temporal	—	—	T2-FLAIR acute: mesiotemporal hyperintensities left hemisphere
Early GAD	5	F	32	24	Right temporal	—	Pos. (S. and L.)	T2-FLAIR acute: normal
Early GAD	6	F	18	1	Right temporal	—	Pos. (S. and L.)	T2-FLAIR acute: volume increase and hyperintensities right amygdala and right hippocampus
Early GAD	7	F	43	8	Right temporal	—	Pos. (S. and L.)	T2-FLAIR acute: hyperintensities left hippocampus
Early GAD	8	F	24	5	Left temporal	—	Pos. (S.; L. not tested)	T2-FLAIR acute: hyperintensities and volume increase left mesiotemporal
Early GAD	9	F	42	5	Left temporal	—	Pos. (S.; L. not tested)	T2-FLAIR acute: hyperintensities left hippocampus and left amygdala
Early GAD	10	M	43	3	Temporal	Steroids	Pos. (S.; L. not tested)	T2-FLAIR acute: hyperintensities left hippocampus and left amygdala
Early GAD	11	F	49	5	Left temporal	—	Pos. (S.; L. not tested)	T2-FLAIR acute: hyperintensities and volume increase right mesiotemporal
Early GAD	12	M	32	2	—	Steroids, plasmapheresis	Pos. (S.; L. not tested)	T2-FLAIR acute: hyperintensities and slide atrophy of right hippocampus
Early GAD	13	M	35	5	Left temporal	—	Pos. (S.; L. not tested)	T2-FLAIR acute: hyperintensities and volume increase left hippocampus and amygdala
Early GAD	14	F	27	5	Temporal	—	Pos. (S. and L.)	T2-FLAIR acute: hyperintensities and volume increase right mesiotemporal
Early GAD	15	M	58	3	Right temporal	—	Neg. (S. and L.)	T2-FLAIR acute: slide hippocampal atrophy bilateral, no signal alterations
Early GAD	16	F	43	11	Left temporal	—	Pos. (S.; L. neg.)	T2-FLAIR acute: hyperintensities and volume increase left hippocampus and amygdala
Early GAD	17	F	26	16	—	—	Pos. (S.; L. not tested)	T2-FLAIR acute: slide volume increase of right amygdala, no signal alterations
Early GAD	18	F	28	0	Left temporal	—	Pos. (S. and L.)	T2-FLAIR acute: hyperintensities and volume increase of both amygdalae
Early GAD	19	M	45	12	Left temporal	—	—	T2-FLAIR acute: hyperintensities and volume increase of left amygdala and anterior hippocampus

*Continued on next page*

**On-line Table 1: Continued**

Study Group	ID	Sex	Age at MR Imaging (yr)	Time between Onset and Scan (mo)	Lateralization EEG	Immunotherapy before MR Imaging Acquisition	Antibody Status (at the Time of MR Imaging Acquisition)	Clinical Imaging
Early GAD	20	M	27	16	Left temporal	–	Neg. (S. and L.)	T2-FLAIR acute: hyperintensities and volume increase of left amygdala
Early GAD	21	F	21	22	Bilateral temporal	–	Pos. (S. and L.)	T2-FLAIR acute: bilateral hyperintensities in amygdalae and hippocampi
Early GAD	22	F	23	17	Normal	–	Pos. (S.; L. neg.)	T2-FLAIR acute: volume increase left amygdala and hyperintensities in left hippocampus
Early GAD	23	F	43	6	Left temporal	–	Pos. (S.; L. not tested)	T2-FLAIR acute: hyperintensities and volume increase of left amygdala and left hippocampus
Early VGKC	24	M	55	14	Normal	Steroids	Pos. (S.; L. not tested)	T2-FLAIR acute: normal
Early VGKC	25	M	60	3	Bilateral temporal	–	Pos. (S.; L. neg.)	T2-FLAIR acute: bilateral hyperintensities increase of amygdala and anterior hippocampus
Early VGKC	26	F	48	22	Left temporal	–	Pos. (S.; L. not tested)	T2-FLAIR acute: hyperintensities and volume increase left hippocampus
Early VGKC	27	M	68	9	Bilateral temporal	Steroids, immunoadsorption	Pos. (S.; L. not tested)	T2-FLAIR acute: bilateral hippocampal hyperintensities and volume increase
Early VGKC	28	F	53	11	Right temporal	–	Pos. (S.; L. not tested)	T2-FLAIR acute: hyperintensities and volume increase of right amygdala; atrophy of the right hippocampus
Early VGKC	29	M	73	11	Left temporal	–	Pos. (S. and L.)	T2-FLAIR acute: volume-increased amygdalae (right > left)
Early VGKC	30	M	70	5	Left temporal	–	Pos. (S. and L.)	T2-FLAIR acute: hyperintensity and volume increase of left amygdala; questionable atrophy right hippocampus
Early VGKC	31	M	67	5	Right temporal	–	Neg. (S.; L. not tested)	T2-FLAIR acute: narrowed hippocampi and left mesiotemporal hyperintensities
Early VGKC	32	F	20	10	Right temporal	Steroids	Pos. (S.; L. not tested)	–
Early VGKC	33	F	61	0	Left temporal	–	Pos. (S. and L.)	T2-FLAIR acute: bilateral hyperintensities and volume increase of amygdalae and anterior hippocampi
Early VGKC	34	M	69	12	Left temporal	–	Pos. (S.; L. not tested)	T2-FLAIR acute: questionable left mesiotemporal hyperintensity and volume increase
Early VGKC	35	M	61	1	Left temporal	Steroids, plasmapheresis	Pos. (S; L. neg.)	T2-FLAIR acute: left hippocampus with subtle atrophy
Early VGKC	36	F	23	0	Left temporal	–	Pos. (S.; L. not tested)	T2-FLAIR acute: questionable bilateral hyperintensity in the pulvinar thalami

*Continued on next page*

**On-line Table 1: Continued**

Study Group	ID	Sex	Age at MR Imaging (yr)	Time between Onset and Scan (mo)	Lateralization EEG	Immunotherapy before MR Imaging Acquisition	Antibody Status (at the Time of MR Imaging Acquisition)	Clinical Imaging
Early VGKC (CASPR2)	37	M	38	6	Left temporal	–	Pos. (S.; L. not tested)	T2-FLAIR acute: bilateral hyperintensities of amygdalae
Early VGKC (CASPR2)	38	M	82	23	Right temporal	–	Pos. (S. and L.)	T2-FLAIR acute: right mesiotemporal hyperintensities and volume increase (especially in amygdala)
Early VGKC (LGII)	39	F	48	4	Right temporal	–	Neg. (S. and L.)	T2-FLAIR acute: hyperintensities and volume increase of right amygdala and hippocampus
Early VGKC (LGII)	40	F	57	2	Right temporal	–	Pos. (S. and L.)	T2-FLAIR acute enlarged mesiotemporal structures, questionable changes in signal
Early VGKC (LGII)	41	F	72	3	Normal	Steroids	Pos. (S. and L.)	–
Early VGKC (LGII)	42	F	71	13	Normal	Steroids	Pos. (S.; L. not tested)	T2-FLAIR acute: signs of atherosclerotic encephalopathy, no mesiotemporal hyperintensities or volume alterations
Early VGKC (LGII)	43	M	65	7	Bilateral temporal	Steroids, immunoadsorption	Pos. (S; L. neg.)	T2-FLAIR acute: microangiopathy
Early VGKC (LGII)	44	M	62	4	No seizures documented	Steroids	Pos. (S.; L. not tested)	T2-FLAIR acute: prominent right amygdala with subtle hyperintensity
Early VGKC (LGII)	45	M	76	6	Normal	Steroids, immunoadsorption, intravenous immunoglobulins	Neg. (S.; L. not tested)	T2-FLAIR acute: global brain atrophy; unspecific periventricular white matter lesions on FLAIR
Early VGKC (LGII)	46	M	74	2	Left temporal	–	Pos. (S; L. neg.)	–
Early VGKC (LGII)	47	M	54	11	Right temporal	Steroids, intravenous immunoglobulins	Neg. (S. and L.)	T2-FLAIR acute: bilateral prominent and signal-enhanced amygdalae with signal enhancement; narrowed hippocampi
Early VGKC (LGII)	48	M	53	7	Normal	–	Neg. (S.; L. not tested)	T2-FLAIR acute: unspecific white matter lesions

**Note:**—S. indicates in serum; L., in liquor; not tested, not tested at the time of the respective MR imaging scan; –, not conducted; Neg., negative; Pos., positive; ID, identification.

<sup>a</sup> Patient characteristics of all patient groups included in the study (early GAD-LE, early VGKC-LE, late GAD-LE, late VGKC-LE).

**On-line Table 2: Patient characteristics and antibody testing—late groups<sup>3</sup>**

Study Group	ID	Sex	Age at MR Imaging (yr)	Time between Onset and Scan (mo)	Lateralization EEG	Immunotherapy before MR Imaging Acquisition	Antibody Status (at the Time of MR Imaging Acquisition)	Clinical Imaging
Late GAD	49	M	29	112	Right temporal	Steroids, azathioprine	Pos. (S.; L. not tested)	Follow-up scan: bilateral abnormal mesiotemporal structures
Late GAD	50	F	32	53	–	Steroids	Pos. (S.; L. not tested)	Follow-up scan: hyperintense left amygdala
Late GAD	51	F	26	64	Left temporal	–	Pos. (S. and L.)	Follow-up scan: volume increase and slight hyperintensity of left amygdala and hippocampus
Late GAD	52	F	24	92	Bilateral temporal	–	Pos. (S.; L. not tested)	Follow-up scan: volume increase and hyperintensity of both amygdalae; hyperintensity of both hippocampi (left > right)
Late GAD	53	F	29	87	Bilateral temporal	–	Pos. (S.; L. not tested)	Follow-up scan: normal mesiotemporal structures
Late GAD	54	F	48	110	–	–	Not tested	–
Late GAD	55	F	31	72	Left temporal	Steroids	Neg. (S. and L.)	Follow-up scan: left mesiotemporal structures appear to be volume-increased
Late GAD	56	F	48	48	–	–	Not tested	–
Late GAD	57	F	21	42	Left temporal	–	Neg. (S. and L.)	Follow-up scan: volume-increased and hyperintense left amygdala
Late GAD	21	F	21	25	–	Steroids	Pos. (S.; L. not tested)	Follow-up scan: volume-increased amygdala (left > right)
Late GAD	2	F	23	83	Left temporal	Steroids, intravenous immunoglobulins	Pos. (S.; L. not tested)	Follow-up scan: atrophy right hippocampus
Late GAD	58	F	27	91	Bilateral temporal	Steroids	Not tested	Follow-up scan: bilateral hippocampal atrophy
Late GAD	3	F	26	27	Left temporal	Steroids	Pos. (S. ; L. not tested)	–
Late GAD	4	M	29	42	Bilateral temporal	Steroids, intravenous immunoglobulins, natalizumab	Pos. (S.; L. not tested)	–
Late GAD	5	F	34	56	–	Steroids, intravenous immunoglobulins	Not tested	Follow-up scan: normal
Late GAD	59	F	30	115	Left temporal	Steroids, intravenous immunoglobulins, immunoadsorption, plasmapheresis, cyclophosphamide	Not tested	Follow-up scan: hyperintensity and volume increase of right amygdala and hippocampus; hyperintensity left hippocampus
Late GAD	6	F	21	35	–	Steroids, immunoadsorption, cyclophosphamide, mycophenolate mofetil	Neg. (S.; L. not tested)	Follow-up scan: subtle bilateral hippocampal atrophy

*Continued on next page*

**On-line Table 2: Continued**

Study Group	ID	Sex	Age at MR Imaging (yr)	Time between Onset and Scan (mo)	Lateralization EEG	Immunotherapy before MR Imaging Acquisition	Antibody Status (at the Time of MR Imaging Acquisition)	Clinical Imaging
Late GAD	8	F	26	21	Left temporal	Steroids, immunoadsorption, mycophenolate mofetil	Not tested	Follow-up scan: hyperintense left mesiotemporal structures; no atrophy
Late GAD	60	M	17	55	–	–	Pos. (S.; L. not tested)	Follow-up scan: questionable signal abnormality left hippocampus
Late GAD	61	M	35	69	–	–	Not tested	Follow-up scan: normal
Late GAD	10	M	48	63	–	Steroids, basiliximab	Not tested	Follow-up scan: left hippocampal atrophy and enlarged left amygdala
Late GAD	11	F	52	50	–	Steroids, basiliximab	Not tested	Follow-up scan: bilateral volume increase of amygdalae
Late GAD	62	F	24	100	–	–	Not tested	Follow-up scan: unclear lesion frontal lobe; all other areas normal
Late GAD	63	M	27	70	–	Steroids	Not tested	Follow-up scan: left hippocampal sclerosis
Late GAD	64	M	24	65	Left temporal	–	Pos. (S. and L.)	Follow-up scan: normal mesiotemporal structures
Late GAD	14	F	31	44	–	Steroids	Pos. (S.; L. not tested)	Follow-up scan: mesiotemporal volume increase and hyperintensity
Late GAD	65	M	51	44	Right temporal	Steroids	Not tested	Follow-up scan: hyperintensity and subtle volume increase of right amygdala and hippocampus
Late GAD	66	F	61	79	Bilateral temporal	Steroids	Pos. (S. and L.)	Follow-up scan: hyperintensity and subtle volume increase of right amygdala and hippocampus and of the anterior left hippocampus
Late GAD	67	M	44	45	Normal	–	Not tested	Follow-up scan: subtle hyperintensity of right hippocampus
Late GAD	68	F	24	31	Right temporal	–	Pos. (S. and L.)	Follow-up scan: hyperintensity of right hippocampus and amygdala
Late GAD	69	M	63	27	Right temporal	–	Pos. (S. and L.)	Follow-up scan: hyperintensity and volume increase right amygdala
Late GAD	70	F	30	75	Left temporal	Steroids, immunoadsorption plasmapheresis	Not tested	Follow-up scan: declining hyperintensity right hippocampus

*Continued on next page*

**On-line Table 2: Continued**

Study Group	ID	Sex	Age at MR Imaging (yr)	Time between Onset and Scan (mo)	Lateralization EEG	Immunotherapy before MR Imaging Acquisition	Antibody Status (at the Time of MR Imaging Acquisition)	Clinical Imaging
Late GAD	71	F	47	69	Left temporal	Steroids	Pos. (S. and L.)	Follow-up scan: hyperintensity and volume increase of the left amygdala
Late VGKC	2	M	64	59	–	Steroids	Not tested	Follow-up scan: bilateral hippocampal atrophy
Late VGKC	3	F	53	73	–	Steroids, tacrolimus	Neg. (S. and L.)	Follow-up scan: normal
Late VGKC	5	F	56	40	–	Steroids, azathioprine	Neg. (S.; L. not tested)	Follow-up scan: left hippocampal sclerosis
Late VGKC	6	M	79	87	Right temporal	Steroids	Pos. (S.; L. not tested)	Follow-up scan: subtle bilateral hippocampal atrophy
Late VGKC	7	M	78	110	Left temporal	Steroids	Pos. (S. and L.)	Follow-up scan: hyperintensity and volume increase of the left amygdala
Late VGKC (CASPR2)	14	M	40	29	–	Steroids, plasmapheresis, mycophenolate mofetil	Not tested	–
Late VGKC	9	F	23	43	–	Steroids	Neg. (S.; L. not tested)	Follow-up scan: subtle mesiotemporal hyperintensity in the left hemisphere
Late VGKC	10	F	68	90	Right temporal	Steroids	Neg. (S.; L. not tested)	Follow-up scan: right hippocampal sclerosis
Late VGKC	11	M	75	84	Right temporal	Steroids, intravenous immunoglobulins	Neg. (S.; L. not tested)	Follow-up scan: questionable left mesiotemporal hyperintensity and swelling
Late VGKC (LGI1)	16	F	52	47	Left temporal	Steroids, intravenous immunoglobulins	Neg. (S.; L. not tested)	Follow-up scan: hyperintensity of the right mesiotemporal structures
Late VGKC (LGI1)	18	F	74	27	Left temporal	Steroids, immunoadsorption	Not tested	–
Late VGKC	13	F	26	37	–	Steroids	Not tested	Follow-up scan: normal
Late VGKC (LGI1)	19	F	73	33	Right temporal	Steroids	Neg. (S.; L. not tested)	Follow-up scan: signs of subcortical arteriosclerotic encephalopathy; normal mesiotemporal structures
Late VGKC	72	F	47	45	–	Steroids	Neg. (S.; L. not tested)	–
Late VGKC	73	F	64	82	Left temporal	Steroids	Neg. (S.; L. not tested)	Follow-up scan: bilateral mesiotemporal hyperintensity (especially left amygdala); no hippocampal sclerosis
Late VGKC (CASPR2)	74	M	52	61	Bilateral temporal	Steroids	Pos. (S. and L.)	Follow-up scan: bilateral mesiotemporal hyperintensity and volume increase

*Continued on next page*

**On-line Table 2: Continued**

Study Group	ID	Sex	Age at MR Imaging (yr)	Time between Onset and Scan (mo)	Lateralization EEG	Immunotherapy before MR Imaging Acquisition	Antibody Status (at the Time of MR Imaging Acquisition)	Clinical Imaging
Late VGKC	75	M	31	91	Left temporal	Steroids	Not tested	Follow-up scan: bilateral hyperintensity and volume increase of amygdalae (left > right)
Late VGKC (CASPR2)	76	M	64	86	—	Steroids	Pos. (S.; L. not tested)	Follow-up scan: global brain atrophy
Late VGKC	77	M	52	51	Left temporal	Steroids	Pos. (S.; L. not tested)	Follow-up scan: hyperintensity and volume increase of left mesiotemporal
Late VGKC (CASPR2)	78	M	53	65	Left temporal	Steroids, immunoadsorption, azathioprine	Pos. (S. and L.)	Follow-up scan: hyperintense mesiotemporal structures right hemisphere
Late VGKC (CASPR2)	79	F	45	47	Left temporal	Steroids	Pos. (S.; L. not tested)	Follow-up scan: cortical atrophy; declining swelling of left amygdala; no hippocampal sclerosis
Late VGKC	80	F	76	67	—	Steroids	Not tested	Follow-up scan: global brain atrophy; microangiopathic white matter disease

**Note:**—indicates not conducted; S., in serum; L., in liquor; not tested, not tested at the time of the respective MR imaging scan; Neg., negative; Pos., positive; ID, identification.

<sup>a</sup> Characteristics of all patient groups included in the study (early GAD-LE, early VGKC-LE, late GAD-LE, late VGKC-LE).

**On-line Table 3: Volumetry of hippocampal subfields in patients and controls—multivariate linear models in early GAD group<sup>a</sup>**

Multivariate Linear Model, $F(11, 44) = 2.33$ , Prob > F = 0.023 ( $n = 46$ ) <sup>b</sup>				
Post Hoc <i>T</i> Tests <sup>c</sup>	Coefficient	Standard Error	<i>T</i> Test	<i>P</i> >   <i>t</i>
Hippocampal tail	-9.1	22.6	-0.40	.690
Subiculum	-11.6	15.8	-0.73	.466
CA1	-64.3	26.2	-2.46	.018 <sup>b</sup>
Presubiculum	0.8	12.0	0.07	.947
Parasubiculum	-7.7	3.7	-2.07	.045 <sup>b</sup>
Molecular layer	-29.9	21.4	-1.40	.168
GC-ML-DG	-12.1	12.6	-0.96	.340
CA3	-17.1	11.2	-1.61	.114
CA4	-12.4	11.4	-1.09	.284
Fimbria	-0.4	4.6	-0.10	.925
HATA	-9.9	3.3	-3.01	.004 <sup>b</sup>

**Note:**—GC-ML-DG indicates granule cell layer of the dentate gyrus; HATA, hippocampus-amygdala transition area; Prob, probability.

<sup>a</sup> On-line Tables 3 to 8 show multivariate linear models including post hoc *t* tests of hippocampal subfield volumes between the different patient groups and their matched controls (as shown in Fig 2).

<sup>b</sup> Significant values.

<sup>c</sup> Protected by the Fisher least-significant difference.

**On-line Table 4: Early VGKC group**

Multivariate Linear Model, $F(11, 48) = 2.48$ , Prob > F = 0.015 <sup>a</sup> ( $n = 50$ )				
Post Hoc <i>T</i> Tests <sup>b</sup>	Coefficient	Standard Error	<i>T</i> Test	<i>P</i> >   <i>t</i>
Hippocampal tail	1.2	21.9	0.05	.957
Subiculum	-16.2	17.7	-0.91	.365
CA1	-19.5	24.0	-0.81	.422
Presubiculum	-2.5	14.4	-0.18	.861
Parasubiculum	-10.0	3.7	-2.68	.010 <sup>a</sup>
Molecular layer	-10.5	21.7	-0.48	.632
GC-ML-DG	-3.1	11.6	-0.27	.791
CA3	-8.7	8.3	-1.05	.301
CA4	-5.2	9.4	-0.56	.581
Fimbria	7.5	7.9	0.95	.347
HATA	-12.8	3.7	-3.43	.001 <sup>a</sup>

**Note:**—GC-ML-DG indicates granule cell layer of the dentate gyrus; HATA, hippocampus-amygdala transition area; Prob, probability.

<sup>a</sup> Significant.

<sup>b</sup> Protected by the Fisher least-significant difference.

**On-line Table 5: Early LGII group**

Multivariate Linear Model, $F(11, 18) = 3.44$ , Prob > $F = 0.001^a$ ( $n = 20$ )				
Post Hoc $T$ Tests <sup>b</sup>	Coefficient	Standard Error	$T$ Test	$P >  t $
Hippocampal tail	21.5	35.0	0.62	.546
Subiculum	21.4	23.6	0.91	.377
CA1	5.5	44.7	0.12	.904
Presubiculum	20.6	18.3	1.13	.275
Parasubiculum	-9.9	5.2	-1.91	.072
Molecular layer	19.9	34.5	0.58	.572
GC-ML-DG	11.8	19.1	0.62	.545
CA3	-5.0	16.0	-0.32	.752
CA4	4.3	16.0	0.27	.787
Fimbria	29.1	8.4	3.47	.003 <sup>a</sup>
HATA	-5.5	6.6	-0.83	.418

**Note:**—GC-ML-DG indicates granule cell layer of the dentate gyrus; HATA, hippocampus-amygdala transition area; Prob, probability.

<sup>a</sup> Significant.

<sup>b</sup> Protected by the Fisher least-significant difference.

**On-line Table 6: Early VGKC group without LGII**

Multivariate Linear Model, $F(11, 28) = 2.75$ , Prob > $F = 0.015^a$ ( $n = 30$ )				
Post Hoc $T$ Tests <sup>b</sup>	Coefficient	Standard Error	$T$ Test	$P >  t $
Hippocampal tail	-17.4	26.9	-0.65	.523
Subiculum	-41.7	23.8	-1.75	.091
CA1	-49.1	29.0	-1.70	.101
Presubiculum	-16.9	19.6	-0.86	.398
Parasubiculum	-11.0	5.3	-2.07	.048 <sup>a</sup>
Molecular layer	-38.7	27.5	-1.41	.169
GC-ML-DG	-16.5	13.9	-1.18	.247
CA3	-15.4	9.4	-1.64	.113
CA4	-15.1	11.5	-1.31	.200
Fimbria	-5.0	11.1	-0.45	.655
HATA	-17.2	4.3	-3.99	<.001 <sup>a</sup>

**Note:**—GC-ML-DG indicates granule cell layer of the dentate gyrus; HATA, hippocampus-amygdala transition area; Prob, probability.

<sup>a</sup> Significant.

<sup>b</sup> Protected by the Fisher least-significant difference.

**On-line Table 7: Late GAD group**

Multivariate Linear Model, $F(11, 64) = 3.65$ , Prob > $F = 0.001^a$ ( $n = 66$ )				
Post Hoc $T$ Tests <sup>b</sup>	Coefficient	Standard Error	$T$ Test	$P >  t $
Hippocampal tail	-3.5	16.0	-0.22	.826
Subiculum	28.4	11.5	2.46	.016 <sup>a</sup>
CA1	29.4	19.2	1.53	.131
Presubiculum	4.1	9.1	0.45	.657
Parasubiculum	2.7	2.3	1.18	.242
Molecular layer	22.4	14.7	1.53	.132
GC-ML-DG	8.1	8.4	0.97	.334
CA3	5.5	8.8	0.62	.538
CA4	6.1	7.5	0.82	.418
Fimbria	5.2	3.9	1.34	.184
HATA	10.1	2.2	4.58	<.001 <sup>a</sup>

**Note:**—GC-ML-DG indicates granule cell layer of the dentate gyrus; HATA, hippocampus-amygdala transition area; Prob, probability.

<sup>a</sup> Significant.

<sup>b</sup> Protected by the Fisher least-significant difference.

**On-line Table 8: Late VGKC group**

Multivariate Linear Model, $F(11, 42) = 1.62$ , Prob > $F = 0.128$ ( $n = 44$ )				
Post Hoc $T$ Tests <sup>a</sup>	Coefficient	Standard Error	$T$ Test	$P >  t $
Hippocampal tail	-0.5	29.0	-0.02	.986
Subiculum	16.8	19.5	0.86	.395
CA1	1.8	28.7	0.06	.951
Presubiculum	7.1	13.3	0.53	.599
Parasubiculum	-6.0	3.7	-1.62	.114
Molecular layer	10.7	23.4	0.46	.651
GC-ML-DG	5.0	11.5	0.43	.667
CA3	0.2	9.3	0.02	.986
CA4	0.8	9.7	0.08	.938
Fimbria	11.0	6.4	1.72	.092
HATA	1.5	4.3	0.34	.734

**Note:**—GC-ML-DG indicates granule cell layer of the dentate gyrus; HATA, hippocampus-amygdala transition area; Prob, probability.

<sup>a</sup> Protected by the Fisher least-significant difference.

**On-line Table 9: Volumetry of amygdala and hippocampus in patients and controls (1-tailed, 2-sample  $t$  tests) in early groups<sup>a</sup>**

23 Early GAD-LE Group + 23 Controls ( $n = 46$ ) and 25 Early VGKC-LE Group + 25 Controls ( $n = 50$ )			
	DOF	$T$ Test	$P >  t $
Early GAD-LE			
Amygdala affected	44	1.92	.031 <sup>b</sup>
Hippocampus affected	44	1.35	
Amygdala unaffected	44	-0.21	>.05
Hippocampus unaffected	44	-0.74	
Early VGKC-LE			
Amygdala affected	48	2.82	.004 <sup>b</sup>
Hippocampus affected	48	0.67	
Amygdala unaffected	48	1.19	>.05
Hippocampus unaffected	48	-0.22	

**Note:**—DOF indicates degrees of freedom; Pr, probability.

<sup>a</sup> One-tailed, 2-sample  $t$  tests of the amygdala and hippocampus in the affected and unaffected hemispheres between patients with LE and matched controls (as shown in Fig 1).

<sup>b</sup> Significant values.

**On-line Table 10: Volumetry of amygdala and hippocampus in patients and controls (1-tailed, 2-sample  $t$  tests) in late groups<sup>a</sup>**

33 late GAD-LE Group + 33 Controls ( $n = 66$ ) and 22 Late VGKC-LE Group + 22 Controls ( $n = 44$ )			
	DOF	$T$ Test	$P >  t $
Late GAD-LE			
Amygdala affected	32	2.19	.036 <sup>b</sup>
Hippocampus affected	32	1.62	
Amygdala unaffected	32	1.56	>.05
Hippocampus unaffected	32	0.99	
Late VGKC-LE			
Amygdala affected	21	1.33	
Hippocampus affected	21	-0.32	
Amygdala unaffected	21	0.08	>.05
Hippocampus unaffected	21	-0.57	

<sup>a</sup> One-tailed, 2-sample  $t$  tests of the amygdala and hippocampus in the affected and unaffected hemispheres between patients with LE and matched controls (as shown in Fig 1).

<sup>b</sup> Significant values.

## ON-LINE APPENDIX:

### 3D-TOF Acquisition Parameters

The FOV was  $200 \times 200 \times 110 \text{ mm}^3$  with a transverse orientation of the slabs. The acquisition and reconstruction voxel size were, respectively,  $0.42 \times 0.73 \times 1.1 \text{ mm}^3$  and  $0.3 \times 0.3 \times 0.55 \text{ mm}^3$ . SENSE acceleration factor = 2.5, TR/TE = 25/3.5 ms, and flip angle =  $20^\circ$  yield an acquisition time of approximately 6 minutes.

### 4D-PCMR Acquisition Parameters

The FOV was  $190 \times 210 \times 32 \text{ mm}^3$ . Acquisition and reconstruction voxel sizes were, respectively,  $1 \text{ mm}^3$  isotropic and  $0.8 \times 0.8 \times 1 \text{ mm}^3$ , with sensitivity encoding acceleration factor, 2; TR/TE, 4.6/2.9 ms; flip angle,  $5^\circ$ ; and background phase error correction.<sup>1</sup> The sequence was triggered by the cardiac frequency using a peripheral pulse unit. The VENC was set to 80 cm/s by default, except for recent acquisitions in which the VENC was reduced to 40 cm/s after stent implantation to improve the low-velocity accuracy at the expense of aliasing artifacts. The positioning of the slices is illustrated in On-line Fig 1. For a heart rate of 65 beats per minute, the number of cardiac phases was 16, yielding an acquisition time of approximately 13 minutes.

### Postprocessing

We combined the 4D-PCMR velocities with the vessel geometric information provided by the 3DRA. The main steps of the workflow (On-line Fig 2) were implemented in Matlab R2016b (MathWorks) and are briefly described below (more details are available in Bouillot et al<sup>2</sup>):

- Segmentation of the 3DRA dataset with a watershed-based algorithm.<sup>3,4</sup> Subsequently, the center line of the segmented vessel was computed in a manner similar to that in Bouillot et al<sup>5</sup> using the VMTK library<sup>6</sup> ([www.vmtk.org](http://www.vmtk.org)).
- Aliasing correction of the 4D-PCMR velocities to remove phase jumps occurring during systole.
- Rigid coregistration of the segmented vessel and the 4D-PCMR data in order to keep only the relevant velocity information within the circulating volume.
- Linear interpolation of the velocity field on a refined grid (grid size of approximately 0.1mm).
- This refined grid together with the surface nodes of the segmented vessel wall were used to compute a Delaunay tetrahedralization of the circulating volume (zero velocities were assumed at the vessel wall). The velocity field described on this tetrahedron mesh served as input data for further quantitative and qualitative analysis and were exported as a VTK file (The Visualization Toolkit; <https://vtk.org>).

### Geometric Parameters and Flow Diversion

In parallel, aneurysm geometric parameters, such as volume, maximum diameter, aspect ratio, and neck size, were measured manually from 3DRA datasets as in Larrabide et al.<sup>7</sup> Potential relationships between these geometric parameters and PVRRs were investigated by means of a linear fit.

The average volume and maximum diameter of the 23 aneurysms were  $378.6 \text{ mm}^3$  (range, 40–1656  $\text{mm}^3$ ) and 9.4 mm (range, 4.4–17.7 mm), respectively. The average aspect ratio and neck

size were 1.32 (range, 0.69–2.32) and 5.5 mm (range, 2.5–13 mm), respectively. No correlations were found between these geometric parameters and the PVRRs (On-line Fig 3;  $R^2 = 0.24, 0.27, 0.02, 0.06$  for volume, maximum size, aspect ratio, and neck size, respectively). Furthermore, no correlation between aneurysm geometric parameters and occlusion outcomes were found (On-line Fig 3, red and blue dots).

### FDS Brand and Flow Diversion

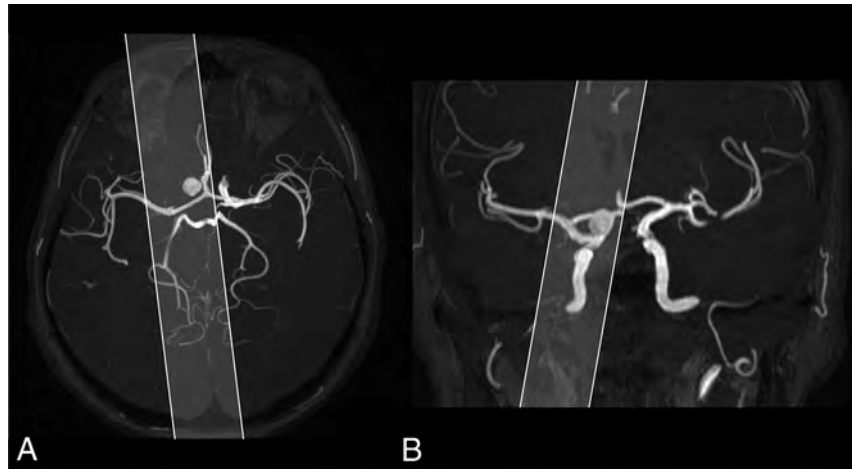
A Kruskal-Wallis test was performed to assess differences between PVRRs and the 3 FDS brands used in this study (PED, FRED, and Silk). We showed that there were no significant differences ( $P = .72$ ) in flow reduction among the 3 different devices implanted in the 23 patients and that the PVRR values for each stent were spread within a close range (On-line Fig 4), meaning that the stent brand did not influence the flow-reduction effect in this study. We also compared the occlusion rate for each implanted device (On-line Table). Even if the PED seems to perform slightly better in inducing thrombosis, we have to consider the small number of FRED and Silk devices used in our cohort, which mitigates these results.

### Time-Averaged Velocities and PVRR

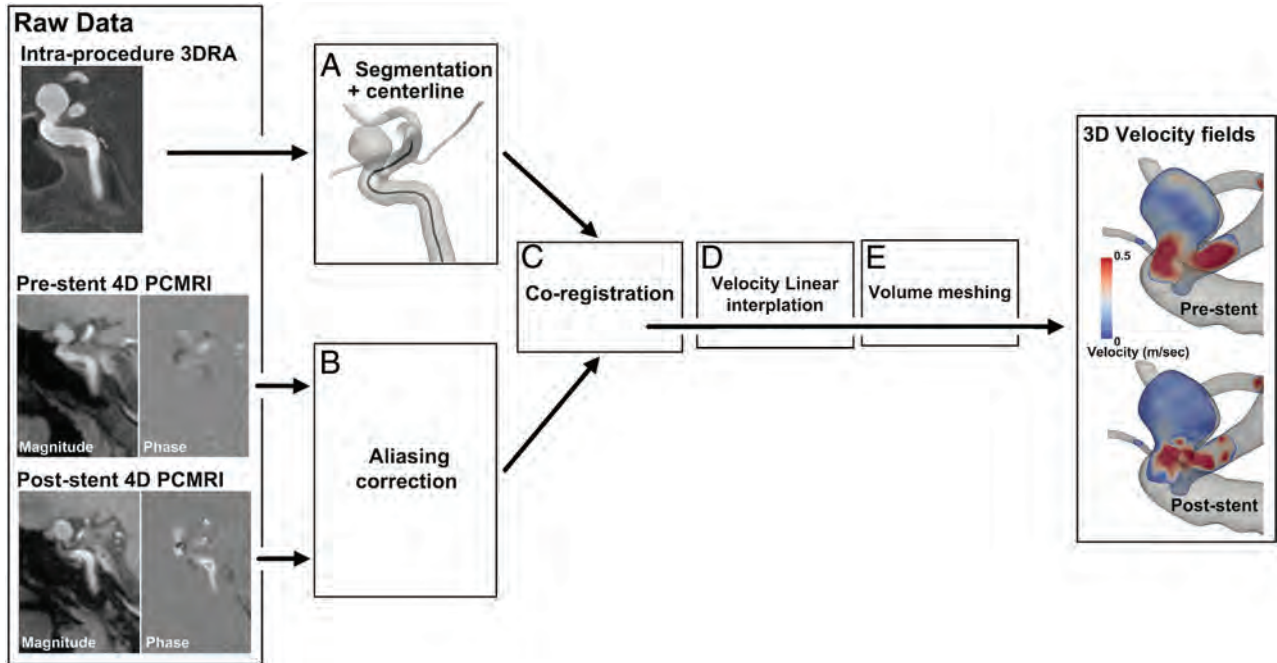
We computed the time-averaged velocity along the cardiac cycle before and after treatment for each patient and searched for correlations between the time-averaged PVRR and the outcomes (On-line Fig 5). As for systolic velocities, the same reduction trend was observed (a wide range of time-averaged velocities before stent placement and converging toward a narrower range after flow diversion). Unlike systolic PVRR showing a trend among the 3 groups of different occlusion times ( $P = .08$ ), no relationship was found between the time-averaged PVRR and the occlusion time ( $P = .46$ ). This might be explained by the time-averaging of the data, which includes proportionally more low-velocity values (below the threshold of 7.7 cm/s), which will affect the PVRR calculation even more.

## REFERENCES

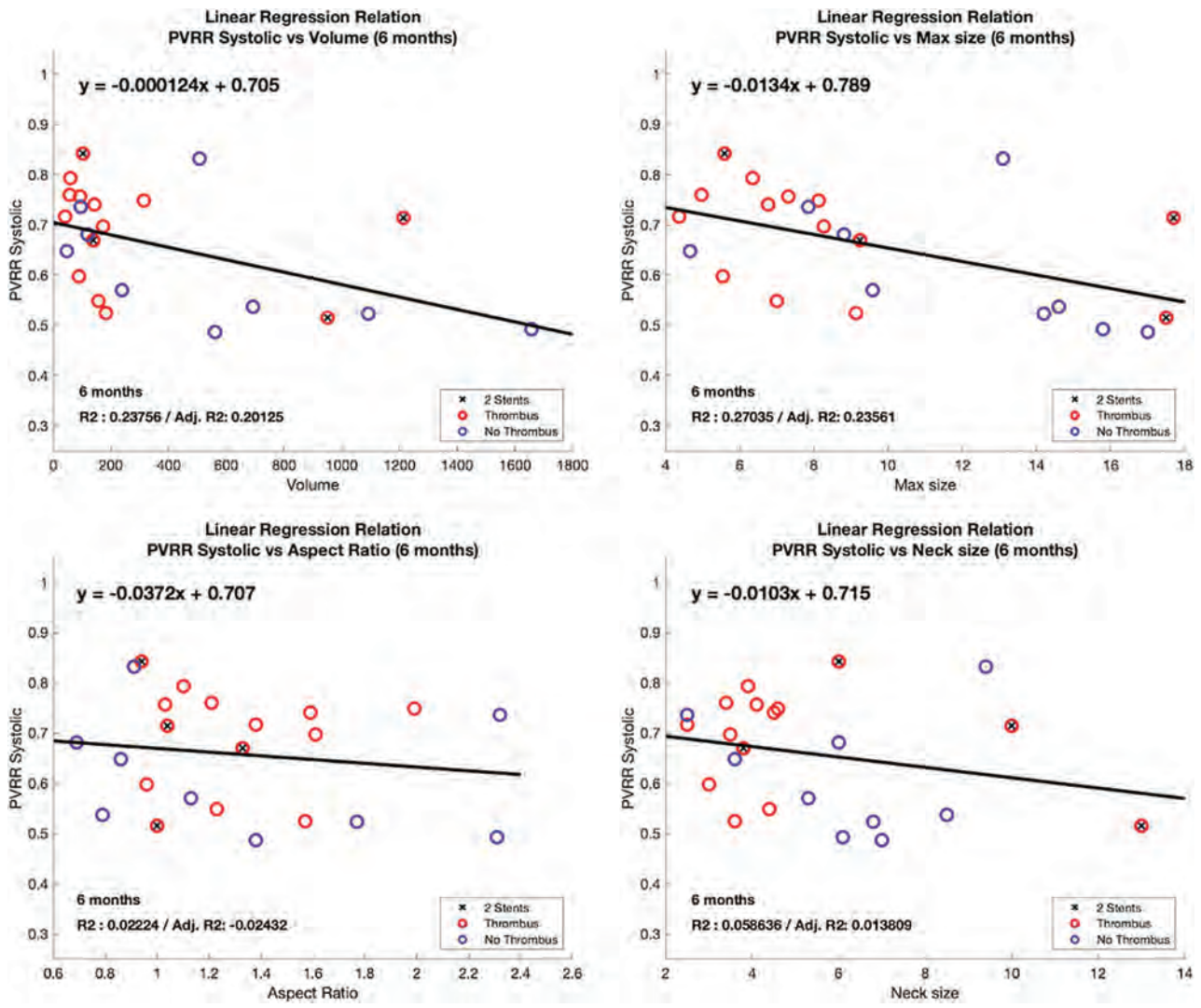
- Walker PG, Cranney GB, Scheidegger MB, et al. **Semiautomated method for noise reduction and background phase error correction in MR phase velocity data.** *J Magn Reson Imaging* 1993;3:521–30 CrossRef Medline
- Bouillot P, Delattre BMA, Brina O, et al. **3D phase contrast MRI: partial volume correction for robust blood flow quantification in small intracranial vessels.** *Magn Reson Med* 2018;79:129–40 CrossRef Medline
- Higgins WE, Ojard EJ. **Interactive morphological watershed analysis for 3D medical images.** *Comput Med Imaging Graph* 1993; 17:387–95 Medline
- Meyer F. **Topographic distance and watershed lines.** *Signal Process* 1994;38:113–25 CrossRef
- Bouillot P, Brina O, Ouared R, et al. **Geometrical deployment for braided stent.** *Med Image Anal* 2016;30:85–94 CrossRef Medline
- Antiga L, Piccinelli M, Botti L, et al. **An image-based modeling framework for patient-specific computational hemodynamics.** *Med Biol Eng Comput* 2008;46:1097–1112 CrossRef Medline
- Larrabide I, Aguilar ML, Morales HG, et al. **Intra-aneurysmal pressure and flow changes induced by flow diverters: relation to aneurysm size and shape.** *AJNR Am J Neuroradiol* 2013;34:816–22 CrossRef Medline



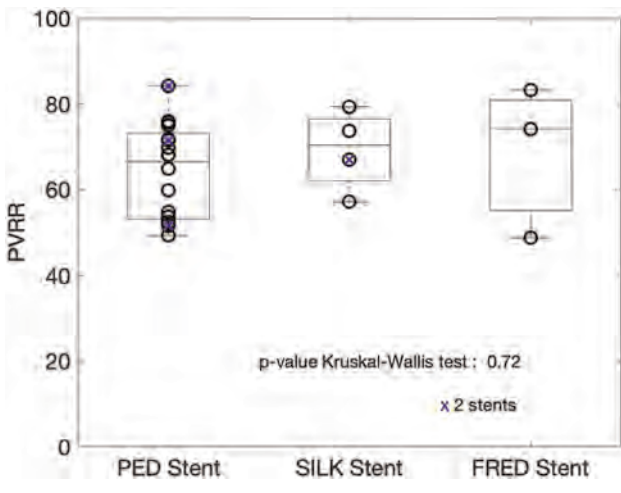
**ON-LINE FIG 1.** Typical MIP of the 3D-TOF (axial [A] and coronal [B] views) with the location of the 4D-PCMR slab (*white area*). Note the double obliquity of the sagittal slices required for complying with the 2 following constraints: 1) avoiding the nose, which is responsible for folding artifacts; and 2) covering the aneurysm bulge and the adjacent ICA.



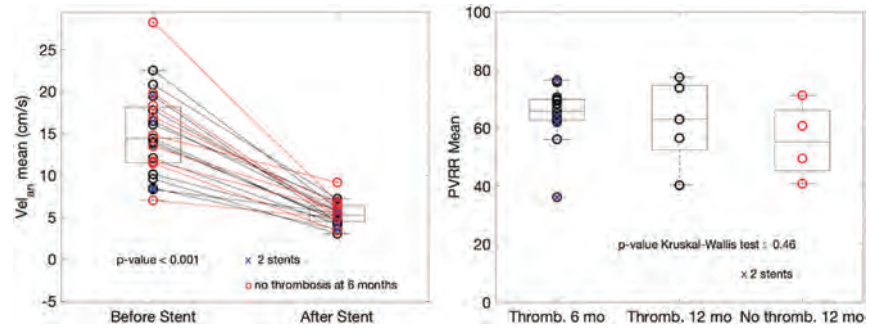
**ON-LINE FIG 2.** Velocity field construction from 4D-PCMR and 3DRA raw datasets. *A*, 3DRA vessel segmentation and center line. *B*, 4D-PCMR aliasing correction. *C*, Vessel geometry, 4D-PCMR coregistration. *D*, Velocity interpolation. *E*, Meshing of the circulating volume.



**ON-LINE FIG 3.** Linear regression between geometric parameters of the aneurysms (volume, maximum size, aspect ratio, and neck size) and flow reduction (PVRR). Red and blue dots represent occlusion and still circulating aneurysms at 6 months, respectively.



**ON-LINE FIG 4.** PVRRs for the 3 different FDs used. Blue cross dots represent patients implanted with 2 stents.



**ON-LINE FIG 5.** *Left*, Intra-aneurysmal time-averaged velocities along cardiac cycle before and after treatment. *Right*, Time-averaged PVRRs for patients thrombosed at 6 and 12 months and not thrombosed at 12 months. *Blue cross dots* represent patients implanted with 2 stents. Thromb indicates thrombosis.

**On-line Table: Occlusion rates at 6 and 12 months for the 3 devices**

Device	6-Month Occlusion	12-Month Occlusion	No Thrombosis at 12 Months
PED (16)	11 (69%)	14 (88%)	2 (13%)
Silk (4)	2 (50%)	3 (75%)	1 (25%)
FRED (3)	1 (33%)	2 (67%)	1 (33%)

## ON-LINE APPENDIX: METHODS

### 1.5/3T MR Imaging Acquisitions

All patients had preliminarily performed diagnostic 1.5/3T studies with dedicated protocols for focal epilepsy using at least one of the following MR imaging systems and protocols:

- 1.5 MR imaging (ACS-NT and Achieva; Philips Healthcare): 3D T1WI fast-field echo, 2D T2 FLAIR, 2D T2WI TSE, 2D T1WI inversion recovery.
- 3T MR imaging (Signa HDx; GE Healthcare): 3D T1WI fast-spoiled gradient-echo, 2D T2 FLAIR, 2D T2WI FSE, and 2D white matter-suppressed FSE inversion recovery.
- 3T MR imaging (Achieva; Philips Healthcare): 3D T1WI fast-spoiled gradient recalled, 3D T2 FLAIR-volume isotropic turbo spin-echo acquisition sequence, 2D T2 FLAIR, 2D T2WI TSE, 2D T2\*-weighted gradient-echo.

### 7T MR Imaging Analysis

The 7T targeted SWAN sequences were also analyzed with quantitative susceptibility mapping (QSM<sup>1</sup>) in 8/12 patients (patients 1–4, 6, 7, 9, and 10). QSM was not performed due to movement artifacts in patients 5 and 8. Briefly, phase data of SWAN acquisitions were preprocessed for Laplacian-based phase unwrapping; the background phase was removed with V-SHARP (variable-kernel sophisticated harmonic artifact reduction for phase).<sup>2</sup> Quantitative susceptibility maps were obtained with the iLSQR (improved sparse linear equation and least-squares) method.<sup>3</sup>

### Histopathologic Assessment

Each surgical specimen was sectioned in 5-mm slabs. Slabs were then fixed in buffered neutral formalin and embedded in paraffin for hematoxylin-eosin staining (all patients). Selected slabs of patients 1, 2, 11, and 12 were also analyzed by Golgi silver staining, thionin, Luxol fast blue.

Immunocytochemistry was performed using antibodies against anti-glial fibrillary acidic protein (GFAP, Zymed Laboratory, San Francisco, California; or Millipore, Temecula, California), neurofilaments (Pan clone DA2, Zymed Laboratory; SMI311, Covance, San Diego, California; or 2F11, Dako, Glostrup, Denmark), intermediate filament protein vimentin (Dako), neuron-specific nuclear protein (Millipore), and myelin basic protein (Dako).

### REFERENCES

1. Haacke EM, Liu S, Buch S, et al. **Quantitative susceptibility mapping: current status and future directions.** *Magn Reson Imaging* 2015;33:1–25 CrossRef Medline
2. Schweser F, Deistung A, Lehr BW, et al. **Quantitative imaging of intrinsic magnetic tissue properties using MRI signal phase: an approach to in vivo brain iron metabolism?** *Neuroimage* 2011;54:2789–2807 CrossRef Medline
3. Li W, Wu B, Liu C. **Quantitative susceptibility mapping of human brain reflects spatial variation in tissue composition.** *Neuroimage* 2011;55:1645–56 CrossRef Medline

**On-line Table 1: Demographic details, histopathology, neuroimaging features, and epilepsy surgery outcome of the study population**

Patient No./Sex/Age at 7T (yr)	Histo-Pathology	Lesion Location	1.5/3T Findings	7T MR Imaging Findings	Engel Class/Follow-Up Duration
1/M/34	FCD IIb	R opercular	1.5T: Transmantle sign Increased T2-weighted signal within the cortex Blurring of GM/WM junction T2-weighted hyperintensity in subcortical WM T2*WI not performed	Transmantle sign Increased T2-weighted signal within the cortex Blurring of GM/WM junction T2-weighted hyperintensity in subcortical WM Intracortical layer in T2*WI Abnormal sulcal/gyral contouring Transmantle sign Blurring of GM/WM junction T2-weighted hyperintensity in subcortical WM T1-weighted hypointensity in subcortical WM	IA/4 yr
2/M/38	FCD IIb	L frontal	1.5T: abnormal sulcal/gyral contouring Transmantle sign Blurring of GM/WM junction T2-weighted hyperintensity in subcortical WM T1-weighted hypointensity in subcortical WM VEN-3D-PCA: normal T2*WI not performed	Abnormal sulcal/gyral contouring Transmantle sign Blurring of GM/WM junction T2-weighted hyperintensity in subcortical WM T1-weighted hypointensity in subcortical WM SWAN: venous drainage abnormalities Intracortical layer in T2*WI	IA/3 yr
3/F/14	FCD IIb	R frontal	3T: increased cortical thickness Abnormal sulcal/gyral contouring Increased T2-weighted signal within the cortex Transmantle sign Blurring of GM/WM junction T2-weighted hyperintensity in subcortical WM T1-weighted hypointensity in subcortical WM	7T demonstrates increased cortical thickness Abnormal sulcal/gyral contouring Increased T2-weighted signal within the cortex Transmantle sign Blurring of GM/WM junction T2-weighted hyperintensity in subcortical WM T1-weighted hypointensity in subcortical WM	IA/2 yr
4/M/9	FCD IIa	R medial parieto-occipital (parasplenic) L frontal	3T: Blurring of GM/WM junction T1-weighted hypointensity in subcortical WM Increased cortical thickness in T2*WI	Intracortical layer in T2*WI Blurring of GM/WM junction T2-weighted hyperintensity in subcortical WM T1-weighted hypointensity in subcortical WM	IA/1 yr
5/F/15	FCD Ib	L frontal	3T: normal MR imaging findings	Normal MR imaging (L frontal subcortical granular appearance of unknown significance)	III/3 yr
6/F/20	FCD Ib	L frontal	3T: normal MR imaging findings	Normal MR imaging findings (subcortical dot of unknown significance)	II/2 yr
7/F/17	FCD IIb	L frontal	3T: increased cortical thickness Abnormal sulcal/gyral contouring Transmantle sign Increased T2-weighted signal within the cortex T2-weighted hyperintensity in subcortical WM	7T demonstrates increased cortical thickness Abnormal sulcal/gyral contouring Transmantle sign Increased T2-weighted signal within the cortex T2-weighted hyperintensity in subcortical WM T1-weighted hypointensity in subcortical WM	III/2 yr

*Continued on next page*

**On-line Table 1: Continued**

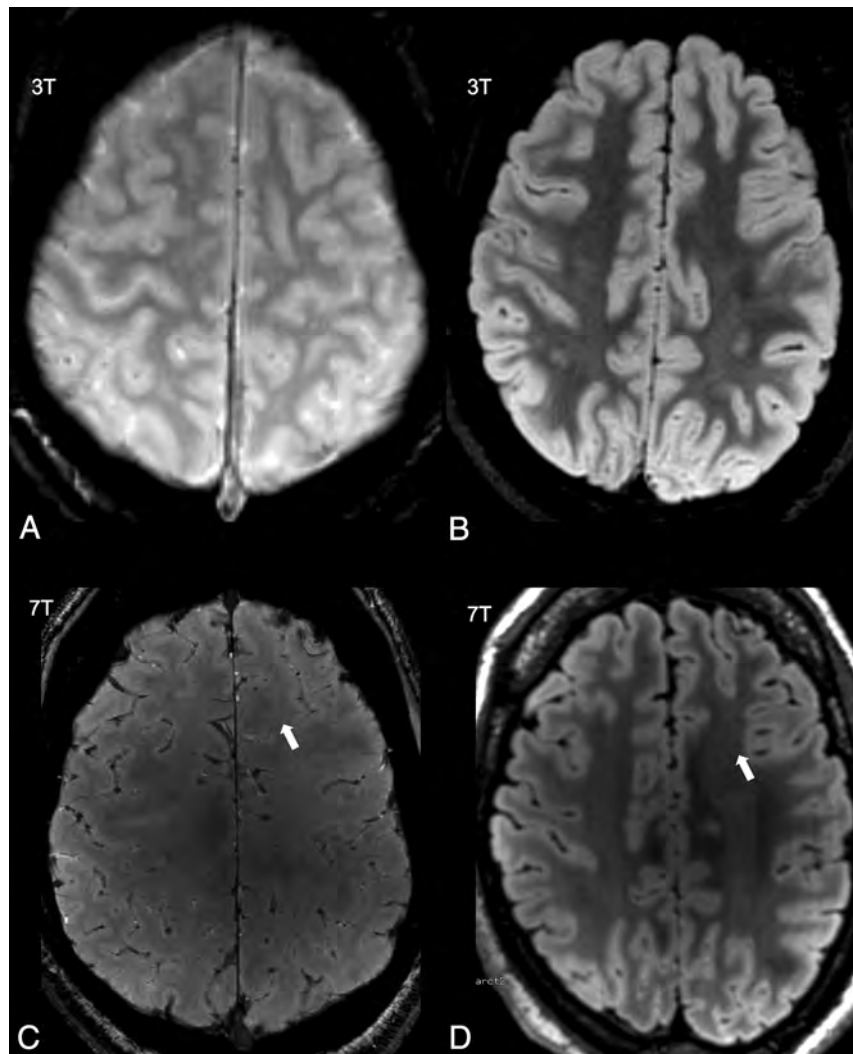
Patient No./Sex/Age at 7T (yr)	Histo-Pathology	Lesion Location	1.5/3T Findings	7T MR Imaging Findings	Engel Class/Follow-Up Duration
8/M/19	FCD IIa	L insular	T1-weighted hypointensity in subcortical WM Increased cortical thickness in T2*WI	Intracortical layer in T2*WI	IA/3 yr
9/M/40	FCD IIa	L frontal	1.5T: blurring of GM/WM junction	Blurring of GM/WM junction	IA/4 yr
10/F/26	FCD IIb	R anterior frontal	1.5T: blurring of GM/WM junction 3T: normal MR imaging findings	Blurring of GM/WM junction Intracortical layer in T2*WI Transmantle sign	IA/3 yr
11/M/23	FCD IIb	L temporo-occipital	1.5T: increased cortical thickness Abnormal sulcal/gyral contouring Transmantle sign Blurring of GM/WM junction T2-weighted hyperintensity in subcortical WM	Increased cortical thickness Abnormal sulcal/gyral contouring Transmantle sign Blurring of GM/WM junction T2-weighted hyperintensity in subcortical WM	IA/2 yr
12/M/25	FCD IIa	L frontal	T1-weighted hypointensity in subcortical WM T2*WI not performed 1.5T: lobar hypoplasia Increased cortical thickness GM/WM blurring T2-weighted hyperintensity in subcortical WM	T1-weighted hypointensity in subcortical WM Inhomogeneous intracortical signal in T2*WI 7T: lobar hypoplasia Increased cortical thickness GM/WM blurring T2-weighted hyperintensity in subcortical WM	IA/2 yr

**Note:**—L indicates left; R, right; PCA, phase contrast angiography; VEN, venography.

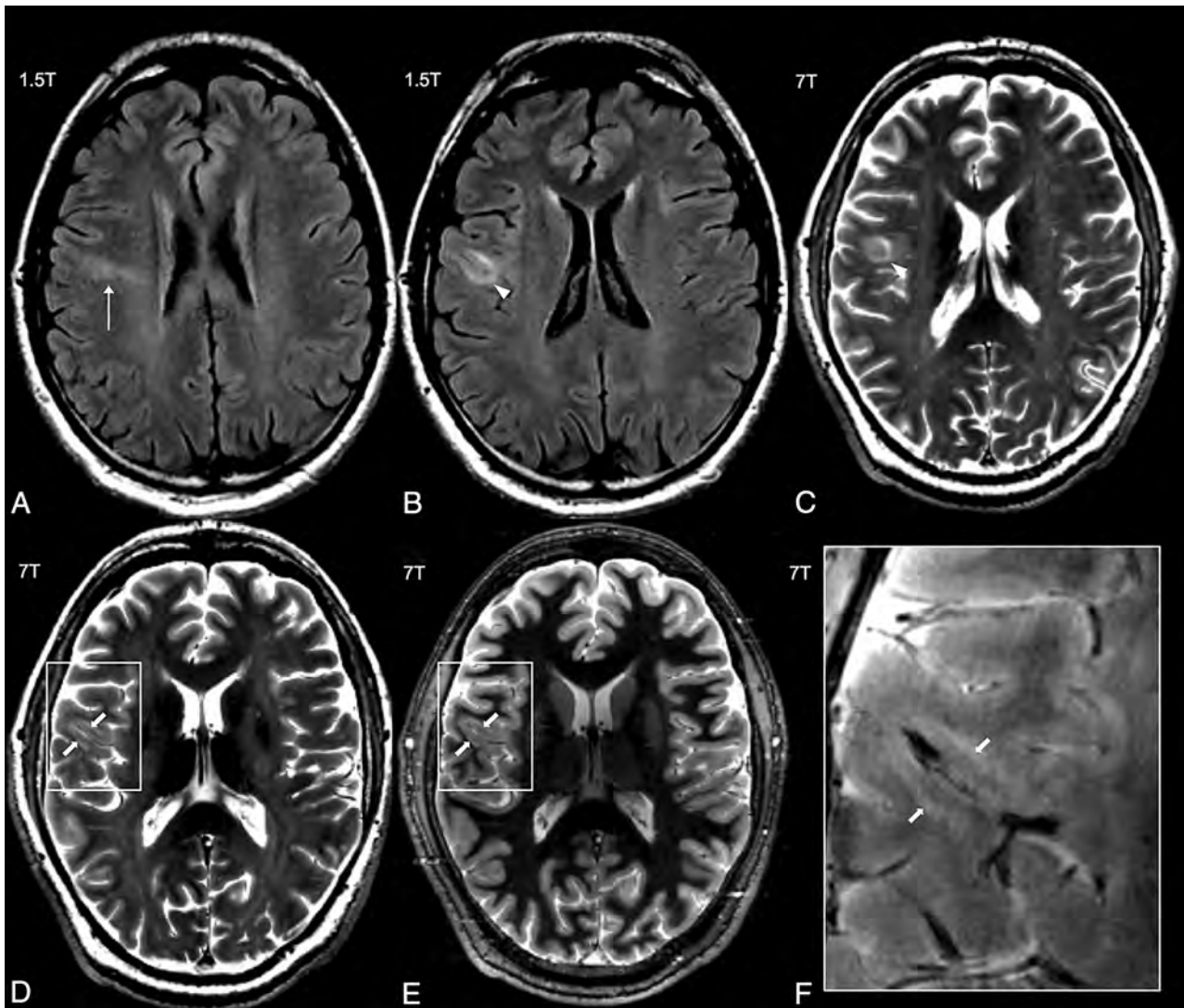
**On-line Table 2: Patients with FCD IIb—correlation between removal of brain regions corresponding to 7T MR findings and epilepsy outcome**

Patient No./ Sex/Age at Operation (yr)	Surgery	Complete Surgical Removal of 7T MR Imaging Findings			Engel Class/ Follow-Up Duration
		Intracortical Layer	Transmantle Sign	Subcortical T2-Weighted Hyperintense WM	
1/M/34	Lesionectomy + corticectomy	Y	N	N	IA/4 yr
2/M/38	Lesionectomy + corticectomy	Y	N	N	IA/3 yr
3/F/14	Lesionectomy + corticectomy	Y	N	Y	IA/2 yr
7/F/17	Lesionectomy + corticectomy	N	N	N	III/2 yr
10/F/26	Lesionectomy + corticectomy	Y	N	NA	IA/3 yr
11/M/23	Lesionectomy + corticectomy	NA	Y	Y	IA/2 yr

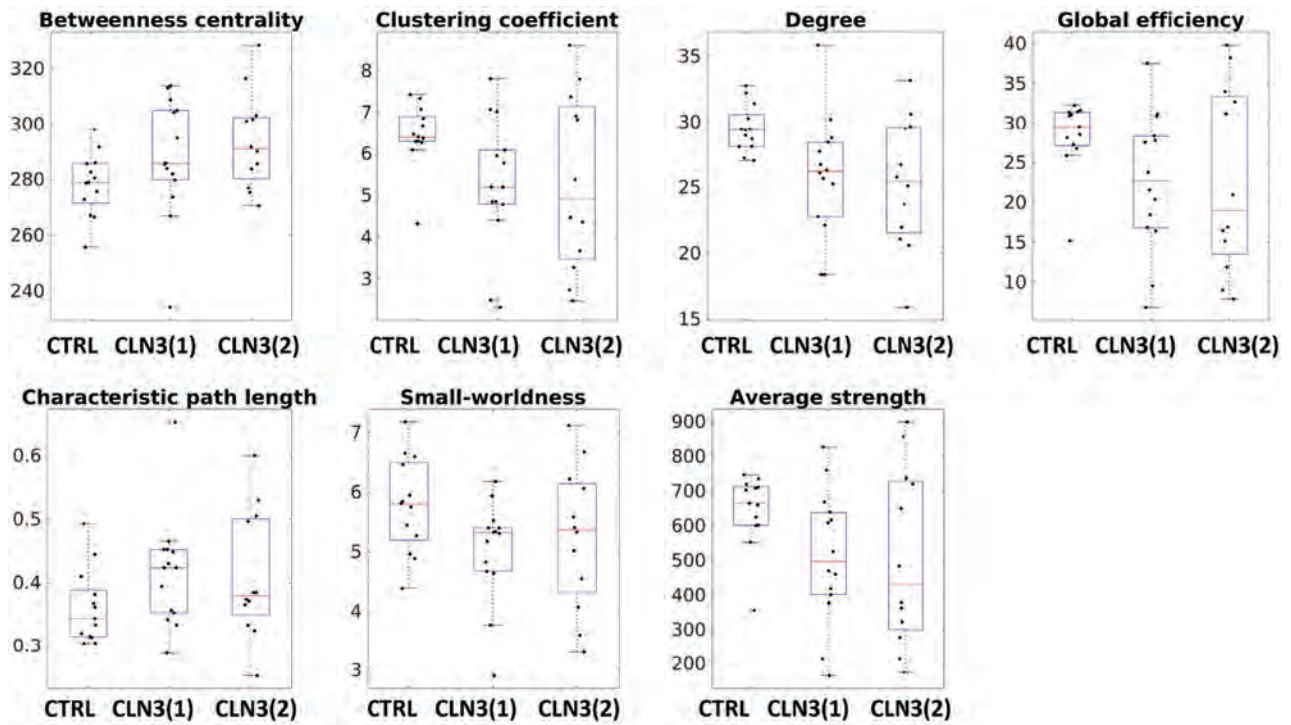
**Note:**—N indicates no; NA, not applicable; Y, yes.



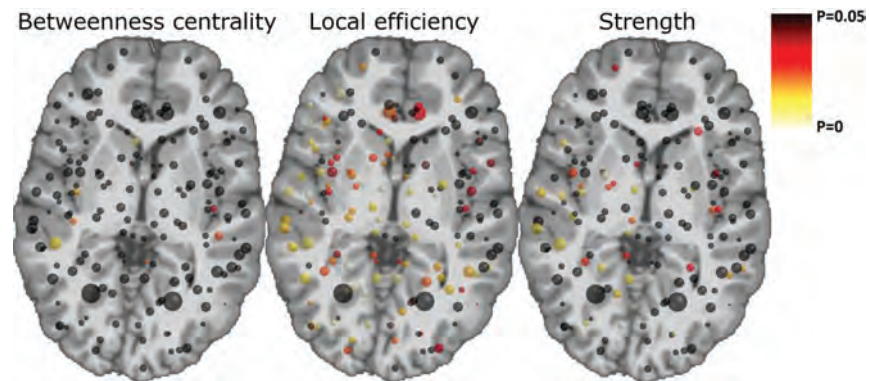
**ON-LINE FIG 1.** Brain imaging of patient 5 (FCD Ib); 3T brain MR imaging (A and B): normal findings on axial T2-weighted\* (A) and FLAIR (B) images. A 7T MR imaging study (C and D). Axial SWI (C) and FLAIR (D) images depict a left frontal subcortical granular appearance of unknown significance (white arrows).



**ON-LINE FIG 2.** Brain imaging of patient 1 (FCD IIb). A 1.5T brain MR imaging study (A and B) shows the transmantle sign (*white arrow*), blurring of GM/WM junction, and T2-weighted hyperintensity in subcortical WM (*arrowhead*) on axial FLAIR images. A 7T brain MR imaging study (C–F) confirms 1.5T findings on the axial T2 images, especially displaying T2-weighted hyperintensity in subcortical WM (*arrowhead* in C). An intracortical layer on T2\*WI (*black line*) is highlighted by axial SWI (F, *white arrows* in *magnified rectangle*) and can also be retrospectively identified on 7T axial T2 images (*white arrows* in D and E).



**ON-LINE FIG 1.** A boxplot of the global graph theoretical properties for the first and second acquisition of patients with CLN3 and the control subjects. Statistically significant differences (Bonferroni corrected) were found in the characteristic path length and degree, both for the first and second acquisition compared with control subjects.



**ON-LINE FIG 2.** Local differences in betweenness centrality, local efficiency, and strength between the first acquisition of the patients with CLN3 and the control subjects. The size of the nodes illustrates the volume of the gray matter region, and the color indicates the statistical significance of the differences ( $P$  values).

Colour legend:

P<0,05
P<0,01
P<0,000305 (Bonferroni corrected P<0,05/164)

### CLN3 1st acquisition vs control subjects

Idx	Label name	Betweenness centrality			Local efficiency			Strength		
		CLN3 1st	CON	P	CLN3 1st	CON	P	CLN3 1st	CON	P
1	Left-Cerebellum-Cortex	722±294	841±433	0,630	0,0085±0,0031	0,01±0,0052	0,215	3143±1662	2194±1097	0,311
2	Left-Thalamus-Proper	789±417	750±388	0,722	0,0091±0,0047	0,0123±0,0052	0,097	1740±621	1848±655	0,485
3	Left-Caudate	619±369	502±292	0,323	0,0077±0,0049	0,0105±0,0041	0,046	849±649	911±342	0,322
4	Left-Putamen	700±430	568±338	0,315	0,0103±0,0055	0,0151±0,0052	0,012	2278±1299	2637±688	0,121
5	Left-Pallidum	410±285	415±208	0,769	0,0093±0,0057	0,0111±0,0034	0,173	1948±580	852±338	0,701
6	Left-Hippocampus	650±466	534±396	0,902	0,0062±0,0026	0,0079±0,0031	0,056	1757±336	728±251	0,226
7	Left-Amygdala	146±154	151±104	0,737	0,0029±0,0018	0,0052±0,0022	0,002	173±53	116±75	0,195
8	Left-Accumbens-area	284±237	366±334	0,529	0,0044±0,0027	0,0061±0,0038	0,164	182±144	213±118	0,602
9	Right-Cerebellum-Cortex	1137±563	748±476	0,162	0,0076±0,003	0,01±0,0048	0,087	2916±1524	2128±1224	0,497
10	Right-Thalamus-Proper	443±319	616±454	0,174	0,0089±0,0041	0,0138±0,0058	0,012	1693±1043	1993±483	0,134
11	Right-Caudate	436±343	400±344	0,687	0,0076±0,0043	0,0111±0,0046	0,028	1837±469	842±341	0,534
12	Right-Putamen	954±410	799±472	0,399	0,0097±0,0057	0,0164±0,008	0,021	2180±955	3254±890	0,004
13	Right-Pallidum	338±205	348±301	0,958	0,0078±0,0035	0,0142±0,0063	0,003	759±333	1037±390	0,031
14	Right-Hippocampus	585±394	343±238	0,090	0,0052±0,0017	0,0097±0,0066	0,017	1564±425	762±393	0,072
15	Right-Amygdala	238±274	425±310	0,129	0,0035±0,0019	0,0061±0,0051	0,026	103±72	202±192	0,027
16	Right-Accumbens-area	218±227	364±341	0,046	0,0048±0,0019	0,0067±0,0046	0,020	1139±121	301±411	0,035
17	ctx_lh_G_and_S_frontomargin	352±294	198±223	0,070	0,0079±0,006	0,0099±0,0046	0,228	612±558	622±672	0,731
18	ctx_lh_G_and_S_occipital_inf	181±173	188±149	0,760	0,0069±0,0038	0,0082±0,004	0,468	534±622	470±379	0,581
19	ctx_lh_G_and_S_paracentral	374±274	346±281	0,593	0,0054±0,0028	0,0095±0,0044	0,010	1509±431	688±374	0,183
20	ctx_lh_G_and_S_subcentral	127±147	202±223	0,201	0,0084±0,0057	0,0107±0,006	0,142	1572±400	511±210	0,816
21	ctx_lh_G_and_S_transv_frontopoli	211±178	155±154	0,605	0,0076±0,0042	0,0095±0,0047	0,159	1559±523	454±418	0,931
22	ctx_lh_G_and_S_cingul-Ant	217±215	282±227	0,173	0,0054±0,0023	0,0093±0,0055	0,031	382±311	576±357	0,144
23	ctx_lh_G_and_S_cingul-Mid-Ant	150±118	224±184	0,157	0,0059±0,0036	0,0082±0,0038	0,050	398±222	388±237	0,502
24	ctx_lh_G_and_S_cingul-Mid-Post	161±119	100±89	0,633	0,0047±0,0024	0,0078±0,0038	0,009	260±138	254±130	0,689
25	ctx_lh_G_cingul-Post-dorsal	227±153	204±130	0,878	0,0033±0,0018	0,0044±0,002	0,135	1123±75	109±77	0,875
26	ctx_lh_G_cingul-Post-ventral	353±279	181±148	0,022	0,0032±0,0017	0,006±0,0038	0,036	148±121	213±158	0,548
27	ctx_lh_G_cuneus	299±193	280±140	0,959	0,0044±0,0022	0,0062±0,0034	0,047	307±146	368±213	0,139
28	ctx_lh_G_front_inf-Opercular	174±174	167±88	0,874	0,0083±0,0056	0,0116±0,0046	0,040	831±819	833±342	0,681
29	ctx_lh_G_front_inf-Orbital	147±170	215±269	0,225	0,0049±0,0027	0,0067±0,0032	0,200	198±282	227±148	0,452
30	ctx_lh_G_front_inf-Triangul	349±163	307±184	0,903	0,0077±0,0047	0,0096±0,0041	0,116	1645±583	637±333	0,428
31	ctx_lh_G_front_middle	336±295	221±155	0,262	0,0128±0,0094	0,0161±0,0057	0,171	1334±758	1682±745	0,294
32	ctx_lh_G_front_sup	824±323	830±349	0,637	0,011±0,0065	0,0153±0,0049	0,031	3748±2198	4799±1763	0,085
33	ctx_lh_G_ins_lg_and_S_cent_ins	202±156	189±167	0,703	0,0047±0,0027	0,006±0,0026	0,280	199±150	185±127	0,744
34	ctx_lh_G_insular_short	343±215	244±201	0,198	0,0052±0,003	0,0077±0,0041	0,057	1243±182	387±200	0,039
35	ctx_lh_G_occipital_middle	285±213	235±166	0,351	0,0073±0,0035	0,0102±0,0042	0,035	1019±893	856±349	0,790
36	ctx_lh_G_occipital_sup	326±196	347±259	0,603	0,0046±0,0021	0,0072±0,0035	0,024	393±331	447±207	0,618
37	ctx_lh_G_oc-temp_lat-fusifor	207±166	178±156	0,975	0,0055±0,002	0,0089±0,0041	0,015	335±239	537±255	0,064
38	ctx_lh_G_oc-temp_med-Lingual	379±235	441±318	0,594	0,0044±0,0016	0,0071±0,0031	0,017	417±355	598±287	0,158
39	ctx_lh_G_oc-temp_med-Parahip	358±233	365±202	0,498	0,005±0,0025	0,0064±0,0027	0,067	1327±207	324±130	0,435
40	ctx_lh_G_orbital	481±332	515±198	0,579	0,0084±0,0053	0,0105±0,0049	0,303	1034±506	1262±596	0,453
41	ctx_lh_G_pariet_inf-Angular	234±190	305±238	0,982	0,0096±0,0056	0,0118±0,0038	0,265	1115±646	961±392	0,284
42	ctx_lh_G_pariet_inf-Supramar	74±73	126±118	0,083	0,0107±0,0062	0,0147±0,005	0,086	971±626	1259±714	0,194
43	ctx_lh_G_parietal_sup	633±415	718±286	0,683	0,0065±0,0033	0,0101±0,0045	0,024	1980±647	1478±607	0,053
44	ctx_lh_G_postcentral	344±314	310±212	0,520	0,0091±0,0053	0,0124±0,0054	0,101	1802±434	1020±422	0,076
45	ctx_lh_G_precentral	381±225	392±352	0,547	0,0115±0,0062	0,0158±0,0044	0,039	1759±1177	1941±615	0,469
46	ctx_lh_G_precuneus	617±476	543±589	0,778	0,0057±0,0024	0,0105±0,0053	0,005	706±347	1131±275	9,4E-04
47	ctx_lh_G_rectus	249±198	131±128	0,202	0,005±0,0029	0,0076±0,0047	0,273	238±165	333±360	0,810
48	ctx_lh_G_subcallosal	271±252	205±250	0,615	0,0026±0,0013	0,0042±0,0027	0,073	180±80	89±63	0,733
49	ctx_lh_G_temp_sup-G_T_transv	64±78	69±76	0,890	0,0043±0,0031	0,0059±0,0027	0,296	177±70	103±91	0,656
50	ctx_lh_G_temp_sup-Lateral	340±230	380±284	0,891	0,0079±0,004	0,0092±0,0031	0,231	1809±528	862±466	0,654
51	ctx_lh_G_temp_sup-Plan_polar	260±166	359±224	0,150	0,0034±0,0025	0,0056±0,0025	0,058	102±82	280±314	0,153
52	ctx_lh_G_temp_sup-Plan_tempo	96±104	134±134	0,487	0,0057±0,0039	0,0098±0,003	0,008	176±121	352±228	0,017
53	ctx_lh_G_temporal_inf	449±387	432±313	0,675	0,0077±0,0039	0,0117±0,0055	0,054	1882±483	1324±704	0,137
54	ctx_lh_G_temporal_middle	416±477	353±231	0,297	0,0092±0,0054	0,0119±0,004	0,098	1954±501	1476±721	0,058
55	ctx_lh_Lat_Fis-ant-Horizont	41±33	87±79	0,080	0,0034±0,0024	0,0046±0,0026	0,445	33±32	50±38	0,563
56	ctx_lh_Lat_Fis-ant-Vertical	49±70	92±94	0,210	0,0037±0,0032	0,006±0,0028	0,026	44±45	70±35	0,084
57	ctx_lh_Lat_Fis-post	111±79	61±63	0,064	0,0044±0,0026	0,0064±0,0035	0,014	181±330	115±59	0,926
58	ctx_lh_Pole_occipital	245±293	324±218	0,431	0,0059±0,0034	0,007±0,0055	0,287	1479±373	417±379	0,550
59	ctx_lh_Pole_temporal	517±274	658±386	0,161	0,0069±0,0037	0,0099±0,0049	0,096	1040±521	1373±630	0,261
60	ctx_lh_S_calcarine	315±216	376±299	0,754	0,0047±0,0021	0,006±0,0033	0,140	1404±187	309±195	0,554

ON-LINE FIG 3. Results of the local graph theoretical analyses in CLN3.

61	ctx_lh_S_central	229±297	265±220	0,581	0.0064±0.0037	0.0088±0.0041	0,053	234±206	361±174	0,024
62	ctx_lh_S_cingul-Marginalis	286±222	172±227	0,228	0.0042±0.0021	0.008±0.0047	0,013	232±221	307±243	0,546
63	ctx_lh_S_circular_insula_ant	111±129	69±108	0,239	0.0043±0.0033	0.0053±0.0028	0,731	199±99	65±38	0,124
64	ctx_lh_S_circular_insula_inf	360±280	229±123	0,037	0.0048±0.0026	0.0075±0.0041	0,036	209±104	326±147	0,031
65	ctx_lh_S_circular_insula_sup	274±250	214±124	0,218	0.0049±0.0034	0.0059±0.0021	0,413	191±147	152±81	0,625
66	ctx_lh_S_collat_transv_ant	164±153	340±270	0,049	0.0049±0.0031	0.0058±0.0025	0,544	199±129	231±146	0,612
67	ctx_lh_S_collat_transv_post	48±58	103±144	0,345	0.0032±0.0018	0.007±0.0067	0,040	128±36	122±137	0,010
68	ctx_lh_S_front_inf	166±166	90±113	0,147	0.0091±0.008	0.0109±0.006	0,137	305±357	242±147	0,698
69	ctx_lh_S_front_middle	129±132	148±147	0,740	0.0063±0.0041	0.0096±0.004	0,018	140±100	239±334	0,572
70	ctx_lh_S_front_sup	235±208	235±216	0,502	0.0109±0.0107	0.0144±0.0072	0,267	381±304	632±293	0,029
71	ctx_lh_S_interm_prim-Jensen	33±37	37±74	0,780	0.0038±0.003	0.0083±0.0057	0,036	148±54	53±37	0,594
72	ctx_lh_S_intrapariet_and_P_trans	338±223	553±547	0,084	0.0055±0.0024	0.0079±0.0032	0,015	1400±206	583±301	0,084
73	ctx_lh_S_oc_middle_and_Lunatus	183±220	209±159	0,749	0.0034±0.0031	0.0046±0.0023	0,174	138±158	113±70	0,940
74	ctx_lh_S_oc_sup_and_transversal	434±567	256±158	0,053	0.0041±0.0018	0.006±0.0034	0,069	224±139	260±211	0,637
75	ctx_lh_S_occipital_ant	54±49	72±54	0,486	0.005±0.0029	0.0063±0.0038	0,163	107±95	110±80	0,615
76	ctx_lh_S_oc-temp_lat	144±173	176±161	0,925	0.0046±0.0022	0.0068±0.0033	0,037	1164±146	202±143	0,253
77	ctx_lh_S_oc-temp_med_and_Lingual	373±396	252±268	0,310	0.0045±0.0021	0.008±0.0047	0,017	317±206	435±149	0,031
78	ctx_lh_S_orbital_lateral	127±121	141±179	0,996	0.0052±0.0039	0.0056±0.0025	0,321	116±146	107±94	0,799
79	ctx_lh_S_orbital_med-olfact	214±471	123±105	0,217	0.0036±0.0023	0.004±0.0022	0,819	87±70	66±44	0,575
80	ctx_lh_S_orbital_H_Shaped	147±166	108±135	0,392	0.0048±0.0038	0.0068±0.0028	0,144	101±96	106±57	0,832
81	ctx_lh_S_parieto_occipital	270±308	302±214	0,773	0.0045±0.0023	0.0064±0.0039	0,045	304±228	319±116	0,421
82	ctx_lh_S_pericallosal	362±268	321±247	0,464	0.0038±0.0017	0.0058±0.0029	0,019	223±134	218±72	0,479
83	ctx_lh_S_postcentral	122±107	260±181	0,025	0.0075±0.0039	0.0092±0.0042	0,230	349±171	385±133	0,256
84	ctx_lh_S_precentral-inf-part	94±97	60±56	0,414	0.0065±0.0036	0.0106±0.0064	0,035	138±116	191±119	0,354
85	ctx_lh_S_precentral-sup-part	72±89	125±156	0,071	0.0072±0.0058	0.0102±0.0027	0,093	109±110	228±121	0,012
86	ctx_lh_S_suborbital	166±152	105±104	0,592	0.003±0.0015	0.0056±0.0042	0,107	180±76	151±216	0,630
87	ctx_lh_S_subparietal	229±186	202±140	0,476	0.0036±0.0011	0.0061±0.004	0,017	225±202	246±170	0,308
88	ctx_lh_S_temporal_inf	103±84	165±177	0,402	0.0046±0.0022	0.0084±0.005	0,009	111±79	311±277	0,017
89	ctx_lh_S_temporal_sup	372±344	171±164	0,085	0.0072±0.0035	0.0101±0.0032	0,018	657±389	786±419	0,490
90	ctx_lh_S_temporal_transverse	85±116	43±75	0,604	0.0036±0.0028	0.0039±0.0029	0,935	59±84	53±95	0,810
91	ctx_rh_G_and_S_frontomargin	354±412	199±161	0,106	0.0069±0.004	0.0108±0.0046	0,019	1450±250	703±461	0,036
92	ctx_rh_G_and_S_occipital_inf	169±184	181±173	0,972	0.0068±0.004	0.0099±0.0045	0,046	430±316	552±457	0,543
93	ctx_rh_G_and_S_pariacentral	234±208	286±165	0,771	0.0048±0.0025	0.0081±0.0041	0,005	265±201	473±287	0,023
94	ctx_rh_G_and_S_subcentral	135±100	109±92	0,308	0.0062±0.0037	0.0106±0.006	0,011	285±143	370±224	0,059
95	ctx_rh_G_and_S_transv_frontopol	340±334	237±278	0,370	0.0084±0.0053	0.0123±0.0059	0,068	716±637	637±275	0,718
96	ctx_rh_G_and_S_cingul-Ant	329±237	339±255	0,624	0.0064±0.0038	0.0101±0.0056	0,059	573±408	650±226	0,885
97	ctx_rh_G_and_S_cingul-Mid-Ant	395±266	173±137	0,007	0.0053±0.0027	0.0102±0.0057	0,006	431±255	562±348	0,376
98	ctx_rh_G_and_S_cingul-Mid-Post	291±310	311±232	0,878	0.0044±0.0015	0.0085±0.004	0,002	268±95	462±191	0,012
99	ctx_rh_G_cingul-Post-dorsal	185±217	164±124	0,554	0.0033±0.0016	0.0055±0.0033	0,054	128±63	150±78	0,433
100	ctx_rh_G_cingul-Post-ventral	221±301	212±174	0,820	0.0034±0.0023	0.0056±0.0031	0,029	1144±129	234±131	0,135
101	ctx_rh_G_cuneus	400±262	588±328	0,170	0.0039±0.0015	0.0066±0.0035	0,007	246±145	432±171	0,001
102	ctx_rh_G_front_inf-Opercular	193±154	155±119	0,777	0.0072±0.0054	0.0141±0.0059	0,010	486±322	1048±615	0,011
103	ctx_rh_G_front_inf-Orbital	80±71	109±87	0,356	0.0043±0.0019	0.0079±0.0029	0,002	115±69	263±207	0,071
104	ctx_rh_G_front_inf-Triangul	225±247	251±272	0,706	0.0064±0.0037	0.0126±0.0061	0,004	421±326	765±282	0,001
105	ctx_rh_G_front_middle	420±302	360±213	0,637	0.0101±0.0054	0.0173±0.0064	0,004	1711±1379	1923±633	0,405
106	ctx_rh_G_front_sup	837±542	1036±700	0,911	0.0104±0.0057	0.0154±0.0065	0,023	3363±2116	4862±1537	0,063
107	ctx_rh_G_Ins_lg_and_S_cent_ins	179±121	205±219	0,828	0.004±0.0025	0.008±0.0052	0,020	117±85	295±241	0,023
108	ctx_rh_G_insular_short	307±148	193±173	0,189	0.0053±0.0035	0.0108±0.007	0,031	296±222	527±287	0,060
109	ctx_rh_G_occipital_middle	376±341	254±208	0,119	0.0077±0.0042	0.0129±0.0051	0,007	1094±872	1381±888	0,526
110	ctx_rh_G_occipital_sup	368±325	608±321	0,213	0.0046±0.0022	0.0074±0.0031	0,012	1452±521	652±335	0,426
111	ctx_rh_G_oc-temp_lat-fusifor	206±222	125±117	0,217	0.0058±0.0025	0.0088±0.0042	0,026	281±179	383±162	0,069
112	ctx_rh_G_oc-temp_med-Lingual	641±416	395±305	0,078	0.0042±0.0012	0.008±0.0047	0,003	431±261	668±308	0,015
113	ctx_rh_G_oc-temp_med-Parahip	343±288	362±240	0,712	0.0041±0.0015	0.0064±0.0031	0,018	234±255	302±168	0,431
114	ctx_rh_G_orbital	550±398	620±456	0,540	0.0075±0.0043	0.0106±0.0045	0,088	1014±543	1231±617	0,463
115	ctx_rh_G_pariet_inf-Angular	254±280	227±140	0,954	0.0099±0.0059	0.0165±0.0061	0,013	1211±855	1834±775	0,053
116	ctx_rh_G_pariet_inf-Supramar	156±183	127±127	0,832	0.0105±0.0055	0.0171±0.0078	0,016	1128±684	1216±634	0,315
117	ctx_rh_G_parietal_sup	663±460	645±415	0,646	0.0055±0.0033	0.0106±0.0051	0,002	631±461	1080±398	0,009
118	ctx_rh_G_postcentral	473±371	379±262	0,180	0.0069±0.0043	0.0136±0.0072	0,001	638±457	1063±472	0,010
119	ctx_rh_G_precentral	400±315	405±369	1,000	0.0095±0.0048	0.0191±0.0106	0,008	1460±1051	2462±818	0,027
120	ctx_rh_G_precuneus	480±387	459±223	0,629	0.0054±0.0026	0.0092±0.0044	0,010	664±378	1219±571	0,011
121	ctx_rh_G_rectus	230±236	250±180	0,246	0.0034±0.0022	0.0052±0.0026	0,043	89±76	150±146	0,115
122	ctx_rh_G_subcallosal	204±148	208±275	0,763	0.0022±0.0009	0.0043±0.0029	0,007	62±49	136±190	0,118
123	ctx_rh_G_temp_sup-G_T_transv	164±107	120±101	0,331	0.0035±0.0025	0.0071±0.0046	0,020	75±79	139±97	0,051
124	ctx_rh_G_temp_sup-Lateral	672±809	415±281	0,065	0.0069±0.0036	0.0129±0.0073	0,008	711±338	1314±648	0,015
125	ctx_rh_G_temp_sup-Plan_polar	363±159	307±208	0,306	0.0041±0.0028	0.0069±0.0035	0,050	185±142	331±202	0,077
126	ctx_rh_G_temp_sup-Plan_tempo	82±76	68±65	0,540	0.0074±0.0051	0.0111±0.0049	0,034	240±184	283±98	0,278
127	ctx_rh_G_temporal_inf	218±187	180±153	0,239	0.0083±0.0048	0.0126±0.0051	0,013	850±449	967±437	0,279
128	ctx_rh_G_temporal_middle	220±156	351±285	0,333	0.0095±0.0051	0.016±0.0083	0,011	1537±786	2261±760	0,012
129	ctx_rh_Lat_Fis-ant-Horizont	116±148	97±126	0,942	0.0034±0.0031	0.0061±0.0032	0,031	162±79	100±99	0,141
130	ctx_rh_Lat_Fis-ant-Vertical	43±85	55±85	0,621	0.0033±0.0033	0.0069±0.0051	0,016	39±56	50±49	0,067

ON-LINE FIG 3. Continued

131	ctx_rh_Lat_Fis-post	144±88	84±70	0,022	0.0052±0.0032	0.007±0.0044	0,096	230±209	124±75	0,462
132	ctx_rh_Pole_occipital	506±422	431±373	0,975	0.0057±0.0026	0.0081±0.0035	0,026	638±366	646±319	0,436
133	ctx_rh_Pole_temporal	585±374	495±323	0,415	0.007±0.0038	0.0105±0.0059	0,039	918±490	1149±526	0,108
134	ctx_rh_S_calcarine	396±221	437±305	0,376	0.0039±0.0012	0.0064±0.003	0,007	266±134	415±273	0,155
135	ctx_rh_S_central	174±117	253±140	0,017	0.0055±0.0039	0.01±0.0055	0,031	232±171	456±274	0,009
136	ctx_rh_S_cingul-Marginalis	177±184	206±200	0,424	0.0045±0.0023	0.0075±0.0036	0,009	197±146	362±203	0,007
137	ctx_rh_S_circular_insula_ant	135±146	44±34	0,493	0.0043±0.0037	0.0065±0.0028	0,169	101±103	99±96	0,897
138	ctx_rh_S_circular_insula_inf	217±132	310±174	0,210	0.0052±0.0029	0.0081±0.0044	0,072	269±138	430±286	0,118
139	ctx_rh_S_circular_insula_sup	191±129	179±135	0,792	0.0037±0.002	0.0064±0.0036	0,030	93±52	131±94	0,133
140	ctx_rh_S_collat_transv_ant	75±85	115±146	0,245	0.0054±0.0034	0.0079±0.006	0,141	138±81	294±287	0,104
141	ctx_rh_S_collat_transv_post	83±109	136±144	0,173	0.0037±0.0037	0.0046±0.003	0,246	51±51	61±43	0,388
142	ctx_rh_S_front_inf	186±150	163±163	0,971	0.006±0.0033	0.0104±0.0066	0,017	300±283	237±168	0,762
143	ctx_rh_S_front_middle	210±229	201±168	0,892	0.0082±0.0069	0.0114±0.0059	0,186	316±275	351±300	0,392
144	ctx_rh_S_front_sup	222±211	292±361	0,378	0.0042±0.0053	0.013±0.0065	0,050	326±201	505±329	0,090
145	ctx_rh_S_interm_prim-Jensen	41±54	20±31	0,428	0.0044±0.0019	0.0079±0.0043	0,012	66±101	45±26	0,745
146	ctx_rh_S_intrapariet_and_P_trans	298±242	340±258	0,886	0.0059±0.0044	0.0098±0.0056	0,022	389±353	605±386	0,028
147	ctx_rh_S_oc_middle_and_Lunatus	129±204	124±81	0,594	0.0028±0.0017	0.0055±0.0033	0,008	71±74	119±125	0,260
148	ctx_rh_S_oc_sup_and_transversal	239±194	436±447	0,679	0.0046±0.0022	0.0066±0.0038	0,003	100±63	321±348	0,010
149	ctx_rh_S_occipital_ant	218±270	88±81	0,301	0.0047±0.0023	0.0091±0.0061	0,019	107±90	284±338	0,052
150	ctx_rh_S_oc-temp_lat	45±67	140±194	0,140	0.0053±0.0031	0.0063±0.0027	0,404	92±72	126±140	0,326
151	ctx_rh_S_oc-temp_med_and_Lingual	190±186	181±135	0,379	0.0043±0.002	0.0062±0.0026	0,039	175±131	203±72	0,192
152	ctx_rh_S_orbital_lateral	101±124	196±269	0,510	0.0042±0.0038	0.007±0.0044	0,066	83±91	171±146	0,143
153	ctx_rh_S_orbital_med-olfact	176±201	118±123	0,852	0.003±0.002	0.0056±0.0039	0,032	75±50	128±92	0,071
154	ctx_rh_S_orbital_H_Shaped	172±226	153±214	0,636	0.0053±0.0028	0.0071±0.0054	0,218	257±356	129±133	0,433
155	ctx_rh_S_parieto_occipital	429±272	504±312	0,406	0.0041±0.0018	0.0068±0.0031	0,004	345±245	425±166	0,101
156	ctx_rh_S_pericallosal	657±479	526±347	0,212	0.0046±0.0027	0.0079±0.0049	0,025	452±395	636±428	0,190
157	ctx_rh_S_postcentral	283±259	275±159	0,942	0.0046±0.0021	0.0099±0.0046	9,4E-04	204±136	444±263	0,012
158	ctx_rh_S_precentral-inf-part	73±89	71±69	0,663	0.0062±0.0036	0.012±0.0065	0,016	184±168	247±134	0,065
159	ctx_rh_S_precentral-sup-part	79±94	193±316	0,080	0.0065±0.0044	0.0124±0.0079	0,027	152±112	289±292	0,072
160	ctx_rh_S_suborbital	72±123	88±112	0,987	0.0024±0.0016	0.0031±0.0022	0,545	37±38	33±24	0,470
161	ctx_rh_S_subparietal	183±151	221±171	0,992	0.0037±0.0027	0.0064±0.0029	0,025	165±138	344±241	0,028
162	ctx_rh_S_temporal_inf	240±273	200±178	0,692	0.0054±0.0045	0.0087±0.0035	0,015	209±198	352±281	0,070
163	ctx_rh_S_temporal_sup	346±229	220±158	0,013	0.0087±0.0048	0.0148±0.0065	0,010	813±374	1348±599	0,012
164	ctx_rh_S_temporal_transverse	64±51	70±69	0,609	0.0036±0.0028	0.0062±0.004	0,047	50±43	77±50	0,141

### CLN3 2nd acquisition vs control subjects

Idx	Label name	Betweenness centrality			Local efficiency			Strength		
		CLN3 2nd	CON	P	CLN3 2nd	CON	P	CLN3 2nd	CON	P
1	Left-Cerebellum-Cortex	970±509	841±433	0,418	0.0081±0.0033	0.01±0.0052	0,226	3566±1685	2194±1097	0,052
2	Left-Thalamus-Proper	1146±392	750±388	0,002	0.008±0.0033	0.0123±0.0052	0,011	1869±699	1848±655	0,909
3	Left-Caudate	648±388	502±292	0,361	0.0064±0.0034	0.0105±0.0041	0,014	559±276	911±342	0,013
4	Left-Putamen	590±384	568±338	0,947	0.0096±0.0039	0.0151±0.0052	0,003	2108±907	2637±688	0,052
5	Left-Pallidum	373±275	415±208	0,601	0.0079±0.0033	0.0111±0.0034	0,020	749±442	852±338	0,473
6	Left-Hippocampus	683±448	534±396	0,199	0.0058±0.0028	0.0079±0.0031	0,050	500±341	728±251	0,018
7	Left-Amygdala	249±245	151±104	0,293	0.0041±0.0024	0.0052±0.0022	0,202	122±156	116±75	0,933
8	Left-Accumbens-area	230±252	366±334	0,245	0.0033±0.0011	0.0061±0.0038	0,021	97±91	213±118	0,012
9	Right-Cerebellum-Cortex	912±508	748±476	0,346	0.0079±0.0029	0.01±0.0048	0,109	3168±1226	2128±1224	0,096
10	Right-Thalamus-Proper	813±440	616±454	0,272	0.0073±0.0031	0.0138±0.0058	0,002	1172±710	1993±483	9,3E-04
11	Right-Caudate	268±145	400±344	0,225	0.0079±0.0036	0.0111±0.0046	0,054	734±452	842±341	0,321
12	Right-Putamen	613±287	799±472	0,205	0.0096±0.0036	0.0164±0.008	0,009	2105±1126	3254±890	8,4E-04
13	Right-Pallidum	544±321	348±301	0,226	0.008±0.0026	0.0142±0.0063	0,005	842±370	1037±390	0,201
14	Right-Hippocampus	561±428	343±238	0,161	0.0054±0.002	0.0097±0.0066	0,035	534±355	762±393	0,066
15	Right-Amygdala	324±261	425±310	0,449	0.0033±0.0008	0.0061±0.0051	0,069	83±39	202±192	0,059
16	Right-Accumbens-area	147±136	364±341	0,052	0.0039±0.0021	0.0067±0.0046	0,053	139±111	301±411	0,215
17	ctx_lh_G_and_S_frontomargin	325±205	198±223	0,166	0.006±0.0022	0.0099±0.0046	0,013	386±377	622±672	0,384
18	ctx_lh_G_and_S_occipital_inf	179±212	188±149	0,945	0.0055±0.0029	0.0082±0.004	0,070	284±286	470±379	0,234
19	ctx_lh_G_and_S_paracentral	363±180	346±281	0,910	0.0035±0.0029	0.0095±0.0044	0,010	607±601	688±374	0,573
20	ctx_lh_G_and_S_subcentral	160±176	202±223	0,497	0.0066±0.0034	0.0107±0.006	0,021	419±372	511±210	0,213
21	ctx_lh_G_and_S_transv_frontopol	181±173	155±154	0,617	0.0067±0.0032	0.0095±0.0047	0,108	321±187	454±418	0,518
22	ctx_lh_G_and_S_cingul-Ant	290±236	282±227	0,869	0.0059±0.0032	0.0093±0.0055	0,080	577±608	576±357	0,928
23	ctx_lh_G_and_S_cingul-Mid-Ant	143±113	224±184	0,207	0.0054±0.0025	0.0082±0.0038	0,050	322±204	388±237	0,449
24	ctx_lh_G_and_S_cingul-Mid-Post	119±126	100±89	0,744	0.0049±0.0024	0.0078±0.0038	0,025	235±211	254±130	0,627
25	ctx_lh_G_cingul-Post-dorsal	172±114	204±130	0,545	0.003±0.0016	0.0044±0.002	0,054	89±59	109±77	0,365
26	ctx_lh_G_cingul-Post-ventral	163±111	181±148	0,486	0.0035±0.0016	0.006±0.0038	0,042	179±198	213±158	0,486
27	ctx_lh_G_cuneus	427±247	280±140	0,091	0.0035±0.0014	0.0062±0.0034	0,018	607±601	368±213	0,122
28	ctx_lh_G_front_inf-Opercular	202±219	167±88	0,540	0.0086±0.0048	0.0116±0.0046	0,043	870±815	833±342	0,822
29	ctx_lh_G_front_inf-Orbital	65±73	215±269	0,053	0.0045±0.0028	0.0067±0.0032	0,063	91±80	227±148	0,009
30	ctx_lh_G_front_inf-Triangular	240±184	307±184	0,251	0.0064±0.0019	0.0096±0.0041	0,012	430±284	637±333	0,026
31	ctx_lh_G_front_middle	532±326	221±155	0,004	0.0106±0.0051	0.0161±0.0057	0,010	1403±804	1682±745	0,224
32	ctx_lh_G_front_sup	765±437	830±349	0,640	0.0102±0.0043	0.0153±0.0049	0,006	4294±2927	4799±1763	0,330

ON-LINE FIG 3. Continued

33	ctx_lh_G_ins_lg_and_S_cent_ins	127±122	189±167	0,283	0.004±0.002	0.006±0.0026	0,026	146±177	185±127	0,362
34	ctx_lh_G_insular_short	360±155	244±201	0,106	0.0041±0.0015	0.0077±0.0041	0,003	256±227	387±200	0,034
35	ctx_lh_G_occipital_middle	474±244	235±166	0,016	0.0064±0.0036	0.0102±0.0042	0,015	732±453	856±349	0,336
36	ctx_lh_G_occipital_sup	331±180	347±259	0,908	0.0046±0.0027	0.0072±0.0035	0,031	407±388	447±207	0,563
37	ctx_lh_G_oc-temp_lat-fusiform	244±154	178±156	0,235	0.0058±0.0028	0.0089±0.0041	0,026	389±287	537±255	0,189
38	ctx_lh_G_oc-temp_med-Lingual	460±312	441±318	0,857	0.0042±0.002	0.0071±0.0031	0,012	308±275	598±287	0,016
39	ctx_lh_G_oc-temp_med-Parahip	497±320	365±202	0,358	0.0046±0.0014	0.0064±0.0027	0,041	283±135	324±130	0,305
40	ctx_lh_G_orbital	538±184	515±198	0,609	0.0061±0.0021	0.0105±0.0049	0,007	798±400	1262±596	0,039
41	ctx_lh_G_pariet_inf-Angular	448±382	305±238	0,138	0.0078±0.0039	0.0118±0.0038	0,002	1041±695	961±392	0,924
42	ctx_lh_G_pariet_inf-Supramar	128±99	126±118	0,845	0.0082±0.0036	0.0147±0.005	2,5E-04	717±567	1259±714	0,022
43	ctx_lh_G_parietal_sup	624±334	718±286	0,348	0.0068±0.003	0.0101±0.0045	0,028	1182±738	1478±607	0,199
44	ctx_lh_G_postcentral	261±211	310±212	0,190	0.0086±0.003	0.0124±0.0054	0,027	996±741	1020±422	0,531
45	ctx_lh_G_precentral	483±373	392±352	0,438	0.0108±0.0048	0.0158±0.0044	0,003	1689±1238	1941±615	0,309
46	ctx_lh_G_preceunus	713±512	543±589	0,536	0.0054±0.0024	0.0105±0.0053	0,006	654±432	1131±275	0,004
47	ctx_lh_G_rectus	211±145	131±128	0,226	0.0039±0.0016	0.0076±0.0047	0,027	217±192	333±360	0,453
48	ctx_lh_G_subcallosal	160±135	205±250	0,835	0.0026±0.0013	0.0042±0.0027	0,056	64±88	89±63	0,364
49	ctx_lh_G_temp_sup-G_T_transv	91±127	69±76	0,889	0.0036±0.0028	0.0059±0.0027	0,077	66±54	103±91	0,294
50	ctx_lh_G_temporal_Middle	486±272	380±284	0,287	0.0062±0.0026	0.0092±0.0031	0,005	694±546	862±466	0,291
51	ctx_lh_G_temp_sup-Plan_polar	371±350	359±224	0,829	0.0036±0.0018	0.0056±0.0025	0,030	166±158	280±314	0,287
52	ctx_lh_G_temp_sup-Plan_tempo	129±127	134±134	0,949	0.0048±0.0033	0.0098±0.003	5,5E-05	207±234	352±228	0,081
53	ctx_lh_G_temporal_inf	380±234	432±313	0,475	0.007±0.003	0.0117±0.0055	0,011	799±498	1324±704	0,036
54	ctx_lh_G_temporal_Middle	300±210	353±231	0,579	0.0069±0.0025	0.0119±0.004	4,8E-04	895±638	1476±721	0,021
55	ctx_lh_Lat_Fis-ant-Horizont	49±47	87±79	0,109	0.0021±0.0015	0.0046±0.0026	0,017	25±35	50±38	0,166
56	ctx_lh_Lat_Fis-ant-Vertical	75±86	92±94	0,587	0.0032±0.0024	0.006±0.0028	0,008	35±55	70±35	0,050
57	ctx_lh_Lat_Fis-post	105±114	61±63	0,362	0.0037±0.002	0.0064±0.0035	0,004	121±140	115±59	0,719
58	ctx_lh_Pole_occipital	258±319	324±218	0,524	0.0051±0.0022	0.007±0.0055	0,252	454±528	417±379	0,984
59	ctx_lh_Pole_temporal	596±251	658±386	0,880	0.006±0.0025	0.0099±0.0049	0,011	1005±886	1373±630	0,181
60	ctx_lh_S_calcarine	380±254	376±299	0,962	0.0041±0.002	0.006±0.0033	0,085	278±169	309±195	0,433
61	ctx_lh_S_central	268±247	265±220	0,990	0.0056±0.002	0.0088±0.0041	0,008	239±181	361±174	0,030
62	ctx_lh_S_cingul-Marginalis	116±73	172±227	0,437	0.004±0.0021	0.008±0.0047	0,011	155±102	307±243	0,070
63	ctx_lh_S_circular_insula_ant	112±128	69±108	0,270	0.0033±0.0016	0.0053±0.0028	0,043	84±76	65±38	0,510
64	ctx_lh_S_circular_insula_inf	289±352	229±123	0,531	0.0047±0.002	0.0075±0.0041	0,026	320±215	326±147	0,699
65	ctx_lh_S_circular_insula_sup	259±160	214±124	0,355	0.0037±0.0017	0.0059±0.0021	8,6E-04	141±132	152±81	0,526
66	ctx_lh_S_collat_transv_ant	216±308	340±270	0,224	0.0042±0.0024	0.0058±0.0025	0,155	235±201	231±146	0,848
67	ctx_lh_S_collat_transv_post	34±59	103±144	0,179	0.003±0.0018	0.007±0.0067	0,058	35±57	122±137	0,053
68	ctx_lh_S_front_inf	183±202	90±113	0,276	0.0084±0.0056	0.0109±0.006	0,186	361±300	242±147	0,390
69	ctx_lh_S_front_Middle	66±116	148±147	0,217	0.0072±0.0037	0.0096±0.004	0,148	119±83	239±334	0,313
70	ctx_lh_S_front_sup	306±275	235±216	0,584	0.0085±0.0043	0.0144±0.0072	0,025	487±478	632±293	0,168
71	ctx_lh_S_interprim-Jensen	61±72	37±74	0,468	0.0031±0.0021	0.0083±0.0057	0,002	71±110	53±37	0,820
72	ctx_lh_S_intrapariet_and_P_trans	408±299	553±547	0,308	0.0051±0.0028	0.0079±0.0032	0,014	359±292	583±301	0,073
73	ctx_lh_S_oc_Middle_and_Lunatus	99±178	209±159	0,080	0.0039±0.0027	0.0046±0.0023	0,388	96±90	113±70	0,461
74	ctx_lh_S_oc_sup_and_transversal	293±353	256±158	0,788	0.0036±0.0024	0.006±0.0034	0,031	120±104	260±211	0,038
75	ctx_lh_S_occipital_ant	63±60	72±54	0,653	0.0031±0.0021	0.0063±0.0038	0,009	86±96	110±80	0,522
76	ctx_lh_S_oc-temp_lat	193±190	176±161	0,914	0.0039±0.002	0.0068±0.0033	0,011	126±112	202±143	0,110
77	ctx_lh_S_oc-temp_med_and_Lingual	219±300	252±268	0,572	0.0054±0.0021	0.008±0.0047	0,093	349±253	435±149	0,151
78	ctx_lh_S_orbital_lateral	90±75	141±179	0,442	0.0046±0.002	0.0056±0.0025	0,248	110±90	107±94	0,962
79	ctx_lh_S_orbital_med-olfact	141±134	123±105	0,891	0.0024±0.0013	0.004±0.0022	0,070	29±18	66±44	0,016
80	ctx_lh_S_orbital-H_Shaped	71±89	108±135	0,427	0.004±0.002	0.0068±0.0028	0,008	69±50	106±57	0,031
81	ctx_lh_S_parieto_occipital	282±191	302±214	0,664	0.0037±0.0015	0.0064±0.0039	0,022	259±222	319±116	0,235
82	ctx_lh_S_pericallosal	461±335	321±247	0,213	0.0039±0.0016	0.0058±0.0029	0,045	214±100	218±72	0,663
83	ctx_lh_S_postcentral	168±188	260±181	0,090	0.0074±0.0038	0.0092±0.0042	0,145	454±366	385±133	0,991
84	ctx_lh_S_precentral-inf-part	60±84	60±56	0,964	0.0072±0.0033	0.0106±0.0064	0,065	173±236	191±119	0,655
85	ctx_lh_S_precentral-sup-part	68±101	125±156	0,235	0.0073±0.0033	0.0102±0.0027	0,027	149±118	228±121	0,081
86	ctx_lh_S_suborbital	188±154	105±104	0,208	0.0036±0.0014	0.0056±0.0042	0,151	132±82	151±216	0,967
87	ctx_lh_S_subparietal	260±261	202±140	0,343	0.0036±0.0019	0.0061±0.004	0,036	198±204	246±170	0,317
88	ctx_lh_S_temporal_inf	157±94	165±177	0,994	0.004±0.0014	0.0084±0.005	0,004	134±106	311±277	0,040
89	ctx_lh_S_temporal_sup	330±275	171±164	0,104	0.0064±0.0025	0.0101±0.0032	5,1E-04	622±393	786±419	0,161
90	ctx_lh_S_temporal_transverse	91±118	43±75	0,315	0.0025±0.0011	0.0039±0.0029	0,159	38±37	53±95	0,780
91	ctx_rh_G_and_S_frontomargin	189±92	199±161	0,877	0.0073±0.0037	0.0108±0.0046	0,014	724±569	703±461	0,765
92	ctx_rh_G_and_S_occipital_inf	138±105	181±173	0,529	0.0053±0.0022	0.0099±0.0045	0,001	295±216	552±457	0,101
93	ctx_rh_G_and_S_paracentral	168±129	286±165	0,082	0.0045±0.0016	0.0081±0.0041	0,006	228±294	473±287	0,040
94	ctx_rh_G_and_S_subcentral	160±121	109±92	0,295	0.0068±0.0034	0.0106±0.006	0,033	434±316	370±224	0,996
95	ctx_rh_G_and_S_transv_frontopoli	270±249	237±278	0,875	0.0072±0.0043	0.0123±0.0059	0,025	516±446	637±275	0,329
96	ctx_rh_G_and_S_cingul-Ant	269±244	339±255	0,591	0.0059±0.0028	0.0101±0.0056	0,019	435±244	650±226	0,031
97	ctx_rh_G_and_S_cingul-Mid-Ant	325±214	173±137	0,044	0.0056±0.0031	0.0102±0.0057	0,015	418±279	562±348	0,295
98	ctx_rh_G_and_S_cingul-Mid-Post	184±149	311±232	0,124	0.0051±0.0028	0.0085±0.004	0,018	318±289	462±191	0,115
99	ctx_rh_G_cingul-Post-dorsal	154±109	164±124	0,796	0.003±0.0016	0.0055±0.0033	0,032	89±72	150±78	0,048
100	ctx_rh_G_cingul-Post-ventral	161±183	212±174	0,402	0.0035±0.0019	0.0056±0.0031	0,042	160±120	234±131	0,156
101	ctx_rh_G_cuneus	339±192	588±328	0,013	0.0032±0.0017	0.0066±0.0035	0,002	127±190	432±171	3,7E-04
102	ctx_rh_G_front_inf-Opercular	309±270	155±119	0,061	0.0074±0.0043	0.0141±0.0059	0,004	678±620	1048±615	0,111

ON-LINE FIG 3. Continued

103	ctx_rh_G_front_inf-Orbital	212±162	109±87	0,102	0,0042±0.0019	0.0079±0.0029	0,002	185±219	263±207	0,451
104	ctx_rh_G_front_inf-Triangular	231±205	251±272	0,913	0,0072±0.0033	0.0126±0.0061	0,020	575±400	765±282	0,151
105	ctx_rh_G_front_middle	424±280	360±213	0,790	0,0103±0.0042	0.0173±0.0064	0,003	1621±1207	1923±633	0,307
106	ctx_rh_G_front_sup	1049±620	1036±700	0,839	0,0097±0.004	0.0154±0.0065	0,010	3687±2334	4862±1537	0,054
107	ctx_rh_G_ins_lg_and_S_cent_ins	262±255	205±219	0,566	0,0045±0.0025	0.008±0.0052	0,038	182±131	295±241	0,121
108	ctx_rh_G_insular_short	196±180	193±173	0,874	0,0056±0.002	0.0108±0.007	0,021	350±184	527±287	0,053
109	ctx_rh_G_occipital_middle	270±215	254±208	0,613	0,0079±0.0034	0.0129±0.0051	0,003	979±693	1381±888	0,145
110	ctx_rh_G_occipital_sup	344±216	608±321	0,031	0,0044±0.0016	0.0074±0.0031	0,003	391±250	652±335	0,034
111	ctx_rh_G_oc-temp_lat-fusiform	223±187	125±117	0,103	0,0051±0.0021	0.0088±0.0042	0,004	305±233	383±162	0,183
112	ctx_rh_G_oc-temp_med-Lingual	486±303	395±305	0,476	0,004±0.0016	0.008±0.0047	0,004	310±223	668±308	0,97E-05
113	ctx_rh_G_oc-temp_med-Parahip	472±249	362±240	0,374	0,0041±0.0016	0.0064±0.0031	0,028	235±166	302±168	0,204
114	ctx_rh_G_orbital	513±354	620±456	0,563	0,0066±0.0022	0.0106±0.0045	0,002	786±581	1231±617	0,062
115	ctx_rh_G_pariet_inf-Angular	185±191	227±140	0,466	0,0102±0.0038	0.0165±0.0061	0,003	1246±756	1834±775	0,036
116	ctx_rh_G_pariet_inf-Supramar	82±99	127±127	0,220	0,0106±0.0053	0.0171±0.0078	0,015	1094±921	1216±634	0,455
117	ctx_rh_G_parietal_sup	489±346	645±415	0,613	0,0054±0.002	0.0106±0.0051	0,001	646±530	1080±398	0,027
118	ctx_rh_G_postcentral	363±311	379±262	0,905	0,0083±0.0029	0.0136±0.0072	0,019	861±602	1063±472	0,299
119	ctx_rh_G_precentral	317±210	405±369	0,479	0,0113±0.0036	0.0191±0.0106	0,020	1929±1264	2462±878	0,199
120	ctx_rh_G_precuneus	788±524	459±223	0,059	0,0082±0.0023	0.0092±0.0044	0,004	775±523	1219±511	0,035
121	ctx_rh_G_rectus	328±237	250±180	0,390	0,0033±0.0018	0.0052±0.0026	0,021	143±139	150±146	0,729
122	ctx_rh_G_subcallosal	163±148	208±275	0,654	0,0022±0.0018	0.0043±0.0029	0,029	57±60	136±190	0,165
123	ctx_rh_G_temp_sup-G_T_transv	117±137	120±101	0,969	0,0034±0.0011	0.0071±0.0046	0,013	54±44	139±97	0,011
124	ctx_rh_G_temp_sup-Lateral	245±196	415±281	0,094	0,0082±0.0035	0.0129±0.0073	0,044	900±595	1314±648	0,101
125	ctx_rh_G_temp_sup-Plan_polar	411±267	307±208	0,197	0,004±0.0017	0.0069±0.0035	0,012	202±116	331±202	0,050
126	ctx_rh_G_temp_sup-Plan_tempo	113±184	68±65	0,583	0,0066±0.0036	0.0111±0.0049	0,008	204±178	283±98	0,072
127	ctx_rh_G_temporal_inf	257±281	180±153	0,452	0,0071±0.0028	0.0126±0.0051	0,001	785±675	967±437	0,188
128	ctx_rh_G_temporal_middle	245±218	351±285	0,527	0,0099±0.0053	0.016±0.0083	0,023	1641±1158	2261±760	0,066
129	ctx_rh_Lat_Fis-ant-Horizont	91±115	97±126	0,957	0,0027±0.0016	0.0061±0.0032	0,003	41±61	100±99	0,100
130	ctx_rh_Lat_Fis-ant-Vertical	17±40	55±85	0,172	0,0019±0.0019	0.0069±0.0051	0,003	14±16	50±49	0,008
131	ctx_rh_Lat_Fis-post	155±172	84±70	0,222	0,0051±0.0032	0.007±0.0044	0,173	168±167	124±75	0,489
132	ctx_rh_Pole_occipital	392±271	431±373	0,615	0,0049±0.0018	0.0081±0.0035	0,009	474±288	646±319	0,119
133	ctx_rh_Pole_temporal	729±489	495±323	0,155	0,0065±0.0027	0.0105±0.0059	0,025	1178±788	1149±526	0,705
134	ctx_rh_S_calcarine	456±195	437±305	0,543	0,0036±0.0014	0.0064±0.003	0,003	265±204	415±273	0,107
135	ctx_rh_S_central	315±204	253±140	0,329	0,0061±0.0033	0.01±0.0055	0,030	257±191	456±274	0,016
136	ctx_rh_S_cingul-Marginalis	156±177	206±200	0,484	0,0046±0.0024	0.0075±0.0036	0,020	213±197	362±203	0,046
137	ctx_rh_S_circular_insula_ant	26±24	44±34	0,071	0,0042±0.0029	0.0065±0.0028	0,073	77±85	99±96	0,432
138	ctx_rh_S_circular_insula_inf	413±271	310±174	0,278	0,005±0.0018	0.0081±0.0044	0,027	346±148	430±286	0,362
139	ctx_rh_S_circular_insula_sup	137±110	179±135	0,330	0,0038±0.0015	0.0064±0.0036	0,020	92±88	131±94	0,209
140	ctx_rh_S_collat_transv_ant	211±411	115±146	0,629	0,0038±0.0018	0.0079±0.006	0,019	158±158	294±287	0,130
141	ctx_rh_S_collat_transv_post	81±93	136±144	0,391	0,0029±0.0015	0.0046±0.003	0,058	45±38	61±43	0,291
142	ctx_rh_S_front_inf	184±147	163±163	0,957	0,0057±0.0022	0.0104±0.0066	0,017	232±243	237±168	0,681
143	ctx_rh_S_front_middle	272±224	201±168	0,526	0,007±0.0041	0.0114±0.0059	0,040	342±407	351±300	0,788
144	ctx_rh_S_front_sup	278±246	292±361	0,871	0,0081±0.0064	0.013±0.0065	0,053	308±237	550±329	0,067
145	ctx_rh_S_interm_prim-Jensen	27±34	20±31	0,682	0,0047±0.0027	0.0079±0.0043	0,030	80±113	45±26	0,447
146	ctx_rh_S_intrapariet_and_P_trans	365±275	340±258	0,777	0,0058±0.003	0.0098±0.0056	0,025	399±241	605±386	0,079
147	ctx_rh_S_oc-middle_and_Lunatus	79±123	124±81	0,156	0,0031±0.0026	0.0055±0.0033	0,039	79±97	119±125	0,390
148	ctx_rh_S_oc_sup_and_transversal	232±241	436±447	0,341	0,0041±0.0022	0.0066±0.0038	0,012	155±118	321±348	0,044
149	ctx_rh_S_occipital_ant	110±109	88±81	0,406	0,0045±0.0012	0.0091±0.0061	0,013	114±68	284±338	0,092
150	ctx_rh_S_oc-temp_lat	90±213	140±194	0,664	0,0059±0.0059	0.0063±0.0027	0,603	90±49	126±140	0,296
151	ctx_rh_S_oc-temp_med_and_Lingual	395±336	181±135	0,088	0,0042±0.0014	0.0062±0.0026	0,011	303±272	203±72	0,382
152	ctx_rh_S_orbital_lateral	125±138	196±269	0,433	0,0038±0.0009	0.007±0.0044	0,025	85±75	171±146	0,134
153	ctx_rh_S_orbital_med-olfact	236±293	118±123	0,132	0,0028±0.0015	0.0056±0.0039	0,021	68±58	128±92	0,078
154	ctx_rh_S_orbital-H_Shaped	106±106	153±214	0,592	0,0048±0.0038	0.0071±0.0054	0,118	87±67	129±133	0,341
155	ctx_rh_S_parieto_occipital	463±421	504±312	0,739	0,0039±0.0021	0.0068±0.0031	0,008	304±193	425±166	0,043
156	ctx_rh_S_pericallosal	701±301	526±347	0,154	0,0046±0.0019	0.0079±0.0049	0,037	525±434	636±428	0,446
157	ctx_rh_S_postcentral	266±358	275±159	0,772	0,0062±0.0028	0.0099±0.0046	0,020	255±131	444±263	0,028
158	ctx_rh_S_precentral-inf-part	115±108	71±69	0,265	0,0062±0.0026	0.012±0.0065	0,008	219±203	247±134	0,337
159	ctx_rh_S_precentral-sup-part	122±102	193±316	0,295	0,0066±0.0031	0.0124±0.0079	0,030	150±112	289±292	0,073
160	ctx_rh_S_suborbital	67±75	88±112	0,554	0,0024±0.0015	0.0031±0.0022	0,349	35±42	33±24	0,924
161	ctx_rh_S_subparietal	357±399	221±171	0,298	0,0041±0.0026	0.0064±0.0029	0,047	224±226	344±241	0,189
162	ctx_rh_S_temporal_inf	180±188	200±178	0,651	0,0046±0.0018	0.0087±0.0035	6,5E-04	192±201	352±281	0,057
163	ctx_rh_S_temporal_sup	462±432	220±158	0,051	0,0085±0.0042	0.0148±0.0065	0,007	1006±634	1348±599	0,152
164	ctx_rh_S_temporal_transverse	67±73	70±69	0,788	0,0031±0.001	0.0062±0.004	0,017	48±64	77±50	0,205

### CLN3 1st vs 2nd acquisition

Idx	Label name	Betweenness centrality			Local efficiency			Strength		
		CLN3 1st	CLN3 2nd	P	CLN3 1st	CLN3 2nd	P	CLN3 1st	CLN3 2nd	P
1	Left-Cerebellum-Cortex	722±294	970±509	0,330	0,0085±0.0031	0.0081±0.0033	0,960	3143±1662	3566±1685	0,356
2	Left-Thalamus-Proper	789±417	1146±392	0,102	0,0091±0.0047	0.008±0.0033	0,606	1740±621	1869±699	0,331
3	Left-Caudate	619±369	648±388	0,704	0,0077±0.0049	0.0064±0.0034	0,794	849±649	599±276	0,481
4	Left-Putamen	700±430	590±384	0,372	0,0103±0.0055	0.0096±0.0039	0,996	2278±1299	2108±907	0,595

ON-LINE FIG 3. Continued

5	Left-Pallidum	410±285	373±275	0,851	0.0093±0.0057	0.0079±0.0033	0,706	1948±580	749±442	0,680
6	Left-Hippocampus	650±466	683±448	0,491	0.0062±0.0026	0.0058±0.0028	0,971	1757±336	500±341	0,215
7	Left-Amygdala	146±154	249±245	0,223	0.0029±0.0018	0.0041±0.0024	0,043	173±53	122±156	0,206
8	Left-Accumbens-area	284±237	230±252	0,397	0.0044±0.0027	0.0033±0.0011	0,306	182±144	97±91	0,159
9	Right-Cerebellum-Cortex	1137±563	912±508	0,383	0.0076±0.003	0.0079±0.0029	0,629	2916±1524	3168±1226	0,401
10	Right-Thalamus-Proper	443±319	813±440	0,030	0.0089±0.0041	0.0073±0.0031	0,526	1693±1043	1172±710	0,422
11	Right-Caudate	436±343	268±145	0,106	0.0076±0.0043	0.0079±0.0036	0,450	1837±469	734±452	0,638
12	Right-Putamen	954±410	613±287	0,019	0.0097±0.0057	0.0096±0.0036	0,832	2180±955	2105±1126	0,605
13	Right-Pallidum	338±205	544±321	0,071	0.0078±0.0035	0.008±0.0026	0,673	759±333	842±370	0,278
14	Right-Hippocampus	585±394	561±428	0,941	0.0052±0.0017	0.0054±0.002	0,354	564±425	534±355	0,611
15	Right-Amygdala	238±274	324±261	0,547	0.0035±0.0019	0.0033±0.0008	0,965	1103±172	83±39	0,703
16	Right-Accumbens-area	218±227	147±136	0,716	0.004±0.0019	0.0039±0.0021	0,791	1139±121	139±111	0,601
17	ctx_lh_G_and_S_frontomargin	352±294	325±205	0,783	0.0079±0.006	0.006±0.0022	0,364	612±558	386±377	0,279
18	ctx_lh_G_and_S_occipital_inf	181±173	179±212	0,575	0.0069±0.0038	0.0055±0.0029	0,314	534±622	284±286	0,256
19	ctx_lh_G_and_S_paracentral	374±274	363±180	0,609	0.0054±0.0028	0.0053±0.0029	0,758	509±431	607±601	0,299
20	ctx_lh_G_and_S_subcentral	127±147	160±176	0,709	0.0084±0.0057	0.0066±0.0034	0,605	572±400	419±372	0,714
21	ctx_lh_G_and_S_transv_frontopoli	211±178	181±173	0,885	0.0076±0.0042	0.0067±0.0032	0,789	559±523	321±187	0,377
22	ctx_lh_G_and_S_cingul-Ant	217±215	290±236	0,355	0.0032±0.0023	0.0059±0.0032	0,099	382±311	179±608	0,041
23	ctx_lh_G_and_S_cingul-Mid-Ant	150±118	143±113	0,869	0.0059±0.0036	0.0054±0.0025	0,851	398±222	322±204	0,944
24	ctx_lh_G_and_S_cingul-Mid-Post	161±119	119±126	0,573	0.0047±0.0024	0.0049±0.0024	0,358	260±138	235±211	0,453
25	ctx_lh_G_cingul-Post-dorsal	227±153	172±114	0,179	0.0033±0.0018	0.003±0.0016	0,645	123±75	89±59	0,188
26	ctx_lh_G_cingul-Post-ventral	353±279	163±111	0,031	0.0032±0.0017	0.0035±0.0016	0,807	148±121	179±198	0,584
27	ctx_lh_G_cuneus	299±193	427±247	0,168	0.0044±0.0022	0.0035±0.0014	0,458	307±146	245±144	0,682
28	ctx_lh_G_front_inf-Opercular	174±174	202±219	0,896	0.0083±0.0056	0.0086±0.0048	0,487	831±819	870±815	0,410
29	ctx_lh_G_front_inf-Orbital	147±170	65±73	0,157	0.0049±0.0027	0.0045±0.0028	0,802	198±282	91±80	0,364
30	ctx_lh_G_front_inf-Triangul	349±163	240±184	0,159	0.0077±0.0047	0.0064±0.0019	0,682	145±583	430±284	0,566
31	ctx_lh_G_front_middle	336±295	532±326	0,132	0.0128±0.0094	0.0106±0.0051	0,729	1334±758	1403±804	0,417
32	ctx_lh_G_front_sup	824±323	765±437	0,523	0.011±0.0065	0.0102±0.0043	0,830	3748±2198	4294±2927	0,093
33	ctx_lh_G_ins_lg_and_S_cent_ins	202±156	127±122	0,460	0.0047±0.0027	0.004±0.002	0,498	199±150	146±177	0,639
34	ctx_lh_G_insular_short	343±215	360±155	0,950	0.0052±0.003	0.0041±0.0015	0,457	243±182	256±227	0,322
35	ctx_lh_G_occipital_middle	285±213	474±244	0,039	0.0073±0.0035	0.0064±0.0036	0,843	1019±893	732±453	0,559
36	ctx_lh_G_occipital_sup	326±196	331±180	0,858	0.0046±0.0021	0.0046±0.0027	0,778	393±331	407±388	0,570
37	ctx_lh_G_oc-temp_lat-fusifor	207±166	244±154	0,347	0.0055±0.002	0.0058±0.0028	0,541	335±239	389±287	0,223
38	ctx_lh_G_oc-temp_med-Lingual	379±235	460±312	0,319	0.0044±0.0016	0.0042±0.002	0,732	417±355	308±275	0,391
39	ctx_lh_G_oc-temp_med-Parahip	358±233	497±320	0,257	0.005±0.0025	0.0046±0.0014	0,955	327±207	283±135	0,902
40	ctx_lh_G_orbital	481±332	538±184	0,943	0.0084±0.0053	0.0061±0.0021	0,183	1034±506	798±400	0,185
41	ctx_lh_G_pariet_inf-Angular	234±190	448±382	0,083	0.0096±0.0056	0.0078±0.0039	0,524	1115±646	1041±695	0,997
42	ctx_lh_G_pariet_inf-Supramar	74±73	128±99	0,149	0.0107±0.0062	0.0082±0.0036	0,362	971±626	717±567	0,597
43	ctx_lh_G_parietal_sup	633±415	624±334	0,955	0.0065±0.0033	0.0068±0.003	0,522	980±647	1182±738	0,135
44	ctx_lh_G_postcentral	344±314	261±211	0,804	0.0091±0.0053	0.0086±0.003	0,973	1802±434	996±741	0,045
45	ctx_lh_G_precentral	381±225	483±373	0,596	0.0115±0.0062	0.0108±0.0048	0,954	1759±1177	1689±1238	0,774
46	ctx_lh_G_precuneus	617±476	713±512	0,931	0.0057±0.0024	0.0054±0.0024	0,931	706±347	654±432	0,768
47	ctx_lh_G_rectus	249±198	211±145	0,711	0.005±0.0029	0.0039±0.0016	0,310	238±165	217±192	0,947
48	ctx_lh_G_subcallosal	271±252	160±135	0,328	0.0026±0.0013	0.0026±0.0013	0,863	180±80	64±88	0,771
49	ctx_lh_G_temp_sup-G_T_transv	64±78	91±127	0,486	0.0043±0.0031	0.0036±0.0028	0,571	177±70	66±54	0,941
50	ctx_lh_G_temp_sup-Lateral	340±230	486±272	0,223	0.0079±0.004	0.0062±0.0026	0,402	809±528	694±546	0,934
51	ctx_lh_G_temp_sup-Plan_polar	260±166	371±350	0,158	0.0034±0.0025	0.0036±0.0018	0,828	102±82	166±158	0,105
52	ctx_lh_G_temp_sup-Plan_tempo	96±104	129±127	0,955	0.0057±0.0039	0.0048±0.0033	0,842	176±121	207±234	0,238
53	ctx_lh_G_temporal_inf	449±387	380±234	0,677	0.0077±0.0039	0.007±0.003	0,897	882±483	799±498	0,999
54	ctx_lh_G_temporal_middle	416±477	300±210	0,342	0.0092±0.0054	0.0069±0.0025	0,342	954±501	895±638	0,830
55	ctx_lh_Lat_Fis-ant-Horizont	41±33	49±47	0,625	0.0034±0.0024	0.0021±0.0015	0,118	33±32	25±35	0,546
56	ctx_lh_Lat_Fis-ant-Vertical	49±70	75±86	0,409	0.0037±0.0032	0.0032±0.0024	0,963	44±45	35±55	0,953
57	ctx_lh_Lat_Fis-post	111±79	105±114	0,921	0.0044±0.0026	0.0037±0.002	0,996	181±330	121±140	0,945
58	ctx_lh_Pole_occipital	245±293	258±319	0,644	0.0059±0.0034	0.0051±0.0022	0,761	479±373	454±528	0,630
59	ctx_lh_Pole_temporal	517±274	596±251	0,248	0.0069±0.0037	0.006±0.0025	0,605	1040±521	1005±886	0,829
60	ctx_lh_S_calcarine	315±216	380±254	0,269	0.0047±0.0021	0.0041±0.002	0,625	404±187	278±169	0,232
61	ctx_lh_S_central	229±297	268±247	0,776	0.0064±0.0037	0.0056±0.002	0,672	234±206	239±181	0,770
62	ctx_lh_S_cingul-Marginalis	286±222	116±73	0,014	0.0042±0.0021	0.004±0.0021	0,911	232±221	155±102	0,425
63	ctx_lh_S_circular_insula_ant	111±129	112±128	0,941	0.0043±0.0033	0.0033±0.0016	0,283	199±99	84±76	0,902
64	ctx_lh_S_circular_insula_inf	360±280	289±352	0,613	0.0048±0.0026	0.0047±0.002	0,913	209±104	320±215	0,049
65	ctx_lh_S_circular_insula_sup	274±250	259±160	0,684	0.0049±0.0034	0.0037±0.0017	0,340	191±147	141±132	0,614
66	ctx_lh_S_collat_transv_ant	164±153	216±308	0,446	0.0049±0.0031	0.0042±0.0024	0,683	199±129	235±201	0,321
67	ctx_lh_S_collat_transv_post	48±58	34±59	0,581	0.0032±0.0018	0.003±0.0018	0,908	28±36	35±57	0,546
68	ctx_lh_S_front_inf	166±166	183±202	0,912	0.0091±0.008	0.0084±0.0056	0,733	305±357	361±300	0,211
69	ctx_lh_S_front_middle	129±132	66±116	0,115	0.0063±0.0041	0.0072±0.0037	0,501	140±100	119±83	0,280
70	ctx_lh_S_front_sup	235±208	306±275	0,218	0.0109±0.0107	0.0085±0.0043	0,726	381±304	487±478	0,088
71	ctx_lh_S_interm_prim-lensen	33±37	61±72	0,310	0.0038±0.003	0.0031±0.0021	0,452	48±54	71±110	0,436
72	ctx_lh_S_intrapariet_and_P_trans	338±223	408±299	0,451	0.0055±0.0024	0.0051±0.0028	0,962	400±206	359±292	0,718
73	ctx_lh_S_oc-middle_and_Lunatus	183±220	99±178	0,377	0.0034±0.0031	0.0039±0.0027	0,561	138±158	96±90	0,602
74	ctx_lh_S_oc_sup_and_transversal	434±567	293±353	0,272	0.0041±0.0018	0.0036±0.0024	0,640	224±139	120±104	0,074

ON-LINE FIG 3. Continued

75	ctx_lh_S_occipital_ant	54±49	63±60	0,597	0.005±0.0029	0.0031±0.0021	0,170	107±95	86±96	0,819
76	ctx_lh_S_oc-temp_lat	144±173	193±190	0,352	0.0046±0.0022	0.0039±0.002	0,609	164±146	126±112	0,927
77	ctx_lh_S_oc-temp_med_and_Lingual	373±396	219±300	0,133	0.0045±0.0021	0.0054±0.0021	0,177	317±206	349±253	0,359
78	ctx_lh_S_orbital_lateral	127±121	90±75	0,349	0.0052±0.0039	0.0046±0.002	0,982	116±146	110±90	0,784
79	ctx_lh_S_orbital_med-olfact	214±471	141±134	0,334	0.0036±0.0023	0.0024±0.0013	0,137	87±70	29±18	0,022
80	ctx_lh_S_orbital-H_Shaped	147±166	71±89	0,061	0.0048±0.0038	0.004±0.002	0,446	101±96	69±50	0,273
81	ctx_lh_S_parieto_occipital	270±308	282±191	0,978	0.0045±0.0023	0.0037±0.0015	0,659	304±228	259±222	0,918
82	ctx_lh_S_pericallosal	362±268	461±335	0,805	0.0038±0.0017	0.0039±0.0016	0,691	223±134	214±100	0,767
83	ctx_lh_S_postcentral	122±107	168±188	0,685	0.0075±0.0039	0.0074±0.0038	0,834	349±171	454±366	0,133
84	ctx_lh_S_precentral-inf-part	94±97	60±84	0,405	0.0065±0.0036	0.0072±0.0033	0,310	138±116	173±236	0,276
85	ctx_lh_S_precentral-sup-part	72±89	68±101	0,751	0.0072±0.0058	0.0073±0.0033	0,795	109±110	149±118	0,194
86	ctx_lh_S_suborbital	166±152	188±154	0,436	0.003±0.0015	0.0036±0.0014	0,233	80±76	132±82	0,083
87	ctx_lh_S_subparietal	229±186	260±261	0,801	0.0036±0.0011	0.0036±0.0019	0,705	225±202	198±204	0,849
88	ctx_lh_S_temporal_inf	103±84	157±94	0,284	0.0046±0.0022	0.004±0.0014	0,622	111±79	134±106	0,525
89	ctx_lh_S_temporal_sup	372±344	330±275	0,599	0.0072±0.0035	0.0064±0.0025	0,749	657±389	622±393	0,915
90	ctx_lh_S_temporal_transverse	85±116	91±118	0,630	0.0036±0.0028	0.0025±0.0011	0,266	59±84	38±37	0,633
91	ctx_rh_G_and_S_frontomargin	354±412	189±92	0,132	0.0069±0.004	0.0073±0.0037	0,522	450±250	724±569	0,038
92	ctx_rh_G_and_S_occipital_inf	169±184	138±105	0,328	0.0064±0.004	0.0053±0.0022	0,342	430±316	295±216	0,264
93	ctx_rh_G_and_S_paracentral	234±208	168±129	0,516	0.0048±0.0025	0.0045±0.0016	0,939	265±201	228±294	0,981
94	ctx_rh_G_and_S_subcentral	135±100	160±121	0,888	0.0062±0.0037	0.0068±0.0034	0,425	285±143	434±316	0,020
95	ctx_rh_G_and_S_transv_frontopol	340±334	270±249	0,492	0.0084±0.0053	0.0072±0.0043	0,939	716±637	516±446	0,653
96	ctx_rh_G_and_S_cingul-Ant	329±237	269±244	0,928	0.0064±0.0038	0.0059±0.0028	0,854	573±408	435±244	0,478
97	ctx_rh_G_and_S_cingul-Mid-Ant	395±266	325±214	0,327	0.0053±0.0027	0.0056±0.0031	0,498	431±255	418±279	0,501
98	ctx_rh_G_and_S_cingul-Mid-Post	291±310	184±149	0,182	0.0044±0.0015	0.0051±0.0028	0,229	268±95	318±289	0,284
99	ctx_rh_G_cingul-Post-dorsal	185±217	154±109	0,509	0.0033±0.0016	0.003±0.0016	0,802	128±63	89±72	0,294
100	ctx_rh_G_cingul-Post-ventral	221±301	161±183	0,862	0.0034±0.0023	0.0035±0.0019	0,867	144±129	160±120	0,596
101	ctx_rh_G_cuneus	400±262	339±192	0,171	0.0039±0.0015	0.0032±0.0017	0,631	246±145	227±190	0,617
102	ctx_rh_G_front_inf-Opercular	193±154	309±270	0,266	0.0072±0.0054	0.0074±0.0043	0,876	486±322	678±620	0,153
103	ctx_rh_G_front_inf-Orbital	80±71	212±162	0,008	0.0043±0.0019	0.0042±0.0019	0,830	115±69	185±219	0,136
104	ctx_rh_G_front_inf-Triangul	225±247	231±205	0,568	0.0064±0.0037	0.0072±0.0033	0,405	421±326	575±400	0,050
105	ctx_rh_G_front_middle	420±302	424±280	0,920	0.0101±0.0054	0.0103±0.0042	0,650	1711±1379	1621±1207	0,758
106	ctx_rh_G_front_sup	837±542	1049±620	0,511	0.0104±0.0057	0.0097±0.004	0,898	3363±2116	3687±2334	0,293
107	ctx_rh_G_ins_lg_and_S_cent_ins	179±121	262±255	0,586	0.004±0.0025	0.0045±0.0025	0,566	117±85	182±131	0,124
108	ctx_rh_G_insular_short	307±148	196±180	0,035	0.0053±0.0035	0.0056±0.002	0,644	296±222	350±184	0,459
109	ctx_rh_G_occipital_middle	376±341	270±215	0,432	0.0077±0.0042	0.0079±0.0034	0,821	1094±872	979±693	0,923
110	ctx_rh_G_occipital_sup	368±325	344±216	0,612	0.0046±0.0022	0.0044±0.0016	0,807	452±521	391±250	0,749
111	ctx_rh_G_oc-temp_lat-fusifor	206±222	223±187	0,849	0.0058±0.0025	0.0051±0.0021	0,559	281±179	305±233	0,442
112	ctx_rh_G_oc-temp_med-Lingual	641±416	486±303	0,226	0.0042±0.0012	0.004±0.0016	0,949	431±261	310±223	0,387
113	ctx_rh_G_oc-temp_med-Parahip	343±288	472±249	0,263	0.0041±0.0015	0.0041±0.0016	0,735	234±255	235±166	0,853
114	ctx_rh_G_orbital	550±398	513±354	0,941	0.0075±0.0043	0.0066±0.0022	0,683	1014±543	786±581	0,551
115	ctx_rh_G_pariet_inf-Angular	254±280	185±191	0,598	0.0099±0.0059	0.0102±0.0038	0,819	1211±855	1246±756	0,733
116	ctx_rh_G_pariet_inf-Supramar	156±183	82±99	0,317	0.0105±0.0055	0.0106±0.0053	0,615	1128±684	1094±921	0,326
117	ctx_rh_G_pariet_sup	663±460	489±346	0,501	0.0055±0.0033	0.0054±0.002	0,785	631±461	646±530	0,550
118	ctx_rh_G_postcentral	473±371	363±311	0,452	0.0069±0.0043	0.0083±0.0029	0,196	638±457	861±602	0,100
119	ctx_rh_G_precentral	400±315	317±210	0,231	0.0095±0.0048	0.0113±0.0036	0,216	1460±1051	1929±1264	0,137
120	ctx_rh_G_preuncus	480±387	788±524	0,213	0.0054±0.0026	0.0051±0.0023	0,961	664±378	775±575	0,234
121	ctx_rh_G_rectus	230±236	328±237	0,103	0.0034±0.0022	0.0033±0.0018	0,799	89±76	143±139	0,082
122	ctx_rh_G_subcallosal	204±148	163±148	0,818	0.0022±0.0009	0.0022±0.0018	0,518	62±49	57±60	0,647
123	ctx_rh_G_temp_sup-G_T_transv	164±107	117±137	0,462	0.0035±0.0025	0.0034±0.0011	0,946	75±79	54±44	0,591
124	ctx_rh_G_temp_sup-Lateral	672±809	245±196	0,019	0.0069±0.0036	0.0082±0.0035	0,165	711±338	900±595	0,085
125	ctx_rh_G_temp_sup-Plan_polar	363±159	411±267	0,818	0.0041±0.0028	0.004±0.0017	1,000	185±142	202±116	0,531
126	ctx_rh_G_temp_sup-Plan_tempo	82±76	113±184	0,663	0.0074±0.0051	0.0066±0.0036	0,938	240±184	204±178	0,968
127	ctx_rh_G_temporal_inf	218±187	257±281	0,679	0.0083±0.0048	0.0071±0.0028	0,657	850±449	785±675	0,894
128	ctx_rh_G_temporal_middle	220±156	245±218	0,931	0.0095±0.0051	0.0099±0.0053	0,573	1537±786	1641±1158	0,288
129	ctx_rh_Lat_Fis-ant-Horizont	116±148	91±115	0,826	0.0034±0.0031	0.0027±0.0016	0,721	62±79	41±61	0,994
130	ctx_rh_Lat_Fis-ant-Vertical	43±85	17±40	0,681	0.0033±0.0033	0.0019±0.0019	0,404	39±56	14±16	0,407
131	ctx_rh_Lat_Fis-post	144±88	155±172	0,981	0.0052±0.0032	0.0051±0.0032	0,830	230±209	168±167	0,752
132	ctx_rh_Pole_occipital	506±422	392±271	0,579	0.0057±0.0026	0.0049±0.0018	0,664	638±366	474±288	0,634
133	ctx_rh_Pole_temporal	585±374	729±489	0,731	0.007±0.0038	0.0065±0.0027	0,904	918±490	1178±788	0,184
134	ctx_rh_S_calcarine	396±221	456±195	0,606	0.0039±0.0012	0.0036±0.0014	0,989	266±134	265±204	0,539
135	ctx_rh_S_central	174±117	315±204	0,109	0.0055±0.0039	0.0061±0.0033	0,734	232±171	257±191	0,567
136	ctx_rh_S_cingul-Marginalis	177±184	156±177	0,961	0.0045±0.0023	0.0046±0.0024	0,664	197±146	213±197	0,432
137	ctx_rh_S_circular_insula_ant	135±146	26±24	0,059	0.0043±0.0037	0.0042±0.0029	0,861	101±103	77±85	0,420
138	ctx_rh_S_circular_insula_inf	217±132	413±271	0,063	0.0052±0.0029	0.005±0.0018	0,797	269±138	346±148	0,137
139	ctx_rh_S_circular_insula_sup	191±129	137±110	0,344	0.0037±0.002	0.0038±0.0015	0,852	93±52	92±88	0,803
140	ctx_rh_S_collat_transv_ant	75±85	211±411	0,097	0.0054±0.0034	0.0038±0.0018	0,188	138±81	158±158	0,471
141	ctx_rh_S_collat_transv_post	83±109	81±93	0,589	0.0037±0.0037	0.0029±0.0015	0,642	51±51	45±38	0,865
142	ctx_rh_S_front_inf	186±150	184±147	0,278	0.006±0.0033	0.0057±0.0022	0,967	300±283	232±243	0,960
143	ctx_rh_S_front_middle	210±229	272±224	0,866	0.0082±0.0069	0.007±0.0041	0,990	316±275	342±407	0,175
144	ctx_rh_S_front_sup	222±211	278±246	0,635	0.0082±0.0053	0.0081±0.0064	0,719	326±201	308±237	0,679

ON-LINE FIG 3. Continued

145	ctx_rh_S_interm_prim-Jensen	41±54	27±34	0,640	0.0044±0.0019	0.0047±0.0027	0,305	166±101	80±113	0,466
146	ctx_rh_S_intrapariet_and_P_trans	298±242	365±275	0,866	0.0059±0.0044	0.0058±0.003	0,994	1389±353	399±241	0,630
147	ctx_rh_S_oc_middle_and_Lunatus	129±204	79±123	0,432	0.0028±0.0017	0.0031±0.0026	0,514	71±74	79±97	0,530
148	ctx_rh_S_oc_sup_and_transversal	239±194	232±241	0,894	0.0037±0.0022	0.0041±0.0022	0,646	100±63	155±118	0,155
149	ctx_rh_S_occipital_ant	218±270	110±109	0,456	0.0047±0.0023	0.0045±0.0012	0,948	107±90	114±68	0,398
150	ctx_rh_S_oc-temp_lat	45±67	90±213	0,341	0.0053±0.0031	0.0059±0.0059	0,839	92±72	90±49	0,709
151	ctx_rh_S_oc-temp_med_and_Lingual	190±186	395±336	0,018	0.0043±0.002	0.0042±0.0014	0,816	175±131	303±272	0,006
152	ctx_rh_S_orbital_lateral	101±124	125±138	0,678	0.0042±0.0038	0.0038±0.0009	0,875	83±91	85±75	0,832
153	ctx_rh_S_orbital_med-olfact	176±201	236±293	0,392	0.003±0.002	0.0028±0.0015	0,905	75±50	68±58	0,952
154	ctx_rh_S_orbital-H_Shaped	172±226	106±106	0,304	0.0053±0.0028	0.0048±0.0038	0,818	257±356	87±67	0,218
155	ctx_rh_S_parieto_occipital	429±272	463±421	0,404	0.0041±0.0018	0.0039±0.0021	0,863	1345±245	304±193	0,715
156	ctx_rh_S_pericallosal	657±479	701±301	0,854	0.0046±0.0027	0.0046±0.0019	0,858	452±395	525±434	0,538
157	ctx_rh_S_postcentral	283±259	266±358	0,980	0.0046±0.0021	0.0062±0.0028	0,105	204±136	255±131	0,291
158	ctx_rh_S_precentral-inf-part	73±89	115±108	0,105	0.0062±0.0036	0.0062±0.0026	0,898	184±168	219±203	0,135
159	ctx_rh_S_precentral-sup-part	79±94	122±102	0,202	0.0065±0.0044	0.0066±0.0031	0,966	152±112	150±112	0,785
160	ctx_rh_S_suborbital	72±123	67±75	0,605	0.0024±0.0016	0.0024±0.0015	0,766	137±38	35±42	0,838
161	ctx_rh_S_subparietal	183±151	357±399	0,352	0.0037±0.0027	0.0041±0.0026	0,625	165±138	224±226	0,204
162	ctx_rh_S_temporal_inf	240±273	180±188	0,455	0.0054±0.0045	0.0046±0.0018	0,875	209±198	192±201	0,655
163	ctx_rh_S_temporal_sup	346±229	462±432	0,868	0.0087±0.0048	0.0085±0.0042	0,799	813±374	1006±634	0,079
164	ctx_rh_S_temporal_transverse	64±51	67±73	0,659	0.0036±0.0028	0.0031±0.001	0,628	150±43	48±64	0,934

ON-LINE FIG 3. Continued

On-line Table: Description of the graph theoretical properties used in this study

Degree	The Number of Adjacent Nodes, ie, Neighbors of the Node
Strength	Total number of streamlines connected from a node to all other nodes
Clustering coefficient	Fraction of the neighbors of a node connected to each other and, thus, forming a triangle
Characteristic path length	Average of the shortest path lengths between each pair of nodes in the network
Global efficiency	Average of the inverse shortest path lengths and is influenced more by short paths, whereas long paths primarily influence the characteristic path length.
Local efficiency	Efficiency of a subgraph formed by the neighborhood of the node
Betweenness centrality	Measures the centrality of the node in the network and is affected by the fraction of the shortest paths passing through the node
Small-worldness	Small-world networks contain both specialized modules and integrating edges; small-worldness is calculated as the ratio between the clustering coefficient and the characteristic path length

**On-line Table: Clinical and genetic data on patients with CHARGE**

Patient No.	Major				Minor				Final Clinical Typology <sup>a</sup>	CHD7 Gene Testing	Protein Variant	Mutation Type	Clinical vs Genetic Diagnosis			
	Ocular	Choanal	Cranial Nerve	Ear	Genital	DD	CHD	GD						Orofacial Clefing	TEF	Facies
1	+	+	+	+	+	+	+	+	+	+	+	+	Definite NA			Clinical
2	+	+	+	+	+	+	+	+	+	+	+	+	Definite NA			Clinical
3	+	+	+	+	+	+	+	+	+	+	+	+	Probable c.632G>A	p.Gly2108Arg	Missense	Genetic
4	+	+	+	+	+	+	+	+	+	+	+	+	Definite ISCN array result: -arr[hg19]8q12.2(61,757,599-61,805,579)x1		Interstitial deletion	Genetic
5	+	+	+	+	+	+	+	+	+	+	+	+	Definite c.3523-2A>C		Splice site	Genetic
6	+	+	+	+	+	+	+	+	+	+	+	+	Definite NA			Clinical
7	+	+	+	+	+	+	+	+	+	+	+	+	Probable NA			Clinical
8	+	+	+	+	+	+	+	+	+	+	+	+	Definite Negative			Clinical
9	+	+	+	+	+	+	+	+	+	+	+	+	Definite c.7957C>T	p.Arg2653X	Stop-gain	Genetic
10	+	+	+	+	+	+	+	+	+	+	+	+	Definite NA			Clinical
11	+	+	+	+	+	+	+	+	+	+	+	+	Definite c.799G>T	p.Glu267X	Stop-gain	Genetic
12	+	+	+	+	+	+	+	+	+	+	+	+	Definite c.4105C>T	p.Arg1339X	Stop-gain	Genetic
13	+	+	+	+	+	+	+	+	+	+	+	+	Probable c.5405-7G>A		Splice site	Genetic
14	+	+	+	+	+	+	+	+	+	+	+	+	Probable Negative			Clinical
15	+	+	+	+	+	+	+	+	+	+	+	+	Probable Positive		NOS	Genetic
16	+	+	+	+	+	+	+	+	+	+	+	+	Definite c.760C>T	p.Gln254X	Stop-gain	Genetic
17	+	+	+	+	+	+	+	+	+	+	+	+	Definite Positive		NOS	Genetic
18	+	+	+	+	+	+	+	+	+	+	+	+	Definite c.3728dupA	p.Asni243LysfsX20	Frameshift	Genetic
19	+	+	+	+	+	+	+	+	+	+	+	+	Definite NA			Clinical
20	+	+	+	+	+	+	+	+	+	+	+	+	Definite Negative			Clinical
21	+	+	+	+	+	+	+	+	+	+	+	+	Negative Positive		NOS	Genetic
22	+	+	+	+	+	+	+	+	+	+	+	+	Definite c.2066delC	p.Thr689SerfsX22	Frameshift	Genetic
23	+	+	+	+	+	+	+	+	+	+	+	+	Probable NA			Clinical
24	+	+	+	+	+	+	+	+	+	+	+	+	Definite NA			Clinical
25	+	+	+	+	+	+	+	+	+	+	+	+	Definite NA			Clinical
26	+	+	+	+	+	+	+	+	+	+	+	+	Definite ISCN array result: arr[hg19]8q12.1q12.2(61,585,541-61,613,066)x1		Interstitial deletion	Genetic
27	+	+	+	+	+	+	+	+	+	+	+	+	Definite c.5350_5374dup25	p.Lys1792ArgfsX5	Frameshift	Genetic
28	+	+	+	+	+	+	+	+	+	+	+	+	Probable Negative			Clinical
29	+	+	+	+	+	+	+	+	+	+	+	+	Probable NA			Clinical
30	+	+	+	+	+	+	+	+	+	+	+	+	Definite c.469 C > T	p.Arg157X	Stop-gain	Genetic
31	+	+	+	+	+	+	+	+	+	+	+	+	Definite c.5607 + 1G>A		Splice site	Genetic
32	+	+	+	+	+	+	+	+	+	+	+	+	Definite NA			Clinical
33	+	+	+	+	+	+	+	+	+	+	+	+	Definite NA			Clinical
34	+	+	+	+	+	+	+	+	+	+	+	+	Probable c.4247C>G	p.Thr1416Arg	Missense	Genetic
35	+	+	+	+	+	+	+	+	+	+	+	+	Probable NA			Clinical

**Note:**—DD indicates developmental delay; CHD, congenital heart disease; GD, growth deficiency; TEF, tracheoesophageal fistula; NOS, not otherwise specified; NA, not applicable; +, present; ISCN, international system for human cytogenetic nomenclature.

<sup>a</sup> Final clinical typology (after Lalani, et al<sup>13</sup>). Definite: 4 major or 3 major/3 minor criteria; Probable/Possible: 1–2 major/3+ minor criteria.